Modulation of Ground and Excited State Dynamics in Donor-Acceptor Organic Functional Small Molecules for Photonics and Biomedical Applications

Thesis submitted to the Indian Institute of Technology Guwahati for the award of

Doctor of Philosophy

In Chemistry

by

Debasish Barman

Roll No. 166122005

Department of Chemistry

Indian Institute of Technology Guwahati

Guwahati-781039, Assam, India

October, 2022

Dedicated to

My parents,

For giving me my life,

Endless love and support throughout my life.

My brothers and sister,

For always standing by me,

Giving continuous care and encouragement.

Statement

I do hereby declare that the work incorporated in this thesis entitled, "**Modulation of Ground and Excited State Dynamics in Donor-Acceptor Organic Functional Small Molecules for Photonics and Biomedical Applications**" is the result of investigations carried out by me under the guidance of Prof. Parameswar Krishnan Iyer, at the Department of Chemistry, Indian Institute of Technology Guwahati, Guwahati, Assam, India.

In keeping with the general practice of reporting scientific observations, due acknowledgements have been made wherever the work described is based on the findings of other investigators. I further declare that this work has not been submitted in part or full to any other university or institute for award of any degree or diploma.

Date: 21st October 2022 **Debasish Barman**

Place: IIT Guwahati, Guwahati

Certificate

This is to certify that the work included in this thesis entitled "**Modulation of Ground and Excited State Dynamics in Donor-Acceptor Organic Functional Small Molecules for Photonics and Biomedical Applications**" submitted by Mr. Debasish Barman, Department of Chemistry, Indian Institute of Technology Guwahati in fulfillment has been carried out under my supervision. I further certify that this work has not been submitted to any other University or Institution in part or full for the award of any degree or diploma.

IIT Guwahati

October, 2022

Parameswar Krishnan Iyer

Thesis supervisor

Department of Chemistry

Indian Institute of Technology Guwahati

Guwahati – 781039, Assam, India

Acknowledgements

I would like to express my sincere appreciation and gratitude to those who have contributed to this thesis and supported me in one way or the other during this truly memorable and overwhelming journey. It is really hard to list all who sincerely helped me, and I would like to thank all of them who have made this thesis possible.

First of all, I am extremely grateful to my supervisor ***Prof. Parameswar K. Iyer*** *for providing me a precious opportunity to work in his group. His continuous support, scientific guidance, deep insights, patience and motivation encouraged me to take up the tasks that otherwise were hard and demanding. I earnestly thank him for having trust in me and giving me total freedom in choosing the direction of my research. I feel fortunate to having him as my mentor who always motivated me with his hard work, dedication and optimism.*

I am highly indebted to my doctoral committee members: ***Prof. Aditya Narayan Panda****,* ***Prof. G. Pugazhenthi****, and* ***Dr. Achalkumar Ammathnadu Sudhakar*** *for assessing my research work regularly. Their insightful advices, suggestions and crucial comments helped me to widen my research from various perspectives and improve my thesis.*

My sincere thanks to ***Prof. Aditya Narayan Panda*** *Sir for helping me to perform the computational calculations.*

The completion of this thesis became possible only with the help of my collaborators, who had provided strong support and guidance along with lab facilities. I sincerely thank my collaborators, ***Dr. P. Rajamalli****, IISc Bangalore, India,* ***Dr. M. Annadhasan****, University of Hyderabad, India,* ***Dr. Anil P. Bidkar****, IIT Guuwahti, India,* ***Prof. Siddhartha Sankar Ghosh****, IIT Guwahati, India,* ***Prof. Rajadurai Chandrasekar****, University of Hyderabad, India,* ***Prof. Eli Zysman-Colman****, University of St Andrews, UK, for their continuous help and support.*

I am also thankful to all the researchers and the staff of the Department of chemistry, center for nanotechnology, central instrument facility, IIT Guwahati for their kind cooperation and support. I am indebted to the staff of student affairs, academic affairs and finance sections of IIT Guwahati for being kind enough to advise and help in their respective roles.

I would like to thank all my past and present lab mates, Dr. Priyanka Dutta, Dr. Himani Kalita, Dr. Ekta Roy, Dr. Radhakrishna Rath, Dr. T. Bhim Raju, Dr. Suresh Vasimalla, Dr. Anamika Dey, Dr. Ashish Singh, Dr. Akhtar Hussain Malik, Dr. Adil Afroz, Dr. Arvin Sain Tanwar, Dr. Sayan Roy Chowdhury, Dr. Dipjyoti Das, Dr. Anamika Kalita, Dr. P. Gopikrishna, Dr. Niranjan Meher, Dr. Rahul Narasimhan, Dr. Subrata, Laxmi Raman Adil, Indrani, Ramesh Babu, Maimur Hossain, Rabindra, Nehal, Ritesh, Retwik, Anwesha, Nasima, Biki, Anita, Kavita, Rajdikshit, Paromita, Tamal, Sushant, Saumalya, Sayantani, Hirok, Priyam, Debika, Tapasi and Dr. Geetmani Singh Nongthombam for their timely help and support. I would also like to thank them for creating a pleasant and vibrant laboratory atmosphere and making my days memorable.

I especially thank ***Dr. P. Gopikrishna****, and* ***Dr. Niranjan Meher*** *for sharing their enormously broad knowledge and showing endless patience. They taught me all the basics, experiments and techniques that were needed.*

I would also especially thank to ***Kavita Narang****,* ***Rajdikshit Gogoi****,* ***Debika Barman****, and* ***Tapasi Sharma*** *for their help, support and finding interest to work with my research fields.*

I am extending my thanks to the guest faculty of INSA summer intern: ***Dr. Avinash L Puyad*** *Sir, and* ***Dr. Chinnusamy Saravanan*** *Sir, for giving me positive encourment and sharing their experience.*

I am also thankful to the master students ***Sujay Paul****,* ***Subhajit Ghosh****,* ***Susmita Buragohain****,* ***Shraoshee Shome****,* ***Manab Kalita****,* ***Manas Kalita*** *whom I co-mentored for their master's project. I am also extending my thanks to the graduate students:* ***Sarang Pande****,* ***Chetan Kumawat****,* ***Abhijeet Kumar****,* ***Sapavat Venkatesh****,* ***Arvind Kumar Nitharwal****,* ***Shubham Maurya*** *whome I co-mentored for their BTP-Projects. Thank you all for your help, support and endless love during the project period, I truly enjoyed with working with you all.*

I would like to thank all my beloved friends for giving moral support and many unforgettable memories during the period of my stay in IIT Guwahati: Dr. Ila Verma, Dr. Tushar Kanta Sahu, Dr. Dilip Kumar Sahu, Dr. Munendra Yadav, Dr. Prasenjit Sarkar, Dr. Ankit Gangrade, Dr. Sourjendu Maity, Vinod Viswakarma, Adit Sha, Sandip Mondal, Bijoy K. Das, Kanu Das, Basab K. Das, Kousik Maji, Subhajit Saha, Santanu Dolai, Chintak Kamalesh Parasar, Dr. Dhirendra Mishra and Dr. Sitakanta Panda.

I am thankful to Department of Science and Technology (DST) for providing the fellowship..

My Ph. D. endeavor could not have been completed without the endless love, support, tolerance and blessings from my family. I am fortunate and blessed enough to have such a caring and supportive parents and siblings. It is because of their prayers, sacrifice and struggle, I am able to live my dream to complete my higher education from a prestigious institute. I am also grateful to my brothers and sister for their eternal love, cooperation and emotional support which had immensely needed to complete this work.

I owe a deep sense of gratitude to my parents for giving me a great life, strength to chase my dreams, and being with me in all my failure and success.

Finally, I am thankful to Almighty God for all your blessings, graces, strength and sustenance that has made me excel and successful in all my academic pursuits!

Debasish Barman

Table of Contents

Thesis Title

Modulation of Ground and Excited State Dynamics of Organic Functional Small Molecules for Photonic and Biomedical Applications

Chapter 4

Hot-Exciton Harvesting *via* Through-Space Single-Molecule Based White-Light Emission and Optical Waveguides

Chapter 5

Aggregation-Induced Hot-exciton Emission via Suppression of Kasha's Rule in Through-space Donor-alkyl Bridge-Acceptor Molecular Rotor

Chapter 7

Manipulation of Triplet Excited-states Procuring Long-lived Delayed Fluorescence *via* Pull-push Electronic Effects in Structurally Tailored Novel AIEgens for Bio-imaging

Abbreviations

	A
α	Alpha
A	Acceptor (Charge)
a.u.	Arbitrary Unit
ACN	Acetonitrile
AFM	Atomic Force Microscopy
ABDA	9,10-anthracenediyl-bis(methylene)dimalonic acid
ACQ	Aggregation Caused Quenching
AIE	Aggregation Induced Emission
AIDF	Aggregation Induced Delayed Fluorescence
AIP	Aggregation Induced Phosphorescence
E_a	Activation Energy
	B
BO	Born-Oppenheimer approximation
β	Beta
Bd	1H-benzo[f]indole
K_d	Binding Constant
	C
CI	Canonical Insertion
$CDCl_3$	Chloroform-*d*
CCDC	Cambridge Crystallographic Data Centre
CT	Charge Transfer
CIE	Commission Internationale de l'Elcairage
CV	Cyclic Voltammetry
	D
δ	Delta Chemical shift (NMR)
°C	Degree Celcius
d	Doublet (NMR)
μ	Dipole Moment
ε	Dielectric Constant
D	Donor (Charge)
D-A	Donor-Acceptor
DF	Delayed Fluorescence
DFL	Dual Fluorescence
DP	Dual Phosphorescence
DMF	Dimethylformamide
DCM	Dichloromethane
DMSO	Dimethyl sulphoxide
DMSO-*d6*	Deuterated dimethyl sulphoxide
DSC	Differential Scanning Calorimetry
	E
J	Exchange Energy
eV	Electron-volt
ET	Energy Transfer
EL	Electroluminescence
EPR	Electron Paramagnetic Resonance
EQE	External Quantum Efficiency
ESD	Excited state dynamics
ESIPT	Excited State Intramolecular Proton Transfer
ESCS	Excited State Charge Separation
ESR	Electron Spin Resonance
	F
f	Oscillator Strength
FC	Franc-Condon
FMO	Frontier Molecular Orbital
k_f	Fluorescence Rate
FTIR	Fourier Transform Infrared
F	Fluorescence
FRET	Förster Resonance Energy Transfer

G

T_g	Glass transition temperature
γ	Gamma
G	Gauss
g	gram

H

h	Hour
Hz	Hertz
HBs	Hydrogen Bonds
HLCT	Hybridized Locally Excited Charge-Transfer
HOMO	Highest Occupied Molecular Orbital
HPS	Hexaphenylsilole
HPLC	High Performance Liquid Chromatography.
HRMS	High-Resolution Mass Spectrometry
XBs	Halogen Bonds

I

IQE	Internal Quantum Efficiency
ISC	Inter System Crossing
IC	Internal Conversion
IRF	IRF Instrument Response Function
K_{ISC}	Intersystem Crossing Rate

K

K	Kelvin

L

LIF	Laser Induced Fluorescence
LUMO	Lowest Unoccupied Molecular Orbital
τ_F	Lifetime of Fluorescence
τ_{DF}	Lifetime of Delayed Fluorescence
τ_{Ph}	Lifetime of Phosphorescence

M

mp	Melting Point
T_m	Melting Temperature
MALDI-TOF MS	Matrix-Assisted Laser Desorption Ionization-Time of Flight Mass Spectroscopy
MECI	Minimum Energy Conical Intersection
MLCT	Metal-Ligand Charge-Transfer
MO	Molecular Orbital
MR	Mechano-Responsive

N

ns	nanoseconds
nm	nanometer
NPs	Nanoparticlaes
NTOs	Natural Transition Orbitals
NMR	Nuclear Magnetic Resonance

O

Δ_f	Orientation Polarizability
OFETs	Organic Field-Effect Transistors
OLEDs	Organic Light Emitting Diodes
OPVs	Organic Photovoltaic Cells
OSMWLE	Organic Single Molecule White Light Emission
OSSLEs	Organic Solid-State Lasers
OWG	Optical Waveguides
α'	Optical loss co-efficient

P

ppm	Parts per million

P

PF	Prompt Fluorescence
PL	Photoluminescence
PhOLED	Phosphorescent OLEDs
PLQY	Photoluminescence Quantum Yield
PMMA	Polymethyl methacrylate
PSs	Photosensitizer
PDT	Photodynamic Therapy
PXRD	Powder X-Ray Diffraction

R

k_r	Rate of Radiative Decay
k_{nr}	Rate of Non-radiative Decay
K_{ISC}	Rate of Inter System Crossing
k_{RISC}	Rate of Reverse Inter System Crossing
RT	Room Temperature
RIM	Rotation In Motion
RIR	Rotation In Restriction
RISC	Reverse Intersystem Crossing
RIV	Rotation In Vibration
ROS	Reactive Oxygen Species
RTP	Room Temperature Phosphorescence
RTDP	Room Temperature Dual Phosphorescence
RB	Round Bottom (flask)
RDG	Reduced Density Gradient

S

ΔE_{ST}	Singlet-Triplet Energy gap
s	Singlet (NMR)
S_n	Singlet Manifold
^1CT	Singlet Charge-Transfer
^1LE	Singlet Locally Excited State
SOC	Spin-orbit Coupling
SC	Single crystal
SAED	Selected Area Electron Diffraction
$^1O_2$	Singlet Oxygen
SOKR	Suppression of Kasha's Rule
SDM	Static Dipole Moment

T

t	Triplet (NMR)
T_m	Triplet Manifold
^3CT	Triplet Charge-Transfer
^3LE	Triplet Charge-Transfer
TRES	Time-Resolved Emission Spectra
TRPL	Time-Resolved Photoluminescence
TSCT	Through-space Charge-Transfer
TTA	Triplet-Triplet Annihilation
TTET	Triplet-Triplet Energy Transfer
TA	Transient Absorption
TADF	Thermally Activated Delayed Fluorescence
TCSPC	Time-correlated Single Photon Counting
TEMPO	(2,2,6,6-Tetramethylpiperidin-1-yl)oxyl
TGA	Thermogravimetric Analysis
TICT	Twisted Intramolecular Charge Transfer
TLC	Thin Layer Chromatography
TPE	Tetraphenylethylene
THF	Tetrahydrofuran

U

UV-Vis	Ultraviolet-visible

CHAPTER 1

Introduction

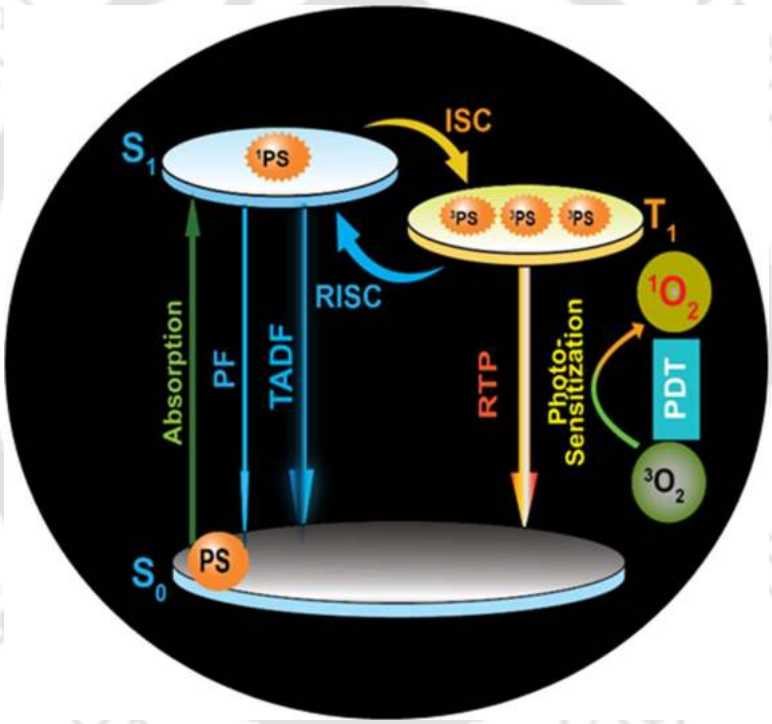

Barman, D., Narang, K., Gogoi, R., Barman, D., Iyer, P. K. *J. Mater. Chem. C*, **2022**, *10*, 8536-8583. https://doi.org/10.1039/D1TC05906H

Barman, D., Gogoi, R., Narang, K., Iyer, P. K. *Front. Chem.* **2020**, *8*, 483. https://doi.org/10.3389/fchem.2020.00483

Abstract

Organic photofunctional materials based on donor-acceptor (D-A) π-conjugated structures with ambient stable triplet-harvesting thermally activated delayed fluorescence (TADF), room temperature phosphorescence (RTP) and aggregation induced emission (AIE) have received immense attention on gathering momentum and rapidly progressing towards commercial application. Successful design strategies of these combined properties are resulted in thermal up-conversion of nonemissive triplets into emissive singlet excitons, increasing the maximum internal efficiency from 25 to 100 % in purely organic systems. In addition, owing to their unique "structure-property correlations" vibrant excited-state properties induced by supramolecular self-assembly, co-assembly leading to improved physicochemical properties and therefore enabling them a potential candidate for multi-platform applications. Throughout the course of this thesis, design and development of new organic D-A and D-σ-A based molecules with their intrinsic structure-property functions along with ground and excited state kinetics are precisely elucidated. The exciting photophysical properties of AIE, TADF and RTP activity and associated mechanism carefully investigated in different new class of single component to multicomponent binary systems (co-crystals) respectively. Of particular note, with the finding of novel chemical structures, few important mechanism was elucidated towards the origin of multimode color-tunable emission white-light emission. Besides the current aspects of excited-state mechanism for model TADF were also presented, mainly regarding the highlights of high-order vibronic coupling and "hot-excitons" with the involvement of three excited states such as singlet charge transfer state (^{1}CT); triplet charge transfer states (^{3}CT); and triplet local excited state (^{3}LE) to come into isoenergetic resonance to achieve high TADF efficiency. In addition, complementary to TADF, RTP, another efficient triplet harvesting mechanism has also been investigated for control release of excitons and to discriminate the individual and/or combined emission from TADF in a structurally rigid or flexible molecular skeleton. Besides, we could solved the dilemma of excited state quenching effect in aggregated or solid state by exploring Anti-Kasha mechanism as reason for AIE behavior. Moreover, it is discussed how to modulate the efficiency of the ambient triplet-harvesting mechanism by varying different molecular conformers that show variant charge-transfer induced color-tunable emission, highly efficient photon transportation as optical waveguiding activity in crystals and generation of toxic reactive oxygen species in aggregated state for image-guided cancer therapy. Collectively, it is shown that variety of emitters and their intrinsic photophysics including a clear structure-property relations, benefitting to employ them into many versatile areas ranging from optoelectronics to biological applications.

1.1.1. Motivation

Light is an auspicious source of existence for living world, especially multicolored bio-luminescence and chemiluminescence from natural light-emitting pigments has made the universe more beautiful. Inspired by nature, human beings imagined and developed organic, inorganic and hybrid-based synthetic materials as a source of photoluminescence and electroluminescence to generate light affordably and made its use for the benefit of living beings in many exciting ways. However, it remains a great challenge to achieve the optimum efficiency level of natural light emitting sources.[1] A substantial amount of research has been conducted to find suitable materials to reach the efficiency level of natural resources, while the discovery of metal and heavy-metal-based hybrid luminescent materials achieved great success and have drawn immense attention in both scientific research and industry.[2] However, these materials in particular are highly expensive, environmentally hazards and rare in global resources, therefore enforcing to search for alternative metal free organic luminescent materials. So far, the development of purely organic materials and investigation of their intrinsic mechanism is an ongoing pursuit over several decades.[3] Organic functional materials endowed numerous advantages by means of molecular diversity, color tunability, intensity, lifetime, biocompatibility, energy consumption, and affordable fabrication cost, including versatile semiconducting functionalities and biological activities. Unlike conventional inorganic conductors and semiconductors, organic functional small molecules and polymers can be synthesized using different cost-effective and simple synthetic strategies with the help of organic and polymer chemistry knowledge. Over the last few decades, the materials community has been making exploration in the field of material sciences, including organic light emitting diodes (OLEDs),[4] organic photovoltaic cells (OPVs),[5] organic field-effect transistors (OFETs),[6] bio-/chemo-/photo-sensors,[7] memories,[8] and even in organic lasers.[9]

Nonetheless, discovery of luminescent materials have emerged as an indispensable research area and remains a principle focus not only in material science but also in biomedical science and technology.[10,11] So far, a large number of π-conjugated luminescent organic molecules have been explored. The majority of the molecules exhibited high fluorescence in dilute solution; however, in solid or aggregated state they usually show reduced emission which limits their efficiency in real time applications.[12] The hydrophobic nature of most of the organic dyes helps them to form aggregates naturally in the thin film of optoelectronic devices and in a hydrophilic biological system; therefore, showed aggregation caused quenching (ACQ) of the fluorophores due to π-π stacking.[13] Remarkably, this major drawback has been overcome after

the concept of aggregation induced emission (AIE) was reported by Ben Zhong Tang group in 2001, which provided a new direction to design solid-state emissive materials. Despite tremendous success in developing AIEgens, most of the organic chromophores rely on singlet emission only, therefore resulting poor efficiency and limited performances because of the non-emissive triplets that are not being utilized for luminescence. It was a great challenge to harvest both singlets and triplets in metal-free organic luminogens which could enhance the efficiency and exploration of the organic emitter to larger extent.[14,15]

In the ongoing pursuit of functional materials development, Adachi and co-workers in 2012 pioneered triplet harvesting thermally activated delayed fluorescence (TADF) materials,[16] a major breakthrough in metal-free organic materials. TADF materials having extremely small singlet-triplet energy gap (ΔE_{ST}), accelerate the reverse intersystem-crossing (RISC) process, performing theoretically 100% internal quantum efficiencies (IQE), in the field of OLEDs.[17,18] In addition, such metal-free organic emitters have the potential for optical waveguide, bioimaging, biosensors, and nanomedicine by virtue of their tailorable synthesis, low-cost input, favorable long-lived emissive feature and excellent biocompatibilities.[19,20]

Great progress has been achieved in the field of AIE, TADF and RTP emitters with versatile design and their utility in multiple application perspectives. Moreover, to meet the demanding requirements of such materials for commercial applications, many issues are yet to be addressed. Therefore, a detailed investigation of structure-property relationships at their molecular to electronic levels of studies are needed for better understanding of the triplet state dynamics. Additionally modulation of stuctural and electronical configurations could produce more optimized future design and improvements to current TADF and RTP structured motifs in a rational manner.

1.1.2. Organic Luminescent Materials

Photoluminescence of π-conjugated molecules was found in the middle of the 19th century. However, electroluminescence remained unknown for almost 100 years. The first observation of electroluminescence in organic materials was in the early 1950s by Bernanose and coworkers.[21] The electroluminescence from an organic molecule, anthracene, was reported by Pope and coworkers in 1963,[22] by applying more than 100V of bias voltage. The achievement did not stimulate much interest as the applied bias was very high. However, in 1987,[23] Tang and VanSlyke made a bilayer structure by thermally evaporating the small molecular weight organic materials, N,N'-diphenyl-N,N'-bis(3-methylphenyl)-1,1'-biphenyl-4,4'-diamine (TPD)

and tris(8-hydroxyquinoline) aluminum (Alq_3) to achieve a total thickness of ~100 nm. Therefore, the utilization of organic molecules into OLEDs, opens a new dimension of electroluminescence which is further widely exploited in the field of lighting technology. Few selective, emerging luminescent organic materials have wielded considerable importance over the past thirty years to advance the material design and related functionality.

In the early stage of luminescent materials exploration, conventional fluorescent small molecules and polymers aroused immense research interest. Yet, certain limitations in the device efficiency due to non-radiative triplets with a share of ~75% of all excitons. Therefore, solely singlet excitons contribution restricts their IQE to only 25% and external quantum efficiency (EQE) to 5%, known to be first generation electroluminescence (Figure 1.1.1a, b).[24] Furthermore, the involvement of Iridium (Ir), Platinum (Pt) and Ruthenium (Ru) based heavy metals into organic framework, turned the non-radiative triplets to radiative phosphorescence via strong metal ligand charge-transfer (MLCT), induced by spin-orbit coupling (SOC) process. By utilizing such phosphorescent materials, a theoretical 100% IQE and 62.5% EQE have been achieved in phosphorescent OLEDs (PhOLEDs) and considered as second generation LEDs (Figure 1.1.1c, d).[25] Over decades, several metal complexes based PhOLEDs with very high efficiencies have been developed since their first report in 1998.[26] However, assimilation of highly expensive and non-environment friendly precious heavy metals further lead to high device fabrication cost and environmental hazards, which pushed the scientific community to research more environment friendly and cheaper alternatives. In this regard, tremendous effort has been manifested to explore alternative approaches like hybridized local charge transfer (HLCT),[27] triplet-triplet annihilation (TTA),[28] including delayed fluorescence (DF) in order to harvest 100% excitons and to overcome the obstacle faced by conventional fast degradable fluorescence/phosphorescence materials.[29] Furthermore, DF materials are found to harvest triplet excitons through an endothermic process, where dark emissive triplets up-converted to bright emissive singlets *via* the reverse intersystem crossing (RISC) process, resulting in significantly enhanced IQE. Moreover, based on the emission pathways, the DF is classified into two types: E-type and P-type.[30] In P-type DF, two triplet fusion occurs, and the phenomenon is known to be TTA. The two triplets combine to give an excited singlet state and a ground state. The excited singlet state then de-excites to the ground state. The main drawback of such materials was found to be limited internal quantum efficiency of ~20-50%. Theoretically, this can achieve only a maximum EQE of 62.5%.[31] In E type DF, energy is supplied to the triplet electron such that it jumps back to the excited singlet state through RISC.

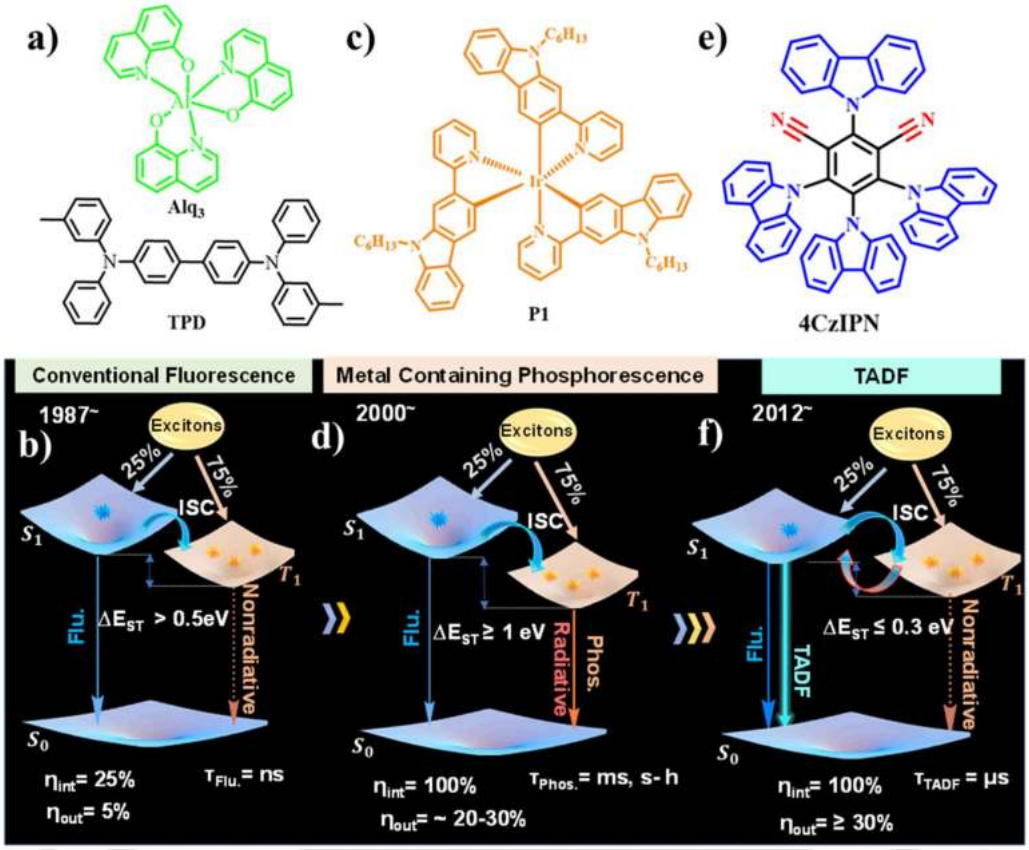

Figure 1.1.1. (a) Chemical structures and (b) illustration of three different Jablonski diagrams for first, second and third generation electroluminescence materials and emission mechanism.

Then the excited singlet state comes to the ground state through the emission of light. This process is also known as thermally activated delayed fluorescence (TADF) that leads to the evolution of third generation OLED (Figure 1.1.1e, f).[16,32] For TADF to occur, the energy gap between the excited triplet state and the excited singlet state must be less than 300 meV that accelerating the feasibility of RISC. The maximum internal quantum efficiency in this process comes out to be 100%. Metal free organic TADF compounds can harvest both singlet and triplet excitons to reach the same QE level as compared to PhOLED emitters.[33] Unlike the sensitivity of triplet state by oxygen, moisture and weak SOC in organic materials, the long-lived delayed fluorescence resulting from the enhanced intersystem crossing (ISC) and RISC from the lowest excited triplet state (T_1) to the lowest excited singlet state (S_1) provided longer lifetimes of microseconds to milliseconds with very high PLQYs. Noticeably, in the last few years, a library of TADF materials are gaining prominence as an inevitable class of luminophores following the invention of first TADF material 4CZIPN by Adachi and coworkers in 2012.[16] The first discovery of TADF, which is previously named as E-type delayed fluorescence, can be dated back to 1961,[34] when the first purely organic TADF material was believed to be found by

Parker and Hatchard in the eosin dye. The first metal-containing TADF material was observed in a Cu(I)-complex by Blasse and co-workers in 1980.[35] In the late 1990s, the efficient delayed fluorescence was further verified in fullerenes by Berberan-Santos and co-workers, and was firstly used in the detection of oxygen and temperature.[36] The attempt to apply TADF materials in OLEDs appeared first in 2009.[37] The device required a rather high onset of current injection around 10 V and 29 V for 100 mA cm^{-2} since the reported TADF OLEDs in 2012 by Adachi group. Complementary to TADF, room temperature phosphorescence (RTP) is another approach that opens new opportunities for optoelectronic, photonic and biological applications.[38,39] RTP is an efficient triplet harvesting mechanism for metal-free organic molecules. The RTP can be achieved solely from the triplet excited state through an enhanced ISC from S_1 to closely lying triplets state ($\geq T_2$) and suppressed nonradiative relaxation from T_1 to the ground state. RTP could exhibit very long lifetime ranges from ms to h (Figure 1.1.2). There are multiple factors that commonly governs the utilization of triplets to enhance the phosphorescence lifetime, including host-guest interaction, presence of heavy atom (such as Br) or multiple heteroatoms (N, O, S), hydrogen/halogen bonding and rigid crystalline structures, triggering the ISC for efficient RTP.[40,41] With increasing interest in the ambient triplet-harvesting organic materials research field, the clarity in the design strategies, related quantum mechanical insights, intrinsinc triplet harvesting mechanism, stabilities, emitting colours and charge transport properties, collectively allow the utilization of non-radiative triplets at larger extent.[42]

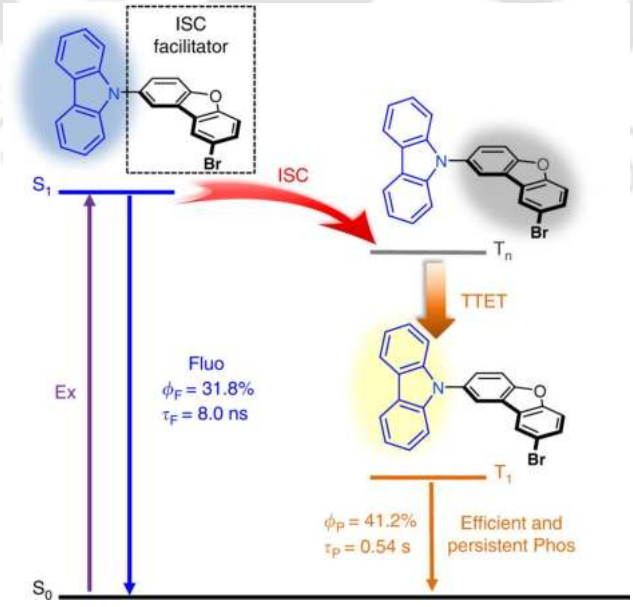

Figure 1.1.2. Representation of metal-free organic phosphorescence molecule and emission mechanism.

1.1.3. Aggregated/Solid State Emission

The increasing demand of highly efficient organic luminescent molecules in aggregated/solid-state for the solution-processed non-doped devices gives them an extra edge over other existing methods for solid-state lighting. However, the major issues of efficiency improvement affected by emission quenching in non-doped thin-film state is mainly due to singlet-triplet annihilation (STA), long lifetime triplet-polaron, and triplet-triplet annihilation (TTA).[43] In addition, organic TADF/RTP molecules that commonly contains high order π-conjugation and heteroatoms in their molecular frameworks have become superior alternatives to realize high fluorescence quantum yields, excellent biocompatibility, good photostability, and low phototoxicity during biological application.[44,45] However, use of triplet-harvesting organic molecules in solid state devices applications or in the biological environment faced great challenges due to the excited state quenching effect caused by π-stack assembly of aromatic structures, which limits their application prospects to a large extent. Usually the hydrophobic nature and presence of high order planar π-conjugation in the chemical structures supresses the radiative pathways via strong π-π stacking and shows aggregation caused quenching (ACQ) effect.[13,46] Therefore, such fluorescent dyes are highly emissive in the solution state whereas completely non-emissive in the solid state. In 2001, the revolutionary discovery of aggregation-induced emission (AIE) by Tang and coworkers who reported a propeller-shaped hexaphenylsilole (HPS)[47] and tetraphenylethylene (TPE)[48]

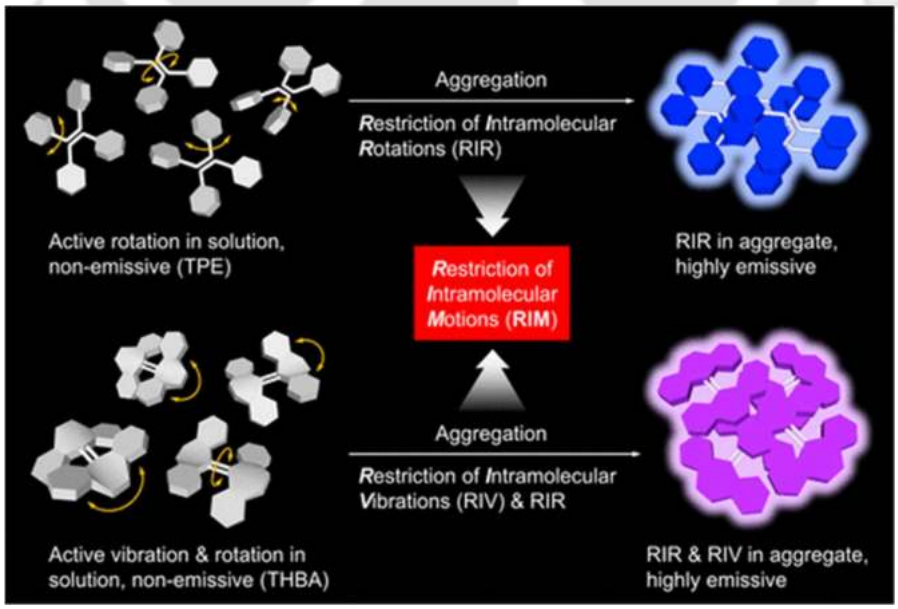

Figure 1.1.3. Schematic illustration of AIE phenomenon of TPE and THBA structures.

derivatives (non-emissive in solution) showed opposite behaviour to ACQ molecules and found to emit intensely at aggregated or in solid state. Restriction of intramolecular rotation and vibration (RIR/RIV) is proposed as a mechanism for this unique AIE phenomenon (Figure 1.1.3).[49] Subsequently, aggregation is a key link between AIE and TADF/RTP properties which enables them as potential chromophores for high-performance optoelectronic OLED devices and other applications of high contrast imaging, including deeper penetration depth over traditional fluorescent molecules.[50] In the optoelectronic devices, the quenching effect of TADF emitters would have been fixed by molecular engineering, and co-existing with AIE behavior that can arrest the rotation or vibration in a highly twisted molecular configuration and therefore non-radiative pathways could easily be prevented (Figure 1.1.4).[51] Besides, at the aggregated state, chromophores are strongly induced by supramolecular non-covalent interactions which increases the number of ISC channels and facilitates the overlapping of excitons from singlet state to triplet excited state excitons and this further reduces the energy gap (ΔE_{ST}) between S_1 and T_1 thereby enhancing delayed luminescence pathway.[52] These luminophores give rise to long lifetimes ranging from nanoseconds to milliseconds even up to seconds and showed very high PLQY.[53] The performances of nondoped OLEDs is improved due to the enhanced PLQY in the aggregation state of TADF emitter.[54] Therefore, there is room for future development of solution-processable AIE-TADF materials-based devices by extending the structural diversity and device engineering strategies. Therefore, there is room for future development of solution-processable AIE-TADF materials-based devices by extending the structural diversity and device engineering strategies.

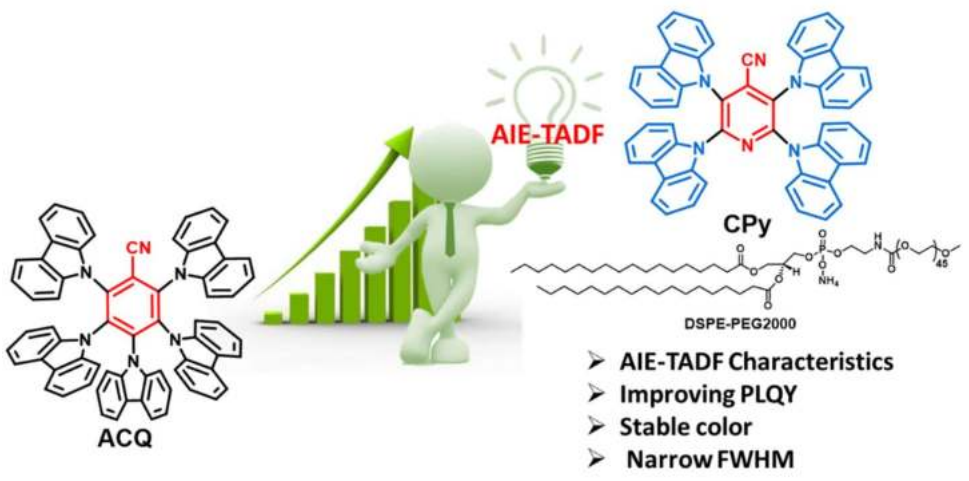

Figure 1.1.4. Representation of AIE-TADF structure and modification.

Inside a biological system, AIEgens may bind with different biomolecules present in the system and due to the influence of the surroundings, the free intramolecular motions of the molecules is constrained, which enhance the radiative decay of the luminophores.[55] By analyzing the nature and intensity of the aggregate emission, some biomolecules and their certain interactions inside the system can be traced.[56] Additionally, the spontaneous aggregation of hydrophobic dyes inside the hydrophilic bio-environment enables AIEgens to easily 'turn-on' followed by impressive fluorescence quantum yield, which is beneficial for improving the spatial resolution of imaging with better contrast.[57] Therefore, in recent years, significant efforts have been devoted to the advancement of efficient design principles and utilizing the triplet management phenomenon of TADF and RTP for biological application.[58,59]

Up to now, substantial contributions have been made to develop a wide variety of AIEgens in both for materials science and biomedical research. Moreover, triplet harvesting AIE-TADF chromophores have accelerated as potential alternatives for diagnosis and treatment of various diseases, especially cancer.[60] TADF emitter could be utilized for conventional bio-imaging and time-resolved luminescence imaging (TRLI) in various complex biological systems for real-time applications.[61]

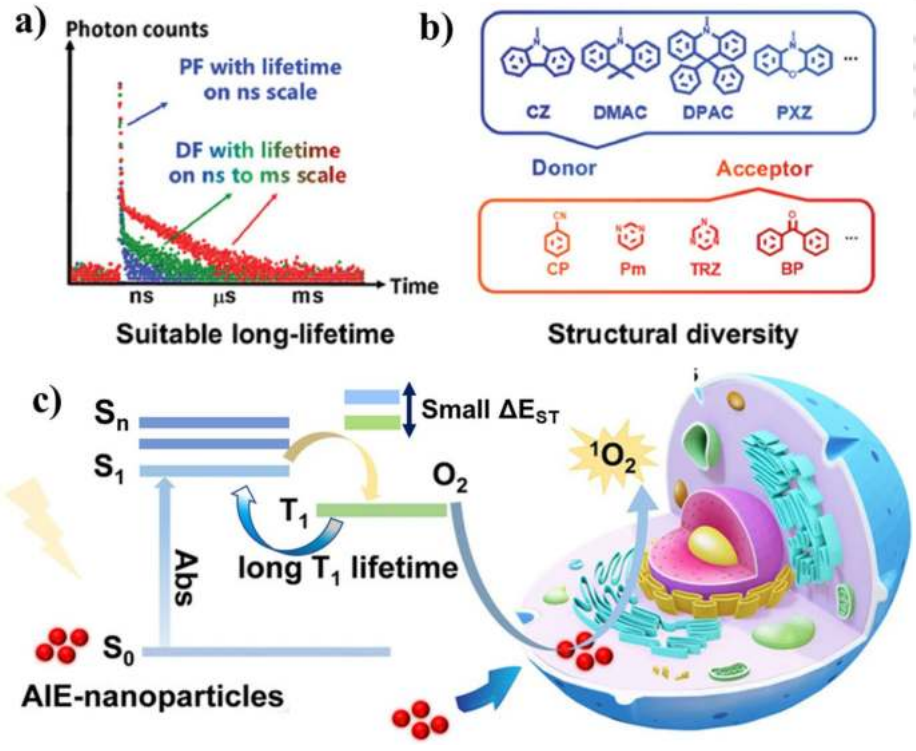

Figure 1.1.5. (a) Transient photoluminescence plot with a different time-scale, (b) Typical donor and acceptor structures used to design AIE-TADF bio-probe (c) Schematic illustration of PDT phenomenon followed by reactive singlet oxygen generation.

Due to the longlived emission feature of AIE-TADF emitters, the collective properties of such family of molecules enable the probe to have more potential for eliminating tissue autofluorescence and improve signal to noise ratio by facilitating a proper delay time between the long-lived emission of dyes and the pulsed excitation light (Figure 1.1.5a, b). In addition, these advanced luminescent materials act as new theranostic agents and could be used as novel metal-free photosensitizers (PSs) for photodynamic therapy (PDT).[62,63] TADF emitters could generate reactive singlet oxygen ($^1O_2$) from surrounding oxygen by taking the energy from the T_1, when it moves back to S_1 during the process of ISC and RISC (Figure 1.1.5c).

1.1.4. Supramolecular Chemistry: Self-assembly to Co-assembly

Molecular assembly is a ubiquitous process in nature, especially the associated chemistry with supramolecular structure, also known as "chemistry beyond the molecule".[64] In particular, self or co-organization of host-guest like molecular building blocks into highly ordered supramolecular structures has gained much interest due to the unique packing-property functions including biocompatibility, chemical and structural diversity, robustness and ease of large-scale synthesis.[65,66]

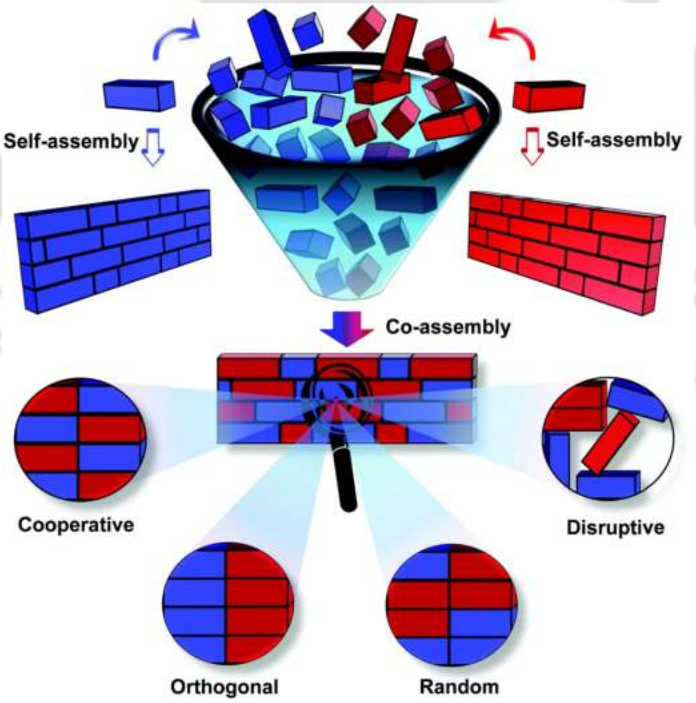

Figure 1.1.6. Schematic illustration of self-assembly and co-assembly using donor-acceptor (blue and red bricks) into an ordered architecture (blue or red wall); mixing them results in charge-transfer complex architecture (wall comprises both blue and red bricks) via four possible supramolecular arrangements such as cooperative, orthogonal (or self-sorting), random and disruptive co-assembly.

In addition, supramolecular architectures spontaneously form well-ordered structures at their both the nano- and the micro-scale that contains all the ground-state molecular information. Therefore, non-covalently bonded D-A-based small π-conjugated structures in particular could be an ideal material to emphasize the functional behavior of the chromophores and decipher their unique "structure-property relationships" at the molecular to electronic level. Therefore, supramolecular D-A assembly has been effectively utilized to produce novel materials with tailored properties for various applications in the fields of material science, engineering, medicine, and biology.[67] Crystal engineering strategy of single component building blocks into ordered multicomponent supramolecular D-A organization has displayed remarkable performances owing to their varying intermolecular interactions viz. hydrogen bonds (HBs), halogen bonds (XBs), π-π stacking including charge-transfer (CT) played a pivotal role to define a clear understanding of "structure-packing-property" including directional interactions, shape/size organization as well as their optoelectronic properties.[68] Besides, different hybrid molecular stacking and definite aggregation patterns such as mixed stack and segregated stack in H- or J-type assembly endow significant contributions to their optoelectronic properties.[69] Nevertheless, till date polymorphs/co-crystals have mainly catered to the pharmaceuticals field.[70] Hence, the evolution of such systems as semiconductors have often been marred by intricate designs or static molecular structures, varied packing modes, and inefficient optical properties, thereby lacking clarity and fails to describe structure-functions correlation in depth. In this regard, small molecule-based organic CT co-crystals are of potential interest due to their versatile arrangements (cooperative, orthogonal, random and disruptive between D-A moieties (represented as blue-red bricks), benefiting realizing superior photonic and electronic performances as compared to the synergistic constituents alone (Figure 1.1.6).[71] Some of such category smolecule showed multiple color emission by applying external stimuli forces such as grinding, recrystallization and solvent fuming, due to the change in its molecular packing mode and distorting their intra- and inter- molecular interactions. Owing to the unique and easy to tune chemical and optical properties, wide range of color switching ability of such system has huge possibilities on structural flexibility in an economical organic molecular platform, are considered as promising avenue for developing the next-generation of electronics devices. To date, organic functional cocrystals have been explored in many exciting applications such as room-temperature ferro-electricity,[72] optical waveguide,[73] pure organic room-temperature phosphorescence,[74] stimulus-response characteristics,[75] photovoltaics,[76] and imaging,[77] etc.

1.1.5. Reference

[1] M. Pope, H. P. Kallmann and P. Magnante, *J. Chem. Phys.,* **1963**, *38*, 2042-2043.

[2] S. Reineke, *Nat. Mater.,* **2015**, *14*, 459-462.

[3] J. Lee, H. F. Chen, T. Batagoda, C. Coburn, P. I. Djurovich, M. E. Thompson and S. R. Forrest. *Nat. Mater.*, **2015**, ***15,*** 92-98.

[4] T. M. Figueira-Duarte, K. Müllen, *Chem. Rev*., **2011**, *111*, 7260-7314.

[5] X. Wan, C. Li, M. Zhang, Y. Chen, *Chem. Soc. Rev.,* **2020**, *49*, 2828-2842.

[6] C. Wang , H. Dong , W. Hu , Y. Liu , D. Zhu , *Chem. Rev*., **2012**, *112*, 2208-2267.

[7] L. E. Kreno , K. Leong , O. K. Farha , M. Allendorf , R. P. Van Duyne , J. T. Hupp , *Chem. Rev*., **2012**, *112*, 1105-1125.

[8] L. Xie , Q. Ling , X. Hou , W. Huang , *J. Am. Chem. Soc*., **2008**, *130*, 2120-2121.

[9] B. K. Yap , R. Xia , M. Campoy-Quiles , P. N. Stavrinou , D. D. C. Bradley, *Nat. Mater*., **2008**, *7*, 376-380.

[10] E. Kim, Y. Lee, S. Lee, S. B. Park, *Acc. Chem. Res.,* **2015**, *48*, 538–547.

[11] J. Zhou, Q. Liu, W. Feng, Y. Sun, F. Li, *Chem. Rev.,* **2015**, *115*, 395–465.

[12] J. Mei, N. Leung, R. Kwok, J. Lam, B. Tang, *Chem. Rev*., **2015**, *115*, 11718-11940.

[13] T. Förster, K. Kasper, *Phys. Chem. (Muenchen, Ger.)* **1954,** *1*, 275– 277.

[14] J. Zhao, W. Wu, J. Suna, S, Guoa, *Chem. Soc. Rev.,* **2013**, *42*, 5323-5351.

[15] J. Guo, Z. Zhao, B. Tang, *Adv. Opt. Mater.,* **2018**, *6*, 1800264.

[16] H. Uoyama, K. Goushi, K. Shizu, H. Nomura, C. Adachi, *Nature,* **2012**, *492*, 234-238.

[17] Y. Tao, K. Yuan, T. Chen, P. Xu, H. Li, R. Chen, C. Zheng, L. Zhang, W. Huang, *Adv. Mater.,* **2014**, *26*, 7931-7958.

[18] Q. Zhang, D. Tsang, H. Kuwabara, Y. Hatae, B. Li, T. Takahashi, S. Y. Lee, T. Yasuda, C. Adachi, *Adv. Mater.,* **2015**, *27*, 2096-2100.

[19] J. Jin, H. Jiang, Q. Yang, L. Tang, Y. Tao, Y. Li, R. Chen, C. Zheng, Q. Fan, K. Y. Zhang, Q. Zhao, W. Huang, *Nat. Commun.,* **2020**, *11*, 842.

[20] N. R. Paisley, S. V. Halldorson, M. V. Tran, R. M. Gupta, S. Kamal, W. R. Algar, Z. M. Hudson, *Angew. Chem., Int. Ed.,* **2021**, *60*, 18630-18638.

[21] A. Bernanose, M. Comte, P. Vouaux, *J. Chim. Phys*., **1953**, *50*, 64-68.

[22] M. Pope, Kallmann, H. P.; Magnante, P. Electroluminescence in Organic Crystals. *J. Chem. Phys*., **1963**, *38*, 2042-2043.

[23] W. Tang, C. VanSlyke, S. A. *Apl. Phys. Lett*., **1987**, *51*, 913-915.

[24] H. Nakanotani, T. Higuchi, T. Furukawa, K. Masui, K. Morimoto, M. Numata, H. Tanaka, Y. Sagara, T. Yasuda, C.Adachi, *Nat. Commun.*, **2014**, *5*, 4016.

[25] C. W. Lee, J. Y. Lee, *Adv. Mater.*, **2013**, *25*, 5450-5454.

[26] M. A. Baldo, D. F. O'Brien, Y. You, A. Shoustiko, S. Sibley, M. E. Thompson, S. R. Forrest, *Nature*, **1998**, *395*, 151-154.

[27] W. J. Li, Y. Pan, L. Yao, H. C. Liu, S. T. Zhang, C. Wang, F. Z. Shen, P. Lu, B. Yang, Y. G. Ma, *Adv. Opt. Mater.*, **2014**, *2*, 892-901.

[28] P.-Y. Chou, H.-H. Chou, Y.-H. Chen, T.-H. Su, C.-Y. Liao, H.-W. Lin, W.-C. Lin, H.-Y. Yen, I.-C. Chena, C.-H. Cheng, *Chem. Commn.,* **2014**, *50*, 6869-6871.

[29] S. Scholz, D. Kondakov, B. Lüssem, K. Leo, *Chem. Rev*., **2015**, *115*, 8449-8503.

[30] C. A. Parker and C. G. Hatchard, *Trans. Faraday Soc.,* **1961**, *57*, 1894–1904.

[31] D. Y. Kondakov, T. D. Pawlik, T. K. Hatwar and J. P. Spindler, *J. Appl. Phys.*, 2009, **106**, 124510.

[32] G. Hong, X. Gan, C. Leonhardt, Z. Zhang, J. Seibert, J. M. Busch, S. Bräse, *Adv.Mater.,* **2021**, *33*, 2005630.

[33] Y. Liu, C. Li, Z. Ren, S. Yan, M.R. Bryce, *Nat. Rev. Mater.,* **2018,** *3*,18020.

[34] C. A. Parker, C. G. Hatchard, *Trans. Faraday Soc.,* **1961**, *57*, 1894-1904.

[35] G. Blasse, D. R. McMillin, *Chem. Phys. Lett.,* **1980**, *70*, 1-3.

[36] M. N. Berberan-Santos, J. M. M. Garcia, *J. Am. Chem. Soc.,* **1996**, *118*, 9391-9394.

[37] A. Endo , M. Ogasawara , A. Takahashi , D. Yokoyama , Y. Kato , C. Adachi, *Adv. Mater.,* **2009**, *21*, 4802-4806.

[38] M. A. Baldo, D. F. O'Brien, Y. You, A. Shoustikov, S. Sibley, M. E. Thompson, S. R. Forrest. *Nature*, **1998**, *395*, 151–154.

[39] W. Zhao, Z. He, B. Z. Tang, *Nat. Rev. Mater.,* **2020**, *5*, 869–885.

[40] W. Zhao, T. S. Cheung, N. Jiang, W. Huang, J. W. Y. Lam, X. Zhang, Z. He, B. Z. Tang, *Nat. Commun.,* **2019**, *10*, 1595.

[41] O. Bolton, K. Lee, H. J. Kim, K. Y. Lin, J. Kim, *Nat. Chem.,* **2011**, *3*, 205–210.

[42] R.Gao, X. Mei, D. Yan, R. Liang, M. Wei, *Nat. Commun.*, **2018**, *9*, 2798.

[43] X. Ban, A. Zhu, T. Zhang, Z. Tong, W. Jiang, Y. Sun, *Chem. Commn.,* **2017**, *53*, 11834-11837.

[44] D. Wang, B. Z. Tang, *Acc. Chem. Res*., **2019**, *52*, 2559-2570.

[45] Kenry, K. C. Chong, B. Liu, *Acc. Chem. Res.,* **2019**, *52*, 3051-3063.

[46] J.B. Birks, *Photophysics of Aromatic Molecules*, Wiley, London, 1970.

[47] J. Luo, Z. Xie, J. Lam, L. Cheng, H. Chen, C. Qiu, H. Kwok, X. Zhan, Y. Liu, D. Zhu, B. Tang, *Chem. Commun.,* **2001**, *18*, 1740-1741.

[48] . J. Q. Shi , N. Chang , C. H. Li , J. Mei , C. M. Deng , X. L. Luo , Z. P. Liu , Z. S. Bo , Y. Q. Dong and B. Z. Tang, *Chem. Commun*., **2012**, *48*, 10675-10677.

[49] R. Hu , N. L. C. Leung and B. Z. Tang , *Chem. Soc. Rev*., **2014**, *43* , 4494-4562.

[50] X. Xiong, F. Song, J. Wang, Y. Zhang, Y. Xue, L. Sun, N. Jiang, P. Gao, L. Tian, X. Peng, *J. Am. Chem. Soc.,* **2014**, *136*, 9590–9597.

[51] S. Xu, T. Liu, Y. Mu, Y. Wang, Z. Chi, C. Lo, S. Liu, Y. Zhang, A. Lien, J. Xu, *Angew. Chem., Int. Ed.,* **2015**, *54*, 874-878.

[52] Kenry, C. Chen, B. Liu, *Nat. Commun.,* **2019**, *10*, 2111.

[53] M. Y. Wong, E. Zysman-Colman, *Adv. Mater.,* **2017**, *29*, 1605444.

[54] T. Shan , Y. L. Liu , X. Y. Tang , Q. Bai , Y. Gao , Z. Gao , J. Y. Li , J. Deng , B. Yang , P. Lu and Y. G. Ma , *ACS Appl. Mater. Interfaces,* **2016**, *8*, 28771 -28779.

[55] F. Sansone, L. Baldini, A. Casnati, R. Ungaro, *New J. Chem*., **2010**, *34*, 2715-2728.

[56] Y. Wu, Q. Chen, Q. Li, H. Lu, X. Wu, J. Ma, H. Gao, *J. Mater. Chem. B,* **2016**, *4*, 6350-6357.

[57] A. Harada, *Acc. Chem. Res.,* **2001**, *34*, 456-464.

[58] Z. Zhao, H. Zhang, J. W. Y. Lam, B. Z. Tang, *Angew. Chem. Int. Ed.,* **2020**, *59*, 9888 – 9907.

[59] F. Ni, N. Li, L. Zhan, C. Yang, *Adv. Opt. Mater.,* **2020**, *8*, 1902187.

[60] J. Zhang, J. Zhang, W. Li, R. Chen, Z. Zhang, W. Zhang, Y. Tang, X. Chen, G. Liu, C.-S. Lee, *Theranostics,* **2017**, *7*, 3007.

[61] Z. Zhu, D. Tian, P. Gao, K. Wang, Y. Li, X. Shu, J. Zhu, Q. Zhao, *J. Am. Chem. Soc.,* **2018**, *140*, 17484-17491.

[62] Z. Liu, W. Shi, G. Hong, W. Chen, B. Song, X. Peng, X. Xiong, F. Song, *J. Controlled Release,* **2019**, *310*, 1-10.

[63] Y.-F. Xiao, J.-X. Chen, S. Li, W.-W. Tao, S. Tian, K. Wang, X. Cui, Z. Huang, X.-H. Zhang, C.-S. Lee, *Chem. Sci*., **2020**, *11*, 888-895.

[64] G. R. Desiraju, *Nature*, **2001**, *412*, 397–400.

[65] J.-M. Lehn, Supramolecular Chemistry: Concepts and Perspectives (VCH, Weinheim, 1995).

[66] X. Zhang, H. Dong, W. Hu, *Adv. Mater.,* **2018**. *30*, 1801048–1801082.

[67] H. Geng, X. Zheng, Z. Shuai, L. Zhu, Y. Yi, *Adv. Mater.,* **2015**, *27*, 1443–1449.

[68] L. Sun, Y. Wang, F. Yang, X. Zhang, W. Hu, *Adv.Mater.,* **2019**, *31*, 1902328.

[69] L. Yu, *Acc. Chem. Res.* 2010, *43*, 1257-1266.

[70] W. Ji, B. Xue, S. Bera, S. Guerin, Y. Liu, H. Yuan, Q. Li, C. Yuan, L. J. W. Shimon, Q. Ma, E. Kiely, S. A. M. Tofail, M. Si, X. Yan, Y. Cao, W. Wang, R. Yang, D. Thompson, J. Li, E. Gazit, *ACS Nano,* 2020, *14*, 10704-10715.

[71] W. Zhu, L. Zhu, Y. Zou, Y. Wu, Y. Zhen, H. Dong, H. Fu, Z. Wei, Q. Shi, W. Hu, *Adv. Mater.,* **2016**, *28*, 5954-5962.

[72] S. Horiuchi, F. Ishii, R. Kumai, Y. Okimoto, H. Tachibana, N. Nagaosa, Y. Tokura, *Nat. Mater.,* **2005**, *4*, 163-166.

[73] X. Y. Fang, X. G. Yang, D. P. Yan, *J. Mater. Chem. C,* **2017**, *5*, 1632-1637.

[74] O. Bolton, K. Lee, H.-J. Kim, K. Y. Lin, J. Kim, *Nat. Chem.,* **2011**, *3*, 205-210.

[75] L. Y. Bai, P. Bose, Q. Gao, Y. X. Li, R. Ganguly, Y. L. Zhao, *J. Am. Chem. Soc.,* **2017**, *139*, 436-441.

[76] S. J. Kang, S. Ahn, J. B. Kim, C. Schenck, A. M. Hiszpanski, S. Oh, T. Schiros, Y.-L. Loo, C. Nuckolls, *J. Am. Chem. Soc.,* **2013**, *135*, 2207-2212.

[77] Y. Wang, W. G. Zhu, W. N. Du, X. F. Liu, X. T. Zhang, H. L. Dong, W. P. Hu, *Angew. Chem., Int. Ed.,* **2018**, *57*, 3963-3967.

1.2.1. Fundamental Concepts

In this chapter, fundamental concepts of photophysical and photochemical processes central to the current investigations were carried out. A qualitative interpretation of the common photophysical transitions and associated description of the electronic energy states are presented, followed by a discussion of the triplet harvesting mechanisms and the applications of triplet harvesting organic materials in OLEDs, OWGs and biological fields.

1.2.1.1. Molecular Orbitals

Metal-free organic materials with their "structure-property and functions" are the principle focus of this thesis. Organic materials mainly consist of carbon and hydrogen, including other atoms such as sulfur, nitrogen and oxygen. An atom is made of electrons and a nucleus, while orbitals are a set of well-defined allowed energies and spatial distributions of the electron around the nucleus. In molecules, atomic orbitals are linearly combined and generate molecular orbitals (MO), which explains the energies and distribution of electrons between two or more atoms.

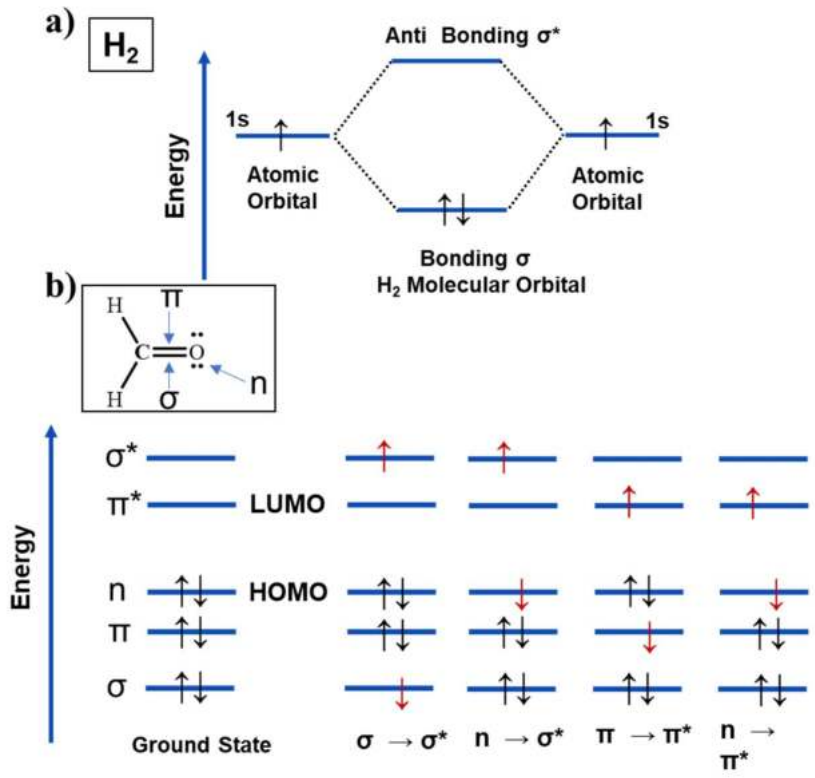

Figure 1.2.1. (a) Schematic representation of molecular orbital for the hydrogen. b) Energy levels of molecular orbitals and all possible electronic transitions in formaldehyde.

Molecular orbitals in the diatomic hydrogen is shown in Figure 1.2.1a. The bonding MO, which is lower in energy (σ) has high occupancy and is lower than the two 1s atomic orbitals of the hydrogen atoms. While the antibonding orbital which is higher in energy (σ*) has low occupency and the electronic wavefunction is in its central node. Hydrogen atoms become bonded when two atoms are kept in close proximity by lowering the electronic energy in the σ orbital at a state of ($E(\sigma(\uparrow\downarrow)) < 2E(1s^1)$). In a molecular system with more electrons, covalent σ bonds are formed either by one s and one p atomic orbital or between two parallel head-to-head p orbitals. When two aligned p atomic orbitals are laterally overlapped and formed π and π^* orbitals, this resulting bond is known to be π bond. Under photo-excitation electron absorbs photon with appropriate energy and gets promoted from a bonding orbital (σ or π) to its corresponding antibonding orbital (σ* or π^*). As shown in Figure 1.2.1b the transition is labelled as $\sigma \rightarrow \sigma^*$ *and* $\pi \rightarrow \pi^*$. Some of the heteroatoms (nitrogen, oxygen and sulphur) containing molecules possess additional non-bonding electrons and form non-bonding orbitals (n). Under photoexcitation a non-bonding electron promotes to an antibonding π^* orbital and giving $n \rightarrow \pi^*$ transition. For an organic molecule, the molecular orbitals are filled by the available electrons in the ground state. In the molecule the highest energy filled orbital is called the highest occupied molecular orbital (HOMO) and the lowest energy empty orbital just above HOMO is called lowest unoccupied molecular orbital (LUMO). In Figure 1.2.1b, molecular orbitals energy levels with all possible molecular orbital transitions are presented.[1]

1.2.2. Excitons in Organic Materials

1.2.2.1. Singlet and Triplet States

An exciton is a coupled state between an excited electron and an associated hole, bound by Coulomb attraction. It can be generated by the recombination of the free electrons and holes under photo-excitation or electrical pumping. After absorbing photon, organic molecules typically undergoes an electronic transition from π-orbital (HOMO) to a π*-orbital (LUMO). This process needs an equal or higher energy of the absorbed photon than the HOMO/LUMO energy gap and a non-zero transition dipole moment (Figure 1.2.2a). Investigation of this transition for any given organic system is very crucial for its photophysical characterization. Subsequently, HOMO/LUMO band values and band gaps are a good model for device science especially it provides the information of carrier

transport and injection in the devices. However, it ignores involving electron-electron interactions and the relative spin of the electrons. These aspects can be addressed using a molecular orbital and energy level model which provide an easier understanding of the origin and the difference between singlet and triplet state (explained later on).

Starting with the Bohr model, electrons show both wave and particle-like behaviours.[2] In an atom, electrons orbit around the dense nucleus in defined energy levels called electronic wave-function $\psi(x, y, z)$. The probability of finding an electron at a particular point in space related to the combination of its spatial coordinates and spin wavefunction, which is further described as the product of ψ and its complex conjugate ψ^*, $\langle\psi^*|\psi\rangle$, at that point. In the quantum mechanical model a set of quntum numbers are used to describe the size, shape and orientation by principle (n), angular (l) and magnetic (m) quantum numbers for one electron hydrogen system, where, $\psi_{nlm}(x, y, z)$ satisfying the Schrödinger equation 1.2.1:

$$\left[\frac{\hat{P}^2}{2m} + V(x,y,z)\right]\psi = \hat{E}\psi \qquad (1.2.1)$$

Where $\hat{P}$ is the momentum operator, m is the electron mass, $V(x, y, z)$ is the potential and $\hat{E}$ is the energy operator. To distinguish electrons that occupy the same orbital, a fourth quantum number is required for multi-electron system, called the spin quantum number (s) which is described as electron angular momentum. Under external magnetic field, the electron's spin can be either spin up ($m_s = +\frac{1}{2}$) or spin down ($m_s = -\frac{1}{2}$) and so $m_s = \pm½$. As per Pauli exclusion principle, no two electrons in an atom can have the same set of quantum numbers.[3,4] Therfore, they must exist in opposite spin states.[5] The spin multiplicity can be determined from s, m= 2s+1. The total m_s is the sum total of the z-components of the electron's inherent spin. For a two-electron system (1s22s22p2): s=0,1, m=1,3 and m_s=1,0,-1. Therefore, four spin eigenstates (m_s =0 and m_s =1,0,-1) are possible, and these differentiate the singlet from triplet states, Figure 1.2.2b). The lowest orbital is occupied by two electrons with antiparallel spins and resulting in a total spin of zero, and this configuration is the lowest energy ground state (S_0) or HOMO. Upon excitation, one electron is promoted from HOMO to LUMO, and a singlet (S_1), antiparallel spins or triplet (T_1, parallel spins) state is formed and adds up to a total s of zero for singlet (m_s = 0) and one for triplet (m_s = -1,0,1), thus on overage 75% of excitons are triplet states, with the remaining 25% being singlets.[6]

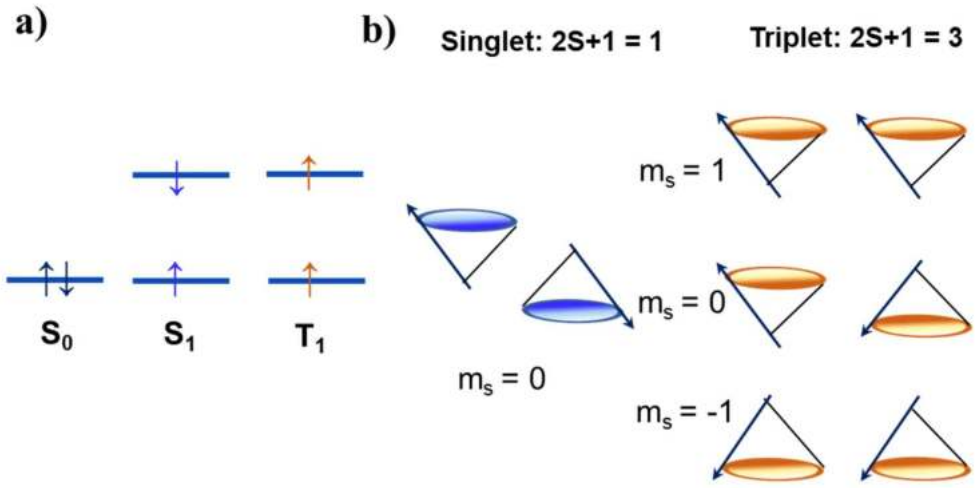

Figure 1.2.2. a) Illustration of ground and excited states in relevant molecular orbital configurations (arrows here indicate the direction of electron spins). b) Illustrating the relative orientations (vector diagram) of two electron spins for singlet and triplet states.

1.2.2.2. Energy Splitting between Singlet and Triplet States

The total energy of the first singlet (E_{S1}) and triplet (E_{T1}) states are considered as the first orbital energy (E_{orb}), the energy associated with the one-electron orbital for a fixed nuclear framework in the excited state. To this is added the Coulomb integration integral (K) and the exchange energy (J), i.e. the first-order correction involving electron-electron repulsion due to the Pauli's principle:

$$E_{S1} = E_{orb} + K + J \qquad (1.2.2)$$

$$E_{T1} = E_{orb} + K - J \qquad (1.2.3)$$

In the equation 1.2.2 and 1.2.3 the sign difference of *J* signifies that the first excited singlet state (S_1) will therefore have higher energy than the first triplet state (T_1). The singlet-triplet energy gap (ΔE_{ST}) is dependent on their exchange energy, calculated using the HOMO and LUMO wave functions, (Φ_H and ψ_L) integrated over the possible two electron positions ($r_1$and r_2):

$$\Delta E_{ST} = E_{S1} - E_{T1} = 2J$$

$$= 2\iint \Phi_H(r_1)\psi_L(r_2)\left(\frac{e^2}{r_1 - r_2}\right)\Phi_H(r_2)\psi_L(r_1)dr_1dr_2 \qquad (1.2.4)$$

A key requirement for TADF emitters is the small ΔE_{ST} which, from equation 1.2.4, comes from increasing the spatial separation of the HOMO and LUMO orbitals ($r_1 - r_2$).[7,8]

1.2.3. Franck-Condon Principle

The transition rate between electronic and vibrational states are related to the similarity of both the electron and nuclear wave functions in the initial and final states. Due to the large mass difference of electron and nuclei in an atom, electron move much faster (10^{-16} -10^{-15} s) than nuclei (10^{-14} - 10^{-13} s). Therefore, it separates the timescales of electron and nuclear motion, resulting the essence of the Born-Oppenheimer (BO) approximation.[9]

According to Fermi's golden rule[10] the transition probability magnitude (P) between an initial state ($\Psi 1$) and a final state ($\Psi 2$) is given by equation 1.2.5;

$$P = \langle \Psi_1 | \mu | \Psi_2 \rangle = \langle \varphi_1 \omega_1 | \mu | \varphi_2 \omega_2 \rangle = \langle \omega_1 | \mu | \omega_2 \rangle \langle \varphi_1 | \varphi_2 \rangle \qquad (1.2.5)$$

where the electronic and vibrational wavefunctions are represented as $\boldsymbol{\omega}$ and φ, respectively. μ is the molecular transition dipole operator and depends on the electron coordinates.

The Franck-Condon (FC) principle states that the vibrational peak intensity in an electronically allowed transition is proportional to the absolute square of the overlap integral of the vibrational wave functions of the initial and final states. While larger orbital overlaps show faster transitions which rely on the BO approximation. The square of the vibrational overlap integral $\langle \varphi_1 | \varphi_2 \rangle$ is known as the Franck–Condon factor, which is proportional to the probability of the transition.

To quantify the intensity or probability of an electronic transition, oscillator strength (f) is used, which is proportional to the square of μ, is:[11,12]

$$f \propto \mu^2 \qquad (1.2.6)$$

For a single excited oscillating electron, f is related to the experimental extinction coefficient ($\boldsymbol{\varepsilon}$) qualitatively given by

$$f \propto \int \varepsilon d\hat{\nu} \qquad (1.2.7)$$

Experimentally, the integral depicts the area under a curve value of the absorption spectrum plotted by the extinction coefficient as a function of wavenumber ν. The oscillator strength, f =1 corresponds to a fully allowed strong electronic transition and f =0 to a forbidden transition.

A schematic of the Franck-Condon principle is depicted in Figure 1.2.3a,b, showing both the electronic levels and vibrational sublevels.

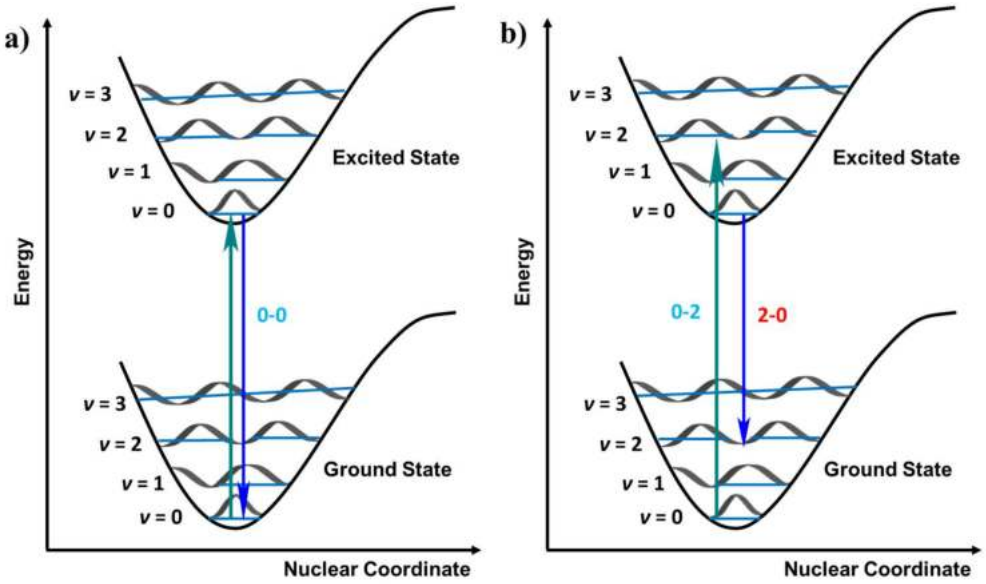

Figure 1.2.3. Representation of energy diagram for the Franck-Condon principle with vertical transitions.

In Figure 1.2.3a, a large orbital overlap of the final excited state of nuclear geometry is essentially an identical shape as the initial ground state of nuclear geometry. Therefore, a 0 - 0 transition will be observed unless forbidden by symmetry. In Figure 1.2.3b. the longer nuclear separation leads to excitation of an electron to an antibonding orbital giving rise to a weaker bond and, therefore, showing a more realistic transition. This transitions between $v = 0$ and $v = 2$, where two vibrational wavefunctions show a large overlap, giving different values (FC factors) for different transitions.

1.2.4. Jablonski Diagram

Figure 1.2.4 illustrates the typical Jablonski diagram with all the possible transitions between states, organized vertically by energy. Thick lines correspond to the electronic state, and there is a series of vibrational states where, each vibrational state is composed of a set of rotational state. Here only electronic and vibrational states are considered for simplicity.

1.2.4.1. Absorption, Fluorescence and Phosphorescence

Absorption and emission is the radiative transition in the form of a photon, occurs between two states of a molecule. Electronic, vibrational and spin wavefunctions of the initial and final states regulate the probability of radiative transition, shape and type, respectively. The radiative transition intensity depends on the type of orbitals involved; therefore, ππ* transitions are more likely intense than nπ* and CT transitions.

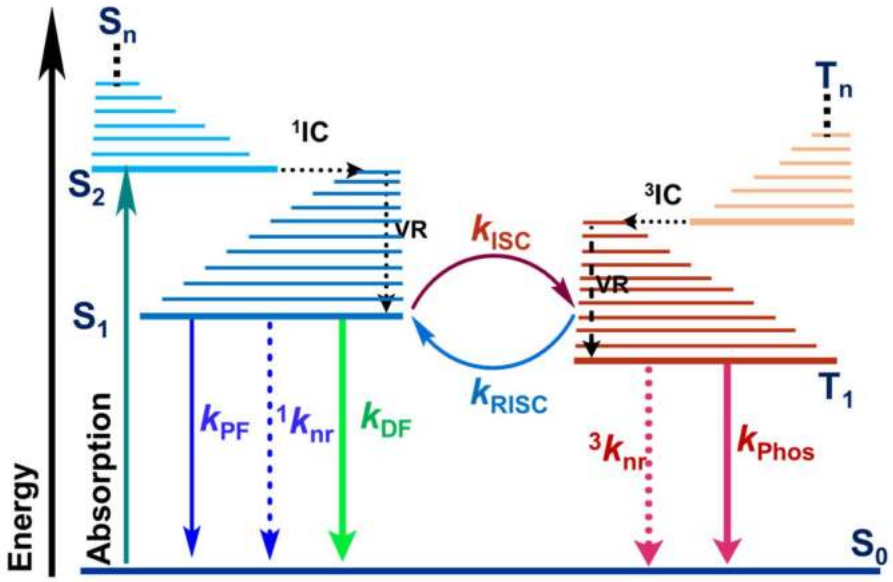

Figure 1.2.4. Jablonski diagram for transitions between relevant vibronic states in an organic molecule. Absorption: upon excitation, the transition from the ground state (S_0) to an excited state with the same multiplicity (S_n) occurs when the photonic energy is higher than the S_n-S_0 gap. Vibrational relaxation (VR) and internal conversion (IC) (as non-radiative, nr, transitions) relax the electron to the lowest possible excited singlet state (S_1). From here, three possible pathways: prompt radiative fluorescence (PF) or nr transitions to the ground state and intersystem crossing (ISC) to the triplet state (T_1). Although formally forbidden, T_1 can also relax to the ground state through radiative (in the form of phosphorescence - PH) or nr transitions. Alternatively, the fourth pathway of reverse ISC (RISC) from T_1 back to S_1 can occur at small S_1-T_1 enegy gap and gives rise to delayed fluorescence (DF) in addition to PF with a magnitude of slower decay rate than the rate of PF in the same spectrum.

The transition strength of these radiative process is known as oscillator strength (*f*). The change of spin, i.e. transition between singlet and triplet states are the weakest transition due to the symmetry forbidden nature.[13] Photon absorption is the first transition where an electron of the molecule is excited from the ground state (S_0) to higher energy states (S_n), which is equivalent to its absorbed photon energy.

Based on the energy difference between the two energy levels, only certain wavelength light can be absorbed during photo-excitation. As per the selection rule ($\Delta S=0$), S_0 to S_n is the exclusive transition for absorption but not S_0 to T_n, because total molecular momentum and geometry conservation is necessary after photo-absorption. The absorption process is very fast in the order of 10^{-15} seconds. After the excitation, the excited electron relaxes to a more thermodynamically stable lowest excited state S_1, through fast internal conversion (IC) and vibrational relaxation process (between 10^{-14} to 10^{-11} seconds). The radiative

transition between S_1 to S_0 is known as fluorescence or prompt fluorescence ($S_1 \rightarrow S_0 + h\nu$) with a fast decay lifetime (pico to nanosecond range) and large rates.

On the other hand, the radiative transition from T_1 to S_0 is known as phosphorescence ($T_1 \rightarrow S_0 + h\nu$) with a long decay lifetime (microseconds to seconds). Normally, phosphorescence (PH) is a spin forbidden transition, which occurs through the intersystem crossing process (ISC) and spin-orbit coupling (SOC) process. When the excited electron is relaxed to S_1, PF, IC and ISC, these three possible subsequent processes compete with each other strongly.

Finally, another class of radiative decay, known as delayed fluorescence (DF), is similar to fluorescence with a longer lifetime (late nano to late microseconds regions). DF occurs due to the repopulation of upconverted electrons in the singlets from triplets by the spin-flip mechanism. Great care must be taken to understand the subtle difference between DF and PH. The oxygen quenching effect needs to be considered in measuring their distinct contribution since both the emissions depend on the lifetime of triplet electrons. Molecular oxygen has a ground state triplet which readily quenches the excited triplets and generates non-radiative transitions. Therefore, high vacuum and low-temperature measurement is necessary to avoid non-radiative decays and get a clear PH spectra.[14]

Absorption and emission transitions are controlled by the Franck-Condon principle in a given molecular system. The wavefunction overlap of the initial and final state governs the intensity of each transition. The change of placement in the electrons results in the nuclei experiencing an electric potential which brings them into motion. After the instantaneous absorption, electrons relax to the lowest vibrational level resulting in emission with redshift from the absorption. The Stokes shift is defined as the difference between the peak of emission and absorption. In the case of TADF molecules, more red-shifted emission is commonly observed due to their unit absorption, which gives rise to the low-energy CT and subsequent ET between D and A units.

1.2.4.2. Intersystem Crossing and Reverse Intersystem Crossing

As per the quantum mechanical rule, the transitions between the different spin multiplicity states are generally forbidden as described above. Therefore, if the molecule is in the singlet state (zero-order approximation), it will remain in the singlet state, however, a compensation between the change in spin and angular momentum by conserving total angular momentum makes the process allowed *via* SOC. Therefore, under strong SOC the

triplet sates acquire a singlet character and vice-versa. Occurrence of spin mixing between S_1 and T_1 of the energy surface at the crossing point, resulting a non-radiative transition called intersystem crossing (ISC). Moreover, atomic size is an important factor in controlling SOC. The magnitude of the SOC is proportional to the size of the atom (SOC $\propto Z^4$). Bigger nuclei accelerate the electrons more and enhance the orbital motion, which further contributes to the overall SOC. Therefore, incorporation of heavy atoms into the chromophoric structure increases the SOC, which is one aspect of "heavy atom affect".[15] El-Sayed's rule states that the strong coupling occurs between a $^S(\pi\pi^*)$ with a $^T(n\pi^*)$ state and vice-versa, resulting in efficient ISC/SOC. In contrast, $^S(\pi\pi^*) \rightarrow {}^T(\pi\pi^*)$ and $^S(n\pi^*) \rightarrow {}^T(n\pi^*)$ are weakly coupled and found to have a negligible SOC.[16,17] At the same time, a reduced energy gap between singlet and triplet states, enabling the flip back of the triplet excitons to the singlet state through reverse ISC.

1.2.5. Thermally-Activated Delayed Fluorescence (TADF)

The fundamental concept of exciton harvesting has been considered as indispensable research in the field of OLED, due to the diverse molecular engineering enhanced SOC strength and successful RISC process at moduled energy gap between singlet and triplet. Therefore, TADF materials are an emerging class of fluorescent small molecules and considered as an alternative to inorganic phosphorescent emitters, pioneered by Adachi and coworkers in 2012. These materials displayed slightly delayed emission and have achieved higher lifetime of up to several microseconds due to the enhancement of ISC and RISC process simultaneously.[18] The basic aspects of TADF materials are favorable to confer the common feature of the molecular design strategy. The most important features of TADF molecules are present in the twisted molecular skeleton with twisted intramolecular charge transfer (TICT) states. A typical Jablonski diagram could explain the TADF phenomenon, wherein, by irradiating light on organic conjugated molecules, the generated excitons can go to the singlet excited state S_1 or even at higher vibrational levels (S_n) (Figure 1.2.4). Through IC and vibrational relaxation these excitons move to S_1 state and finally return to S_0 by releasing fluorescence. Parallelly excited state singlets can move to triplet excited state *via* ISC and release as non-radiative phosphorescence. Alternatively, at a certain condition such as small ΔE_{ST} and gaining thermal activation due to steric reason by molecular vibration, triplet excitons reverse back to lowest singlet and resulting in a delayed fluorescence with fluorescence, and that DF is termed as TADF.[19]

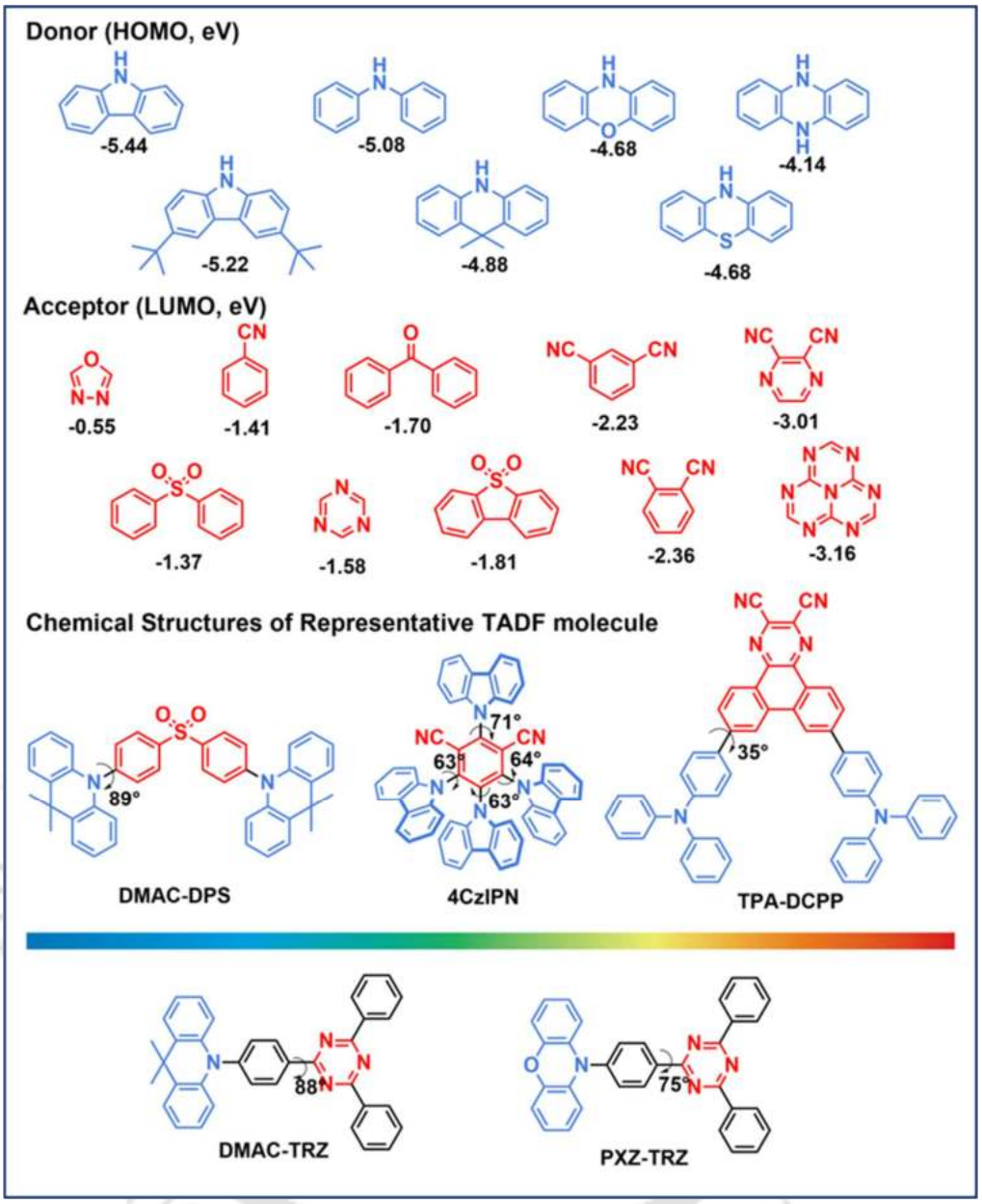

Figure 1.2.6. Chemical structures of common donor and acceptor molecules used to design TADF emitter include the deep-blue emitter DMAC-DPS, the sky-blue emitter DMAC-TRZ, the green emitter 4CzIPN , the green-yellow emitter PXZ-TRZ and the red emitter TPA-DCPP. The colour bar depicts the blue to red emission wavelength of the TADF molecules.

Therefore, it is necessary to have a twisted molecular geometry between donor- and acceptor with their spatially separated HOMO and LUMO, resulting in a sufficiently small ΔE_{ST} value for RISC process to occur, which is generally less than 0.3 eV (Figure 1.2.5).[20,21] The rate of RISC can be calculated by using the Equations-1.2.8. As per the selection rules ISC is a spin forbidden transition, but these transitions can be partially allowed if the energy gap (ΔE_{ST}) is small.

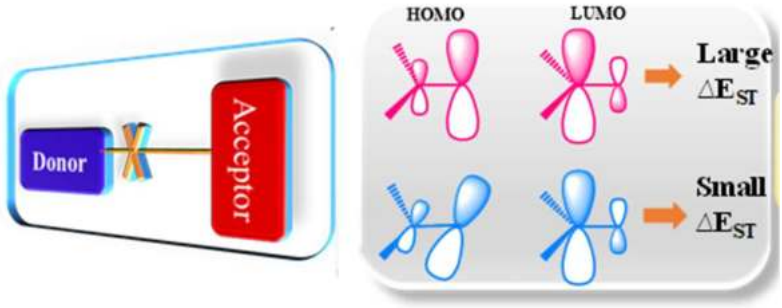

Figure 1.2.5. Schematic of the orthogonal orientation of donor-acceptor in a TADF structure and, depending on their HOMO/LUMO overlap geometry, leads to large or small energy gap.

$$k_{RISC} \propto \exp\left(-\frac{\Delta E_{ST}}{k_B T}\right) \qquad (1.2.8)$$

1.2.6. Excited State Dynamics for TADF

1.2.6.1. Ideal TADF Model

In the ongoing pursuit of metal-free organic TADF materials development and related fundamental mechanism investigation, the current TADF model and its intrinsic mechanism is quite fascinating. In contrast to the earlier assumptions, the forbidden transitions between ^{1}CT and ^{3}CT as SOC between states of the same spatial orbital is zero. Notably, for efficient TADF, a significant contribution of SOC is important *via* mixing between singlet and triplet manifolds with the involvement of different characters of each state. A local triplet (^{3}LE) state with ππ* character could interact with ^{1}CT form with the nπ* or mixed nπ*/ππ*character to produce SOC and RISC process.[22] Further, thermal activation for RISC is reduced by the nonadiabatic coupling with mixing between ^{3}LE and ^{3}CT and/or forming an equilibrium between these two states. According to the second-order perturbation theory, the lowering of the energy gap occurs because activation energy (E_a) is dominated by the energy gap of ^{1}CT-^{3}CT rather than the energy gap of ^{1}CT-^{3}LE. Therefore, the intermediate ^{3}LE state act as a mediator to the RISC and TADF process showed an important effect on the E_a energy and associated different energy gaps while explaining TADF mechanism.[23]

Finally, according to second-order perturbation theory and by considering the vibronic coupling of ^{1}CT-^{3}LE, the rate of RISC can then be defined as equation 1.2.9[24]

$$k_{RISC} = \frac{2\pi}{h}\left|\frac{\langle 1\psi_{CT}|\hat{H}_{SO}|3\psi_{LE}\rangle\langle 3\psi_{LE}|\hat{H}_{vib}|3\psi_{CT}\rangle}{\delta(3E_{LE} - 3E_{CT})}\right|^2 \delta(3E_{LE} - 3E_{CT}) \qquad (1.2.9)$$

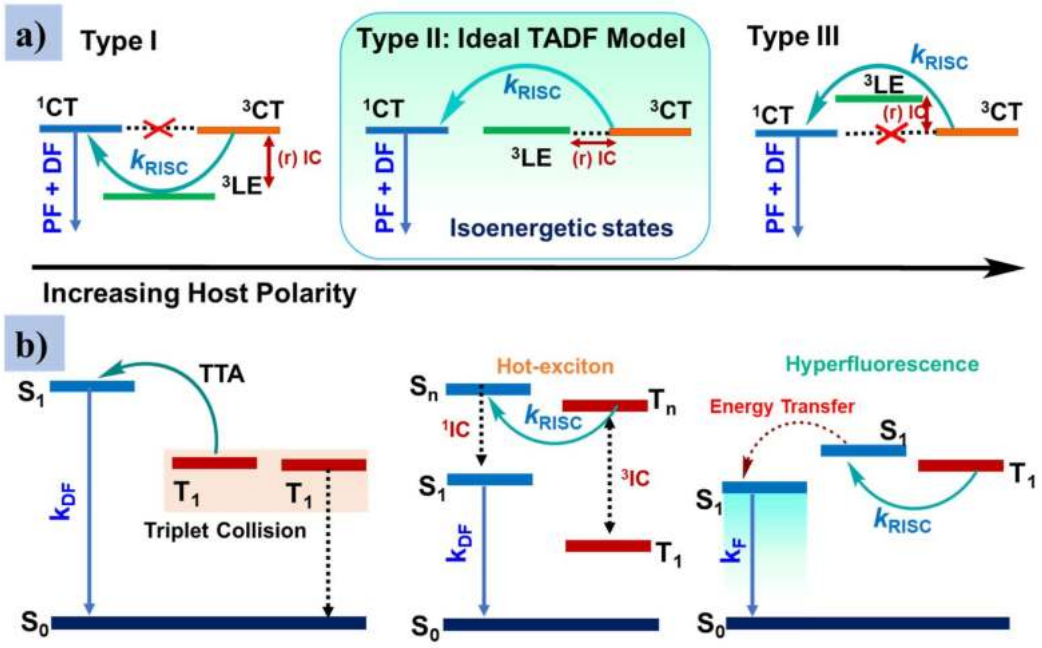

Figure 1.2.6. (a) Schematic energy-level diagrams of ^{1}CT-^{3}LE-^{3}CT states for different types of TADF mechanism. (b) Representation for the generation of DF with alternative mechanisms left) triplet-triplet annihilation (TTA), middle) hot-excitons or upper state crossing and (c) hyperfluorescence. The sky-blue shed area in hyperfluorescence refers to a conventional fluorescence-emitting guest and the (right) to a TADF sensitizer.

Based on all the experimental and computational results, there are three types of TADF mechanism described as Type-I where ^{3}LE state goes from being above to almost isoenergetic as Type-II and below the CT manifold is a Type-III mechanism. Among these, the minimized energy gaps between ^{1}CT-^{3}LE and ^{3}CT-^{3}LE is more sought for efficient TADF shown in Figure 1.2.7a.[25] With the emergence of TADF materials and better understanding on how to control the excited state dynamics, few other mechanisms were also proposed *i.e.* triplet-triplet annhilation (TTA), hot-exciton contribution as upper-state crossing and hyperfluorescence as described below.

1.2.6.2. Triplet-Triplet Annihilation (TTA)

TTA is a P-type[26] DF, a bimolecular process that governs the singlet formation from two triplets: $T_1 + T_1 \xrightarrow{k_{TTA}} S_n + S_0 + \text{heat}$; then DF proceeds from the S_1 state to S_0. The equation presents that TTA occurs from the collision of two triplets, where one triplet gets promoted to an upper excited state (S_n), while the other one relaxes back to the S_0 state, as shown in Figure 1.2.7b (left). Triplet collisions lead to the different excitons of singlets (total spin S = 0), triplets (S = +1) or quintets (S = +2) as per the spin conservation rule and depending on the spin of both triplets, but not experimentally observed. However, TTA can produce the theoretical maximum η_{int}, of 62.5 % *via* triplet fusion mechanism. Although, TTA achieved smaller efficiency than TADF but has longer device lifetime and operational stability.[27]

1.2.6.3. Hot-exciton: Higher-lying State Crossing

Upper state or crossing also known as "hot exciton" involves RISC between higher-lying singlet (S_n) and triplet (T_m) excited states, $T_m \xrightarrow{k_{RISC}} S_n$ which is followed by relaxation to the S_1 state and finally DF as shown in Figure 1.2.7b (middle). Though this approach could not reach η_{int} of 100 %, due to the increased competition of the triplet manifold (^{3}IC) resulting in non-radiative decays which limits their performance. However, a specific kind of single molecular structure displayed dual and/or multimode emission with the involvement of upper state crossing to produce high efficiency white-light in combination with fluorescence, DF and phosphorescence respectively.[28]

1.2.6.4. Hyperfluorescence

Hyperfluorescence is considered as fourth-generation lighting emitters. It is based on the TADF and fluorescence molecules where TADF is being used as sensitizer (St) to pump the radiative decay of the fluorescent probe. After harvesting the triplet and high yield population of singlet by TADF emitter, a subsequent energy transfer (E_n. T.) into the fluorescent guest emitter greatly increases the performance of the emitting guest (G) as: $(T_2)^{St} \xrightarrow{k_{RISC}} (S_1)^{St} \xrightarrow{En.\ T.} .(S_1)G$, (as shown in Figure 1.2.7b, right). By taking advantage of very high PLQY and RISC, avoiding direct injection to the guest, the η_{ext} of typical fluorescent emitters can greatly improve and reduce exciton loss.[29,30] Addition of fluorescence guest emitter to the system, the device stability can also improve due to reduced excited state lifetime. However, further optimization of suitable TADF sensitizer and finding guest

fluorescent emitter for hyperfluorescence systematic research is still necessary in this topic. Nonetheless, theoretically, this system offers the great advantage of increasing efficiency by keeping their colour purity of these typical fluorescence materials.

1.2.7. Room Temperature Phosphorescence (RTP)

Room temperature phosphorescence (RTP) is another effective triplet harvesting mechanism in metal-free organic molecules. Complementary to TADF materials, the discovery of organic RTP emitters has attracted great attention due to the low-cost synthesis, versatile molecular design and good processability, thereby showed potential for optoelectronic and biological applications, such as OLEDs,[31] imaging,[32] sensing,[33] optical thermometry[34] and anti-counterfeiting.[35] A simplified schematic of the RTP mechanism is illustrated in Figure 1.2.8a. In principle, under photo-excitation, the excitons from S_1 accumulate in the excited triplet manifolds (T_m) *via* a spin-flipping ISC process, followed by a radiative decay transition from T_1 to S_0, and the emission known as phosphorescence. Subsequently, the phosphorescence emission is concurrently competitive with nonradiative relaxations with thermal and collisional processes; therefore, phosphorescence is commonly seen only at low temperatures.[36] However, if the molecular vibration is suppressed and ISC rate is enhanced, efficient RTP can be achieved at room temperature. The rate constant of ISC (k_{ISC}) at room temperature is expressed in equation 1.2.10 as per first-order perturbation theory and Marcus semiclassical approach.[37]

$$k_{ISC} \propto \frac{\langle 1_\psi | \hat{H}_{SO} | 3_\psi \rangle^2}{\Delta E_{ST}} \qquad (1.2.10)$$

where 1_ψ, 3_ψ and ($\hat{H}_{SO}$) denoted the total electronic wavefunctions of singlet/triplet excited states and electrons spin-orbit coupling operator respectively. This shows that k_{ISC} is proportional to the $\hat{H}_{SO}$. Therefore, SOC played a significant role for phosphorescence. Several strategies were employed to enhance SOC including the incorporation of heavy atom (*e.g.* Br and I), halogen and/or hydrogen bonding, H-aggregation, rigid host matrix and high crystallinity, respectively Figure 1.2.8b.[38]

1.2.7.1. Excited-State Dynamics for RTP

According to El-Sayed's rule, to enhance the rate of ISC and achieve efficient SOC the radiationless transition between the two excited states involves the need to be changed in the orbital type. For example, the allowed transition between $^1(\pi,\pi*)$ and $^3(n,\pi*)$ leads to faster ISC than the relatively forbidden transition between $^1(\pi,\pi*)$ and $^3(\pi,\pi*)$ in the

absence of the heavy-atom effect or other SOC processes. To generate high yield triplet emission the rate of ISC must be higher than other competitive fluorescence-like transitions.[39] In the equation 1.2.10, the Hamiltonian ($\hat{H}_{SO}$) operator bears two parts: one as pure imaginary operator and other heavy-atom constant, where, the pure imaginary operator corresponds to the rotation of an orbital wavefunction at 90°. Therefore, the forbidden $^1(\pi,\pi*)$ to $^3(\pi,\pi*)$ transition is because SOC operator couples with the out-of-plane π-orbitals and becomes zero. On the contrary, the coupling of SOC operator couples the out-of-plane π-orbitals and the in-plane n orbital, and results in $^1(\pi,\pi*)$ to $^3(n,\pi*)$ or $^1(n,\pi*)$ to $^3(\pi,\pi*)$ as allowed transition Figure 1.2.8c. Therefore, the presence of n-orbital can promote SOC in a carbonyl group or heteroatoms (*e.g.* N, O, S and P) containing organic moieties. Like benzophenone, the ISC is allowed by the El-Sayed's rule and facilitated by a small energy difference (ΔE_{ST}).[40]

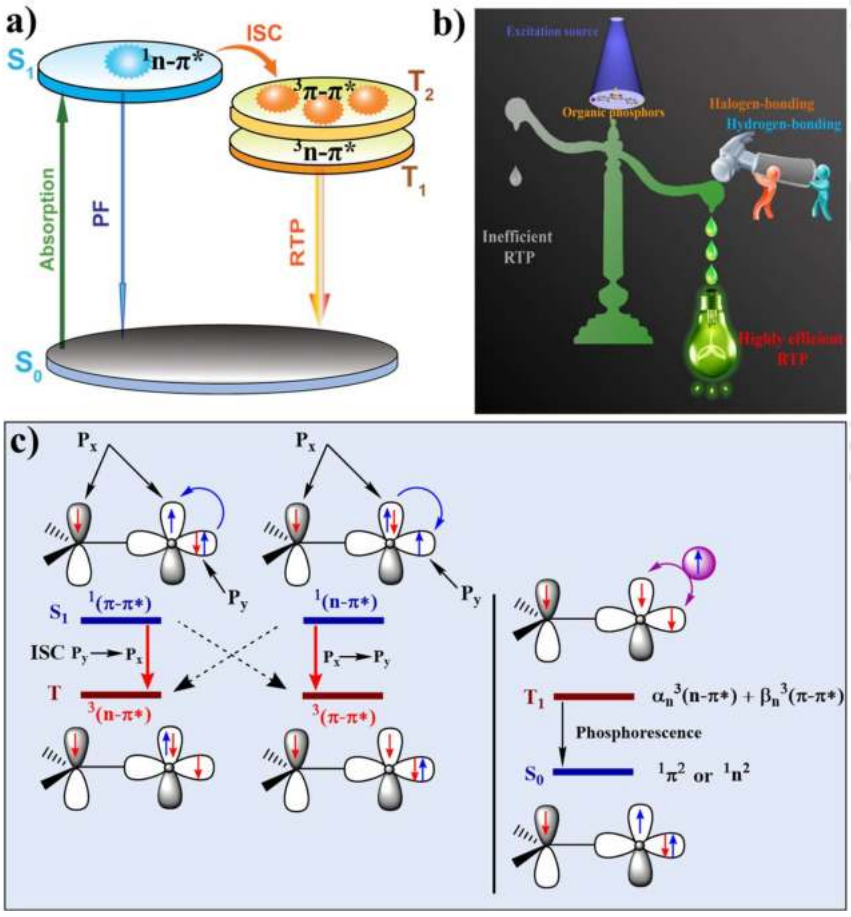

Figure 1.2.8. a) Jablonski diagram for room-temperature phosphorescence. b) Illustration of the triplet triggering factors for efficient RTP. c) Schematic representation of the El-Sayed's rule for allowed (solid lines) and forbidden (dotted lines) ISC and molecular-orbital hybridization of the lowest triplet states for tuning the rate of phosphorescence decay.

1.2.8. Lifetimes and Quantum Yields

The probability of a transition (radiative or non-radiative) per unit time between states describes the transition rate constant (k) as depicted in the Jablonski diagram. With the expression of transition rate constant, the excited state lifetime depicted as lifetime (τ) = $1/k$ and quantum yield as $\Phi = k/\Sigma k$ is associated during transition between states. More importantly, the rate constants of different relevant transitions provide crucial information to characterize and evaluate the potential of new organic materials for various applications. To distinguish each transition rates and the associated different kinetic process is denoted as a subscript: the rate constant of a non-radiative, ISC and RISC process is depicted as k_{nr}, k_{ISC}, and k_{RISC}, respectively. The rate constants of the fluorescence and phosphorescence radiative decays are represented by k_f and k_{ph}, respectively.

The lifetime of any chromophore is defined as the average time approximately a chromophore spends in the excited state before decaying to the ground state by emitting a photon.[41] In organic molecules, fluorescence decay from singlet excited state timescale within the range of tens of picoseconds to hundreds of nanoseconds, while the triplet excited state lifetime ranges from microseconds to milliseconds. The lifetimes of fluorescence (τ_f) and phosphorescence (τ_{ph}) are given by;

$$\tau_f = \frac{1}{k_f + k_{nr}^S + k_{ISC}} \qquad (1.2.11)$$

$$\tau_{ph} = \frac{1}{k_{ph} + k_{nr}^T} \qquad (1.2.12)$$

The efficiency of radiative decay in organic molecules is measured by photoluminescence quantum yield (PLQY, Φ), defined as the ratio of the number of photons emitted to the number of photons that are absorbed to generate the emission. The fraction of excited molecules that decays to the ground state as a form of fluorescence known as fluorescence quantum yield (Φ_F) and is given by;[1]

$$\Phi_F = \frac{k_f}{k_f + k_{nr}^S + k_{ISC}} = k_f \tau_f \quad (1.2.13)$$

The efficiency of the triplet formation as a form of quantum yield of ISC (Φ_{ISC}), also referred as the triplet yield (Φ_T) and denoted as;

$$\Phi_{ISC} = \frac{k_{ISC}}{k_f + k_{nr}^S + k_{ISC}} = k_{ISC} \tau_f \quad (1.2.14)$$

While the efficiency of RISC quantum yield (Φ_{RISC}), *i.e.* singlet yield (Φ_S) representing the yield of upconverted triplet to the singlet state, is mentioned as;

$$\Phi_{RISC} = \frac{k_{RISC}}{k_{RISC} + k_{nr}^{T} + k_{Ph}} \qquad (1.2.15)$$

The Phosphorescence quantum yield (Φph) is given by;

$$\Phi_{Ph} = \frac{k_{ph}}{k_{Ph} + k_{nr}^{T}} \Phi_{ISC} = \Phi_{ISC} k_{Ph} \tau_{ph} \qquad (1.2.16)$$

Rate constants can be calculated with the value of the quantum yields and lifetimes, according to the following equations;[8]

$$k_f = \frac{\Phi_F}{\tau_f} \qquad (1.2.17)$$

$$k_{ISC} = \frac{\Phi_{ISC}}{\tau_f} \qquad (1.2.18)$$

$$k_{nr}^{S} = \frac{1}{\tau_f} - k_f - k_{ISC} \qquad (1.2.19)$$

$$k_{RISC} = \frac{1}{\tau_{df}} \frac{\Phi_{RISC}}{1 - \Phi_{ISC}\Phi_{RISC}} = \frac{\Phi_{RISC}}{\tau_{df}} \left(\frac{\Phi_{pf} + \Phi_{df}}{\Phi_{df}} \right) \qquad (1.2.20)$$

Experimentally, $\Phi\tau_f$ and τ_{df} can be determined to calculate the various rate constants respectively.

1.2.9. Factors Affecting on TADF and RTP

1.2.9.1. Molecular Oxygen and Singlet Oxygen Generation

Molecular oxygen (O_2) is a non-polar, paramagnetic molecule that is very important while studying the photophysics of an organic molecule. Since it has two symmetrical electron spins on the ground triplet state, it is a notable exception. According to the Pauli exclusion principle, two anti-symmetrical electrons are occupying the HOMO (anti-bonding π* orbitals of same energy, P_x and P_y) or the ground triplet state. Subsequently, molecular oxygen can easily take the triplets of neighbouring molecule generated under photoexcitation and further transfer the energy from T_1 of the molecule to the T_0 of oxygen and behave as a triplet quencher and the phenomenon is known as photosensitization (Figure 1.2.9).[42] Due to this reason, characterization of the triplet harvesting mechanism

for TADF and RTP must be studied in absence of oxygen or air. Therefore, the presence of 20.8% oxygen in air effectively quenches the triplet emission such as phosphorescence and delayed fluorescence (by upconverted triplet) of organic chromophores, limiting the utilitiy of such emitters. Moreover, after photosensitization process the molecular oxygen gets converted to toxic singlet oxygen and is known as a reactive oxygen species (ROS). The generated ROS can be useful in bio-sensing, imaging and therapeutic applications because in living organisms oxygen has a significant importance and its level is quite relevant to the human cell activity.[43,44]

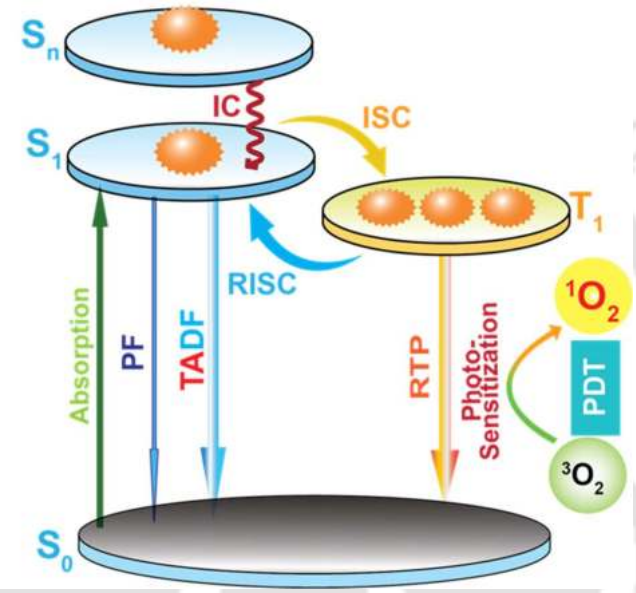

Figure 1.2.9. Schematic illustration of long-lived triplet inducing reactive singlet oxygen generation from surrounding ground triplet oxygen.

1.2.9.2. Host:Guest Interactions

Most organic emitters suffers from concentration induced excited state quenching and lead to decrease of the radiative decay efficiency, requiring the use of supporting host matrices.[45] Although recent studies shows that concentration quenching effect can be reduced by effective design strategies bypassing the need for host environment and a simplified device architecture. However, the lack of progress in appropriate design strategies for this specific topic remains slow.[46] Subsequently, the effects of host interactions induced chromophore orientation is another interesting topic that has been growing attention.[47] Over several years, three key strategies were developed, such as rigid matrix, exiplex and sensitization respectively. In all the cases emissive material is randomly embeded into a rigid host material (having good film forming properties and ambipolar

characteristics). In the thin film, such inert host matrices reduce the molecular aggregation and oxygen quenching related issues by rigidifying the environment.[48] Moreover, at low concentrations of guest/donor in the rigid host matices, appropriate alignment of HOMO/LUMO within host, guest and other associated charge injection layer, the host will have the function of promoting charge/energy transport and exciton formation in the emissive guest molecule (Figure 1.2.10). For efficient charge/energy transportation and to avoid triplet quenching in the devices, the triplet energy of the host molecule must be higher than the guest molecule. For efficient RTP materials, the host has a significant effect to characterize the inherent triplet-harvesting mechanism.

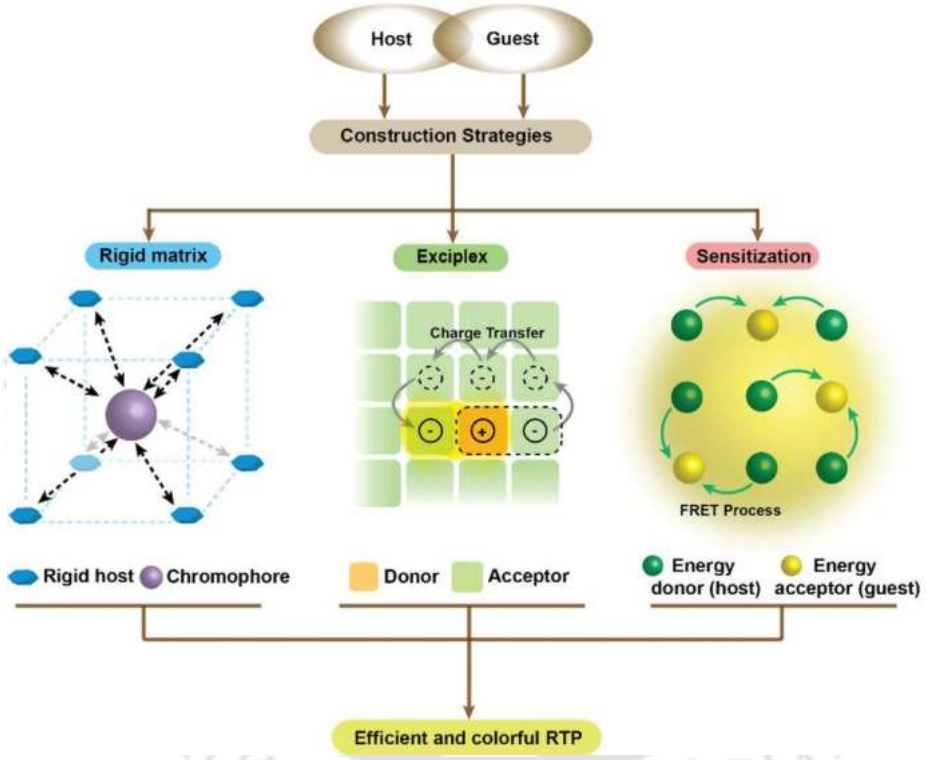

Figure 1.2.10. Schematic drawing of different construction strategies for host-guest RTP material systems.

1.2.9.3. Solvatochromism

In Figure 1.2.11 it is shown that the minimization of the energy gap can be controlled from the CT energy onset. Although, initially CT is controlled by adjusting the appropriate polarity of the host and embedding it into the TADF emitter. However, for a D-A architecture, twisted intramolecular charge transfer (TICT) played great importance in exhibiting TADF property owing to the inherent dipole moment.[49] Due to the large dipole moment of the CT state, the solute molecules strongly interact with local solvent molecules

and reorient to form favourable dipolar interactions. In the ground and excited state geometries, the dipolar interactions are different. For a TADF molecule, rearrangement of the solvent shell around the molecule, shield the molecular dipole and therefore lowers the total energy of the system. Collectively, this interaction changes the emission spectrum of the TADF emitter in terms of position, intensity, and shape of the spectroscopic bands. The most obvious effect is, change in the emission colour in solutions with different polarity, also known as solvatochromic effects, or solvatochromism.[50]

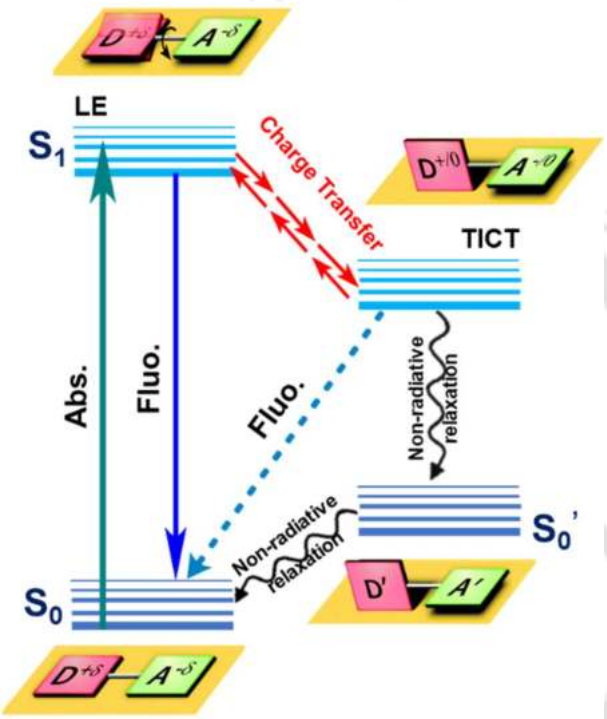

Figure 1.2.11. Illustration of twisted intramolecular charge transfer (TICT) dynamics.

A negative solvatochromism is defined by its hypsochromic shift and refers to higher energy blue-shifted emission, whereas positive solvatochromism is depicted by its bathochromic shift and refers to lower energy red-shifted emission.[51] The polarity of the environment can not change the LE emission profile, as LE does not possess any dipole moment. Therefore, optimization of environment polarity (or doped into appropriate polarity of the host) is necessary to shift the CT down towards the ^{3}LE to minimize the ΔE_{ST} gap for achieving TADF.

1.2.9.4. Packing Effects

Ground state and excited state geometry of the emitter can be regulated by the packing of the molecule. In particular, variation of packing arrangement effects the dihedral angle of the D-A structure. Therefore, the LE and CT state character is strongly affected due to the separation of HOMO/LUMO and conjugation across the emitter effects the excited state properties.[52] Moreover, in aggregate/solid state fluorescence lifetime and spectral shift are stimulated by special structural alignments, classified as H-, J- and X- aggregate, which arises from the orientation of coupled transition dipole between interacting chromophores (Figure 1.2.12). While the angle between the structural alignment of the interacting molecules and transition dipole orientation is known as the "*slippage angle*". The long axis of one molecule and the line connecting the centers of the molecules formed this "*slippage angle*". According to Kasha's theory, the angles <54.7° are for high slippage aggregates, and a head-to-tail orientation of the transition dipoles leads to J- and X-aggregation.[53] However, as the angles >54.7° are for low slippage aggregates and parallel orientation of the transition dipoles, they lead to H-aggregation.[54] The difference in aggregation pattern effects both the ground state and excited state properties. Therefore, H-aggregation shows hypsochromically shifted or blue-shifted (higher energy) absorption and fluorescence spectra with a relatively broad emission spectrum and longer excited state lifetime than monomer.[55]

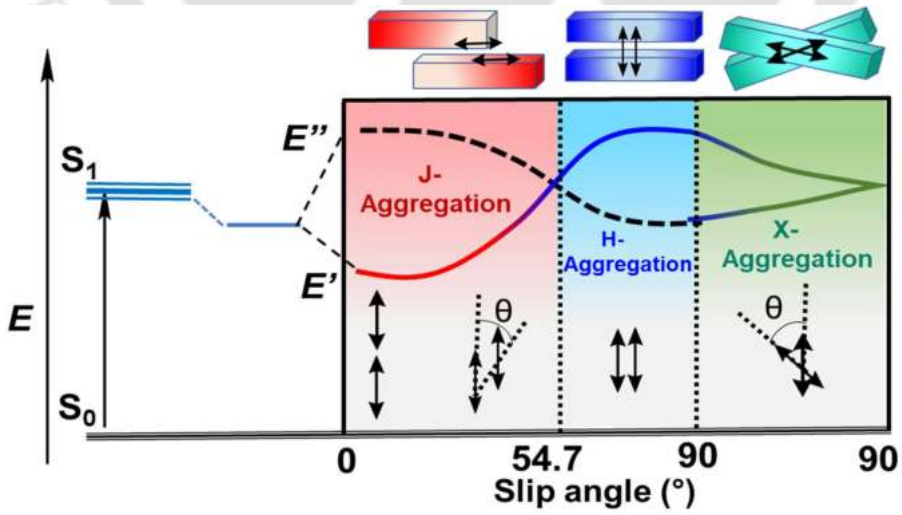

Figure 1.2.12. Illustration of excited states energy splitting diagram for molecular J-aggregate, H-aggregate, X-aggregate with slippage angle of transition dipoles coupling configuration.

In contrast, bathochromically shifted or red-shifted (lower energy) absorption and emission observed due to J- and X-aggregation, with a narrow emission band and reduced excited state lifetime compared to the monomer. Therefore, dihedral angle of D-A and slippage angle of molecules in the aggregated state effectively influence the TADF and RTP performance of an emitter.

1.2.10. Aggregation Induced emission and Excited-State Dynamics

Over the last two decades, substantial research on AIE-active materials has been conducted in material science, analytical chemistry, and life sciences.[56,57] Hence, AIE luminogens have sparked the curiosity on mechanistic aspects of bright solid state luminescence in various segments of the scientific community. Research on the mechanisms of quenching in solution and emission in the solid state began after the discovery of prototypical AIEgens like pentaphenylsilole and tetraphenylethene (TPE), where restriction of both rotation (RIR) and vibration (RIV) is proposed as a reason of fluorescence enhancement in aggregates/solid state.[58] By principle, RIR and RIV control the non-radiative decay pathways to exhibit AIE.[59,60] Further investigations depicted that few other AIE phenomena occur as a consequence of multiple processes which includes E/Z isomerization, J-type aggregation, twisted intramolecular charge transfer (TICT) and excited state intramolecular proton transfer (ESIPT), respectively in variety of molecular systems Figure 1.2.13a,b.[61-63] Despite a few well-explored mechanisms for each and every independent system, no general mechanism has been elucidated for AIE in a rational manner. Eventually, a question comes to mind "*What is essential in the AIE mechanism?*"

1.2.10.1. Potential Energy Surface Crossing

To answer this question, we must consider the necessary theoretical calculations and experiments for independent quantum chemical aspects of minimum energy conical intersection (MECI) and potential energy surface (PES) in the excited states during non-radiative decays.[64] In solution, the distorted structure of MECI is easily accessed while it becomes difficult to access in the solid state. The accessibility of the conical intersection (CI) mainly regulates the non-radiative decay rate and fluorescence quantum yield, which can be explained based on the PES mechanism **(**Figure 1.2.13c**)**.[65.66] In solution, the non-radiative decay is promoted due to the low-lying conical intersection and therefore fast internal conversion leads to low PLQY. In contrast, at the aggregated/solid state, large

amplitude modes such as ring puckering prohibits the internal conversion, therefore enhancing the PLQY significantly.

1.2.10.2. Anti-Kasha's Emission

Mostly, traditional fluorophores reported till date were found to emit light by following Kasha's rule,[67] which states that radiative decay (fluorescence / phosphorescence) occurs only from the lowest exited states to ground state (S_1/T_1 to S_0), irrespective of the initial photoexcited state.[68] Yet, as an exception to this rule, anti-Kasha's rule could be accomplished by retardation of ultrafast vibrational relaxation and internal conversion from higher excited states to S_1 if the energy gap between S_n-S_1 is quite large.[69] By restricting access to the crossing of PES, the excited molecule on higher excited states (>S_1) shows bright emissions due to the high energy barrier. In particular, emission from states other than S_1 and T_1 is extremely difficult to realize in condensed/solid-state owing to a significant amount of fast vibration or collisional relaxation in the upper-lying excited states. On the contrary, the participation of many higher-lying excited singlet (S_n) and triplet (T_m) states could result in dual-/multi-mode emissions *via* anti-Kasha mechanism.[70]

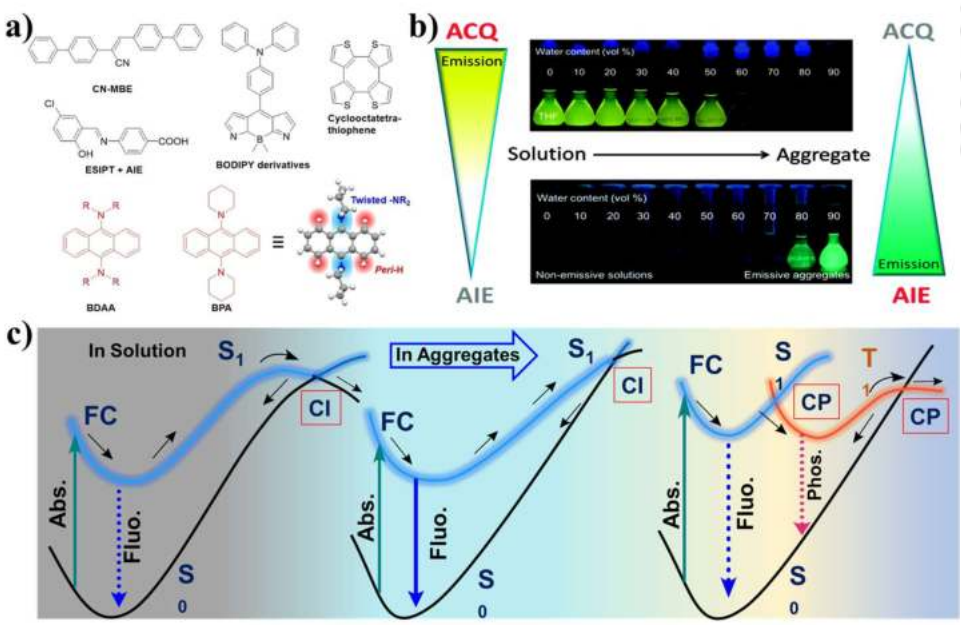

Figure 1.2.13. (a) Chemical structures of unconventional AIEgens. (b) Images of ACQ and AIE phenomenon. (c) Schematic illustration of a AIE typical potential energy surface (PES). Left: Low conical intersection (CI) causes competition between fluorescence and internal conversion through a CI. Middle: If a CI is sufficiently high, fluorescence becomes dominant. Right: In some cases, an ISC to the triplet state occurs, where phosphorescence ensures.

Many experimental and theoretical efforts have been devoted to accomplishing anti-Kasha emissive molecular rotors because such emissive pathways can ideally avoid additional consumption from internal conversions and other forms of electronic relaxation. These features are beneficial for the improved luminescent quantum efficiency in aggregated/solid state.[71] Therefore, anti-Kasha effect opens new possibilities for the fundamental understanding of the new-generation emissive materials, especially focusing on multi-wavelength emissions or AIE effect.[72]

1.2.11. Single Molecule White-Light Emission and Excited-State Dynamics

White-light-generating emitters have great potential for use in flat-panel displays and have attracted broad interest in future light sources.[73,74] Conventional strategy of white-light emission from multicomponent organic white-light emitters were accomplished by the rational blending of red/green/blue or blue/orange emitters, which covers the complete visible-light emission spectrum region. Usually, white-light emission is exhibited *via* multicomponent fluorescent blends,[75] that typically include monomer/excimer complex,[76] inter/intramolecular charge transfer (ICT),[77] Förster resonance energy transfer (FRET),[78] and excited-state intramolecular proton transfer (ESIPT),[79] etc. However, white radiative decay from both singlet and triplet excitons has been recently found in TADF and RTP molecules.[80-82] Moreover, the development of single molecule white light emitters (SMWLEs) with multi-functional additional exciting key properties are under investigation owing to their superior performances, no phase segregation, no colour aging with improved stability, good reproducibility and simple device fabrication protocols.[83] In addition, by introducing AIE functionality in white TADF emitters, efficient device results have been realized by overcoming the complex material arrangements and by appropriate doping of materials into the host to achieve high EQE.[84] Thus, simple material based high performance organic white-light emitter fabrication is still a challenge. Moreover, an ever-increasing demand to use them as solution-processed non-doped fabrication technique gives them an extra edge over other existing methods for solid-state lighting. Recently, a few strategies have been developed such as: a) dual fluorescence from two states: commonly LE, CT, dual LE and dual CT states could generate white light via structural isomerism, ESIPT, and excimer formation (Figure 1.2.14a)[85] b) fluorescence and phosphorescence: by adjusting the equilibrium between singlet and triplet excitons after photoexcitation, the strength of ISC could be manipulated (Figure 1.2.14b)[86] c) dual phosphorescence with Anti-Kasha's behavior: (Figure 1.2.14c)

A rare but interesting phenomenon which violates Kasha's rule and the molecules can emit light from a higher excited state[87,82] (e.g., S_n and T_n, n≥2), originally discovered in azulene in 1955. Such molecules displayed dual phosphorescence typically at two conditions,

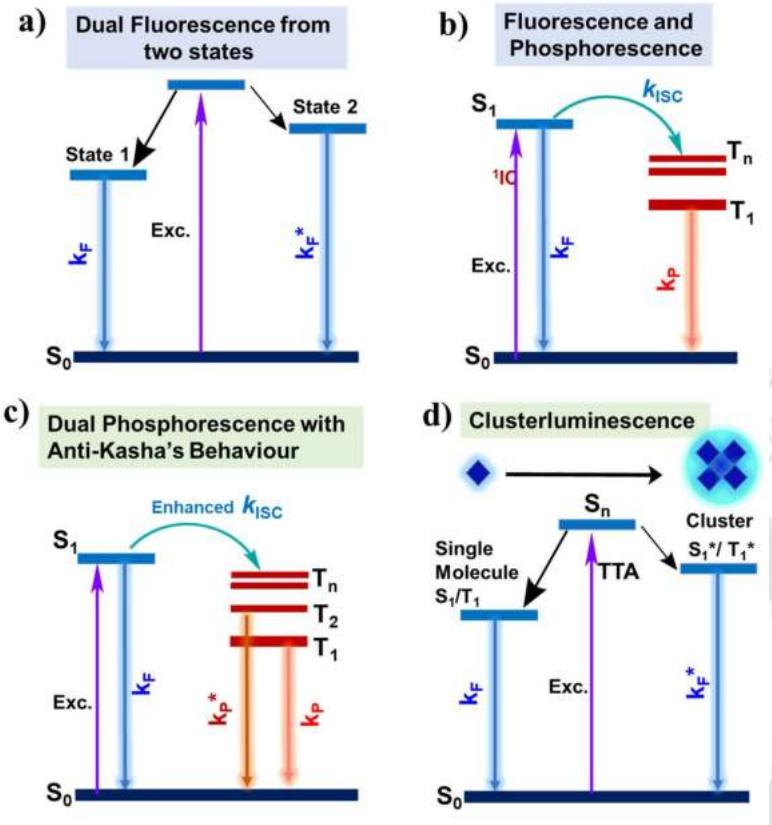

Figure 1.2.14. General scheme to achieve white-light emission from single-component organic aggregates.

1) at the large energy difference between T_n, (n≥2) and T_1, 2) radiative rate of a higher triplet state is much faster than that of T_1, collectively resulting in dual phosphorescence from two triplet states, d) clusteroluminescence: unlike traditional through-bond conjugation based white emissive compounds, many nonconjugated or poorly conjugated systems such as polystyrene and maleimide emit white light in the aggregated state, by forming clusters and this exceptional photophysical process is termed as clusteroluminescence (Figure 1.2.14d).[88] Strong intermolecular and intramolecular interactions including electronic delocalization and coupling between electron-rich groups (e.g., carbonyl, hydroxyl, and sulfhydryl groups) can generate new emissive species, therefore playing a vital role in stabilizing the excitons to produce clusteroluminescence.

1.2.12. References

[1] B. Valeur, M. N. Berberan-Santos, *Molecular fluorescence: principles and applications* (John Wiley & Sons, 2012).

[2] L. De Broglie, *Particules de spin 1/2* (Gauthier-Villars, Paris, 1952).

[3] B. Wardle, *Principles and applications of photochemistry* (John Wiley & Sons, 2009).

[4] A. Köhler, H. Bässler, Triplet states in organic semiconductors, *Mater. Sci. Eng. R Rep.,* **2009***, 66*, 71-109.

[5] W. Pauli, Exclusion principle, Lorentz group and reflection of space-time and charge.

[6] D. J. Griffiths, D. F. Schroeter, *Introduction to quantum mechanics* (Cambridge University Press, 2018).

[7] N. J. Turro, V. Ramamurthy, J. C. Scaiano, *Principles of molecular photochemistry: an introduction* (University science books, 2009).

[8] F. B. Dias, T. J. Penfold, A. P. Monkman, *Methods Appl. Fluoresc.,* **2017**, *5*, 012001.

[9] M. Born, R. Oppenheimer, Zur quantentheorie der molekeln. *Annalen der Physik,* **1927**, *389*, 457-484.

[10] P. A. M. Dirac, *Proc. R. Soc. London. Ser. A. Math. Phys. Sci.,* **1927**, *114*, 243-265.

[11] W. Heitler, *The quantum theory of radiation,* Courier Corporation, **1984**.

[12] E. J. Bowen, *The chemical aspects of light,* Clarendon Press, **1949**.

[13] M. Kasha, *Discuss. Farad. Soc.,* **1950**, *9*, 14-19.

[14] A. Köhler, H. Bässler, *Electronic Processes in Organic Semiconductors*, **2015**.

[15] K. S. Yook, J. Y. Lee, *Adv. Mater.,* **2012**, *24***,** 3169–3190.

[16] M. A. Baldo, D. F. O'Brien, Y. You, A. Shoustikov, S. Sibley, M. E. Thompson, S. R. Forrest, *Nature,* **1998**, *395***,** 151–154.

[17] M. A. El-Sayed, *Acc. Chem. Res.,* **1968**, *1,* 8–16.

[18] Z. Yang, Z. Mao, Z. Xie, Y. Zhang, S. Liu, J. Zhao, J. Xu, Z. Chi, M. P. Aldred, *Chem. Soc. Rev.,* **2017**, *46*, 915-1016.

[19] P. Rajamalli, N. Senthilkumar, P. Gandeepan, P. –Y. Huang, M. –J. Huang, C. –Z. Ren-Wu, C.-Y. Yang, M.-J. Chiu, L.-K. Chu, H. –W. Lin, C. –H. Cheng, *J. Am. Chem. Soc.,* **2016**, *138*, 628−634.

[20] J. H. Kim, J. H. Yun, J. Y. Lee, *Adv. Opt. Mater.,* **2018**, *6*, 1800255.

[21] X. –K. Chen, Y. Tsuchiya, Y. Ishikawa, C. Zhong, C. Adachi, J. –L. Brédas, *Adv. Mater.,* **2017**, *29*, 1702767.

[22] B. T. Lim, S. Okajima, A. K. Chandra, E. C. Lim, *Chem. Phys. Lett.,* **1981**, *79*, 22–27.

[23] J. Gibson, A. P. Monkman, T. J. Penfold, *Chem. Phys. Chem.,* **2016**, *17*, 2956–2961.

[24] C. M. Marian, *J. Phys. Chem. C,* **2016**, *120*, 3715–3721.

[25] X.-K. Chen, S.-F. Zhang, J.-X. Fan, A.-M. Ren, *J. Phys. Chem. C,* **2015**, *119*, 9728–9733.

[26] C. A. Parker, *Proc. R. Soc. London. Ser. A. Math. Phys. Sci.,* **1963**, *276*, 125–135.

[27] D. Y. Kondakov, *Philos. Trans. R. Soc. A Math. Phys. Eng. Sci.,* **2015**, *373*, 20140321–20140321.

[28] . T. Northey, T. J. Penfold, *Org. Electron.,* **2018**, *59*, 45–48.

[29] . K.-H. Kim, S.-J. Yoo, J.-J. Kim, *Chem. Mater.,* **2016**, *28*, 1936–1941.

[30] S. K. Jeon, H. Park, J. Y. Lee, *ACS Appl. Mater. Interfaces,* **2018**, *10*, 5700–5705.

[31] R. Kabe, N. Notsuka, K. Yoshida, C. Adachi, *Adv. Mater.,* **2016**, *28*, 655-660.

[32] G. Zhang, G. M. Palmer, M. W. Dewhirst, C. L. Fraser, *Nat. Mater.,* **2009**, *8*, 747.

[33] O. S. Wolfbeis, Sensor paints. *Adv. Mater.,* **2008**, *20*, 3759-3763.

[34] L. Jethi, M. M. Krause, P. Kambhampati, *J. Phys. Chem. Lett.,* **2015**, *6,* 718-721.

[35] L. Xiao, Y. Wu, J. Chen, Z. Yu, Y. Liu, J. Yao, H. Fu. *J. Phys. Chem. A*, **2017**, *121*, 8652-8658.

[36] W. Zhao, Z. He, J. W.Y. Lam, Q. Peng, H. Ma, Z. Shuai, G. Bai, J. Hao, B. Z. Tang, *Chem,* **2016**, *1*, 592-602.

[37] K. Schmidt, S. Brovelli, V. Coropceanu, D. Beljonne, J. Cornil, C. Bazzini, T. Caronna, R. Tubino, F. Meinardi, Z. Shuai, J.-L. Brédas. *J. Phys. Chem. A,* **2007**, *111*, 10490-10499.

[38] M. A. El-Sayed, Spin-Orbit coupling and the radiationless processes in nitrogen heterocyclics. *J. Chem. Phys.,* **1963**, *38*, 2834-2838.

[39] C. M. Marian, Spin{orbit coupling and intersystem crossing in molecules. *Wiley Interdisciplinary Reviews: Comp. Mol. Sci.,* **2012**, *2*, 187-203.

[40] M. A. El-Sayed *J. Chem. Phys.,* **1963**, *38*, 3032.

[41] D. M. Hercules, Fluorescence and phosphorescence analysis: principles and applications. *Fluorescence and Phosphorescence Analysis: Principles and Applications/Ed. David M. Hercules. New York, NY: Interscience Publishers,* **1966**, *c1966*.

[42] N. J. Turro, *Modern Molecular Photochemistry* (University Science Books, Sausalito CA, 1991)

[43] C. Schweitzer, R. Schmidt, *Chem. Rev.,* **2003**, *103,* 1685-1757.

[44] . W. Tian, L. Deng, S. Jin, H. Yang, R. Cui, Q. Zhang, W. Shi, C. Zhang, X. Yuan, G. Sha, *J. Phys. Chem. A,* **2015**, *14*, 3393-3399.

[45] P. L. dos Santos, J. S. Ward, M. R Bryce, A. P. Monkman, *J. Phys. Chem. Lett.,* **2016**, *7***,** 3341–3346.

[46] X. Zhang, M. W. Cooper, Y. Zhang, C. Fuentes-Hernandez, S. Barlow, S. R. Marder, B. Kippelen, *ACS Appl. Mater. Interfaces,* **2019**. *11*, 12693–12698.

[47] Y. Watanabe, H. Sasabe, J. Kido, *Bull. Chem. Soc. Jpn.,* **2019**, *92***,** 716–728.

[48] Z. Xie, X. Zhang, H. Wang, C. Huang, H. Sun, M. Dong, L. Ji, Z. An, T. Yu, W. Huang *Nat Commun*., **2021**, *12*, 3522.

[49] T. Northey, J. Stacey, T. J. Penfold, *J. Mater. Chem. C,* **2017**, *5,* 11001–11009.

[50] S. Nigam, S. Rutan. *Appl. Spec.,* **2001**, *55*, 362A-370A

[51] A. Marini, A. Munoz-Losa, A. Biancardi, B. Mennucci, *J. Phys. Chem. B,* **2010**, *114*, 17128-17135.

[52] P. L. dos Santos, J. S. Ward, D. G. Congrave, A. S. Batsanov, J. Eng, J. E. Stacey, T. J. Penfold, A. P. Monkman, M. R. Bryce *Adv. Sci.,* **2018**, *5***,** 1700989.

[53] F. Wurthner, T. E. Kaiser, C. R. Saha-Moller, *Angew. Chem. Int. Ed.,* **2011**, *50*, 3376-3410.

[54] D. Chaudhuri, D. Li, Y. Che, E. Shafran, J. M. Gerton, L. Zang, J. M. Lupton, *Nano Lett.,* **2011**, *11*, 488-492

[55] S. Ma, S. Du, G. Pan, S.Dai, B. Xu, W. Tian, *Aggregate,* **2021**, *2*, e96.

[56] D. Ding, K. Li, B. Liu, B. Z. Tang, *Acc. Chem. Res.,* **2013**, *46*, 2441 – 2453.

[57] J. Mei, Y. Hong, J. W. Y. Lam, A. Qin, Y. Tang, B. Z. Tang, *Adv. Mater.,* **2014**, *26*, 5429 – 5479.

[58] Z. Zhao, B. He, B. Z. Tang, *Chem. Sci.,* **2015**, *6*, 5347 – 5365.

[59] S. Yin, Q. Peng, Z. Shuai, W. Fang, Y.-H. Wang, Y. Luo, *Phys. Rev., B* **2006**, *73*, 205409.

[60] N. L. C. Leung, N. Xie, W. Z. Yuan, Y. Liu, Q. Wu, Q. Peng, Q. Miao, J. W. Y. Lam, B. Z. Tang, *Chem. Eur. J.,* 2014, 20, 15349 – 15353.

[61] R. Hu, E. Lager, A. Aguilar-Aguilar, J. Liu, J. W. Y. Lam, H. H. Y. Sung, I. D. Williams, Y. Zhong, K. S. Wong, E. PeÇaCabrera, B. Z. Tang, *J. Phys. Chem. C,* **2009**, *113*, 15845 – 15853.

[62] P. Song, X. Chen, Y. Xiang, L. Huang, Z. Zhou, R. Wei, A. Tong, *J. Mater. Chem.,* **2011**, *21*, 13470 – 13475.

[63] Z. Zhao, X. Y. Zheng, L. L. Du, Y. Xiong, W. He, X. X. Gao, C. L. Li, Y. J. Liu, B. Xu, J. Zhang, F. Y. Song, Y. Yu, X. Q. Zhao, Y. J. Cai, X. W. He, R. T. K. Kwok, J. W. Y. Lam, X. H. Huang, D. L. Phillips, H. Wang, B. Z. Tang, *Nat. Commun.,* **2019**, *10*, 2952.

[64] S. Sasaki, K. Igawa, G. Konishi, *J. Mater. Chem. C,* **2015**, *3*, 5940 – 5950.

[65] S. Sasaki, S. Suzuki, W. M. C. Sameera, K. Igawa, K. Morokuma, G. Konishi, *J. Am. Chem. Soc.*, **2016**, *138*, 8194 – 8206.

[66] S. Sasaki, S. Suzuki, K. Igawa, G. Konishi, *J. Org. Chem.,* **2017**, *82*, 6865 – 6873.

[67] A. P. Demchenko, V. I. Tomin, P.-T. Chou, *Chem. Rev.,* **2017,** *117*, 13353-13381.

[68] M. Kasha, *Discuss. Faraday Soc.,* 1950, *9*, 14-19.

[69] S. Scuppa, L. Orian, A. Donoli, S. Santi, M. Meneghetti, *J. Phys. Chem. A,* **2011**, *115*, 8344-8349.

[70] O. Yushchenko, G. Licari, S. Mosquera-Vazquez, N. Sakai, S. Matile, E. Vauthey, *J. Phys. Chem. Lett.,* **2015**, *6*, 2096-2100.

[71] H. Qian, M. E. Cousins, E. H. Horak, A. Wakefield, M. D. Liptak, I. Aprahamian, *Nat. Chem.,* **2017**, *9*, 83-87.

[72] B. H. Jhun, D. Y. Jeong, S. Nah, S. Y. Park, Y. You, *J. Mater. Chem. C,* **2021**, *9*, 7083-7093.

[73] Y. Liu, M. Nishiura, Y. Wang, Z. Hou, *J. Am. Chem. Soc.,* **2006**, *128*, 5592.

[74] G. M.Farinola, R.,Ragni, *Chem. Soc. Rev.,* **2011**, *40*, 3467-3482.

[75] Y. Yang, M. Lowry, C. M. Schowalter, S. O. Fakayode, J. O. Escobedo, X. Xu, H. Zhang, T. J. Jensen, F. R. Fronczek, I. M. Warner, R. M. Strongin, *J. Am. Chem. Soc.,* **2006**, *128*, 14081.

[76] Y.-H. Chen, K.-C. Tang, Y.-T. Chen, J.-Y. Shen, Y.-S. Wu, S.-H. Liu, C.-S. Lee, C.-H. Chen, T.-Y. Lai, S.-H. Tung, R.-J. Jeng, W.-Y. Hung, M. Jiao, C.-C. Wu, P.-T. Chou, *Chem. Sci.,* **2016**, *7*, 3556.

[77] H. Naito, K. Nishino, Y. Morisaki, K. Tanaka, Y. Chujo, *Angew. Chem., Int. Ed.,* **2017**, *56*, 254.

[78] D. K. Maiti, R. Bhattacharjee, A. Datta, A. Banerjee, *J. Phys. Chem. C,* **2013**, *117*, 23178.

[79] K.-C. Tang, M.-J. Chang, T.-Y. Lin, H.-A. Pan, T.-C. Fang, K.-Y. Chen, W.-Y. Hung, Y.-H. Hsu, P.-T. Chou, *J. Am. Chem. Soc.,* **2011**, *133*, 17738.

[80] B. Xu, Y. Mu, Z. Mao, Z. Xie, H. Wu, Y. Zhang, C. Jin, Z. Chi, S. Liu, J. Xu, Y.-C. Wu, P.-Y. Lu, A. Lien, M. R. Bryce, *Chem. Sci.,* **2016**, *7*, 2201.

[81] B. Xu, H. Wu, J. Chen, Z.Yang, Z. Yang, Y.-C. Wu, Y. Zhang, C. Jin, .-Y. Lu, Z. PChi, S. Liu, J. Xu, M. Aldred, *Chem. Sci.,* **2017**, *8*, 1909.

[82] Z. He, W. Zhao, J. W. Y. Lam, Q. Peng, H. Ma, G. Liang, Z. Shuai, B. Z. Tang, *Nat. Commun.,* **2017**, *8*, 416.

[83] H. Al-Attar, A. Monkman, *Adv. Funct. Mater.,* **2012,** *22*, 3824.

[84] Z. Chen, C.-L. Ho, L. Wang, W.-Y. Wong, *Adv. Mater.,* **2020***, 32*, 1903269.

[85] N. A. Kukhta, M. R. Bryce, *Mater. Horiz.,* **2021***, 8*, 33–55.

[86] J. Wang, X. Gu, H. Ma, Q. Peng, X. Huang, X. Zheng, S. H. P. Sung, G. Shan, J. W. Y. Lam, Z. Shuai, B. Z. Tang, *Nat. Commun.,* **2018**, *9*, 2963.

[87] Z. He, W. Zhao, J. W. Y. Lam, Q. Peng, H. Ma, G. Liang, Z. Shuai, B. Z. Tang, *Nat. Commun.,* **2017**, 8, 416.

[88] H. Zhang, Z. Zhao, P. R. McGonigal, R. Ye, S. Liu, J. W.Y. Lam, R.T.K. Kwok, W. Z. Yuan, J. Xie, A. L. Rogach, B. Z.Tang, *Mater. Today*, **2019**, *32*, 275–292.

Synopsis

The content of this present thesis entitled "***Modulation of Ground and Excited State Dynamics in Donor-Acceptor Organic Functional Small Molecules for Photonics and Biomedical Applications"*** comprises of seven chapters.

Chapter 1: This chapter includes research motivation, fundamental aspects, background and summary of conventional to current organic photo-functional molecules with their exciting excited-state dynamical properties and versatile applications in the following chapters.

Chapter 2: This chapter presents two kinetically controlled supramolecular charge transfer (CT) complexes were conceptualized from a trimorphic molecular donor denoted as "twisted aromatic hydrocarbon" (TAH), with p-fluoranil (TFQ) and p-chloranil (TCQ) in water, organic solvent, and solvent-free methods. Elucidating their co-assembling mechanism revealed that segmentation of the TAH with acceptors, spontaneously formed a distinct "H-type mixed stack" and "J-type segregated stack", regulated by blue/red-shifted CT interactions. By utilizing the structural transformational ability of the self-assembled TAH, the mechanistic aspects for the rapid nanoscopic co-assembly formation were precisely demonstrated experimentally and theoretically. The trimorphs and co-crystals of TAH could be disassembled resulting in turn-on emission by applying various external stimuli and being repeatedly reconfigured, thus providing a unique "structure-property relationship" and new TAH-based materials. This unique concept offers color-specific polymorphism and CT-complex formation strategy involving a simple class of functional materials having co-operative network forming ability using the twisted molecular donor.

Chapter 3: This chapter demonstrates the use of twisted donor, TAH with various rigid planar acceptors of octafluoronaphthalene (OFN), tetrafluoropterepthanitrile (TFPN) and 1,2,4,5-tetracyanobenzene (TCNB) for switchable excited-state properties and optical wave-guide functions. The integrated four fluorescent color-tunable dynamic co-crystals, TAHOFN, color-specific polymorphs of TAHTFPN_G and TAHTFPN_O including triplet harvesting thermally activated delayed fluorescence (TADF) properties of TAHTCNB were prepared by adjusting the strength of acceptor units. A structural transformation into hybrid stacking mode, H-type mixed stack and J-type segregated stack *via.* dissimilar CT-properties, results into tunable energy band gap, variable CT degree and presence of hydrogen-bonding interactions between aromatic cores conveying improved

physicochemical properties. In addition, co-crystals displayed active optical wave-guiding properties with ultra-low optical loss co-efficient (0.44 dB/μm for TAHOFN, 0.0742 dB/μm for TAHTFPN and 0.0837 dB/μm for TAHTCNB). These findings provide considerable insights and open up a new way for the future design and development of novel multifunctional materials *via.* a universal "dynamic luminescent co-crystal engineering" strategy.

Chapter 4: This chapter demonstrates through-space donor-alkyl bridge-acceptor (D-σ-A) luminogens are developed as new organic single-molecule white light emitters (OSMWLEs) involving multiple higher lying singlet (Sn) and triplet (Tm) states (hot-excitons). Experimental and theoretical results confirm the origin of white light emission due to the co-existence of prompt fluorescence from locally excited state, thermally activated delayed fluorescence (TADF), and fast/slow dual phosphorescence color mixing simultaneously. Notably, the fast phosphorescence is inherited by trace amounts of isomeric impurities from commercial carbazole, while H-/J-aggregation results in slow phosphorescence. Single crystal X-ray structures, and the alkyl chain length induced supramolecular self-assembly greatly influence the solid-state optical properties. Remarkably, the 1D-microrod crystals of OSMWLEs demonstrate the first examples of triplet harvesting waveguides by self-guiding the generated phosphorescence through light propagation along its longitudinal axis. This work thus highlights an uncommon design strategy to achieve multi-functional OSMWLEs with in-depth mechanistic insights and optical waveguiding applications endowing them as potentially new class of white emissive materials.

Chapter 5: This work presents a series of through-space donor-alkyl bridge-acceptor (D-σ-A) luminogens, BT2OxCz [2,2'-(5-(3-(9H-carbazol-9-yl)alkoxy)-1,3-phenylene)bis(benzothiazole)] (x = 3, 4, 5 and 6) as new anti-Kasha emissive AIEgens conveyed for the first time. Experimental and theoretical results confirmed that the origin of AIE, co-existence of dual fluorescence and phosphorescence in water at room temperature are realized via multiple higher-lying excited states (hot excitons), especially from the bright emissive states of S7/S5 and T3, that have never been observed previously via suppression of Kasha's rule (SOKR). Precise photophysical studies, single-crystal structures and quantum-mechanical (static and dynamic) studies revealed that large energy gaps (ΔEST) between S7/S5 and S1 states (T3 and T1 states) along with an abundance of small ΔEST between singlet charge transfer (1ICT) and triplet locally excited (3LE) states

facilitates reverse intersystem crossing (rISC) resulting in TADF and RTP simultaneously. Single crystal structures depicted that alkyl chain length induced supramolecular self-assembly displayed distinct H- and J-aggregation, including strong intra and intermolecular hydrogen bonds suppressing internal conversions and promoting intersystem crossing within the upper excited states and making possible multi-mode emissions by evolving hot-excitons. Structural rigidity/flexibility presents a unique molecular skeleton for achieving multi-colored emissions of two different reversible mechanoresponsive behavior viz. mechanoluminescence and mechanochromism in powder and polymer films, respectively. This work thus highlights an uncommon design strategy of multifunctional AIEgens with in-depth mechanistic insights, endowing them as a potentially new class of anti-Kasha emissive materials.

Chapter 6: Image-guided photodynamic therapy (PDT) has been acknowledged as one of the most demonstrative therapeutic modalities for cancer treatment, owing to its precision, non-invasiveness and improved imaging ability. Unlike, conventional photosensitizers (PSs) with low contrast imaging, weaker sensitivity and dark cytotoxicity, herein, we have designed and synthesized a series of purely organic PSs denoted as BTMCZ, BTMPTZ and BTMPXZ, exhibiting thermally activated delayed fluorescence (TADF) and aggregation induced emission (AIE) characteristics. Experimental and theoretical studies revealed that modulation of donor in the PSs enables to finely adjust energy gap (ΔEST) via second-order spin-orbit perturbation, involving lowest singlet (1CT) and higher-lying triplet (3LE) states along with rigid crystal packing of H-, X, and J-type aggregation greatly influencing Color-tunable up-converted luminescence. Further, confocal-microscopy-based cellular uptake study confirms the internalization of nano-probe PSs and BTMCZ enables to generate reactive oxygen species (ROS) under white-light irradiation, which efficiently kills the cancer cells.

Chapter 7: Purely organic luminescent materials with aggregation induced emission (AIE) and thermally activated delayed fluorescence (TADF) have appeared as a new library of benign luminophores for versatile applications. Yet, the fundamental understanding of their exceptional 'structure-property relationship' is still in its infancy. Herein, four triplet harvestig luminogens namely BTMCZBr2, BTMCZCN2, BTMCZOMe2 and BTMCZPy2 were facilely synthesized to decipher their intrinsic structure-property functions and further used for cell imaging application. A novel benzothiazole-methanone acceptor core has been explored with common donor carbazole moiety. By introducing electron donating and

withdrawing segments (EWS and EDS) in the carbazole donor, efficiently triggering the pull-push electronic effects via different locally excited (LE) and charge-transfer (CT) states, demonstrating a unique examples of long-lived luminescent organic materials. Interestingly, EWS substituted molecules BTMCzBr2 and BTMCzCN2 showed hybridized locally excited charge-transfer (HLCT) emission and long lifetime, while EDS contained molecules BTMCzOMe2 and BTMCzPy2 showed efficient TADF property and very high PLQY. Experimental studies and computational results revealed a clear understanding of the singlet-triplet excited state dynamics, appropriate structural modifications, controlled electronic effects, and supramolecular self-assembly which are important prerequisites to demonstarte the 'structure-property-functions correlations' at the electronic level. Single-crystal X-ray structures of EWS adopted organic solvents while EDG adopted water molecule in the crystal lattice and depicting different solvent polarity induced optical properties. Among four fluorophores, BTMCzPy2 was found to be an efficient AIE-TADF emitter and exhibited a good cellular uptake and bright cell-imaging efficacy.

CHAPTER 2

Stimuli-Responsive Trimorphs and Charge-Transfer Complexes of a Twisted Molecular Donor

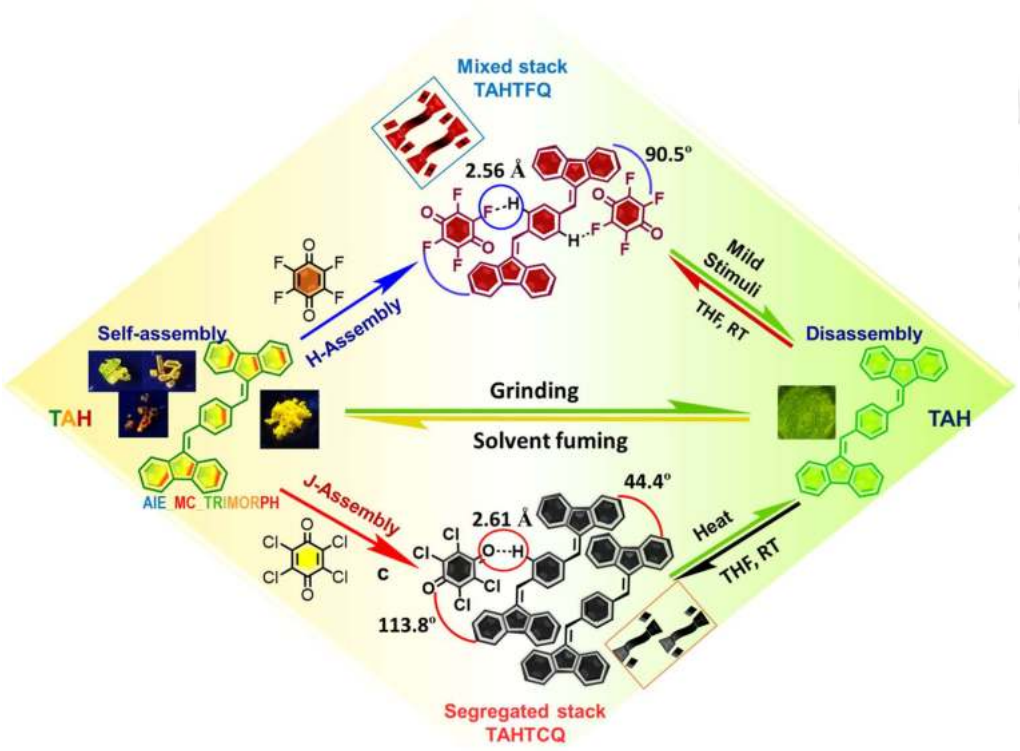

Barman, D., Gopikrishna, P., Iyer, P. K. *Langmuir,* **2021**, *37*, 8024−8036.
https://doi.org/10.1021/acs.langmuir.1c01172

Abstract

Supramolecular self-assemblies and co-assemblies possess multiple non-covalent interactions, highly ordered structures and multifunctional properties. Yet the fundamental understanding of their 'structure-property relationship' remains very challenging. Herein, two kinetically controlled supramolecular charge transfer (CT) complexes were conceptualized from a trimorphic molecular donor denoted as "twisted aromatic hydrocarbon" (TAH), with p-Fluoranil (TFQ) and p-Chloranil (TCQ) in water, organic solvent and solvent-free methods. Elucidating their co-assembling mechanism, revealed that segmentation of the TAH with molecules having planar deficient cores spontaneously formed distinct "H-type mixed stack" and "J-type segregated stack", regulated by blue/red-shifted charge-transfer, π-π stacking including weak C-H···F and C-H···O noncovalent bonding interactions significantly. By utilizing the structural transformational ability of the self-assembled TAH, the mechanistic aspects for the rapid nanoscopic co-assembly formation were precisely demonstrated experimentally and theoretically. The trimorphs and co-crystals of TAH could be disassembled resulting in turn-on emission by applying various external stimuli and being repeatedly reconfigured, thus, providing unique structure-property relationship and new TAH-based materials. This unique concept offers color-specific polymorphism and CT-complex formation strategy involving simple class of functional materials having co-operative network forming ability using the twisted molecular donor.

2.1 Introduction

Organic single and multicomponent supramolecular charge transfer complexes are key platforms that are generating exciting and newer functional properties over the last few decades.[1] Essentially, highly ordered assemblies have aroused widespread attention, due to the huge prospects of their dynamic and tunable condensed state properties such as specific module packing-arrangement, topological ordering, molecular conformations, phase to phase transformation.[2] Thus, multicomponent solids with non-covalent interactions have emerged with exciting photophysical processes and semiconducting functionalities that have broadened their application perspectives.[3] These solids are now widely employed in two-photon absorption,[4] room temperature phosphorescence,[5] ambipolar transistors,[6] organic photovoltaics,[7] ferroelectricity,[8,9] electric response,[10] organic stimuli responsive (SR) luminophores,[11] security inks,[12] data storage,[13] multiplexing[14] and artificial muscles.[15]

Few efforts have been devoted to generate multi-conformational assembly from single component systems, especially luminescent polymorphs.[16-19] These comprise a rare class of organic materials, that exist in multiple forms within a self-assembled single component system and have drawn considerable interest as effective pharmaceutical in-gredients,[20,21] and renewable energy applications.[22] Additionally, self-assembly conversions in single component system may also offer an effective route to achieve fascinating supramolecular co-crystal structures which have not been reported yet.

Unlike the straightforward single component crystallization from solution due to the inherent association behavior in solid-state,[23] rapid multicomponent supramolecular co-assembly construction remains relatively difficult.[24-26] Consequently, appropriate structural match, controlled molecular packing, regular growth morphology, and fundamental understanding of crystallization kinetics pathways of assembly formation remains unclear. Subsequently, in non-covalently bonded binary architecture, achieving appropriate alignment and packing patterns are important prerequisites to realize 'structure-property relationship' at the molecular level.[27] Notably, to establish superior functionality in co-assembled systems, various types of hydrogen bonds (HBs), halogen bonds (XBs), π-π stacking including CT interactions are exhibited by complementary chemical and geometrical recognition elements.[28] In principle, these crucial factors, define directional interactions, shape/size organizations, and account for the highly organized packing and morphology.[29] In addition, electron rich donors (D) and deficient acceptors (A) based co-

crystals have natural propensity to assemble via two different packing motifs viz. π-π stacking, such as mixed stack packing,[30] and segregated stack packing,[31] which greatly induce their physicochemical properties.[32] These structure related packing information and evolving non-covalent interactions are endowed to preserve the integrity of structural interiors, especially for D-A systems, owing to the synergistic effect of these individual components.[33] Yet, multicomponent solids are eventually reported in only metals and inorganic alloys[34] and as planar host/guest aromatic hydrocarbons or in nonplanar heteroaromatics.[35,36]

As an unique feature, the optical properties of mechanoresponsive (MR) materials can be tuned by applying external force without altering the structural features.[37,38] In general, the emission color of the organic materials are precisely governed by their molecular packing via intermolecular interactions. MR materials are tightly or loosely packed in the solid state and their luminescence properties can be altered by external mechanical forces, such as grinding, crushing, shearing and stretching.[39] To realize the MR mechanism, few classes of organic materials have been designed which upon grinding transforms the crystalline phase into amorphous and characterized by powder XRD analysis.

To address the challenge of constructing binary pure organic co-assembled D-A 1D and 2D CT co-crystals, few promising strategies employing planar heteroaromatics based design and impressive functional properties endowed with comprehensive structure-property relationship were reported.[40,41] Subsequently, the stimuli-responsive functional behavior of some co-crystals were found to be rare, tuned by non-covalent bonding disruption under external stimuli forces.[42,43] However, the conceptualization of fully twisted aromatic hydrocarbon (TAH) molecules based co-crystals remains unexplored yet.[44,45]

Herein, a kinetically controlled simple assembling strategy was developed to construct binary co-assembly structures from polymorphic TAH. Further, the mechanism for distinct supramolecular co-operative network formation, regulated by π-π, CT and two different C-H···F and C-H···O interactions, including specifically controlled dynamic stimuli-responsive behavior thereafter was also elucidated. The mono-substituted dibenzofulvene derivative45 (referred as TAH), was synthesized via a modified single step catalyst free procedure (Scheme 2.1 & Figure A2.1-A2.3). This extended π-conjugated twisted donor molecule enables to exhibit regular self-assembly with conformational transformations leading to tricolored trimorphic behavior and tunable condensed state emission property. Further, spontaneous assembling properties of TAH were utilized to build heteromolecular

co-crystal structures TAHTFQ/TAHTCQ and to deliberately investigate their tailored growth morphology, unique "H-type mixed stack" and "J-type segregated stack" packing motifs that provided vital clues to derive the structure-property relationships.

Since TAH is devoid of any heteroatom or donor-acceptor units while possessing highly twisted rotor groups, it was difficult to ascertain their functional properties and co-assembled structures with planar guest molecules. Nonetheless, the dynamic stimuli responsiveness of TAH and TAHTFQ/TAHTCQ were also analyzed carefully with precisely controlled reversible emission switching features under multiple external stimuli. These results provide new prospects to construct well-ordered functional co-assemblies by integrating highly twisted fully aromatic TAH core with planar acceptor molecules in water, without requiring any stabilizing agents. This strategy thus opens an effective new avenue to build robust structure-property relationship towards the construction of TAH based multi-component organic materials

2.2. Experimental Section

2.2.1. Materials

9H-fluorene, 1,4-phthalaldehyde, p-Fluoranil, p-Chloranil and potassium hydroxide were purchased from Sigma-Aldrich and used without further purification. Absolute ethanol, THF and chloroform were distilled over calcium chloride.

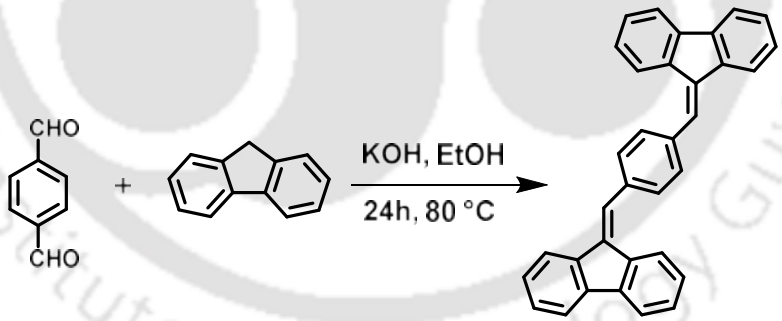

Scheme 2.1.. Synthetic procedure of twisted aromatic hydrocarbon (TAH), termed TAH.

2.2.2. Synthesis and Characterization

2.2.2.1. Synthesis of 1,4-Bis(fluorenylidenemethyl)benzene (TAH)

A mixture of potassium hydroxide (1g, 18 mmol) and 9H-fluorene (3g, 18 mmol) were dissolved in absolute ethanol. The resulting solution was refluxed for 1 hour under inert atmosphere. 2g of benzene-1,4-dicarbaldehyde (15 mmol) was added into reaction mixture and refluxed for 12 hours. The yellow color precipitate was filtered and washed several times with ethanol to give pure product as a bright yellow solid compound TAH.

(Yield: 74 %); ^{1}H NMR (600 MHz, $CDCl_3$) δ (ppm): 7.82 (d, J=7.1 Hz, 1H), 7.74 (d, J=6.2 Hz, 4H), 7.70 (s, 2H), 7.40 (m, J= 7.3 Hz, 1H), 7.35 (m, 2H), 7.12 (t, J= 8.1 Hz, 1H).^{13}C NMR (150 MHz, $CDCl_3$) δ (ppm): 141.53, 139.61, 139.34, 137.05, 136.05, 136.84, 129.72, 128.86, 128.48, 127.21, 126.96, 126.86, 124.53, 120.44, 119.98, 119.79. MALDI-TOF MS: $[M - H]^+$ calcd: 430.17; found: 429.15. Melting point: ~210 °C.

2.2.3. Measurement and Methods

2.2.3.1. FTIR and Raman Spectral Analysis

All the FTIR data were collected using a PerkinElmer instrument, where samples were first embedded in a KBr pellet following the standard protocol. Application. Raman spectra analysis was done using a laser micro-Raman system (Horiba Jobin Vyon, LabRam HR) with 633 nm laser excitation.

2.2.3.2. Absorption and PL Spectra Measurement

The fluorescence and absorption spectra were measured with PerkinElmer, Model Lambda-25 spectrometer and Horiba-Fluoromax4 with Varian Cary Eclipse spectrometer respectively. The absolute quantum yields were measured by using the Horiba Fluoromax (Jobin Yvon equipped with Integrating sphere) absolute quantum yield spectrometer. The time-resolved fluorescence lifetimes were investigated with the time-resolved fluorescence studies were performed using an Edinburgh Life Spec II instrument.

2.2.3.3. Electrochemical Measurements

Electrochemical measurements were carried out using a CH Instruments 760D electrochemical workstation at a scan rate of 50 mV/s. A three-electrode cell with platinum wire counter electrode, glassy carbon working electrode and Ag/Ag+ reference electrode was employed. Tetrabutylammonium hexafluorophosphate (0.1 M) in acetonitrile was used as supporting electrolyte and Fc+ /Fc couple was used as internal reference. A thin film was casted from 10 µL, 1 mM solution of sample in THF on the working electrode and the measurements were performed at room temperature under inert atmosphere.

2.2.3.4. Thermal Analysis

The transition temperatures and associated enthalpy changes were determined by differential scanning calorimeter (Q20 DSC) under nitrogen atmosphere with a heating rate of 10 °C/min. Thermogravimetric analyses (TGA) were carried out with a Mettler-Toledo TGA/SDTA 851e thermogravimetric analyzer in a temperature range of 30-600 °C under nitrogen atmosphere at 5 °C min^{-1} heating rate.

2.2.3.5. Electron Microscopic Visualization

TAHTFQ, and TAHTCQ 3D-nanocubes were examined by scanning electron microscopy (FESEM) (Zeiss, Model: Sigma-300). All water drop casted samples were gold-sputtered under vacuum to achieve a thin layer of conductive gold coating on the micro/nano crystalline samples. Atomic force microscopy (AFM) analysis were performed dropcasted sample over silicon substrate, in AFM, Asylum Cypher, Oxford Instruments. Transmission electron microscopy (TEM, JEOL JEM-2100F). Dynamic light scattering (DLS) measurements were taken with a Zetasizer Nano ZS90(model no ZEN3690) instrument.

2.2.3.6. X-ray Diffraction Analysis

The powder X-ray diffraction measurements of the powder and thin films were performed using a Rigaku SmartLab X-ray diffractometer where copper Kα (λ = 1.54 Å) was used as the source with 9 kW power. The XRD patterns for the 2θ range of 5°−50° were measured at the scan rate 0.3°/s. Single-crystal structures of TAH, TAHTFQ, and TAHTCQ were obtained on X-ray diffractometer on Agilent. The single crystal x-ray diffractometer is equipped with Mo X-ray source (Mova), CCD detector (Eos), Oxford cryo system (80-500K) and crystal AlisPRO software and Autochem softwares. SC-XRD data were collected at 293 K. All the self-assembled crystal and co-assembled crystal structures were solved by SHELXT with direct methods. All the non-hydrogen atoms were located by SHELXT directly and refined anisotropically by SHELXL2018 with least squares methods.

2.2.3.7. Thermophoresis Measurements

The binding affinity of the co-assemblies were determine by the affinity of a binding reaction, a series of titration of one binding partner was performed, while the fluorescent binding partner (TAH) kept constant concentration. The binding affinity of TFQ was found to be very high rather TCQ to TAH when the titration made from 0.1mM to 10 mM concentration. The change in the thermophoretic signal leads to a modest K_d value of 176.32 ± 2.45 μM with full sigmoidal curve for TAHTFQ whereby relatively weakly integrative TCQ results K_d=278.10 ± 0.73 μM. The error bar denoting the s.d. of each data poin calculated from independent thermophoresis measurements.

2.2.3.8. Growth of Single Crystals

Three different self-assembled trimorphic crystals of TAH, green (G), orange (O), and red (R), were obtained in different organic solvent mixtures such as ethyl acetate-hexane for green, chloroform for orange and chloroform-ethyl acetate for red color crystals at room temperature by solvent diffusion method. Where co-assembled crystals of TAHTFQ (red) and TAHTCQ (black) prepared from solution phase technique by using THF as a solvent

at 1:1 ratio of individual components (TAH and TFQ/TCQ) at ambient conditions at slow evaporation technique.

2.2.3.9. NMR Experiments

The distinct interaction between donor TAH and acceptor TFQ/TCQ was observed by 1HNMR spectra, where protons associated with TAHTFQ exhibited downfield shift whereas TAHTCQ protons showed moderate upfield shift. The experiment was carried out by dissolving TAH and TFQ/TCQ in equivalent ratio of 1:1 in CDCl3 at room temperature. Since all the above molecules were highly soluble in most common solvents, we choose non-polar CDCl3. At the same time, 1:1 ratio was chosen based on the kinetic and PL study results, which revealed that 1:1 ratio is an effective ratio for co-assembly formation.

2.2.3.10. On Surface Disassembly Characterization

On surface co-assembly preparations conducted on glass substrate, firstly 50 mM TAH was drop-casted over micro glass slides, which showed green emissive under 365 nm UV-light. Eventually by adding equivalent molar ratios of TFQ and TCQ over TAH, immediately red and black color (at day light) TAHTFQ and TAHTCQ co-assembly formed which are non-emissive under 365 nm UV-light. Further thermo-responsive disassembly behavior and reversible co-assembly of TAHTFQ & TAHTCQ were carried out by applying controlled thermal energy in a sophisticated hotplate (IKA). Under heat non-emissive co-assemblies are separated and turns to emissive pristine TAH molecules. Interestingly, TAHTFQ turns to emissive at 80 ºC, where TAHTCQ turns at 100 ºC, however both dis-assemblies were reversibly co-assembled by treating with THF solvent at room temperature.

2.2.3.11. Theoretical Calculations

The growth morphologies of TAHTFQ and TAHTCQ co-assembled crystals were calculated by using the Materials Studio software, based on the attachment energy theory. The molecular structure was first optimized on the basis of the experimental crystal structure. The geometric and energy calculations were performed using the Forcite and Morphology modules. The highest occupied molecular orbital (HOMO), lowest unoccupied molecular orbital (LUMO), and of single-component crystals and multicomponent crystals were calculated by density functional theory (DFT). All DFT calculations in this study were performed by employing the combination of Becke3−Lee−Yang−Parr (B3LYP) hybrid functional and 6-31G(d,p) basis set using the Gaussian 09 package under 298.15 K temperature and 1 atm pressure. The calculated structures, energy level very much close to experimental results. Combined with the Single-crystal X-ray diffraction (SC-XRD) crystal data, the Hirshfeld surfaces, electrostatic

potential, and molecular orbital were simulated by CrystalExplorer 3.1.51 The Hirshfeld surfaces and the electrostatic potential (ESP) were mapped with dnorm using STO-3G basis set at the Hartree-Fock theory.

2.3. Results and Discussion

2.3.1. Polymorphism and Optical Properties of TAH Crystals

The polymorphism behavior of TAH was demonstrated by obtaining three trimorphic crystals, green (G), orange (O), and red (R), in different organic solvent(s) / mix solvents such as ethyl acetate-hexane for green, chloroform for orange and chloroform-ethyl acetate for red color crystals at room temperature via solvent diffusion method (Figure 2.1a). Emission spectra of these crystals exhibited three distinct emission bands centered at 555 nm, 573 nm and 598 nm, including CIE (International Commission on Illumination) co-ordinate values of (0.39, 0.56), (0.46, 0.61) and (0.51,0.47) for G-crystal, O-crystal and R-crystal respectively (Figure 2.1b, c). Moreover, structural topologies of the twisted TAH revealed that the three polymorphic single crystals exhibited non-planar structures with minor differences in their dihedral angles between TAH moieties and phenyl-bridge of 171.08° and 170.79° for G-crystal, 170.69° and 170.87° for O-crystal and 170.89° and 171.22° for R-crystal. [Figure 2.2(a, b, c), Figure A2.4a, Table A2.1]

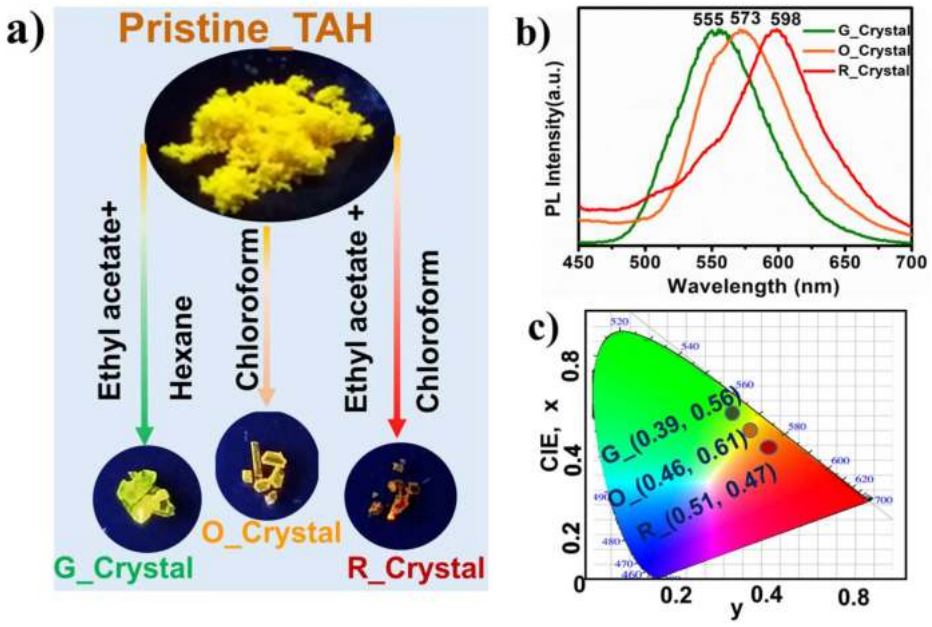

Figure 2.1. Trimorphism and condensed state characterization of TAH: (a) Solvent assisted three different color (green, orange & red) crystals. (b & c) PL spectra of G-crystal, (λ_{max}= 555 nm) O-crystal (λmax= 573 nm) and R-crystal λ_{max}= 595 nm) and their respective CIE coordinate diagram.

In O- and R-crystals, two adjacent molecules are assembled via π···π (3.398 Å & 3.395 Å) intermolecular interactions, and further, these dimers are arranged in ladder type chain structures, stabilized by CH···π (2.75 Å) intermolecular interactions. Hence, these conformations are very favorable to increase the degree of conjugation, leading to red-shifted emission (~573 nm and ~598 nm). On the other hand it is assumed that G-crystals are in monomeric form and stabilized by weak CH···π (2.74 Å) and CH···π (2.89 Å) intermolecular interactions. Additionally, the influence of solvent polarity on structural transformations and emission change was verified by TD-DFT calculations (Gaussian 09 package) in various nonpolar to polar solvent systems (Figure A2.4b). As expected, solvent polarity strongly effects their bandgap (E_g) and photoluminescence quantum yield (PLQY) of the respective crystals with the values of 2.30 eV, 2.25 eV and 2.13 eV calculated from crystal geometry, while absolute PLQY values of 35.84 %, 29.56 % and 28.18 % for crystals, depicted as gradual decrease and corresponding to green, orange and red color crystals, respectively (Figure 2.2d). Furthermore, the condensed state photophysical properties of the twisted TAH were elucidated using absorption and photoluminescence (PL) spectra, by varying the water content (W_c) in THF solution at constant TAH concentrations (~3 x 10^{-5} M). TAH absorbs at 364 nm in THF, whereas in water it bathochromically shifted to 400 nm confirmed by recording excitation and absorption study (Figure A2.4c, d).

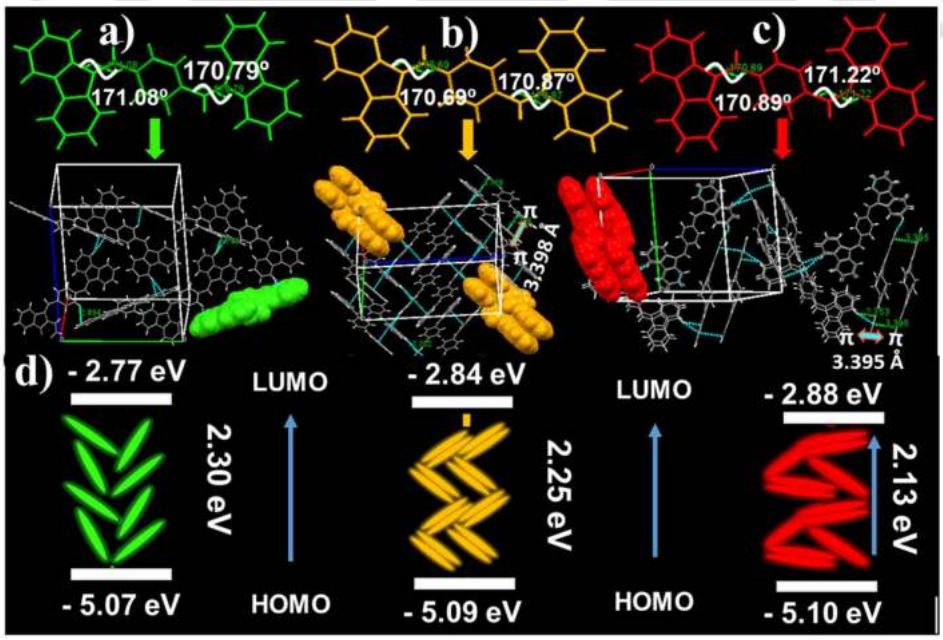

Figure 2.2. (a, b & c) SC-XRD structures of the three G-crystal, O-crystal and R-crystal and their packing interactions. (d) Theoretical energy band gap (inset: illustration of crystal packing).

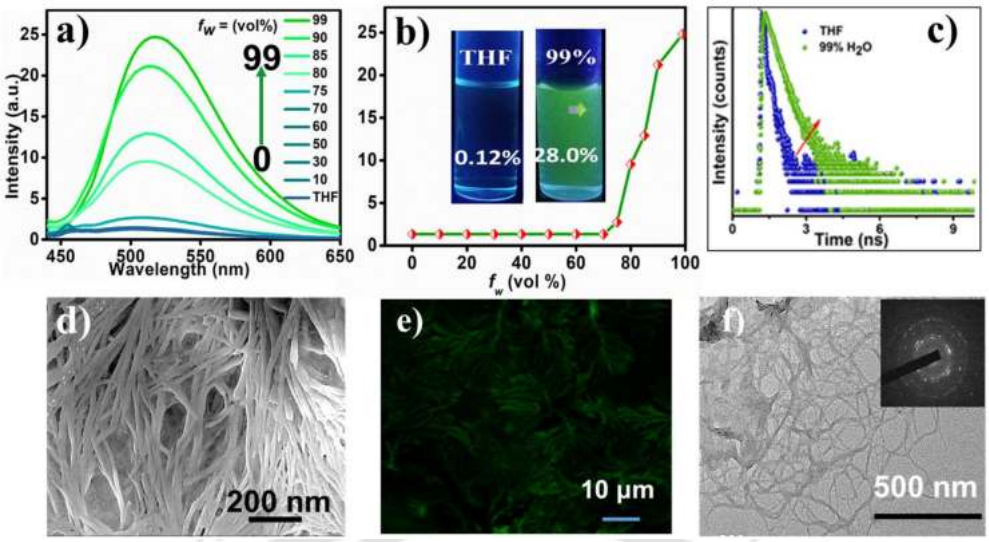

Figure 2.3. AIE property of TAH: (a & b) Fluorescence spectra and relative intensity (inset: fluorescence images were captured under 365 nm UV lamp), (c) Fluorescence lifetime in THF and 99% Wc. (d). Microribbon morphologies by FESEM (scale-200 nm). (e) Confocal images (scale-10µM). (f) FETEM (0.5µM) analysis was conducted from drop-casted nano-aggregates (0.1 µM conc.) over carbon coated copper grid at RT.

Fluorescence spectra and the relative PL intensity (inset: images taken under 365 nm UV-lamp), average lifetime (τ_{av} = 1.90 ns) and quantum yield (PLQY = 28.05%) were much higher in 99% W_c than in THF solution (τ_{av} = 1.42 ns and PLQY = 0.12%) as shown in Figure 2.3a, b c. The enhanced emission and accompanying results could be attributed to restricted intramolecular free rotation due to microribbon (~10-20 µM) type self-aggregate formation in 99% Wc, referred as aggregation induced emission (AIE)[46,47] and con-firmed by FESEM, CLSM and FETEM analysis (Figure 2.3d, e, f).

2.3.2. Optical Properties and Growth Morphology for Co-crystals

Precise alterations in single component based self-assembly offers an effective route to achieve exciting supramolecular structures.[48] Based on this premise, a rapid and spontaneous supramolecular co-crystal formation strategy was conceptualized for TAH in aqueous medium at ambient condition without any stabilizers / capping assistance (unlike use of surfactants previously)[49] (Figure 2.4a & Figure A2.5a). The supramolecular co-crystals were grown from THF as well as solvent-free rapid approaches, such as simple rubbing of TAH thin films with p-Fluoranil (TFQ) or p-Chloranil (TCQ) films (Figure A2.5b, c). Moreover the co-assembly formation with precursor TAH (~2 x 10^{-5} M concentration) could be kinetically monitored by UV-visible absorbance study,

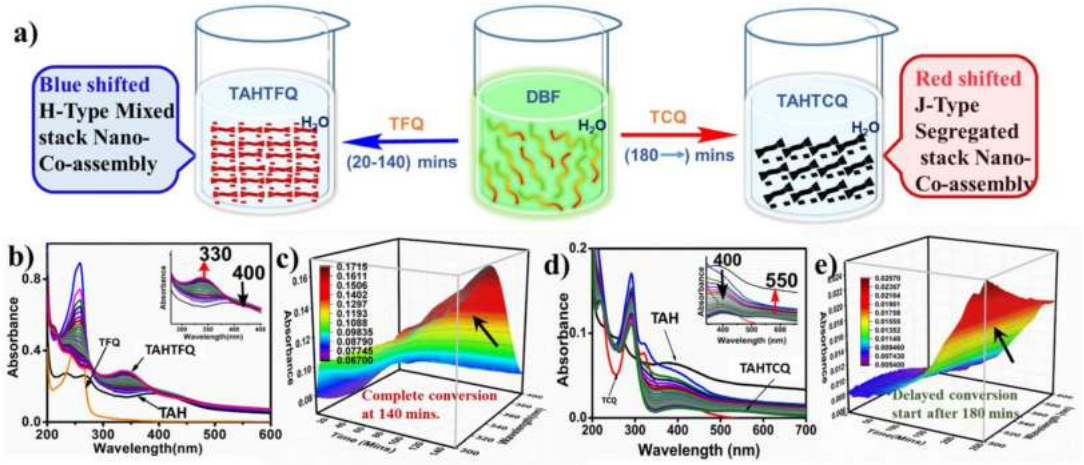

Figure 2.4. (a) Illustrations of aqueous phase co-crystal formulation from TAH. (b & d) Blue and red-shifted UV-visible absorbance spectra of formed TAHTFQ and TAHTCQ from TAH, TFQ and TCQ at different time interval. (c & e) 3D-contour plot for fast and slow association.

where initially, a CT band was found at 400 nm. On adding TFQ to TAH and carefully monitoring the CT band associations, 70 nm blue-shifted new peak appeared at 330 nm after 20 minutes, suggesting initiation of an H-type mixed stack co-crystal formation of TAHTFQ and the association was completed within 140 minutes (Figure 2.4b). However, TCQ addition to TAH comprises a self-ordered J-type TAHTCQ co-crystal, and 150 nm red-shifted new peak gradually appeared at 550 nm after ~180 minutes, which was initiated but slightly delayed, and the full conversion prolonged ahead (Figure 2.4d). The spontaneous initiation and complete association of TAHTFQ and TAHTCQ co-crystals were accounted from the contour diagram, plotted with absorbance as a function of wavelength and time (Figure 2.4c, e). Notably, the slower co-crystal of TAHTCQ is likely due to the large 'chlorine' atoms of TCQ that sterically congested the intermolecular association among chromophore molecules leading to comparatively weaker interaction with oxygen atoms. In order to observe the controlled and regular water dispersible nano-co-assemblies of TAHTFQ and TAHTCQ from microribbons of single component TAH, low-magnification (scale bar: 1 & 2 μm) FESEM images (Figure 2.5a, c) (inset high magnification, scale bar: 200 nm) were acquired. These images revealed very uniform blocks of TAHTFQ crystals with D= 368 nm, L= 185 nm, W= 15.8 nm size and relatively larger assemblies of TAHTCQ with D = 1.57 μm, L= 563 nm, W= 418 nm size. Low-magnification TEM images (scale bar 500 nm) also consisted regular cubic shape of block co-crystals (Figure 2.5b, d).

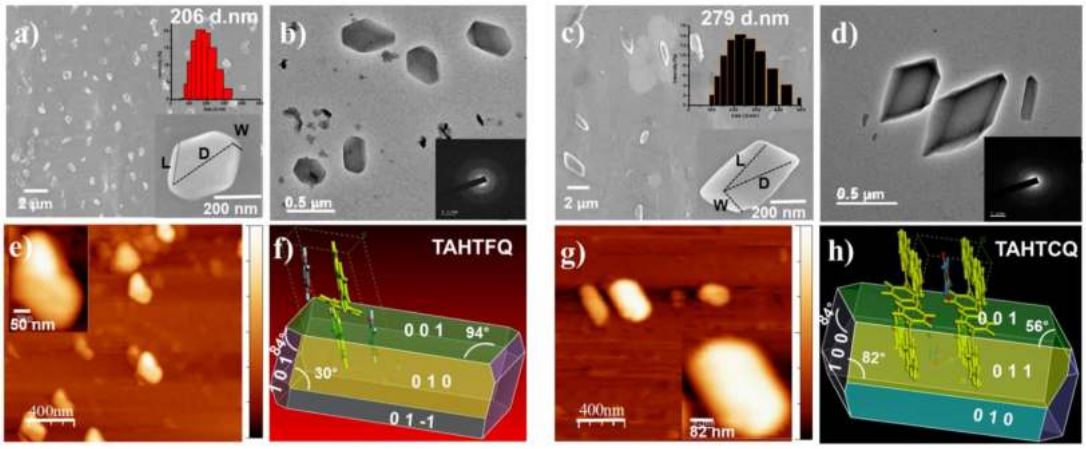

Figure 2.5. (a & c) Low-magnification (scale bar: 1 & 2 µm) FESEM images (inset high magnification, scale bar: 200 nm) (Insets: DLS 206 d.nm for TAHTFQ and 279 d.nm for TAHTCQ). (b & d) Low-magnification TEM images (Inset: SAED pattern). (e & g) AFM images with height profile (400 nm scale bar). (f & h) Growth morphologies by Material studio 17 software for TAHTFQ and TAHTCQ based on the calculated energies.

However, no crystal lattice and diffraction pattern was observed in selected area electron diffraction (SAED) analysis, attributed to the highly energetic electron beams irradiation, destroying the crystal structures[50] (inset Figure 2.5b, d), thereby turning them to amorphous domains and signifying thermoresponsive feature of the co-crystals. This observation further supported by temperature dependent powder X-ray diffraction and thermogravimetric analysis studies which is mentioned in later part of discussion. To study the morphology of these blocks, AFM images were recorded from drop-casted samples over silicon substrate at very dilute concentration (1 x 10^{-5} M) in 400 nm scale bar (Figure 2.5e, g). The height and RMS roughness of 47.01 nm, 4.95 nm for TAHTFQ and 41.56 nm, 4.45 nm for TAHTCQ, including some heterogeneous population of aggregates on surface, could be due to the incomplete co-assembly formation at very dilute concentration. Growth morphologies were predicted by Material studio 17 software[51] for TAHTFQ and TAHTCQ co-crystals based on the calculated energies (Tables A2.2 & A2.3). The calculated attachment energy suggests a cubic block morphology at different crystal facets for the binary growth model which is very similar to the experimental morphological results (Figure 2.5f, h). Thus, the self-assembled crystals to co-crystals conversions are effectively mediated by C-H···F and C-H···O weak interactions, π-π stacking, and CT interactions upon incorporating TFQ/TCQ into the donor TAH structure and displaying characteristics similar to the bulk co-crystals grown directly from solution and their detailed perspective structure-property relationship are elaborated below.

2.3.3. Co-crystals Characterization

Bulk co-crystals were prepared instantly (within 30 s) from solution phase method, and optimized at different equivalent ratios of TAH:TFQ/TCQ during co-crystallization (Figure A2.5d, e). Solid state UV-vis spectra suggested that the blue and red shifted co-crystal show features similar to the aqueous phase absorbance of TAH, TAHTFQ and TAHTCQ respectively (Figure A2.5f). Notably, both the co-crystals were effectively formed at equal molar ratios in water, while SC-XRD structure also confirmed both the TAHTFQ and TAHTCQ formed in 1:1 ratios respectively. The highly planar electron rich cloud is available in fluorene moiety in the twisted and *trans* geometry of the TAH which enables to accommodate two deficient electron centers of TFQ and TCQ, effectively via charge transfer and other noncovalent bonding interactions overcoming the minor steric hinderance. These results, encouraged us to investigate critically the dissimilarity in charge-transfer / packing interactions, morphological behavior and elucidate the mechanism of fast/slow co-assembling process. The rapid doping of TFQ and TCQ in the twisted TAH was supported by Fourier transform infrared (FTIR) spectra, Raman spectra, and PXRD.

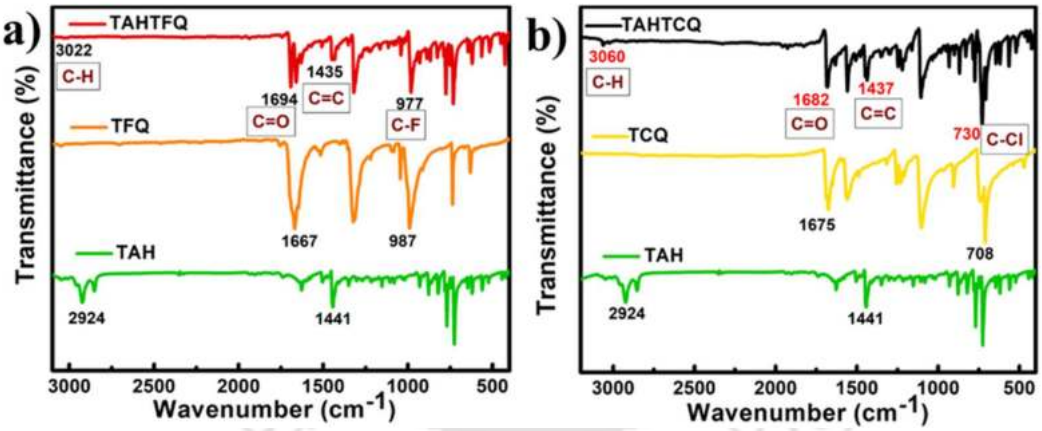

Figure 2.6. (a & b) FTIR spectra of TAH crystals (green line), TFQ (orange line), TCQ (yellow line) TAHTFQ (red line) and TAHTCQ (black line).

The characteristic FTIR peaks at 987 cm^{-1}, 1667 cm^{-1} of C–F and C=O bonds in TFQ shifted to 977 cm^{-1} and 1694 cm^{-1}, whereas the peak at 2924 cm^{-1} for C-H bond of TAH shifted to 3022 cm^{-1} for TAHTFQ (Figure 2.6a). The 708 cm^{-1}peak of C-Cl bond and 1675 cm^{-1} of C=O bond in TCQ shifted to 730 cm^{-1} and 1682 cm^{-1} and the C-H bond shifted from 2924 cm cm^{-1} to 3060 cm^{-1} for TAHFTCQ (Figure 2.6b), respectively.

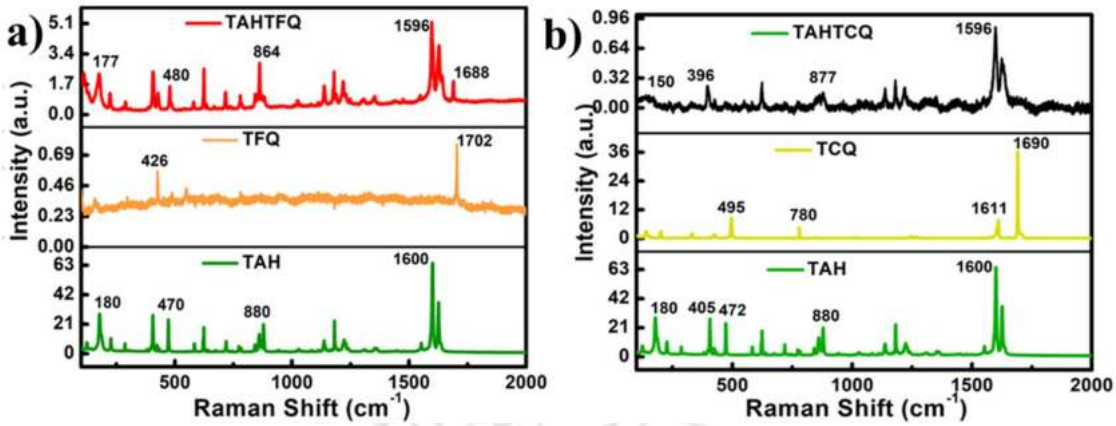

Figure 2.7. (a & b) Raman spectra of TAH (deep green line), TFQ (orange line), TCQ (greenish yellow line), TAHTFQ (red line) and TAHTFQ (black line).

For instance, FTIR study revealed that the successful involvement of electron rich hydrocarbon (TAH) and electron deficient quinone (TFQ and TCQ) cores effectively induced shifting in stretching frequencies and lead to distinct packing interactions due to the presence of different electronegative atom (F/Cl) upon co-assembly formation. Furthermore, significant Raman shift of TAH occurred from 1600 cm^{-1}, 880 cm^{-1}, 470 cm^{-1} to 1596 cm^{-1}, 864 cm^{-1}, 480 cm^{-1} for TAHTFQ (Figure 2.7a), and 1596 cm^{-1}, 877 cm^{-1} for TAHTCQ (Figure 2.7b) respectively. These results clearly demonstrated, a prominent CT caused by electron-rich TAH and the electron-deficient quinones are redistributed over their electron clouds, due to electrostatic Coulomb interactions. Correspondingly, the C-H···F for TAHTFQ and C-H···O for TAHTCQ, resulted in structural changes leading to the stretching peak being shifted significantly.[52] Further, the degree of CTs (ρ) defined as ρ ($0 \leq \rho \leq 1$), which denotes physical properties like conductivity and packing of co-crystals which can be understood from equation-2.1. A modest 0.139e ρ value for TAHTCQ and 0.05e ρ for TAHTFQ was calculated by employing this formula.[53, 54]

$$\rho = \frac{1}{2}\left(\left[1 - \frac{x_{CT} - y_{CT}}{x_N - y_N}\right] + \left[1 - \frac{z_{CT} - y_{CT}}{z_N - y_N}\right]\right) \qquad (\text{Equation} - 2.1)$$

where x, y, and z represents the bond lengths assigned in TFQ and TCQ, the subscript "CT" denotes bonds in the acceptor when it is in the CT complex TAHTFQ/TAHTCQ, and the subscript "N" refers to bonds in neutral TAH (Figure 2.8).

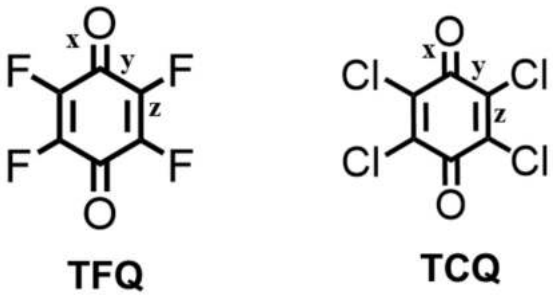

Figure 2.8. Chemical structures of TFQ and TCQ; Degree of CT calculated based on marked (x, y, z) bonds in neutral TFQ and TCQ.

This investigation suggested that the modest value of ρ with high order CT favors J-type segregated packing for TAHTCQ, whereas, the low ρ value of TAHTFQ, preferred to be a mixed stack H-type assembly. Hence, the degree of CT interaction in twisted co-crystals clarifies the mode of packing segmentation and provides key mechanistic information to endow the 'structure functionality' relationship for further development of twisted donor based supramolecular co-assemblies.

2.3.4. Crystal Structure Analysis

Single-crystal X-ray diffraction (SCXRD) and PXRD measurements were performed for TAHTFQ and TAHTCQ co-crystals to confirm the molecular stacking and non-covalent interactions. SCXRD-structure analysis at unit cell and multi-cell crystal packing arrangements. Both the co-crystals of TAHTFQ and TAHTCQ exhibited triclinic crystal lattice with P-1 space group, whereas, the parent TAH trimorphs (G, O, & R-crystal) showed orthorhombic crystal lattice with Pbca space group (Table A2.4). Upon co-crystallization a mixed-stack packing mode was observed in TAHTFQ, where TAH and TFQ units were stacked orthogonally (90.5º) and alternately (D-A-D-A), linked via H···F interactions, π-π interactions (distances 2.56Å and 3.40 Å) by face-to-face stacking along [001] direction with a mean distance of 3.32Å where the distance between TAH-TAH and TFQ-TFQ is 6.51Å (Figure 2.9a, b & c). Successively, TAH and TCQ units are placed at an angle 113.8° in TAHTCQ, and is comprised of a segregated packing mode, where TAH and TCQ are stacked on each other individually (DD-AA) connected through H···O, interactions (C-H···O) with a distance of 2.61Å and π-π interactions of 3.50Å respectively. In addition, face-to-edge stacking along [001] direction with a mean distance of 3.78Å, including 7.37Å distance was also observed between TAH-TAH and TCQ-TCQ (Figure 2.9d, e & f).

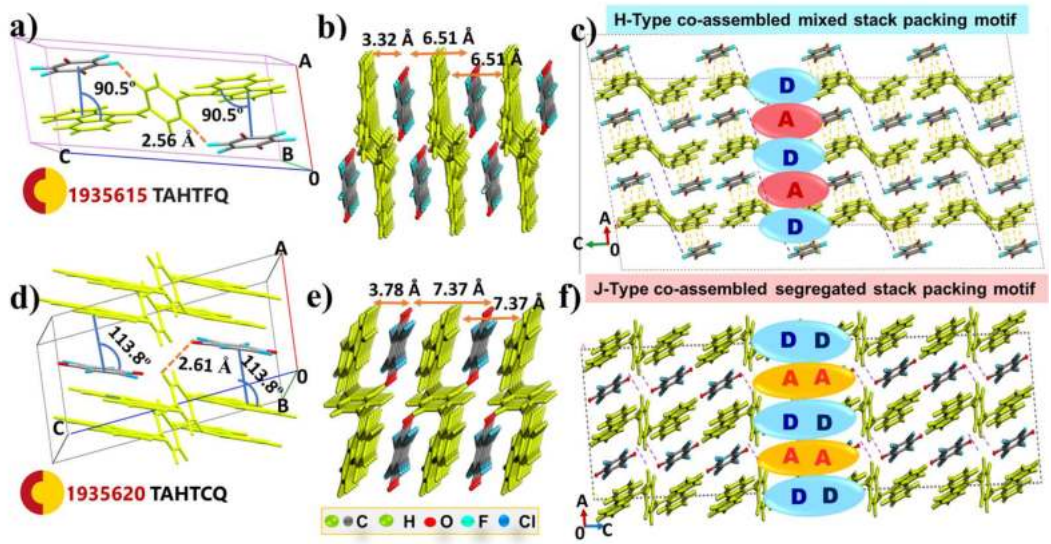

Figure 2.9. (a & b). Single-crystal XRD structure of TAHTFQ and TAHTCQ co-crystal in unit cell. (c & d) Top view of stacked architectures and relative distances from each constituent. (e & f) Side view in bulk packing pattern of "mixed stack" TAHTFQ and "segregated stack" TAHTCQ co-crystals.

Figure 2.10a is a simplified representation of the molecular packing modes and energy diagram in co-assembly, as H-aggregation and J-aggregation and their dipole stacking in the solid state.[55] Similar co-facial brickwork mixed stack configuration (H-type) and segregated configuration (J-type) were also observed for TAHTFQ and TAHTCQ respectively. Therefore, the strong assembly along the π-π direction with large π-overlap and ideal co-facial configuration ($\theta > 54.7°$) of the TAHTFQ co-crystal evidently showed the occurrence of H-type Co-crystals. In contrast, finite π-conjugated cores and large intermolecular rotation ($\theta < 54.7°$) of the TAHTCQ co-crystal indicated the presence of hybrid J-type assembly in the combined crystal packing. Besides, the flexible dihedral angle (40.00°, 38.85°) between phenyl core and dibenzofulvene has been fixed with two different angle (47.11° for TAHTFQ and 48.51° for TAHTCQ) upon co-crystallization with TFQ and TCQ respectively (Figure A2.8a). Twisted angle between two planes of planar TAH and central phenyl planes are 43.28°, 53.93° and 54.39° for TAH crystal, TAHTFQ TAHTCQ co-crystals respectively, influenced by the interactive orientation of the guest quinone molecules. Thus, bulk packing in SC-XRD structure for TAHTFQ showed close contact with symmetrical alignment among TAH and TFQ cores, whereas in TAHTCQ an unsymmetrical alignment with long distance contact has observed (Figure A2.8b, c).

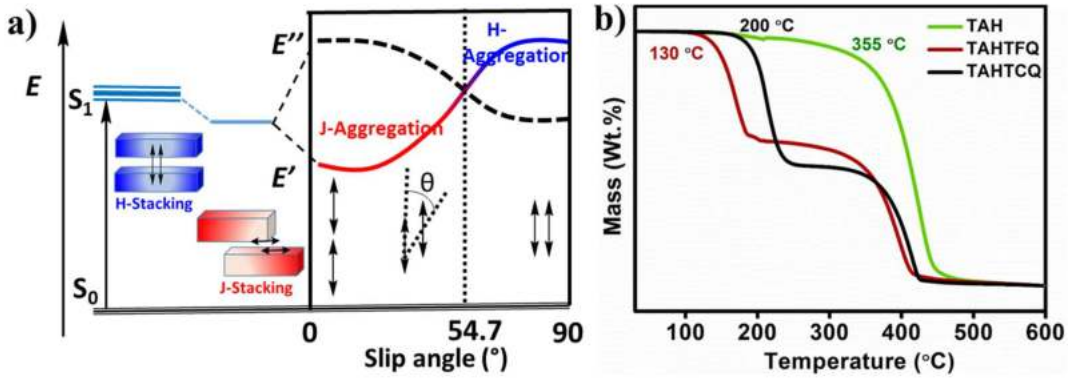

Figure 2.10. (a) Energy diagram illustration of co-crystals for the classification of molecular packing modes; inset: brickwork stacking arrangements and dipole stacking modes in the solid state for TAHTFQ and TAHTCQ. (b) Dissimilar thermal stability by TGA analysis for TAH, TAHTFQ and TAHTCQ.

Further, simulation studies based on the minimum attachment energy principle,[56] indicated that in both the co-crystals π–π stacking was the preferential growth direction in [001] plane having approximately 52% and 48% of possible interactions satisfied, which led to the formation of cubic blocks (Tables A2.2, A2.3). The difference in packing orientation, angles and non-covalent interactions influenced the thermal stability of co-crystals profoundly. On this view The thermal stability of the kinetically controlled products studied by thermogravimetric analysis (TGA) confirmed that the J-type TAHTCQ was relatively more stable up to 200 °C compared to the H-type TAHTFQ, which degraded rapidly at 130 °C, however, the parent TAH molecule was highly stable up to 355 °C. (Figure 2.10b).

The experimental PXRD of TAHTFQ and TAHTCQ were nearly similar to the simulated results. To interpret the defined packing pattern, d-space (Å) values were calculated from their single co-assembled structures (Figure 2.11a). The fine and well-defined diffracted peak patterns for both the co-crystals with the disappearance of several peaks from precursor TAH crystal confirms the involvement of both the neutral constituents, leading to highly ordered architectures. Specifically, d-space (Å) values were calculated to be 3.17, 2.82 for TAHTFQ and 3.47, 2.70, 2.20, 1.91 for TAHTCQ, indicating that the co-crystals were dominated by multiple interactions such as π-π stacking, non-covalent (C-H···F, C-H···O) and CH-π interactions (Figure 2.11b). More diffraction peaks seen at low d-spacing values for TAHTCQ suggested that the interactions are likely in higher-order for TAHTFQ co-crystal.

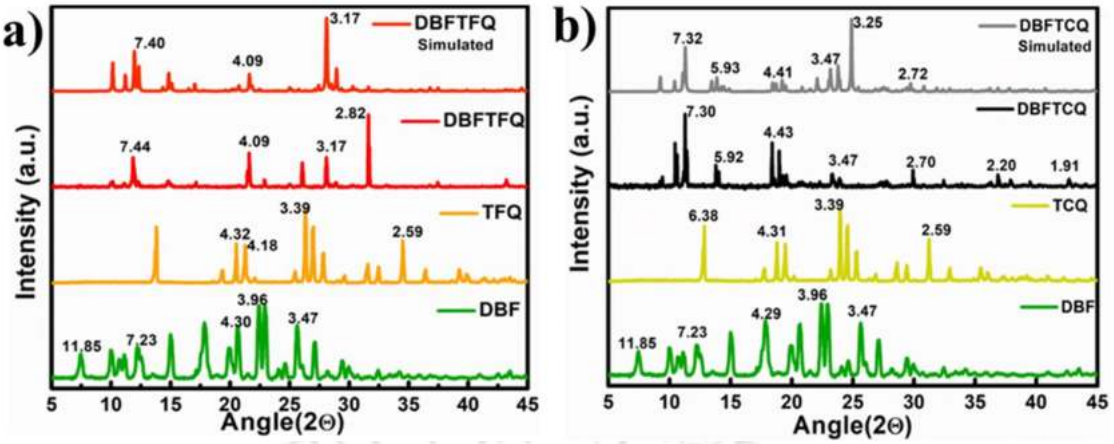

Figure 2.11. (a & b) Experimental PXRD pattern for TAH (green line), TFQ (orange line), TFQ (yellow line), TAHTFQ with calculated PXRD (red line), and TAHTFQ with calculated PXRD (black line).

The ^{1}H NMR spectra revealed that the aromatic protons of TAH in TAHTFQ exhibited large downfield shifts, while those in TAHTCQ co-crystal showed negligible upfield shifts (Figure A2.6), signifying very distinct interactions between the TAH and the planar guest molecules at post co-crystal formation process at room temperature. The presence of more electronegative fluorine atom results in extracting electron density from the electron rich TAH hydrocarbon as compared to the lesser electronegative chlorine of TCQ. Thus, NMR results further support their very different packing modes and faster co-assembly of TAHTFQ and relatively slower co-assembly of TAHTCQ. More precisely time dependent ^{1}HNMR study revealed that TAHTFQ showed faster downfield chemical shift in10 mins while TAHTCQ showed relatively slower upfield shift in 15 mins (Figure A2.7**)**. Such information has been elusive and provided valuable insights on the interaction of planar electron deficient cores with TAH chromophore.

2.3.5. Fast/Slow Co-assembly and Emission Quenching Mechanism of Co-Crystals

The fast/slow assembly for TAHTFQ/TAHTCQ was also established by calculating binding affinity (K_d) using thermophoresis experiments,[57] where the strength of the interaction between fluorescent TAH and TFQ/TCQ was measured by detecting changes in the fluorescence intensity while different concentration of TFQ/TCQ to TAH is applied over time (Figure 2.12a, b). Eventually, K_d was calculated from a fitted curve of normalized fluorescence plotted against the concentration of acceptors (TFQ/TCQ) (Figure 2.12c). TAHTFQ demonstrated a full sigmoidal curve with good K_d value (176.32 ± 2.45 μM) depicting rapid and spontaneous interactions. Similarly, multiple non-covalent interactions

via close H···F (2.56 Å) contact and orthogonal π-cloud involvement (operative π-π stacking) including strong CT interaction, enabled the rapid association between donor and acceptor molecules, supported by SC-XRD structure analysis of co-crystals. Simulation studies were performed to investigate the fast / slow co-assembly formation, π-π stacking and non-covalent (C-H···F, C-H···O) interactions by electrostatic potential (ESP) mapping and their corresponding two-dimensional (2D) fingerprint plots by employing CrystalExplorer 3.1 software.[58] Further, ESP mapped on Hirshfeld surface on TAH in TAHTFQ co- crystal exhibited bright red spot with short-contacts (3.40 Å) and with a C-H···F distance of 2.56Å (Figure 2.12d) which demonstrated the effective interactions with acceptor TFQ, favoring rapid co-crystal formation. However, comparatively longer close contact (3.50 Å) with connected C-H···O distance of 2.61 Å (Figure 2.12e), including absence of a red spot on TAH in TAHTCQ supported the weaker interactions thereby slow co-crystallization was observed.

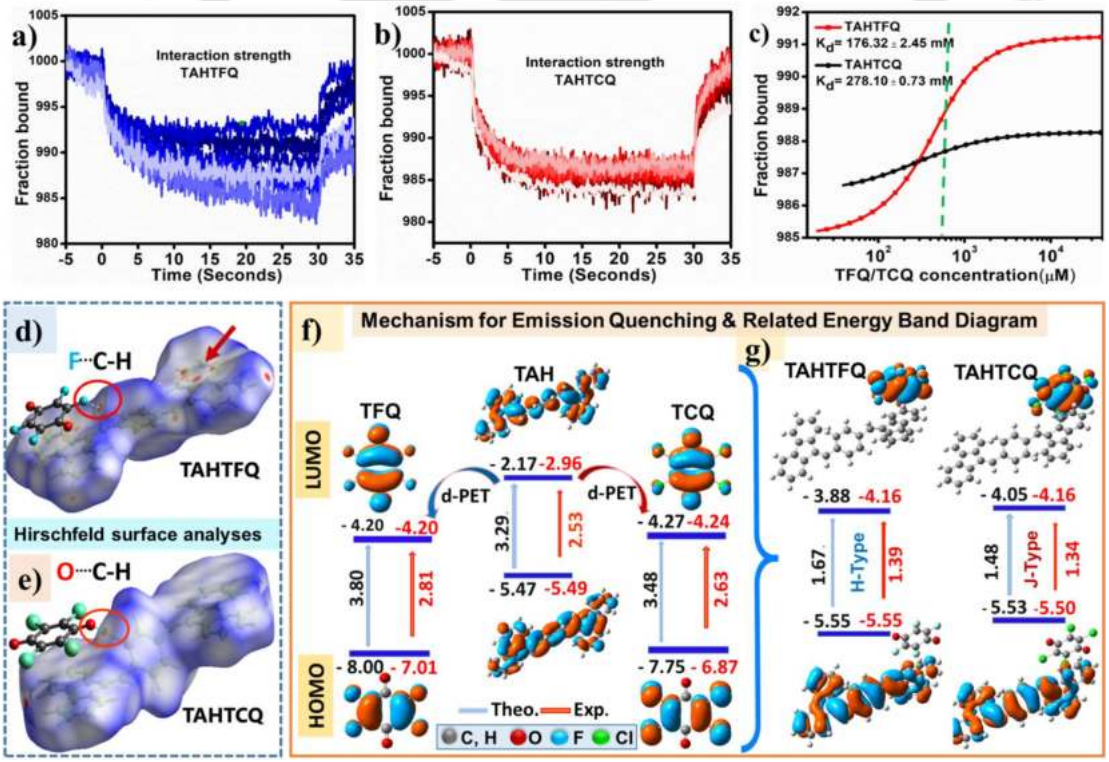

Figure 2.12. (a, b & c) Interaction strength depicted with fluorescence intensity as a function of different concentration of TFQ/TCQ to TAH with applied time followed by binding affinity (K_d) calculated for TAHTFQ and TAHTCQ, respectively. (d & e) ESP and the fingerprint plots including effective, non-covalent C-H···F (2.56 Å) and C-H···O (2.61 Å) bonding interaction of the TAH is mapped on the Hirshfeld surface in TFQ and TCQ respectively. (f & g) Emission quenching mechanism, blue/red-shifted packing accompanying the energy profile was attributed by DFT/TD-DFT and cyclic voltammetry (CV) studies.

The 2D fingerprint plots of TAH and TFQ/TCQ across the surface revealed atom-atom type contacts, where ESP patterns are mainly related to the surface contacts of H···F (24.2%), H···O (9.9%), C···H (9.9%) and C···C (11.4%) for TAHTFQ (Figure A2.8a) while, TAHTCQ exhibited H···Cl (26.1%), H···O (13.8%), C···H (10.9%) and C···C (13.2%) interactions (Figure A2.8b) which are larger in value than those of TAHTFQ. These results confirm the effect of bigger size chlorine atoms as responsible for weakening the interactions. Density functional theory (DFT/TD-DFT) calculations were performed to determine the twisted electronic structure of TAH and associated 'structure-property relationship' for co-assembled structures with TFQ/TCQ.[59] The TAHTFQ and TAHTCQ co-crystals were non-fluorescent, attributed to the static emission quenching of TAH via donor-excited photoinduced electron transfer (PET) mechanism.[60,61] This donor-excited PET mechanism was also supported by HOMO-LUMO energy level values of TAH and TFQ/TCQ calculated by DFT and CV studies (Table A2.5). The experimentally obtained LUMO values for TFQ and TCQ were -4.24 eV and -4.20 eV, offering a strong probability of d-PET from LUMO of TAH (-2.96 eV) (Figure 2.12f). In addition, the existence of moduled CT interactions in both TAHTFQ and TAHTCQ effectively revealed the stacking motif supported by HOMO-LUMO low/high energy bandgap profile in TAHTFQ and TAHTCQ. As observed, both the co-crystals had very narrow bandgaps relative to TAH, TFQ and TCQ (Table A2.5).

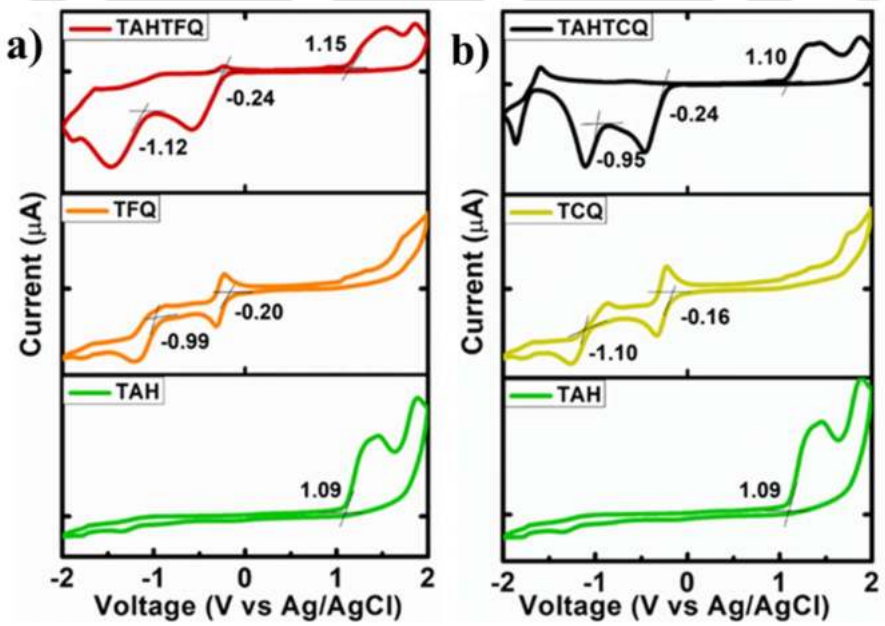

Figure 2.13. (a & b) Cyclic voltammetry (CV) curves of TAH crystals (green line), TFQ/TCQ (orange/yellow line) and TAHTFQ/TAHTCQ (red/black line).

HOMO of the co-crystals is located on the donor hydrocarbon (TAH), whereas LUMO allied with the acceptors TFQ and TCQ, leading to well separated electronic distribution, clearly indicating the CT characteristics of the co-crystals (Figure 2.12g). Further, the energy band-gap values obtained from computational and experimental (CV) in Figure 2.13 results are very proximate, where the association of TFQ with TAH resulted in H-type higher band-gap value of 1.67 eV for TAHTFQ. However, TCQ assembly offers J-type TAHTCQ (1.48 eV) and is in agreement with the UV-visible blue shifted (330 nm) and red shifted (550 nm) absorption band respectively.

2.3.6. Reversible Stimuli-Responsiveness of Trimorphs and Co-crystals

The mechanoresponsive (MR) behavior of polymorphic forms of TAH, such as G-, O-, and R-crystals including pristine powder were demonstrated by applying controlled mechanical force and reconfigured back by dichloromethane solvent fuming (Figure 2.14a).[62]

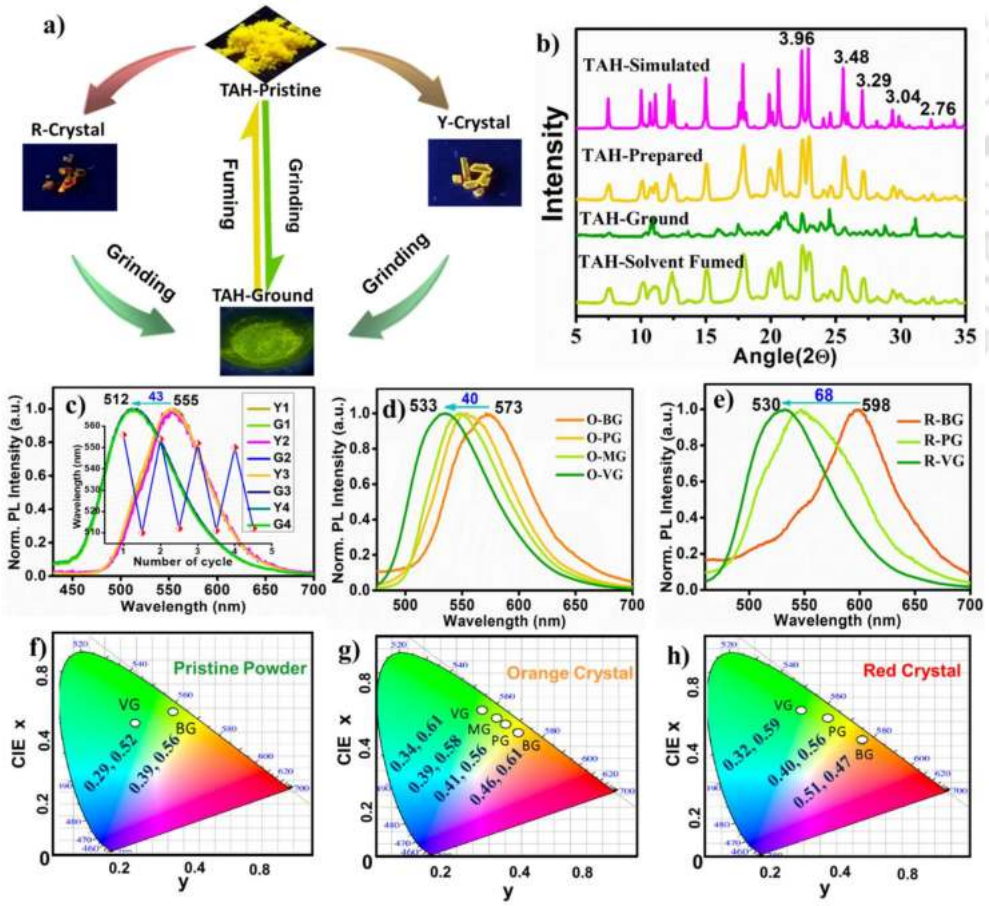

Figure 2.14. (a) A schematic illustration of self-assembled and disassembled reversible cycle of trimorphs. (b) Powder XRD pattern, in case of grounded TAH, very weak diffractions were observed depicting amorphous domain. PL spectra after repeated grinding-fuming cycles for the yellow crystalline powder of TAH (Y: yellow phase, G: green phase) (c). PL spectra of orange and red color crystals of TAH, before and after grinding (d & e). CIE co-ordinate diagrams of grounded G/O/R crystals (f, g & h).

PXRD analysis also supported the stimuli-controlled emission switching and disassembly features of TAH due to the subsequent crystalline to amorphous phase transformations. The sharp diffraction peaks observed at 3.96 Å to 2.76 Å [d-space values (Å)] disappear upon mechanical stimuli, in this low-d-space region in PXRD typically revealing the π-π and strong packing interactions region (red dotted line, Figure 2.14b). On applying external stimuli, the bright yellow crystalline powder of TAH (555 nm), turned into amorphous green emissive powder (512 nm, ~43 nm) depicting MR characteristics which recovered upon dichloromethane solvent fuming (Figure 2.14c, inset: reversible grinding-fuming cycle is shown). The orange and red crystals exhibited multicolor emissions upon grinding; with partial grinding (PG), moderate grinding (MG), and vigorous grinding (VG), all of which were reversible. The emission color of the crystals were also modified from orange (573 nm) or red (598 nm) to green (533 nm or 530 nm) with a large blue-shift of ~40 nm for orange crystal and ~68 nm for red crystal (Figure 2.14d, e). Hence, crystals with tunable emission were observed which upon mechanical stimuli transform into amorphous phase, with the disappearance of sharp peaks and blue-shifted enhanced emission (512 nm) Table A2.6). The emission specific trimorphism and mechanochromism behavior were confirmed by plotting the CIE coordinate diagrams for color purity (Figure 2.14f, g & h). Stimuli-responsive disassembly behavior of both the co-assemblies TAHTFQ and TAHTCQ were also investigated alike to their twisted precursor TAH by disrupting the well-organized supramolecular packing, resulting in pristine amorphous TAH. The experiment was conducted in co-assembled crystals obtained from solution phase and on surface techniques (Figure 2.15a, b & Figure A2.10). Initially, mechanoresponsive (MR) characteristics were tested by applying mechanical force and further thermal stimuli[63] was subjected on both the co-crystals to inspect their thermo-responsive (TR) property. Notably, precisely controlled thermal treatment of the co-assemblies, resulted in a rapid response for TAHTFQ at 80 °C, whereas, TAHTCQ needed more time with high temperature at 100 °C to exhibit thermochromic feature (Figure A2.10). The TR results of the co-crystals were supported by temperature dependent powder X-ray diffraction studies at three different temperatures at 25 ºC, 50 ºC and 100 ºC with the powder form of the crystals. Surprisingly, with rising temperature, multiple broad diffraction peaks were observed which is similar to the disassembled and amorphous parent TAH diffraction pattern, confirming thermo-responsive behavior of co-crystals and recovery of parent molecular donor (Figure A2.11).

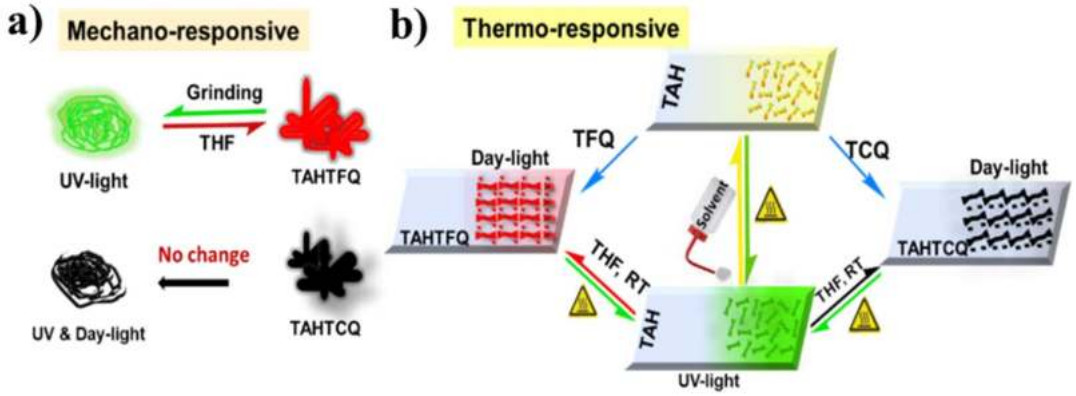

Figure 2.15. (a & b) Illustrations of on-surface mechanoresponsive (MR) and thermoresponsive (TR) properties of TAHTFQ and TAHTCQ cocrystals.

PL emissions of both the co-crystals were suppressed, which demonstrated that multiple non-covalent interactions were indeed potentially strong to self-organize back to their original forms even at extreme stimuli conditions (Figure 2.16c, d**).** Further, TGA study in Figure 2.10b demonstrated fast degradation at 130 °C for TAHTFQ, and relatively slow degradation at 200 °C for TAHTCQ, and a common thermal decomposition curve at 355 °C observed for both co-crystals due to the higher stability for the parent TAH. Further, physicochemical and tunable mechanical properties[64,65] of the integrated co-crystals upon thermal stimuli exhibited to turn on green emission with amorphous TAH, since TFQ and TCQ were displaced from the supramolecular co-crystals (blue dotted line in Figure 2.16a, **b**) by disruption of the non-covalent interactions. Moreover, reversible TR behavior was established by performing solvation after grinding and heating, wherein PXRD persists at d- values 2.26 Å and 5.72 Å for TAHTFQ. Additionally, the observed phenome-non was also supported by DSC results, which revealed a well-matched endothermic phase transition (melting) at 204 °C observed for amorphous TAH and different exothermic crystalline phase transitions observed at 78 °C, 122 °C and 178 °C from single-component and binary co-assembled systems respectively (Figure 2.16e). The PL studies confirmed the MR behavior, where ~8 nm blue-shifted enhanced emission at 522 nm was observed for TAHTFQ rather than precursor TAH (MC emission at 530 nm) whereas TR for TAHTCQ exhibited almost no emission switching and found at 510 nm, which is very close to disassembled TAH emission 512 nm. Importantly, both the dis-assemblies were instantly recovered and spontaneously assembled back by adding few drops of THF over grounded and heated co-assemblies.

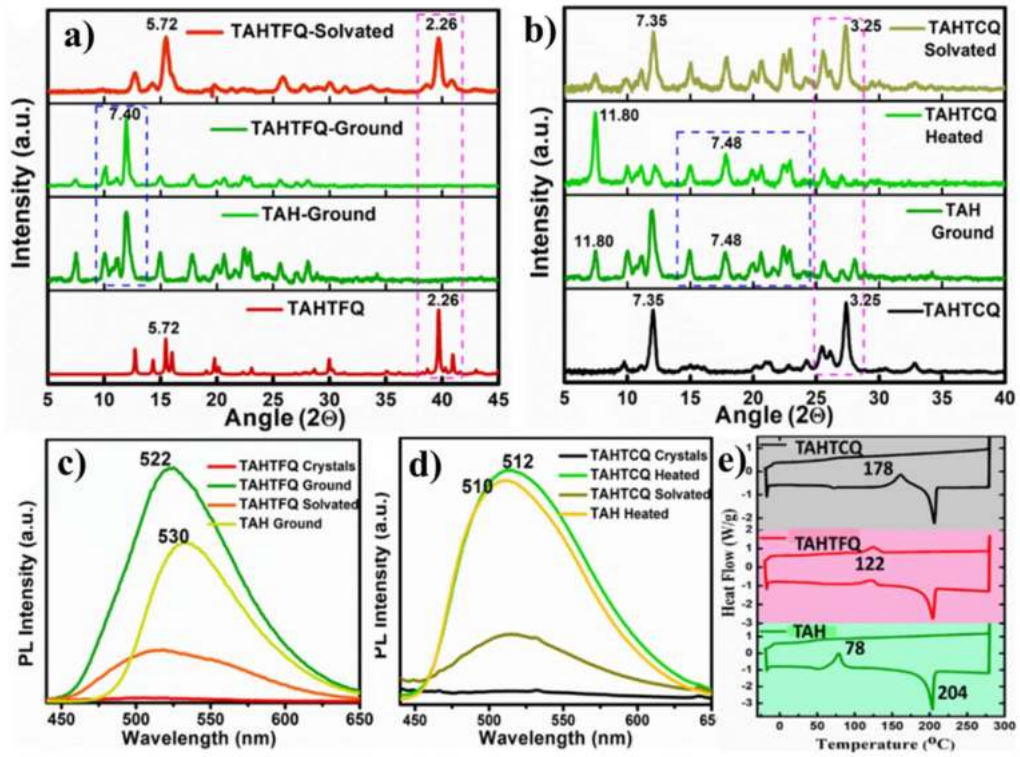

Figure 2.16. (a & b) PXRD patterns for the self-organized co-crystals TAHTFQ/TAHTCQ and disassembly to TAH. (c & d) Emission switching behavior in PL-spectra recorded at pristine, grounded and solvated condition. (g).DSC studies were performed which exhibited endothermic transition at 204 °C for amorphous TAH and different exothermic crystalline phase transitions were observed at 78 °C, 122 °C and 178 °C from single-component and binary co-assembled systems respectively.

2.4. Conclusion

Two new classes of kinetically controlled "H-type mixed stack" and "J-type segregated stack" supramolecular co-crystals were conceived from a simple stimuli-active trimorphic "twisted aromatic hydrocarbon (TAH)". Structural transformations ability of TAH offered heteromolecular network formation of TAHTFQ and TAHTCQ in the presence of strong oxidant p-Fluoranil and p-Chloranil respectively. These functional co-crystals, present an effective and simple approach to control CT functionality and well-defined packing which directed the mechanistic pathway for co-operative network formation by tailoring distinct nano range growth morphology, in water, without altering polymorphic characteristics of TAH and are bestowed with typical 'structure-property relationship' aspects. Combined with the experimental studies and computational analysis, the rapid and spontaneous co-assembly formation with emission quenching mechanism was found to be governed by two distinct non-covalent interactions, different electronegative substitution, and charge density of acceptors and the dissimilar binding affinity of the guest molecules. Thus, precisely, the

generation of two distinct packing motifs and turn on emission with an ability to self-organize reversibly even upon severe and mild to extensive stimuli exploitation was demonstrated. Exploring co-assembly formation of such unusual twisted aromatic hydrocarbon structures in water has enriched the perception on their structure related nano to bulk properties, enabling the construction of unique stimuli-responsive functional non-covalent assemblies, tailoring distinct nano growth morphology and next-generation optoelectronic devices thereby broadening the application of co-crystal based supramolecular materials.

2.5. References

[1] J. E. Anthony, *Chem. Rev.,* **2006,** *106*, 5028-5048.

[2] F. H. Herbstein, Oxford University Press, New York, **2006**.

[3] R. Li, W. Hu, Y. Liu, D. Zhu, *Acc. Chem. Res.,* **2010**, *43*, 529-540.

[4] L. Sun, W. Zhu, W. Wang, F. Yang, C. Zhang, S. Wang, X. Zhang, R. Li, H. Dong, W. Hu, *Angew. Chem. Int. Ed.,* **2017**, *56*, 7831-7835.

[5] M. Yamashina, M. M. Sartin, Y. Sei, M. Akita, S. Takeuchi, T. Tahara, M. Yoshizawa, *J. Am. Chem. Soc.,* **2015**, 137, 9266-9269.

[6] Y. S. Zhao, J. Wu, J. Huang, *J. Am. Chem. Soc.,* **2009**, *131*, 3158-3159.

[7] S. J. Kang, S. Ahn, J. B. Kim, C. Schenck, A. M. Hiszpanski, S. Oh, T. Schiros, Y.-L. Loo, C. Nuckolls, *J. Am. Chem. Soc.,* **2013**, *135*, 2207-2212.

[8] S. Horiuchi, F. Ishii, R. Kumai, Y. Okimoto, H. Tachibana, N. Nagaosa, Y. Tokura, *Nat. Mater.,* **2005**, *4*, 163-166.

[9] A. S. Tayi, A. K. Shveyd, A. C. H. Sue, J. M. Szarko, B. S. Rolczynski, D. Cao, T. J. Kennedy, A. A. Sarjeant, C. L. Stern, W. F. Paxton, W. Wu, S. K. Dey, A. C. Fahrenbach, J. R. Guest, H. Mohseni, L. X. Chen, K. L. Wang, J. F. Stoddart, S. I. Stupp, *Nature,* **2012**, *488*, 485-489.

[10] K. Yan, M. Long, T. Zhang, Z. Wei, H. Chen, S. Yang, J. Xu, *J. Am. Chem. Soc.,* **2015**, *137*, 4460-4468.

[11] G. Liu, J. Liu, X. Ye, L. Nie, P. Gu, X. Tao, Q. Zhang, *Angew. Chem. Int. Ed.,* **2017**, *56*, 198-202.

[12] K. Cai, J. Xie, D. Zhang, W. Shi, Q. Yan, D. Zhao, *J. Am. Chem. Soc*., **2018**, *140*, 5764-5773.

[13] X. Hou, C. Ke, C. J. Bruns, P. R. McGonigal, R. B. Pettman, J. F. Stoddart, *Nat. Commun.,* **2015**, *6*, 6884.

[14] Y. Lu, J. Zhao, R. Zhang, Y. Liu, D. Liu, E. M. Goldys, X. Yang, P. Xi, A. Sunna, J. Lu, Y. Shi, R. C. Leif, Y. Huo, J. Shen, J. A. Piper, J. P. Robinson, D. Jin, *Nat. Photonics.,* **2013**, *8*, 32-36.

[15] Y. Liu, A. H. Flood, P. A. Bonvallet, S. A. Vignon, B. H. Northrop, H.-R. Tseng, J. O. Jeppesen, T. J. Huang, B. Brough, M. Baller, S. Magonov, S. D. Solares, W. A. Goddard, C.-M. Ho, J. F. Stoddart, *J. Am. Chem. Soc.,* **2005**, *127*, 9745-9759.

[16] L. Yu, *Acc. Chem. Res.,* **2010**, *43*, 1257-1266.

[17] T. Beyer, G. M. Day, S. L. Price, *J. Am. Chem. Soc.,* **2001**, *123*, 5086-5094.

[18] J. Thun, L. Seyfarth, J. Senker, R. E. Dinnebier, J. Breu, *Angew. Chem. Int. Ed.,* **2007**, *46*, 6729-6731.

[19] G. Giri, R. Li, D.-M. Smilgies, E. Q Li, Y. Diao, K. M. Lenn, M. Chiu, D. W. Lin, R. Allen, J. Reinspach, S. C. B. Mannsfeld, S. T Thoroddsen,. P. Clancy, Z. Bao, A. Amassian, *Nat. Commun.,* **2014**, *5*, 3573.

[20] L. A. Hardegger, B. Kuhn, B. Spinnler, L. Anselm, R. Ecabert, M. Stihle, B. Gsell, R. Thoma, J. Diez, J. Benz, J.-M. Plancher, G. Hartmann, D. W. Banner, W. Haap, F. Diederich, *Angew. Chem., Int. Ed.,* **2011**, *50*, 314-318.

[21] C. B. Aakeroy, S. Forbes, J. Desper, *J. Am. Chem. Soc.,* **2009**, *131*, 17048-17049.

[22] A. S. Tayi, A. Kaeser, M. Matsumoto, T. Aida, S. I. Stupp, *Nat. Chem.,* **2015**, *7*, 281-294.

[23] C. A. Gunawardana, C. B. Aakeröy, *Chem. Commun.,* **2015**, *54*, 14047-14060.

[24] T. Shirman, D. Freeman, Y. D. Posner, I. Feldman, A. Facchetti, M. E. van der Boom, *J. Am. Chem. Soc.,* **2008**, *130*, 8162-8163.

[25] D. Braga, L. Maini, F. Grepioni, *Chem. Soc. Rev.,* **2013**, *42*, 7638-7648.

[26] W. Zhu, R. Zheng, Y. Zhen, Z. Yu, H. Dong, H. Fu, Q. Shi, W. Hu, *J. Am. Chem. Soc.,* **2015**, *137*, 11038-11046.

[27] J. D. Wuest, *Nat. Chem.,* **2012**, *4*, 74-75.

[28] N. A. Mir, R. Dubey, G. R. Desiraju, *Acc. Chem. Res.,* **2019**, *52*, 2210-2220.

[29] Sun L., Y. Wang, F. Yang, Zhang X., W. Hu, *Adv. Mater.,* **2009**, *31*, 1902328.

[30] L. Zhu, Y. Yi, Y. Li, E.-G. Kim, V. Coropceanu, J.-L. Brédas, *J. Am. Chem. Soc.,* **2012**, *134*, 2340-2347.

[31] J. Ferraris, V. Walatka, J. H. Perlstei, D. O. Cowan, *J. Am. Chem. Soc.,* **1973**, *95*, 948-949.

[32] J. Zhang, W. Xu, P. Sheng, G. Zhao, D. Zhu, *Acc. Chem. Res.,* **2017**, *50*, 1654-1662.

[33] M. Boterashvili, M. Lahav, S. Shankar, A. Facchetti, M. E. van der Boom *J. Am. Chem. Soc.,* **2014**, *136*, 11926-11929.

[34] M. Dabros, P. R. Emery, V. R. Thalladi, *Angew. Chem. Int. Ed.,* **2007**, *46*, 4132-4135.

[35] S. K. Park, J. H. Kim, T. Ohto, R. Yamada, A. O. F. Jones, D. R. Whang, I. S. Cho, Oh, J. H. Hong, J. E. Kwon, J. H. Kim, Y. Olivier, R. Fischer, R. Resel, J. Gierschner, H. Tada, S. Y. Park, *Adv. Mater.,* **2017**, *29*, 1701346.

[36] B. Lu, X. Fang, D. Yan, *ACS Appl. Mater. Interfaces,* **2020**, *12*, 31940-31951.

[37] Y. Ishijima, H. Imai, Y. Oaki, *Chem.* **2017,** *3,* 509-521.

[38] . Mei, He. Tian, *Matter,* **2020***, 3,* 329-332.

[39] D. Barman, R. Gogoi, K. Narang, P. K. Iyer, *Front. Chem.* **2020**, *8*, 483.

[40] M.-P. Zhuo, Y.-C. Tao, X.-D. Wang, Y. Wu, S. Chen, L.-S Liao, Jiang, L. *Angew. Chem. Int. Ed.,* **2018**, *130*, 11470-11474.

[41] X. Ye, Y. Liu, Q. Guo, Q. Han, C. Ge, S. Cui, L. Zhang, X. Tao, *Nat. Commun*., **2019**, *10*, 761.

[42] Y. Liu, A. Li, S. Xu, W. Xu, Y. Liu, W. Tian, B. Xu, *Angew. Chem., Int. Ed*. **2020**, *59*, 15098.

[43] G. Liu, J. Liu, X. Ye, L. Nie, P. Gu, X. Tao, Q. Zhang, *Angew .Chem., Int.Ed.* **2017**, *56*,198 -202.

[44] H. Jiang, P. Hu, J. Ye, K. K. Zhang, Y. Long, W. Hu, C. Kloc, *J. Mater. Chem. C,* **2018**, *6*, 1884-1902.

[45] H. Shao, X. Chen, Z. Wan, P. Lu, *J. Phys. Chem. B,* **2007**, *111*, 10386-10396.

[46] J. Mei, N. L. C. Leung, R. T. K. Kwok, J. W. Y. Lam, B. Z. Tang, *Chem. Rev.,* **2015**, *115*, 11718-11940.

[47] V. Ramamurthy, S. Jockusch, M. Porel, *Langmuir* **2015**, *31*, 5554-5570.

[48] M. Pakhira, D. P. Chatterjee, D. Mallick, R. Ghosh, A. K. Nandi, *Langmuir,* **2021**, *37*, 4953-4963.

[49] Y. Huang, J. Xing, Q. Gong, L.-C. Chen, G. Liu, C. Yao, Z. Wang, H.-L. Zhang, Z. Chen, Q. Zhang, *Nat. Commun.,* **2019**, *10*, 169.

[50] R. F Egerton, P. Li, M. Malac, *Micron,* **2004**, 35, 399-409.

[51] Winn, D.; Doherty, M. F., Modeling crystal shapes of organic materials grown from solution. *AIChE Journal* **2000**, *46*, 1348-1367.

[52] C. R. Newman, C. D. Frisbie, D. A. da Silva Filho, J.-L. Brédas, P. C. Ewbank, K. R. Mann, *Chem. Mater.* **2004,** *16*, 4436-4451.

[53] J. B. Torrance, *Acc. Chem. Res.* **1979,** *12*, 79-86.

[54] K. P. Goetz, A. Fonari, D. Vermeulen, P. Hu, H. Jiang, P. J. Diemer, J. W. Ward, M. E. Payne, C. S. Day, C. Kloc, V. Coropceanu, L. E. McNeil, O. D. Jurchescu, *Nat. Commun.,* **2014**, *5*, 5642.

[55] W. Ji, B. Xue, S. Bera, S. Guerin, Y. Liu, H. Yuan, Q. Li, C. Yuan, L. J. W. Shimon, Q. Ma, E. Kiely, S. A. M. Tofail, M. Si, X. Yan, Y. Cao, W. Wang, R. Yang, D. Thompson, J. Li, E. Gazit, *ACS Nano* **2020**, *14*, 10704-10715.

[56] I. Rosbottom, J. K. Roberts, R. Docherty, *Cryst. Eng. Comm.,* **2015**, *17*, 5768-5788.

[57] C. J. Wienken, P. Baaske, U. Rothbauer, D. Braun, S. Duhr, *Nat. Commun*., **2010,** *1*, 100.

[58] S. K. Wolff, D. J. Grimwood, J. J. McKinnon, M. J. Turner, D. Jayatilaka, M. A. Spackman, University of Western Australia, **2012**.

[59] M. J. Frisch, *et.al.* Gaussian, Inc., Wallingford CT, 2013.Gaussian, Inc., Wallingford CT, **2013**.

[60] T. Ueno, Y. Urano, K.-I. Setsukinai, H. Takakusa, H. Kojima, K. Kikuchi, K. Ohkubo, S. Fukuzumi, T. Nagano, *J. Am. Chem. Soc.,* **2004**, *126*, 14079-14085.

[61] N. Meher, P. K. Iyer, *Angew. Chem. Int. Ed.,* **2018**, *57*, 8488-8492.

[62] X. Wang, C. Qi, Z. Fu, H. Zhang, J. Wang, H.-T. Feng, K. Wang, B. Zou, J. W. Y. Lam, B. Z. Tang, *Mater. Horiz.* **2021,** *8*, 630-638.

[63] V. G. Saraswatula, D. Sharada, B. K. Saha, *Cryst. Growth Des.*, **2018**, *18*, 52-56.

[64] Y. Sun, Y. Lei, H. Dong, Y. Zhen, W. Hu, *J. Am. Chem. Soc.,* **2018**, *140*, 6186-6189.

[65] W. Ji, B. Xue, S. Bera, S. Guerin, L. J. W. Shimon, Q. Ma, S. A. M. Tofail, D. Thompson, Y. Cao, W. Wang, E. Gazit, *Mater. Today* **2020**, *42*, 29-40.

Appendix: Additional data for **Chapter 2**

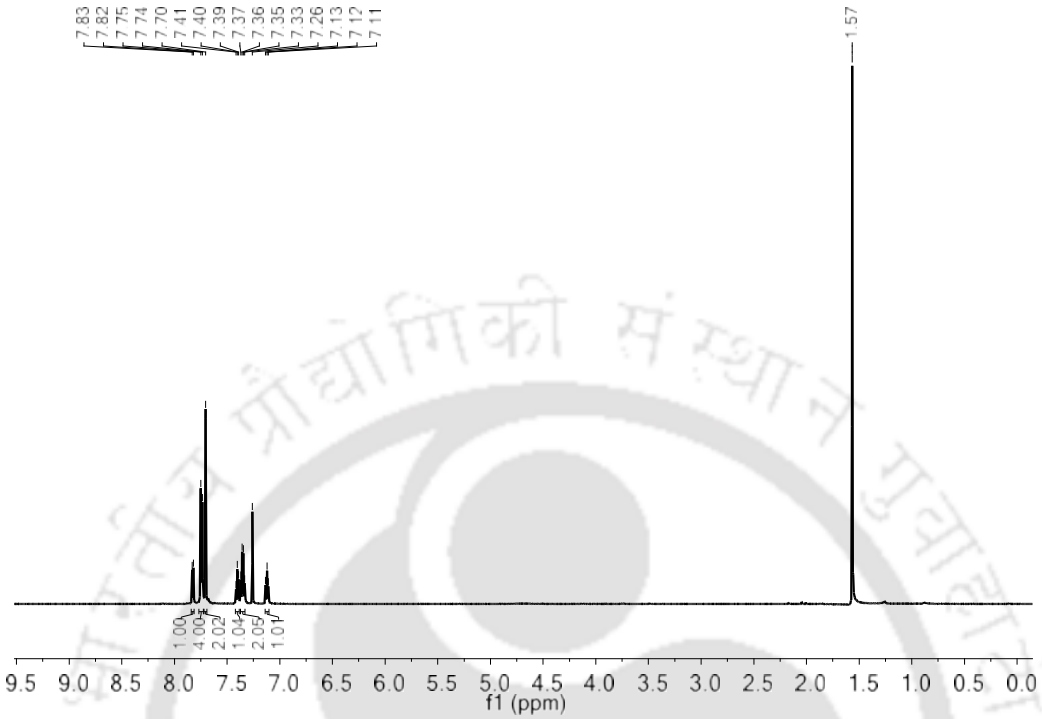

Figure A2.1. ^{1}H NMR spectra of TAH luminogen in $CDCl_3$ at 298K.

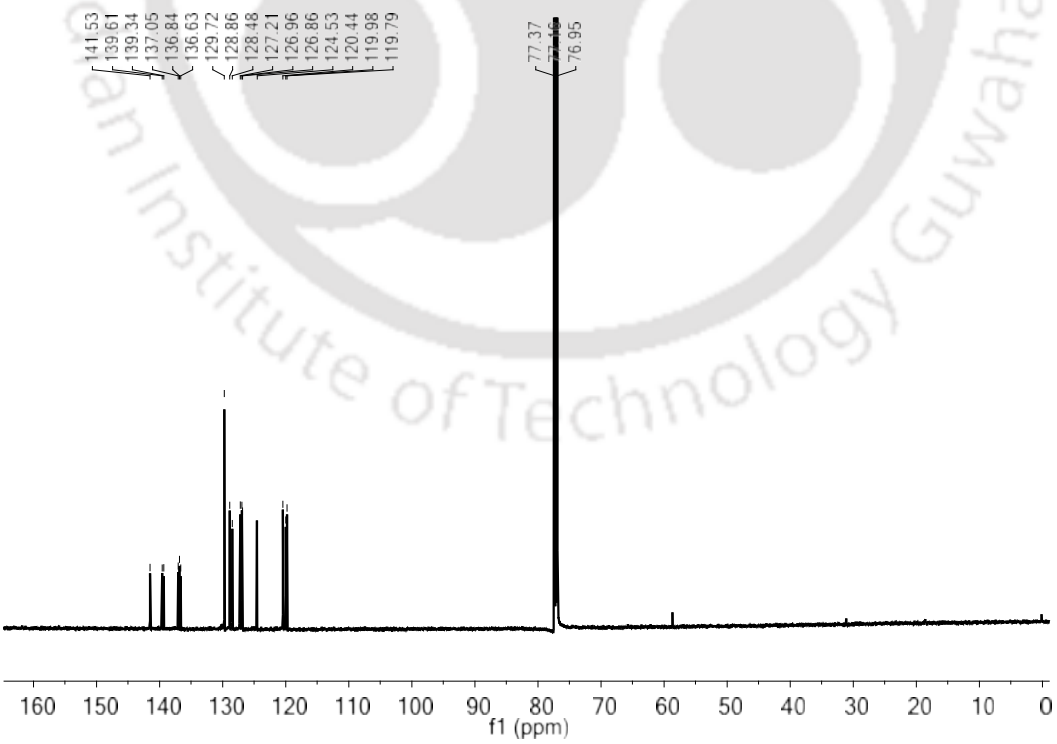

Figure A2.2. ^{13}C NMR spectra of TAH luminogen in $CDCl_3$ at 298K.

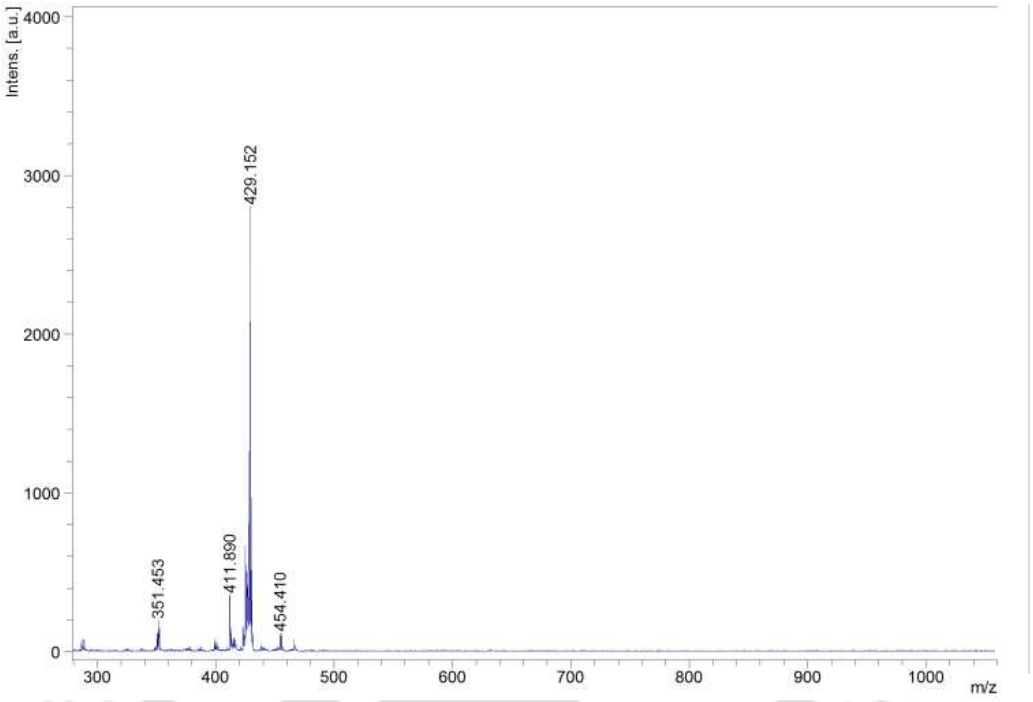

Figure A2.3. MALDI-TOF MS spectra of TAH luminogen.

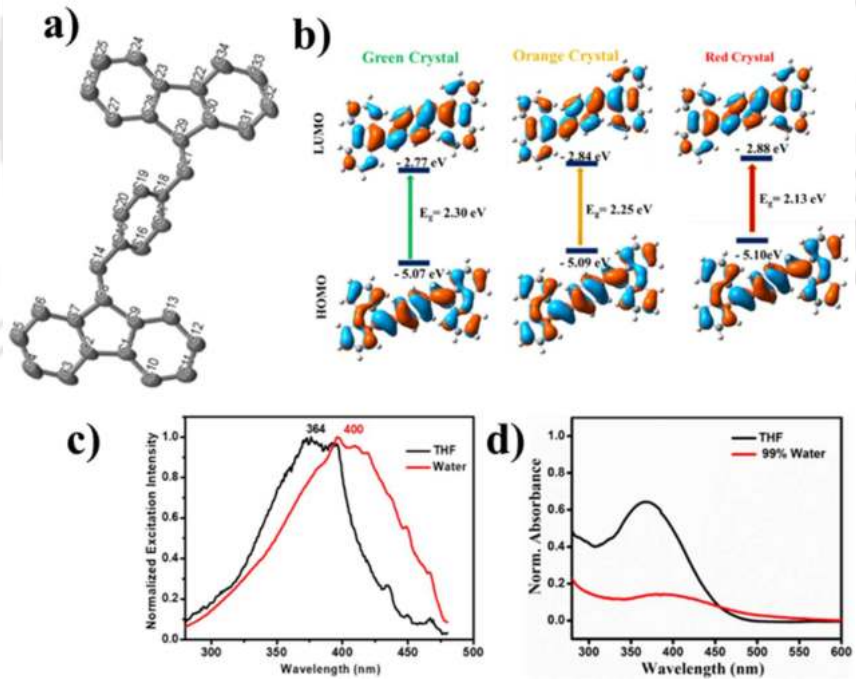

Figure A2.4. (a) Ellipsoids molecular structure of TAH. (b)Trimorphism behavior of the TAH by TD-DFT, B3LYP/6-31G (d,p) [cpcm, solvent=Heptane, Chloroform and THF].; With increasing solvent polarity band gap decreases significantly 2.30 eV, 2.25 eV and 2.13 eV for green, orange and red crystal respectively. (c)Solvent-induced change in absorbance at the excitation wavelength in THF and water. (d) Absorption spectra in THF and 99% water. The absorption spectra at condensed state of the luminogens exhibited single broad absorption band in water at 400 nm and in THF at 364 nm.

Table A2.1. Conformational deformations by Bond angles (in Å) and dihedral angles (in degree) of trimorphic G, O, R-TAH mechanophore.

Bond lengths/Bond Angles	G-Crystal	O-Crystal	R-crystal
C8-C14	1.349	1.348	1.349
C14-C15	1.466	1.464	1.466
C18-C21	1.469	1.463	1.469
C21-C29	1.343	1.341	1.344
C7-C8-C14-C15	171.05	171.22	171.23
C18-C21-C29-C30	170.53	170.89	170.66

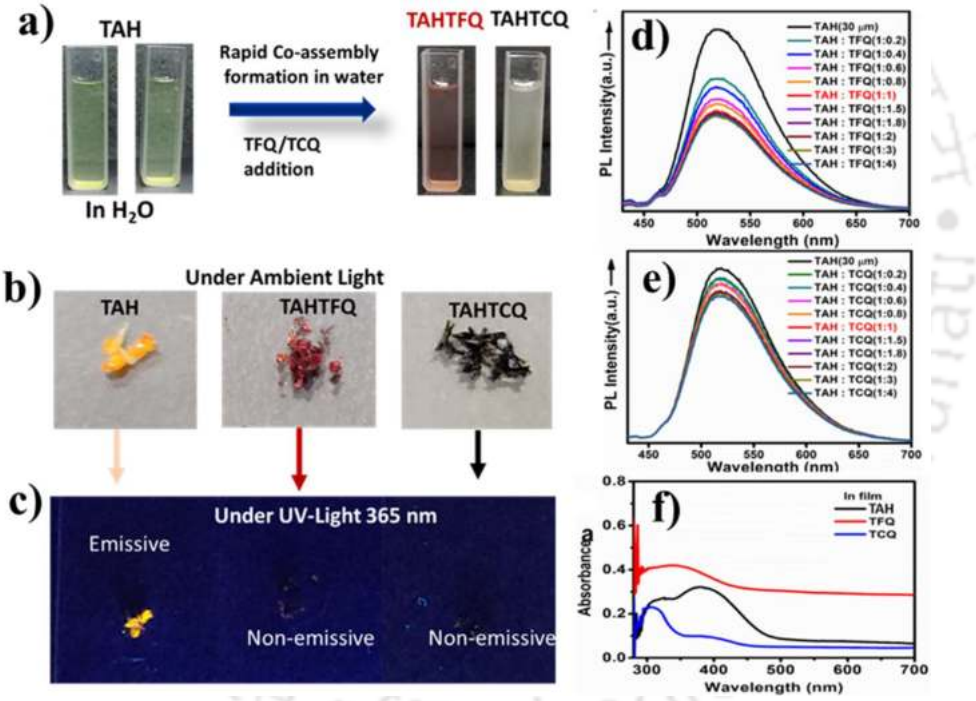

Figure A2.5. (a) A visual color change of supramolecular 3D-coassembly formation for TAHTFQ while TAHTCQ in aqueous medium (Milli-Q grade) by addition of TFQ & TCQ (20 mM) to DBF (20 mM). (b) TAH orange crystals and non-emissive co-assembled crystals of TAHTFQ (red) and TAHTCQ (black) prepared from solution phase technique by using THF as a solvent at equimolar concentrations of individual components at RT. (c) DBF crystals are emissive where DBFTFQ and DBFTCQ crystals are non-emissive, photograph taken under 365 nm UV-light. (d & e) Fluorescence at different equivalent ratios of TAH:TFQ/TCQ. (f) Solid state UV-vis spectra of TAH, TAHTFQ and TAHTCQ suggested that the blue and red shifted co-assemblies as similar to the absorption in aqueous phase.

Table A2.2. Calculated attachment energies of different crystal facets of TAHTFQ

hkl	Dhkl/Å	Eatt(Total)/kcal mol-1	Eatt(vdW)/kcal mol-1	% Total facet area
{ 0 0 1}	13.75501856	-17.4473219	-15.25308817	52.46959536
{ 0 1 0}	8.61278943	-42.28774375	-37.00590106	15.46102209
{ 0 1 -1}	7.07855931	-38.25250233	-32.66361513	8.24961203
{ 1 0 1}	6.92236923	-45.05388762	-38.0075819	15.26677349

Table A2.3. Calculated attachment energies of different crystal facets of TAHTCQ

hkl	Dhkl/Å	Eatt(Total)/kcal mol-1	Eatt(vdW)/kcal mol-1	% Total facet area
{ 0 0 1}	14.27817764	-22.24043691	-17.66534248	48.54670273
{ 0 1 0}	9.1540294	-50.80600283	-43.46326299	9.16237547
{ 0 1 1}	7.6284247	-39.73488938	-35.91609497	18.53079964
{ 1 0 0}	6.93162506	-55.23521704	-46.55439061	13.62520067

Table A2.4. Crystallographic data and structure refinement parameters of TAH trimorphs, TAHTFQ and TAHTCQ co-assemblies.

Compound	**TAH-Green**	**TAH-Orange**	**TAH-Red**	**TAHTFQ**	**TAHTCQ**
Empirical formula	$C_{34}H_{22}$	$C_{34}H_{22}$	$C_{34}H_{22}$	$C_{34}H_{22},C_6F_4O_2$	$C_{34}H_{22},C_6Cl_4O_2$
CCDC NO	1860140	1585865	1860220	1935615	1935620
Temperature/K	293 (2)	293 (2)	296 (2)	293 (2)	293 (2)
Crystal system	orthorhombic	orthorhombic	orthorhombic	triclinic	triclinic
Space group	Pbca	Pbca	Pbca	P -1	P -1
a/Å	10.759(3)	10.7726(4)	10.7705(19)	6.5187(11)	7.3722(5)
b/Å	17.616(4)	17.6372(7)	17.623(3)	9.1305(16)	9.069(1)
c/Å	23.624(6)	23.6168(8)	23.643(4)	15.218(3)	14.8974(14)
α/°	90.00	90.00	90.00	80.786(16)	94.027(9)
β/°	90.00	90.00	90.00	77.885(16)	99.706(7)
γ/°	90.00	90.00	90.00	73.818(15)	91.048(7)

Volume/Å^3	4477(2)	4487.2(3)	4487.6(13)	845.5(3)	978.88(16)
Z	8	8	8	2	2
ρ_{calc}mg/mm^3	1.277	1.275	1.274	1.553	1.564
m/mm^{-1}	0.072	0.072	0.072	0.128	0.623
F(000)	1808	1808	1808	402.0	466.0
Index ranges	-13 ≤ h ≤ 13, -22 ≤ k ≤ 21, -29 ≤ l ≤ 29	-12 ≤ h ≤ 12, -17 ≤ k ≤ 20, -27 ≤ l ≤ 28	-14 ≤ h ≤ 14, -23 ≤ k ≤ 23, -31 ≤ l ≤ 30	-7 ≤ h ≤ 7, -10 ≤ k ≤ 10, -13 ≤ l ≤ 18	-9 ≤ h ≤ 9, -12 ≤ k ≤ 11, -19 ≤ l ≤ 10
Reflections collected	153523	12859	70396	5267	7468
Independent reflections	4609[R(int) = 0.1977]	3932[R(int) = 0.0330]	5645[R(int) = 0.0344]	2993[R(int) = 0.0276]	4404[R(int) = 0.0369]
Data/restraints/parameters	4609/0/307	3932/0/307	5645/0/307	2993/0/262	4404/0/262
Goodness-of-fit on F^2	1.131	0.932	0.878	1.058	1.052
Final R indexes [I>=2σ (I)]	R1 = 0.0824, wR2 = 0.1726	R1 = 0.0503, wR2 = 0.1386	R1 = 0.0499, wR2 = 0.0499	R1 = 0.0500, wR2 = 0.1056	R1 = 0.0637, wR2 = 0.1385
Final R indexes [all data]	R1 = 0.1487, wR2 = 0.2084	R1 = 0.0869, wR2 = 0.1708	R1 = 0.0917, wR2 = 0.1612	R1 = 0.0750, wR2 = 0.1263	R1 = 0.1182, wR2 = 0.1753

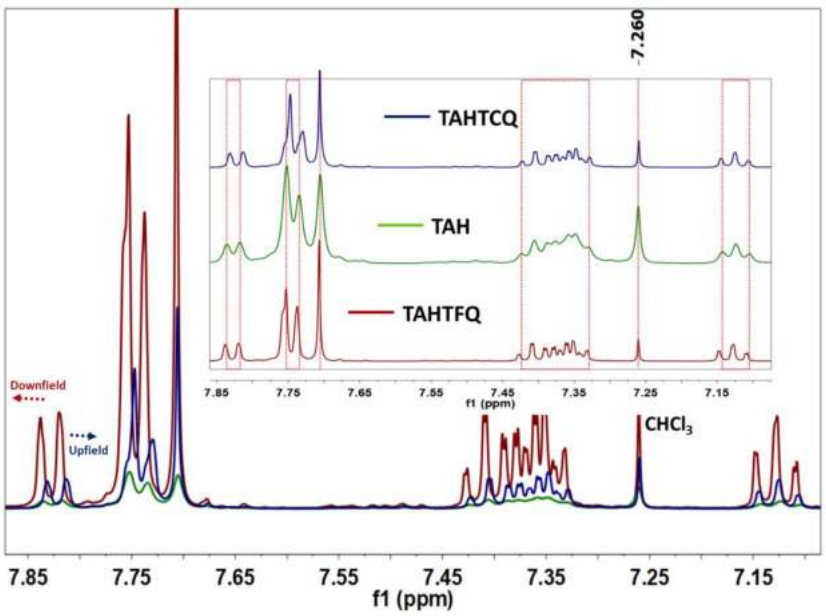

Figure A2.6. A superimposed (inset stacked) ^{1}HNMR spectra of TAH, TAHTFQ and TAHTCQ recorded in $CDCl_3$ at room temperature. ^{1}HNMR spectra revealed that after co-crystals formation, aromatic protons of TAHTFQ shifted downfield and while TAHTCQ was shifted upfield.

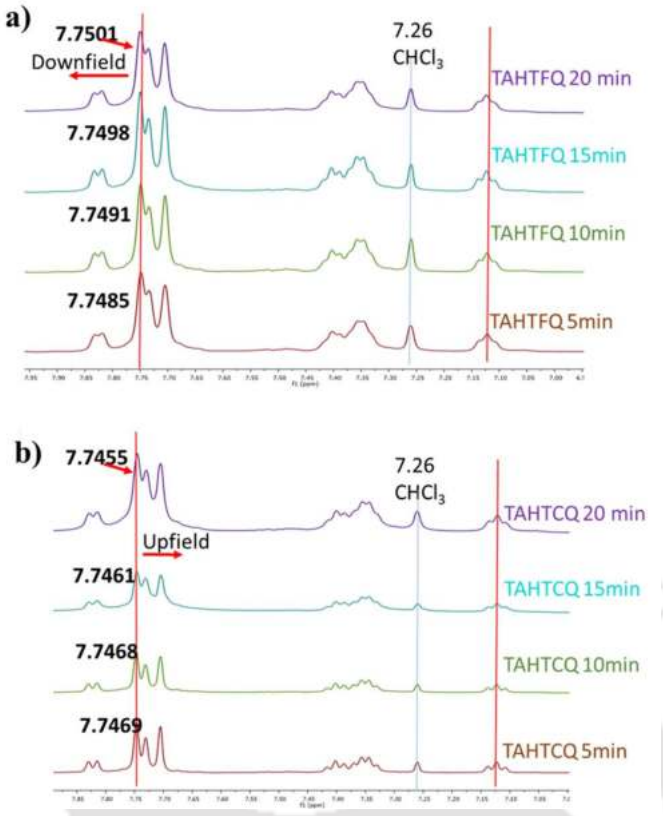

Figure A2.7. (a & b) Time-dependent stacked ^{1}HNMR spectra of TAHTFQ and TAHTCQ recorded in $CDCl_3$ at room temperature. ^{1}HNMR spectra revealed that TAHTFQ co-crystals formed fast (moved to downfield within 10 mins) while TAHTCQ formed slow starts moved to upfield within 15 mins, aromatic protons of TAHTFQ shifted downfield and while TAHTCQ was shifted upfield.

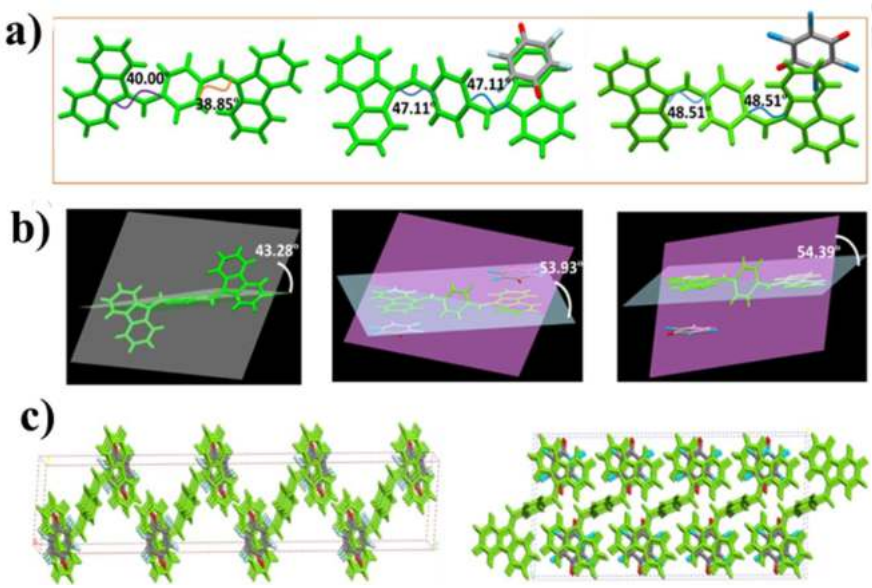

Figure A2.8. (a) Flexible dihedral angle b/w phenyl core and di-benzofulvene has been fixed with two different angle upon co-crystallization with TFQ and TCQ. (b) Twisted angle between two planes of planar TAH and central phenyl planes are 43.28°, 53.93° and 54.39° ° for TAH crystal, TAHTFQ TAHTCQ co-crystals respectively influenced by the interactive orientation of the guest molecules. (c) Bulk packing of SC-XRD structure for TAHTFQ showing close contact with symmetrical alignment between TAH and TFQ cores, whereas in TAHTCQ an unsymmetrical alignment with long distance contact was found.

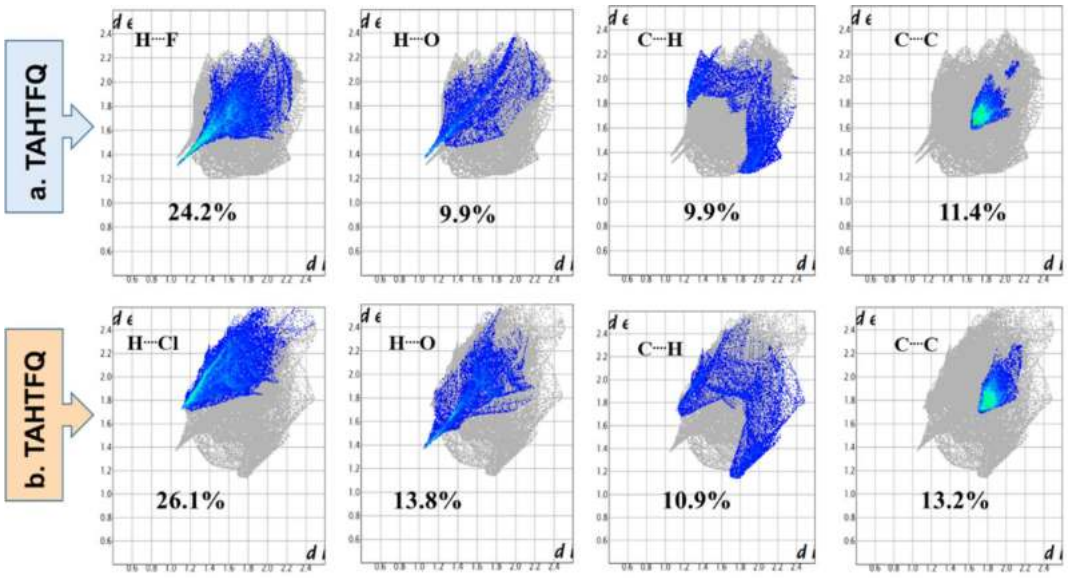

Figure A2.9. (a & b) 2D Finger print for surface to atom intermolecular interactions mapped on Hirshfeld surface in TAHTFQ and TAHTCQ.

Table A2.5. The energy levels calculated from cyclic voltammetry and DFT

Compound			Experimental data				DFT data (eV)		
	E_{ox}/V	E_{red}/V	E_{HOMO} /eV	E_{LUMO} /eV	E_{opt}/ eV	H-L Gap eV	HOMO	LUMO	H-L Gap
TAH	1.09	-	-5.49	-2.96	2.53	2.53	-5.47	-2.17	3.29
TFQ	-	-0.20	-7.01	-4.20	2.81	2.81	-8.00	-4.20	3.80
TCQ	-	-0.16	-6.87	-4.24	2.63	2.63	-7.75	-4.27	3.48
TAHTFQ	1.15	-0.24	-5.55	-4.16	-	1.39	-5.55	-3.88	1.67
TAHTCQ	1.10	-0.20	-5.50	-4.16	-	1.34	-5.53	-4.05	1.48

Table A2.6. CIE coordinate values of the TAH mechanophore

	Yellow powder	X, Y coordinates	Orange crystals	X, Y coordinates	Red crystals	X, Y coordinates
Before Grinding (BG)	556	0.39, 0.56	573	0.46, 0.51	598	0.51, 0.47
Partial Grinding (PG)	-	-	554	0.41, 0.56	550	0.40, 0.56
Moderate Grinding (MG)	-	-	547	0.39, 0.58	-	-
Vigorous Grinding (VG)	510	0.29, 0.52	533	0.34, 0.61	530	0.32, 0.59

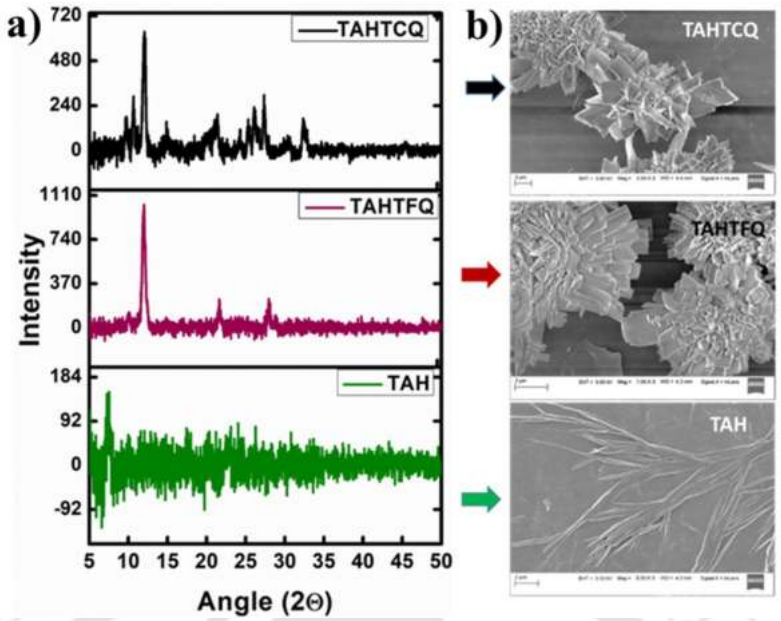

Figure A2.10. Instant on surface co-crystals sample preparation was done by simple drop-casting technique and co-crystalswere confirmed by thin film XRD studies (a), FESEM image recorded to investigate the distinct morphology on the surface (b) for TAH (green) TAHTFQ (magenta) and TAHTCQ (black) respectively.

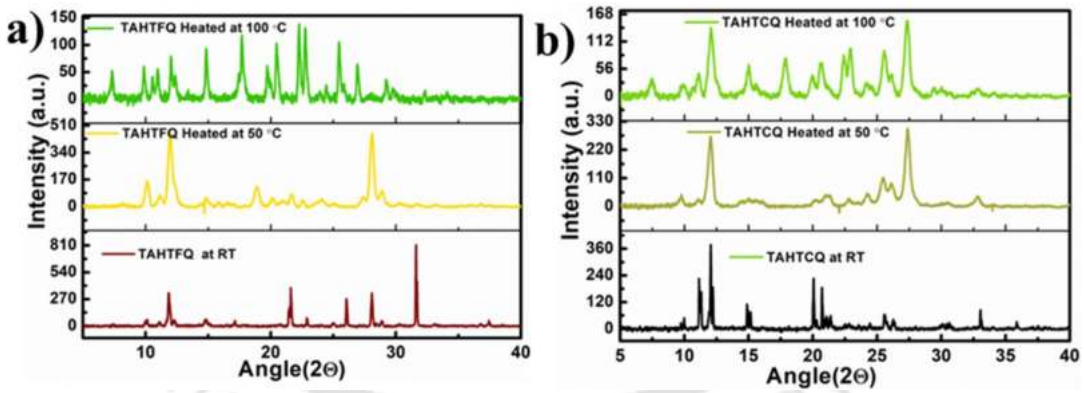

Figure A2.11. Thermo-Responsive feature of the co-crystals were supported by temperature dependent-PXRD study, at three different temperatures at 25 ºC, 50 ºC and 100 ºC with the powder form of the crystals were recorded. The PXRD pattern of (a) for TAHTFQ and (b) for TAHTCQ showed with rising temperature multiple broad diffraction peaks was observed which is similar to the disassembled amorphous TAH diffraction pattern, confirming thermo-responsive behavior of co-crystals.

CHAPTER 3

Through-Space Charge-Transfer Induced Color-Tunable Luminescent Co-crystals: Polymorphism, Isomerism, Thermally Activated Delayed Fluorescence and Optical Waveguides

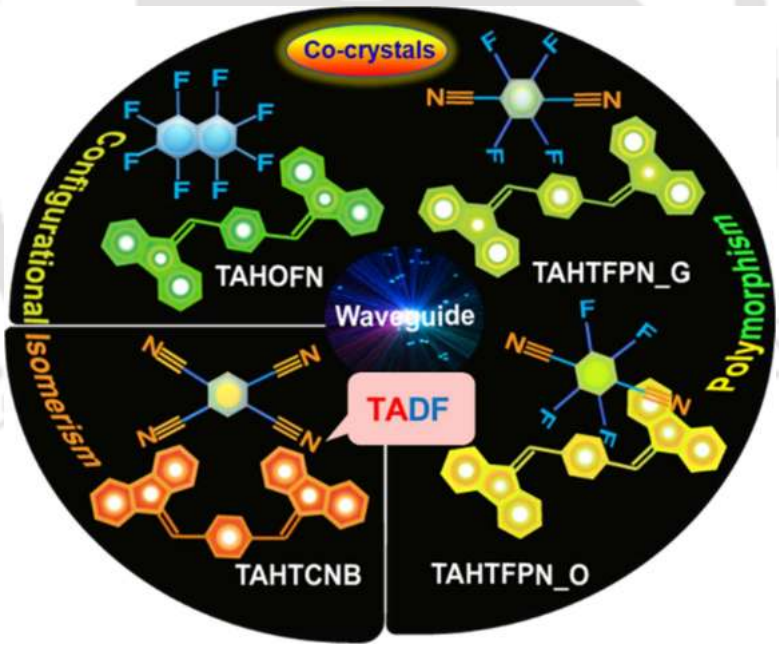

Barman, D., Annadhasan, M., Rajamalli, P., Chandrasekar, R., Iyer, P. K. (*Chem. Sci.* Under Review).

Abstract

Photofunctional co-crystal engineering strategies based on donor-acceptor π-conjugated system facilitates expedient molecular packing, consistent morphology, and switchable optical properties, conferring synergic 'structure-property relationship' and optoelectronic functions. In this work, four color-tunable bright co-crystals have been formulated by modulating the excited-state properties via variable through-space charge-transfer (TSCT) interactions in the presence of twisted aromatic hydrocarbon (TAH) donor and three diverse planar acceptors. Remarkably, by adjusting the strength of acceptor units, a structural transformation into hybrid stacking modes are resulting color-specific polymorphs and an unprecedented configurational isomer. Interestingly, the cis-isomeric co-crystal exhibits unusual triplet-harvesting thermally activated delayed fluorescence (TADF) characteristics, a major breakthrough in hydrocarbon based multicomponent systems. Structural analysis via single crystal X-ray studies and simulations reveal weak non-bonding interactions that regulated the ordered packing, tunable energy band gap and variable degree of TSCT that collectively enriched the physicochemical properties of these co-crystals (PLQY = ~77%). Impressively, the 1D-microrod co-crystals demonstrates as an exceptional class of both singlet and triplet harvesting waveguides by self-guiding the generated fluorescence and TADF, along its longitudinal axis at ultra-low optical loss co-efficient (~0.0742, 0.0837 dB/μm). These findings provide a considerable insights to explore the scope in multicomponent crystals design strategy and optoelectronic functions.

3.1. Introduction

Organic photofunctional materials based on co-crystals, have received immense attention owing to their unique molecular stacking, long-range assembly, high photoluminescence efficiency and improved semiconducting functionality.[1,2] Co-crystal engineering of single component building blocks into ordered multicomponent supramolecular organization has displayed remarkable performances in organic solid-state lasers (OSSLs),[3] ambipolar organic field-effect transistors (OFETs),[4] organic light-emitting transistors (OLETs),[5,6] multi-stimuli-responses (MSR),[7] two-photon absorption[8] and optical waveguides (OWGs).[9-20] Few organic functional co-crystals possess extremely ordered and finely engineered architectures that offering defects free crystal lattice, free grain boundary, well-defined morphology (1D/2D), and efficient signal input/output properties,[21] that stimulated to light propagation feature and showed attractive properties for waveguide applications in next-generation telecommunication technologies.[22,23] Thereafter, many attempts were devoted to develop such co-crystals, among which electron-rich donor (D) and electron-deficient acceptor (A) based charge-transfer co-assemblies were demonstrated to be the best approaches so far.[24,25] Versatile intermolecular interactions viz. hydrogen bonds (HBs), halogen bonds (XBs), π-π stacking including charge-transfer (CT) played a pivotal role to define directional interactions, shape/size organization as well as their multifunctional behavior.[26-28] Specifically, organic CT co-crystals are of potential interest due to their versatile arrangements between D-A moieties, benefiting to realize superior photonic and electronic performances as compared to the lone synergistic constituents.[9,29] Besides, different hybrid molecular stacking and definite aggregation patterns such as mixed stack and segregated stack in H- or J-type assembly endows significant contribution to their optoelectronic properties.[30,31] Recent studies have shown that the color-tunable polymorphs provide promising directions for the modulation of luminescent behavior and presents immense prospects for the exploration of novel optical waveguide feature and optoelectronic applications.[32,33] Nevertheless, polymorphs/co-crystals till date have mainly catered to the pharmaceuticals field.[34,35] Hence, the evolution of such systems as semiconductors have often been marred by intricate designs or static molecular structures, varied packing modes and inefficient optical properties, thereby lacking clarity and fails to describe structure-functions correlation in depth.[36]

Nevertheless, the ongoing pursuit of emerging fluorescent materials, and harvesting triplets in pure organic molecules is a great challenge. Few CT-active organic emitters have enabled to harvest triplet excitons *via* an effective reverse intersystem crossing (RISC) process at low splitting energy (ΔE_{ST}), which dictate as thermally activated delayed fluorescence (TADF).[37, 38] The small ΔE_{ST} between lowest singlet (S_1) and triplet (T_1) states allowed non-radiative triplet population inversion to regenerate radiative singlet with the aid of thermal energy and delayed fluorescence from S_1 to S_0. A typical TADF emitter designed by direct covalent bonding at orthogonally linked D-A moieties, offered very high quantum efficiency, longer life-time and improved device performances, thus, receiving significant interest in the area of OLEDs.[39,40] However, the existence of TADF-co-crystals based emitters are seldom found in literature,[41] presumably due to either the lack of insights into mostly reported co-crystals design or the planar co-formers remains ineffective to fulfill the stringent requirement for TADF process. Since most of the reported co-crystal structures were constructed by using highly planar and rigid constituents, they showed inefficient intermolecular interactions and notorious aggregation caused quenching (ACQ) behavior during co-crystallization.[42]

One of our recent report, we demonstrated that CT co-crystal engineering relying on non-planar twisted aromatic hydrocarbon (TAH) donor and electron-deficient planar acceptors, could be an ideal way to precisely decipher the structure-properties relationships at molecular level.[43] However, an efficient and dynamic organic luminescent co-crystal design with modulation of excited states *via* through-space charge-transfer (TSCT) induced color-tunable emission with high photoluminescence quantum yield (PLQY), remains an unexplored domain so far.[10, 44] Since, TAH holds a strong electron-donating ability and tunable energy band they demonstrate fascinating optoelectronic properties owing to their electron-rich π-conjugated molecular structures. Hence, TAH-based donor is favorable to newer photo functionality by a greater extent as they possess inherent aggregation induced emission (AIE) behavior *via* restriction in rotation (RIR) in solid state.[45, 46] Moreover, the dynamic nature of TAH can easily be deformed by external factors such as solvent, temperature, diverse crystal packing, interactive CT-strength at different crystallization environments, that encouraged to achieve unprecedented co-crystals of polymorphs and configurational isomers, thereby providing newer avenues to construct novel co-crystals with unusual physical properties.[31,47] Hence, if the combined advantages of two major co-crystal engineering strategies of molecular polymorphism and configurational isomerism

were synergized, the route and design to achieve novel photofunctional materials would be broadened. In addition, sterically hindered TAHs donor-based CT co-crystals with spatially oriented rigid assembly could offer efficient TADF characteristics. Therefore, TAHs based co-crystals, not only showed multi-phase structural transformation, but also modulates the emission properties, morphologies, improved thermal stability and superior photon harvesting behavior in their supramolecular scale as compared to previously reported traditional planar donor counter parts.[30, 48] Therefore, rational design of TAH-based multifunctional co-crystals with color-tunable luminescence, promising TADF characteristics, including optical waveguide performances in polymorphs/isomeric structures, remains particularly unidentified to date.

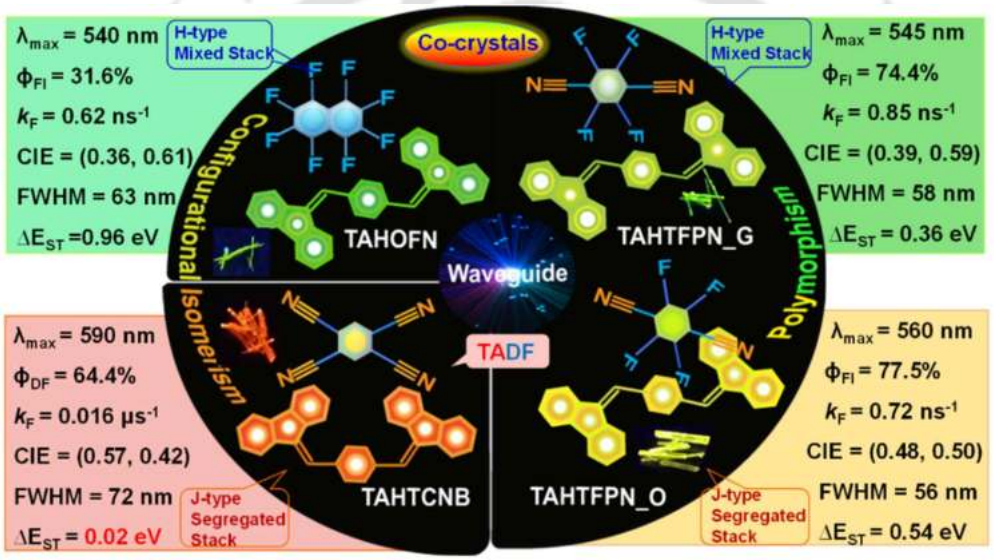

Figure 3.1. Schematic illustration of luminescent co-crystals TAHOFN, TAHTFPN_G, TAHTFPN_O and TAHTCNB composed of twisted aromatic hydrocarbon donor (TAH) and planar acceptors octafluoronapthalene (OFN), tetra-fluoropterepthonatonitrile (TFPN) and tetracyanobenzene (TCNB) with their respective tunable packing oriented col-or-tunable polymorphs and configurational isomeric binary assembly structures.

Herein, a series of four novel TAH-based luminescent CT-co-crystals were successfully formulated by using simple building blocks, referred as TAHOFN, TAHTFPN_G, TAHTFPN_O, and TAHTCNB. All the CT-complexes displayed dissimilar fluorescence colors such as off-green, bright green, yellow and red emissions of TAHOFN, TAHTFPN_G, TAHTFPN_O and TAHTCNB respectively. Notably, among the four co-crystals TAHTFPN-G and TAHTFPN-O are the color-specific polymorphs, and are stable in *trans* form, while TAHTCNB exhibited unusual triplet harvesting configurational *cis*-isomer by preserving the integrity of structural interiors of the TAH (**Figure 3.1).**

Experimental and theoretical results suggested that all the integrated co-crystals exhibited tunable energy band gap, variable TSCT degree and multiple noncovalent interactions between aromatic cores, conveying defined packing with directionality and specificity to their self-assembly structures, thereby giving bright luminescence (ϕ_F = ~ 77%) and active singlet-triplet utilized wave-guide performances. These co-crystals showed different stacking arrangements (H-type mixed stack and J- type segregated stack aggregation packing) that resulted in markedly different optical properties in solid-state.[28,30] The very high rigidity in hindered *cis*-geometry leads to narrow E_g and ΔE_{ST} for TAHTCNB co-crystals, hence, exhibiting strong red emission (~600 nm) as well as triplet harvesting TADF-characteristics a new avenue for purely hydrocarbon based TADF-co-crystals design. TAH co-crystals exhibited, uniform chain-like molecular arrangements through continuous π-π interactions, and their surface inclined dipole moment (μ) benefited to rationalize the unidirectional photon propagation at very low optical loss coefficient. Overall, this work presents very unusual multifunctional properties by utilizing the difference in rigid and flexible co-crystalline assembly into tunable macroscopic geometrical, morphological and emission properties, including mechanistic insights and photon harvesting characteristics.[41] Consequently, this work not only confirms that constructing polymorphic and configurational isomeric co-crystals can be an effective way to design novel luminescent CT-co-crystals but also presents a clear understanding on the relationship between variant self-assembly designs, color-tunablity and self-guiding singlet-triplet optical waveguides for the first time.

3.2. Experimental Section

3.2.1. Materials

1,4-Bis(fluorenylidenemethyl)benzene denoted as TAH prepared from our previously reported procedure.[44] Octafluoronaphthalene (OFN), Tetrafluoropterepthanitrile (TFPN) and 1,2,4,5-Tetracyanobenzene (TCNB) were purchased from Sigma-Aldrich and used without further purification. Tetrahydrofuran (THF) were purchased from local vendors and further dried and purified.

3.2.2. Preparation of Co-crystals

TAHOFN co-crystal was prepared by using 1:1 stoichiometric mixture of TAH (500 mg, 1.17 mmol) and OFN (316 mg, 1.17 mmol) dissolved in anhydrous THF and kept at RT. When, THF was evaporated a yellowish color solution turns to rod-like green crystals after 1 day.

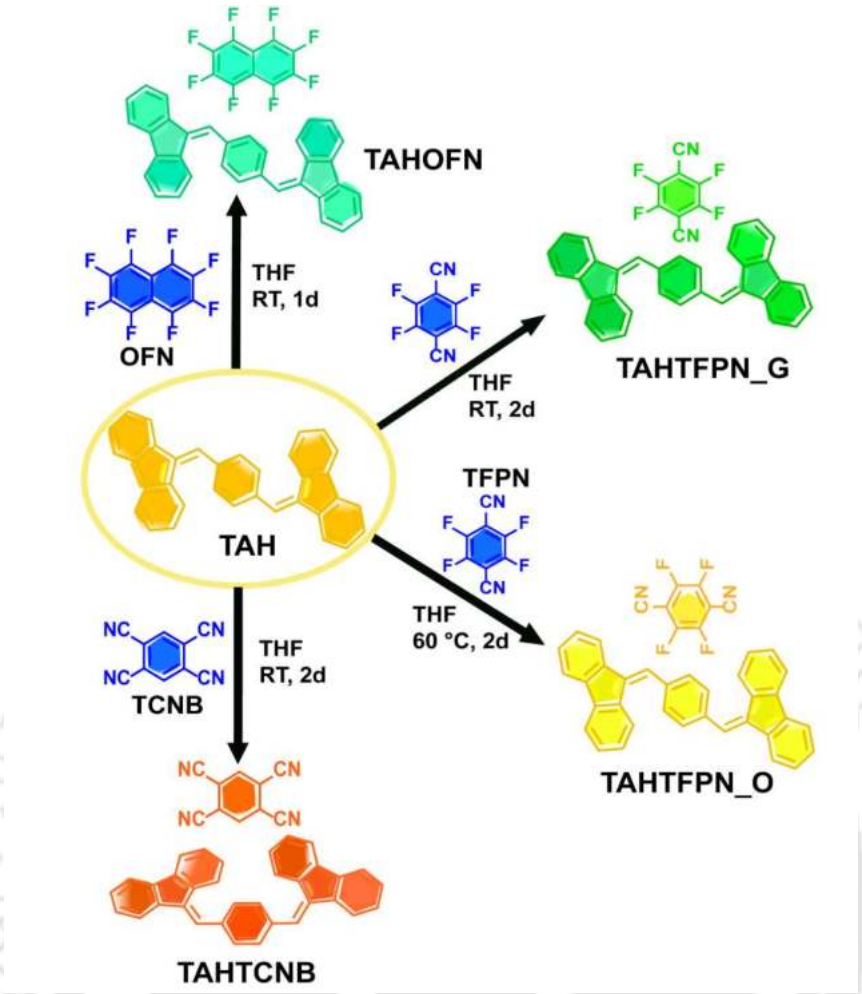

Scheme 3.1. Synthetic procedure of color-tunable co-crystals TAHOFN, TAHTFPN_G, TAHTFPN_O and TAHTCNB from the constituent precursors.

TAHTFPN_G co-crystal was prepared by using 1:1 stoichiometric mixture of TAH (500 mg, 1.17 mmol) and TFPN (232 mg, 1.17 mmol) dissolved in anhydrous THF and kept at RT. When, THF was evaporated a yellowish color solution turns to rod-like green color crystals after 2 day.

TAHTFPN_O co-crystal was prepared by using 1:1 stoichiometric mixture of TAH (500 mg, 1.17 mmol) and TFPN (232 mg, 1.17 mmol) dissolved in anhydrous THF and 60 °C temperature applied. When, THF was evaporated a yellowish color solution turns to rod-like orange color crystals were obtained after 2 day.

TAHTCNB co-crystal was prepared by using 1:1 stoichiometric mixture of TAH (500 mg, 1.17 mmol) and TFPN (207 mg, 1.17 mmol) dissolved in anhydrous THF and kept at RT. When, THF was evaporated a yellowish color solution turns to rod-like red color crystals obtained after 2 day.

3.2.3. Measurements and Methods

3.2.3.1. FTIR and Raman Spectral Analysis

Fourier transform infrared (FTIR) spectra of all samples were recorded in a Perkin Elmer instrument in attenuated total reflectance (ATR) mode. Raman spectra analysis was done using a laser micro-Raman system (Horiba Jobin Vyon, LabRam HR) with 633 nm laser excitation.

3.2.3.2. X-ray Diffraction Analysis

The powder X-ray diffraction measurements of the powder and thin films were performed using a Rigaku SmartLab X-ray diffractometer where copper K_α (λ = 1.54 Å) was used as the source with 9 kW power. The XRD patterns for the 2θ range of 5°−50° were measured at the scan rate 0.3°/s. Single-crystal structures of TAHOFN, TAHTFPN_G, TAHTFPN_O and TAHTCNB were obtained on X-ray diffractometer on Agilent. The single crystal x-ray diffractometer is equipped with Mo X-ray source (Mova), CCD detector (Eos), Oxford cryo-system (80-500K) and crystal AlisPRO software and Autochem softwares. Single crystal x-ray diffraction (SCXRD) data were collected at 293 K. All the self-assembled crystal and co-assembled crystal structures were solved by SHELXT with direct methods. All the non-hydrogen atoms were located by SHELXT directly and refined anisotropically by SHELXL2018 with least squares methods. The revised data have been deposited with the Cambridge Crystallographic Data Centre (CCDC) (accession codes CCDC 2109333, 2109336, 2109335, and 2109337). The stacking structure and intermolecular interactions of the co-assembly were analyzed *via* Mercury and Materials Studio software.

3.2.3.3. Solid-State Absorbance and Emission Studies

The fluorescence and absorption spectra were measured with PerkinElmer, Model Lambda-25 spectrometer and Horiba-Fluoromax4 with Varian Cary Eclipse spectrometer respectively. The absolute quantum yields were measured by using the Horiba Fluoromax (Jobin Yvon equipped with Integrating sphere) absolute quantum yield spectrometer. The time-resolved fluorescence lifetimes were investigated with the time-resolved fluorescence studies were performed using an Edinburgh Life Spec II instrument.

$$\tau_{av} = \frac{\{(\alpha_1.\tau_1) + (\alpha_2.\tau_2)\}}{(\alpha_1 + \alpha_2)}$$

Where τ_{av} is average decay time tau's(τ) are decay components and alphas(α) respective amplitudes.

3.2.3.4. Transient Absorption (TA) and Laser-Induced Fluorescence (LIF) Measurements

TA and LIF were performed in an LP980-KS spectrometer configured with a visible PMT detector for kinetic data and an ICCD detector for spectral data acquisition. These detectors were mounted on different ports of the LP980 spectrograph, allowing rapid switching between spectral and kinetic detection. Measurements at 77 K were performed in an Oxford Instruments OptistatDN cryostat placed in the sample chamber of the LP980. The cryostat temperature is controlled from the LP980 operating software, L900. During measurements at room temperature, the slides were either mounted inside the cryostat or in a film sample holder (L-F04). Pump pulses at 355 nm were produced by a Litron Nano S 130-10 laser. The pump pulse width was ~5 ns and its energy was ~20 mJ/pulse. The white-light probe beam was generated by the Xe lamp in the LP980, operating in pulsed mode and producing pulses with a duration of 6 ms. Pumponly and probe-only backgrounds were subtracted automatically by the L900 software when necessary. Some Laser-Induced Fluorescence (LIF) measurements were performed with a 370 nm longpass filter before the emission monochromator to eliminate the interference from scattered pump light on the spectra.

3.2.3.5. EPR Study

Electron Paramagnetic Resonance (EPR) spectra were recorded on a JES-FA200 ESR spectrometer, at room temperature with microwave power, 0.995 mW; microwave frequency, 9443.961MHz; and modulation amplitude, 2.

3.2.3.6. Microscopic Studies

The morphology and crystallinity of the co-crystals were examined by scanning electron microscopy (FESEM) (Zeiss, Model: Sigma-300). All drop casted samples were gold-sputtered under vacuum to achieve a thin layer of conductive gold coating on the micro/nano crystalline samples. Atomic force microscopy (AFM) analysis were performed drop-casted sample over silicon substrate, in AFM Asylum Cypher, Oxford Instruments. Transmission electron microscopy (TEM, JEOL JEM-2100F) were recorded from the drop casted on carbon film coated copper grid (size 300 mesh).

3.2.3.7. Electrochemical Measurements

Electrochemical measurements were carried out using a CH Instruments 760D electrochemical workstation at a scan rate of 50 mV/s. A three-electrode cell with platinum wire counter electrode, glassy carbon working electrode and Ag/Ag+ reference electrode was employed. Tetrabutylammonium hexafluorophosphate (0.1 M) in acetonitrile was used as supporting electrolyte and Fc+ /Fc couple was used as internal reference. A thin film

was casted from 10 µL, 1 mM solution of sample in THF on the working electrode and the measurements were performed at room temperature under inert atmosphere.

Figure A3.1 explains the CV curves and the onset values that are obtained and the corresponding energy levels are tabulated in Table A3.5. Both the luminogens displayed only oxidation curves and by substituting the onset values of oxidation into $E_{HOMO} = -[(E_{ox}-E_{1/2}\text{ (ferrocene)}) + 4.8\text{ eV}]$ the HOMO energy levels were obtained. The LUMO of the monomers were estimated from the optical band gap (E_{opt}).

3.2.3.8. Thermal Analysis

The transition temperatures and associated enthalpy changes were determined by a differential scanning calorimeter (Q20 DSC) under a nitrogen atmosphere with a heating rate of 10 °C/min. Thermogravimetric analyses (TGA) were carried out with a Mettler-Toledo TGA/SDTA 851e thermogravimetric analyzer in a temperature range of 30-600 °C under a nitrogen atmosphere at a 5 °C min^{-1} heating rate.

3.2.3.9. Computational Studies

The highest occupied molecular orbital (HOMO), lowest unoccupied molecular orbital (LUMO), and of single-component crystals and multicomponent crystals were calculated by density functional theory (DFT). All DFT and time dependent density functional theory (TD-DFT) calculations in this study were performed by employing the combination of Becke3-Lee-Yang-Parr (B3LYP) hybrid functional and 6-31G (d,p) basis set using the Gaussian 16 package. The calculated structures, energy levels are good agreement with experimental results. The growth morphologies of co- crystals were calculated by using the Materials Studio software, based on the attachment energy theory. The molecular structure was first optimized on the basis of the experimental crystal structure. The geometric and energy calculations were performed using the Forcite and Morphology modules.

Combined with the SCXRD crystal data, the Hirshfeld surfaces, electrostatic potential, and molecular orbital were simulated by CrystalExplorer 3.1.51 The Hirshfeld surfaces and the electrostatic potential (ESP) were mapped with dnorm using STO-3G basis set at the Hartree-Fock theory.

3.2.3.10. Confocal Micro Spectroscopy studies

The experiments were carried out using a Wi-Tec alpha 200 laser confocal optical microscope facility equipped with a Peltier-cooled CCD detector. 355/405/488/785 nm lasers were used as an excitation source. The excitation and collection of signals from the output of the microstructure were performed by an upright microscope (20×; NA: 0.6). The

output signal collection was performed using 20× objective for every 0.3 ms and the signal was sent to a CCD detector through a multimode optical fiber of diameter 100 μm (core). The time taken to complete one set of experiment is dependent upon the solvent evaporation time. All measurements were performed at ambient condition and images were processed by using WI-TEC 2.0 software.

All other fluorescence microscopic images were captured using a ZEISS Axio Vert.A1 inverted microscope with 10X objective. All digital pictures were taken with a canon power shot SX420 IS digital camera.

3.3. Results and Discussion

3.3.1. Co-crystals Design and Formulation

Four color-tunable fluorescent rod-shaped single-crystalline co-crystals denoted as TAHOFN, TAHTFPN_G, TAHTFPN_O and TAHTCNB were prepared *via* solvent diffusion method from THF, by using 1:1 stoichiometry ratio of the precursor molecules. While TAH, a dibenzofulvene derivative, was chosen as an electron-rich twisted non-planar donor and octafluoronaphthalene (OFN), tetrafluoropterepthanitrile (TFPN) and 1,2,4,5-Tetracyanobenzene (TCNB) cores were chosen as an electron-deficient planar acceptor. TAH co-assembled very promptly (within 48 hours) and resulted in rod-like four distinct colored CT complexes. Notably, color-specific polymorphic co-crystals were obtained by controlling the temperature during co-crystalization such as at room temperature (RT) for TAHTFPN_G and at 60°C for TAHTFPN_O, while others were grown at RT (Scheme 3.1).

Co-crystal structures and distinct packing modes *via* supramolecular interactions were analyzed by single crystal X-ray diffraction crystallography method. Rod-like single crystals were grown with the two most common packing mode viz. H-type mixed stacking exhibiting -D-A-D-A- columns with face-to-face π-π overlapping for off-green emissive TAHOFN and bright green emissive TAHTFPN_G (Figure 3.2a, b), whereas, J-type segregated stacking mode showed an appropriate slippage of face-to-face overlapping in separated -D-D- and -A-A- columns for the yellow emissive TAHTFPN_O and red emissive TAHTCNB (Figure 3.2c, d). Luminescence characteristics of the prepared single co-crystals were recorded *via* fluorescence microscopy, and the images were collected under 405 nm excitation (Figure 3.2e). These differences in mixed stack and segregated stack packing modes resulted in markedly unique optical properties of the co-crystals.

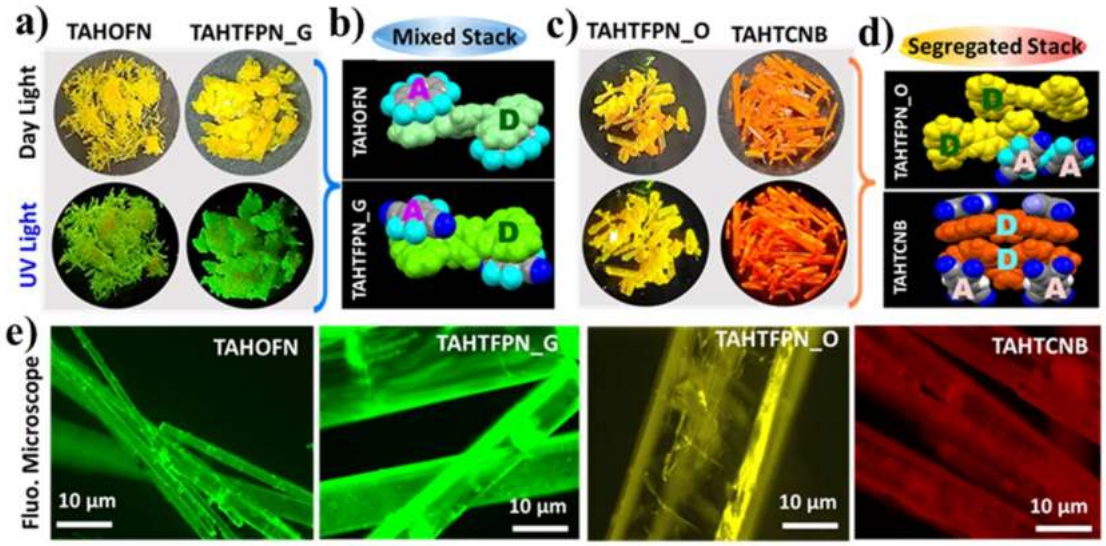

Figure 3.2. Optical properties of co-crystals: (a-d) Images of prepared co-crystals (under daylight and 365 nm UV-lamp) and two different stacking modes of TAHOFN, TAHTFPN_G, TAHTFPN_O and TAHTCNB. (e) Fluorescence Microscope images of the prepared single co-crystals.

3.3.2. Characterization of Co-crystals

To explore the "structure-functionalilty relationship" and color-tunable properties based on molecular packing and distinct CT-modalities of the formulated co-crystals, a simple π-conjugated dibenzofulvene derivative (TAH) was chosen and its co-crystallization with variable fluorine (-F) and cyano (-CN) substituted OFN, TFPN and TCNB planar small aromatic cores were studied. Based on the affinity of charge-transfer, π-π stacking, and intermolecular HBs between F and N atom in acceptor with the active hydrogen in hydrocarbon donor, the two simple molecules were expected to co-assemble and produce distinct supramolecular arrangements with switchable optoelectronic properties.[49] Moreover, to prove the formation of CT complexes (co-crystals), Fourier transform infrared (FTIR) spectroscopy measurements, Raman scattering, powder X-ray diffraction (PXRD), thermogravimetric analysis (TGA), differential scanning calorimetry (DSC) were employed.

FT-IR spectroscopy of co-crystals were analyzed to characterize the π-π stacking, and intermolecular HBs and CT-interactions between donor and acceptors during co-crystal formation. In all the co-crystals the complete involvement of both co-formers was observed with a certain shift of their stretching frequencies.[50]

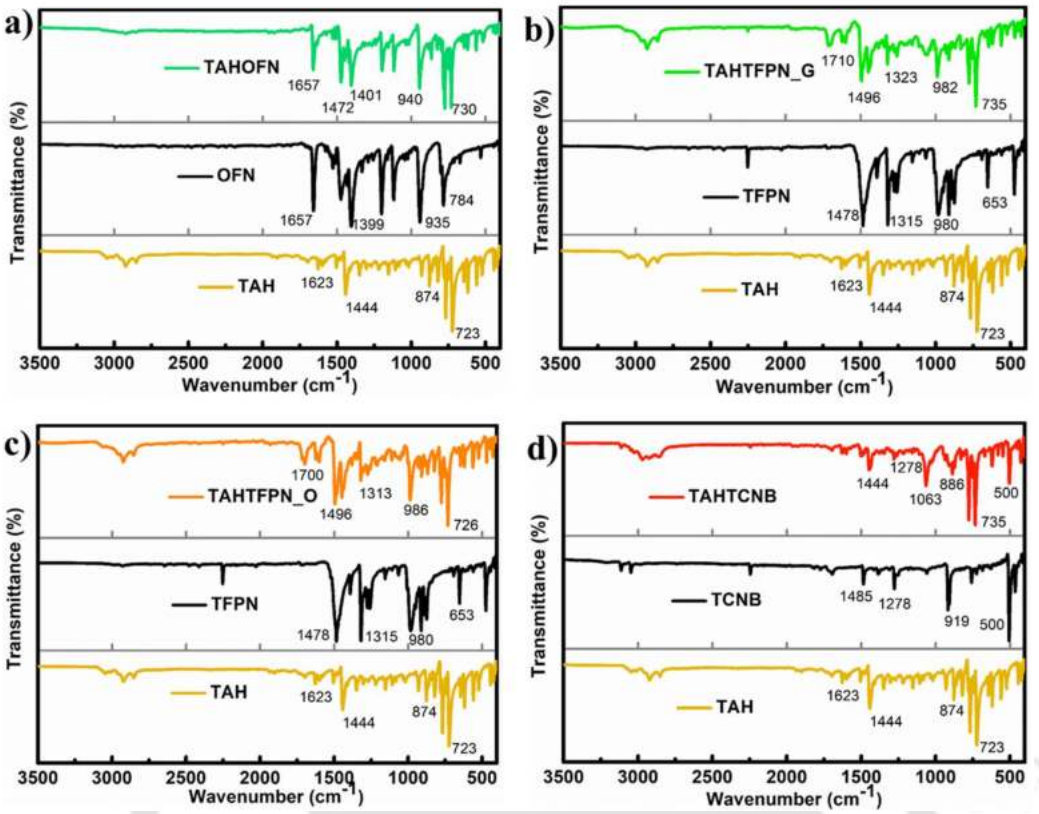

Figure 3.3. (a-d) FTIR spectra of TAH crystals (yellow line), OFN, TFPN, TCNB (black line), where the co-crystals of TAHOFN (off-green line), TAHTFPN_G (green line), TAHTFPN_O (orange line) and TAHTCNB (red line) respectively.

For the co-crystal TAHOFN band of FT-IR, the C-F stretching vibration peak in OFN at 1399 cm^{-1} became strong and shifted to 1401 cm^{-1}, while C-H bending frequency of TAH peaks at 1444 cm^{-1} shifted to 1472 cm^{-1} (Figure 3.3a). Substantially, for co-crystal TAHTFPN_G and TAHTFPN_O, the peak of C-F stretching vibration in TFPN at 1315 cm^{-1} became strong and shifted to 1323 cm^{-1}, 1313 cm^{-1} while C-H bending frequency of TAH in both co-crystal, peaks at 1472 cm^{-1} shifted to 1496 cm^{-1} (Figure 3.3b, c). For the co-crystal TAHTCNB no significant CN stretching vibration shift occurred; however, C-H stretching frequency at 919 cm^{-1} shifted to 886 cm^{-1} and became weak. Further, a new peak also appeared at 1063 $cm^{-1,}$ which could be due to the strong CT-complexation (Figure 3.3d). Furthermore, micro-Raman spectroscopy was first applied with the laser irradiation on the crystal surface for collecting signals and demonstrated an entirely different peak in the Raman spectrum compared to the co-former signals.

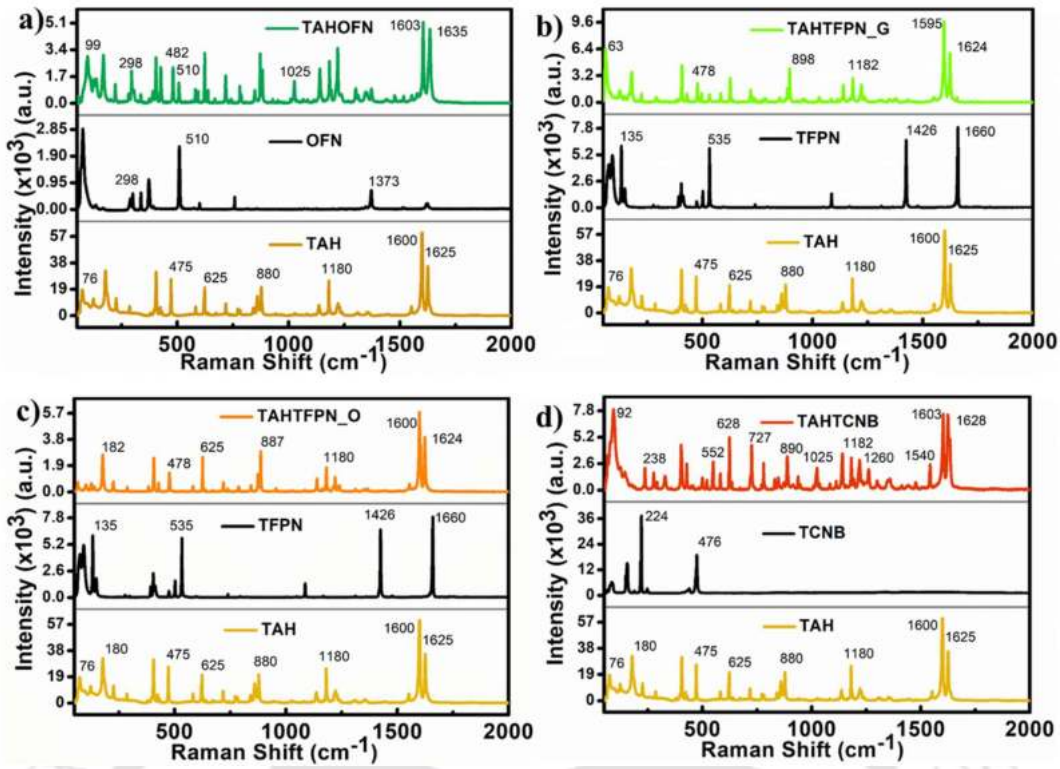

Figure 3.4. (a-d) Raman spectra of TAH crystals (yellow line), OFN, TFPN, TCNB (black line), where the co-crystals of TAHOFN (dark-green line), TAHTFPN_G (green line), TAHTFPN_O (orange line) and TAHTCNB (red line) respectively.

Moreover, most of the frequencies of the precursors displayed a small shift from their pure forms and the disappearance of a few stretching frequencies of TAH and other acceptors of OFN (1373 cm^{-1}), TFPN (1426 cm^{-1}) and TCNB (476 cm^{-1}) in the solid co-crystals, caused the variation in CT and HB interactions on the co-assembly formation (Figure 3.4a-3.4d). In addition, a new peak was observed at 1025 cm^{-1} in TAHOFN and 898 cm^{-1} in TAHTFPN_G, while multiple new frequencies of 552 cm^{-1}, 727 cm^{-1}, 1025 cm^{-1}, 1260 cm^{-1} were seen in TAHTCNB. Hence, mico-Raman scattering analysis further evidenced the complete involvement of small guest acceptors into the crystal lattice of donor TAH. More importantly, the appearance of newer peaks in the co-crystals clearly depicted the presence of intermolecular interactions.[48] In contrast, PXRD confirmed the co-crystallization of the twisted TAH system in the presence and absence of planar OFN, TFPN and TCNB. Compared to pure TAH and other OFN, TFPN and TCNB, the appearance of several new characteristic peaks in TAHOFN co-crystals (9.44°, 11.63°, 14.32°, 19.60°, 22.48°, 31.99°), TAHOFN_G co-crystals (10.78°, 12.57°, 18.40°, 26.26°, 36.96°) TAHOFN_O co-crystals (8.84°, 11.48°, 11.68°, 15.16°, 22.73°, 28.10°) and TAHTCNB co-crystals (5.46°, 7.54°,

11.48°, 17.25°, 24.12°. 27.80°) whereas the absence of several original peaks from pure TAH (7.40°, 12.37°, 17.75°, 22.88°, 27.06°), OFN (23.43°, 25.17°, 30.00°), TFPN (17.00°, 23.37°, 33.22°) and TCNB (18.65°, 22.58°, 30.00°) was observed upon co-crystallization, depicting the new molecular arrangement and co-assembly formation (Figure 3.5a-3.5d). Although TAHTFPN_G and TAHTFPN_O co-crystals were composed of similar co-former, the entirely different diffraction patterns suggested a packing transition and polymorphic behavior.[49] It is noteworthy to mention that all the simulated PXRD patterns calculated from SC-XRD geometry of co-crystals exactly matched with the experimentally obtained XRD patterns.

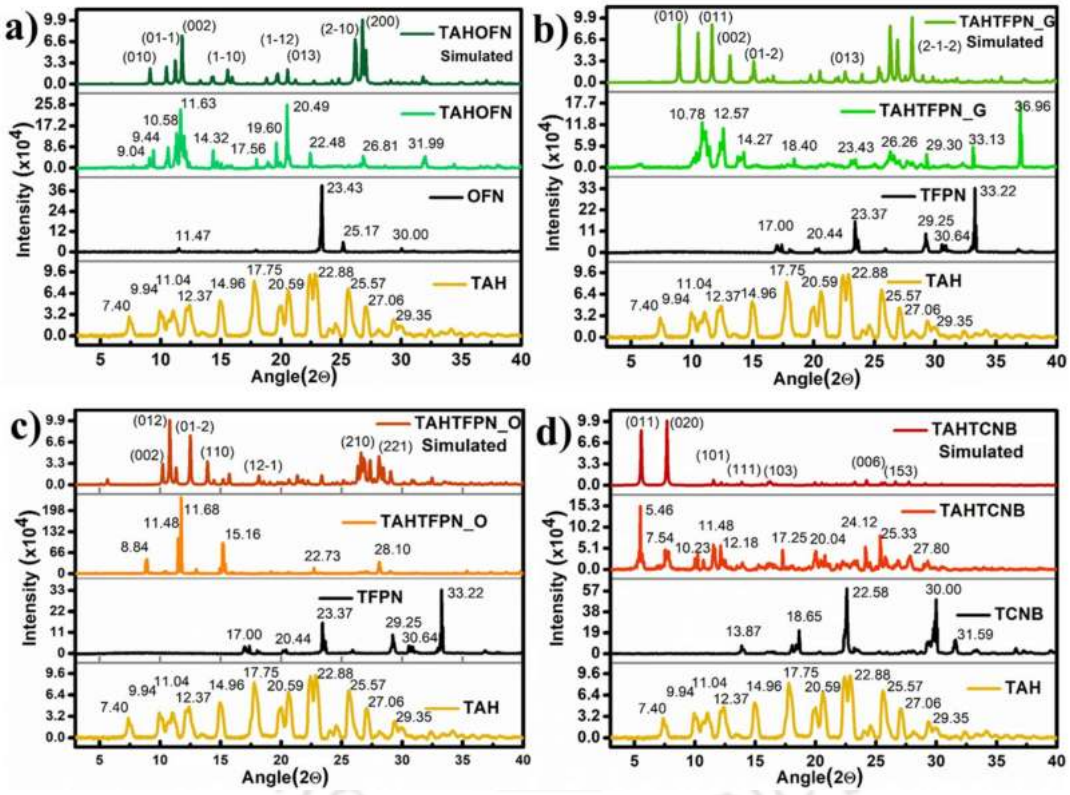

Figure 3.5. (a-d) PXRD patterns for TAH crystals (yellow line), OFN, TFPN, TCNB (black line), where the co-crystals of TAHOFN (off and dark green line: pristine and simulated), TAHTFPN_G (off and dark green line: pristine and simulated), TAHTFPN_O (off and dark orange line: pristine and simulated) and TAHTCNB (off and dark line: pristine and simulated) respectively.

Further, the thermal stability of the individual precursors and co-crystals studied by TGA (Figure 3.6a-3.6d) demonstrated the appearance of new peak for co-crystals with two thermal degradations at 135 °C, 360 °C for TAHOFN, 120 °C, 360 °C TAHTFPN_G, 140 °C, 360 °C for TAHTFPN_O and 235 °C, 360 °C for TAHTCNB, compared to the pure TAH (360 °C), OFN (75 °C), TFPN (125 °C) and TCNB (210 °C) peaks. Hence, TGA study

reveals that the formation of co-crystals and high thermal stability of TAHTCNB (235 °C) unlike the three other co-crystals, while among the two polymorphs, TAHTFPN_O is thermally more stable than TAHTFPN_G. Notably, pure TAH showed high thermal stability rather than other co-former (OFN, TFPN, TCNB). These findings also suggested that co-crystals with the more thermally stable TAH donor (360 °C) produced a new packing mode that improves the thermal stability relative to pure constituents. Furthermore, DSC study showed an endothermic peak at 211 °C, 220 °C, 190 °C, and 196 °C for TAH, TAHOFN, TAHTFPN_G, and TAHTFPN_O, while TAHTCNB exhibited multiple peaks at 107 °C, 207 °C, 217 °C and 263 °C respectively (Figure 3.7). DSC results corroborated the melting point of the respective co-crystals. Interestingly, TAHTCNB presents various other peaks, which are presumably due to isomeric transition and presence of some solvent molecule in the crystal lattice. Moreover, the dissimilar melting transition for all the co-crystals clearly justified the involvement of several non-covalent interactions that regulate their molecular packing.[49]

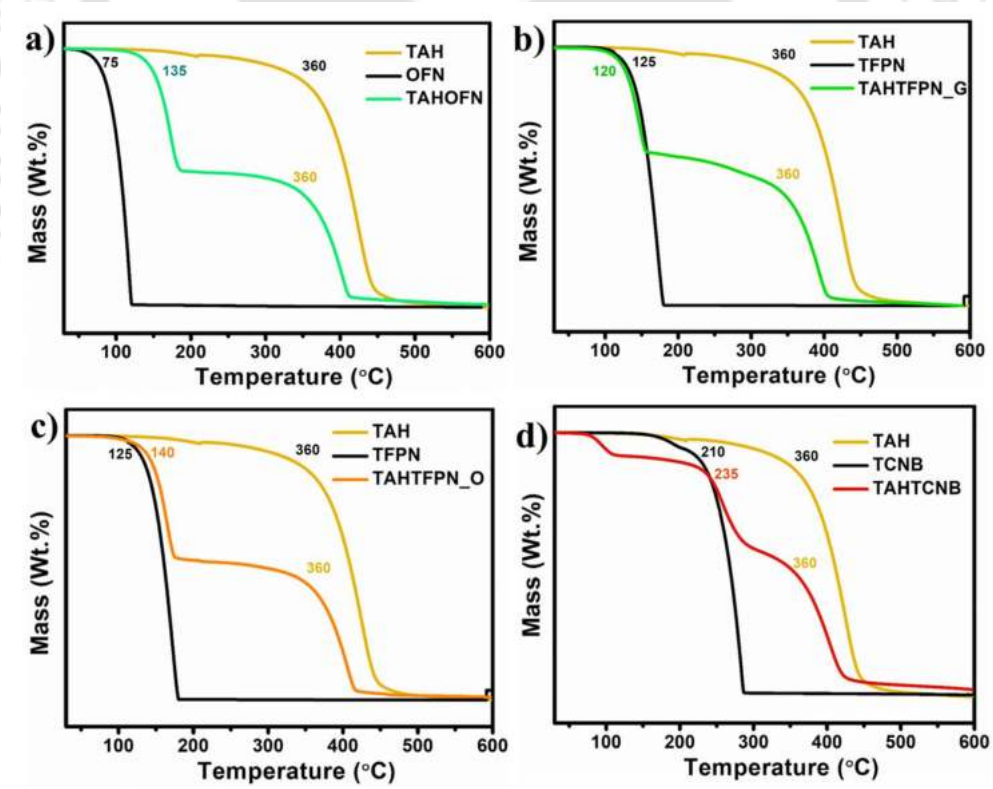

Figure 3.6. Thermogravimetric analysis (TGA) for TAH crystals (yellow line), OFN, TFPN, TCNB (black line), where the co-crystals of TAHOFN (dark-green line), TAHTFPN_G (green line), TAHTFPN_O (orange line) and TAHTCNB (red line) respectively.

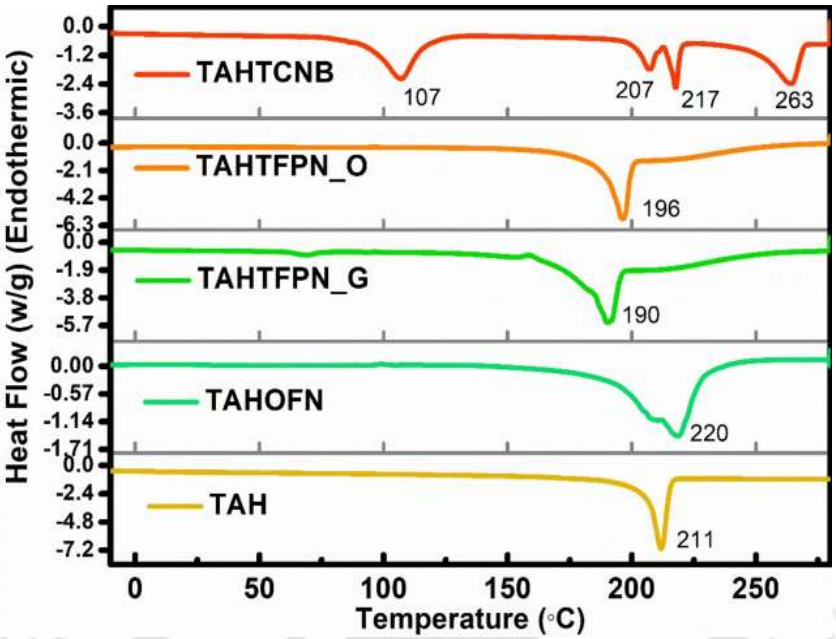

Figure 3.7. Differential scanning calorimetry (DSC) study for TAH (yellow line), TAHOFN (off green line), TAHTFPN_G (green line), TAHTFPN_O (orange line) and TAHTCNB (red line) respectively.

Collectively, all the above-mentioned studies suggest, the successful formulation of co-crystals with different stacking and rigid packing between electron-rich TAH and electron-deficient OFN, TFPN and TCNB, respectively.

3.3.3. Optical Properties of Co-crystals

Solid crystalline state optical properties for the polymorphic and configurational isomeric co-crystals of TAHOFN, TAHTFPN_G, TAHTFPN_O and TAHTCNB were elucidated by using absorption (UV-Vis), photoluminescence (PL) as well as the time-resolved PL (TRPL) based spectroscopic measurements. Co-crystals TAHOFN, TAHTFPN_G exhibited blue-shifted absorption at 460 and 430 nm whereas TAHTFPN_O and TAHTCNB showed a red-shifted absorption at 490 and 500 nm related to the absorption of parent TAH (485 nm), deciphering TSCT interactions between constituent precursors (Figure 3.8). The photo emissive properties of co-crystals have been further investigated at ambient condition. The steady state PL spectra for all co-crystals displayed a broad emission range from 450 to 700 nm, while clear red-shifted emission peaks were observed with wavelength maximum mainly located at λ_{max} = 540, 545, 560 and 590 nm with full-width half maxima (FWHM) 63, 58, 56 and 72 nm respectively (Figure 3.9a).

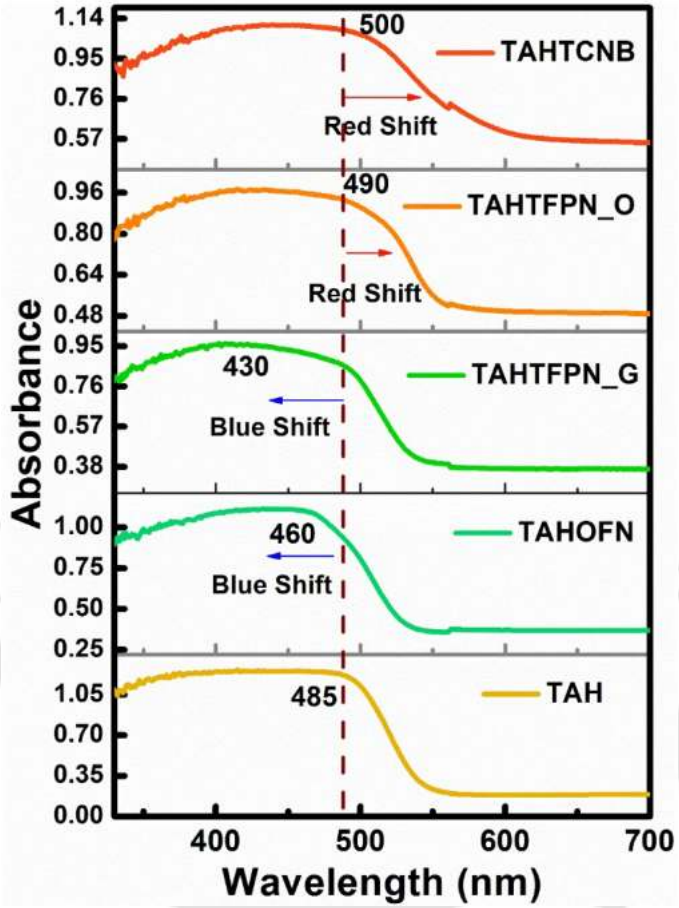

Figure 3.8. Diffuse reflection absorption spectra of TAH (yellow line), TAHOFN (off green line), TAHTFPN_G (green line), TAHTFPN_O (orange line) and TAHTCNB (red line) respectively.

As compared to the precursor molecules, very high PLQY has been determined to be 31.6%, 74.4%, 77.5% and 64.4% for TAHOFN, TAHTFPN_G, TAHTFPN_O and TAHTCNB, respectively, through an absolute method by using an integration sphere. To the best of our knowledge, such high PLQY values (77.5%) for co-crystalline materials, reporting for the first time.[38,41] Exact emission colors were calculated from the Commission Internationale de L'Eclairage (CIE) chromaticity coordinates values of (0.36, 0.61) for TAHOFN, (0.39, 0.59) for TAHTFPN (0.48, 0.50) for TAHTFPN and (0.57, 0.42) for TAHTCNB respectively (Figure 3.9b). To further understand the excited state information, the fluorescence decays were recorded at solid crystalline form using TRPL at time-correlated single photon counting (TCSPC) method and the average life-time (τ_{av}) values of 0.50, 0.87, 1.06 and 38.81 ns were recorded for TAHOFN, TAHTFPN_G, TAHTFPN_O, TAHTCNB respectively (Figure 3.9c). Unlike, single exponential decay profile of former three co-crystals, TAHTCNB exhibited tri-exponential decay presumably due to the prompt locally excited (LE) state and presence of delayed species.

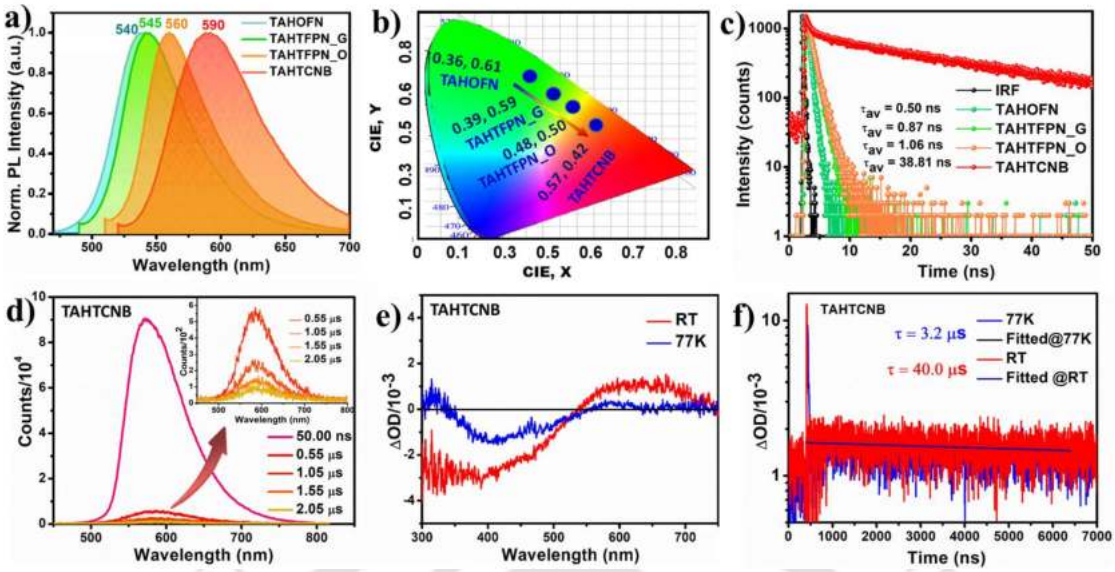

Figure 3.9. (a) Steady state PL spectra of all the afforded co-crystals in solid-state, TAHOFN, TAHTFPN_G, TAHTFPN_O and TAHTCNB exhibited red-shifted emission wavelength maximum at 540, 545, 560 and 590 nm respectively. (b) CIE-coordinates for the integrated co-crystals revealed color purity from green and yellow to red emissions. (c) Time-resolved photoluminescence life-time (TRPL) for all the co-crystals in solid state. (d) Laser-induced fluorescence (LIF) spectra for TAHTCNB at ns and μs pulse delay revealed delayed fluores-cence behavior of red co-crystal. (e) Transient absorption (TA) spectra at room temperature (RT) and 77K for TAHTCNB. (f) Transient decay kinetics spectra corroborate increment of life-time, 40 μs at RT from 3.2 μs at 77K, confirming TADF characteristics.

Besides, longer fluorescence life-time (38.81 ns) was observed for TAHTCNB as compared to the other three congeners due to the involvement of additional excited states and attaining non-radiative relaxation from the excitonic coupling at different multiplicities.[10,51] Additional details on excited-state life-time fitting values of the co-crystals of polymorph and conformational isomer are summarized in Table A3.1-A3.4. The radiation constants (k_F) of co-crystals were calculated to be 0.62 ns^{-1}, 0.85 ns^{-1}, 0.72 ns^{-1} and 0.016 ns^{-1} by using the formula $k_F = \phi_{PL}/\tau$, which is a much smaller value than the single component or/and other typical CT crystals.[9,52] These, small k_F values corroborate, the fluorescence is originated from CT state. Furthermore, broad FWHM and accompanying delayed species could be attributed to the strong CT and triplet contribution on the red-shifted broad emission in TAHTCNB. To confirm TADF property laser-induced fluorescence (LIF) study was performed by applying nanoseconds (50 ns) and microseconds (0.55, 1.05, 1.55 and 2.05 μs) pulse laser excitation for 0.5 wt% PMMA doped TAHTCNB film (Figure 3.9d). Interestingly, a delayed emission spectra was observed at various μs delay pulse laser excitation, referred as TADF.[10,53] The triplet harvesting behavior of TAHTCNB was further confirmed by transient absorption (TA) spectra and decay kinetics analysis at room

temperature (RT) and 77K, respectively (Figure 3.9e). As expected TA spectra depicted a positive signal near 600 nm while life-time was found to be 40.0 μs, which is twelve times higher than that at 77K temperature (3.2 μs) (Figure 3.9f). The red emissive TAHTCNB co-crystal experiences a rare intermolecular steric strain due to the *cis*-configuration adopted by TAH, thereby generating unusual supramolecular architecture, which could suppress the non-radiative relaxation and assist to harvest triplets *via* an effective RISC process at reduced ΔE_{ST} to obtain efficient TADF property. All the optical properties are summarized in **Table 3.1.**

3.3.4. Intrinsic Color-tunable Emission Mechanism

The process of co-assembly with hydrocarbon donor and various acceptors demonstrated an alternate stacking mode which facilitates the efficient TSCT and/or energy transfer between D-A, to achieve high PLQY. Consequently, the exciting optical properties of co-crystals motivated us to investigate more critically the dissimilarity in CT/packing interactions and mechanistically determine the process of co-crystaliization.[45,54] Therefore, theoretical simulations were carried out to clearly understand the mechanism of blue/red-shifted absorption/fluorescence and TADF activities, including their dissimilar TSCT behavior in the co-assembled structures by employing time-dependent density functional theory (TD-DFT) calculations from Gaussian 16 programme.[55] Frontier molecular orbitals (FMOs) for all the co-crystals were calculated by using the B3LYP/6-31G(d,p) basis set and level from their single-crystal geometries. The calculated HOMO values are determined to be -5.51, -5.58, -5.48 and -5.55 eV, whereas the LUMO values are -2.76, -2.69, -2.80 and -3.52 eV respectively (Figure 3.10a_i, b_i, c_i, d_i), therefore, the related band gap was calculated to be 2.75, 2.89, 2.68 and 2.03 eV for TAHOFN, TAHTFPN_G. TAHTFPN_O and TAHTCNB, respectively which is in good agreement with experimental bandgap values (2.75, 2.35, 2.32 and 2.03 eV) obtained from cyclic voltammetry (CV) (Figure A3.1 and Table A3.5). Besides, the energy level for different spin multiplicity states were determined to be S_1 = 3.19 eV and T_1 = 2.23 eV for TAHOFN, S_1 = 2.45 eV and T_1 = 2.09 eV for TAHTFPN_G, S_1 = 2.26 eV and T_1 = 1.72 eV for TAHTFPN_O, S_1 = 1.95 eV and T_1 = 1.93 eV for TAHTCNB. Thus, the energy splitting (ΔE_{ST}) values were determined to be 0.96, 0.36, 0.54 and 0.02 eV for TAHOFN, TAHTFPN_G, TAHTFPN_O and TAHTCNB respectively.

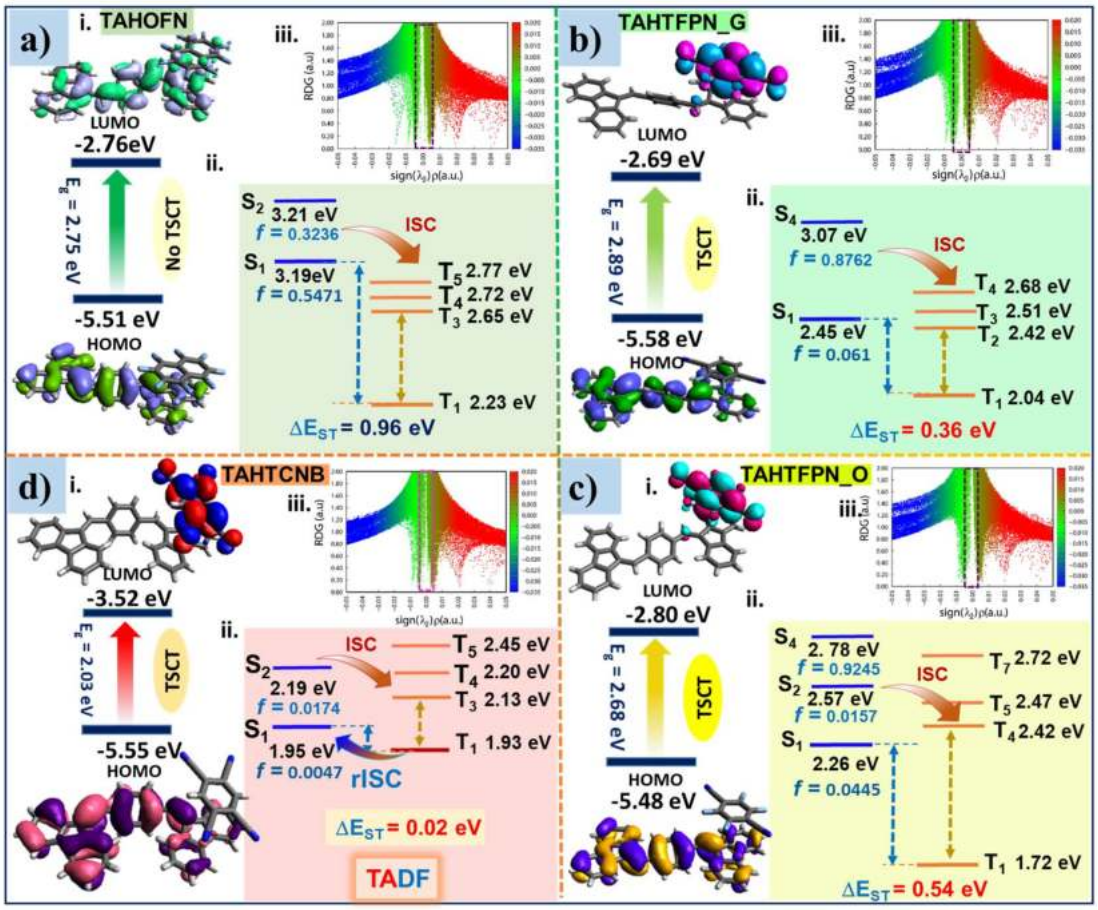

Figure 3.10. Computational calculations (TD-DFT) for blue/red-shifted TSCT, singlet/triplet energy gap and emission mechanism using Gaussian 16 at B3LYP/631G (d,p) level of study: (a_i, b_i, c_i and d_i) Frontier molecular orbitals (FMOs); HOMO/LUMO distributions and bandgaps. (a_ii, b_ii, c_ii and d_ii) Emission energy calculations for different singlets/triplets with their corresponding energy splitting's (ΔE_{ST}). (a_iii, b_iii, c_iii and d_iii) The functions of reduced density gradient (RDG) and Sign (λ_2)ρ iso-surface map with an isovalue of 0.5 for TAHOFN, TAHTFPN_G, TAHTFPN_O and TAHTCNB respectively.

Unlike very small ΔE_{ST} values of TAHTCNB other three co-crystals exhibited large ΔE_{ST} values (>0.3 eV) and stable trans architecture of TAH, which hinders the RISC process thereby found to be TADF inactive.[44] All the above-mentioned observations were shown in their corresponding Jablonski diagram at different active excited singlets and triplets (Figure 3.10a_ii, b_ii, c_ii, d_ii). Furthermore, to reveal the dissimilar intermolecular noncovalent interactions which induced the emission from excited states, the functions of reduced density gradient (RDG) and sign (λ_2)ρ were calculated for all the co-crystals using TDDFT geometry with Multiwfn software.[56] RDG analysis confirmed the presence of clear high density of weak interactions (green region) and larger steric hindrance (brown region) between D and A segments in TAHTCNB as compared to TAHOFN, TAHTFPN_G and TAHTFPN_O, which could effectively restrict the molecular vibrations and prevent

energy loss of the excited molecules and revealing TADF susceptibility (Figure 3.10a_iii, b_iii, c_iii, d_iii). The combination of *cis*-conformation of the electron-donating TAH molecular structure and the strong electron-withdrawing benzonitrile moiety are beneficial for the sterically stressed intermolecular-CT characteristics (Figure A3.2), that collectively leads to small ΔE_{ST} (0.02 eV) between S_1 and T_1, and promotes efficient RISC process that resulted in TADF emission.[57] Remarkably, TAHTCNB presents a first example of intermolecular TSCT-based red-emissive and waveguide active TADF co-crystal. Precisely, the HOMO-LUMO energy profile and dissimilar TSCT character provides significant insights to rationalize the blue/red-shifted emission or absorption for all four complexes. Unlike, TAHOFN**,** the co-crystal of other three congeners showed robust CT character with narrower band gaps, consistent with their experimentally obtained UV-visible wavelength and CV values. TAHOFN co-crystal showed weak fluorescence, attributed to the close π-π interaction and static emission quenching of TAH *via* photoinduced electron transfer (PET) mechanism.[58] (Figure A3.3). However, TAHTFPN-G, TAHTFPN-O and TAHTCNB showed weak π-π interaction and significant TSCT, due to the high energy donor HOMO and acceptor LUMO as compared to single constituent TAH. Besides, separated localization of HOMO/LUMO and strong electronic coupling benefited from the blue/red-shifted emission or absorption. FMOs distribution suggested that HOMO of the three co-assemblies were mainly located on the donor hydrocarbon (TAH), whereas LUMO aligned with the acceptors TFPN and TCNB, leading to well separated HOMO and LUMO, clearly indicating the TSCT characteristics of the co-assemblies (Figure A3.4-A3.5).[10, 59] In addition, the existence of moduled TSCT interactions for co-crystals were revealed by their related stacking motif, and described from their respective HOMO-LUMO bandgaps. Therefore, an association of OFN and TFPN with TAH resulted in blue-shifted, H-type mixed stack packing with higher energy bandgap co-crystal of green emissive TAHOFN, TAHTFPN_G, whereas other assemblies of TFPN and TCNB with TAH offered a red-shifted J-type segregated stack packing with low bandgap yellow and red emissive co-crystals of TAHTFPN_O and TAHTCNB respectively. Notably, the obtained bandgap energy profile is in agreement with experimentally obtained UV-visible blue-shifted wavelength of 460/430 nm for TAHOFN/TAHTFPN_G co-crystal and red-shifted absorption wavelength of 490 and 500 nm for TAHTFPN_O and TAHTCNB respectively as compared to single component TAH absorption wavelength at 485 nm.

Table 3.1: Summary of photophysical studies of co-crystals in solid crystalline state.

Co-crystals	λ_{UV} (nm)	λ_{PL} (nm)	CIE (x, y)	HOMO (eV)	LUMO (eV)	E_g (eV)	ΔE_{ST} (eV)	τ_{av} (PF) (ns)	τ_{av} (DF) (μs)	ϕ_{PL} (%)	K_F (ns^{-1})[a]	μ (D)	α' (dB/μm)
TAHOFN	460	540	0.36, 0.61	-5.51	-2.76	2.75	0.96	0.50	-	31.6	0.62	0.80	0.44
TAHOFN_G	430	545	0.39, 0.59	-5.58	-2.69	2.89	0.36	0.87	-	74.4	0.85	1.31	0.0742
TAHOFN_O	490	560	0.48, 0.50	-5.48	-2.80	2.68	0.54	1.06	-	77.5	0.72	1.56	-
TAHTCNB	500	590	0.57, 0.42	-5.55	-3.52	2.03	0.02	38.81	40.0 (RT), 3.2 (77K)	64.4	0.016	1.62	0.0837

Radiation constants [$k_F = \phi/\tau$] calculated from fluorescence QY and lifetime of crystals at RT in air.

Overall, experimental UV-visible/PL spectrum and theoretical band structures revealed that on increasing the electron-withdrawing nature of the acceptors into the donor, a narrow bandgap and red-shifted TSCT-complex could be successfully achieved. Furthermore, the distinct packing modes of CT-complexes play an important role in dominating their optoelectronic properties. Electron spin resonance (ESR) measurements were carried out to study the relationship between packing, CT interactions and optoelectronic features in the TSCT complex.[9,29] The strong TSCT interactions are favorable for the reduced bandgap and red-shifted emission which is directly influenced by the electronic redistribution and bond-length variation in the TSCT complex. In contrast, a prominent ESR signal (g factor = 2.145 at room temperature) was observed for TAHTCNB, which consisted of the ground state TSCT interaction character (Figure A3.6**)**. Notably, the ESR signal was found to be weaker for TAHTFPN complex and almost no signal was observed for TAHOFN and precursor TAH. Therefore we speculate that a significant ESR signal for TAHTCNB originates due to the strong electronic coupling and TSCT interaction with dense segregated stacking, resulting in large red-shifted delayed emission as compared to other mixed stacked weak TSCT complexes. In order to understand the red-shifted CT-emission mechanism for all four co-crystals accurately, the degree of TSCT (ρ) was calculated which is vital to describe the amount of charge transfer between donor and acceptor. The prominent CT caused by electron-rich hydrocarbon and electron-deficient benzonitrile moieties redistributed their electron clouds, including electrostatic Coulomb interactions, which directly influenced the degree of CT in the co-crystals. Correspondingly, single-crystal X-ray geometry displayed the change in C-C bond length

of acceptors in CT-complexes, as compared to the neutral form of OFN, TFPN and TCNB, which resulted in the structural changes leading to the stretching peak being shifted significantly. Further, the degree of CTs (ρ) is defined as ρ (0≤ ρ ≤1), which denotes physical properties like conductivity and packing of co-crystals, and can be obtained from equation-2.1.[60] A modest 0.915e, 0.725e, 0.580e and 0.229e ρ value for TAHOFN, TAHTFPN_G, TAHTFPN_O and TAHTCNB confirms the gradual decrease of CT degree because of weakening of the interactions between the pair of D-A molecules. Subsequently, the high value of ρ reveals mixed stack packing mode while relatively low ρ represents segregated stack packing mode.[29]

$$\rho = \frac{1}{2}\left(\left[1 - \frac{x_{CT} - y_{CT}}{x_N - y_N}\right] + \left[1 - \frac{z_{CT} - y_{CT}}{z_N - y_N}\right]\right) \quad (\text{Equation} - 2.1)$$

in which x, y, and z refer the bond lengths assigned in OFN, TFPN and TCNB, the subscript "CT" and "N" denote when the bonds are in CT complex, and the bonds in the neutral state of acceptors (Figure 3.11).

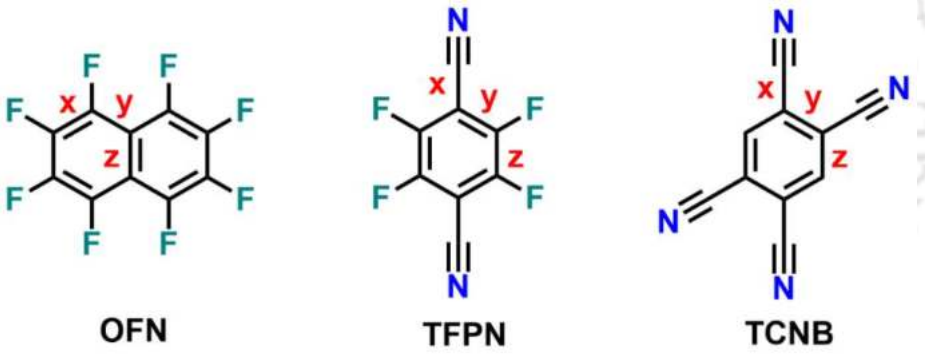

Figure 3.11. Chemical structures of OFN, TFPN and TCNB molecule, where, x, y, and z are the bond length of carbon-carbon bond at neutral state.

3.3.5. Crystal Structure-packing-property Analysis

Supramolecular aggregated structures and molecular packing greatly influence the optical properties of π-conjugated materials in solid-state and confirms unique "structure-function correlations".[61] Therefore, to clearly understand the mode of packing induced color-tunable fluorescent behavior at their atomic level, SC-XRD structures were solved and analyzed in detail for all four integrated co-crystals. The SC-XRD structures of co-crystal showed three triclinic and space groups of *P-1* for TAHOFN (CCDC NO 2109333), TAHTFPN-G (CCDC NO 2109336) and TAHTFPN-O (CCDC NO 2109335).

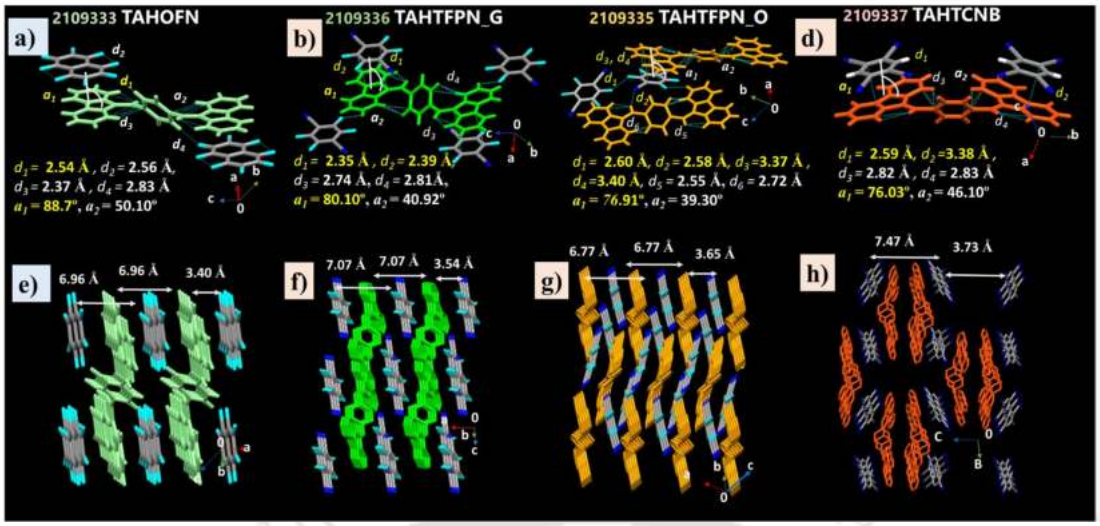

Figure 3.12. Single crystal X-ray diffraction (SC-XRD) analysis for TAHOFN, TAHTFPN_G, TAHTFPN_O and TAHTCNB: (a-d) SC-XRD structure of co-crystals in unit cell and interactive noncovalent bonding distances and angles at intra and intermolecular fashion. (e-h) Top view of for all four co-crystals at their bulk stacked architectures and relative distances from each constituent.

Whereas, TAHTCNB exhibited orthorhombic crystal system and *Pnmm* a space group (CCDC NO 2109337). Detailed crystal data collection and refinement parameters of co-crystals are summarized in Table A3.6. In the SC-structures of co-crystals, each donor molecule is connected with adjacent acceptor molecules *via* multiple intra- and inter-molecular interactions. In particular, HBs, π-π and TSCT interactions play a crucial role as non-covalent bonding between a pair of D-A structures due to the presence of N/F atoms in electron-deficient acceptors OFN, TFPN and TCNB.[8,62] Face to face orthogonal stacking between TAH and OFN aromatic cores was observed for TAHOFN with an angle of 88.7° and a intermolecular HBs (d_1 =C-F···H-C, 2.54 Å) were observed between π-stacked OFN, where F atom in OFN linked to adjacent H atom present in bridge phenyl ring of TAH donor (Figure 3.12a). Subsequently, multiple intramolecular CH-π interactions (d_2, d_3 d_4 = 2.56 Å, 2.37 Å 2.83 Å) with a dihedral angle of 50.10° was observed between dibenzofulvene (TAH) and bridge phenyl ring in TAH donor. Similarly, TAHTFPN_G displayed an orthogonal stacking angle of 80.10° with intermolecular HB (d_1 =C-N···H-C, 2.35 Å) and π-π stacking interaction (d_2= 2.39 Å) between TFPN and TAH. Intramolecular interaction was also seen as CH-π interactions (d_3, d_4 = 2.74 Å, 2.81Å) with a dihedral angle of 40.92° in TAH donor (Figure 3.12b). Moreover, the polymorphic crystal structure of TAHTFPN_O showed slightly staggered stacking between TAH and

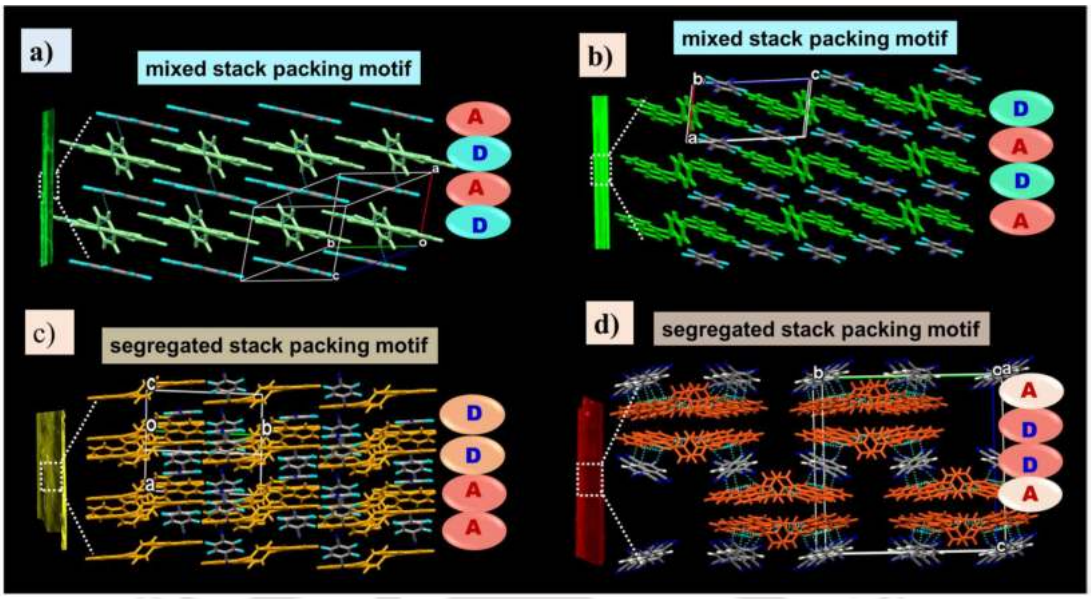

Figure 3.13. (a-d) Side view in bulk packing pattern and representation of "mixed stack" TAHOFN and TAHTFPN-G and "segregated stack" TAHTFPN_O and TAHTCNB co-crystals respectively.

TFPN with an angle of 76.91°, while two HBs (d_1 = C-F···H-C, 2.60 Å and d_2 = C-N···H-C, 2.58 Å) and two π-π stacking (d_3, d_4 = 3.37 Å, 3.40 Å) interactions were realized. Likewise, close intramolecular CH-π interactions (d_1, d_2 = 2.55 Å, 2.72 Å) with a low dihedral angle 39.30° was also apparent in TAH donor (Figure 3.12c). Nonetheless, the configurational *cis*-isomer of TAHTCNB displayed intense staggered stacking between TAH and TCNB with an angle of 76.03° and intermolecular HB and π-π stacking (d_1 = C-N···H-C, 2.59 Å and d_2 = $C_{\pi-\pi}$, 3.83 Å) interactions. The *cis*-conformation of TAH was stabilized by intramolecular CH- π interactions (d_3, d_4 = 2.82 Å, 2.83 Å) with a dihedral angle of 46.10° between the two planes of TAH and central phenyl planes in TAH (Figure 3.12d). Also, the bulk crystal packing demonstrates a mixed-stack packing mode for TAHOFN and TAHTFPN-G, along a-axis into alternating donor TAH and acceptor OFN/TFPN in a -A-D-A-D- based symmetrical alignment with a very close contact distance of 3.40 Å and 3.54 Å, respectively (Figure 3.12e, f). Meanwhile, a segregated stack packing mode along a- and b-axis was seen for TAHTFPN-O and TAHTCNB between TAH and TFPN/TCNB stacked on each other relatively at far distance of 3.65 Å and 3.73 Å, individually in a -DD-AA- based unsymmetrical fashion (Figure 3.12g, h). Meanwhile, the distance between TAH-TAH, OFN-OFN, TFPN-TFPN, TCNB-TCNB was found to be 6.96 Å, 7.07 Å, 6.77 Å and 7.47 Å, respectively.

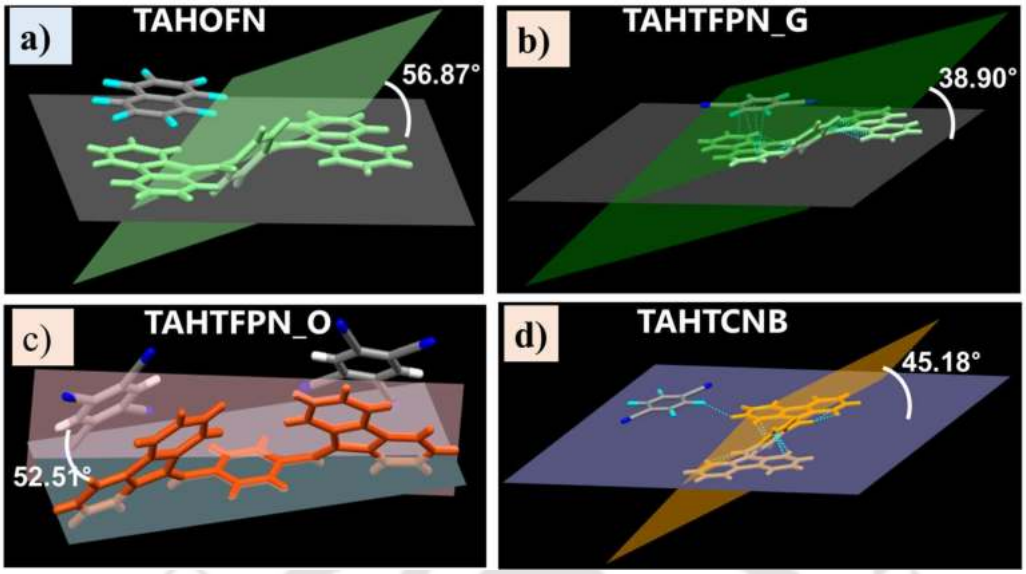

Figure 3.14. Polymorphic co-crystals**:** (a-d) Twisted angle between two planes of planar TAH and central phenyl planes in trans-TAHOFN, TAHTFPN_G, TAHTFPN_O and cis-TAHTCNB co-crystals respectively. Difference interactive orientation to the guest molecules resulted in variable conformations of TAH, revealing polymorphism features of all the afforded co-crystals.

Intramolecular CH-π interactions enhance the planar propensity of TAH unit as to central phenyl ring which creates enough accommodation of the acceptors to its TAH aromatic cores successively. Despite the *cis*-conformation of TAH in TAHTCNB co-crystals, the other three co-crystals preserved the stable *trans* conformation of the TAH molecule. Thus a strong dimer was stabilized through two intermolecular H-bonds and π-π stacking that resulted in molecular chain-like assemblies with layer-by-layer arrangement with one layer composed of donor TAH molecules and the next containing acceptor OFN/TFPN/TCNB molecules interacting via different face to face or edge-to-edge stacking (Figure 3.13a-3.13d). The dynamic nature of TAH in the co-crystals and non-bonding interactions are shown and summarized in Figure 3.14, A3.7 and Table A3.7. Further, electrostatic potential (ESP) mapping and their corresponding two-dimensional (2D) fingerprint plots were performed to further justify the presence of π-π stacking and intermolecular HB interactions from CrystalExplorer 3.1 software (Figure A3.8-A3.11).[63] Therefore, the SC-XRD analysis clarified the abundance of multiple intermolecular interactions and enabled the formation of distinct and highly ordered packing modes, which confer tunable optical behaviors of the co-crystals. Precisely, co-crystallization induced structural transformation into hybrid stacking modes with two distinct arrangements between D-A such as face-to-face H-aggregation offers blue-shifted mixed-stacking, whereas J-aggregation is found to

be a staggered arrangement and leads to red-shifted segregated stacking. Moreover, rigid and dense sheet and wave-like network for the co-crystals benefits to restrict vibrational relaxation and prevents excitons quenching.[45,64] The low PLQY of TAHOFN can be assigned to the formation of local H-aggregates between TAH and OFN molecules, which leads to a high non-radiative deactivation rate. The presence of plenty of large intermolecular interactions and staggered orientation reduces the fluorescence quenching effect, resulting in high PLQY and revealing clear insights of structure-function correlation which directs into light propagating waveguide applications.[25-29]

3.3.6. Microscopic Morphology Visualization Studies

Photophysical and optoelectronic properties are largely affected by the size and morphology of materials.[45] Noncovalent interactions are crucial to define directional interactions and shape/size organizations in the morphologies of various structures like spheres, rods, rectangles and helixes for organic micro/nanocrystals, which influences the performances in the optoelectronic devices.[65,66] Further, multiple weak interactions leads to structural transformation and produce polymorphs or geometrical isomers which are responsible for the formation of different morphologies and optical properties. Therefore, in order to visualize controlled and regular 1D/2D morphology of the co-crystals, low-magnification (scale bar: 5.0 μm and 2.0 μm) FESEM images were obtained from the drop casted films on silicon coated glass plate (Figure 3.15a-3.15d). FESEM images manifested extremely uniform rod shape of the TAHOFN and 2D sheet-like for TAHTFPN_G crystals with size (D= 0.6, 1.15 μm, L= 12, 3.7 μm, W= O.42, 0.5 μm) and relatively small size prism shaped and rod-like 1D morphology of TAHTFPN_O and TAHTCNB with size (D = 1.8, 0.6 μm, L= 2.8, 20.0 μm, W= 0.35, 0.2 μm). Low-magnification TEM images (scale bar 2 μm) also consisted of the regular 2D and 1D shapes of the co-assemblies (Figure 3.15e-3.15h). However, a defined diffraction pattern was observed in SAED analysis, attributed to the high crystallinity of the co-assembly structures (inset Figure 4e-h). Further, to visualize the surface morphology, AFM images have also been recorded (scale bar 1 μm) and the afforded images are akin to the FESEM and FETEM images (Figure 3.15i-3.15l). The height and RMS roughness was found to be 323.0, 100.3, 101.9, 122.82 nm and 158.75, 22.93, 36.37, 35.37 nm, for TAHOFN, TAHTFPN_G, TAHTFPN_O and TAHTCNB respectively.

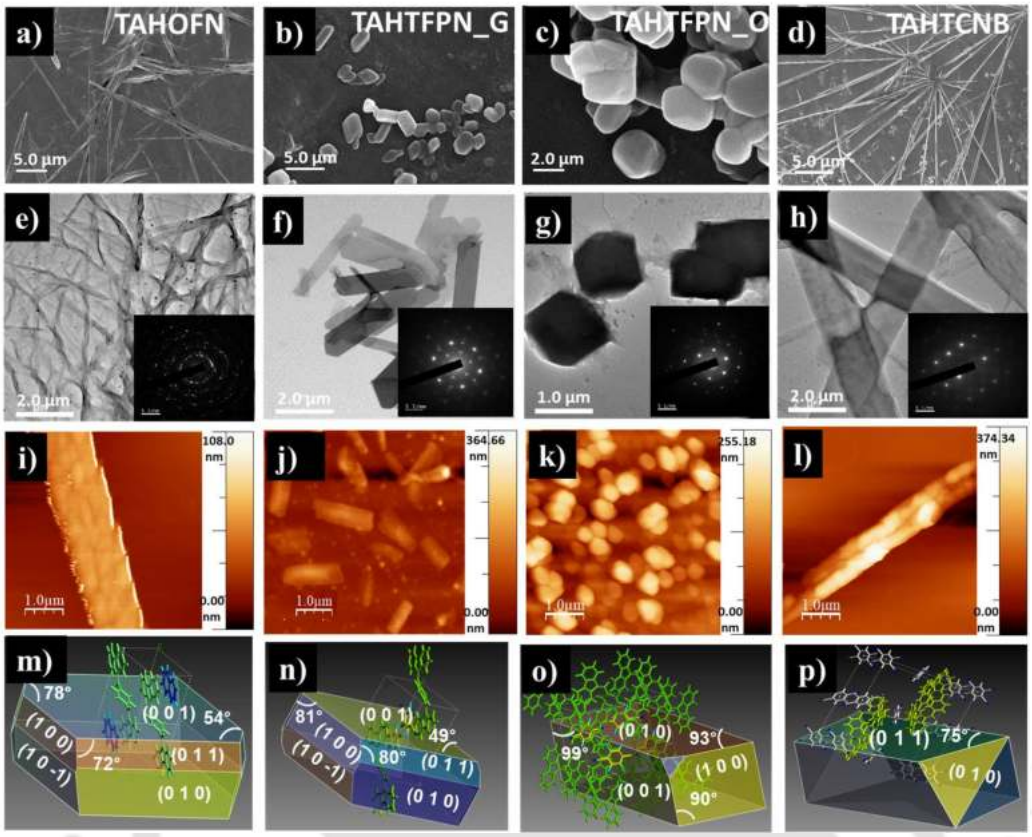

Figure 3.15. Microcrystals size and morphology visualization for all four co-crystals of TAHOFN, TAHTFPN_G, TAHTFPN_O and TAHTCNB: (a-d) Low-magnification (scale bar: 2 & 5 µm) FESEM images. (e- h) Low-magnification TEM images (scale bar 2 µm) of crystals (inset SAED pattern collected for crystallinity). (i-l) AFM images with height profile (1 µm scale bar). (m-p) Growth morphologies were anticipated by Material studio 17 software from all four co-crystals single crystals geometry based on the calculated attachment energies calculations, respectively.

Moreover, uniform supramolecular π-stacked co-assemblies through anisotropic interactions lead to perfectly orthogonal/parallel assembly, benefiting to obtained smooth surface topography in 2D block-shaped and 1D-sheet/rod-shaped crystal growth. Further, growth morphologies of the co-crystals were simulated and predicted by using Bravais-Friedel-Donnay-Harker (BFDH) theory and attachment energy principle in Material Studio software.[67,68] Simulated morphology provides multiple fast growing crystal facets of {0 0 1}, {0 1 0}, {0 1 1}, {1 0 0}, and {1 0 -1} for both TAHOFN and TAHTFPN_G, whereas a different surface areas of 54.04%, 15%, 9.52%, 5.61% and 9.48% for TAHOFN, and 47.02%, 17.28%, 12.45%, 11.83% and 8.80% for TAHTFPN_G respectively (Figure 3.15m, n and Table A3.8-A3.9). Subsequently, the crystal facets of {0 0 1}, {0 1 0}, {1 0 0}, and {1 1 1} with surface areas of 36.04%, 46.67%, 16.69%, and 0.58% for TAHTFPN_O, while for TAHTCNB, only two crystal facets {0 1 1}, {1 0 1} with surface

areas of 85.99% and 14% was predicted (Figure 3.15o, p and Table A3.10-A3.11). Therefore, TAHOFN and TAHTFPN_G grows into rod and 2D sheet-like crystal in the preferential growth direction at {0 0 1}, where TAHTFPN_O and TAHTCNB grows into cubic prism and rod-shaped crystal in the {0 1 0} and {0 1 1} direction thereby facilitating easy light transmission feature along the major growth direction, respectively. Remarkably, simulated morphology which is consistent with the experimental observation is anticipated to be regular prism and 1D sheet/rod like shaped structures with the length direction along c axis. In addition, the lowest energy single-crystal geometry presents that the acceptors OFN, TFPN and TCNB were located above the dibenzofulvene core with counter pitch angle 88.7°, 80.10°, 76.91° and 76.03° in TAHOFN, TAHTFPN_G, TAHTFPN_O and TAHTCNB CT-complexes, respectively (Figure 3.16).

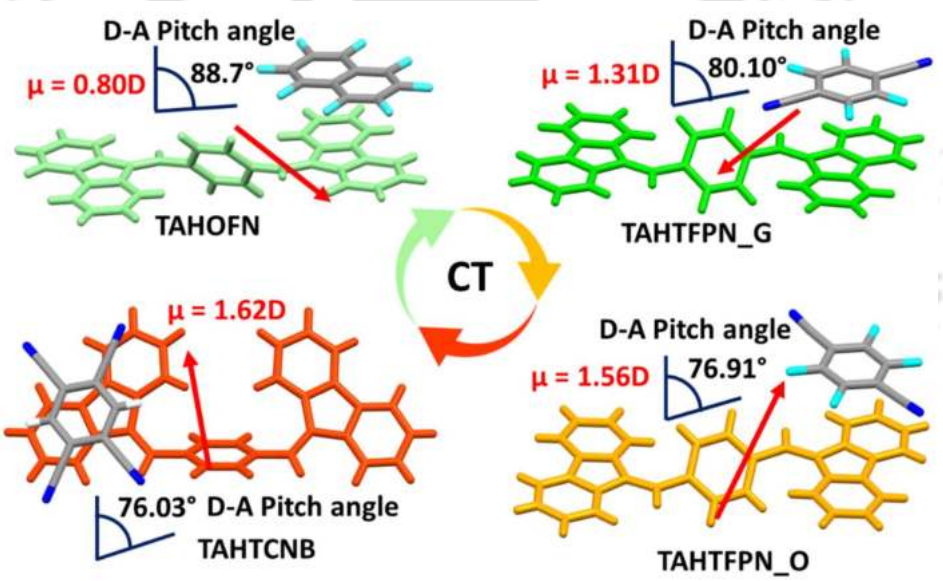

Figure 3.16. Orientation of dipole moment (μ) and pitch angles between D-A obtained from TD-DFT and SC-XRD structures of TAHOFN, TAHTFPN_G, TAHTFPN_O and TAHTCNB.

Therefore, a gradual decrement of counter pitch angle with low overlap between D-A suggests that the weaker interaction was encountered due to the variation in packing modes from mixed stack to segregated stack, which is consistent with the above analysis and favorable for red-shifted emission.[9,39] However, the static dipole moment (SDM) of TAHOFN, TAHTFPN_G, is directed from the acceptors OFN and TFPN to the donor TAH, and were calculated as 0.80D, 1.31D. Notably, SDM of TAHTFPN_O and TAHTCNB is directed from donor TAH to the acceptors TFPN and TCNB, and were calculated as 1.56D and 1.62D, respectively. The low CT degree and high SDM further confirms the weak CT

in the ground state of the yellow polymorph TAHTFPN_O and *cis*-isomer TAHTCNB CT-complexes. Thus, modulating molecular packing and μ with desirable morphology via anisotropic interactions in π-conjugated co-assembly is not only important for fundamental study but also has practical implications.

3.3.7. Optical Waveguide Study

All the photophysical studies clearly showed their distinctive emissive property relative to the individual crystals. While exposing the prepared co-crystals under UV light (365 nm), the ends of the crystals showed bright emissions. This observation triggered us to explore their optical wave guiding studies. The optical wave guiding experiments were performed for individual rod-like microcrystals using a confocal microscopy setup in transmission-mode geometry. A diode laser 405 nm was used as an excitation source, exciting at the left terminus of the microcrystal generated bright greenish luminescence for TAHOFN and TAHTFPN_G, while bright orange-red emission was generated from TAHTCNB microcrystals, which was transmitted to its opposite end. To examine excitation position dependent PL signal modulation, experiments were performed for all three microcrystals. For this purpose microcrystals of length of 21, 135 and 201 μm were selected and excited at different distances i.e., 21, 18, 14, 10, 5.8, 3.0 μm for TAHOFN, 135, 111, 91, 70, 47, 23 μm for TAHTFPN_G, and 201, 165, 133, 100, 62, 29 μm for TAHTCNB microcrystals.

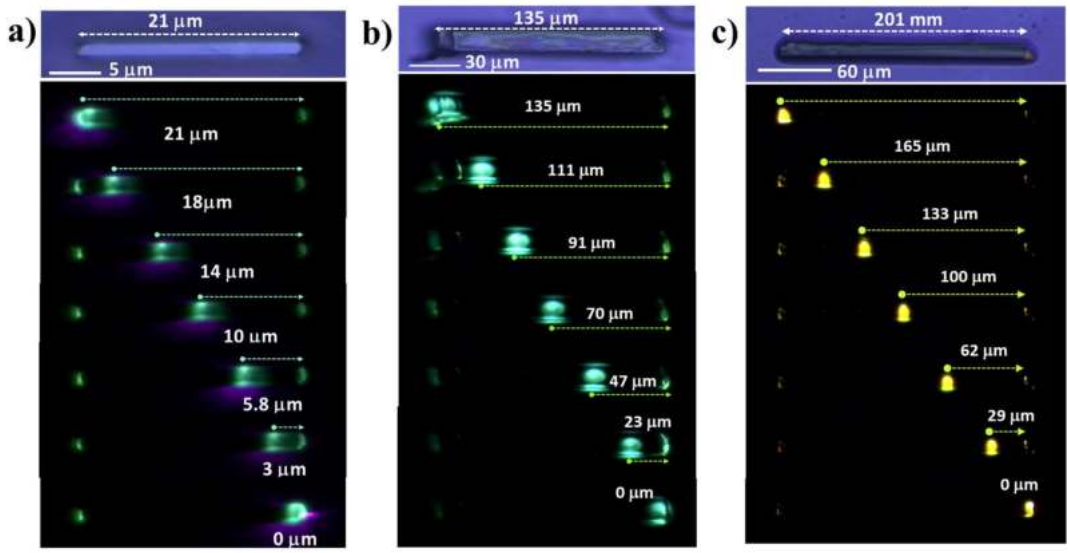

Figure 3.17. Optical waveguide study: (a-c) Micro PL images of micro-crystals for TAHOFN, TAHTFPN_G and TAHTCNB microcrystals; a focused 405 nm excitation laser source was used to excite micro-rods at seven different positions.

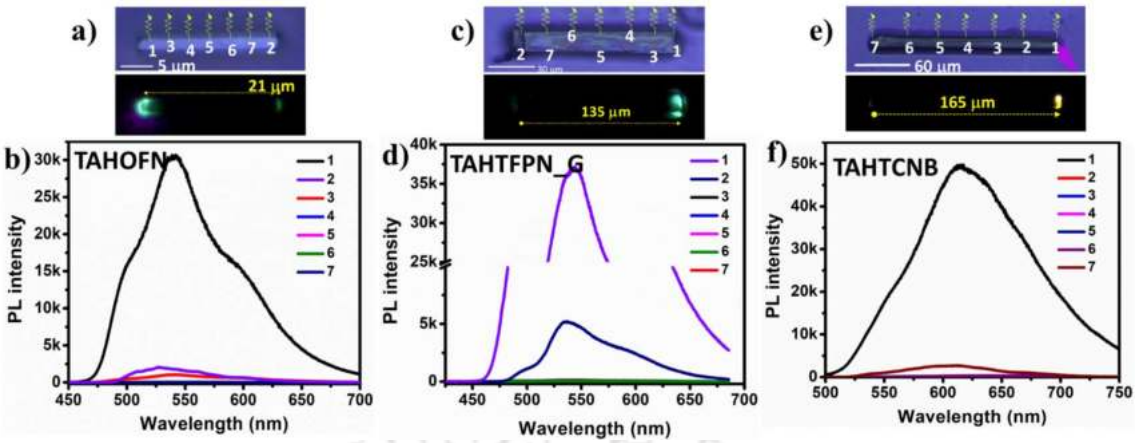

Figure 3.18. (a) Confocal microscopic images of microcrystals. (b) Spatially resolved spectra of TAHOFN, TAHTFPN_G and TAHTCNB co-crystals: Excitation position was kept constant and PL signals were collected at different positions.

Subsequently, the light transducing behavior of microcrystals was investigated for TAHOFN, TAHTFPN_G, and TAHTCNB crystals, respectively, under ambient conditions. The PL images of TAHOFN, TAHTFPN_G and TAHTCNB show strong greenish and orange-red emissions at the tips for the respective microcrystals (Figure 3.17a-3.17c). Spatially resolved spectra for all three microcrystals were recorded by keeping the excitation position constant and PL signals were collected at different positions for TAHOFN, TAHTFPN_G and TAHTCNB microcrystals (Figure 3.18). Strikingly, the PL spectrum showed narrow bandwidth spectrum covering 450-700 nm with distinct fluorescence and TADF emission peaks centered at 545, 550 and 600 nm for TAHOFN, TAHTFPN_G and TAHTCNB, respectively (Figure 3.19a-3.19c), which matched exactly with the PL emission observed for crystalline powder forms of the co-crystals.[10] Noticeably, the spectral profiles did not shift with the excitation position. However, with an increase of distance from the excitation point to terminus, the PL intensity gradually decreased at the left terminus. The optical loss co-efficient (α') was obtained from distance-dependent PL spectra, whereas the PL intensities were recorded at the illuminated position (I_{body}) and collected at the terminus of the crystals (I_{tip}) within the micro-rod crystals (Figure 3.19d-3.19f). By fitting the exponential decay function, $I_{tip}/I_{body} = \exp(-\alpha' D)$,[69,70] where D is the distance between the illuminated position and the collection position of the crystal, and α is the loss coefficient (where $\alpha' = 4.34\alpha$), the α' values were determined to be as low as 0.44 dB/µm for TAHOFN, 0.0742 dB/µm for TAHTFPN_G and 0.0837 dB/µm for TAHTCNB, respectively.

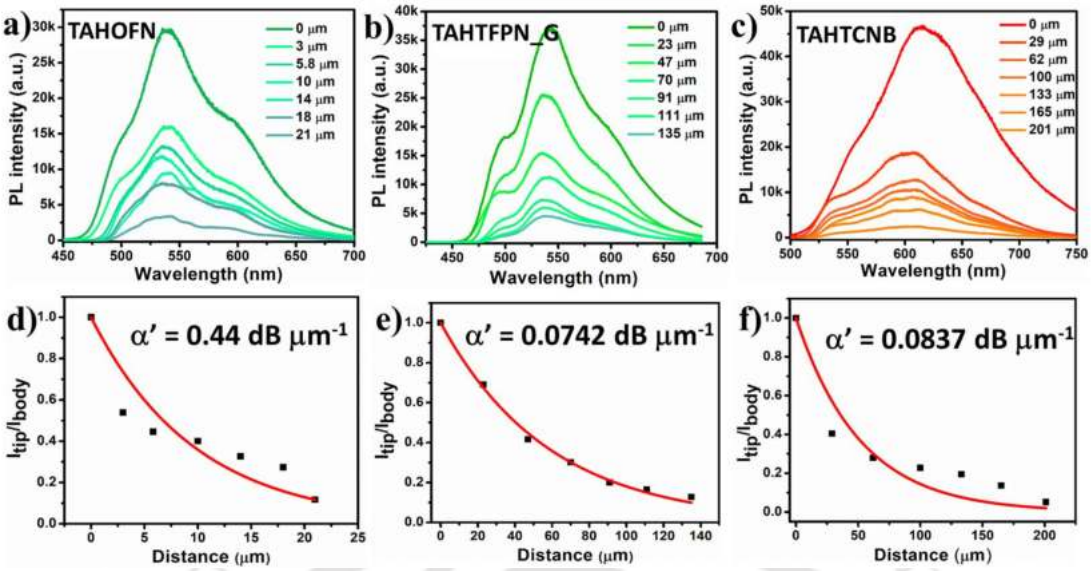

Figure 3.19. Optical waveguide study: (a-c) Emission spectra at the end of the microcrystals for TAHOFN, TAHTFPN_G and TAHTCNB, the bright line is the emission spectra at the illuminated position. (d-f) Estimation of the optical loss coefficient (α) from the plot of I_{tip}/I_{body} versus the light propagation distance.

These results are suggested that a very good optical waveguide performance of this crystalline organic fluorescent and TADF microcrystal. Notably, these α' values are lower than most of state-of-the-art 1D optical waveguides materials (Table A3.12).[33]The observed efficient optical waveguide properties and low α' value for TAHTFPN_G rather than TAHOFN can be explained by a few important factors such as large CT, high PLQY, well-defined crystallinity, defects free packing, smooth surface and weak coupling between μ and light propagation, leading to no reabsorption and a low loss of the optical waveguides.[25,44] On the contrary the α' value of TAHCNB is comparatively higher than TAHTFPN_G microcrystal because of occurrence of triplet contribution in the TADF emission. Therefore, our developed micro-co-crystals acts as a light transducer by self-guiding its fluorescence and TADF emission via linear light propagation along its longitudinal axis.

3.4. Conclusion

In summary, exploration of new photofunctional luminescent crystals, mechanistic understanding of color-tunable solid-state emission and finding appropriate applications is a formidable challenge for purely organic multicomponent organic system. This work presents a series of four rationally designed color-tunable CT co-crystals of TAHOFN, TAHTFPN_G, TAHTFPN_O and TAHTCNB developed by utilizing the non-planar twisted donor TAH and planar acceptors OFN, TFPN and TCNB. The co-crystals,

TAHTFPN_G and TAHTFPN_O, possess different fluorescence color-specific polymorphs, while TAHTCNB is an unusual configurational cis-isomer exhibiting an exceptional TADF feature, a major breakthrough for a pure hydrocarbon donor based co-crystal. Further, a very broad agreement of experimental and theoretical results confirmed the complete involvement of co-formers and the formation of new co-crystals and their structural modulations with intrinsic excited state dynamics for bright fluorescence. With the increasing acceptor strength, the co-crystals exhibited decrease in energy band gap and ΔE_{ST} including variable degree of through-space CT characteristics leading to different tunable optical properties, blue/red-shifted fluorescence, up-conversion luminescence including singlet and triplet harvesting optical waveguide performances. These, co-crystals exhibited different multiple intermolecular noncovalent bonding, TSCT and π-π interactions which regulated different stacking modes such as H-type mixed stack and J-type segregated stack between co-former units and resulted in dynamic co-crystals with improved physicochemical functions. Consequently, the combined investigations of dense crystal packing, regular supramolecular organization, morphology, desired orientation of μ, and variable CT in the co-crystals resulted in improved OWGs by self-guiding the generated fluorescence and TADF, through light propagation along its longitudinal axis at ultra-low optical loss co-efficient (α') respectively. Collectively, this work explored a new class of polymorphs and a rare configurational isomer in the co-crystal systems which precisely described the unusual "structure-functionality relationship", by achieving high excitons utilization efficiency with low optical loss wave-guiding features in color-tunable co-crystals for the first time.

3.5 References

[1] Y. Wang, L. Sun, C. Wang, F. Yang, X. Ren, X. Zhang, H. Dong, W. Hu, *Chem. Soc. Rev.,* **2019**, *48*, 1492-1530.

[2] J. Li, K. Zhou, J. Liu, Y. Zhen, L. Liu, J. Zhang, H. Dong, X. Zhang, L. Jiang, W. Hu, *J. Am. Chem. Soc.,* **2017**, *139*, 17261-17264.

[3] X. Wang, Z. -Z. Li, M. -P. Zhuo, Y. Wu, S. Chen, J. Yao, H. Fu, *Adv. Funct. Mater.,* **2017**, *27*, 1703470.

[4] S. K. Park, S. Varghese, J. H. Kim, S. -J. Yoon, O. K. Kwon, B. -K. An, J. Gierschner, S. K. Park, *J. Am. Chem. Soc.,* **2013**, *135*, 4757-4764.

[5] M. A. McCarthy, B. Liu, E. P. Donoghue, I. Kravchenko, D. Y. Kim, F. So, A. G. Rinzle, *Science,* **2011**, *332*, 570-573.

[6] Z. Qin, H. Gao, H. Dong, W. Hu, *Adv. Mater*., **2021**, *33*, 2007149.

[7] Y. Liu, A. Li, S. Xu, W. Xu, Y. Liu, W. Tian, B. Xu, *Angew. Chem. Int. Ed.,* **2020**, *59*, 15098-15103.

[8] L. Sun, W. Zhu, W. Wang, F. Yang, C. Zhang, S. Wang, X. Zhang, R. Li, H. Dong, W. Hu, *Angew. Chem. Int. Ed.,* **2017**, *56*, 7831-7835.

[9] W. Zhu, L. Zhu, Y. Zou, Y. Wu, Y. Zhen, H. Dong, H. Fu, Z. Wei, Q. Shi, W. Hu, *Adv. Mater.* **2016**, *28*, 5954-5962.

[10] D. Barman, M. Annadhasan, R. Chandrasekar, P. K. Iyer, *Chem. Sci.,* **2022**, *13*, 9004-9015.

[11] J. Ravi, M. Annadhasan, A. Vinod Kumar, R. Chandrasekar, *Adv. Funct. Mater.,* **2021**, *31*, 2100642.

[12] M. Rohullah, V. V. Pradeep, J. Ravi, A. V. Kumar, R. Chandrasekar, *Angew. Chem.Int. Ed.,* **2022**,*61,* e2022021.

[13] M. Annadhasan, A.R. Agrawal, S. Bhunia, V.V. Pradeep, S. S. Zade, C. M. Reddy, R. Chandrasekar, *Angew. Chem. Int. Ed.,* **2020**, *59,* 13852-13858.

[14] C. A. Masmanidis, H. H. Jaffe, R. L. Ellis, *J. Phys. Chem.,* **1975,** *79*, 2052-2061.

[15] R. Chandrasekar, *Small,* **2021**, *17*, 2100277.

[16] K. Takazawa, J. Inoue, K. Mitsuishi, T. Takamasu, *Adv. Mater.,* **2011**, *23*, 3659-3663.

[17] M. Annadhasan, S. Basak, N. Chandrasekhar, R. Chandrasekar, *Adv. Opt. Mater.,* **2020**, *8*, 2000959.

[18] Z. Lu, Y. Zhang, H. Liu, K. Ye, W. Liu, H. Zhang, *Angew. Chem. Int. Ed.,* **2020**, *59*, 4299-4303.

[19] D. P. Karothu, G. Dushaq, E. Ahmed, L. Catalano, S. Polavaram, R. Ferreira, L. Li, Liang, S. Mohamed, M. Rasras, P. Naumov, *Nat. Commun.,* **2021**, *12*, 1326.

[20] M. P. Zhuo, J. J. Wu, X. D. Wang, Y. C. Tao, Y. Yuan, L. S. Liao, *Nat. Commun.,* **2019**, *10*, 3839.

[21] W. Zhu, R. Zheng, X. Fu, H. Fu, Q. Shi, Y. Zhen, H. Dong, W. Hu, *Angew. Chem., Int. Ed.,* **2015**, *54*, 6785- 6789.

[22] F. Di Benedetto, A. Camposeo, S. Pagliara, E. Mele, L. Persano, R. Stabile, R. Cingolani, D. Pisignano, *Nat. Nanotechnol.,* **2008**, *3*, 614-619.

[23] J. M. Halabi, E. Ahmed, L. Catalano, D. P. Karothu, R. Rezgui, P. Naumov, *J. Am. Chem. Soc.,* **2019**, *141*, 14966-14970.

[24] Y. Liu, Q. Zeng, B. Zou, Y. Liu, B. Xu, W. Tian, *Angew. Chem., Int. Ed.,* **2018**, *57*, 15670-15674.

[25] L. Sun, W. Zhu, X. Zhang, L. Li, H. Dong, W. Hu, *J. Am. Chem. Soc.,* **2021**, *143*, 19243-19256.

[26] M. -P. Zhuo, Y. -C. Tao, X. -D. Wang, Y. Wu, S. Chen, L. –S. Liao, L. Jiang, *Angew. Chem. Int. Ed.,* **2018**, *130*, 11470-11474.

[27] S. Z. Li, B. Lu, X. Y. Fang, D. P. Yan, *Angew. Chem., Int. Ed*., **2020**, *59*, 22623-22630.

[28] A. Narayanan, D. Cao, L. Frazer, A. S. Tayi, A. K. Blackburn, A. C. H. Sue, J. B. Ketterson, J. F. Stoddart, S. I. Stupp, *J. Am. Chem. Soc.,* **2017**, *139*, 9186-9191.

[29] M. -P. Zhuo, Y. Yuan, Y. Su, S. Chen, Y. -T. Chen, Z. -Q. Feng, Y. -K. Qu, M. -D. Li, Y. Li, B. -W. Hu, X. -D. Wang, L. -S. Liao, *Adv. Mater.,* **2022**, 2107169.

[30] W. Ji, B. Xue, S. Bera, S. Guerin, Y. Liu, H. Yuan, Q. Li, C. Yuan, L. J. W. Shimon, Q. Ma, E. Kiely, S. A. M. Tofail, M. Si, X. Yan, Y. Cao, W. Wang, R. Yang, D. Thompson, J. Li, E. Gazit, *ACS Nano,* **2020**, *14*, 10704–10715.

[31] Y. Liu, H. Hu, L. Xu, B. Qiu, J. Liang, F. Ding, K. Wang, M. Chu, W. Zhang, M. Ma, B. Chen, X. Yang, Y. S. Zhao, *Angew. Chem., Int. Ed.,* **2020**, *59*, 4456-4463.

[32] S. Ma, Y. Liu, J. Zhang, B. Xu, W. Tian, *J. Phys. Chem. Lett.,* **2020**, *11*, 10504-10510.

[33] B. Lu, X. Fang, D. Yan, *ACS Appl. Mater. Interfaces,* **2020**, *12*, 31940-31951.

[34] L. Yu, *Acc. Chem. Res.,* **2010**, *43*, 1257-1266.

[35] T. Beyer, G. M. Day, S. L. Price, *J. Am. Chem. Soc.,* **2001**, *123*, 5086-5094.

[36] K. M. Steed, J. W. Steed, *Chem. Rev.,* **2015**, *115*, 2895-2933.

[37] H. Uoyama, K. Goushi, K. Shizu, H. Nomura, C. Adachi, *Nature,* **2012**, *492*, 234-238.

[38] S. Hirata, Y. Sakai, K. Masui, H. Tanaka, S. Y. Lee, H. Nomura, N. Nakamura, M. Yasumatsu, H. Nakanotani, Q. Zhang, K. Shizu, H. Miyazaki, C. Adachi, *Nat. Mater.,* **2015**, *14*, 330-336.

[40] M. Y. Wong, E. Zysman-Colman, *Adv.Mater.,* **2017**, *29*, 1605444.

[41] P. Rajamalli, N. Senthilkumar, P. Y. Huang, C. C. Ren-Wu, H. W. Lin, C. H. Cheng, *J. Am. Chem. Soc.,* **2017,** *139*, 10948-10951.

[42] L. Sun, W. Hua, Y. Liu, G. Tian, M. Chen, M. Chen, F. Yang, S. Wang, X. Zhang, Y. Luo, W. Hu, *Angew. Chem., Int. Ed.,* **2019**, *58*, 11311-11316.

[43] J. Mei, N. L. C. Leung, R. T. K. Kwok, J. W. Y. Lam, B. Z. Tang, *Chem. Rev.,* **2015**, *115*, 11718-11940.

[44] D. Barman, P. Gopikrishna, P. K. Iyer, *Langmuir,* **2021**, *37*, 8024-8036.

[45] D. Liu, J. De, H. Gao, S. Ma, Q. Ou, S. Li, Z. Qin, H. Dong, Q. Liao, B. Xu, Q. Peng, g. Z. Shuai, W. Tian, H. Fu, X. Zhang, Y. Zhen, W. Hu, *J. Am. Chem. Soc.,* **2020**, *142*, 6332-6339.

[46] Y. Huang, J. Xing, Q. Gong, L.-C. Chen, G. Liu, C. Yao, Z. Wang, H.-L. Zhang, Z. Chen, Q. Zhang, *Nat. Commun.,* **2019**, *10*, 169.

[47] T.; Jimbo, M.; Tsuji, R.; Taniguchi, K.; Sada, K. Kokado, *Cryst. Growth Des.,* **2018**, *18*, 3863-3869.

[48] X. Han, Y. Lei, Q. Liao, H. Fu, *Angew.Chem. Int. Ed.,* **2021**, *133*, 3074-3078.

[49] J.-J. Wu, Z.-Z. Li, M.-P. Zhuo, Y. Wu, X.-D. Wang, L.-S. Liao, L. Jiang, *Adv. Opt. Mater.,* **2018**, *6*, 1701300.

[50] Y. Huang, Q. Gong, J. Ge, P. Tang, F. Yu, L. Xiao, Z. Wang, H. Sun, J. Yu, D. -S. Li, Q. Xiong, Q. Zhang, *ACS Nano,* **2020**, *14*, 15962-15972.

[51] Y. -L. Lei, Y. Jin, D. -Y. Zhou, W. Gu, X. –B. Shi, L. S. Liao. S. –T. Lee, *Adv. Mater.,* **2012**, *24*, 5345-5351.

[52] R. J. Dillon, C. J. Bardeen, *J. Phys. Chem. A,* **2011**, *115*, 1627-1633.

[53] M. Etherington, J. Gibson, H. Higginbotham, T. J. Penfold, A. P. Monkman, *Nat Commun.,* **2016**. *7*, 13680.

[54] J. Harada, M. Ohtani, Y. Takahashi, T. Inabe, *J. Am. Chem. Soc*., **2015**, *137*, 4477-4486.

[55] L. Zhu, E. –G. Kim, Y. Yi, J. –L. Brédas, *Chem. Mater.,* **2011**, *23*, 5149-5159.

[56] T. Lu, F. W. Chen, *J. Comput. Chem.,* **2012**, *33*, 580-592.

[57] P. Rajamalli, F. Rizzi, W. Li, M. A. Jinks, A. K. Gupta, B. A. Laidlaw, I. D. W. Samuel, T. J. Penfold, S. M. Goldup, E. Zysman-Colman, *Angew. Chem. Int. Ed*., **2021**, *60*, 12066-12073.

[58] N. Meher, P. K. Iyer, *Angew. Chem. Int. Ed.,* **2018**, *57*, 8488-8492.

[59] Y. Wang, H. Wu, P. Li, S. Chen, L. O. Jones, M. A. Mosquera, L. Zhang, K. Cai, H. Chen, X. -Y. Chen, C. L. Stern, M. R. Wasielewski, M. A. Ratner, G. C. Schatz, J. F. Stoddart, *Nat Commun.,* **2020**, *11*, 4633.

[60] K. P. Goetz, A. Fonari, D. Vermeulen, P. Hu, H. Jiang, P. J. Diemer, J. W. Ward, M. E. Payne, C. S. Day, C. Kloc, V. Coropceanu, L. E. McNeil, O. D. Jurchescu, *Nat. Commun.,* **2014**, *5*, 5642.

[61] M. Boterashvili, M. Lahav, S. Shankar, A. Facchetti, M. E. van der Boom *J. Am. Chem. Soc.,* **2014**, *136*, 11926-11929.

[62] H. Wang, Q. Li, J. Zhang, H. Zhang, Y. Shu, Z. Zhao, W. Jiang, L. Du, D. L. Phillips, J. W. Y. Lam, H. H.Y. Sung, I. D. Williams, R. Lu, B. Z. Tang, *J. Am. Chem. Soc.,* **2021**, *143*, 9468-9477.

[63] I. Rosbottom, J. K. Roberts, R. Docherty, *CrystEngComm.,* **2015**, *17*, 5768-5788.

[64] O. Bolton, K. Lee, H.-J. Kim, K. Y. Lin, J. Kim, *Nat. Chem.,* **2011**, *3*, 205.

[65] X. Ye, Y. Liu, Q. Guo, Q. Han, C. Ge, S. Cui, L. Zhang, X. Tao, *Nat. Commun*., **2019**, *10*, 761.

[66] Y. Sun, Y. Lei, H. Dong, Y. Zhen, W. Hu, *J. Am. Chem. Soc.,* **2018**, *140*, 6186-6189.

[67] D. Winn, M. F. Doherty, *AIChE J.,* **2000** *46*, 1348-1367.

[68] H. Liu, X. Cao, Y. Wu, Q. Liao, J. A. Jiménez, F. Würthner, H. Fu, *Chem. Commun.,* **2014**, *50*, 4620-4623.

[69] M. Annadhasan, D. P. Karothu, R.' Chinnasamy, L. Catalano, E. Ahmed, S. Ghosh, P. Naumov, R. Chandrasekar, *Angew.Chem.Int.Ed*., **2020**, *59*, 13821-13830.

[70] Z. Ding, H. Shang, Y. Geng, S. –T. Zhang, Z. Huo, Z. Yang, B. Li, W. Xu, S. Jiang, *J. Phys. Chem. Lett., **2021**, 12*, 4585-4592.

Appendix: Additional data for **Chapter 3**

Table A3.1. Time resolved PL Decay of TAHOFN co-crystal Ex. 405 nm and Em. 540 nm.

❖ **Exponential Components Analysis (Reconvolution)**

Fitting range : [112; 510] channels

χ^2 : 0.997

	B_i	ΔB_i	f_i (%)	Δf_i (%)	τ_i (ns)	$\Delta\tau_i$ (ns)
1	0.1570	0.0018	100.000	3.524	0.505	0.012

Shift : 0.307 ns (± 0.419 ns)

Decay Background : 1.142 (± 0.139)

IRF background : 0

Table A3.2. Time resolved PL Decay of TAHTFPN_G co-crystal Ex. 405 nm and Em. 545 nm.

❖ **Exponential Components Analysis (Reconvolution)**

Fitting range : [112; 640] channels

χ^2 : 1.009

	B_i	ΔB_i	f_i (%)	Δf_i (%)	τ_i (ns)	$\Delta\tau_i$ (ns)
1	0.1347	0.0015	100.000	1.574	0.967	0.004

Shift : 0.236 ns (± 0.643 ns)

Decay Background : 1.096 (± 0.139)

IRF background : 0

Table A3.3. Time resolved PL Decay of TAHTFPN_O co-crystal Ex. 405 nm and Em. 560 nm.

❖ **Exponential Components Analysis (Reconvolution)**

Fitting range : [113; 1500] channels

χ^2 : 1.003

	B_i	ΔB_i	f_i (%)	Δf_i (%)	τ_i (ns)	$\Delta\tau_i$ (ns)
1	0.1388	0.0022	100.000	1.876	1.064	0.003

Shift : 0.122 ns (± 0.873 ns)

Decay Background : 1.023 (± 0.062)

IRF background : 0

Table A3.4. Time resolved PL Decay of TAHTCNB co-crystal Ex. 405 nm and Em. 590 nm.

❖ **Exponential Components Analysis (Reconvolution)**

Fitting range : [113; 3900] channels

χ^2 : 1.034

	B_i	ΔB_i	f_i (%)	Δf_i (%)	τ_i (ns)	$\Delta\tau_i$ (ns)
1	0.0763	0.0052	2.970	0.858	0.570	0.126
2	0.0115	0.0006	4.142	0.229	5.253	0.018
3	0.0433	0.0004	92.888	0.830	31.432	0.0004

Shift : 0.098 ns (± 3.634 ns)

Decay Background : 8.010 (± 1.265)

IRF background : 0

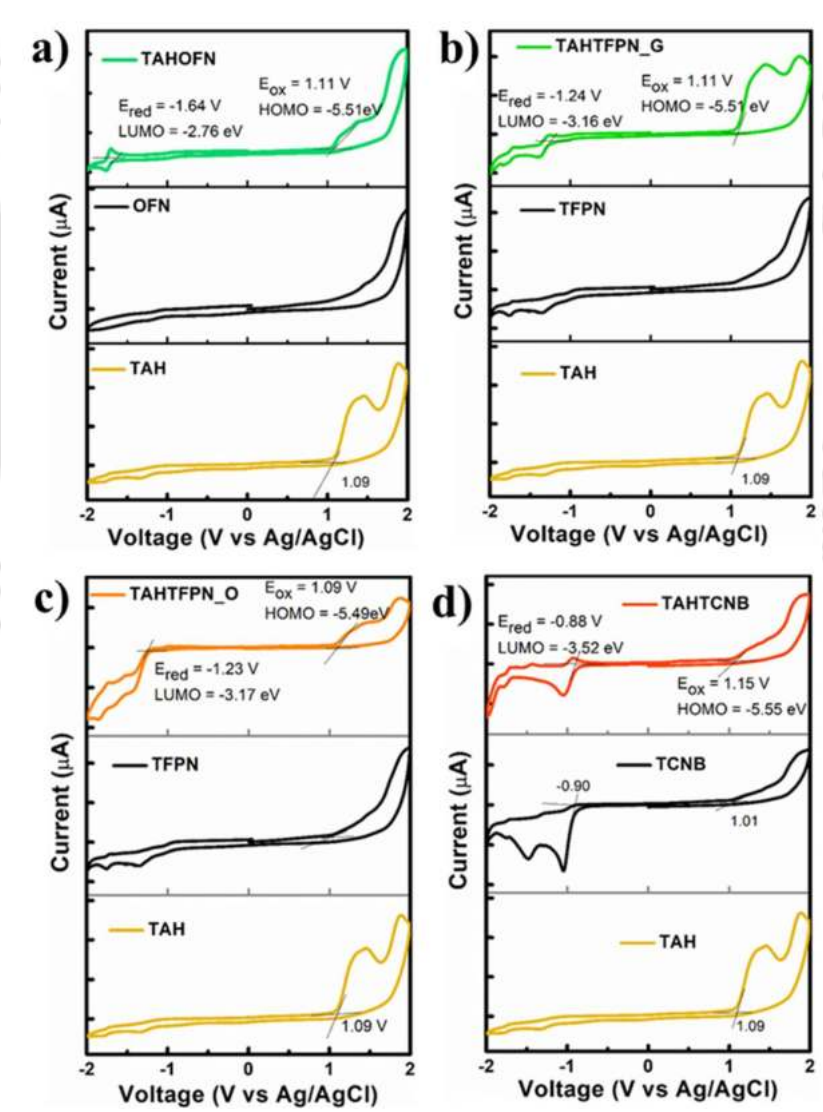

Figure A3.1. (a-d) Cyclic voltammetry (CV) curves of TAH crystals (yellow line), OFN, TFPN, TCNB (black line) where cocrystals of TAHOFN (off-green line), TAHTFPN_G (green line) TAHTFPN_O (orange line) where TAHTCNB (red line) respectively.

Table A3.5. The energy levels calculated from cyclic voltammetry and DFT.

Compound	Experimental data						DFT data (eV)		
	E_{ox}/V	E_{red}/V	E_{HOMO} /eV	E_{LUMO} /eV	E_{opt}/ eV	H-L Gap eV	HOMO	LUMO	H-L Gap
TAH	1.09	-	-5.49	-2.96	2.53	2.53	-5.47	-2.17	3.29
TAHOFN	1.11	-1.64	-5.51	-2.76	-	2.75	-5.51	-2.76	2.75
TAHTFPN_G	1.11	-1.24	-5.51	-3.16	-	2.35	-5.58	-2.69	2.89
TAHTFPN_O	1.09	-1.23	-5.49	-3.17	-	2.32	-5.48	-2.80	2.68
TAHTCNB	1.15	-0.88	-5.55	-3.52	-	2.03	-5.55	-3.52	2.033

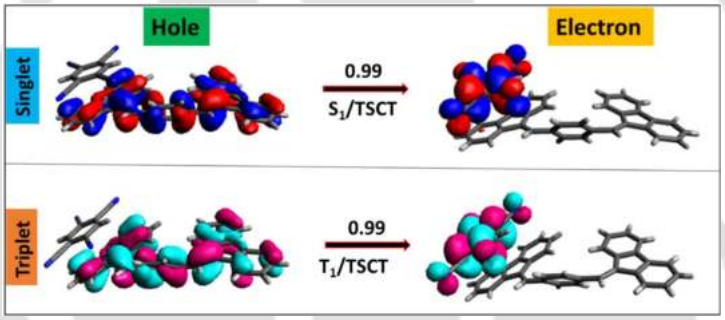

Figure A3.2. Natural transition orbitals (NTOs) for lowest excited singlet and triplet excited states in TAHTCNB.

Figure A3.3. Mechanism of weak fluorescence (a-PET & d-PET) for TAHOFN by DFT/TD-DFT calculated HOMO/LUMO energy band diagram for conformer TAH and OFN.

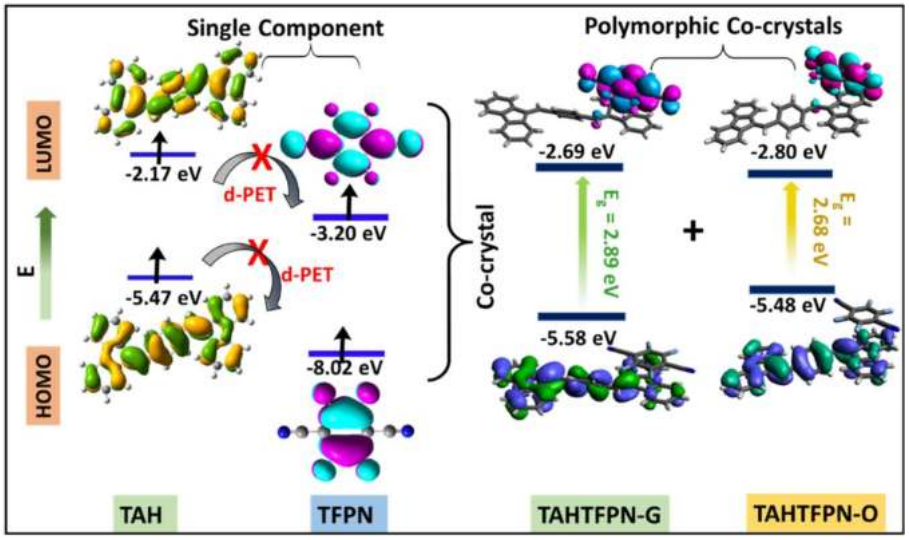

Figure A3.4. Color-tunable fluorescence and CT mechanism for the polymorphic co-crystals of TAHTFPN_G and TAHTFPN_O by DFT/TD-DFT calculated HOMO/LUMO energy band diagram for the conformer TAH and TFPN.

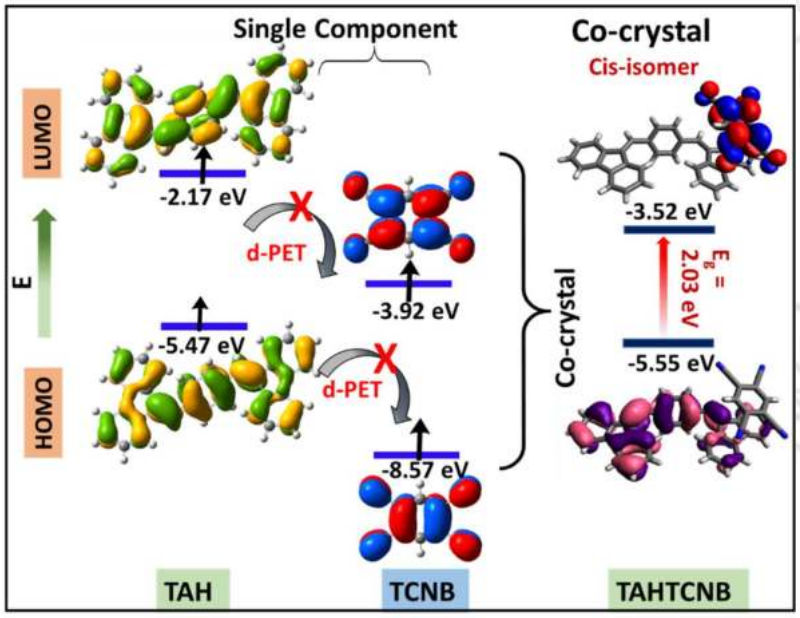

Figure A3.5. Red fluorescence and strong narrow band CT mechanism for the cis-isomeric co-crystals of TAHTCNB by DFT/TD-DFT calculated HOMO/LUMO energy band diagram for the conformer TAH and TCNB.

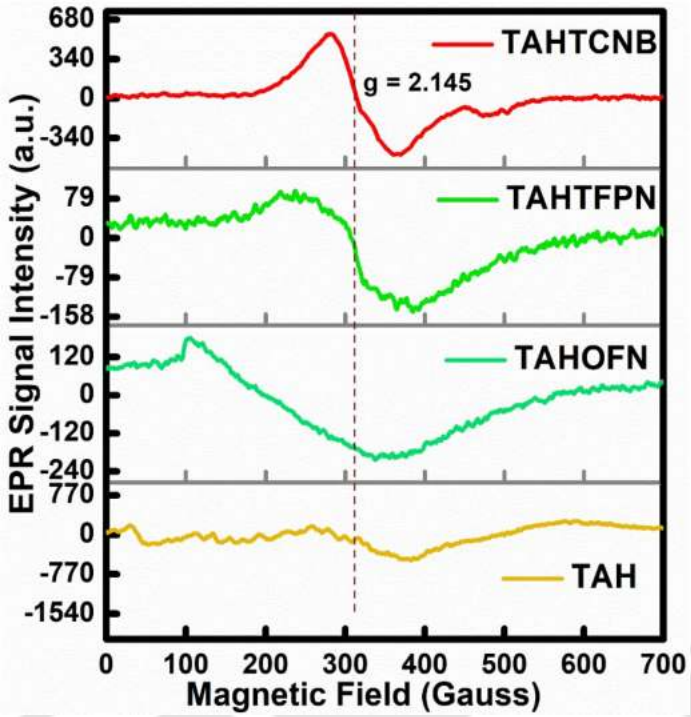

Figure A3.6. Electron spin resonance (ESR) spectra for TAH (yellow line), TAHOFN (off green line), TAHTFPN_G (green line) and TAHTCNB (red line).

Table A3.6. Crystallographic data and structure refinement parameters of TAHOFN, TAHTFPN_G, TAHTFPN_O and TAHTCNB co-crystals.

Compound	TAHOFN	TAHTFPN_G	TAHTFPN_O	TAHTCNB
Empirical formula	$C_{44}H_{22}F_8$	$C_{42}H_{24}F_4N_2$	$C_{42}H_{24}F_4N_2$	$C_{44}H_{24}N_4$
CCDC NO	2109333	2109336	2109335	2109337
Temperature/K	293 (2)	293 (2)	293 (2)	293 (2)
Crystal system	triclinic	triclinic	triclinic	orthorhombic
Space group	P -1	P -1	P -1	P n m a
a/Å	6.9672(6)	7.0777(7)	6.777(4)	8.1658(6)
b/Å	9.9719(12)	9.9789(12)	15.869(11)	22.9815(16)
c/Å	15.3125(11)	13.6987(13)	17.567(9)	22.0149(19)
α/°	91.687(8)	95.475(9)	80.15(5)	90
β/°	100.664(7)	98.390(8)	88.60(4)	90
γ/°	103.036(9)	94.383(9)	86.25(5)	90
Volume/Å^3	1015.72(17)	948.77(18)	1857.2(19)	4131.4(6)

Z	2	2	2	4
ρ_{calc}mg/mm^3	1.595	1.454	1.514	0.979
m/mm^{-1}	0.144	0.114	1.022	0.058
F(000)	490	422	860	1264.4830
Index ranges	-8 ≤ h ≤ 7, -11 ≤ k ≤ 11, -18 ≤ l ≤ 18	-9 ≤ h ≤ 8, -11 ≤ k ≤ 13, -18 ≤ l ≤ 18	-7 ≤ h ≤ 7, -17 ≤ k ≤ 17, -19 ≤ l ≤ 19	-6 ≤ h ≤ 9, -27 ≤ k ≤ 13, -17 ≤ l ≤ 26
Reflections collected	6600	7707	44322	10016
Independent reflections	3593[R(int) = 0.0726]	4310[R(int) = 0.0799]	5355[R(int) = 0.1135]	3732
Data/restraints/parameters	3593/0/316	4310/0/280	5355/0/559	3732/0/217
Goodness-of-fit on F^2	1.060	1.081	1.238	1.0477
Final R indexes [I>=2σ (I)]	R1 = 0.0692, wR2 = 0.1610	R1 = 0.0847, wR2 = 0.2073	R1 = 0.1426, wR2 = 0.2831	R1 = 0.1207, wR2 = 0.3363
Final R indexes [all data]	R1 = 0.1424, wR2 = 0.2120	R1 = 0.1307, wR2 = 0.2466	R1 = 0.1520, wR2 = 0.2888	R1 = 0.1796, wR2 = 0.3792

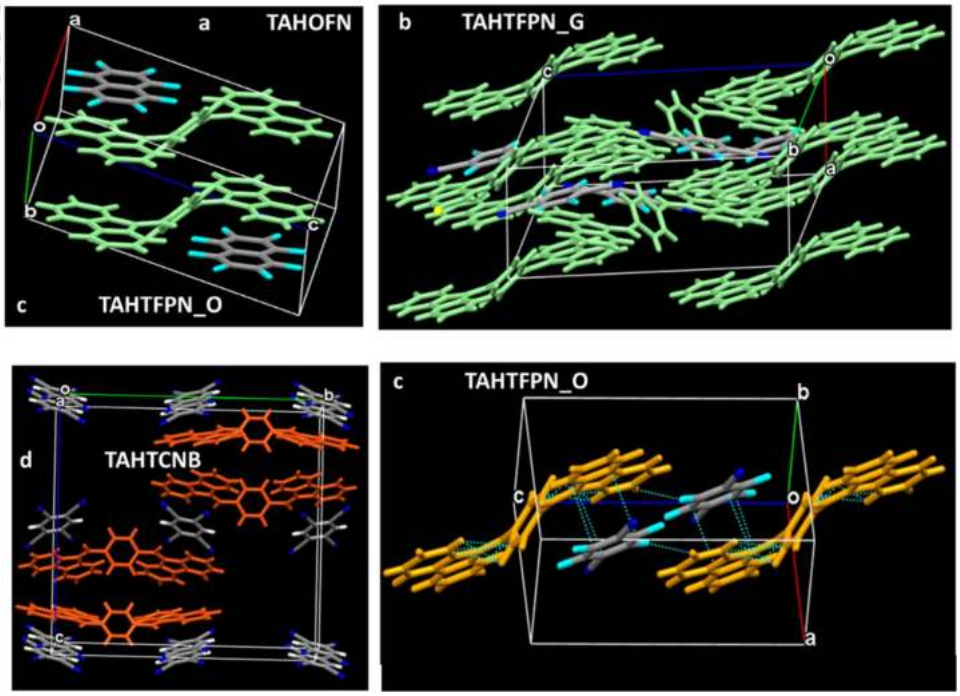

Figure A3.7. Unit cell packing in the SC-XRD structure for TAHOFN, TAHTFPN_G, TAHTFPN_O, TAHTCNB showing close contact with mixed stack and segregated stack alignment between TAH and OFN, TFPN and TCNB cores.

Table A3.7. SCXRD-crystal structural analysis with non-covalent interactions and dihedral angle for all the afforded co-crystals.

Single Crystals	Inter-molecular Interactions Close contact distance (Å)					Intramolecular Interactions Close contact distance (Å)			Dihedral Angle (Degree)	
	CH-F	CH-N	CH-π	D-$A_{π-π}$	D-$D_{π-π}$	F-F	CH-N	CH-π	Inter D-A	Intra In TAH
TAHOFN	2.54	-	-	3.40	6.96	2.56	2.663	2.37 2.83	88.7	50.10
TAHTFPN_G	-	2.35	2.39	3.54	7.07	-	-	2.74 2.81	80.10	40.92
TAHTFPN_O	2.60	2.58	3.37	3.65	6.77	-	-	2.55 2.72	76.91	39.30
TAHTCNB	-	2.59	3.38	3.73	7.47	-	-	2.82 2.83	76.03	46.10

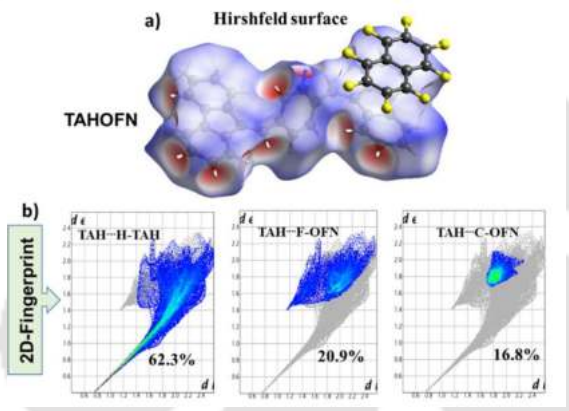

Figure A3.8. 2D Finger print for surface to atom intermolecular interactions mapped on Hirshfeld surface in TAHOFN.

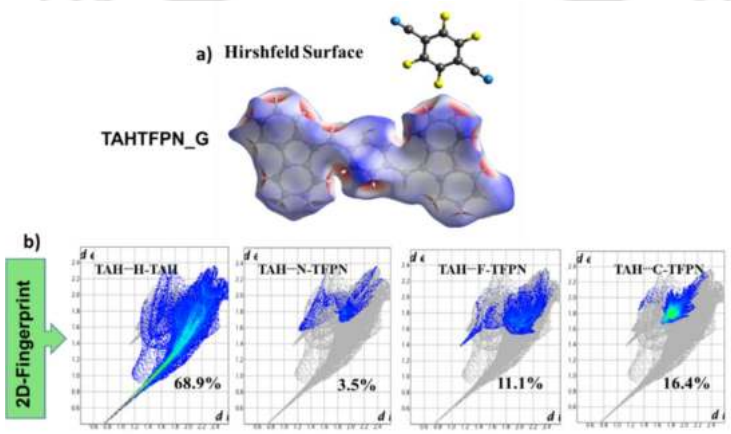

Figure A3.9. 2D Finger print for surface to atom intermolecular interactions mapped on Hirshfeld surface in TAHTFPN_G.

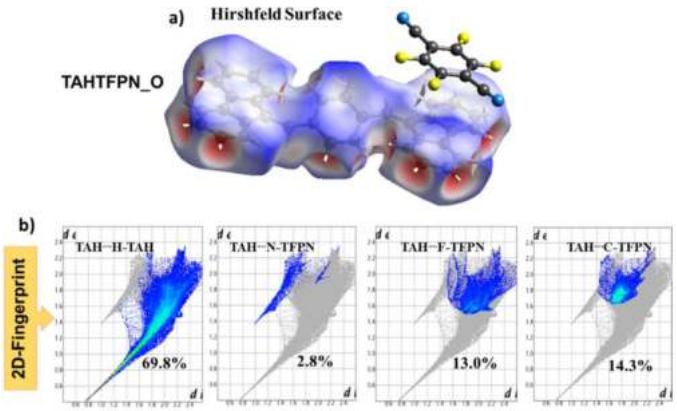

Figure A3.10. 2D Finger print for surface to atom intermolecular interactions mapped on Hirshfeld surface in TAHTFQ (top)/TAHTCQ (bottom).

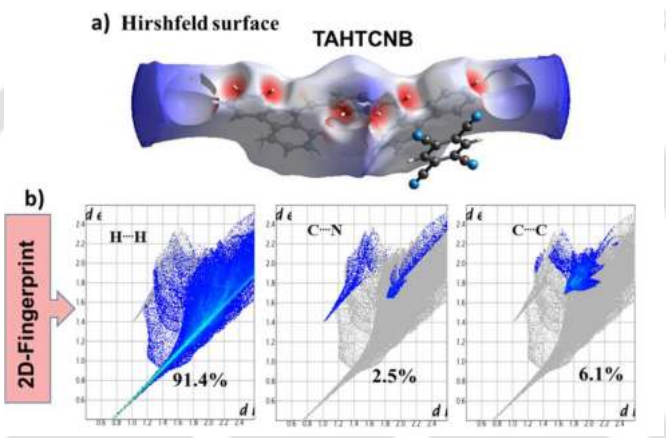

Figure A3.11. 2D Finger print for surface to atom intermolecular interactions mapped on Hirshfeld surface in TAHTFQ (top)/TAHTCQ (bottom).

Table A3.8. Calculated attachment energies of different crystal facets of TAHOFN co-crystal.

hkl	Dhkl/Å	Eatt(Total)/kcal mol^{-1}	Eatt(vdW)/kcal mol^{-1}	% Total facet area
{ 0 0 1}	15.0063956	-15.18404728	-13.11742205	54.04771092
{ 0 1 0}	9.68802304	-36.38145248	-32.67298273	15.00237552
{ 0 1 1}	7.8767392	-32.25494214	-29.52227144	9.5240967
{ 1 0 0}	6.65484113	-47.72987075	-42.12068768	5.6110776
{ 1 0 -1}	6.58258643	-45.92078761	-39.57714372	9.48065437

Table A3.9. Calculated attachment energies of different crystal facets of TAHTFPN_G co-crystal.

hkl	Dhkl/Å	Eatt(Total)/kcal mol^{-1}	Eatt(vdW)/kcal mol^{-1}	% Total facet area
{ 0 0 1}	13.47278056	-18.0184494	-15.36076162	47.0257642
{ 0 1 0}	9.89148587	-36.2122139	-31.10511264	17.28027921
{ 0 1 1}	7.59166391	-30.89557461	-27.07515935	12.45274387
{ 1 0 0}	6.97242549	-45.30159773	-36.49290066	11.83982621
{ 1 0 -1}	6.6237172	-44.90672448	-36.92410463	8.8037205

Table A3.10. Calculated attachment energies of different crystal facets of TAHTFPN_O co-crystal.

hkl	Dhkl/Å	Eatt(Total)/kcal mol^{-1}	Eatt(vdW)/kcal mol^{-1}	% Total facet area
{ 0 0 1}	17.30647421	-43.66871097	-32.54464608	36.04655729
{ 0 1 0 }	15.60484159	-33.75079862	-31.07773417	46.67710968
{ 1 0 0 }	6.76187634	-91.92433018	-75.2539478	16.69519411
{ 1 1 1}	6.12567428	-104.9041868	-82.94611497	0.58113891

Table A3.11. Calculated attachment energies of different crystal facets of TAHTCNB co-crystal.

hkl	Dhkl/Å	Eatt(Total)/kcal mol^{-1}	Eatt(vdW)/kcal mol^{-1}	% Total facet area
{ 0 1 1}	15.89762085	-33.06173254	-26.3911915	85.99938491
{ 1 0 1}	7.65609364	-109.5026191	-69.24039722	14.00061509

Table A12: A brief summary of the previous report on various optically waveguide active molecular crystals.

Name	Emission peak / nm	Fluorescent lifetime / ns	Delayed Fluorescent lifetime / µs	PLQY	Loss co-efficient	Reference
2-acetyl-6dimethylaminonaphthalene (ADN)	450	-	-	-	0.069 dB/µm	*Angew. Chem.*, 2013, *125*, 8875-8879
2-acetyl-6-methylaminonaphthalene (AMN)	540	-	-	-	0.076 dB/µm and 0.457 dB/µm along different directions	*Angew. Chem.*, 2013, *125*, 8875-8879
2,2′-((5,5′-(3,7-dicyano-2,6 bis(dihexylamino) benzo[1,2 b:4,5-b′]difuran 4,8- diyl)bis(thiophe-ne-5,2-diyl)) bis(methanylylidene))dimalononitrile (BDFTM)	676	2.02	-	16%	0.06 dB/µm	Adv. Funct. Mater. 2014, 24, 4250-4258
One-dimensional (1D) ribbon-like perylene crystals	580	-	-	5%	0.072 dB/µm	*J. Mater. Chem. C,* 2014, *2*, 9695-9700
Two-dimensional (2D) square-like perylene crystals	580	-	-	5%	0.099 and 0.101 dB/µm along different directions	J. Mater. Chem. C, 2014, 2, 9695-9700
BDTVA (a 9,10-distyrylanthracene derivative)	509	1.96	-	50%	0.000275 dB/µm	*ACS Photonics*, 2015, *2*, 313-318
The cocrystal of trans-1,2 bis(4pyridyl)ethylene and 1,2,4,5tetracyanobenzene	436	6.13	-	19%	0.26 dB/µm (isotropic 2D waveguide)	Angew. Chem. Int. Ed., 2015, 54, 6785 6789
The cocrystal of 1,2-di(4pyridyl)ethylene and 1,3,5-trifluoro2,4,6-triiodobenzene	440	1.66	-	26.1%	0.19 dB/µm	J. Am. Chem. Soc., 2015, 137, 1103811046
A solvate composed of a carbazole and cyano-substituted tetraphenylethylene derivative cocrystalized with DMF	458	2.45	-	41%	0.00804 dB/µm	*Small*, 2016, *47*, 6554-6561
A solvate composed of a carbazole and cyano-substituted tetraphenylethylene derivative cocrystalized with $CHCl_3$	481	1.93	-	65%	0.00708 dB/µm	*Small*, 2016, *47*, 6554-6561

A solvate composed of a carbazole and cyano-substituted tetraphenylethylene derivative cocrystalized with CH_2Cl_2	522	3.01	-	40%	0.00301 dB/μm	*Small*, 2016, *47*, 6554-6561
The cocrystal of 4-(1-naphthylvinyl) pyridine and 1,2,4,5tetracyanobenzene	about 550	7.5	-	6.8%	0.040-0.11 dB/μm	*Adv. Mater.,* 2016, *28*, 5954-5962
PyB (composed of two chromophores of a pyrene unit and a rhodamine B moiety)	492	6.73	-	3.52%	0.00669 dB/μm at 440 nm and 0.00351 dB/μm at 497 nm	ACS Appl. Mater. Interfaces, 2017, 9, 8910-8918
BCZ (a carbazole-containing βdiketonate derivative)	567	-	-	37%	0.033 dB/μm	Adv. Funct. Mater., 2017, 27, 1700332
2,5-dihydro-3,6-bis(octylamino) terephthalate doped with 3,6-bis(octylamino) terephthalate	572	12.7	-	56%	0.000272 dB/μm at 576 nm and 0.000196 dB/μm at 615 nm	*Adv. Mater.,* 2018, *30*, 1800814
The cocrystal of 4,4'-((1*E*,1'*E* (2,5dimethoxy-1,4-phenylene)bis(ethene 2,1-diyl))dipyridine and 1,4diiodotetrafluorobenzene	525	-	-	-	0.0145 dB/μm at 525 nm for microtubes; 0.0341 dB/μm for microrods	*J. Mater. Chem. C,* 2018, *6*, 9594-9598
7-(diethylamino)coumarin-3- aldehyde	564	8.25	-	7.5%	0.0058 dB/μm	Mater. Chem. Front., 2018, 2, 910-916
(*E*)-1-(4-(dimethylamino) phenyl)iminomethyl-2-hydroxyl-naphthalene	615	-	-	43%	0.00027 dB/μm for the straight, 0.000274 dB/μm for the bent state	Angew. Chem. Int. Ed., 2018, 57, 8448 -8452
dimethyl 2,5-bis((2hydroxyethyl)amino)terephthalate	641	6.1	-	8%	0.000351 dB/μm for the straight state; 0.000376 dB/μm for the bent state	J. Phys. Chem. Lett., 2019, 10, 1437-1442

2,5-dimethoxybenzene-1,4dicarboaldehyde	499	4.0	-	42%	0.00120 dB/μm	*ChemPlusChem*, 2019, *84*, 247-251
1,4-trimethylsilylethynyl anthracene (TMS ANT)	538		-	-	about 0.002 dB/μm	*Chem. Mater.* 2019, *31*, 1775-1783
1,2,3,4-Tetrafluoro-5,8bis(trimethylsilylethynyl)anthracene (F4 TMS ANT)	559	-	-	-	about 0.0013 dB/μm	*Chem. Mater.* 2019, *31*, 1775-1783
The 1D cocrystal of fluoranthene and 1,2,4,5-tetracyanobenzene	about 550	80	-	74%	0.0181 dB/μm along [100] direction	Nat. Commun., 2019, 10, 761
The 2D cocrystal of fluoranthene and 1,2,4,5-tetracyanobenzene	about 550	80	-	74%	0.0084, 0.0139 and 0.0147 dB/μm along [001], [012] direction, respectively	Nat. Commun., 2019, 10, 761
1,4-bis((*E*)-4-(1,2,2triphenylvinyl)styryl)-2,5dimethoxybenzene (TPDSB)	526	1.70	-	85.6%	0.012-0.020 dB/μm	J. Phys. Chem. Lett., 2019, 10, 679-684
The 1D cocrystal of 9-anthracene carboxylic acid and 1,2,4,5tetracyanobenzene (9AC-TCNB)	583 and 652	τ_1 = 2.38 ns (40.63%) and τ_2 = 6.71 ns (59.31%) at 583 nm; τ = 5.87 ns (96.69%) at 652 nm	-	-	0.006706 dB/μm at 583 nm; 0.006602 dB/μm at 652 nm	Adv. Optical Mater., 2020, 8, 1901280
The 2D cocrystal of 9-anthracene carboxylic acid and 1,2,4,5tetracyanobenzene (9AC-TCNB)	650	-	-	-	0.0068306 dB/μm at 650 nm	Adv. Optical Mater., 2020, 8, 1901280
One of polymorphic 2D cocrystals composed of 4-(4-dimethylaminostyryl)quinolone and 1,4-diiodotetrafluorobenzene (*M*DFCs)	515	0.24	-	12%	0.0140 dB/μm, 0.0520 dB/μm and 0.0540 dB/μm along different directions	Angew. Chem. Int. Ed., 2020, 59, 44564463.
One of polymorphic 2D cocrystals composed of 4-(4-dimethylaminostyryl)quinolone and 1,4-diiodotetrafluorobenzene (*T*DFCs)	565	1.91	-	11%	0.104 dB/μm, 0.115 dB/μm and 0.108 dB/μm	Angew. Chem. Int. Ed., 2020, 59, 44564463.

Tri-phenylene (TP)-2,3,5,6-tetrafluoro-7,7,8,8-tetracyanoquinodimethane (F4TCNQ) CT organic complex	770	11.3 ns	-	5.4%	0.060 dB μm^{-1}	*Adv.Mater.* 2022, *34*, 2107169.
Trans-1,2-Diphenylethylene and 1,2,4,5-tetracyanobenzene	580	31.5 ns	τ_1 = 0.69 ms and τ_2 = 2.94 ms	13.77%	-	Angew. Chem. Int. Ed., 2019, 58, 11311 –11316.
Calix[3]acridan (C[3]A) and 1,2-dicyanobenzene (DCB)	500	152 ns	5.2 µs	70%	-	Angew. Chem. Int. Ed., 2022, 61, e202117872.
Through-space cocrystals of twisted aromatic hydrocarbon (TAH) donor and octafluoronaphthalene (OFN), tetrafluoropterepthanitrile (TFPN) and 1,2,4,5-tetracyanobenzene (TCNB) denoted as TAHOFN, TAHTFPN_G, TAHTFPN_O and TAHTCNB	540 545 560 590	0.50 ns 0.87 ns 1.06 ns 38.81 ns	4.0 µs	31.6% 74.4% 77.5% 64.4%	OWG loss coefficient: 0.44 dB/µm, 0.0742 dB/µm 0.0837 dB/µm	Present work

CHAPTER 4

Hot-Exciton Harvesting *via* Through-Space Single-Molecule Based White-Light Emission and Optical Waveguides

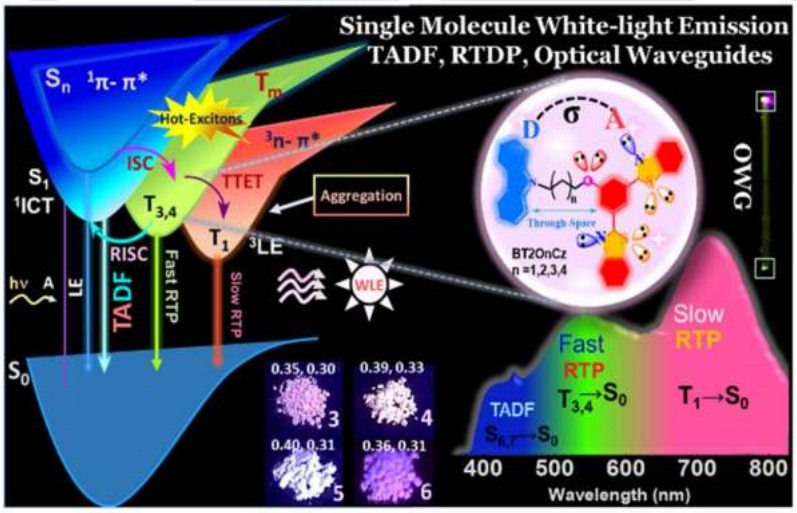

Barman, D., Annadhasan, M., Chandrasekar, R., Iyer, P. K. *Chem. Sci*., **2022**, *13*, 9004-9015.

DOI: https://doi.org/10.1039/D2SC02172B

Abstract

Through-space donor-alkyl bridge-acceptor (D-σ-A) luminogens are developed as new organic single-molecule white light emitters (OSMWLEs) involving multiple higher lying singlet (S_n) and triplet (T_m) states (hot-excitons). Experimental and theoretical results confirm the origin of white light emission due to the co-existence of prompt fluorescence from locally excited state, thermally activated delayed fluorescence (TADF), and fast/slow dual phosphorescence color mixing simultaneously. Notably, the fast phosphorescence is inherited by trace amounts of isomeric impurities from commercial carbazole, while H-/J-aggregation results in slow phosphorescence. Single crystal X-ray structures, and the alkyl chain length induced supramolecular self-assembly greatly influence the solid-state optical properties. Remarkably, the 1D-microrod crystals of OSMWLEs demonstrate the first examples of triplet harvesting waveguides by self-guiding the generated phosphorescence through light propagation along its longitudinal axis. This work thus highlights an uncommon design strategy to achieve multi-functional OSMWLEs with in-depth mechanistic insights and optical waveguiding applications endowing them as potentially new class of white emissive materials.

4.1 Introduction

Organic single-molecule white light emitters (OSMWLEs)[1] have stimulated enormous interest owing to their potential applications in next-generation white light-emitting diodes (WLEDs),[2] sensing,[3] anti-counterfeiting,[4] biological imaging[5,6] and optical waveguides (OWGs).[7] The unique photophysical processes governing broad visible spectrum emission of OSMWLEs are fundamentally very intriguing. Majority of WLEs reported, thus far, rely on harnessing singlet excitons either in a single molecule and/or polymers[8] or multicomponent fluorescent blends.[9] These systems typically include monomer/excimer complex,[10] inter/intramolecular charge transfer (ICT),[11] Förster resonance energy transfer (FRET),[12] excited-state intramolecular proton transfer (ESIPT),[13] and dual (prompt/delayed) fluorescence (DFL).[14] In contrast, weakly susceptible triplet excitons in organic molecules adopt the non-radiative pathways, and dissipate as heat energy instead of light due to the poor spin-orbit coupling (SOC), thereby exhibiting dim phosphorescence.[15] Besides, triplet excitons show high quenching propensities in the presence of moisture and molecular oxygen at room temperature (RT), while, phosphorescence from organics generally exists only at cryogenic temperature.[16] These limitations impede the effective utilization of both singlet and triplet energy, especially to generate white light in purely organic compounds. Essentially, phosphorescent OSMWLE have immense prospects of triplet harvesting features at ambient condition. They offer alternatives to conventional emitters due to the favourable no phase segregation, no colour aging, uniform film-forming ability and simple device fabrication.[17,18] However, due to ineffective molecular design and lack of fundamental insights on the excited-state dynamic (ESD) process, the origin of white light emission (WLE) is often overlooked.

Recently, multiple radiative decays from both singlet and triplet excitons generating WLE were presented in organic molecules by assimilating typical FL or thermally activated delayed FL (TADF) and room temperature phosphorescence (RTP) or two distinct dual-phosphorescence (DP).[19-22] Strategically, an engineered TADF emitter possesses well-separated highest occupied molecular orbital (HOMO), and lowest unoccupied molecular orbital (LUMO), comprising small singlet-triplet splitting (ΔE_{ST}), that can harvest triplet excitons through efficient reverse intersystem crossing (RISC) process.[23] After the first report of seminal TADF emitter 4CZIPN,[24] tremendous efforts have been devoted to explore new materials based on triazines, oxadiazoles, cyanobenzenes, sulfones and benzothiazole cores.[25] These molecules with a common electron donor-acceptor (D-A)

dyad/triad structures exhibit narrow ΔE_{ST} and robust TADF.[26] On the other hand, long-lived RTP from organic luminogens were realized by populating triplet excitons on introducing heavy atom effect, El-Sayed's rule, and charge transfer (CT) state into bipolar molecular skeleton involving carbazole, carbonyl, borate, sulfone, and phenothiazine respectively.[27-29] Subsequently, crystal packing, polymer matrices and rigid host, enhance the SOC to promote intersystem crossing (ISC) process by suppressing the non-radiative dissipation.[30] Nonetheless, recent breakthroughs in ultra-long organic phosphorescence due to trace amounts of isomeric impurity (in carbazole or boronic acid-based systems) promoted the realization of stable phosphorescence emission at ambient conditions without any protection from moisture or molecular oxygen.[31,32] Although, few triplet harvesting mechanistic processes are known, through-space triplet-triplet energy transfer (TTET) remains a key photophysical process, which defines the exchange of both spin and energy between a pair of molecules or intramolecular fragments located at a short distance of <10 Å and releases free energy (exothermic) via Dexter-type channel.[33] The anisotropic one dimensional (1D) molecular crystals could harvest excitons and display robust light propagation on account of a long-range ordered molecular π-π stacking, free grain boundary, and efficient light guiding propensity.[34] Such type of high refractive index and defect free crystal perform as excellent optical waveguides (OWGs) suitable for next-generation photonic and communication technologies.[35,36]

In order to address the challenge of constructing multifunctional OSMWLE, few promising strategies that rely on simple material design with inherent triplet harvesting mechanism have been reported[37-41] (Figure 4.1). These reports confirm that nearly all the WLEs, rely on conventional knowledge of crystallization and external/internal heavy atom effect in a directly connected D-A system. Despite, the progress in designing WLEs, the potential solid state application at RT using a combination of multiple excited states in purely organic molecules are unexplored. Thus far, optical crystals with hot-exciton harvesting OSMWLE having DFL and DP demonstrating efficient OWG attribute has not been reported to the best of our knowledge. In this work, four through-space charge transfer (TSCT) OSMWLE materials have been designed and synthesized, denoted as BT2OxCz (x=3, 4, 5 and 6), which contain acceptor 2,2'-(1,3-phenylene)bis (benzothiazole) [BT2] and donor carbazole [Cz], connected via a series of odd/even alkyl chain. The synthesized BT2OxCz molecular crystals exhibit highly sought after DFL and DP at RT. Experimental and theoretical results

attribute the origin of WLE to substantially high lying manifold singlet and triplet excited states. A key conceptual insight of the emission process in solid state is prompt fluorescence (locally excited emission) and TADF, accompanied by DP at RT. Further, the enhancement of SOC via fine adjustment of moderate ΔE_{ST} (~0.50 - 0.55 eV) between S_1 and T_1 with collateral narrow ΔE_{ST} (~0.02 - 0.12 eV) between S_1 and T_3/T_4 facilitates efficient ISC and RISC to upsurge the TADF and RTP simultaneously. By varying the chain length between D and A, singlet and triplet states could be manipulated to realize a broadband visible range emission in powder, polymethyl methacrylate (PMMA) doped thin-films and in single molecular crystals. Notably, sterically constrained shorter chain BT2OxCZ (x=3, 4, 5) molecules display TADF and RTP. In contrast, the longest chain analogue BT2O6Cz exhibits relatively intense RTP, owing to dimer formation and subsequent inter-TSCT. Moreover, sterically strained 'J-aggregation' and geometrically relaxed 'H-aggregation' in the crystal lattice enable harvesting of singlet and triplet-excitons, simultaneously. Remarkably, 1D crystals of BT2O3Cz and BT2O6Cz efficiently guide triplet-harvesting light along their long axes with low optical loss coefficient (α'= 0.3260 dB/μm, and 0.2158 dB/μm respectively).

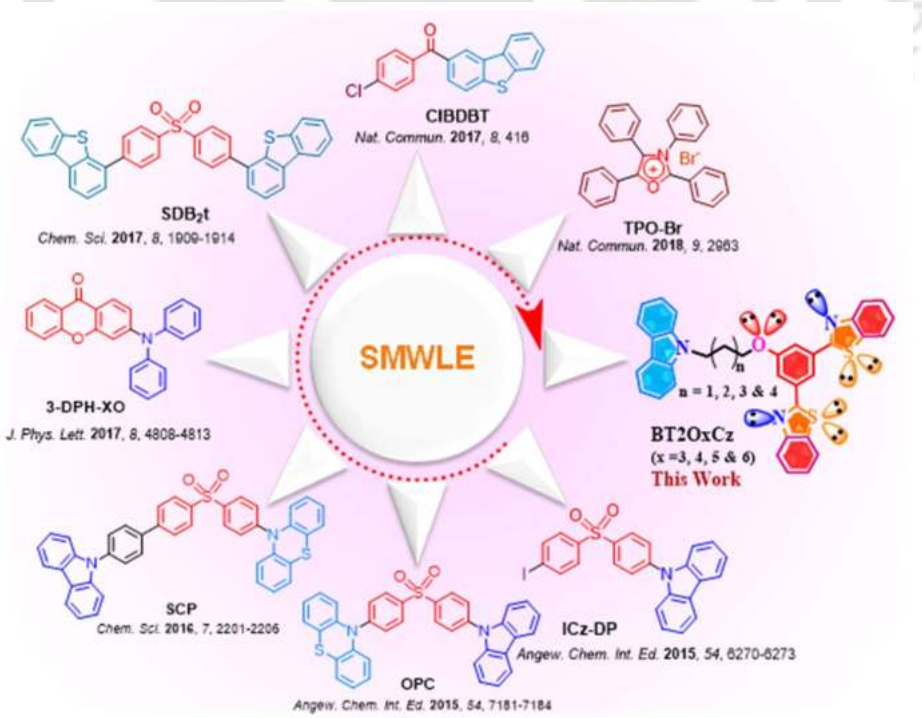

Figure 4.1. State-of-the-art reported organic single molecule white light emitters (OSMWLEs), in this work, the design of through-space donor-σ-acceptor [BT2OxCz (x= 3, 4, 5 & 6)] derivatives of various alkoxy group connected between 9H-carbazol and di substituted phenyl benzothiazole moiety.

4.2. Experimental Section

4.2.1. Materials

Benzothiazole, 1,1'-(5-hydroxy-1,3-phenylene)bis(ethan-1-one), carbazole, 1,3-dibromopropane, 1,4-dibromobutane, 1,5-dibromopentane, 1,6-dibromohexane, sodium hydride, potassium hydroxide, potassium iodide, potassium carbonate and glycerol were purchased from Sigma-Aldrich and used as such without further purification**.** All the solvents used like dimethylsuphoxide, acetone, chloroform and hexane were purified prior to use according to the standard protocol and stored in molecular sieves.

4.2.2. Synthesis and Characterizations

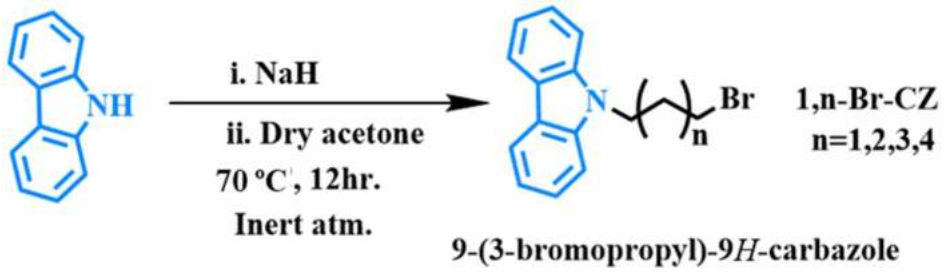

Scheme 4.1. Synthesis of 1, n-Br-Cz [9-(n-bromalkyl,)-9H-Carbazole] (1,n-BrCz).

Carbazole (1g, 5.98 mmol) was dissolved in dry acetone (about 20 ml) in a 100 ml RB then 287 mg of NaH (11.96 mmol) was added to the solution. With the evolution of H_2 gas, the colorless solution became turbid. After 45 minutes, 1.2 equivalent of dibromo alkane (7.17 mmol) (1, 4- dibromo butane; 1, 5- dibromo pentane; 1, 6- dibromo hexane) was added to the mixture of solution and refluxed at 70 ºC for 12 hours. The turbit solution was turn to clear honey color. Then stopped the reaction and TLC checked, a new intense spot was observed. After that, the solvent was removed with the help of vacuum and the obtained crude solid was worked up with DCM and distilled H_2O followed by brine solution for three times until the base was completely removed from the organic portion and the organic layer was dried over anhydrous Na_2SO_4. The mixture was purified by column chromatography by using silica gel (100-200 mesh size) with hexane/dichloromethane (19:1 v/v) as eluent, colorless solid was obtained. The colorless solids were further recrystallized with 20% DCM: hexane mixture and calculate yield of 90% for all the 1,n-Cz-Br (n= 3,4,5,6) compounds. Further, characterize all the derivatives using ^{1}H, ^{13}C and HRMS respectively

4.2.2.1. 1, 3-Br-Cz [9-(3-bromopropyl)-9H-Carbazole] : ^{1}H NMR (600 MHz, $CDCl_3$), δ (ppm): δ 8.15 (d, J = 7.8 Hz, 1H), 7.52 (dd, J = 4.0, 1.4 Hz, 2H), 7.29 (ddd, J = 7.9, 5.3, 2.7 Hz, 1H), 4.51 (t, J = 6.6 Hz, 1H), 3.40 (t, J = 6.2 Hz, 1H), 2.47 – 2.43 (m, 1H). ^{13}C NMR (151 MHz, CDCl3) δ 140.37 (s), 125.84 (s), 123.01 (s), 120.43 (s), 119.16 (s), 108.61 (s), 77.26 (s), 77.05 (s), 76.84 (s), 40.94 (s), 31.98 (s), 30.81 (s).

HRMS (ESI) peaks of m/z value of (M & M+2) was calculated 288.0388, 290.0367 and observed 288.0389, 290.0373.

4.2.2.2. 1, 4-Br-Cz [9-(4-bromobutyl)-9H-Carbazole] : ^{1}H NMR (600 MHz, $CDCl_3$), δ (ppm): δ 8.14 (d, J = 7.7 Hz, 1H), 7.50 (t, J = 7.6 Hz, 1H), 7.43 (d, J = 8.2 Hz, 1H), 7.27 (t, J = 7.3 Hz, 1H), 4.38 (t, J = 7.0 Hz, 1H), 3.41 (t, J = 6.5 Hz, 1H), 2.08 (d, J = 7.7 Hz, 1H), 1.95 (d, J = 8.3 Hz, 1H). ^{13}C NMR (151 MHz, $CDCl_3$) δ 140.28 (s), 125.74 (s), 122.89 (s), 120.45 (s), 118.96 (s), 108.54 (s), 77.26 (s), 77.05 (s), 76.84 (s), 42.18 (s), 33.21 (s), 30.25 (s), 27.68 (s).

HRMS (ESI) peaks of m/z value of (M & M+2) was calculated 302.0544, 304.0524 and observed 304.0561, 304.0545.

4.2.2.3. 1, 5-Br-Cz [9-(5-bromopentyl)-9H-Carbazole] : ^{1}H NMR (400 MHz, $CDCl_3$), δ (ppm): δ 7.99 (d, J = 7.8 Hz, 1H), 7.35 (t, J = 7.6 Hz, 1H), 7.27 (d, J = 8.2 Hz, 1H), 7.12 (t, J = 7.4 Hz, 1H), 4.18 (t, J = 7.1 Hz, 1H), 3.21 (t, J = 6.7 Hz, 1H), 1.75 (ddd, J = 11.3, 7.6, 4.7 Hz, 2H), 1.41 (t, J = 3.7 Hz, 1H). ^{13}C NMR (101 MHz, $CDCl_3$) δ 140.22 (s), 125.56 (s), 122.74 (s), 120.29 (s), 118.74 (s), 108.45 (s), 77.26 (s), 76.94 (s), 76.63 (s), 42.67 (s), 33.23 (s), 32.35 (s), 28.06 (s), 25.78 (s)

HRMS (ESI) peaks of m/z value of (M & M+2) was calculated 316.0701, 318.0680 and observed 316.0707, 318.0690.

4.2.2.4. 1, 6-Br-Cz [9-(6-bromohexyl)-9H-Carbazole] : ^{1}H NMR (600 MHz, $CDCl_3$), δ (ppm): δ 8.14 (d, J = 7.7 Hz, 1H), 7.50 (t, J = 7.2 Hz, 1H), 7.43 (d, J = 8.2 Hz, 1H), 7.27 (t, J = 7.4 Hz, 1H), 4.33 (t, J = 7.1 Hz, 1H), 3.38 (t, J = 6.7 Hz, 1H), 1.94 – 1.90 (m, 1H), 1.85 – 1.81 (m, 1H), 1.51 – 1.47 (m, 1H), 1.44 – 1.40 (m, 1H). ^{13}C NMR (151 MHz, $CDCl_3$) δ 140.36 (s), 125.62 (s), 122.80 (s), 120.38 (s), 118.77 (s), 108.60 (s), 77.26 (s), 77.05 (s), 76.84 (s), 42.83 (s), 33.80 (s), 32.55 (s), 28.83 (s), 27.92 (s), 26.46 (s)

HRMS (ESI) peaks of m/z value of (M & M+2) was calculated 330.0857, 330.0837 and observed 332.0864, 332.0846.

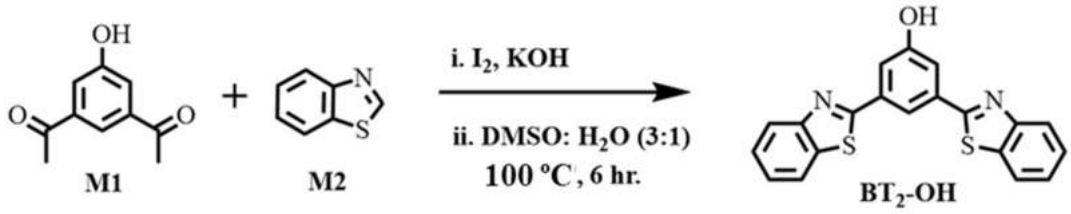

Scheme 4.2. Synthesis of 3,5-bis(benzothiazol-2-yl)phenol (BT2OH) via in-situ cross coupling:\.

1,1'-(5-hydroxy-1,3-phenylene)bis(ethan-1-one) (2g, 11.2 mmol), benzothiazole (3g, 22 mmol), iodine (5.6g, 22 mmol) and potassium hydroxide (1.23g, 22 mmol) were taken in DMSO : water (3:1) at room temperature. The mixture was heated up to 100 °C and the completion of the reaction was monitored using analytical TLC technique. After 12 h the reaction mixture was cooled to at room temperature. Then the crude mixture was extracted with ethyl acetate and washed with aqueous sodium thiosulfate solution for several times. Then it was dried over anhydrous Na_2SO_4 and concentrated under reduced pressure. Then the obtained blue solid compound was finally purified recrystallization in methanol and proceed for next step.

Scheme 4.3. 2,2'-(5-(3-(9H-carbazol-9-yl)alkoxy)-1,3phenylene)bis(benzothiazole) [BT2OxCz, x=3,4,5,6].

For this reaction the reagent K_2CO_3 was dried in an oven for overnight in about 200 °C to remove the trace of moistures. In an inert atmosphere (Ag-gas), taking 0.56 mole of BT_2-OH and 154.8 mg of K_2CO_3 in a 100 ml RB followed by the addition of about 15 ml of NMP solvent. The mixture was stirred well on the magnetic stirrer to dissolve the K_2CO_3 at 70 °C After 45 minutes of standing of the solution, adding 1 equiv. of 1, n-Br-Cz (1, 4-Br-Cz = 198.7 mg; 1, 5-Br-Cz = 210 mg 1, 6-Br-Cz = 217.9 mg) to the reaction mixture with a pinch amount of KI. The reaction was refluxed for 12 hours at 70 °C. In these

reactions, the solution for the first time is deep blue color then after 30-45 minutes later, the color of the solution was changing gradually from deep blue to violet to green color. Again, the solution was retained its early color after 12 hours. TLC was checked and the reaction was stopped (TLC solvent was 1:1 v/v DCM: Hexane). The solvent was removed with the help of vacuum RV and the reaction mixture was worked up with DCM and distilled H_2O followed by Brine (NaCl) for several times until the base was removed from the organic portion and the organic layer was dried with anhydrous Na_2SO_4. The residue was purified by silica gel (100-200 mesh) with coulomb chromatography using solvent (Hexane/dichloromethane 19:1 v/v; 9:1 v/v; 5.6:1 v/v with the respect of polarity of the products) as the eluent to obtain a desired product (white color in amorphous state).

4.2.2.5. 2,2'-(5-(3-(9H-carbazol-9-yl)propoxy)-1,3-phenylene)bis(benzothiazole) [BT2O3Cz]:

^{1}H NMR (600 MHz, $CDCl_3$), δ (ppm): δ 8.34 (s, 1H), 8.11 (dd, J = 7.7, 4.6 Hz, 4H), 7.95 (d, J = 7.9 Hz, 2H), 7.78 (d, J = 1.2 Hz, 2H), 7.53 (t, J = 7.2 Hz, 2H), 7.49 (d, J = 8.2 Hz, 2H), 7.43 (t, J = 7.6 Hz, 4H), 7.22 (t, J = 7.4 Hz, 2H), 4.64 (t, J = 6.6 Hz, 2H), 4.16 (t, J = 5.5 Hz, 2H), 2.47 – 2.43 (m, 2H). ^{13}C NMR (151 MHz, CDCl3) δ 166.82 (s), 154.00 (s), 140.44 (s), 135.75 (s), 135.22 (s), 126.55 (s), 125.85 (s), 125.58 (s), 123.47 (s), 122.96 (s), 121.76 (s), 120.42 (s), 119.54 (s), 119.06 (s), 115.64 (s), 108.61 (s), 77.26 (s), 77.05 (s), 76.84 (s), 65.37 (s), 39.46 (s), 28.68 (s).

HRMS (ESI) peaks of m/z value was calculated 568.1517 and observed 568.1485.

4.2.2.6. 2,2'-(5-(4-(9H-carbazol-9-yl)butoxy)-1,3-phenylene)bis(benzothiazole) [BT2O4Cz]:

^{1}H NMR (600 MHz, $CDCl_3$), δ (ppm): δ 8.34 (s, 1H), 8.14 – 8.12 (m, 4H), 7.96 (d, J = 7.9 Hz, 2H), 7.76 (d, J = 1.2 Hz, 2H), 7.54 (s, 2H), 7.50 (dd, J = 5.6, 4.7 Hz, 4H), 7.44 (s, 2H), 7.27 (d, J = 10.7 Hz, 2H), 4.48 (s, 2H), 4.19 (s, 2H), 2.19 (s, 2H), 1.96 (dd, J = 13.7, 6.8 Hz, 2H). ^{13}C NMR (151 MHz, $CDCl_3$) δ 166.88 (s), 159.78 (s), 154.01 (s), 140.40 (s), 135.70 (s), 135.23 (s), 126.52 (s), 125.75 (s), 125.54 (s), 123.45 (s), 122.93 (s), 121.76 (s), 120.45 (s), 119.34 (s), 118.91 (s), 115.58 (s), 108.67 (s), 77.26 (s), 77.05 (s), 76.84 (s), 68.15 (s), 42.77 (s), 29.74 (s), 27.04 (s).

HRMS (ESI) peaks of m/z value was calculated 582.1674 and observed 582.1686.

4.2.2.7. 2,2'-(5-((5-(9H-carbazol-9-yl)pentyl)oxy)-1,3-phenylene)bis(benzothiazole) [BT2O5Cz]: ^{1}H NMR (600 MHz, $CDCl_3$), δ (ppm): δ 8.35 (s, 1H), 8.14 (dd, J = 7.8, 4.0 Hz, 4H), 7.97 (d, J = 7.8 Hz, 2H), 7.77 (d, J = 1.2 Hz, 2H), 7.56 (t, J = 7.6 Hz, 2H), 7.53 – 7.48 (m, 4H), 7.45 (d, J = 7.2 Hz, 2H), 7.29 (s, 2H), 4.41 (t, J = 7.1 Hz, 2H), 4.17 (t, J =

6.2 Hz, 2H), 2.04 (s, 2H), 1.93 (s, 2H), 1.67 (s, 2H).^{13}C NMR (151 MHz, $CDCl_3$) δ 166.96 (s), 159.89 (s), 154.00 (s), 140.40 (s), 135.64 (s), 135.21 (s), 126.52 (s), 125.69 (s), 125.54 (s), 123.43 (s), 122.86 (s), 121.76 (s), 120.41 (s), 119.22 (s), 118.82 (s), 115.60 (s), 108.66 (s), 77.26 (s), 77.05 (s), 76.84 (s), 68.23 (s), 42.96 (s), 29.11 (s), 28.85 (s), 23.94 (s). HRMS (ESI) peaks of m/z value for was calculated 596.1830 and observed 596.1842.

4.2.2.8. 2,2'-(5-((6-(9H-carbazol-9-yl)hexyl)oxy)-1,3-phenylene)bis(benzothiazole) [BT2O6Cz]: ^{1}H NMR (600 MHz, $CDCl_3$), δ (ppm): δ 8.33 (s, 1H), 8.11 (t, J = 7.5 Hz, 4H), 7.94 (d, J = 7.8 Hz, 2H), 7.76 (s, 2H), 7.53 (t, J = 7.6 Hz, 2H), 7.47 (dd, J = 16.9, 9.8 Hz, 4H), 7.42 (d, J = 8.0 Hz, 2H), 7.23 (t, J = 7.3 Hz, 2H), 4.36 (t, J = 7.2 Hz, 2H), 4.14 (t, J = 6.3 Hz, 2H), 1.98 – 1.94 (m, 2H), 1.86 – 1.82 (m, 2H), 1.59 – 1.56 (m, 2H), 1.52 – 1.48 (m, 2H). ^{13}C NMR (151 MHz, $CDCl_3$) δ 166.99 (s), 159.96 (s), 154.02 (s), 140.42 (s), 135.64 (s), 135.22 (s), 126.51 (s), 125.59 (d, J = 18.1 Hz), 123.43 (s), 122.84 (s), 121.75 (s), 120.39 (s), 119.17 (s), 118.77 (s), 115.62 (s), 108.66 (s), 77.26 (s), 77.05 (s), 76.84 (s), 68.36 (s), 42.98 (s), 29.13 (s), 28.99 (s), 27.10 (s), 25.96 (s).

HRMS (ESI) peaks of m/z was calculated 610.1987 and observed 610.1993.

4.2.3. Measurements and Methods

4.2.3.1. Structural Characterization

All the reactions were carried out in oven dried (~100 °C) round bottom flasks under argon atmosphere unless otherwise mentioned. The ^{1}H and ^{13}C NMR spectra were recorded by using deuterated solvents ($CDCl_3$) in Bruker 600 MHz NMR spectrometer. Chemical shifts (δ) are expressed relative to the resonances of the residual non-deuterated solvent for ^{1}H [$CDCl_3$: ^{1}H (δ) = 7.26 ppm], and ^{13}C [$CDCl_3$:^{13}C(δ) = 77.0 ppm]. Absolute values of the coupling constants are given in Hertz (Hz), regardless of their sign. Multiplicities are abbreviated as singlet (s), doublet (d), doublet of doublets (dd), triplet (t), multiplet (m), and broad (br).

4.2.3.2. Compounds Purification

High-performance liquid chromatogram (HPLC) spectra were recorded from Shimadzu UFLC system. Before running, each sample was purified through 0.22 µm filter to remove any aggregates. The flow rate was fixed at 1.0 mL/min, the injection volume was 20 µL and each sample was run for 20 min. The absorption wavelength used was set at 300 nm. 100 % percent of acetonitrile was used as the running buffer.

4.2.3.3. Optical Characterization

The fluorescence and absorption spectra were measured with PerkinElmer, Model Lambda-25 spectrometer and Horiba-Fluoromax4 with Varian Cary Eclipse spectrometer

respectively. The absolute quantum yields were measured by using the Horiba Fluoromax (Jobin Yvon equipped with Integrating sphere) absolute quantum yield spectrometer. The time-resolved fluorescence lifetimes were investigated with the time-resolved fluorescence studies were performed using an Edinburgh Life Spec II instrument. Temperature-dependent (77K-300K) PL and lifetime measurements were carried out using a liquid nitrogen-cooled optical cryostat (Optistat, Oxford Instruments) attached to an Edinburgh FSP-920 instrument.

4.2.3.4. Morphology Visualization

The morphology and crystallinity of the synthesized BT2OxCz (x=3, 4, 5, & 6) were examined by scanning electron microscopy (FESEM) (Zeiss, Model: Sigma-300). All water drop casted samples were gold-sputtered under vacuum to achieve a thin layer of conductive gold coating on the micro/nano crystalline samples. Atomic force microscopy (AFM) analysis were performed drop-casted sample over silicon substrate, in AFM, Asylum Cypher, Oxford Instruments. Transmission electron microscopy (TEM, JEOL JEM-2100F). Dynamic light scattering (DLS) measurements were taken with a Zetasizer Nano ZS90 (model no ZEN3690) instrument. All of the FTIR data were collected using a PerkinElmer instrument. All digital pictures were taken with a canon power shot SX420 IS digital camera.

4.2.3.5. Single crystal X-ray Diffraction (XRD) data

Single-crystal structures of BT2O3Cz, and BT2O6Cz were obtained on X-ray diffractometer on Agilent. The single crystal x-ray diffractometer (SC-XRD) is equipped with Mo X-ray source (Mova), CCD detector (Eos), Oxford cryo system (80-500K) and crystal AlisPRO software and Autochem softwares. SCXRD data were collected at 293 K. All the crystal structures were solved by SHELXT with direct methods. All of the non-hydrogen atoms were located by SHELXT directly and refined anisotropically by SHELXL2018 with least squares methods. The revised data have been deposited with the CCDC (accession codes CCDC 1969742, and 1969743). The stacking structure and intermolecular interactions of the BT2O3Cz and BT2O6Cz were analyzed via Murcury and Materials Studio software. The powder X-ray diffraction measurements of the powder and thin films were performed using a Rigaku SmartLab X-ray diffractometer where copper Kα (λ = 1.54 Å) was used as the source with 9 kW power. The XRD patterns for the 2θ range of 5°−50° were measured at the scan rate 0.3°/s.

4.2.3.6. Transient Absorption (TA) and Laser-Induced Fluorescence (LIF) Measurements

TA and LIF were performed in an LP980-KS spectrometer configured with a visible PMT detector for kinetic data and an ICCD detector for spectral data acquisition. These detectors were mounted on different ports of the LP980 spectrograph, allowing rapid switching between spectral and kinetic detection. Measurements at 77 K were performed in an Oxford Instruments OptistatDN cryostat placed in the sample chamber of the LP980. The cryostat temperature is controlled from the LP980 operating software, L900. During measurements at room temperature, the slides were either mounted inside the cryostat or in a film sample holder (L-F04).Pump pulses at 355 nm were produced by a Litron Nano S 130-10 laser. The pump pulse widthwas ~5 ns and its energy was ~20 mJ/pulse. The white-light probe beam was generated by the Xe lamp in the LP980, operating in pulsed mode and producing pulses with a duration of 6 ms. Pumponly and probe-only backgrounds were subtracted automatically by the L900 software when necessary. Some Laser-Induced Fluorescence (LIF) measurements were performed with a 370 nm longpass filter before the emission monochromator to eliminate the interference from scattered pump light on the spectra.

4.2.3.7. General Characterization

The transition temperatures and associated enthalpy changes were determined by differential scanning calorimeter (Q20 DSC) under nitrogen atmosphere Thermogravimetric analyses (TGA) were carried out with a Mettler-Toledo TGA/SDTA 851e thermogravimetric analyzer in a temperature range of 30-600 °C under nitrogen atmosphere at 5 °C min^{-1} heating rate.

4.2.3.8. Computational Studies

Combined with the SXRD crystal data, the Hirshfeld surfaces, electrostatic potential, and molecular orbital were simulated by CrystalExplorer 3.1.51. The Hirshfeld surfaces and the electrostatic potential (ESP) were mapped with dnorm using STO-3G basis set at the Hartree-Fock theory. Vertical and transitions energies with the highest occupied molecular orbital (HOMO), lowest unoccupied molecular orbital (LUMO), of single-component crystals were calculated by density functional theory (DFT). All DFT and TDDFT calculations in this study were performed by employing the combination of Becke3-Lee-Yang-Parr (B3LYP) hybrid functional and 6-31G(d,p) basis set using the Gaussian 16 package. The calculated structures, energy level very much close to experimental results.

The growth morphologies of BT2O3Cz and BT2O6Cz crystals were calculated by using the Materials Studio software, based on the attachment energy theory. The molecular

structure was first optimized on the basis of the experimental crystal structure. The geometric and energy calculations were performed using the Forcite and Morphology modules.

4.3. Results and Discussion

4.3.1. Materials Design Principles

By considering important aspects of OSMWLEs, a through-space rational design strategy was developed to achieve solid-state WLE at RT. The conceived TADF and DP luminogens (BT2OxCz, x=3, 4, 5 and 6) bear a donor Cz and an acceptor BT2 connected via short (three/four membered) and long (five/six membered) alkyl chains viz. BT2O3Cz, BT2O4Cz, BT2O5Cz, and BT2O6Cz. The key requisites to achieve white-emission in organic molecules depends on the following quantum-mechanical aspects and few stringent requirements, which include: 1) Singlet excitons equilibration with parent and other accessible excited states (e.g., $\geq S_1$), favouring RISC from $\geq T_2$ via a small ΔE_{ST} producing TADF.[42] 2) Utilization of triplet excitons either from the distinct radiative decay of the T_1 states (populated via TTET/IC, from $\geq T_2$) or directly from $\geq T_3$ by evolving with $\geq S_1$ via a mixed ISC process. 3) Realization of stable phosphorescence from a small amount of impurity that could protect against triplet exciton quenching and result in faster decay from $\geq T_3$.[31]

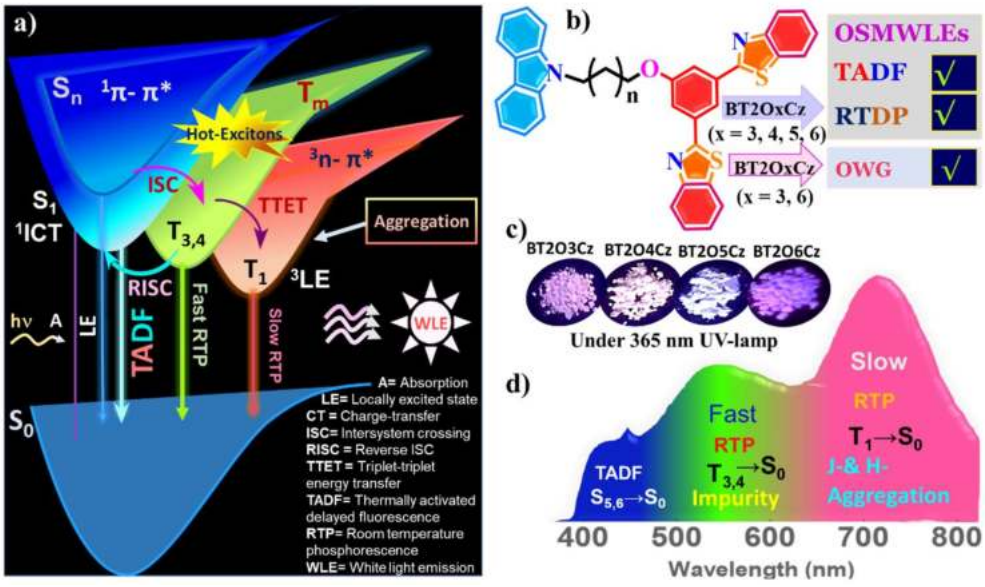

Figure 4.2. (a) Proposed Jablonski diagram illustrating OSMWLE emission mechanism. (b) Chemical structures of OSMWLE BT2OxCz (x=3, 4, 5 and 6). (c) Pristine powder images of pf BT2OxCz captured under 365 nm UV lamp. (d) Illustration of excitons distribution in WLE emission spectra.

4) Faster decay of $\geq T_3$ to counterbalance the smaller extents with T_1 to facilitate radiative decay from $\geq T_3$ and T_1, producing DP. 5) By creating the excited state charge-separation (ESCS) involving the hot-excitons in highly-flexible molecular systems and controlling the complex excited-state dynamics, solid state white light emission could be generated. Collectively, these aspects are directly influence and contribute to the higher-lying singlet and triplet energy ($\geq S_4/S_7$ and $\geq T_8/T_{10}$) states allowing TADF and RTP simultaneously. The proposed Jablonski diagram illustrates the prominent photophysical processes and relative energy levels involved in fine tuning of the higher-lying excited states for WLE emission for the integrated OSMWLEs (Figure 4.2a).

4.3.2. Synthetic Strategyfor BT2OxCZ (x = 3, 4, 5 and 6) OSMWLEs

In Figure 4.2b the intriguing chemical structure of 2,2'-(5-(3-(9H-carbazol-9-yl)alkoxy)-1,3-phenylene) bis (benzothiazole) (BT2OxCz, x= 3, 4, 5 and 6) were synthesized using simple two-step substitution reaction with 3,5-bis(benzothiazol-2-yl)phenol (BT2OH) in presence of 9-(3-bromoalkyl)-9H-carbazole (1, n-CzBr, n = 3, 4, 5 and 6). 3,5-bis(benzothiazol-2-yl)phenol was synthesized via in-situ cross-coupling reaction and 9-(3-bromoalkyl)-9H-carbazole from base substitution reaction (Scheme 4.1-4.3). Detailed structural characterizations using NMR (^{1}H and ^{13}C), and HRMS are shown in Figure A4.1-A4.25. The electron-accepting (3,5-bis(benzothiazol-2-yl)phenoxy) unit bearing large number of lone pairs and the presence of two sulphur atoms makes the conjugated fragment highly electron deficient. D-A units are connected through-space via various non-conjugated alkyl chains. The electron balance in the molecule happens via through-space charge transfer (TSCT) from electron rich Cz to electron deficient BT2O unit. Moreover, by changing the length of alkyl chain (propyl, butyl, pentyl and hexyl), the resultant molecules (BT2OxCz, x=3, 4, 5 and 6) show an impressive tunable WLE at RT in solid state. From their crystal structures and computational optimized geometry it was observed that the shorter chain length containing molecules adopt large twisted conformations rather than the structurally relaxed longer chain molecules. Geometrically strained BT2O3Cz and BT2O4Cz molecules showed strong twisted intramolecular charge transfer (TICT) feature rather than more relaxed BT2O5Cz and BT2O6Cz which formed dimers. However, in solid-state all the emitters exhibited distinct TADF and RTP properties with Commission Internationale de l'éclairage (CIE) coordinate values very close to pure WLE (0.33, 0.33).

4.3.3. Solid State Optical Properties

A clear mechanistic insight on the origin of WLE was methodically studied with the crystalline powders obtained from the slow evaporation of chloroform/hexane (8:2) solution. To decipher the intrinsic solid state WLE details, PL and TRPL characteristics were investigated for all the through-space BT2OxCz emitters in their crystalline/amorphous powders. UV-visible spectra for shorter chain BT2O3Cz and BT2O4Cz exhibited absorption bands at 350 and 315 nm, respectively. In contrast, longer chain BT2O5Cz and BT2O6Cz showed comparatively broader absorption bands at 340 and 350 nm, respectively (Figure 4.3a-d**,** solid black lines). The broad absorption for longer chain emitters can be attributed to the dimeric assembly evident from the crystal packings. Further, steady state optical emission spectrum recorded (Figure 4.3a-d, blue dotted line) for all the BT2OxCzs, displayed a broad emission spectrum with multiple peaks covering 400 to 700 nm region. Remarkably, an intense peak around ~430 nm was observed for all the emitters and other broad and weak shoulder peaks at ~550 and >600 nm, suggesting multimode emission due to the combined existence of fluorescence and phosphorescence.

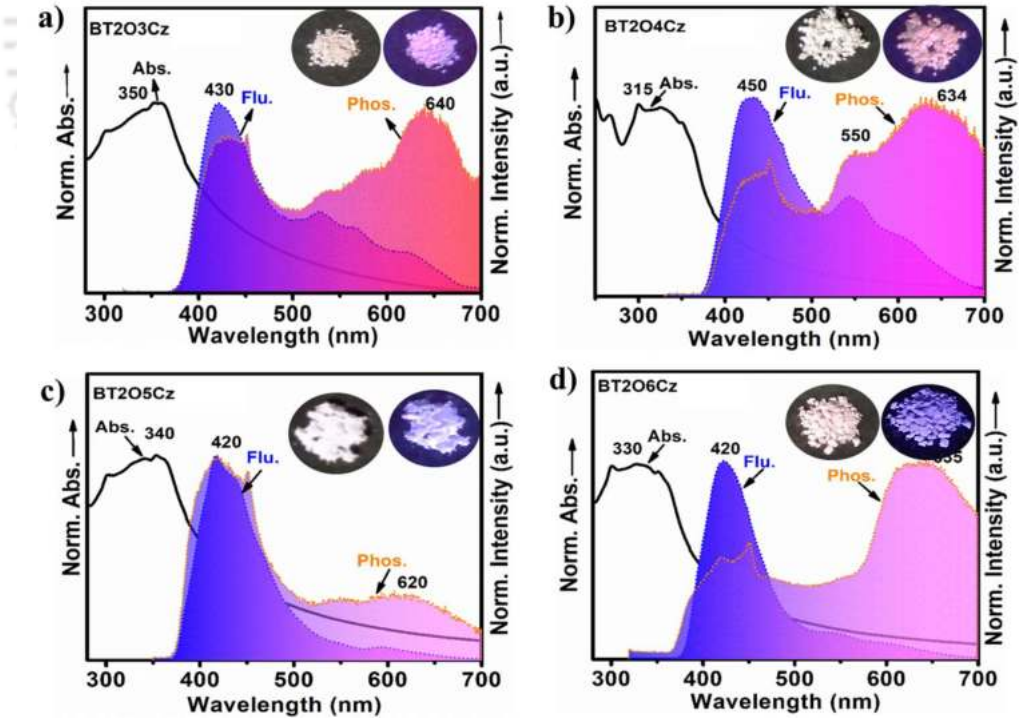

Figure 4.3. Solid state Photophysical Properties of the OSMWLEs: (a-d) Ultraviolet-visible absorption, steady state fluorescence and phosphorescence spectra in crystalline powder form for all the OSMWLEs of BT2OxCz (x=3, 4, 5 and 6) (inset photograph at daylight and 365 nm UV-lamp).

Besides, the intensities of later peaks for BT2O5Cz and BT2O6Cz gradually decrease with increasing chain length due to the weakening of TSCT property. Likewise, the solid state phosphorescence spectra of all the WLE BT2OxCz showed multiple peaks distributed over visible region (Figure 4.3a-d, orange dotted line). A weaker fluorescence band (blue shaded), superimposes with steady state fluorescence at ~430 nm, whereas intense phosphorescence signals (red shaded) appear at green (~550 nm) and near-IR region (640, 634, 620 and 635 nm) for BT2O3Cz, BT2O4Cz, BT2O5Cz, and BT2O6Cz). These signals were also found to be identical with steady state faint shoulder emission band (>600 nm). However, BT2O5Cz exhibited bright fluorescence and showed weak phosphorescence because of its amorphous nature. To confirm the ascertained hypothesis for BT2O5Cz, powder X-ray diffraction (PXRD)/thin film XRD and FETEM study was conducted with pristine OSMWLEs at RT (Figure A4.25, A4.26). In both the XRD patterns, broad and weak peaks were observed for BT2O5Cz relating to its amorphous nature, whereas, other emitters of BT2OxCz (x = 3, 4, 6) showed sharp diffracting peak patterns at low d-spacing region (marked in red dotted box) depicting high degree of crystallinity. In the FETEM, despite the micro-rod shaped morphologies of the OSMWLEs, the selected area (electron) diffraction (SAED) images showed a clear amorphous nature of BT2O5Cz powder (Figure A4.27) which does not affect the singlets. Hence, it had bright fluorescence and due to lack of rigid crystallinity, non-radiative deactivations of triplets has not been fully circumvented, thereby it showed weak phosphorescence. Notably, with increasing chain length, BT2O5Cz and BT2O6Cz exhibited blue-shifted phosphorescence, probably due to the less geometrical strain reduced thermal relaxation of high lying triplet energy.

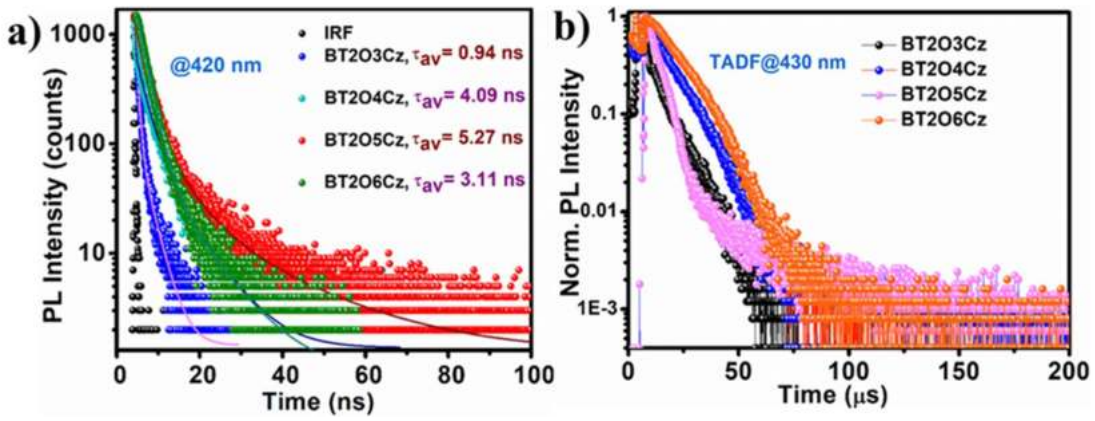

Figure 4.4. Prompt fluorescence/LE lifetime (a) and delayed fluorescence lifetime (b) recorded in crystalline powder form for all the emitters, BT2OxCz (x=3,4,5 & 6) at 420 and 430 nm respectively.

Therefore, we hypothesized that the former blue emission at 430 nm originated from a higher singlet state (>S_1) and TADF in nature. However, the latter peaks are assigned as room temperature dual phosphorescence (RTDP) emission, derived from low (T_1) and high lying triplet states (>T_1). Subsequently, to confirm that the shorter wavelength blue emission arises from singlet states, the lifetime recorded at 430 nm, showed a bi-exponential decay comprising a ns range lifetime, due to the prompt locally excited emission (τ_{PF} = 0.94, 4.09, 5.27 and 3.11 ns for all BT2OxCz WLEs) (Figure 4.4a) and a microsecond (µs) range lifetime for delayed components (τ_{DF} = 11.5, 11.4, 55.0 and 17.3 µs) (Figure 4.4b). Long average lifetime (5.27 ns and 55 µs) for BT2O5Cz further confirms the prominent fluorescence nature of the emitter compared to the other three emitters. Besides, longer wavelength green/red region peaks are actually derived from triplet state. To validate this, lifetime studies were carried out at ambient and inert condition for all the emitters. As expected, the average lifetime calculated from bi-exponential decays, showed huge enhancement from 6.77 to 68.07 µs for BT2O3Cz (λ_{em} = 640 nm), 10.89 to 18.89 µs for BT2O4Cz (λ_{em} =634 nm), 21.65 to 30.75 µs for BT2O5Cz (λ_{em} = 620 nm) and 20.72 to 29.12 µs for BT2O6Cz (λ_{em} = 635 nm) (Figure 4.5a-d) at inert conditions.

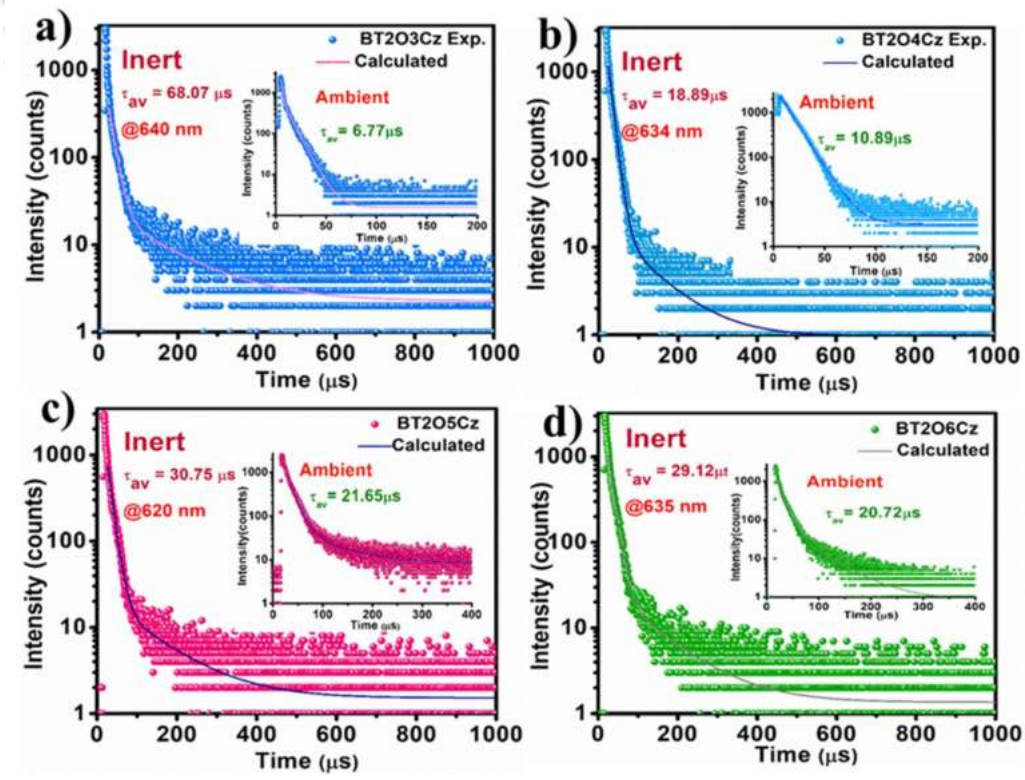

Figure 4.5. (a-d) Time-resolved PL based delayed lifetime recorded for BT2OxCz (x=3, 4, 5 and 6) at ambient and inert conditions at RT.

Notably, the higher lifetime for BT2O5Cz and BT2O6Cz was presumably due to the thermally elevated phosphorescence while the comparatively lesser lifetime for BT2O3Cz and BT2O4Cz was because of TADF emission at ambient condition. Further, the temperature-dependent delayed emission and their corresponding lifetime were verified by recording at 100, 150, 200and 300 K respectively for BT2O3CZ and BT2O6Cz (4.6a-f).

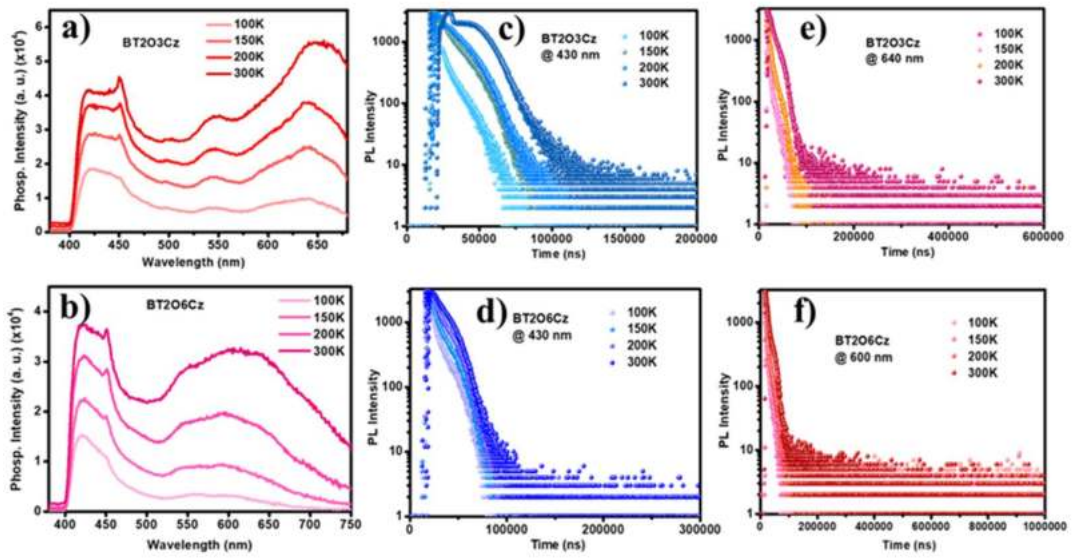

Figure 4.6. Temperature dependent study: (a & b) Temperature dependent phosphorescence spectra. (c & d) Delayed fluorescence decay at 430 nm. (e & f) Phosphorescence decay recorded in crystalline powder form for for BT2O3Cz and BT2O6Cz at 640 nm.

Collectively, peaks at ~430 and ~600 nm with their delayed lifetime were verified as TADF and thermally elevated RTP in character. In contrast, delayed intensity and lifetime increase with increasing temperature from 100 to 300K, providing concrete evidence to simultaneously support the thermally activated singlet and triplet excitons release process at RT. In the temperature dependency results we observed anomalous behaviour for the OSMWLEs, which can be explained by considering the following aspects: (1) presence of isomeric impurity acts as charge traps and generates charge-separated excited states which are responsible for fast phosphorescence decay (at 550 nm emission with μs lifetime), (2) at elevated temperature hotter excitons are produced that may prefer direct transition from higher-lying states ($T_3/T_4 \rightarrow S_0$) or goes via TTET for favourable relaxation to feed T_1 thereby resulting in 600 nm red phosphorescence (3) communications among these emitting states at local minima by thermal motions (e.g., vibrations) may be weaken at low temperatures so that hot excitons remain obscured. (Experimental results related to these properties were discussed in the "Mechanism for multi-emission section") Moreover, the

longest phosphorescence lifetime (68.07 μs) for BT2O3Cz can be attributed by the high crystallinity, densely packed supramolecular assembly (ρ_{cal} =1.400 mg/mm^3), intermolecular electronic coupling and through-space TICT effect in sterically strained molecular structure. Phosphorescence QY for all the BT2OxCz powders was calculated to be 4.5%, 4.4%, 5.3% and 13.3%. The radiative rate constant (k_r) were calculated to be 6.72 x10^7 s^{-1}, 4.08 x10^7 s^{-1}, 2.55 x10^7 s^{-1}, and 6.14 x10^7 s^{-1} and non-radiative rate constants (k_{nr}) were found to be 1.40 x10^4 s^{-1}, 0.87 x10^4 s^{-1}, 0.40 x10^4 s^{-1}, and 0.42 x10^4 s^{-1}, for all BT2OxCz WLEs. These results signify that excitons were being utilized at maximum extent for radiative decay (x10^7) under photo-illumination. Further, ISC and RISC rate constants calculated from PLQY and lifetime values of the prompt and delayed components, were estimated to be k_{ISC} = 7.5 x10^6 s^{-1}, 1.53 x10^6 s^{-1}, 1.25 x10^6 s^{-1}, 0.75 x10^6 s^{-1} and k_{RISC} = 1.47 x10^5 s^{-1}, 0.24 x10^5 s^{-1}, 0.46 x10^5 s^{-1}, 0.48 x10^5 s^{-1} , for BT2OxCz (x=3-6) respectively (Summarized in Table A4.1).[43] To obtain clear insights of phosphorescence emission at molecular level, including elimination of the molecular aggregation effect and to restrict non-radiative motion, a set of control experiments were conducted on spin-coated films after doping all the BT2OxCz WLEs at 0.5 wt% and 5 wt% concentration into PMMA in inert condition using dry toluene. Phosphorescence spectrum in low concentrated films (0.5%) exhibited three distinct peaks located at 450 nm (TADF), 545 nm (fast RTP, τ_{av} = ~80 μs) and 700 nm (slow RTP, τ_{av} = ~2.5 ms) covering entire visible range (Figure 4.7a, b), clearly suggesting, exclusion of molecular oxygen in the rigid polymer matrix, allowing significant RTP contribution (triplet excitons are dominated over singlet excitons). Notably, in films, there was a ~20 nm bathochromic shift than powder form with no change in peak positions for all the four emitters, which could be due to the restriction in molecular motion (RIM), strong intramolecular interactions rigidifying the structural conformation and resulting in suppression of non-radiative deactivations.[44] The colour purity and uniform single molecular surface morphologies were established from the CIE diagram and atomic force microscope (AFM) topography, respectively (Figure A4.28 and A4.29). However, molecular aggregation caused the quenching effect reducing the RTP efficiency of highly concentrated (5.0 wt%) PMMA-doped film. As expected, the film displayed only a broad fluorescence and no phosphorescence at RT (Figure A4.30). This result suggests that conformational rigidity in the proximity of phosphors is more important than the environmental matrix rigidity.

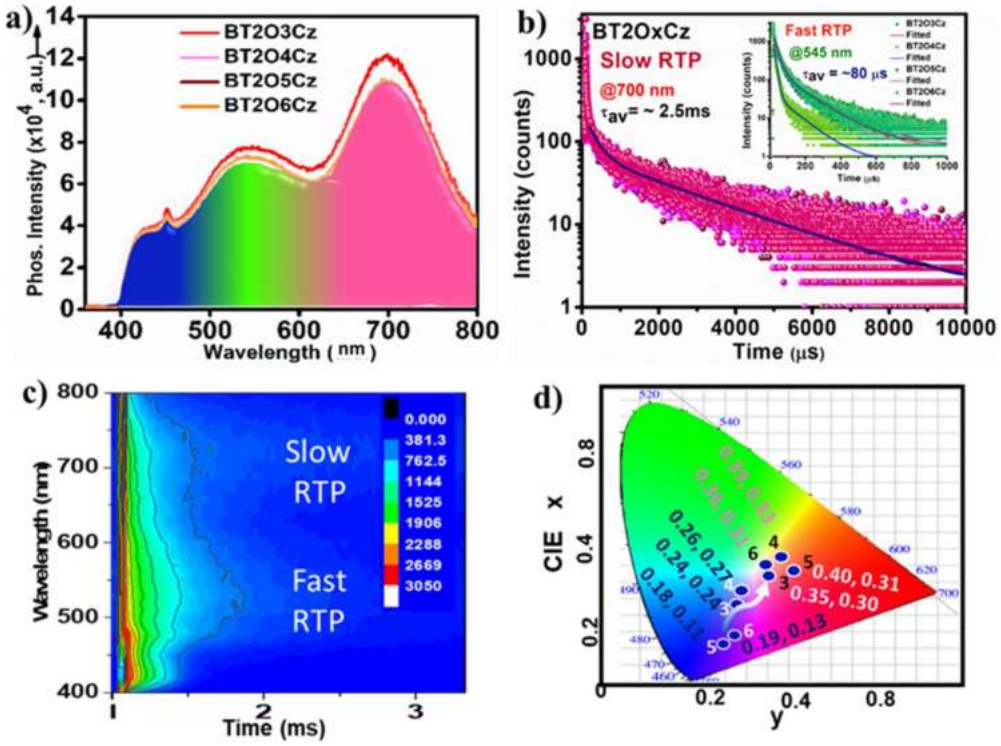

Figure 4.7. (a) Multiple delayed emissions for a rigid PMMA (0.5 wt%) doped spin-coated film for all the OSMWLEs. (b & c) Life-time decay and Time resolved emission spectra (TRES) for BT2O3Cz at 545 and 700 nm phosphorescence emission. (d) CIE coordinate diagram for the steady state (blue) and delayed emission (white) for all the OSMWLEs.

Moreover, the two distinct triplet emission peaks from 0.5 wt% PMMA-doped film due to boosted ISC allowed triplet excitons migration from high lying T_m to T_1 state via intramolecular TTET process[33] which was further elucidated by recording time-resolved emission spectra (TRES) at RT. The TRES spectra of model PMMA-doped BT2O3Cz exhibited two persistent delayed emission bands in millisecond (ms) lifetime region within 400 to 800 nm wavelength (Figure 4.7c). Here the emission band centered at 545 nm was inherited from high energy level of T_3/T_4 states, corresponding to fast RTP, whereas the emission at 700 nm stems through TTET process from T_3/T_4 to low energy stable T_1 state revealing slow RTP. It has also been observed that these compounds adopted broad and switchable emission colours by changing their excitation source. Upon steady state excitation the emission colour for crystalline powder had CIE coordinates near the blue region (0.24, 0.24) for BT2O3Cz, (0.26, 0.27) for BT2O4Cz, (0.18, 0.11) for BT2O5Cz and (0.19, 0.13) for BT2O6Cz. These CIE values revealed that OSMWLEs turn bluer with increasing chain length. In contrast, a very close pure white CIE (0.33, 0.33) was obtained upon excitation of microsecond pulse as a source. The obtained phosphorescence CIE

values were (0.35, 0.30) for BT2O3Cz, (0.39, 0.33) for BT2O4Cz, (0.40, 0.31) for BT2O5Cz and (0.36, 0.31) for BT2O6Cz (Figure 4.7d). The shorter and longer chain containing emitters emit close to pure white, likely due to the strong packing and wider overlaps of dual fluorescence and phosphorescence in the crystalline state that enabled the suppression of triplet non-radiative decays and promoted equilibrium in their states. Furthermore, considering the photostability of TADF and thermally elevated phosphorescence were involved, phosphorescence spectra and decays were recorded for the neat film of model compound BT2O3Cz in heated conditions (298K, 323K, 353K and 373K). The phosphorescence spectra of heated film exhibited distinct TADF and phosphorescence with increasing temperatures and relatively higher intensity was observe at temperature 353 K. Notably, at RT (298K) no distinguishable peaks at 550 and 600 nm was observed which may be due to the quenching effect in neat film. However, peaks were distinguished at elevated temperatures because of hot-excitons contributions in their respective emission sources. Moreover, no significant difference in life-time was observed in the film signifying good photo-stability of BT2O3Cz (Figure A4.31). The overall photophysical properties are summarized in Table 4.1, which identifies the multimode emission and their vital difference in various states.

Table 4.1: Summary of photophysical studies of BT2OxCz (x=3, 4, 5 and 6) in solid crystalline powder and PMMA-doped spin coated films.

OSMW LEs	**λ_{UV} (nm)**	**λ_{PL} (nm)**	**λ_{Phos} (nm)**		**τ_{av} (ns)**	**τ_{av} (μs)**		**ϕ_P**	**k_r ($x10^7$ s^{-1})[a]**	**k_{nr} ($x10^4$ s^{-1})[b]**	**K_{ISC} ($x10^6$ s^{-1})**	**K_{RISC} ($x10^5$ s^{-1})**
	Solid	Solid	Solid	Film	Solid	Solid Air/ Inert	Film	Phos. RT	Solid Air/RT	Solid Air/RT	Solid Air/RT	Solid Air/RT
BT2O3 Cz	350	415 530 567	430 540 640	430 535 700	0.94	6.77 68.07	71.7 3220	4.5	6.72	1.40	7.5	1.47
BT2O4 Cz	320	430 540 610	445 546 633	430 535 700	4.09	10.89 18.89	76.8 2059	4.4	4.08	0. 87	1.53	0.24
BT2O5 Cz	340	420 540	420 615	430 535 700	5.27	21.65 30.76	85.5 7222	5.3	2.44	0. 40	1.25	0.46
BT2O6 Cz	325	415 538	450 630	430 535 700	3.11	20.72 29.12	74.2 2270	13.3	6.14	0. 42	0.75	0.48

Radiative and non-radiative decay rate [$^a k_r = \phi/\tau$, $^b k_{nr} = (1-\phi)/\tau$] calculated from QY and delayed lifetime of crystals at RT in air.

4.3.4. Mechanism for Multi-emission

Furthermore, to understand the actual origin of all the independent emissions observed for solids and thin film of BT2OxCZ emitters, steady state PL spectra, PLQY and TRPL emission of neat films of each moieties Cz, BT2OH and mixture (Cz:BT2OH = 1:1) were recorded. This experiment also facilitates discrimination of all independent excited states involved for the fluorescence and phosphorescence (Figure 4.8). Steady state PL was observed at 375, 420 and 400 nm with PLQY values of 7.79%, 4.61% and 9.54% for Cz, BT2OH and mixtures (Cz:BT2OH = 1:1), respectively. These results clearly depict that every individual moiety contributed towards $^1\pi$-π^*, ^{1}n-π^* and ^{1}ICT transitions independently to the singlet emission.

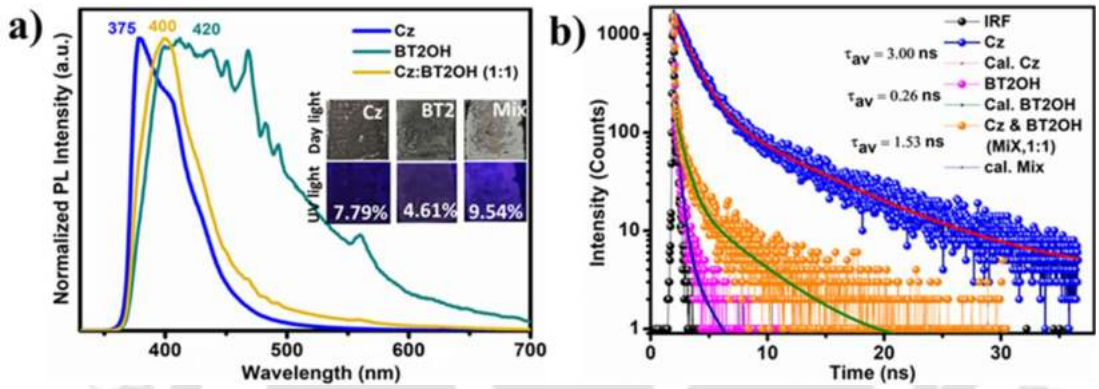

Figure 4.8. Film PL spectra and TRPL of each moiety (Cz, BT2OH) and mixture (Cz:BT2OH = 1:1) (a &b).

Furthermore, average lifetime value of 3.0, 0.26 and 1.53 ns with biexponential fit results were observed for Cz, BT2OH and the mixture (Cz:BT2OH = 1:1), from prompt and delayed species, respectively. To precisely understand ~~on~~ the multi-emission sources (centred at 430, 550 and 700 nm), we hypothesized first that the 430 nm emission resulted from higher lying singlets. To verify this, excitation wavelength-dependent emission studies were performed for BT2O3Cz and BT2O6Cz. A series of excitation wavelengths were used to excite the luminogens, and the PL spectra illustrated the bright state emission (λ_{em} = 430 nm) which disappears when excitation shifted to a longer wavelength (λ_{ex} = 300 to 500 nm) from normal excitation (λ_{ex} = ~320 nm) (Figure 4.9a, b).

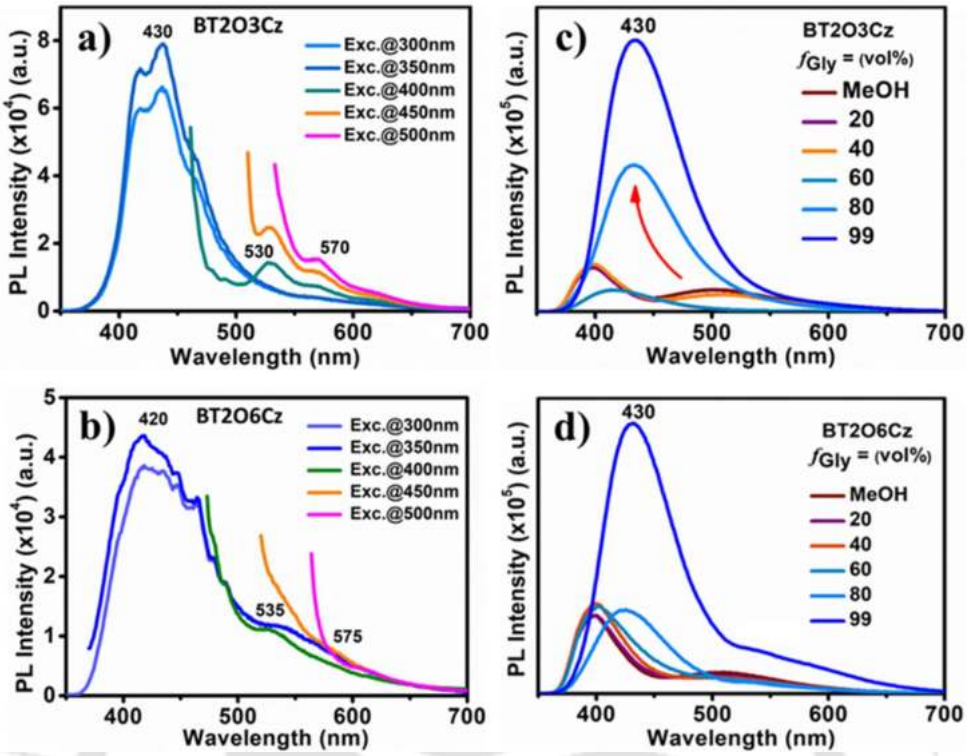

Figure 4.9. (a & b) Excitation-dependent corrected emission spectra of compound BT2O3Cz and BT2O6Cz. The bright state fluorescent spectra that were obtained after exciting at λex = 320 nm, where dark state spectra were obtained by exciting λex = 500 nm and amplified by two times for the sake of clarity. (c & d) Fluorescence spectra of compound BT2O3Cz and BT2O6Cz in mixtures of glycerol and methanol of increased solvent viscosity and results in an almost fifteen fold increase in emission intensity.

Moreover, on excitation at λ_{ex} = 500 nm a red-shifted dark emission feature emerges at ~530 and ~570 nm, indicating that the molecule relaxes to the lower energy dark states viz. S_1/S_2. By fixing the excitation wavelength to a lower energy (500 nm), weak emission was observed from a lower-lying excited state (the dark state, which in this scenario is S_1). This experiment proved that the main emission is from an energy level higher than S_1, while, S_1 is a weakly emissive one and corroborates the existence of dark states via SOKR.[45] Further, viscosity-induced enhanced fluorescence of BT2OxCz (x =3 and 6) were also studied in various micro-viscous environments where a binary mixture, glycerol (Gly) and methanol was used to regulate the viscosity of the medium (Figure 4.9c, d). The emission maxima initially shifted to longer wavelength with increasing Gly fraction (f_{Gly}) due to ICT. However, tenfold enhanced emission intensity was observed at 80% f_{Gly}, compared to methanol solution. Since, in the low viscous medium, excitation to the emissive excited state followed by rotation about the rotor axis significantly decreases the energy gap between the emissive and dark excited states, it resulted in a rapid internal conversion (IC) to S_1. While in high viscous medium or in aggregated state, the non-radiative deactivation

of the twisted complex is circumvented by suppressing IC from >S_1 state to dark S_1 state, due to restricted rotation thereby resulting in huge fluorescence enhancement.

Further, to shed light on 550 nm emission, alkyl chain containing carbazole units were taken independently, ensued in ultra-long room temperature phosphorescence emission (URTP)[4,31] of up to several seconds afterglow (removing UV-excitation) for four, five and six carbon chain containing carbazole moieties respectively. Moreover, steady state PL spectra of 1, nCzBr exhibited a sharp prompt fluorescence band near 375 nm and a shoulder phosphorescence peak at 550 nm (Figure 4.10a, b).

Therefore, phosphorescence spectra recorded in air showed very distinct band centered at ~550 nm with the lifetime values of 95.1 μs, 187.5 ms, 47.57 ms and 126.2 ms for 1,3CzBr, 1,4CzBr, 1,5CzBr and 1,6CzBr, respectively (Figure 4.10c, d). URTP emissions were further captured under UV-light (365 nm) at both on and off conditions (Figure 4.11a).

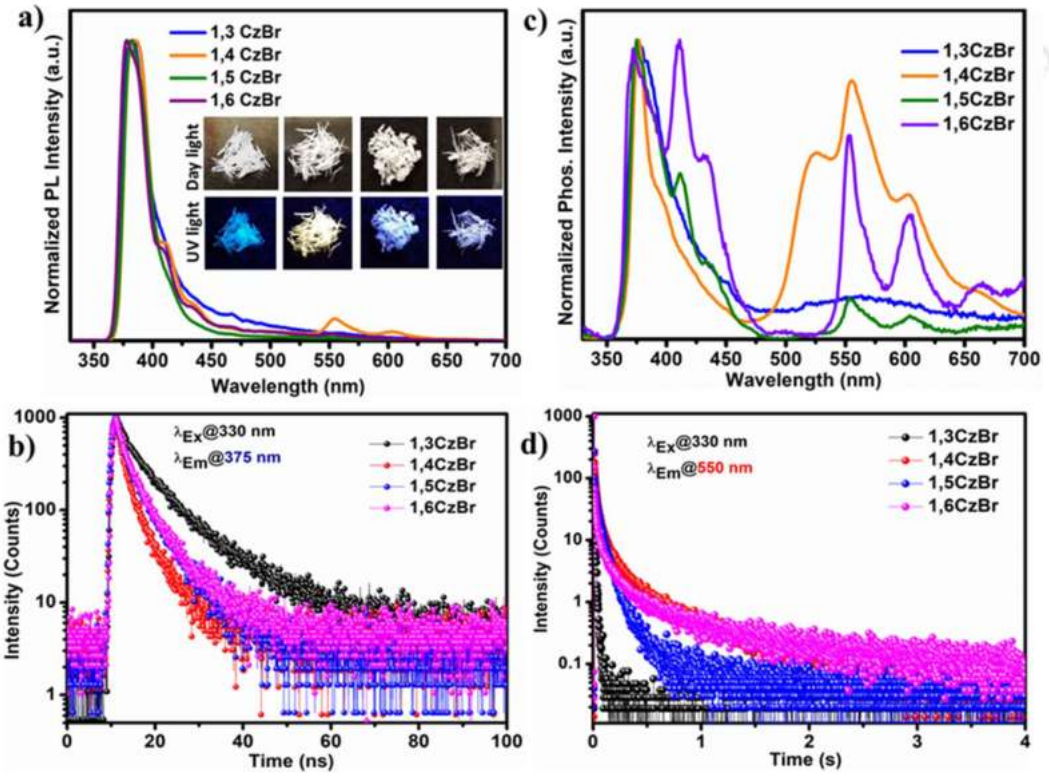

Figure 4.10. Ultra-long room temperature phosphorescence (URTP) study for various alkyl chain containing carbazole unit, 1,n CzBr (n =3, 4, 5, & 6). (a) Steady state PL spectra exhibited a sharp band near 375 nm due to delayed fluorescence and shoulder peaks near 550 nm, due to phosphorescence. (b) Phosphorescence spectra were recorded in air and found to be very distinct phosphorescence centered at ~ 550 nm. (c and d) Prompt fluorescence decay (ns) and phosphorescence decay (ms) was recorded in air for 375 and 550 nm respectively.

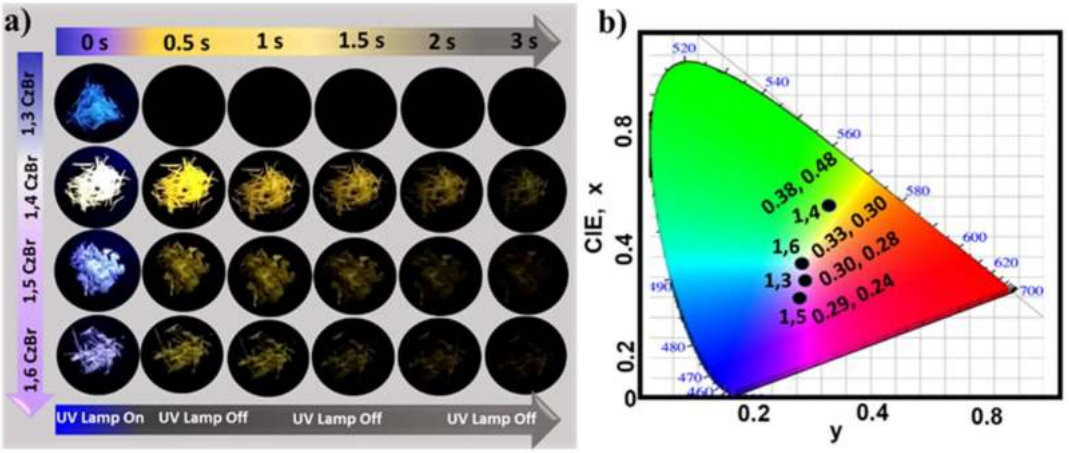

Figure 4.11. (a) URTP emissions were further captured under UV-light (365 nm) at both on and off conditions. (b) CIE-coordinates values revealed the white phosphorescence emission for 1,6 CzBr.

CIE-coordinates values revealed the white phosphorescence emission for 1, 6 CzBr (Figure 4.11b). More interestingly, the fast RTP at ~550 nm emission of BT2OxCz exactly matched with the URTP emission of bromo alkylated carbazole derivatives. Notably, it is reported that URTP emission can be observed due to the presence of trace amounts of isomeric impurity [1H-benzo[f]indole (Bd)] of commercial carbazole derivatives.[31] Therefore, the fast phosphorescence emission from the present BT2OxCz emitter is also inherited because of the impurity effect confirmed by HPLC analysis (Figure 4.12a, b and Figure A4.32). The hypothesis was further confirmed by laser-induced fluorescence (LIF) spectra and transient absorption (TA) study. We recorded LIF spectra for BT2O6Cz at 77 K and RT from LP980 at varying delays after the pump pulse (Figure 4.13a and Figure A4.33-A4.35**).** The LIF spectra demonstrated that on moving from ns to µs delay, distinctive phosphorescence was observed in the range of 500-700 nm. Further, TA study was conducted with the PMMA doped spin-coated film (0.5%) of BT2O6Cz, and two distinct positive transient absorption signals appeared at ~550 and ~700 nm at 77 K while at RT both peaks increased and the 700 nm TA signal dominated (Figure 4.13b). Besides, kinetic TA trace also exhibited exponential decay profile. (Figure A4.36). These results clearly depicted that the trace amounts of alkylated carbazole isomeric impurity generates charge-separated states (hot-excitons) and results in fast and stable phosphorescence at 550 nm. Consecutively, the hotter excitons (emissive higher-lying triplet excited states T_3/T_4) are likely feeding the lowest T_1 state via TTET at RT.

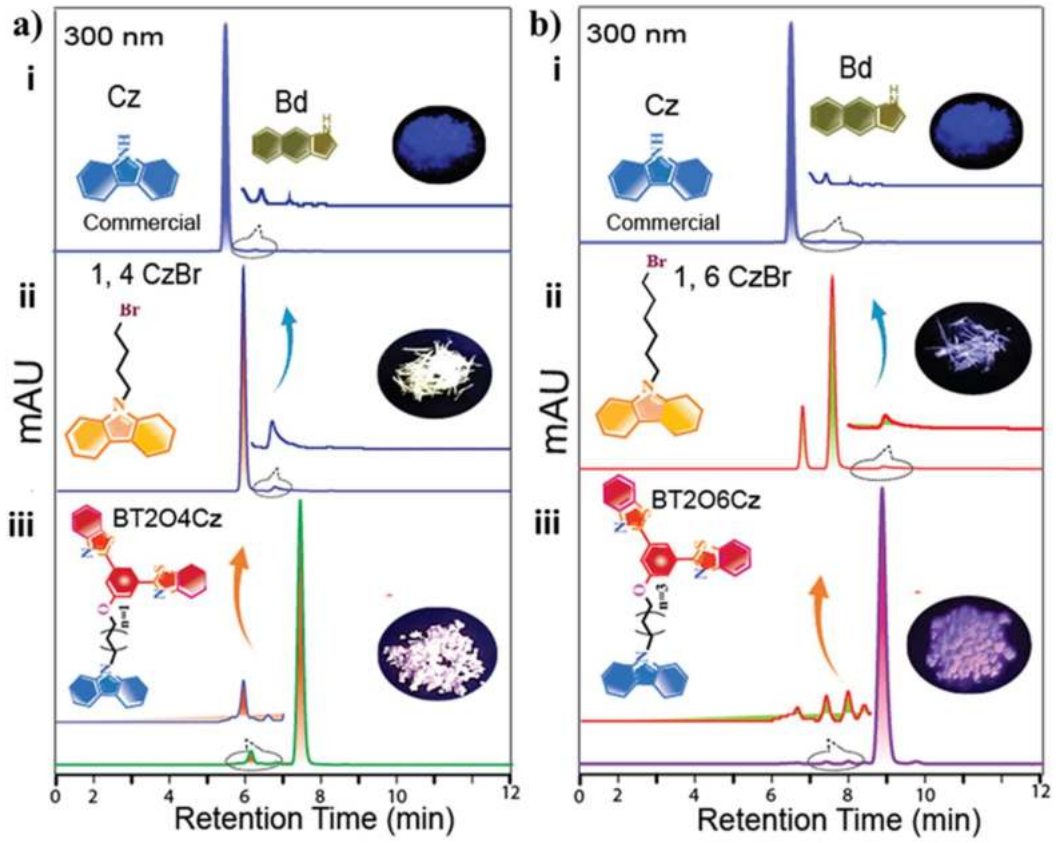

Figure 4.12. Impurity effect on solid-state emission mechanism: (a & b) High-performance liquid chromatography (HPLC) spectra of commercial Cz (i) 1,4CzBr, 1,6CzBr crystals (ii) and BT2O4Cz, BT2O6Cz crystals (iii) monitored at 300nm with acetonitrile as eluent. All the crystals up to final compound inherits an impurity peak of BD compounds. Chemical structure of all the compounds were shown with inset photograph of each crystal captured under 365 nm UV-lamp.

Substantially, the communication is cut off at 77 K, indicative of such a higher triplet excited states that are being separated from the lowest T_1.[46] At the same time, ~700 nm emission has also been rationalized as due to due to aggregation-induced supramolecular non-covalent interactions evolving alkyl chains furnishing tight molecular packing via dimerization and circumventing non-radiative decays in solid state.

4.3.5. Computational Calculations:

To investigate the intrinsic insights and support the experimentally obtained multimode emission results, quantum-mechanical calculations were performed for BT2O3Cz and BT2O6Cz from their optimized single crystal structure geometry using Gaussian 16 program.[47] Density functional theory (DFT) and time dependent density functional theory (TD-DFT) were performed for at B3LYP/6-31G (d,p) level up to the 10^{th} states at their different spin multiplicities (Figure 4.14a, b and Figure A4.37).

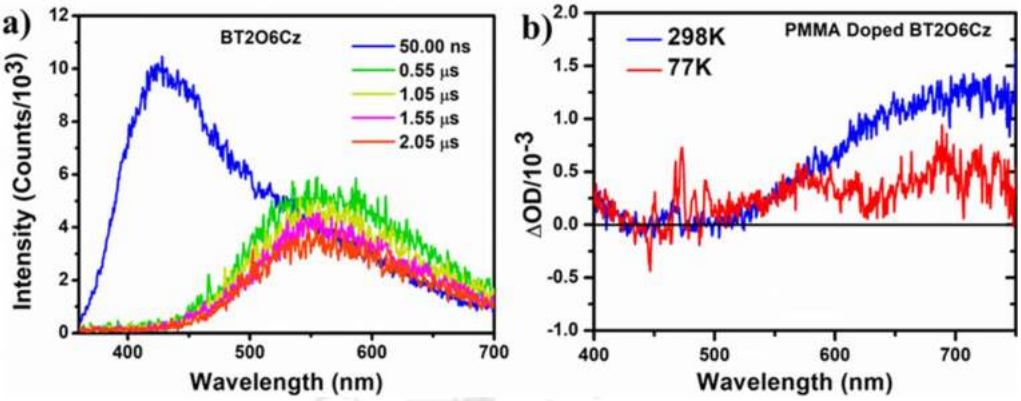

Figure 4.13.(a) Laser induce fluorescence (LIF) spectra of BT2O6Cz acquired at RT in LP980 at varying delays after the pump pulse (color coding in the graph). (b) Transient absorption (TA) spectra of PMMA doped BT2O6Cz spin-coated film (0.5%) acquired with the ICCD at 298 K (blue) and 77 K (red).

Frontier molecular orbitals (FMO), results displayed well separated electron density distributions in their respective HOMO and LUMO with a wider band gap profile (3.61/3.48 eV) depicting TSCT behaviour of these emitters (Figure 4.14ai, bi). Nonetheless, a zero energy splitting (0.02 and 0.12 eV) between S_1 and T_3/T_4 strongly favours efficient RISC process, where, relatively larger differences of S_1 (3.24, 3.03 eV) and T_1 (2.74, 2.39 eV) leads to moderate ΔE_{ST} value of 0.50 and 0.71 eV for BT2O3Cz and BT2O6Cz, (Figure 4.14 aii, bii) which corresponds to the basic prerequisite for displaying a simultaneous TADF and RTP emission.[19,20] Energy band gap and ΔE_{ST} values suggest a strong susceptibility of TADF for shorter chain and intense RTP for longer chain emitter respectively. Further, active manifold ISC channels were also investigated by sequential adiabatic energies related to ground state for S_1, $>S_1$ and T_1 to higher triplet states of up to 10th state and their corresponding major frontier orbital contributions are summarized in Table A4.2-A4.9. Noticeably, the oscillator strength (*f*) at S_1-S_3 states for both the emitters were found to be zero (*f*=0), indicating that lowest S_1 state is a non-emissive state. Large *f* values were observed beyond S_4 / S_5 depicting the electronic relaxation from higher-lying states ($>S_4$) contributing as an emissive state which is unusual and reverse of conventional and many experimental results. Moreover, ambient delayed fluorescence or phosphorescence emission by harvesting the triplet state is a very difficult process, as most of the organic molecules undergo S_1 (π- π^*) $\rightarrow$ T_1 (π- π^*) forbidden ISC transition. However, in the present molecules, natural transition orbitals (NTOs) calculation suggested that S_1 and $>S_1$ is a pure ^{1}ICT and ^{1}LE (π- π^*) character while T_1 and T_3 having ^{3}LE (n- π^*) character (Figure A4.38).

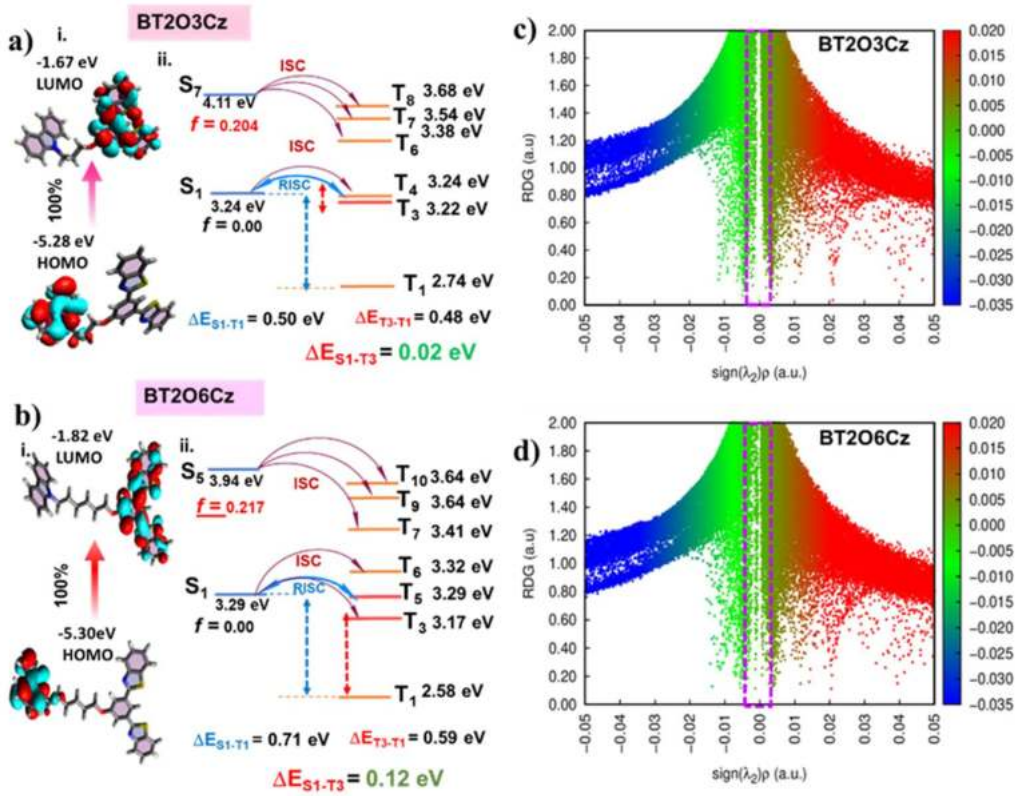

Figure 4.14. Computational calculations: (ai &bi) HOMO and LUMO density distributions with the corresponding band gap profiles, (aii and bii) Adiabatic energy transitions dependent oscillator strength (*f*) and possible manifold active ISC channels and energy splitting (ΔE_{ST}) for BT2O3Cz and BT2O6Cz from Gaussian 16 package at B3LYP-6-31G(d,p) level of theory. (c and d) The functions of reduced density gradient (RDG) and Sign (λ_2)ρ isosurface map with an isovalue of 0.5 for BT2O3Cz and BT2O6Cz respectively.

Therefore, the multimode emissions by the involvement NTOs corresponding to higher excited states producing ^{1}ICT → ^{3}LE and ^{1}LE → ^{3}LE/^{3}ICT transitions (allowed transition) within singlet and triplet (S_n and T_m) manifold resulting in substantial enhanced SOC thereby leading to TADF and RTP simultaneously. These theoretical findings are feasible to rationalize the simultaneous process of TADF and RTP that occurred from higher-lying states (hot-excitons).[48] Furthermore, to reveal the dissimilar intramolecular non-covalent interactions which induced the emission from excited states, the functions of reduced density gradient (RDG) and Sign (λ_2)ρ were calculated for BT2O3Cz and BT2O6Cz using TD-DFT geometry with Multiwfn software.[49] RDG analysis (Figure 4.14c, d) confirms the presence of obvious intramolecular attractive interactions (green region) and larger steric hindrance (brown region) between D-A and long alkyl chain segments in BT2O6Cz which could effectively restrict the intramolecular vibrations and prevent energy loss of the excited molecules and revealing more RTP susceptibility. In contrast, the short alkyl chain

linked conformation of BT2O3CZ exhibits relatively weak intramolecular interactions, which is a common phenomenon found in general TADF molecules.[50]

4.3.6. Supramolecular Structures and Luminescence

To explore deeper understanding of supramolecular interactions, molecular packing arrangements induced TADF, RTP emission in solid state, the single-crystal X-ray structures were analyzed carefully. Crystal structures of BT2O3Cz (CCDC 1969742) and BT2O6Cz (CCDC 1969743) were obtained by very slow evaporation of chloroform/hexane (8:2) solvents.

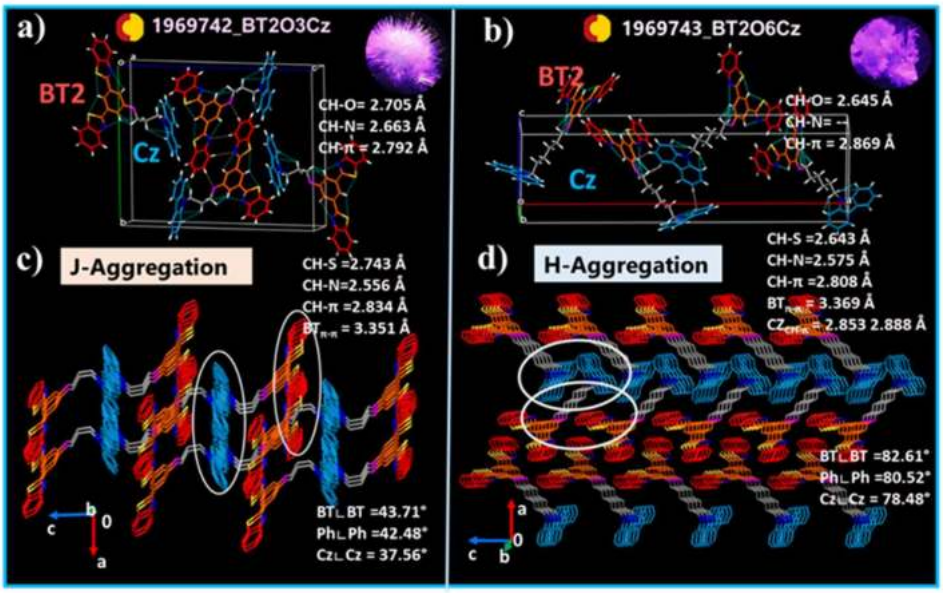

Figure 4.15. SC-XRD and PXRD analysis: (a & b) Single-crystal XRD structure of BT2O3Cz and BT2O6Cz OSMWLEs in unit cell (inset: single crystals images captured under 365nm UV lamp). (c & d) Side view of bulk stacked architectures, relative distances and angles from each constituent, are shown to exhibit distinct J-type and H-type aggregation pattern for BT2O3Cz and BT2O6Cz OSMWLEs.

Unfortunately, the crystal structure of BT2O4Cz and BT2O5Cz could not be solved. Two needle-like crystals of BT2O3Cz and BT2O6Cz exhibited monoclinic and orthorhombic crystal system with P 21/c and Pca 21 space group (crystal structure information summarized in Table A4.10). Both the molecules exhibited multiple intra- and intermolecular interactions via hydrogen bonding due to the presence of N/O/S atoms and other non-covalent interactions such as weak CH-π, π-π, and through-space CT (Figure 4.15a, b). These interactions enable formation of rigid and dense 3D network which further assists to restrict vibrational relaxation and prevents excitons quenching.[51] The intramolecular hydrogen bonds involving S and N atoms were close to active hydrogen on the phenyl in the acceptor unit (C-S···H: 2.74 Å; C-N···H: 2.55 Å in BT2O3Cz and C-

S···H: 2.64 Å; C-N···H: 2.57 Å in BT2O6Cz), and enhances the co-planarity of three units [two benzothiazole (BT) and central phenyl core], evidenced by their short contact distances and torsions angles of 170.60° and 173.50°. Other intramolecular interactions involved the active hydrogen present in alkyl chain with the π-cloud of donor carbazole (Cz) unit (C-H···π: 2.83 Å; π···C-H: 2.72 Å in BT2O3Cz and C-H···π: 2.80 Å; π···C-H: 2.75 Å in BT2O6Cz). Additionally, multiple intermolecular interactions was also apparent in both the crystal structures. Intermolecular hydrogen bonding by a N atom present in BT and O atom present in the alkoxy chain in BT2O3Cz (C-H···N: 2.66 Å, C-H···O: 2.70 Å) also interacts non-covalently with nearby set of molecules creating a rigid 3D molecular framework, thereby reducing the non-radiative deactivations. However, BT2O6Cz, exhibited a single intermolecular hydrogen bond, involving O atom in the alkoxy chain (C-H···O: 2.64 Å). Unlike hydrogen bonds, many other intermolecular strong interactions were also observed due to the presence of active hydrogen atoms.

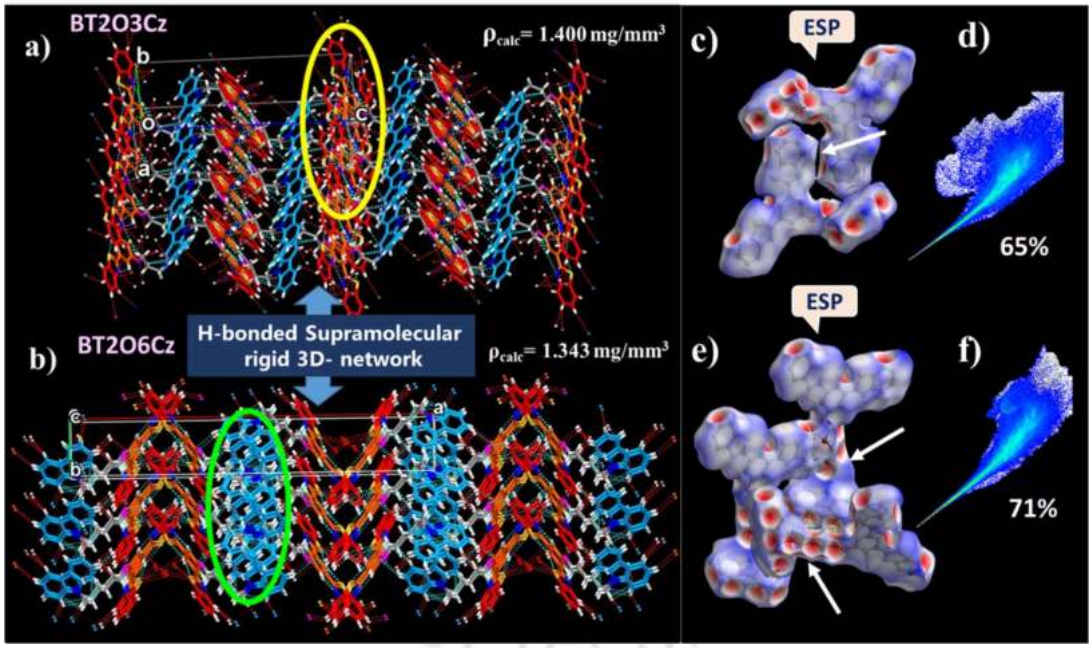

Figure 4.16. (a & b) Top view in bulk intramolecular packing of rigid BT2O3Cz and BT2O6Cz O. (c & d) Electrostatic potential (ESP) and (e & f) 2D finger plot mapped on the Hirshfeld surface in the BT2O3Cz and BT2O6Cz OSMWLEs.

While the BT2O6Cz showed more intermolecular interactions involving carbazole (Cz), alkyl chain hydrogens and S atom in BT (C-H···π: 2.85 Å; 2.86 Å and π···S: 3.31 Å) than BT2O3Cz which displayed only C-H···π: 2.79 Å interaction. Besides, very weak π-π stacking between two BT units in BT2O6Cz (3.35 Å, 3.36 Å) leads to dimeric structure,

whereas, BT2O3Cz exhibits J-aggregated structure (slip angle 43.71° between BT cores, 37.56° between Cz cores). BT2O6Cz exhibits H-aggregated structure (slip angle 82.61° between BT cores, 78.48° between Cz cores), (Figure 4.15c, d) and this dimeric form is stabilized by multiple non-covalent interactions and separated electron clouds of individual D-A units (detailed SC-structural analysis summarized in Table A4.11). These key factors enabled considerably weak π-π stacking, leading to strengthening of TSCT interactions. Additionally, their bulk crystal tight packing shows that H-aggregated BT2O6Cz leads to overall denser molecular packing rather than J-aggregated BT2O3Cz in their crystalline state, that suppressed the vibrational deactivations and activates the radiative channels[52] (Figure 4.16a, b). Simulation studies by electrostatic potential (ESP) mapping and their corresponding two-dimensional (2D) fingerprint plots (Crystal Explorer 3.1 software) substantiated the packing and interactions (π-π stacking and intermolecular HB interactions). The ESP mapped on Hirshfeld surface of BT2O3Cz / BT2O6Cz exhibited bright red spots on the strongly linked hydrogen bonds which clearly demonstrated the effective interactions, influencing their emission properties[53] (Figure 4.16c, e**).** 2D fingerprint plot suggested that the overall interactions for BT2O6Cz were higher (71%) than BT2O3Cz (65%) (Figure 4.16d, f). Therefore, the rigid interlocked BT2O3Cz and the involvement of donor (Cz) group and longer alkyl chain interactions in BT2O6Cz inhibited internal conversions and photochemical reactions which facilitated the emissions from higher lying excited states, resulting in enhanced delayed fluorescence and phosphorescence at RT. SC-XRD analysis Figure S56-S58. The X-ray powder diffraction (XPRD) peaks of crystalline powder obtained from as-synthesized pristine compounds exactly matched with the simulated patterns obtained from SCXRD-structure analysis (Figure 4.17a). The BT2O3Cz crystal grew preferentially along [011], whereas BT2O6Cz grew along [200] with planar layered structures. The BT2O6Cz exhibited multiple diffraction peaks at low d-space region (θ = 20-30°) (highlighted in orange dotted line) compared to BT2O3Cz confirming more non-covalent interactions and high packing density due to alkyl chain and dimer formations.

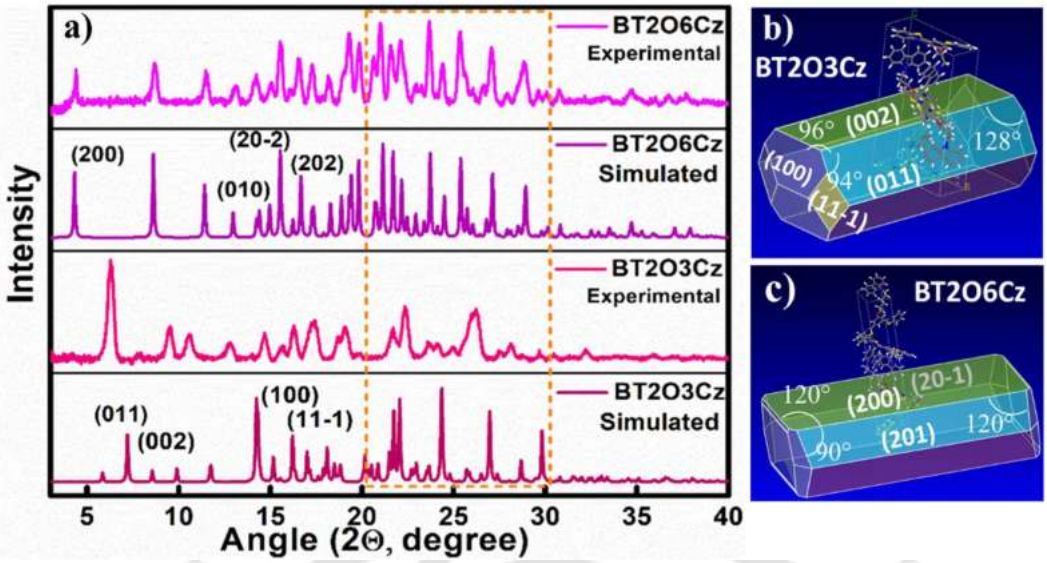

Figure 4.17. (a) Powder X-ray diffraction (PXRD) characterization of BT2O3Cz and BT2O6Cz. (b & c) Simulated crystal growth.

The calculated attachment energy[54] suggests a rod like growth morphology at different crystal facets (001), (002), (100) and (11-1) in BT2O3Cz with high attachment energy and (200), (201), (20-1) and (101) in BT2O6Cz displayed relatively less attachment energy for the binary growth model. Moreover, (001) and (002) is the primary crystal growth facet for BT2O3Cz while (200) is for BT2O6Cz (Figure 4.17b, 4.17c and Tables A4.12 and A4.13). Overall, these studies reveal the contribution of denser supramolecular non-covalent interactions, self-assembly induced solid-state packing, growth morphology and thermal stability profoundly on their ESD and multi-emissions. Further, the H-aggregated molecular packing greatly impedes the higher triplet state stabilization thereby favouring phosphorescence for longer chain BT2O6Cz. The densely packed crystalline state is a key strategy to realize triplet emission for most organic phosphorescent materials.[55] The solid state features of BT2O3Cz and BT2O6Cz motivated us to probe the triplet-harvesting optical wave-guiding properties in their single crystal states. We performed single-crystal micro-spectroscopy studies on crystals of BT2O3Cz and BT2O6Cz of length ≈202.9 μm and ≈75.6 μm.

4.3.7. Optical Waveguide Study

A diode laser 405 nm (continuous wave) was used as an excitation source. Excitation at the left terminal of the microcrystal generated bright greenish-white luminescence which subsequently propagated and out-coupled at the opposite terminal (Figure 4.18a, b).

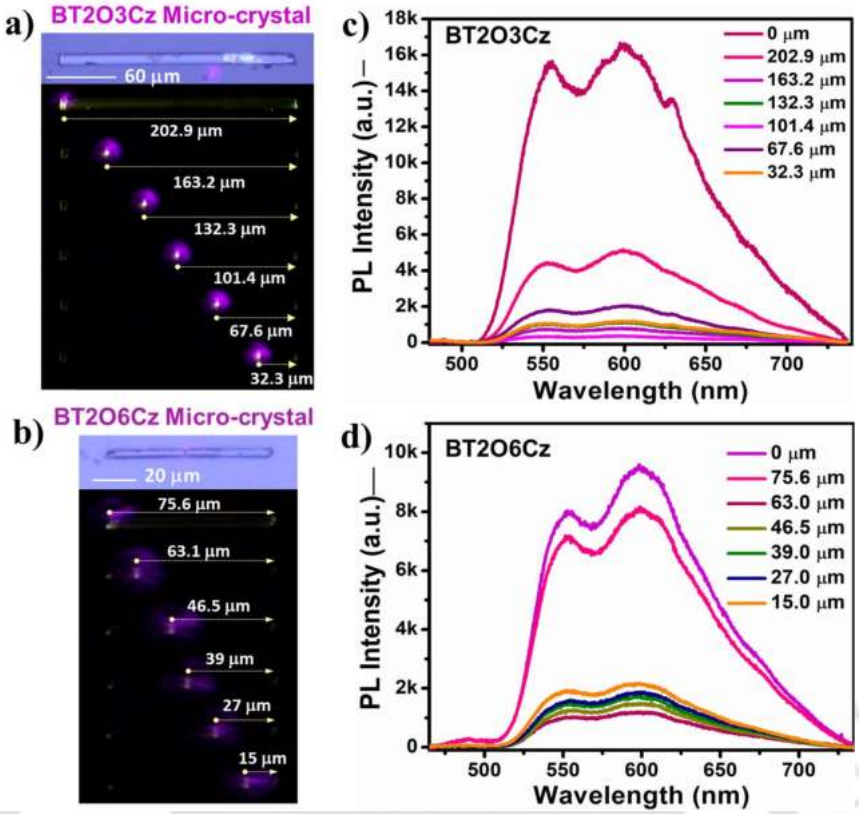

Figure 4.18. Optical waveguide study: (a & b) Optical and PL images of microcrystals of BT2O3Cz and BT2O6Cz showing excitation at different positions with a 405 nm laser. (c & d) PL spectra recored at the end of the BT2O3Cz and BT2O6Cz microcrystals

The microcrystals were excited at different points along their long axes (202.9, 163.2, 132.3, 101.4, 67.6, 32.3 and 0 µm for BT2O3Cz and 75.6, 63.1, 46.5, 39, 27, 15 and 0 µm for BT2O6Cz). The recorded broad band PL spectra covered 500-750 nm region and notably, two distinct phosphorescence peaks appeared at 550 and 600 nm. These peaks exactly match with the triplet emission of crystalline powders of OSMWLEs. Noticeably, the spectral profiles did not shift with the excitation position. However, with an increase of light propagation distance, the PL intensity gradually decreased due to propagation-induced optical loss (Figure 4.18c, d). By fitting of an exponential decay function, $I_{out}/I_{in} = \exp^{(-\alpha D)}$, where D is the distance between the illuminated position and the signal collection point of the crystal, the loss coefficient α' (where α'=4.34α) were determined to be as low as 0.3260 dB/µm and 0.2158 dB/µm for BT2O3Cz and BT2O6Cz respectively (Figure 4.19a, b).[56] These data suggest good optical wave-guiding performance of these crystalline organic phosphorescent micro-rods (Figure 4.19c, d). Notably, these α' values are lower than most of state-of-the art 1D optical waveguide materials such as solvate crystals, metal-organic

framework and hybrid perovskite crystals.[57,58] These results confirm the triplet-harvesting light propagation ability of microcrystals suitable for photonic device applications.

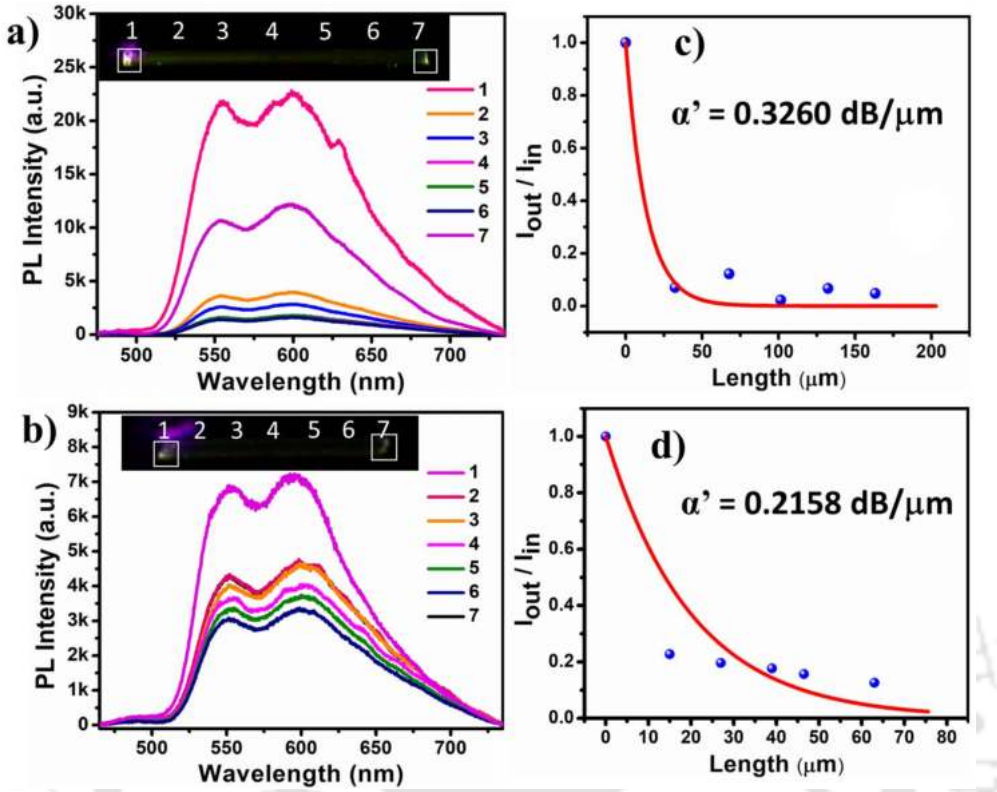

Figure 4.19. (a & b) Spatially resolved PL spectra obtained at each point keeping the excitation position constant. (c & d) Estimation of the optical loss coefficient (α') from the plot of Iout/Iin versus the light propagation distance

4.4. Conclusion

In summary, four through-space charge transfer (TSCT) OSMWLE materials, BT2OxCz (alkyl spacer x = 3, 4, 5 and 6) were reported, that displayed multi-functional properties involving hot-excitons contributions i.e. high lying S_n (singlet) and T_m (triplet) manifold via charge-separated states. The bridging alkyl chain-length between D-A and a trace amount of carbazole isomer plays a crucial role to control the excited state relaxation processes and fine tunes the emission behaviour in solid state and PMMA doped film states, respectively. The integrated heavy atom free and amorphous OSMWLEs with shorter chain BT2O3Cz, BT2O4Cz and BT2O5Cz displayed TADF-RTP while longer chain BT2O6Cz was more susceptible to exhibit intense RTP at ambient conditions. Notably, two distinct fast/slow phosphorescences were realized where the fast phosphorescence was inherited by trace amounts of isomeric impurities of commercial carbazole, while H-/J-aggregation

results in slow phosphorescence. Theoretical studies provided valuable information on effective manifold ISC channel and narrow ΔE_{ST} values (0.02/0.50 and 0.12/0.71 eV) strongly supporting the experimental results in the isolated and dimeric form of the emitters from their single crystal geometry. Transient PL studies revealed the co-existence of thermally elevated fluorescence-phosphoresce at the same time. Remarkably, the single-crystal structure illustrates that aggregation induced densely packed supramolecular crystals of BT2O3Cz and BT2O6Cz exhibited self-guided triplet-harvesting light propagation capability along the primary growth direction with low optical loss coefficient. Overall, this new approach presents a unique strategy to obtain efficient photonic materials by stressing the importance of modulating and optimizing the bridging groups to achieving multi-emissions in a single molecule. The multifunctional OSMWLEs based on dual fluorescence and dual phosphorescence from a single component system demonstrates the first example of simultaneous observation of LE, TADF, RTDP and optical wave-guiding properties.

4.5. References

[1] Y. Liu, M. Nishiura, Y. Wang, Z. Hou, *J. Am. Chem. Soc*., 2006, **128**, 5592-5593.

[2] G. M. Farinola, R. Ragni*, Chem. Soc. Rev*., 2011, **40**, 3467-3482.

[3] P. Lehner, C. Staudinger, S. M. Borisov, I. Klimant, *Nat. Commun*., 2014, **5**, 4460.

[4] L. Bian, H. Shi, X. Wang, K. Ling, H. Ma, M. Li, Z. Cheng, C. Ma, S. Cai, Q. Wu, N. Gan, X. Xu, Z. An, *J. Am. Chem. Soc.,* 2018, **140**, 10734-10739.

[5] T. Maldiney, A. Bessière, J. Seguin, E.Teston, S. K. Sharma, B. Viana, A. J. J. Bos, P. Dorenbos, M. Bessodes, D. Gourier, D. Scherman, C. Richard, *Nat. Mater.,* 2014, **13**, 418-426.

[6] W.-L. Zhou, Y. Chen, Q. Yu, H. Zhang, Z.-X. Liu, X.-Y. Dai, J.-J. Li, Y. Liu, *Nat. Commun.,* 2020, **11**, 4655.

[7] a) H. Liu, Z. Lu, Z. Zhang, Y. Wang, H. Zhang, *Angew. Chem. Int. Ed.,* 2018, **57**, 8448-8452; b) Z. Lu, Y. Zhang, H. Liu, K. Ye, W. Liu, H. Zhang, *Angew. Chem. Int. Ed*., 2020, **59**, 4299–4303.

[8] S. Shao, J. Ding, L. Wang, X. Jing, F. Wang, *J. Am. Chem. Soc.,* 2012, **134**, 20290-20293.

[9] a) Y. Yang, M. Lowry, C. M. Schowalter, S. O. Fakayode, J. O. Escobedo, X. Xu, H. Zhang, T. J. Jensen, F. R. Fronczek, I. M. Warner, R. M. Strongin, *J. Am. Chem. Soc.,* 2006, **128**, 14081-14092; b) S. Basak, YSLV Narayana, M. Baumgarten, K. Müllen, R. Chandrasekar, *Macromolecules,* 2013, **46**, 362-369.

[10] Y.-H. Chen, K.-C. Tang, Y.-T. Chen, J.-Y. Shen, Y.-S. Wu, S.-H. Liu, C.-S. Lee, C.-H. Chen, T.-Y. Lai, S.-H. Tung, R.-J. Jeng, W.-Y. Hung, M. Jiao, C.-C. Wu, P.-T. Chou, *Chem. Sci.,* 2016, **7**, 3556-3563.

[11] H. Naito, K. Nishino, Y. Morisaki, K. Tanaka, Y. Chujo, *Angew. Chem., Int. Ed.,* 2017, **56**, 254-259.

[12] D. K. Maiti, R. Bhattacharjee, A. Datta, A. Banerjee, *J. Phys. Chem. C,* 2013, **117**, 23178-23189.

[13] K.-C. Tang, M.-J. Chang, T.-Y. Lin, H.-A. Pan, T.-C. Fang, K.-Y. Chen, W.-Y. Hung, Y.-H. Hsu, P.-T. Chou, *J. Am. Chem. Soc*., 2011, **133**, 17738-17745.

[14] Z. Xie, C. Chen, S. Xu, J. Li, Y. Zhang, S. Liu, J. Xu, Z. Chi, *Angew. Chem. Int. Ed*., 2015, **54**, 7181-7184.

[15] C. A. Masmanidis, H. H. Jaffe, R. L. Ellis, *J. Phys. Chem.,* 1975, **79**, 2052-2061.

[16] M. A. El-Sayed, *Acc. Chem. Res.* 1971, **4**, 23-31.

[17] D. Lee, O. Bolton, B. C. Kim, J. H. Youk, S. Takayama, J. Kim, *J. Am. Chem. Soc*., 2013, **135**, 6325-6329.

[18] H. A-Attar, A. Monkman, *Adv. Funct. Mater.,* 2012, **22**, 3824-3832.

[19] L. Zhan, Z. Chen, S. Gong, Y. Xiang, F. Ni, X. Zeng, G. Xie, C. Yang, *Angew. Chem., Int. Ed.,* 2019, **58**, 17651-17655.

[20] H.-T. Feng, J. Zeng, P.-A. Yin, X.-D. Wang, Q. Peng, Z. Zhao, J. W. Y. Lam, B. Z. Tang, *Nat. Commun.,* 2020, **11**, 2617.

[21] Z. Mao, Z. Yang, Y. Mu, Y. Zhang, Y.-F. Wang, Z. Chi, C.-C. Lo, S. Liu, A. Lien, J. Xu, *Angew. Chem., Int. Ed.,* 2015, **54**, 6270-6273.

[22] L. Huang, L. Liu, X. Li, H. Hu, M. Chen, Q. Yang, Z. Ma, X. Jia, *Angew. Chem., Int. Ed.,* 2019, **58**, 16445-16450.

[23] X.-K. Chen, D. Kim, J.-L. Brédas, *Acc. Chem. Res.,* 2018, **51**, 2215-2224.

[24] H. Uoyama, K. Goushi, K. Shizu, H. Nomura, C. Adachi, *Nature,* 2012, **492**, 234-238.

[25] Y. Im, M. Kim, Y. J. Cho, J.-A. Seo, K. S. Yook, J. Y. Lee, *Chem. Mater.,* 2017, **29**, 1946-1963.

[26] A. Pershin, D. Hall, V. Lemaur, J.-C. Sancho-Garcia, L. Muccioli, E. Zysman-Colman, D. Beljonne, Y. Olivier, *Nat. Commun.,* 2019, **10**, 597.

[27] O. Bolton, K. Lee, H.-J. Kim, K. Y. Lin, J. Kim, *Nat. Chem*., 2011, **3**, 205.

[28] W. Zhao, Z. He, J. W. Y. Lam, Q. Peng, H. Ma, Z. Shuai, G. Bai, J. Hao, B. Z. Tang, *Chem,* 2016, **1**, 592.

[29] H. Han, E.-G. Kim, *Chem. Mater.,* 2019, **31**, 6925-6935.

[30] (a) Y. Xie, Y. Ge, Q. Peng, C. Li, Q. Li, Z. Li, *Adv. Mater.,* 2017, **29**, 1606829. (b) J. Yang, X. Zhen, B. Wang, X. Gao, Z. Ren, J. Wang, Y. Xie, J. Li, Q. Peng, K. Pu, Z. Li, *Nat. Commun.,* 2018, **9**, 840.

[31] C. Chen, Z. Chi, K. C. Chong, A. S. Batsanov, Z. Yang, Z. Mao, Z. Yang, B. Liu, *Nat. Mater.,* 2020, **20**, 175.

[32] C. Chen, K. C. Chong, Y. Pan, G. Qi, S. Xu, B. Liu, *ACS Materials Lett.,* 2021, **3**, 1081-1087.

[33] W. Zhao, T. S. Cheung, N. Jiang, W. Huang, J. W. Y. Lam, X. Zhang, Z. He, B. Z. Tang, *Nat. Commun.,* 2019, **10**, 1595.

[34] S. Hayashi, S. -Y. Yamamoto, D. Takeuchi, Y. Ie, K. Takagi, *Angew. Chem. Int. Ed.,* 2018, **57**, 17002-17008.

[35] F. Di Benedetto, A. Camposeo, S. Pagliara, E. Mele, L. Persano, R. Stabile, R. Cingolani, D. Pisignano, *Nat. Nanotechnol.,* 2008, **3**, 614 – 619.

[36] J. M. Halabi, E. Ahmed, L. Catalano, D. P. Karothu, R. Rezgui, P. Naumov, *J. Am. Chem. Soc.,* 2019, **141**, 14966−14970.

[37] B. Xu, Y. Mu, Z. Mao, Z. Xie, H. Wu, Y. Zhang, C. Jin, Z. Chi, S. Liu, J. Xu, Y.-C. Wu, P.-Y. Lu, A. Lien, M. R. Bryce, *Chem. Sci.,* 2016, **7**, 2201-2206.

[38] Y. Zhang, Y. Miao, X. Song, Y. Gao, Z. Zhang, K. Ye, Y. Wang, *J. Phys. Chem. Lett.,* 2017, **8**, 4808-4813.

[39] B. Xu, H. Wu, J. Chen, Z. Yang, Z. Yang, Y.-C. Wu, Y. Zhang, C. Jin, .-Y. Lu, Z. PChi, S. Liu, J. Xu, M. Aldred, *Chem. Sci.,* 2017, **8**, 1909-1914.

[40] Z. He, W. Zhao, J. W. Y. Lam, Q. Peng, H. Ma, G. Liang, Z. Shuai, B. Z. Tang, *Nat. Commun.,* 2017, **8**, 416.

[41] J. Wang, X. Gu, H. Ma, Q. Peng, X. Huang, X. Zheng, S. H. P. Sung, G. Shan, J. W. Y. Lam, Z. Shuai, B. Z. Tang, *Nat. Commun.,* 2018, **9**, 2963.

[42] I. Bhattacharjee, N. Acharya, H. Bhatia, D. Ray, *J. Phys. Chem. Lett.,* 2018, **9**, 2733-2738.

[43] D. Barman, K. Narang, R. Gogoi, D. Barman, P. K. Iyer, *J. Mater. Chem. C,* 2022, **10**, 8536-8583.

[44] X.-K. Chen, Y. Tsuchiya, Y. Ishikawa, C. Zhong, C. Adachi, J.-L. Brédas, *Adv. Mater.,* 2017, **29**, 1702767.

[45] H. Qian, M. E. Cousins, E. H. Horak, A. Wakefield, M. D. Liptak, I. Aprahamian, *Nat. Chem.,* 2017, **9**, 83-87.

[46] T. Wang, Z. Hu, X. Nie, L. Huang, M. Hui, X. Sun, G. Zhang, *Nat. Commun.,* 2021, **12**, 1364.

[47] M. J. Frisch, et al., Gaussian 16 Revision C.01 (Gaussian, Inc., Wallingford CT, USA, 2016).

[48] Y. Xu, P. Xu, D. Hu, Y. Ma, *Chem. Soc. Rev.,* 2021, **50**, 1030-1069.

[49] T. Lu, F. W. Chen, *J. Comput. Chem.,* 2012, **33**, 580–592.

[50] Z. Yang, Z. Mao, C. Xu, X. Chen, J. Zhao, Z. Yang, Y. Zhang, W. Wu, S. Jiao, Y. Liu, M. P. Aldred, Z. Chi, *Chem. Sci.,* 2019, **10**, 8129-8134.

[51] X.-N. Li, M. Yang, X.-L. Chen, J.-H. Jia, W.-W. Zhao, X.-Y. Wu, S.-S. Wang, L. MengC.-Z. Lu, *Small,* 2019, **15**, 1903270.

[52] Z. An, C. Zheng, Y. Tao, R. Chen, H. Shi, T. Chen, Z. Wang, H. Li, R. Deng, X. Liu and W. Huang, *Nat. Mat, er.,* 2015, **14**, 685-690.

[53] Z. Yang, C. Xu, W. Li, Z. Mao, X. Ge, Q. Huang, H. Deng, J. Zhao, F. L. Gu, Y. Zhang, Z. Chi, *Angew. Chem., Int. Ed.,* 2020, **59**, 17451-17455.

[54] D. Winn, M. F. Doherty, *AIChE J.*, 2000, **46**, 1348-1367.

[55] a) Y. Li, K. Wang, Q. Liao, L. Fu, C. Gu, Z. Yu, H. Fu, *Nano Lett.,* 2021, **21**, 7, 3287–3294. b) M. Godumala, A.V. Kumar, R. Chandrasekar, *J. Mater. Chem.* C, 2021, **9**, 14115-14132. (c) H. Liu , Z. Bian , Q. Cheng , L. Lan , Y. Wang, H. Zhang, *Chem. Sci.,* 2019, **10**, 227-232.

[56] W. Yuan, J. Cheng, X. Li, M. Wu, Y. Han, C. Yan, G. Zou, K. Müllen, Y. Chen, *Angew. Chem., Int. Ed.,* 2020, **59**, 9940−9945.

[57] B. Lu, X. Fang, D. Yan, *ACS Appl. Mater. Interfaces,* 2020, **12**, 31940−31951.

[58] S. Du, S. Ma, B. Xu, W. Tian, *J. Phys. Chem. Lett.,* 2021, **12**, 9233−9238.

Appendix: Additional data for **Chapter 4**

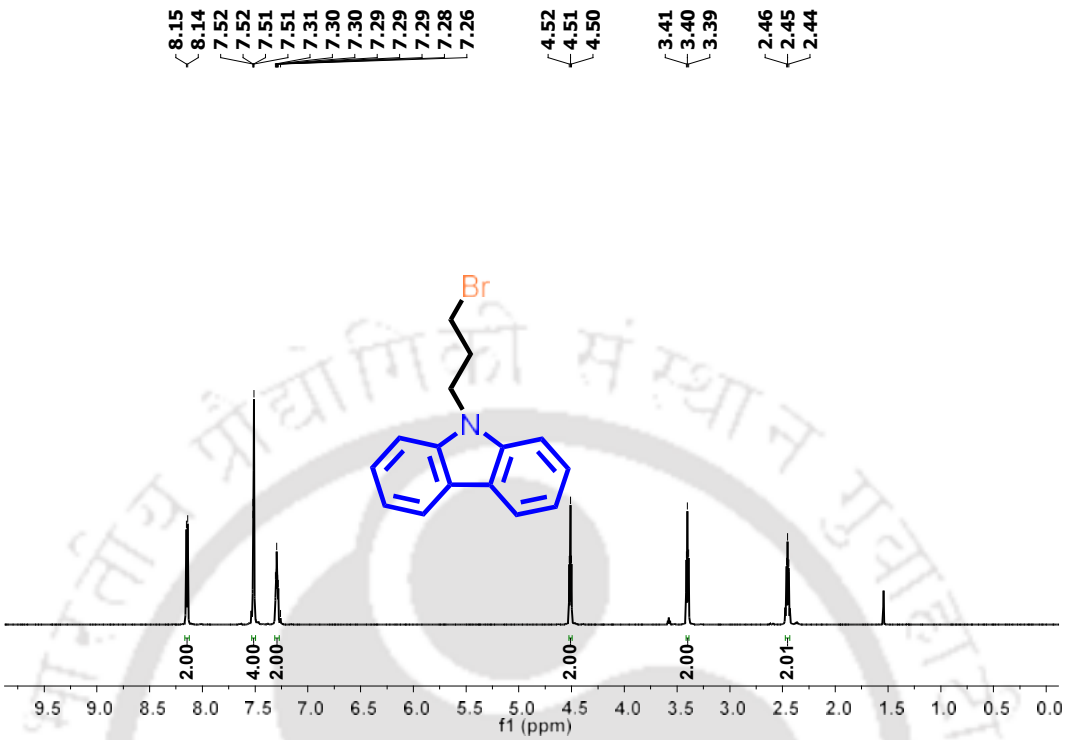

Figure A4.1. ^{1}H NMR spectra of 1,3-CzBr in $CDCl_3$ at 298K.

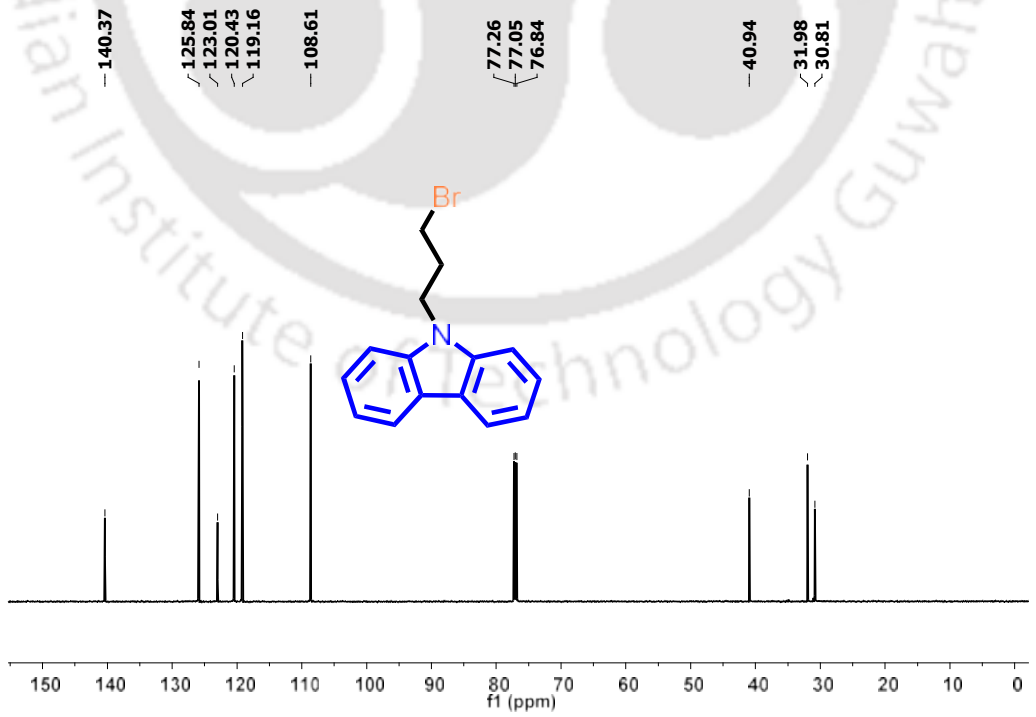

Figure A4.2. ^{13}C- NMR spectra of 1,3-CzBr in CDCl3 at 298K.

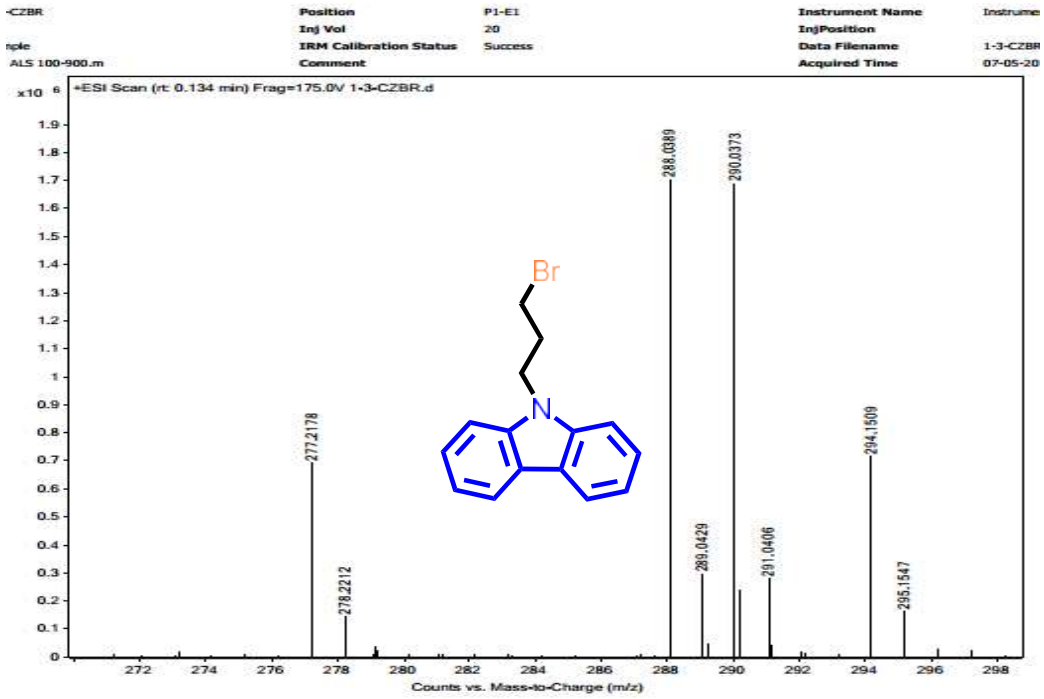

Figure A4.3. HRMS (ESI) peaks of m/z value for $[1,3\text{-CzBr} + H]^+$ (M & M+2) was calculated 288.0388, 290.0367 and observed 288.0389, 290.0373 at 298K in Acetonitrile solvent.

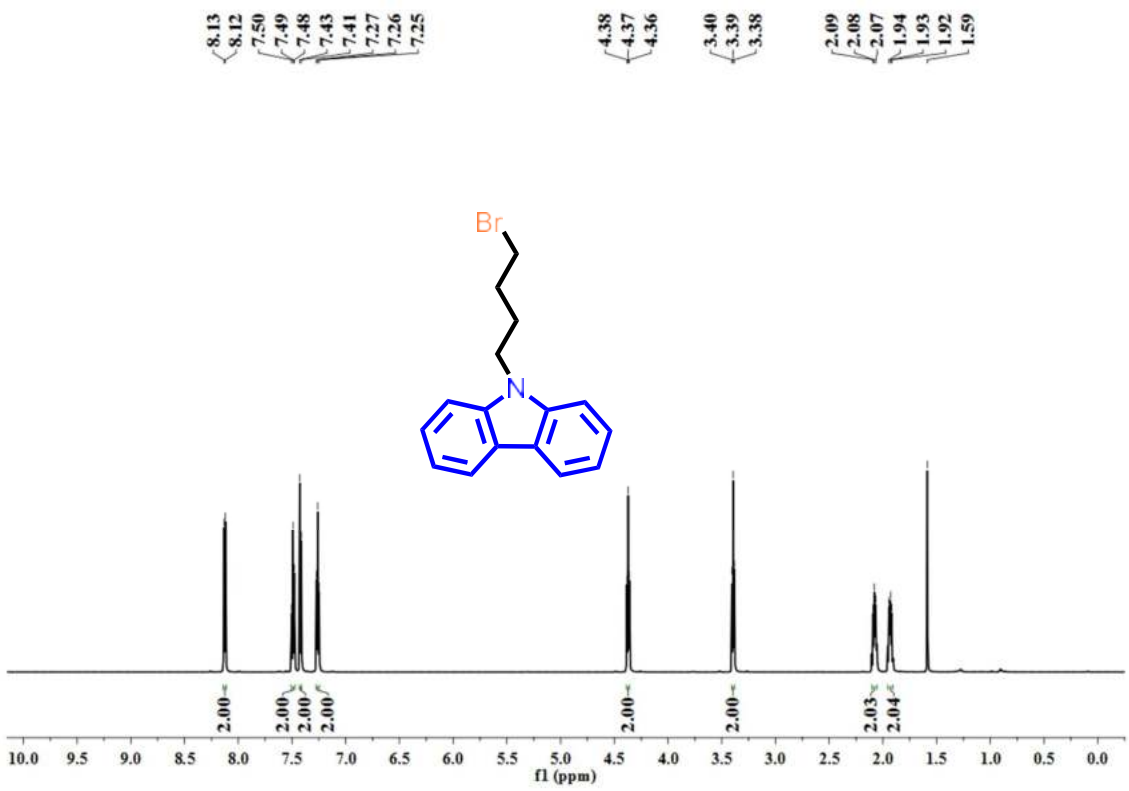

Figure A4.4. ^1H NMR spectra of 1,4-CzBr in $CDCl_3$ at 298K.

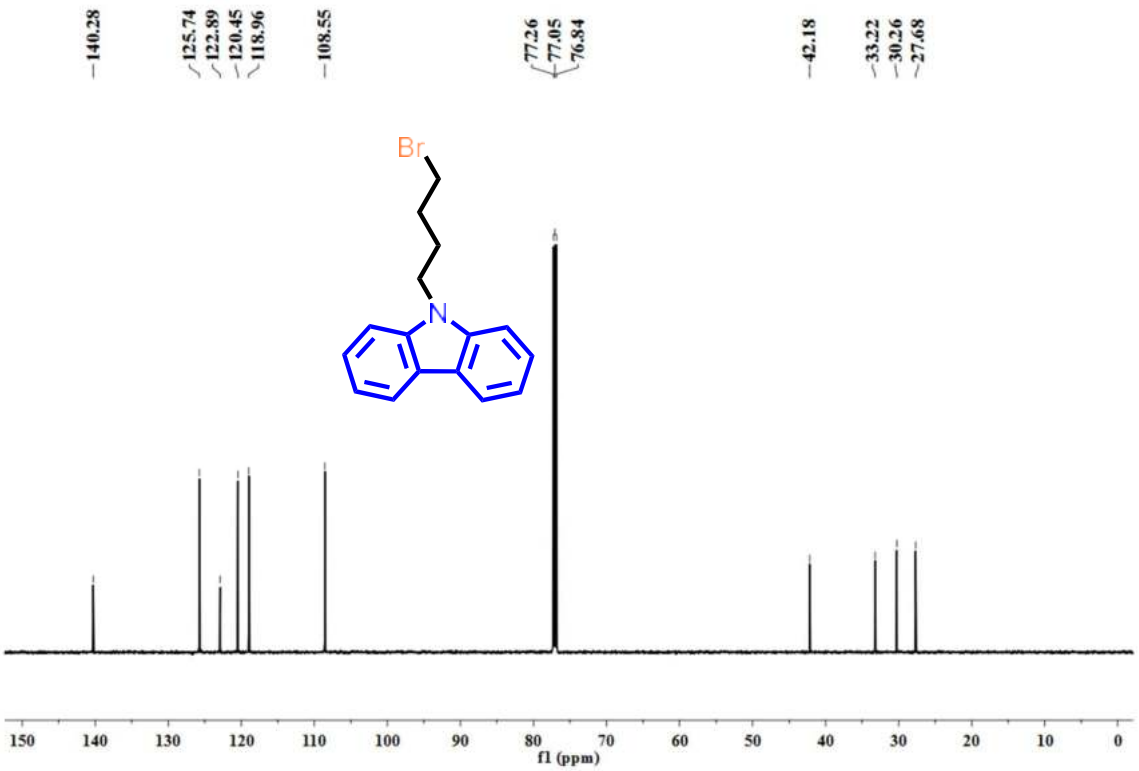

Figure A4.5. ^{13}C NMR spectra of 1,4-CzBr in $CDCl_3$ at 298K.

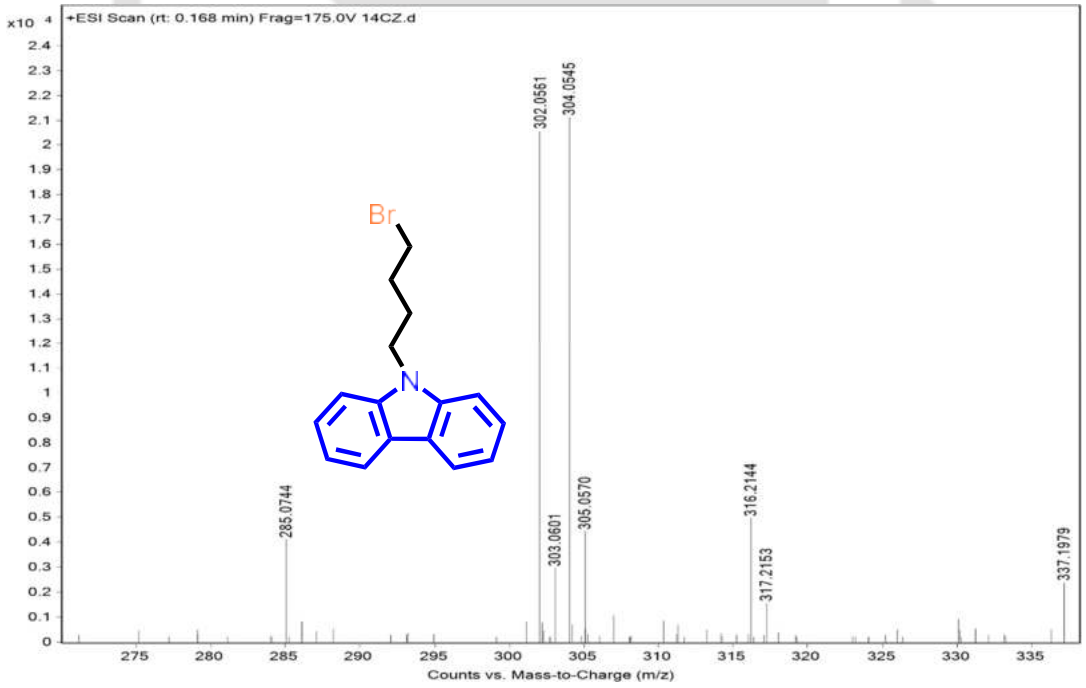

Figure A4.6. HRMS (ESI) peaks of m/z value for $[1,4\text{-CzBr} + H]^+$ (M & M+2) was calculated 302.0544, 304.0524 and observed 304.0561, 304.0545 at 298K in Acetonitrile solvent.

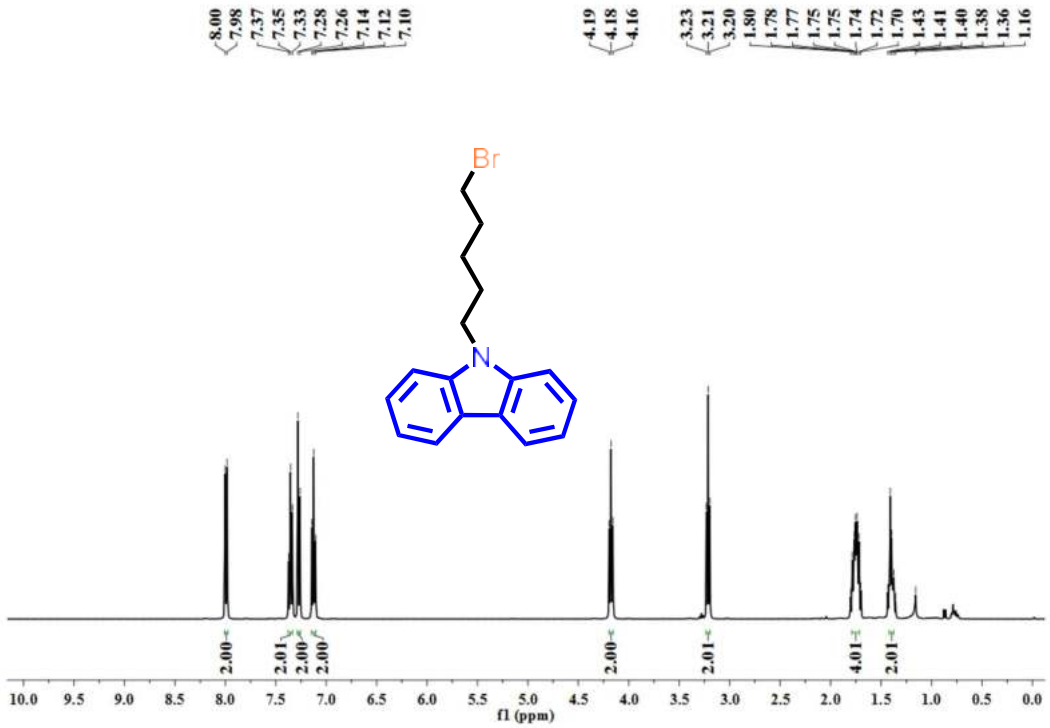

Figure A4.7. ^{1}H NMR spectra of 1,5-CzBr in $CDCl_3$ at 298K.

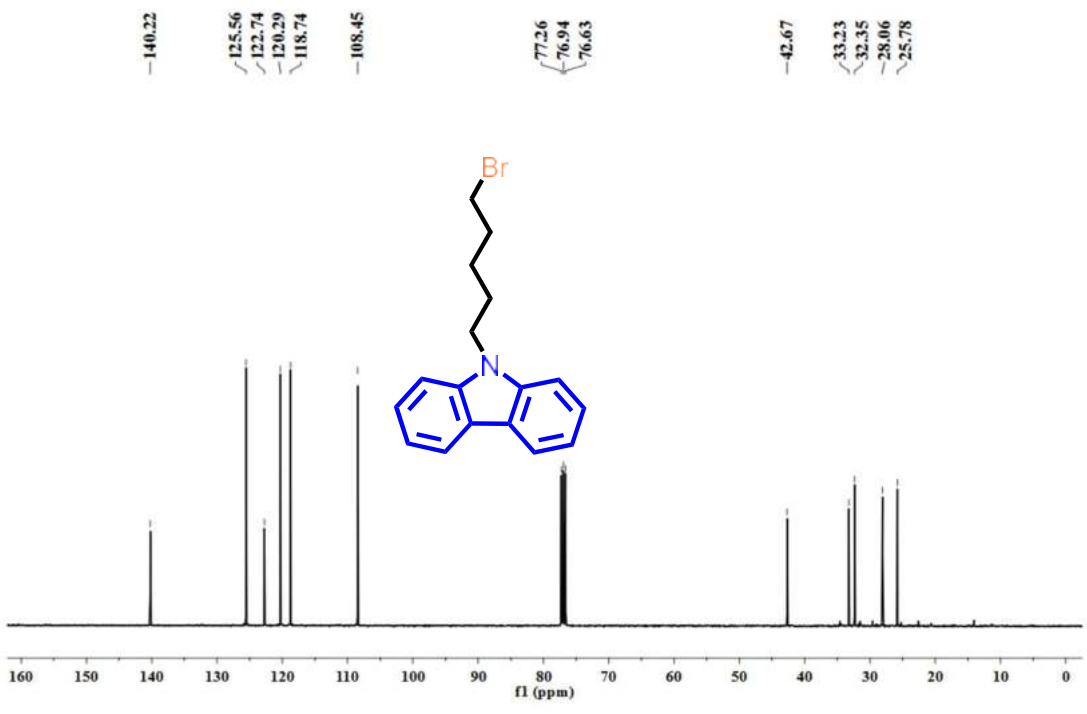

Figure A4.8. ^{13}C- NMR spectra of 1,5-CzBr-Cz in $CDCl_3$ at 298K.

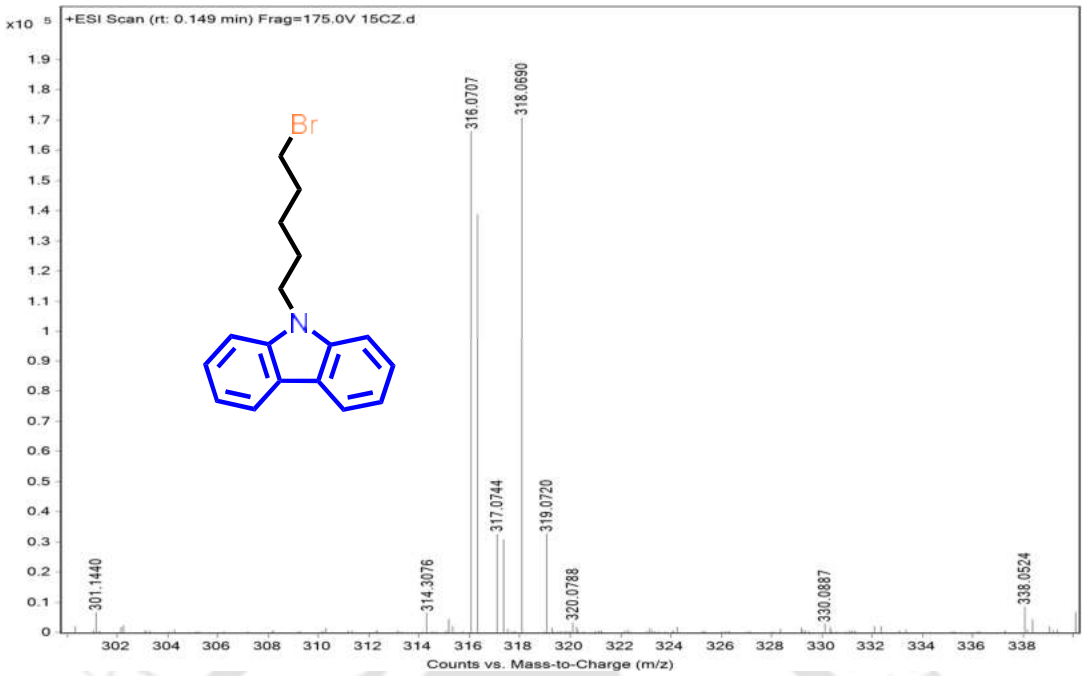

Figure A4.9. HRMS (ESI) peaks of m/z value for $[1,5\text{-CzBr} + H]^+$,(M & M+2) was calculated 316.0701, 318.0680 and observed 316.0707, 318.0690 at 298K in Acetonitrile solvent.

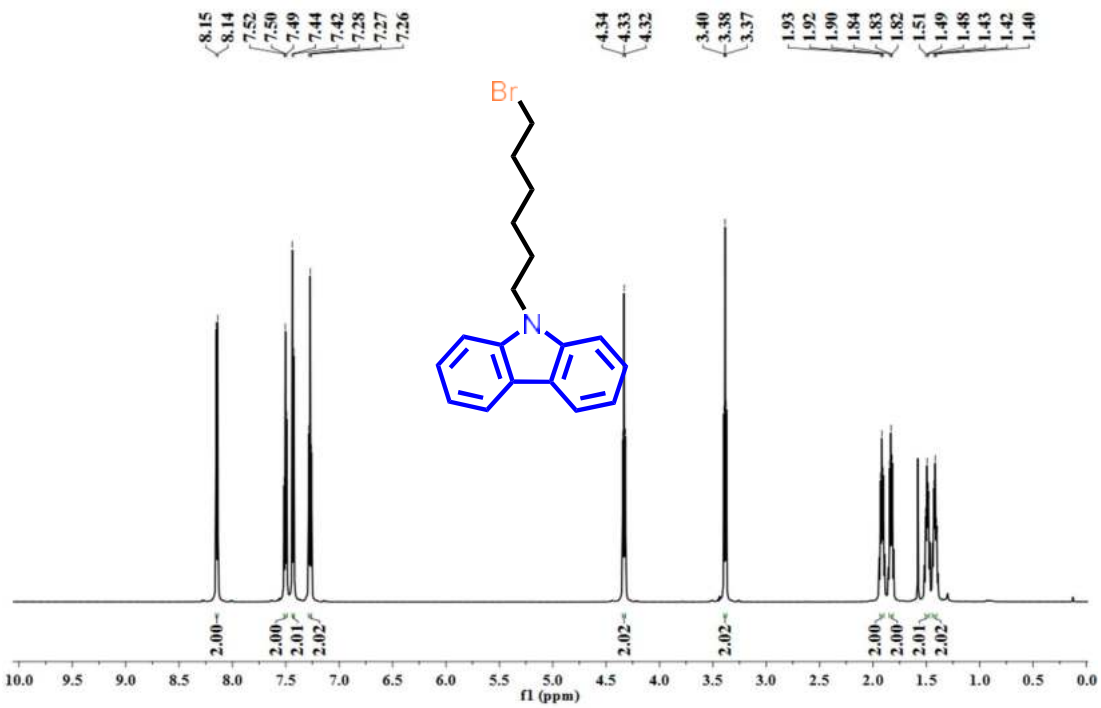

Figure A4.10. ^1H NMR spectra of 1,6-CzBr in $CDCl_3$ at 298K.

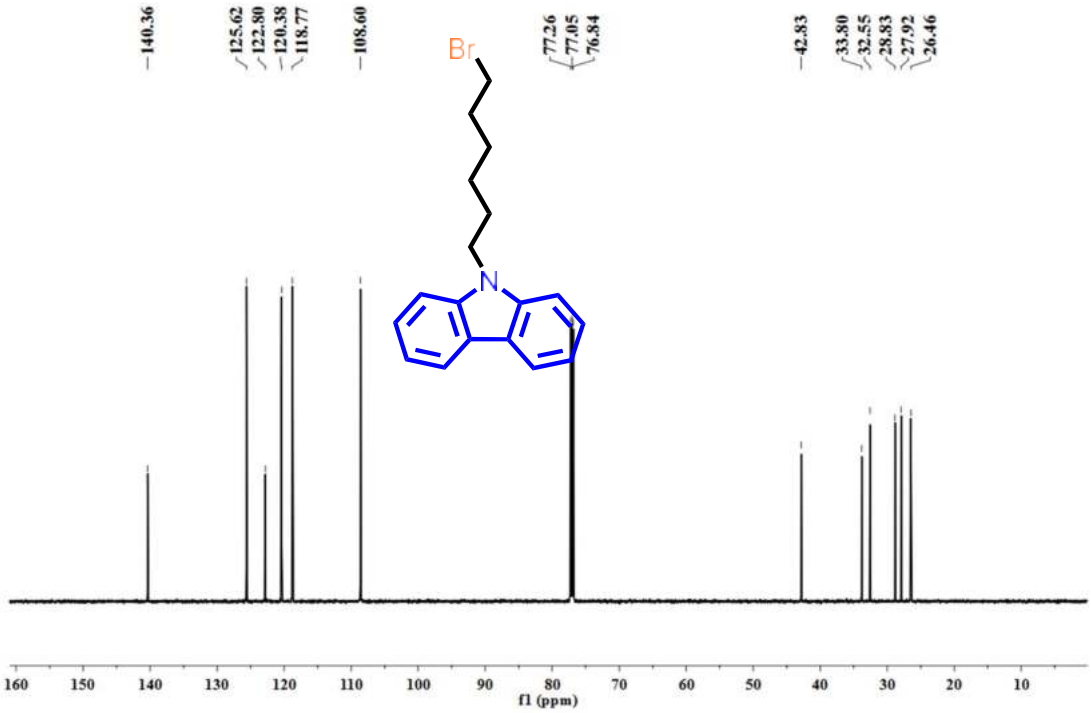

Figure A4.11. ^{13}C- NMR spectra of 1,6-CzBr-Cz in $CDCl_3$ at 298K.

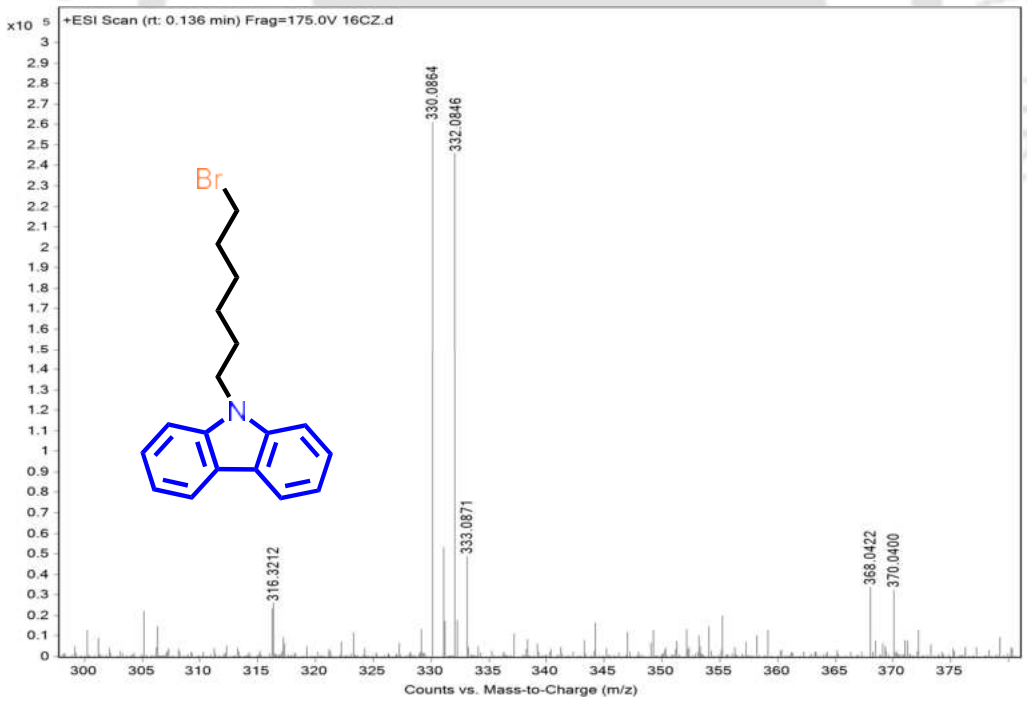

Figure A4.12. HRMS (ESI) peaks of m/z value for [1,6-CzBr + H]+ ,(M & M+2) was calculated 330.0857, 330.0837 and observed 332.0864, 332.0846 at 298K in Acetonitrile solvent.

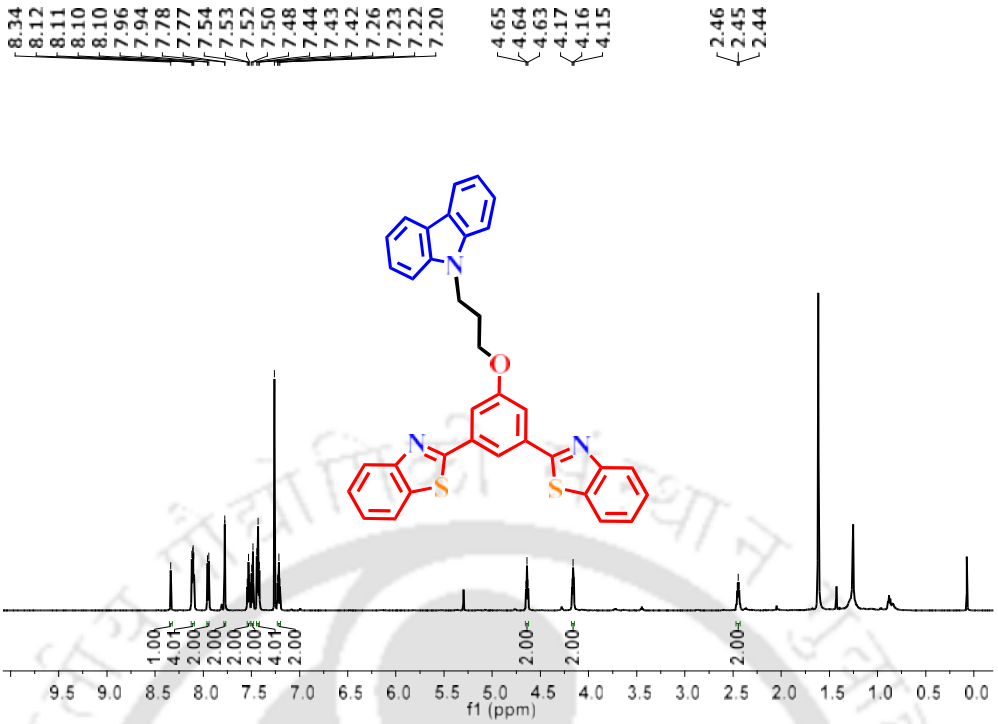

Figure A4.13. ^{1}H NMR spectra of BT2O3Cz in $CDCl_3$ at 298K.

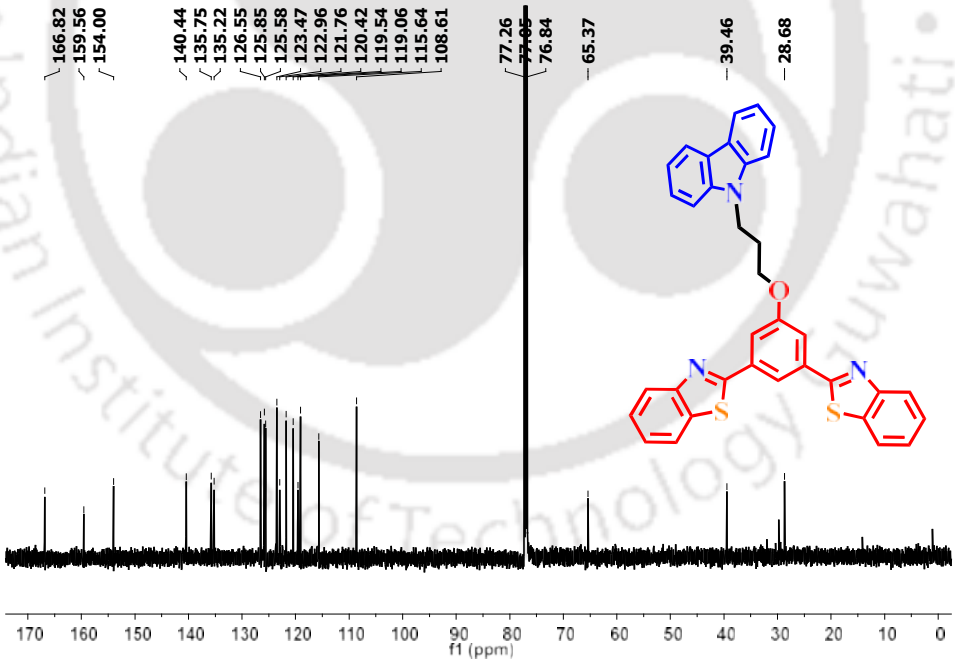

Figure A4.14. ^{13}C- NMR spectra of BT2O3Cz in $CDCl_3$ solvent at 298 K.

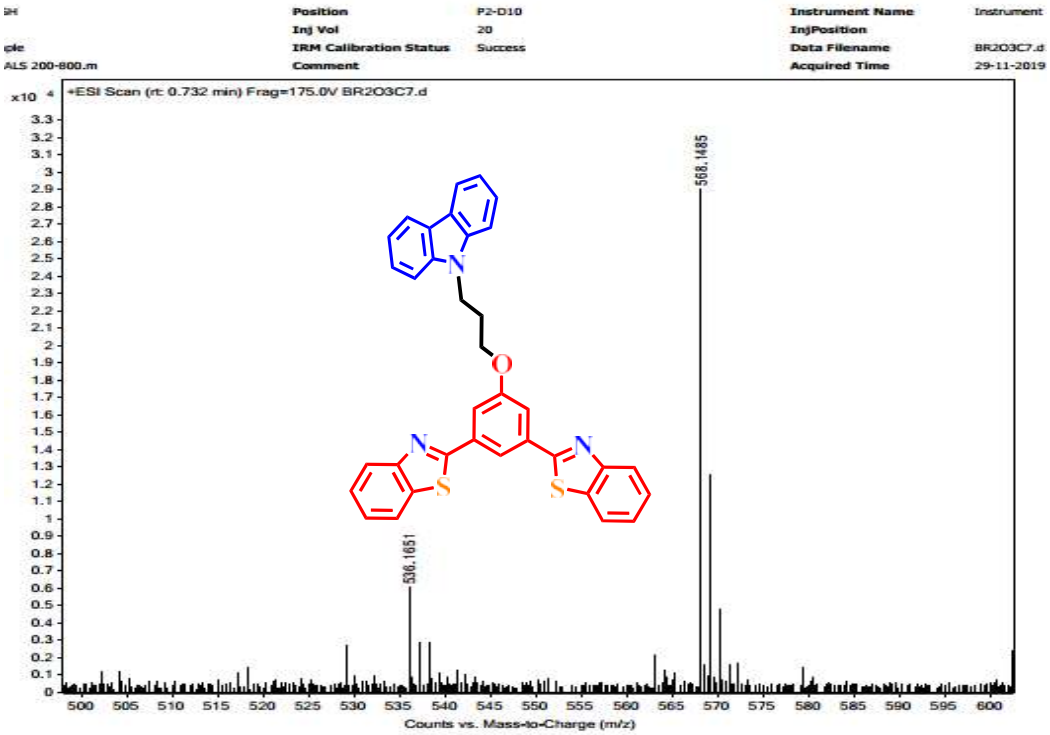

Figure A4.15. HRMS (ESI) peaks of m/z value for $[BT2O3Cz + H]^+$ was calculated 568.1517 and observed 568.1485 at 298K in Acetonitrile solvent.

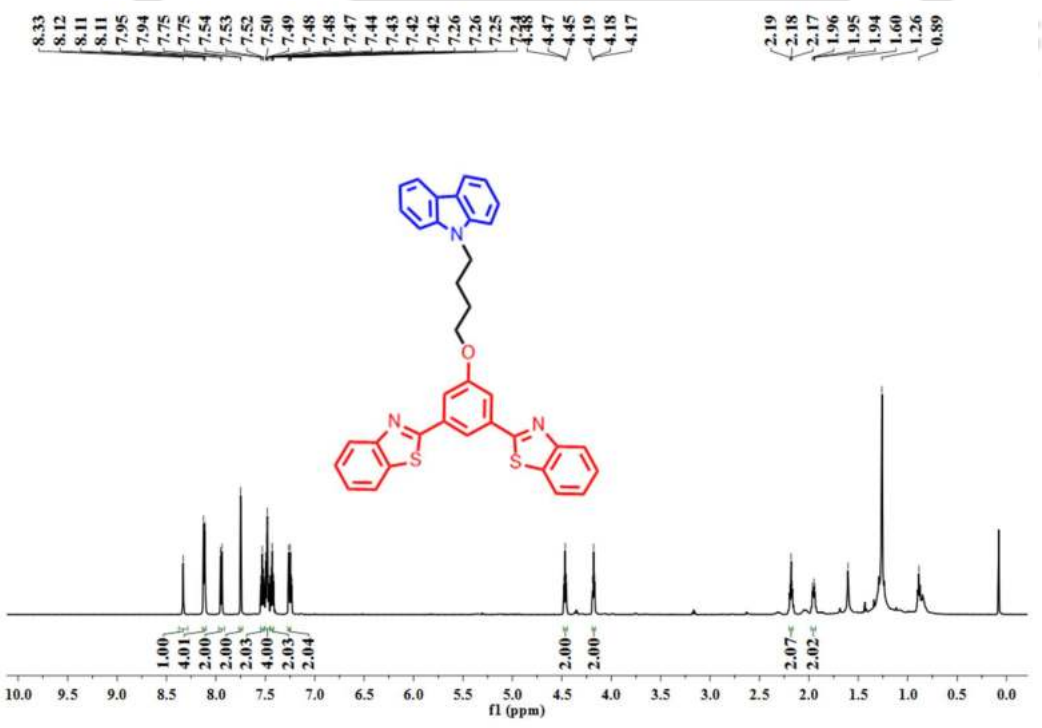

Figure A4.16. ^1H NMR spectra of BT2O4Cz in $CDCl_3$ at 298K.

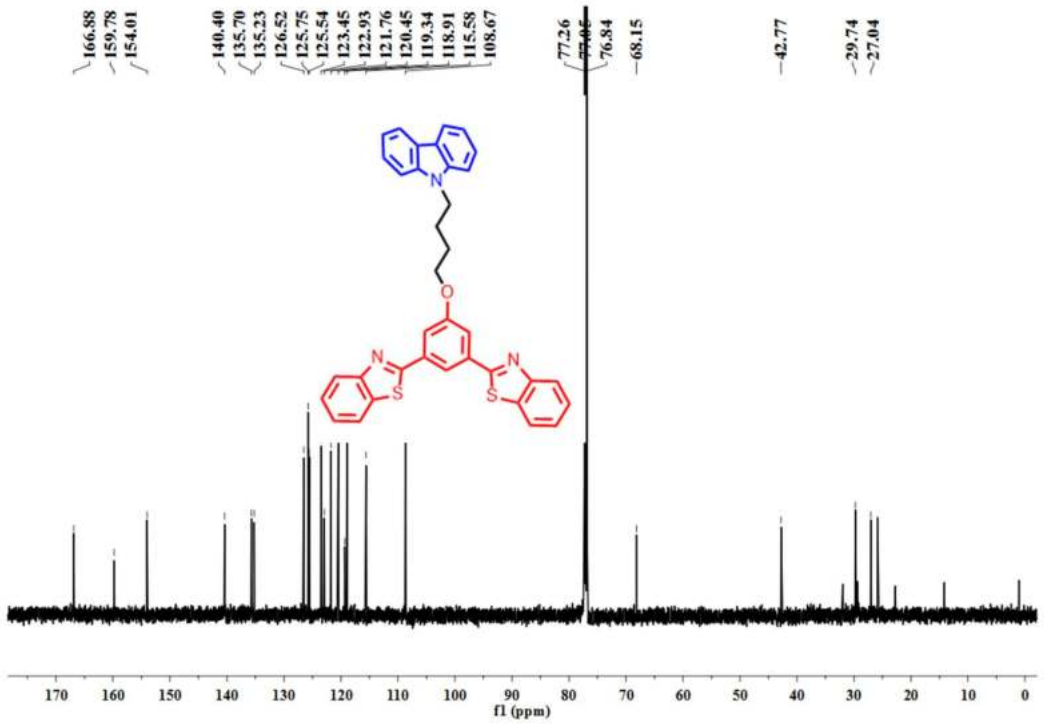

Figure A4.17. ^{13}C- NMR spectra of BT2O4Cz in $CDCl_3$ solvent at 298 K.

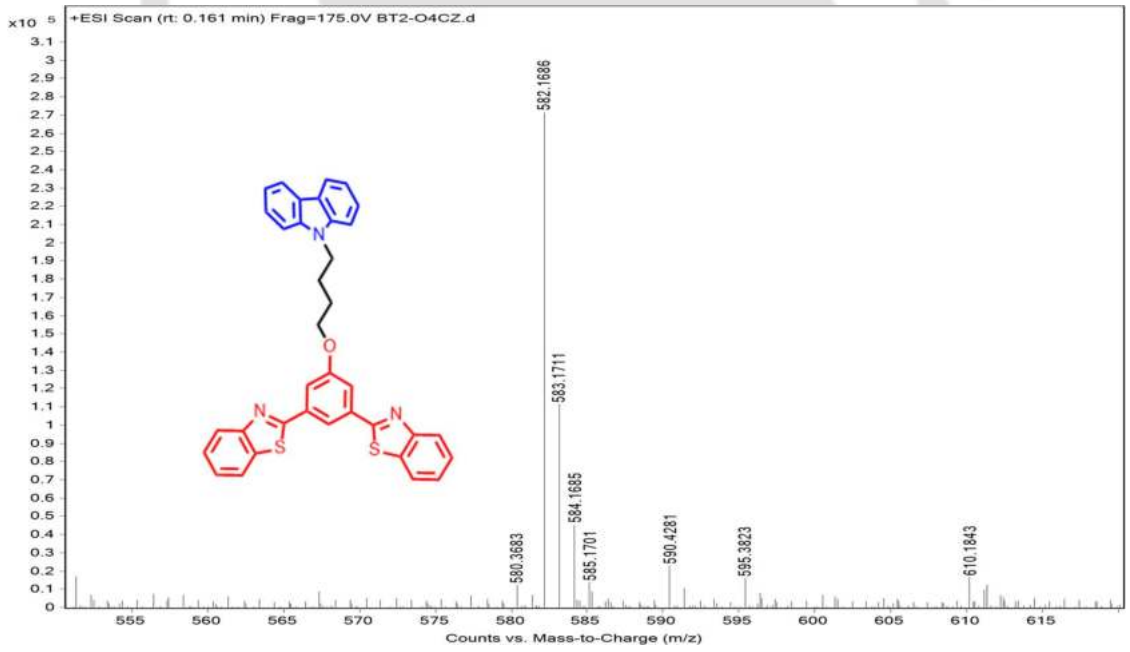

Figure A4.18. HRMS (ESI) peaks of m/z value for $[BT2O4Cz + H]^+$ was calculated 582.1674 and observed 582.1686 at 298K in HPLC Acetonitrile solvent.

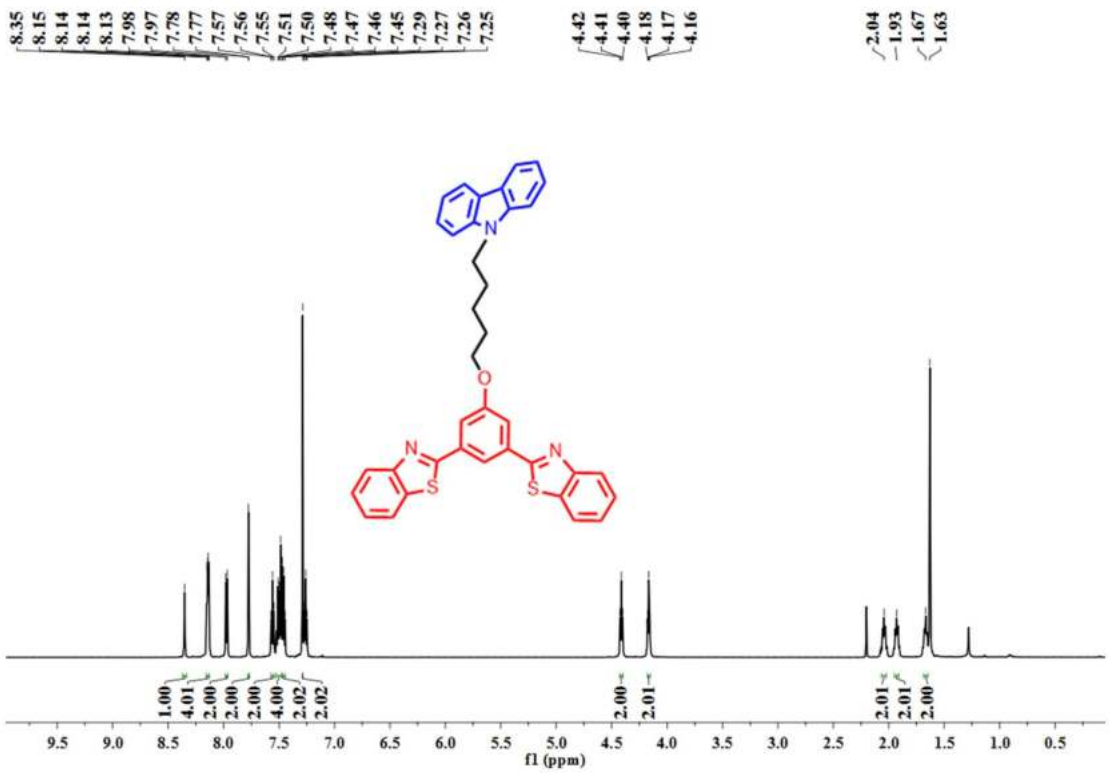

Figure A4.19. ^{1}H NMR spectra of BT2O5Cz in $CDCl_3$ at 298K.

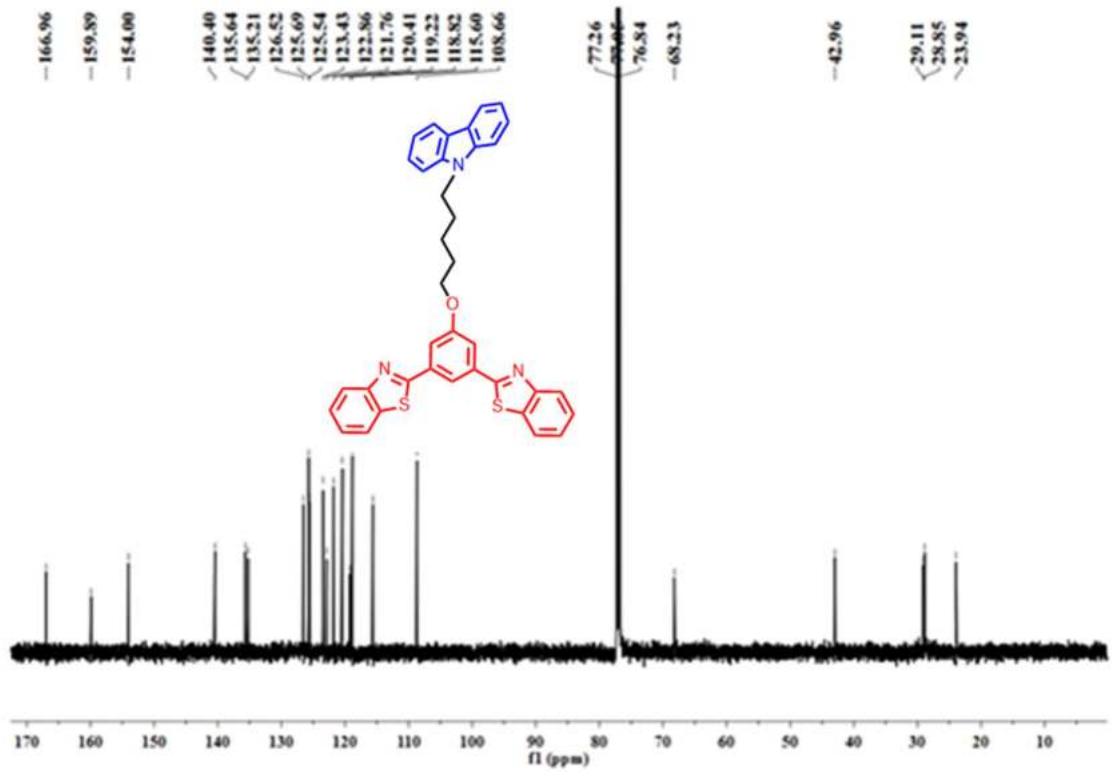

Figure A4.20. ^{13}C- NMR spectra of BT2O5Cz in $CDCl_3$ solvent at 298 K.

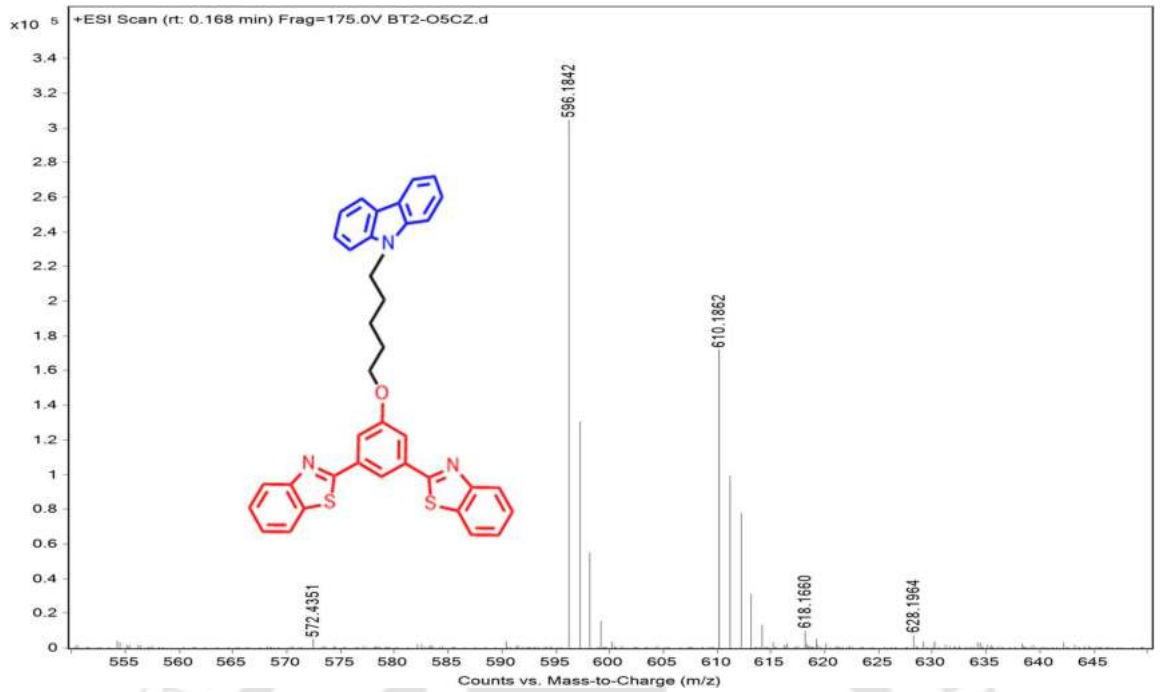

Figure A4.21. HRMS (ESI) peaks of m/z value for $[BT2O5Cz + H]^+$ was calculated 596.1830 and observed 596.1842 at 298K in HPLC Acetonitrile solvent.

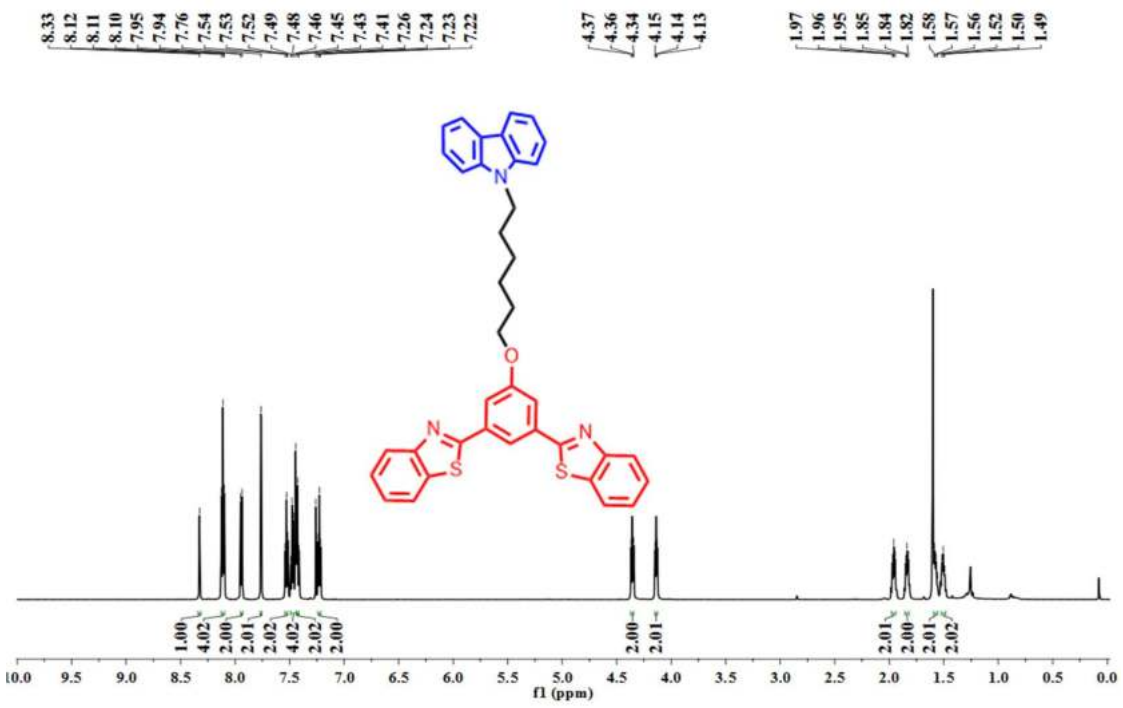

Figure A4.22. ^1H NMR spectra of BT2O6Cz in $CDCl_3$ at 298K.

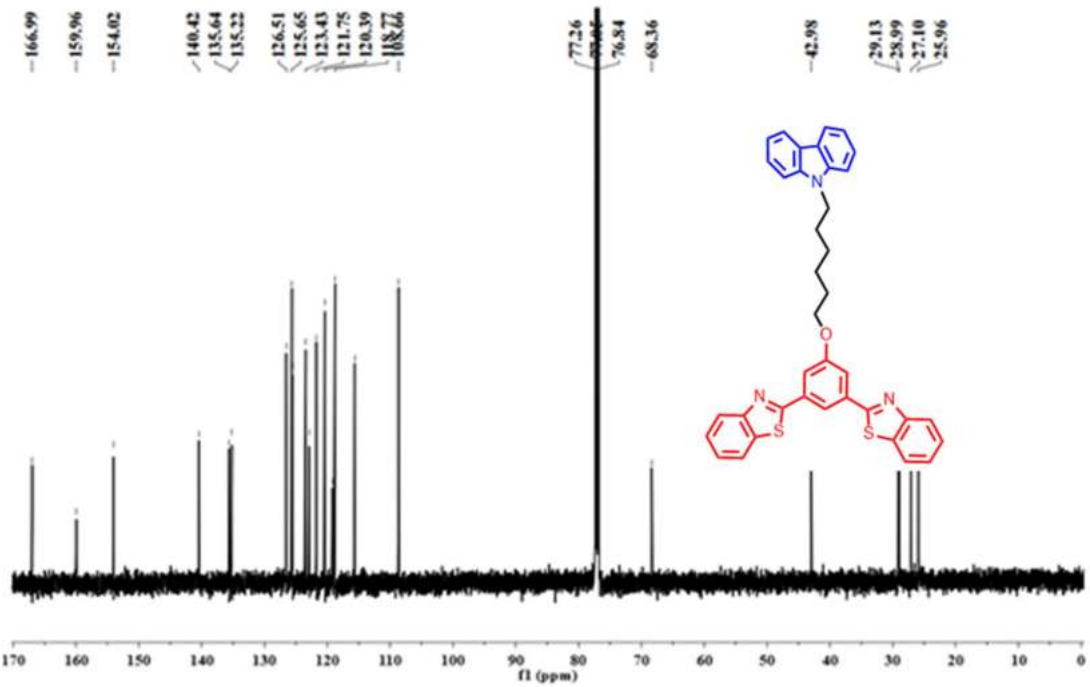

Figure A4.23. ^{13}C- NMR spectra of BT2O6Cz in $CDCl_3$ solvent at 298 K.

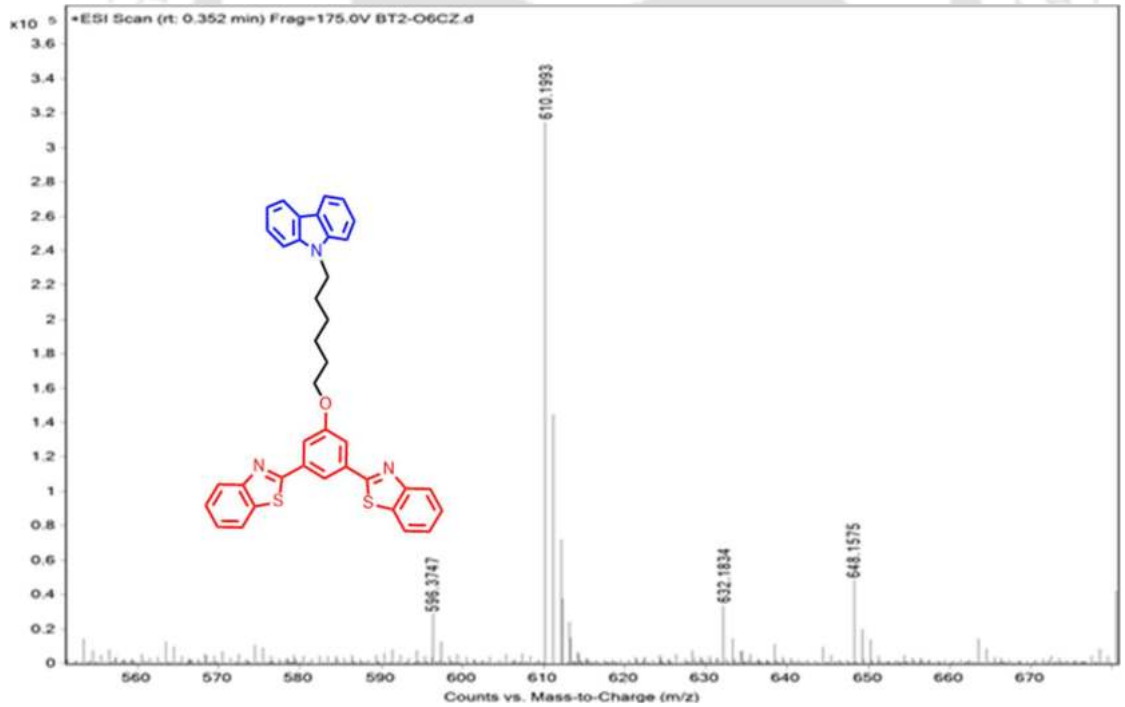

Figure A4.24. HRMS (ESI) peaks of m/z value for $[BT2O6Cz + H]^+$ was calculated 610.1987 and observed 610.1993 at 298K in HPLC Acetonitrile solvent.

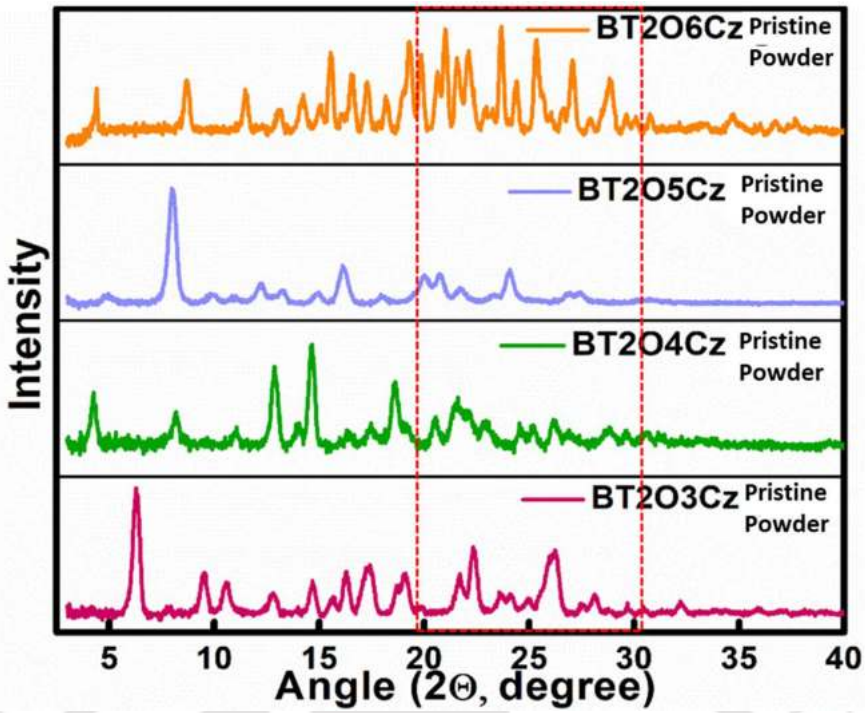

Figure A4.25. PXRD for all the emitters, BT2OxCz (x=3, 4, 5 & 6) at their pristine powder form.

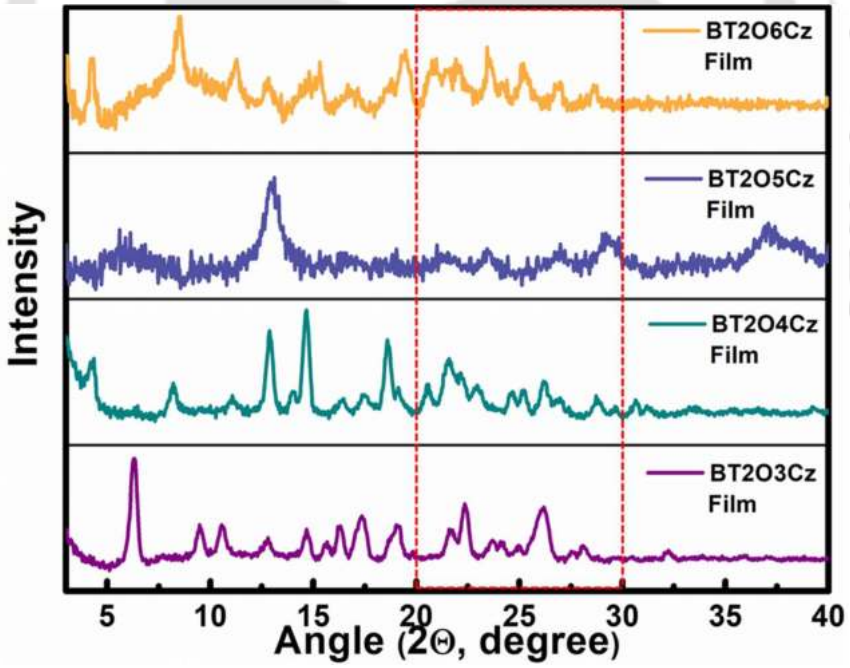

Figure A4.26. Thin film XRD for all the emitters, BT2OxCz (x=3, 4, 5 & 6) at their drop-casted thin film state. In both XRD patterns, the broad peaks observed for BT2O5Cz, whereas, other emitters of BT2OxCz (x =3,4,6) showed sharp diffracting peak patterns at low d-spacing region (marked in red dotted box) depicting high degree of crystallinity of BT2OxCz (n =3,4,6) and amorphous nature of BT2O5Cz.

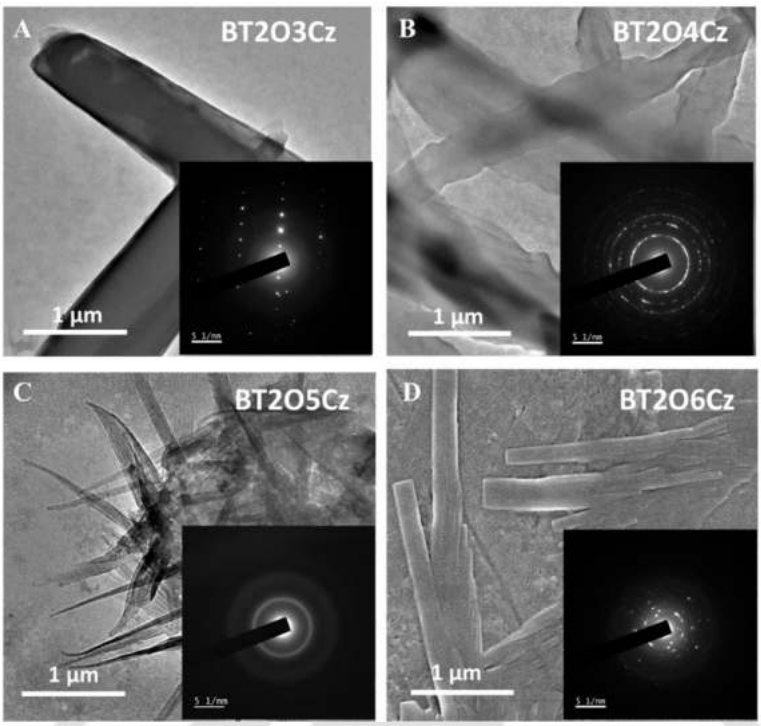

Figure A4.27. FETEM images (inset: SAED images) of BT2OxCz (x=3, 4, 5 & 6). Samples were prepared from THF solution and by drop casting technique on copper grid (400 mesh). All the emitters exhibited nearly similar micro-rod shaped morphology. However, SAED images showed amorphous nature of BT2O5Cz, while all other emitters are found to be crystalline in nature.

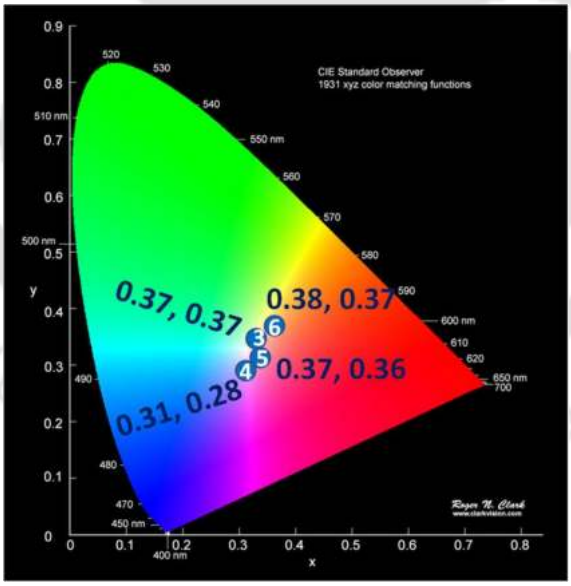

Figure A4.28. CIE diagram plotted for 0.5 % PMMA doped spin coated film for BT2OxCz (x=3, 4, 5 & 6).

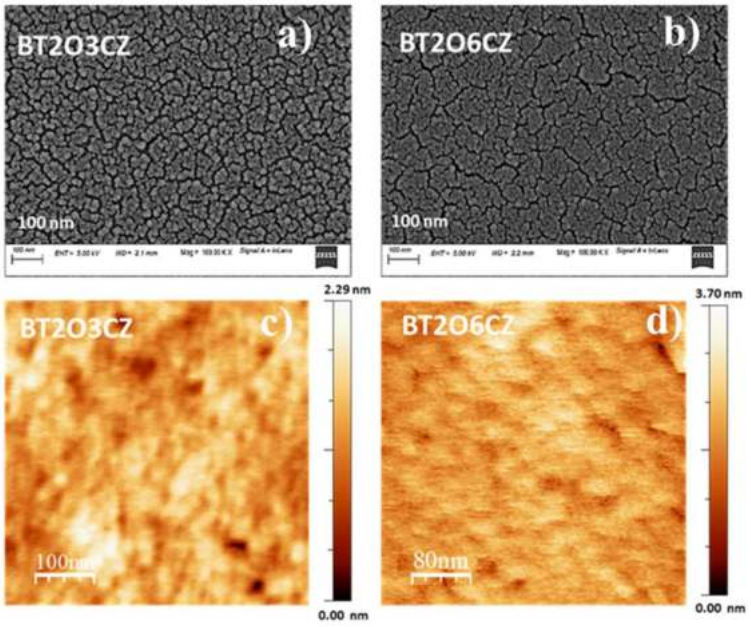

Figure A4.29. AFM images recorded for 0.5 % PMMA doped spin coated film for BT2O3Cz and for BT2O6Cz respectively.

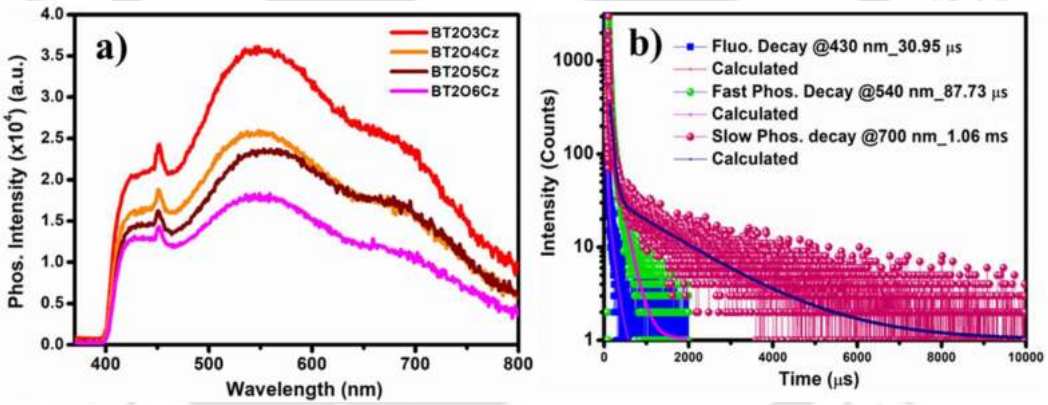

Figure A4.30. (a) Phosphorescence spectra recorded for 5.0 % PMMA doped spin coated film for BT2OxCz (x=3, 4, 5 and 6). (b) Phosphorescence decay recorded for 5.0 % PMMA doped spin coated film for BT2O3Cz for the respective emission band centered at 430, 540 and 700 nm respectively.

Table A4.1. Summary of Excited state kinetics for solid powder form of all the OSMWLEs.

Emitters	k_P ($\times 10^7$ s^{-1})	k_D ($\times 10^5$ s^{-1})	k_F ($\times 10^7$ s^{-1})	k_{IC} ($\times 10^7$ s^{-1})	k_{ISC} ($\times 10^6$ s^{-1})	k_{RISC} ($\times 10^5$ s^{-1})
BT2O3Cz	106	1.47	25.5	80.4	7.5	1.47
BT2O4Cz	24.4	0.91	4.8	3.8	1.53	0.24
BT2O5Cz	18.9	0.46	3.0	15.7	1.25	0.46
BT2O6Cz	32.1	0.48	5.4	26.3	0.75	0.48

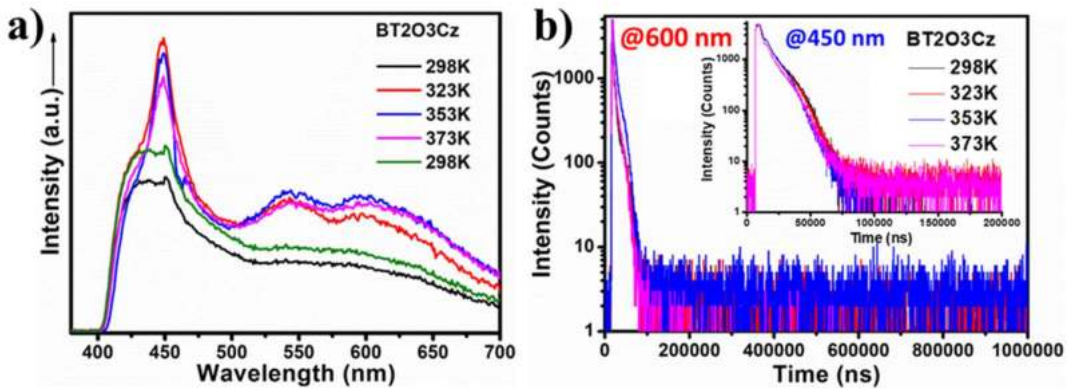

Figure A4.31. (a & b) Phosphorescence spectra and decay recorded at different temperatures for white film for BT2O3Cz for the respective TADF and phosphorescence band centered at 450 and 600 nm respectively.

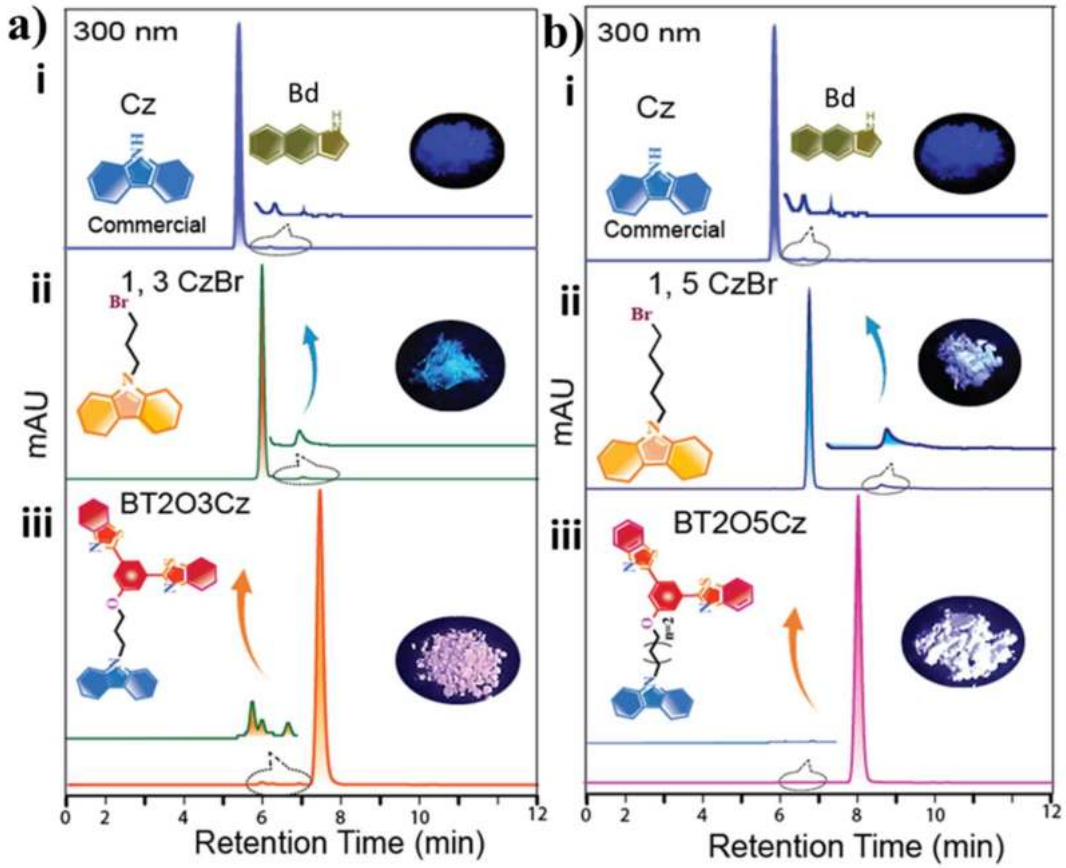

Figure A4.32 (a & b) HPLC spectra of commercial Cz (i), 1,3CzBr, 1,5CzBr crystals(ii) and BT2O3Cz, BT2O5Cz crystals (iii) monitored at 300nm with acetonitrile as eluent. For all the crystals up to final compounds inherits an impurity peak of Bd compounds. Chemical structure of all the compounds were shown with inset photograph of each crystal captured under 365 nm UV-lamp.

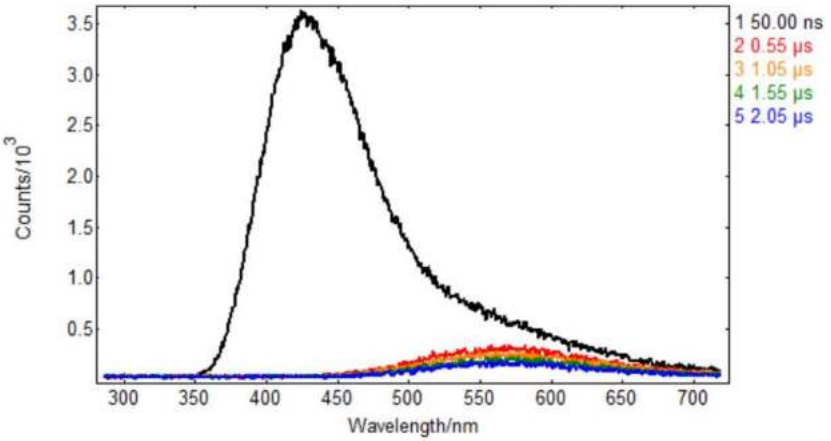

Figure A4.33. LIF spectra of BT2O4Cz acquired at 77K in LP980 at varying delays after the pump pulse (colour coding in the graph). Measurement conditions: λ exc = 355 nm, Spectrograph bandwidth = 2 nm, ICCD gate width = 1 µs, 15 averages / point.

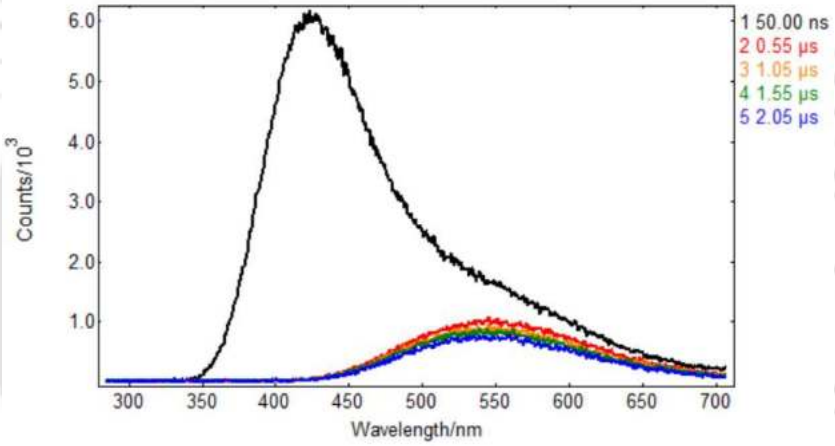

Figure A4.34. LIF spectra of BT2O4Cz acquired at room temperature in LP980 at varying delays after the pump pulse (colour coding in the graph). Measurement conditions: λ exc = 355 nm, Spectrograph bandwidth = 2 nm, ICCD gate width = 1 µs, 15 averages / point.

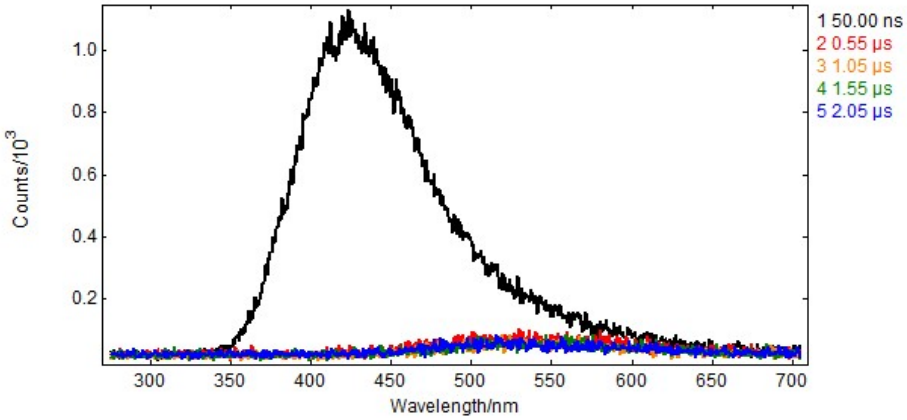

Figure A4.35. LIF spectra of BT2O6Cz acquired at 77K in LP980 at varying delays after the pump pulse (colour coding in the graph). Measurement conditions: λ exc = 355 nm, Spectrograph bandwidth = 2 nm, ICCD gate width = 1 µs, 15 averages / point.

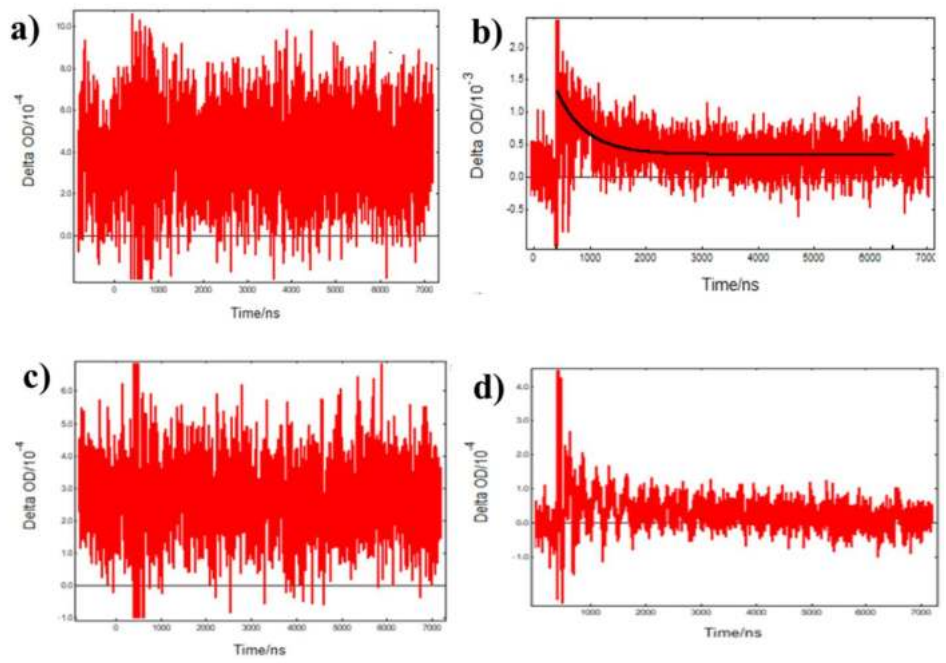

Figure A4.36. Kinetic TA traces of BT2O4Cz and BT2O6Cz at 550 nm measured at (a) 77K and (b) room temperature. Measurement conditions: λ pump = 355 nm, Spectrograph bandwidth = 1.20 nm, 800 averages.

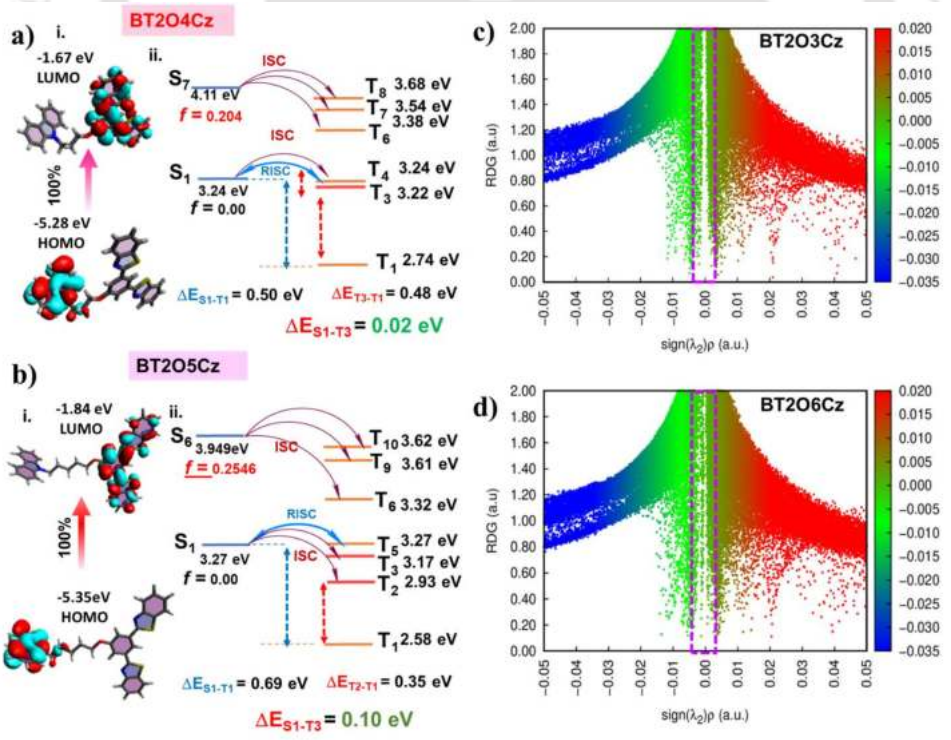

Figure A4.37. Computational calculations: (ai and bi) HOMO and LUMO density distributions with the corresponding band gap profiles, (aii and bii) TDDFT energy transitions dependent oscillator strength (*f*) and possible manifold active ISC channels and energy splitting (ΔE_{ST}) for BT2O4Cz and BT2O5Cz from Gaussian 16 package at B3LYP-6-31G(d,p) level of theory. (c and d) The functions of reduced density gradient (RDG) and Sign $(\lambda_2)\rho$ isosurface map with an isovalue of 0.5 for BT2O4Cz and BT2O5Cz respectively.

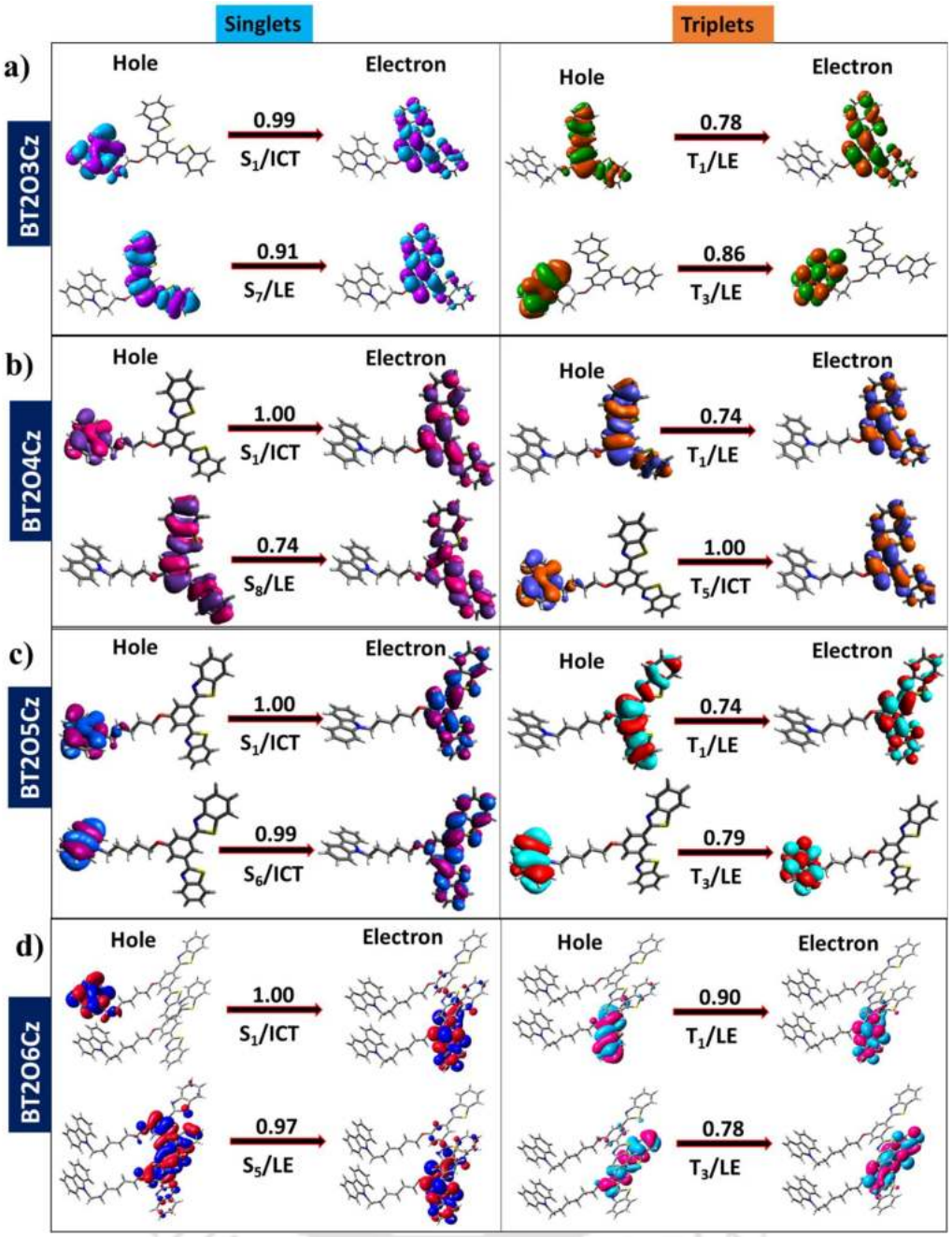

Figure A4.38. Natural transition orbitals (NTOs) for different singlet and triplet excited states in BT2OxCz (x=3,4,5 and 6).

Table A4.10. Crystallographic data and structure refinement parameters of BT2O3Cz and BT2O6Cz crystal.

Compound	**BT2O3Cz**	**BT2O6Cz**
Empirical formula	C35 H25 N3 O S2	C38 H31 N3 O S2
CCDC NO	1969742	1969743
Temperature/K	296	293
Crystal system	monoclinic	orthorhombic
Space group	P 21/c	P c a 21
a/Å	5.737(5)	40.9226(8)
b/Å	19.159(18)	6.2134(1)
c/Å	24.68(2)	11.8600(2)
α/°	90.00	90.00
β/°	96.66(3)	90.00
γ/°	90.00	90.00
Volume/Å^3	2694(4)	3015.63(9)
Z	4	4
ρ_{calc}mg/mm^3	1.400	1.343
m/mm^{-1}	0.234	1.883
F(000)	1184.0	1280.0
Index ranges	-6≤ h ≤ 6, -22 ≤ k ≤ 22, -29 ≤ l ≤ 29	-48 ≤ h ≤ 48, -7 ≤ k ≤ 7, -14 ≤ l ≤ 14
Reflections collected	94738	18331
Independent reflections	4760	5301[2794]
Data/restraints/parameters	4760/0/370	5301/0/397
Goodness-of-fit on F^2	1.045	1.014
Final R indexes	R1 = 0.0850, wR2 = 0.2065	R1 = 0.0547, wR2 = 0.1278

Table A4.11. Summarized table of SCXRD-crystal structural analysis with non covalent interactions, dihedral and slip angle informations.

Single Crystals	Intra-molecular Interactions Close contact distance (Å)					Intermolecular Interactions Close contact distance (Å)					Sweep Angle (Degree)		
	CH-S	CH-N	CH-π	π-CH	$BT_{\pi-\pi}$	$CZ_{C\ H-\pi}$	CH-O	CH-N	CH-π	π-S	BT-BT	Ph-Ph	Cz-Cz
BT2O3Cz	2.743	2.556	2.834	2.726	3.351	-	2.705	2.663	2.792	-	96.19	51.91	47.75
BT2O6Cz	2.643	2.575	2.808	2.752	3.369	2.852.88	2.645	-	2.869	3.310	42.03	37.74	137.86

Table A4.12. Calculated attachment energies of different crystal facets for BT2O3Cz.

hkl	Dhkl/Å	Eatt(Total)/kcal mol^{-1}	Eatt(vdW)/kcal mol^{-1}	% Total facet area
{ 0 1 1 }	15.09541	-73.40388503	-70.00425858	50.61294073
{ 0 0 2 }	12.25673	-59.41677538	-59.91612851	31.19920067
{ 1 0 0 }	5.698286	-169.7176518	-155.2817056	6.91903336
{ 1 1 -1 }	5.461538	-172.7664881	-161.2503639	5.36009409

Table A4.13. Calculated attachment energies of different crystal facets for BT2O6Cz.

hkl	Dhkl/Å	Eatt(Total)/kcal mol^{-1}	Eatt(vdW)/kcal mol^{-1}	% Total facet area
{ 2 0 0}	20.4613	-55.3638598	-48.23128222	52.38292617
{ 2 0 1}	10.26091359	-123.5714912	-108.106391	14.0966025
{ 2 0 -1}	10.26091359	-123.5714912	-108.106391	14.0966025
{ 0 1 0}	6.2134	-177.4611538	-168.3216253	14.36666498

CHAPTER 5

Aggregation-Induced Hot-exciton Emission *via* Suppression of Kasha's Rule in Through-space Donor-alkyl Bridge-Acceptor Molecular Rotor

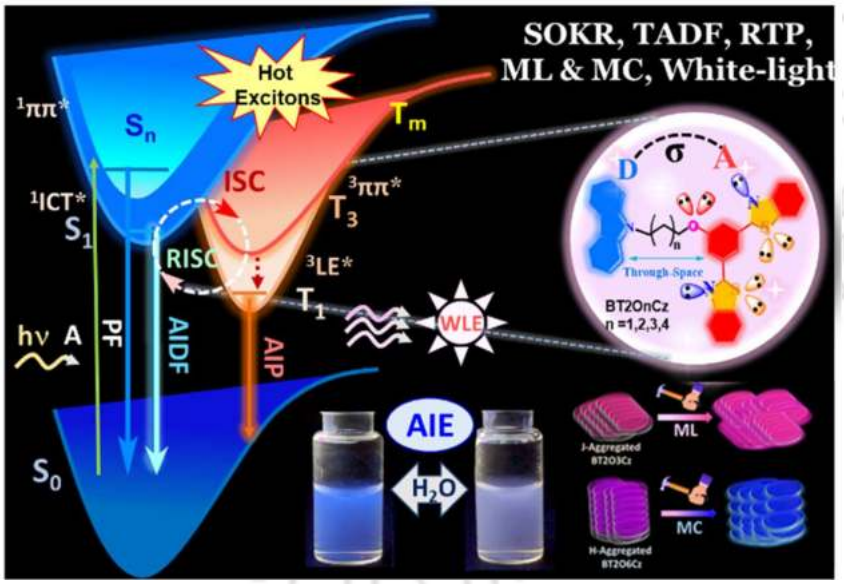

Barman, D., Iyer, P. K. *J. Phys. Chem. C,* **2023**, XX, XXXX (Accepted)

Abstract

The advancement of novel multifunctional emitters and their comprehensive insights into the underlying mechanism for the origin of aggregated state emission in purely organic molecules is a challenging task. This work presents a series of through-space donor-alkyl bridge-acceptor (D-σ-A) luminogens, BT2OxCz [2,2'-(5-(3-(9H-carbazol-9-yl)alkoxy)-1,3-phenylene)bis(benzothiazole)] (x = 3, 4, 5 and 6) as new anti-Kasha emissive AIEgens conveyed for the first time. Experimental and theoretical results confirmed that the origin of AIE, co-existence of dual fluorescence and phosphorescence in water at room temperature are realized via multiple higher-lying excited states (hot excitons), especially from the bright emissive states of S_7/S_5 and T_3, that have never been observed previously via suppression of Kasha's rule (SOKR). Precise photophysical studies, single-crystal structures and quantum-mechanical (static and dynamic) studies revealed that large energy gaps (ΔE_{ST}) between S_7/S_5 and S_1 states (T_3 and T_1 states) along with an abundance of small ΔE_{ST} between singlet charge transfer (^{1}ICT) and triplet locally excited (^{3}LE) states facilitates reverse intersystem crossing (rISC) resulting in TADF and RTP simultaneously. Single crystal structures depicted that alkyl chain length induced supramolecular self-assembly displayed distinct H- and J-aggregation, including strong intra and intermolecular hydrogen bonds suppressing internal conversions and promoting intersystem crossing within the upper excited states and making possible multi-mode emissions by evolving hot-excitons. Structural rigidity/flexibility presents a unique molecular skeleton for achieving multi-colored emissions of two different reversible mechanoresponsive behavior viz. mechanoluminescence and mechanochromism in powder and polymer films, respectively. This work thus highlights an uncommon design strategy of multifunctional AIEgens with in-depth mechanistic insights, endowing them as a potentially new class of anti-Kasha emissive materials.

5.1 Introduction

Aggregation-induced emission (AIE) based luminogens with multifunctional behaviors have drawn potential interest to the discipline of material chemistry both in fundamental research and practical applications, mostly in organic light-emitting diodes (OLEDs),[1,2] sensing,[3] anti-counterfeiting,[4] bio-imaging[5] and cancer therapeutics.[6,7] For instance, classical organic luminogens suffer notorious aggregation-caused quenching (ACQ) effect at high concentrations owing to their self-aggregation *via* strong π-π stacking in aromatic structures, which greatly impedes the wide utility of such materials.[8-9] Conversely, AIE effect obviates the major issues of emission quenching by restricted intramolecular motions and rotations (RIM/RIR) which suppress non-radiative deactivation and promote an enhanced emission at aggregated/solid-state.[10,11] However, this conventional mechanism is unable to explain low contrast imaging in many sensitive micro viscus biological environments, thereby limiting their practical applications.[12] Besides, the lack of novel molecular design and intricate insights into the excited-state dynamic (ESD) processes and the origin of AIE remains an infusive task so far.[13] Moreover, utilization of traditional fluorophores reported till date were found to emit light by following Kasha' rule,[14] which states that radiative decay (fluorescence/phosphorescence) occurs only from the lowest exited states to the ground state (S_1/T_1 to S_0), irrespective of the initial photoexcited state.[15] Yet, as an exception to this rule, suppression of Kasha' rule (SOKR) could be accomplished by retardation of ultrafast vibrational relaxation and internal conversion from higher excited states to S_1 when the energy gap between S_n-S_1 is quite large.[16,17] In particular, emission from states other than S_1 and T_1 is extremely difficult to realize in condensed/solid-state owing to a significant amount of fast vibration or collisional relaxation in the upper-lying excited states. On the contrary, participation of many higher-lying excited singlet (S_n) and triplet (T_m) states could result in dual-/multi-mode emissions *via* SOKR mechanism.[18,19] Although, many experimental and theoretical efforts have been devoted to accomplishing anti-Kasha emissive molecular rotors, yet such emissive pathways can ideally avoid additional consumption from internal conversions and other forms of electronic relaxation, which is beneficial for the improved luminescent quantum efficiency.[20] Therefore, the anti-Kasha effect opens new possibilities to the fundamental understanding for the new-generation emissive materials, especially focusing on multi-wavelength emissions or AIE effect.[21] Nevertheless, in the past few years, few anti-Kasha emissive materials are developed on BODIPY, azulenes, pyrene and thiones-based derivatives.[19,20-23] In these

systems, dual or multi-mode emission bands were observed from a single molecule by breaching the Kasha's rule and typically relied on few possible mechanisms *viz*. monomer/excimer complex,[24] inter/intramolecular charge transfer (ICT),[25] Förster resonance energy transfer (FRET),[26] excited-state intramolecular proton transfer (ESIPT),[27] and by constructing supramolecular self-assembles.[28] Notably, reverse intersystem crossing (rISC) between higher excited triplets to singlets, large oscillator strength and low energy splitting (ΔE_{ST}) might confer thermally activated delayed fluorescence (TADF) emission.[29] Unfortunately, weakly susceptible triplets in organic molecules prevail the non-radiative pathways, and dissipate as heat energy instead of light due to the poor spin-orbit coupling (SOC), thereby exhibiting dim room temperature phosphorescence (RTP).[30] Hence, organic phosphorescence generally exists only at cryogenic temperature due to the high triplet quenching propensities in the presence of moisture and molecular oxygen at ambient conditions.[31] These limitations seriously impede to harvesting both higher-lying singlet and triplet energy in order to realize dual emission of TADF and RTP simultaneously in water and remain as a stimulating research area. In this context, anti-Kasha emission from a through-space donor (D) and acceptor (A) design strategy by using carbazole and benzothiazole based molecular rotors is not explored yet.[18,32] Profoundly, the presence of many heteroatoms in these aromatic structures may contribute to the emissive transfer among different multiplicities in higher excited states deciphering SOKR.[33] While, heteroatoms in aromatic structures also prevail in multiple strong intermolecular hydrogen-bonding, intra-/inter molecular charge-transfer and weak π-π interactions which generally regulate distinct H- and J-type aggregated self-assembly fashion and are obvious to assist for generating the TADF and RTP.[34] Therefore, the combination of such multi-emission sources from anti-Kasha states could be optimized to cover the entire visible spectrum thereby white-light emission (WLE) can be generated in a single molecular structure.[20,35] A typical dual fluorescence-phosphorescence based behavior is likely observed in highly rigid crystalline systems, which displayed two common properties such as mechanochromism (MC)[36] a reversible emission switching behavior and mechanoluminescence (ML)[37] an enhanced emission intensity under external mechanical stimulations. However, to the best of our knowledge, there are no such definitive examples of such multi-functionality in a single molecule that could display several key-functional behaviors like AIE, TADF-RTP (*via* SOKR) and multi-stimuli-responsive MC/ML simultaneously. Development of such new multifunctional molecular

rotors with deep quantum-mechanical insights for the origin of aggregated state emission for a single molecular rotors remains till date a challenging task.

Herein, four through-space charge transfer (TSCT) based anti-Kasha emissive AIEgenic rotors have been designed and synthesized, denoted as BT2OxCz (x=3, 4, 5 and 6), which contains 2,2'-(1,3-phenylene)bis (benzothiazole)[BT2] as an acceptor and carbazole [Cz] as a donor, connected *via* a series of odd/even alkyl chains. Integrated molecules exhibited dual fluorescence emission (DFE) in the aggregated state, such as locally excited state (LE) and TADF, while RTP was also seen together in a single molecular structure. Experimental and theoretical results attributed the origin of AIE and DE, due to the involvement of higher-lying excited singlet and triplet manifolds *via* SOKR. Notably, it could be envisaged that the SOC was immensely boosted on fine adjustment of singlet and triplet state manifolds resulting in both narrower ΔE_{ST} (~0.02 - 0.12 eV) and wider ΔE_{ST} (0.50 and 0.55 eV), thereby facilitating the efficient ISC and RISC to upsurge the TADF and RTP simultaneously. Precisely a key conceptual insight for the AIE emission process in the condensed state has been illustrated to be *via* SOKR and confirmed by rigorous experimental studies and quantum-mechanical calculations. The energy difference between the emissive higher-lying excited state (S_7) and the lowest excited state (S_1) was found to be approximately at 7,300 cm^{-1}, as per energy gap law, this much difference in energy is sufficient for the retardation of internal conversion to dark S_1 state to validate SOKR.[38] Notably, sterically constrained shorter chain BT2O3CZ, BT2O4CZ and BT2O5CZ displayed relatively intense TADF, while the longer chain BT2O6Cz exhibited RTP, owing to dimer formation, that resulted in inter-TSCT and denser packing with multiple non-covalent interactions as compared to other three congeners. Moreover, SC-XRD analyses showed two distinct packing motif, sterically strained 'J-aggregation' and geometrically relaxed 'H-aggregation' which decipher ambient stable triplet emission. Additionally, the shorter chain emitters showed ML due to the rigid packing structure while geometrically more relaxed longer chain emitters exhibited color tunable MC behavior. Through this work a new concept enabling to investigate condensed state multi-mode emission mechanisms and their intrinsic color switching multi-mechanoresponsive (MR) behavior has been established.

5.2. Experimental Section

5.2.1. Materials

All the materials used for this work are similar to chapter 4.

5.2.2. Synthesis and Characterizations

Synthesis and characterization were performed for all the four compounds in this work is followed by the similar protocol of chapter 4.

5.2.3. Measurements and Methods

5.2.3.1. Optical Characterization

The fluorescence and absorption spectra were measured with PerkinElmer, Model Lambda-25 spectrometer and Horiba-Fluoromax4 with Varian Cary Eclipse spectrometer respectively. The absolute quantum yields were measured by using the Horiba Fluoromax (Jobin Yvon equipped with Integrating sphere) absolute quantum yield spectrometer. The time-resolved fluorescence lifetimes were investigated with the time-resolved fluorescence studies were performed using an Edinburgh Life Spec II instrument. Temperature-dependent (77K-300K) PL and lifetime measurements were carried out using a liquid nitrogen-cooled optical cryostat (Optistat, Oxford Instruments) attached to an Edinburgh FSP-920 instrument.

5.2.3.2. Morphology Visualization

The morphology and crystallinity of the synthesized BT2OxCz (x=3, 4, 5, & 6) were examined by scanning electron microscopy (FESEM) (Zeiss, Model: Sigma-300). All water drop casted samples were gold-sputtered under vacuum to achieve a thin layer of conductive gold coating on the micro/nano crystalline samples. Atomic force microscopy (AFM) analysis were performed drop-casted sample over silicon substrate, in AFM, Asylum Cypher, Oxford Instruments. Transmission electron microscopy (TEM, JEOL JEM-2100F). Dynamic light scattering (DLS) measurements were taken with a Zetasizer Nano ZS90 (model no ZEN3690) instrument. All of the FTIR data were collected using a PerkinElmer instrument. All digital pictures were taken with a canon power shot SX420 IS digital camera.

5.2.3.3. General Characterization

The transition temperatures and associated enthalpy changes were determined by differential scanning calorimeter (Q20 DSC) under nitrogen atmosphere Thermogravimetric analyses (TGA) were carried out with a Mettler-Toledo TGA/SDTA

851e thermogravimetric analyzer in a temperature range of 30-600 °C under nitrogen atmosphere at 5 °C min^{-1} heating rate.

The growth morphologies of BT2O3Cz and BT2O6Cz crystals were calculated by using the Materials Studio software, based on the attachment energy theory. The molecular structure was first optimized on the basis of the experimental crystal structure. The geometric and energy calculations were performed using the Forcite and Morphology modules.

5.2.3.4. Computational Studies

Combined with the SXRD crystal data, the Hirshfeld surfaces, electrostatic potential, and molecular orbital were simulated by CrystalExplorer 3.1.51. The Hirshfeld surfaces and the electrostatic potential (ESP) were mapped with dnorm using STO-3G basis set at the Hartree-Fock theory.

Vertical and transitions energies with the highest occupied molecular orbital (HOMO), lowest unoccupied molecular orbital (LUMO), of single-component crystals were calculated by density functional theory (DFT). All DFT and TDDFT calculations in this study were performed by employing the combination of Becke3-Lee-Yang-Parr (B3LYP) hybrid functional and 6-31G(d,p) basis set using the Gaussian 16 package. The calculated structures, energy level very much close to experimental results.

Furthermore, DFT and TDFT calculations were employed for ground state and excited states (S_1, S_7 and S_{10}) electronic structure to obtained surface potential energy of compound BT2O3Cz. The potential energy as a function of dihedral angle were developed by a series of constrained geometry optimizations from single-crystal structure employing the same density functional and basis set as described above. For each constrained geometry optimization, the dihedral angle of the molecular rotor was held constant, while all other bond lengths and angles were allowed to fully relax. 36 different geometries were generated for the BT2O3Cz where the rotor dihedral angle was varied in 10° increments. The total SCF energy of each constrained geometry optimization was used to assess the ground state electronic energy of each species as a function of rotor angle. The UV/Vis absorption (Abs) spectra of compounds were simulated based upon the TDDFT data from Gaussian 16.

Further SOC and SOC-TDFT studies were calculated using Orca 4.2.0 software package. First, geometry optimization of BT2O3Cz and BT2O6Cz was carried out in vacuum with B3LYP functional and the 6-31G basis set for all atoms. The vibrational frequencies computed on the optimized geometry of BT2O3Cz and BT2O6Cz where time-dependent density functional theory (TD-DFT) under Tamn-Dancoff approximation (TDA) was

employed to obtain the first 10 singlet excited states. The first triplet was optimized from the ground state of UKS calculation. SOC on top of the TD-DFT results was included by using quasi-degenerate perturbation theory. In order to compute the fluorescence and phosphorescence spectra, the path integral approach implanted in the ORCA_ESD module B3LYP functional and DEF2-SVP DEF2-SVP/C GRID4 ESD (FLUOR/PHOS) was used with the same protocol as above for the SCF and TD-DFT. Further, the effect of temperature is completely accounted in exact way by choosing TEMP under ESD for different temperature dependent fluorescence and phosphorescence studies at 77K, 200K and 298K respectively.

5.2.3.5. Formula Used for Lifetime and Solvatochromism Studies

$$\tau_{av} = \frac{\{(\alpha_1.\tau_1) + (\alpha_2.\tau_2)\}}{(\alpha_1 + \alpha_2)} \qquad \text{Equation 5.1}$$

Where τ_{av} is avarage decay time tau's(τ) are decay components and alphas(α) respective amplitudes.

$$\nu_A - \nu_F = \frac{2\Delta f}{hC}\frac{(\mu_E - \mu_G)^2}{a^3}, \qquad \Delta f = \frac{\varepsilon - 1}{2\varepsilon + 1} - \frac{n^2 - 1}{2n^2 - 1} \qquad \text{Equation 5.2}$$

In which $\boldsymbol{\nu_A}$ is the wavenumber of the absorption, $\boldsymbol{\nu_F}$ is the wavenumber of the emission, h is Planck's constant, C is the speed of light, a is the cavity radius and $\boldsymbol{\Delta f}$ is the orientation polarizability where $\boldsymbol{\Delta f}$ is defined by the dielectric constant ε and the refractive index n.

5.3. Results and Discussion

5.3.1. Materials Design Strategy

In this work, we proposed a series of TSCT based anti-Kasha emissive molecular structures 2,2'-(5-(3-(9H-carbazol-9-yl)alkoxy)-1,3 phenylene) bis (benzothiazole) (BT2OxCz, x = 3, 4, 5, 6) which was synthesized and chararcterized by following similar protocols described in the previous chapter 4A. Structurally, the electron-accepting unit (3,5-bis(benzothiazol-2-yl) phenoxy) bearing a large number of lone pairs and the presence of two sulphur atoms makes the conjugated fragment highly electron deficient. The deficiency of electrons is fulfilled *via* TSCT by an electron-donating carbazole group, connected through various non-conjugated alkyl chain (Figure 5.1a). It is well known that heavy atoms free benzothiazole and carbazole serve as a unique platform for producing excitons harvesting

luminescence molecules owing to their spin allowed transition between the π-π* and n-π* states as per El-Sayed rule,[31] which therefore exhibited a high quantum yield.

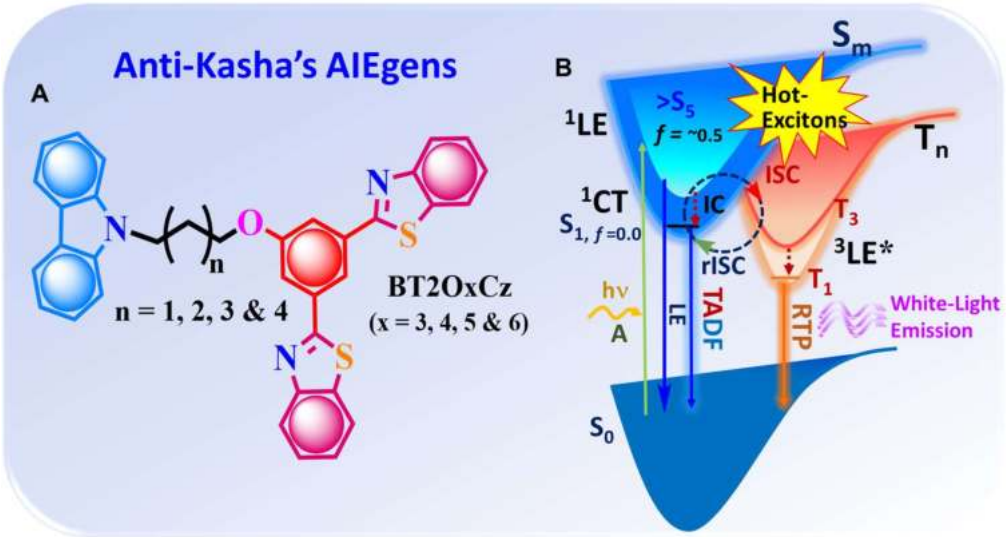

Figure 5.1. (a) Chemical structure of synthesized molecular rotors BT2OxCZ (x=3,4,5 and 6). (b) Jablonski diagram illustrating Anti-Kasha's emission sources.

However, in the present system, by changing the length of alkyl chain (propyl, butyl, pentyl and hexyl), the resultant molecules. (BT2OxCz, x=3, 4, 5 and 6) showed multi-emissions sources by encompassing LE, TADF and RTP in the aggregated state by suppressing the Kasha's principle. However, dual fluorescence emission is primarily governed by hot-excitonic states (high-oscillator-strength states) *via* multiple competitive process such as higher-lying singlet ^{1}π-π* state to lower-lying ^{1}ICT as LE and ^{1}ICT occurs by two-step processes by higher-lying singlet ^{1}π-π*(LE) to triplet ^{3}n-π*(LE) state followed by rISC from ^{3}LE* to the ^{1}ICT. On the other hand RTP was realized by the emergence of the high-lying ^{1}π-π* to ^{3}n-π* transition simultaneously (Figure 5.1b). Single-crystal structures and computationally optimized structures revealed that the shorter chain length containing BT2O3Cz and BT2O4Cz adopt large twisted conformations and thereby it showed strong twisted intramolecular charge transfer (TICT) and AIE feature rather than the structurally relaxed longer chain BT2O5Cz and BT2O6Cz. Besides, in condensed state all the emitters exhibited distinct TADF and RTP properties with very close to pure WLE as per Commission Internationale del'éclairage (CIE) coordinate values of (0.33, 0.33). Subsequently, a clear mechanistic insight on the origin for this AIE and WLE by virtue of utilization of hot-excitons and distinct color switching behavior was illustrated for the first time.

5.3.2. Condensed and Solution State Optical Properties

Based on the premise that self-assembled AIE luminogens offered a singlet-triplet-harvesting feature in water,[39,40] the singlet emission of all the BT2OxCz luminogens were precisely investigated by using UV-visible and photoluminescence (PL) studies. AIE was performed by changing various water/THF fractions (f_w) while solvatochromism studies were carried out using different polarity solvents at constant sample concentrations (~3 x 10^{-5} M). All BT2OxCz congeners exhibit absorption at 305 nm in THF and other water fractions (f_w), whereas in the aggregated state (99% f_w), shorter chain BT2O3Cz showed red-shifted absorption centered at 360 nm due to J-aggregation, while BT2O6Cz displayed relatively blue-shifted absorption located at 345 nm due to H-aggregation (Figure 5.2a-d**).**

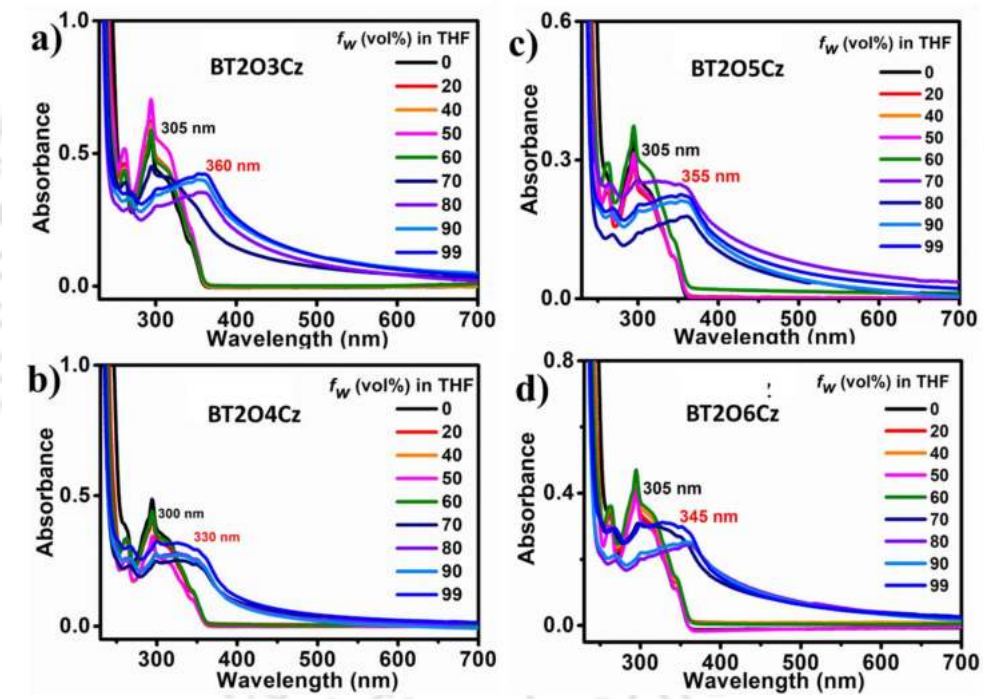

Figure 5.2. (a-d) UV-visible absorbance spectra of BT2OxCz (x=3,4,5 and 6) at various THF/water fractions (f_w).

Steady-state emission spectra and their relative intensities were recorded at various f_w ratios. Further, all the molecular rotors exhibited blue-fluorescence at ~455 nm in solution (THF), which upon a gradual increment of up to 60% f_w, showed decreased PL intensities with increased solvent polarity with a red shift from 460 to 500 nm due to the TICT effect (Figure 5.3a-5.3d for BT2OxCz). Further, the relative PL intensity increased significantly and reached a maximum of 99% f_w at ~430 nm (Figure 5.3e-5.3h for BT2OxCz). An intense

AIE-TICT phenomenon was observed for BT2O3Cz and BT2O4Cz at 99% f_w. Nevertheless, BT2O5Cz and BT2O6Cz exhibited relatively weak AIE, including no clear TICT effect. Although, no noticeable change was observed for AIE emission maxima (~430 nm) with increasing chain length, a prominent locally excited peak occurs at 375 nm. Besides, a bathochromic shift was observed with increasing solvent polarity (solvatochromism behavior), which profoundly impacts their through space TICT-features *via* excited states stabilization which is a positive sign to be efficient TADF emitters (Figure 5.3i-5.3l for BT2OxCz).[41] The presence of LE and through-space TICT emission can also easily be distinguished from this study.

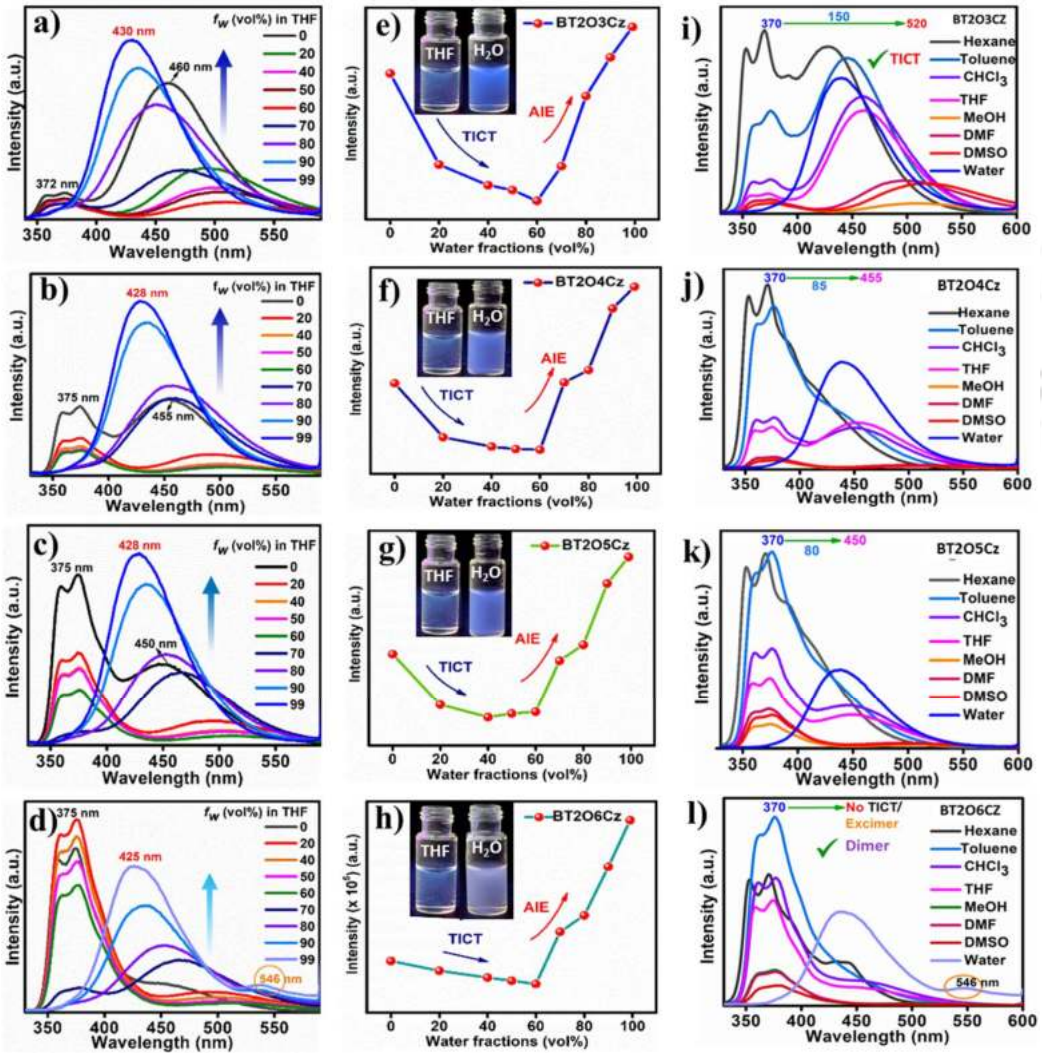

Figure 5.3. Condensed and Solution state Photophysical Properties of the AIEgens**:** (a-d) Fluorescence spectra and (e-h) relative intensity graph of TICT-AIE, intense emission for BT2OxCz at the constant concentration ($2x10^{-5}$ M), at various water/THF fractions (inset images taken under 365 nm UV-lamp). (i and l) Solvatochromism study: Fluorescence spectra in different polarity solvents of BT2OxCz.

Therefore, a tunable excited state resulted in significant solvatochromism behavior of 150 nm red shift in BT2O3Cz, 85 and 80 nm red-shifts for BT2O4Cz and BT2O5Cz, whereas BT2O6Cz displayed no such TICT effect. Therefore, with increasing chain length, the through-space TICT effect gradually diminishes and the LE state emission (375 nm) dominated over CT emission (430 nm), due to the long separation between D-A segments and highly planar cores present in the BT2O5Cz and BT2O6Cz respectively. The extent of solvatochromism was further verified by the Lippert-Mataga plot,[42] where the stokes-shift of BT2O3Cz and BT2O6Cz in different solvents were plotted against their ET(30) values and fitted with a straight line (Figure A5.1 –A5.2) Notably, stokes shift and emission maxima of BT2O3Cz shows a regular increment and positive slope, whereas, BT2O6Cz showed a negative slope with an increase in solvent polarity. Especially, the emission increment was significantly higher in case of shorter chain rotors BT2OxCz (x=3,4) rather than longer chain rotors BT2OxCz (x=5,6). Notably, unlike the other three emitters, BT2O6Cz showed dual peaks; the usual AIE peak at 430 nm and a new peak at 546 nm, likely due to the dimer or excimer emission at 99% fw (Figure 5.3i orange circle).

Furthermore, to better understand the properties of the excited states TRPL study was performed for all BT2OxCz rotors in water and THF where, lifetime for the 430 nm AIE peak, a bi-exponential decay with a sharp enhancement of average lifetime (τ_{av} = 6.13, 5.70, 4.77, 4.66 ns) was seen at 99% f_w than in THF (τ_{av} = 1.38, 1.68, 0.74 and 1.46 ns) respectively (Figure 5.4a-d for BT2OxCz). These results confirmed that the TSCT emission reduces by increasing the chain length and is consistent with the steady-state emission spectra in the aggregated state. The AIE lifetime (ns) in water showed a long tail with bi-exponential decay profile which necessitated determining the involvement of delayed species contribution in the condensed state. Thus, the phosphorescence spectrum exhibited as aggregation-induced delayed fluorescence (AIDF) at 430 nm and an additional aggregation-induced phosphorescence (AIP)[43] peak at >600 nm in 99% f_w with the τ_{av} = 114.61, 91.61, 7.86 and 114.98 μs (Figure 5.5a, b). PL quantum yields were calculated to be 24.1%, 20.1%, 16.4% and 17.2%. The decay constants of radiative (k_r) and non-radiative (k_{nr}) decays were calculated by using the formula $k_r = \phi/\tau$ and $k_{nr} = 1-\phi/\tau$ for BT2OxCz. Therefore, K_r are calculated to be 2.09 ms^{-1}, 2.18 ms^{-1}, 20.86 ms^{-1} and 1.49 ms^{-1} while K_{nr} values are 6.63 ms^{-1}, 8.73 ms^{-1}, 106.36 ms^{-1} and 7.20 ms^{-1} respectively. CIE-coordinate values were found to be (0.31, 0.29) for BT2O3Cz, (0.31, 0.28) for BT2O4Cz, (0.27, 0.26) for BT2O5Cz and (0.36, 0.33) for BT2O6Cz (Figure 5.5c).

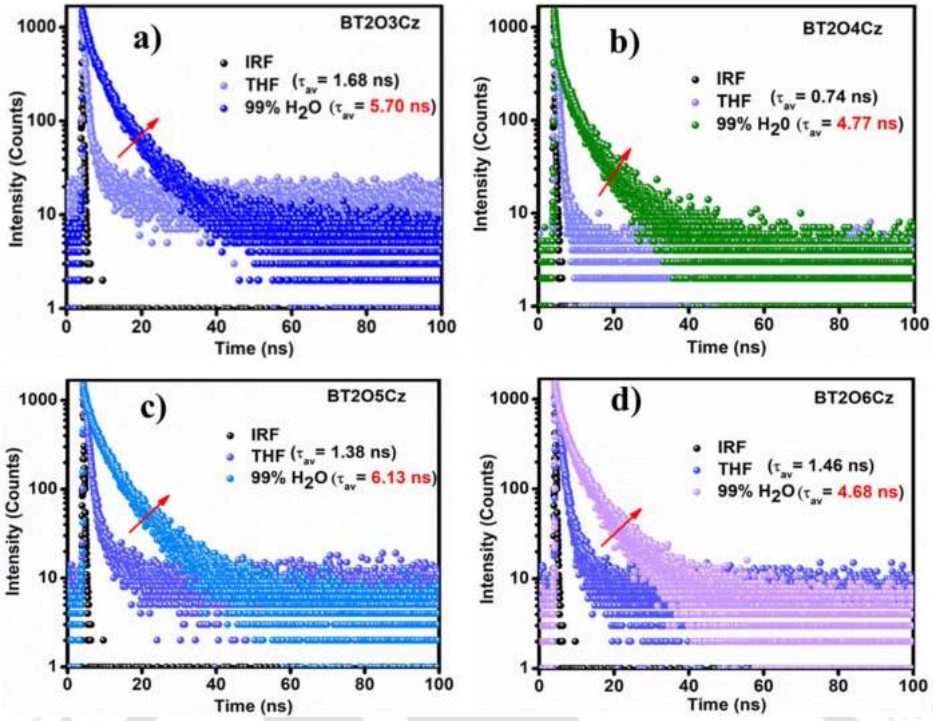

Figure 5.4. (a-d) Fluorescence lifetime study for BT2OxCz (x= 3, 4, 5 & 6) in aggregated state, to investigate the aggregation enhanced the life-time of the emitter.

Notably, BT2O6Cz showed more prominent white phosphorescence emission, due to the dimeric form in the condensed state, whereas BT2O5Cz showed intense AIDF and very weak AIP emission in the aggregated state due to its amorphous nature. These results concur that both AIDF and AIP belong to aggregation-induced fluorescence-phosphorescence (AIFP) emission in water, and the observed bright AIE emission was presumably could be due to the SOKR.[44] Concentration-dependent PL studies showed a simultaneous increment of both the peaks with increasing concentration, suggesting that the 546 nm peak was due to the dimer formation[45] in 99% f_w (Figure 5.5d). The enhanced emission and accompanying results could be attributed to strong TSCT and restricted intramolecular free rotation due to the structural rigidity and flexibility of non-conjugated alkyl chain. All the solution and condensed state photophysical properties are summarized in Table 5.1. Unlike, conventional AIE mechanism involving RIR, RIM, TICT and ESIPT, a rare class of anti-Kasha's mechanism was detected here, providing quantum mechanical insights for AIE emission at 430 nm which originates from upper lying singlet state (>S_1) for all the BT2OxCz luminogens.

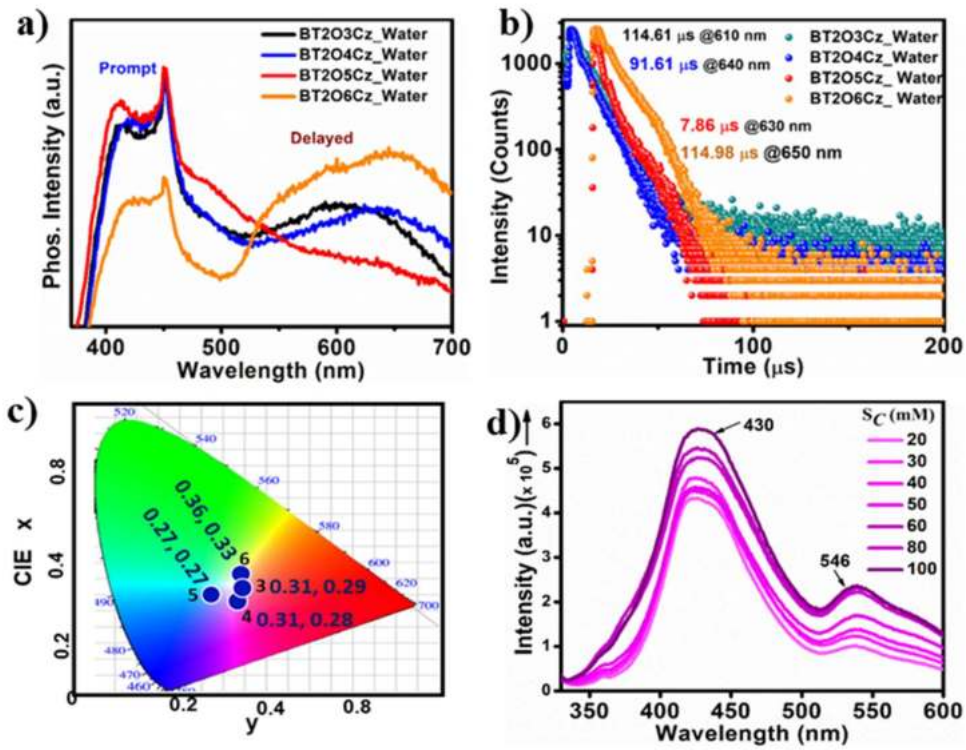

Figure 5.5. (a & b) Delayed emission spectra and delayed lifetime for all BT2OxCz in 99% (f_w) at µs-pulse excitation (λ_{ex} = 300 nm). (c) CIE co-ordinate diagram plotted against the delayed emission in 99% (f_w). (d) Concentration dependent fluorescence spectra for BT2O6Cz.

Table 5.1: Summary of photophysical studies of BT2OxCz (x=3, 4, 5 and 6) in solution and condensed state.

AIEgens	**λ_{abs}(nm)**		**λ_{em} (nm) (steady state)**		**Stocks Shift (cm^{-1}) (CT)**	**τ_P (ns)**	**τ_D (µs)**	**Φ_{PL}**	**k_r^a ($x10^3$ s^{-1})**	**k_{nr}^b ($x10^3$ s^{-1})**
State	Soln.	H_2O	Soln.	H_2O	Soln.	H_2O	H_2O	H_2O	H_2O	H_2O
BT2O3Cz	305	360	370, 520	430	0.00135	6.13	114.61	24.1	2.09	6.63
BT2O4Cz	300	330	375, 455	428	0.001136	5.70	91.61	20.1	2.18	8.73
BT2O5Cz	305	355	375, 450	428	0.0010	4.77	7.86	16.4	20.86	106.36
BT2O6Cz	305	345	375	425	-	4.66	114.98	17.2	1.49	7.20

Radiative and non-radiative decay rate [$^a k_r = \phi/\tau$, $^b k_{nr} = (1-\phi)/\tau$] calculated from fluorescence QY and delayed lifetime in water at RT.

To understand underlying insights, excitation wavelength dependent emission studies were performed where a series of excitation wavelengths were used to excite the luminogens, and the PL spectra illustrated the bright state emission (λ_{em} = 430 nm) which disappears when excitation shifted to longer wavelength (λ_{ex} = 300 to 500 nm) from normal excitation (λ_{ex} = ~320 nm) (Figure 5.6a-d for BT2OxCz). Moreover, on excitation at λ_{ex} = 500 nm a red-shifted dark emission feature emerges at ~530 and ~570 nm; indicating that the molecule relaxes to the lower energy dark states *viz.* S_1/S_2. By fixing the excitation wavelength to a lower energy (500 nm), weak emission was observed from a lower-lying excited state (the dark state, which in this scenario is S_1). This experiment proved that the main emission is from an en-ergy level higher than S_1, while, S_1 being a weakly emissive one and corroborating the existence of dark states via SOKR. Further, viscosity induced enhanced fluorescence of all the BT2OxCz were also studied in various micro-viscous environment where a binary mixture, glycerol (Gly) and methanol was used to regulate the vis-cosity of the medium (Figure 5.7a-d for BT2OxCz). The emission maxima initially shifted to longer wavelength with increasing Gly fraction (f_{Gly}) due to ICT. However, ten-time enhanced emission intensity was observed at 99 % fGly, compared to methanol solution.

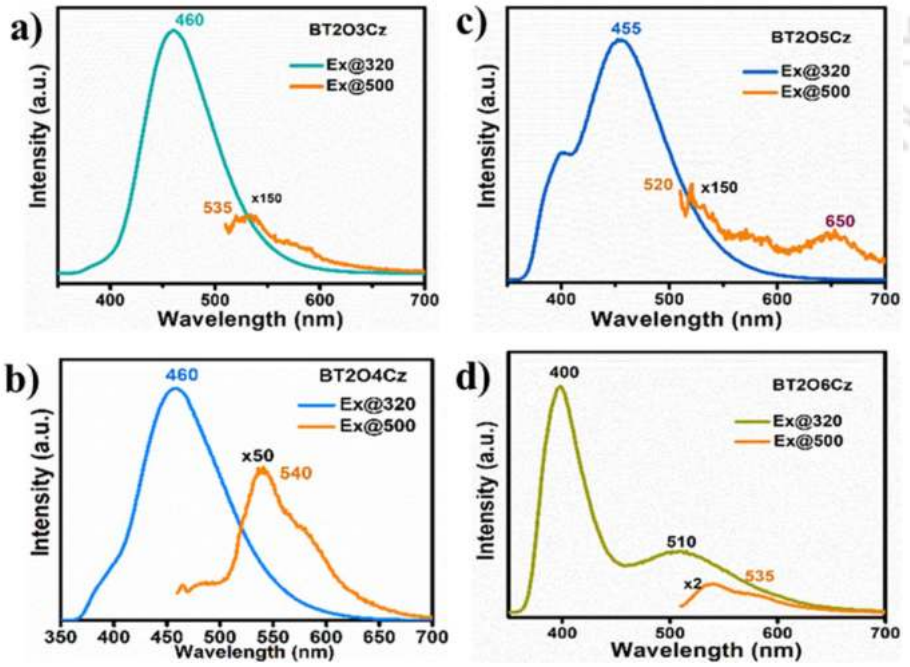

Figure 5.6. (a-d) Excitation wavelength dependent fluorescence spactra for BT2OxCz, BT2OxCz (x= 3, 4, 5 & 6).

Since, in the low viscus medium, excitation to the emissive excited state followed by rotation about the rotor axis significantly decreases the energy gap between the emissive and dark excited states, resulting in a rapid internal conversion (IC) to S1. While in high viscous medium or in aggregated state, the non-radiative deactivation of the twisted complex is circumvented by suppressing IC from >S1 state to dark S1 state, due to restricted rotation thereby resulting huge fluorescence enhancement.

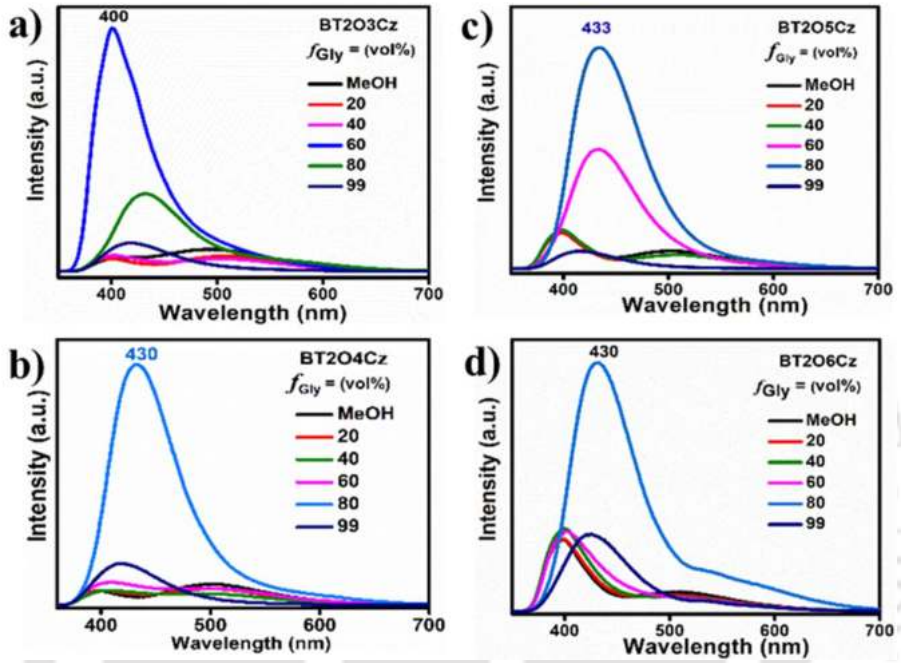

Figure 5.7. (a-d) Fluorescence spectra of BT2OxCz(x= 3, 4, 5 & 6).at various fractions of methanol and glycerol mixtures.

5.3.3. Self-assembly and Nanocrystalline Behavior for AIEgens

The supramolecular self-assembly in water and nanocrystalline behavior of BT2OxCz were studied by FESEM, TEM and AFM. The low-magnification FESEM images (scale bar: 2 μm) (Figure 5.8a-5.8d) (inset high magnification, scale bar: 400 nm) were obtained from drop casted film of aggregates prepared on aluminium coated glass substrate. Structurally rigid BT2O3Cz showed round structures, BT2O4Cz exhibited sheet like structures, while BT2O5Cz and BT2O6Cz had extremely uniform spherical nanoparticles with slightly varying size (~350 nm) in low-magnification TEM images (scale bar 500 nm) (Figure Figure 5.8e-5.8h). Unlike BT2O5Cz, SAED analysis attributed high order crystallinity of all the other three emitters Further, AFM (scale bar 2 μm), also consisted the regular and crystalline assembly with RMS roughness and height of 36.56, 76.24 nm for BT2O3Cz,

38.27, 172.04 nm for BT2O4Cz, 36.26, 84.42 nm for BT2O5Cz and 52.94, 161.76 nm for BT2O6Cz, ensuring well-ordered morphology with increasing chain length (Figure 5.8i-5.8l). The actual nanoparticle formation and their size distribution was further investigated by using dynamic light scattering (DLS) at 99% W_c. DLS showed shrinking of nanoparticles size distribution on decreasing chain-length, size: ~270 nm for shorter chain BT2O3Cz and BT2O4Cz, and ~230 nm for longer chain BT2O5Cz and BT2O6Cz emitters respectively. This regular morphology and DLS results prove that the defined self-assembly and nano-crystalline nature of the emitters increase with increasing hydrophobic alkyl chain length.

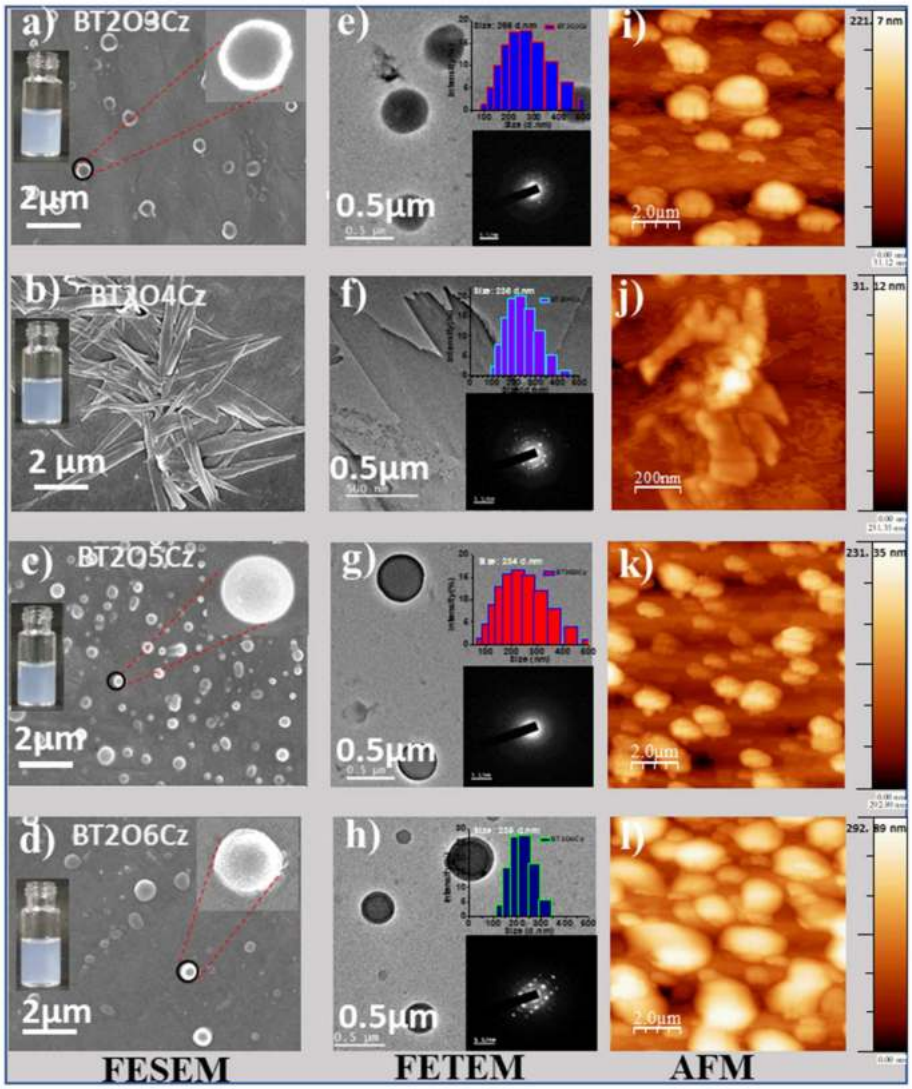

Figure 5.8. Nano-morphology for all the BT2OxCz (x=3,4,5 & 6) emitters at their condensed state: (a-d) FESEM images (scale bar 2µm, inset aggregation formation image under day light). (e-h) FETEM images [(scale bar 0.5 µm, inset: SEAD pattern and DLS at 99% (fw)]. (i-l) AFM images (scale bar 2µm).

5.3.4. SC-crystal Structures Analysis

Furthermore, to decipher the internal mechanism for AIDF and AIP emission at condensed, supramolecular interactions and molecular packing in single-crystal structures were carefully investigated. SC-structures of BT2O3Cz (CCDC 1969742) and BT2O6Cz (CCDC 1969743) were obtained by very slow evaporation of chloroform/hexane (8:2) solvents. Two needle-like crystals exhibited monoclinic and orthorhombic crystal systems with P 21/c and Pca 21 space group for BT2O3Cz and BT2O6Cz.[32] As shown in Figure 5.9a, b) BT2O3Cz presented a twisted conformation while BT2O6Cz exhibited relatively planar orientation due to the shorter distance (7.3 Å) in former as compared to the longer distance (11 .2 Å) latter crystal between D-A respectively. Interestingly, two separate planar cores were found from their respective D-A cores by strong intramolecular bonding. In the acceptor, the core bearing two benzothiazole (BT) units forms a rigid planar structure with an adjacent phenyl core with a torsion angle of 7.8°, 10.7° for BT2O3Cz and 8.85°, 4.94° for BT2O6Cz by strong intramolecular interactions (C-S···H, 2.743 Å, C-N···H, 2.556 Å in BT2O3Cz and C-S···H, 2.643 Å, C-N···H, 2.575 Å in BT2O6Cz). Whereas, rigid and planar carbazole (Cz) moiety oriented two opposite directions related to orthogonally connected alkyl chain and through-space linked acceptor core with a torsion angle of 107.7° and 99.34°, respectively. Structural rigidity in Cz due to intramolecular interactions involved active hydrogen present in alkyl chain with the π-cloud of donor carbazole (Cz) unit (C-H···π, π···C-H, 2.834 Å, 2.723 Å in BT2O3Cz and C-H···π, π···C-H, 2.808 Å, 2.755 Å in BT2O6Cz). Therefore, two separate planar structures in a single molecule allow to form dimer *via* intermolecular π-π stacking and other non-covalent interactions. In the dimeric structures, BT2O3Cz exhibited strong π-π interaction between BT cores (BTπ···π, 3.351 Å) and two adjacent molecules interlocked tightly, whereas very weak π-stacking (BTπ···π, 6.213 Å) was observed for BT2O6Cz. Consequently, these dimeric forms were stabilized by multiple non-covalent interactions and separated electron clouds of individual D-A units, which would become much more beneficial to restrict vibrational relaxation and prevent excitons quenching.[46] Besides, an abundance of other multiple intermolecular interactions was also apparent in both the SC-structures due to the presence of many heteroatoms (N, O, S) and active hydrogen atoms in the alkyl chain. Intermolecular hydrogen bond by a N atom present in BT and O atom present in the alkoxy chain in BT2O3Cz (C-H···N, C-H···O, 2.663 Å, 2.705 Å) also interacts with another nearby set of molecules enabling to create a rigid 3D framework (Figure 5.9c, d).

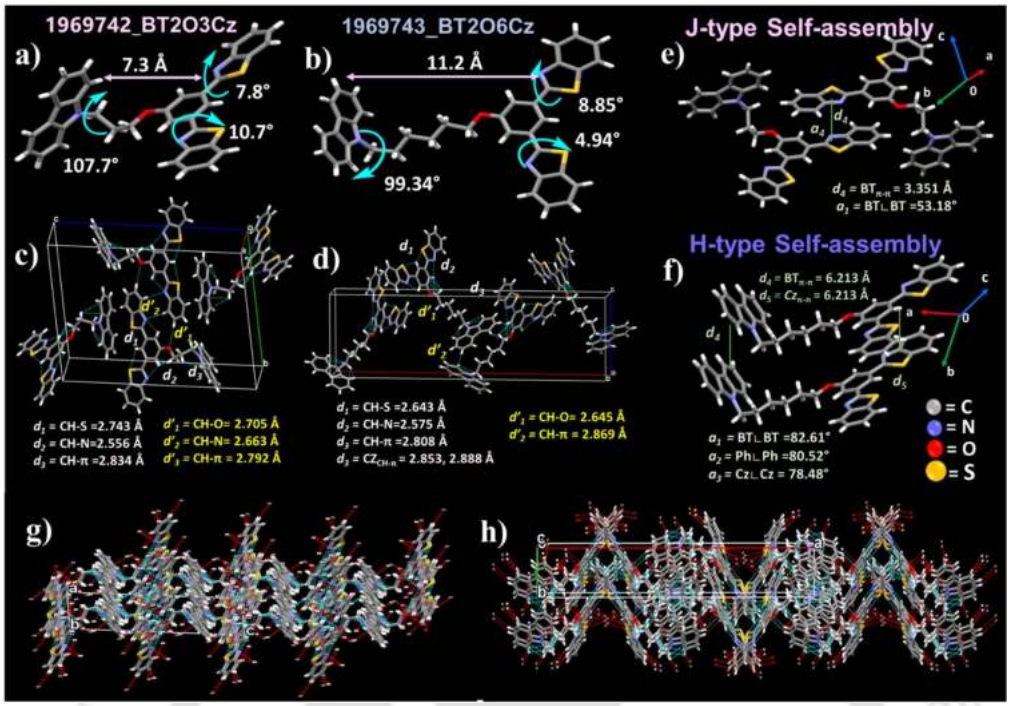

Figure 5.9. Single-crystal X-ray diffraction (SC-XRD) analysis: (a & b) monomeric SC-XRD structure of BT2O3Cz and BT2O6Cz AIEgens. (c. d) Unit cell structures and relative active, interactive distances through noncovalent weak interactions. (e & f) Dimeric assembly in single crystals showed distinct J-type and H-type aggregation patterns via π-π stacking distances and slip angles for BT2O3Cz and BT2O6Cz. (g & h) Top view in bulk intramolecular packing of rigid BT2O3Cz and comparatively dense intermolecularly rigid packing for BT2O6Cz.

Moreover, BT2O6Cz, exhibited a single intermolecular hydrogen bond, exhibited through O atom in the alkoxy chain (C-H···O, 2.645 Å). Unlike hydrogen bonds, many other intermolecular strong interactions were also observed due to the presence of active hydrogen atoms, while the BT2O6Cz showed more intermolecular interaction by Cz and alkyl chain hydrogens and S atom in BT (C-H···π, 2.853 Å, 2.88 Å and π···S, 3.313 Å) rather than BT2O3Cz which showed only C-H···π, 2.792 Å. Besides, BT2O3Cz exhibits J-aggregated structure (slip angle 53.18° between BT cores) while BT2O6Cz exhibits H-aggregated structure (slip angle 82.61° between BT cores, 80.52° between Cz cores) (Figure 5.9e, f).

Additionally, their bulk crystal packing shows a 3D-network and H-aggregated BT2O6Cz leads to overall denser molecular packing rather than J-aggregated BT2O3Cz in their crystalline state that suppressed the vibrational deactivations and activated the radiative channels[47] (Figure 5.9g, h). As a consequence, the dense packing and rigid assembly inhibited internal conversions and photochemical reactions, which facilitated the emissions from all possible excited states resulting TADF and RTP emissions simultaneously. Powder

X-ray diffraction (PXRD) analysis performed with the powder form obtained from as-synthesized pristine compounds and exhibited the sharp and intense multiple diffractions revealed microcrystalline nature. Notably, a large number of sharp diffraction peaks were seen in the low d-spacing region (2θ, 20°-30°) for higher chains containing B2O6Cz, which could be due to high-order inter-molecular noncovalent interactions rather than other congeners, triggering intense triplet utilization (Figure A5.3). Overall, these studies deciphering denser supramolecular non-covalent interactions, self-assembly and solid-state packing motif contributed very profoundly to their ESD and multi-emission properties.[20] Further, the H-aggregated molecular packing and involvement of spacer significantly impedes the higher triplet state stabilization, thereby favoring phosphorescence emission for longer chain BT2O6Cz.

5.3.5 Computational Results

In order to confirm the SOKR emissions in the aggregated state, the excited state processes were analyzed carefully by using two sets of computational methods. While static quantum-mechanical calculations were performed for BT2O3Cz and BT2O6Cz using Gaussian 16 program,[48] ESD studies were carried out with ORCA 4.2.0 software.[49] Starting with SC-X-ray geometries, calculations were carried out at Grimme's dispersion corrected B3LYP/6-31G (d,p) level of theory to compute the frontier molecular orbitals (FMO). Additionally, time-dependent (TD) DFT calculations were performed to find vertical emission energies, including oscillator strength (*f*) up to the 10th states at their different spin multiplicities in isolated and dimeric geometries (Figure 5.10ai-5.1di) at B3LYP/6-31G(d,p) level. Test calculations were also carried out using BPV86, PBE0, and M062X functionals. However, it was observed that B3LYP results matched better with the experimental λ_{abs} (Figure A5.4 for BT2O3Cz and Figure A5.5 for BT2O6Cz). Hence, B3LYP functional was used for these through-space systems.

Experimentally, it has been observed that BT2O3Cz and BT2O6Cz are likely to be found in isolated and dimeric forms, respectively. Computational results are consistent with the experimental observations.[32] In all the cases, the electron density distributions for their HOMO and LUMO were found to be well separated. While HOMOs are mainly located at donor carbazole units, LUMOs are localized at acceptor benzothiazole units. Moreover, the monomer of BT2O3Cz and dimer of BT2O6Cz show high LUMO energies of -1.67, -1.84 eV (and deep HOMO, -5.28, -5.10 eV) with electrochemical band gaps of 3.61 and 3.26 eV, respectively.

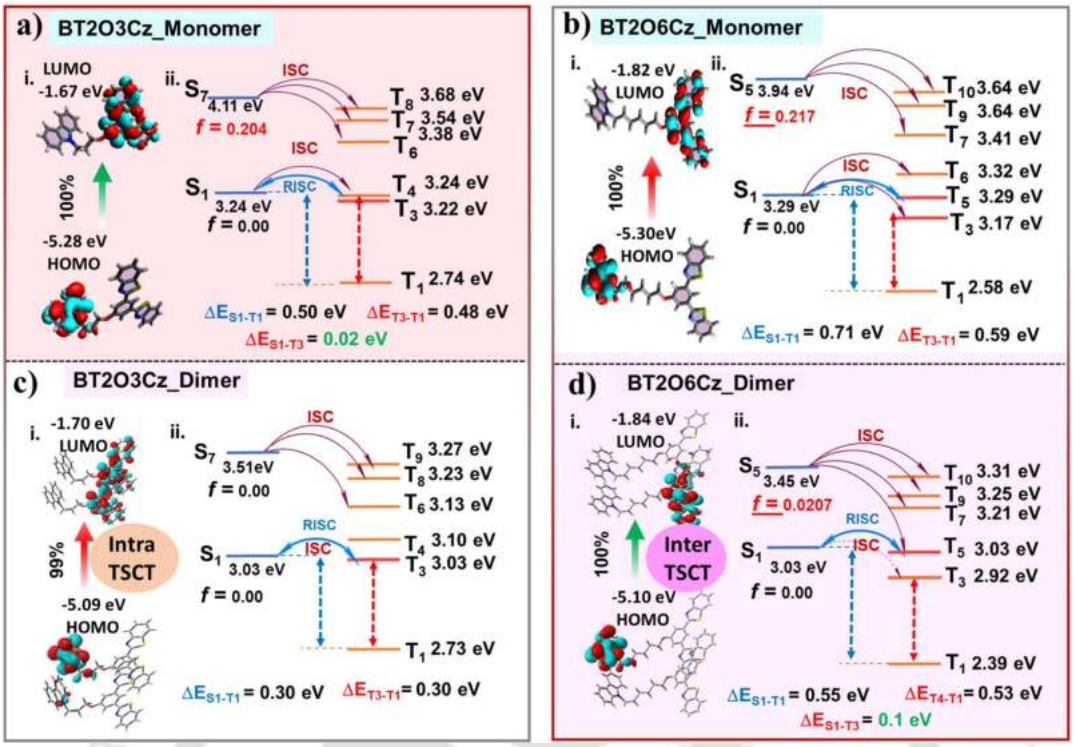

Figure 5.10. Computational calculations (a-d): Electron density distributions and energies of HOMO and LUMO for BT2O3Cz and BT2O6Cz in their monomers (ai, bi) and dimers (ci, di). Emission energies and possible active manifolds of ISC channels and the corresponding energy splittings are aslo shown for monomers (aii, bii) and dimers (cii, dii).

These wider band gaps for the emitters correspond to the basic prerequisite for displaying TADF/RTP property. Further, the HOMO-1 and LUMO+1 orbitals also show well-separated density distributions indicating the involvement of higher energy states for radiative decays. While intra-electronic FMO distributions are observed for BT2O3Cz in both isolated and dimer forms depicting intra-TSCT characters, inter-electronic distributions are seen for BT2O6Cz, where the separated HOMO and LUMO densities are located in two different molecules corroborating inter-TSCT character. (Figure A5.6).Active manifold of ISC channels was also investigated by computing vertical emission energies to the ground state from S_1, S_6/S_7 and T_1 - T_8/T_{10} states and their corresponding major frontier orbital contributions (summarized in Table A5.1-A5.4) for both isolated and dimeric geometries. Surprisingly, the oscillator strength (*f*) values for S_1, S_2 and S_3 states for both the emitters are found to be zero (*f*=0) (Figure 5.10aii-5.10dii), indicating that the S_1 state is non-emissive, which is in contrast to the conventional Kasha's formulation.[50] As mentioned earlier, few other functionals such as BPV86, PBE0, and M062X were also attempted. However, *f* value was still found to be zero for S_1, including

the large difference in energies between S_1 and $>S_1$ states, indicating that S_1 is indeed a dark state. The large *f* values for S_7, S_8 and S_{10} are 0.2039, 0.6071 and 0.3902, respectively, for BT2O3Cz (monomer). Similarly, *f* values of S_5, S_8 and S_9 are 0.0207, 0.0618 and 0.0881, respectively, for BT2O6Cz (dimer).

In addition, in case of BT2O3Cz, S_4 possesses an *f* value of 0.1019 indicating that this state could also take part in radiative relaxation and ISC processes. Nonetheless, a zero energy splitting between S_1 and T_3 (0.02 eV and 0.10 eV) strongly favors efficient RISC processes, where relatively well-separation of S_1 (3.24 and 3.03 eV) and T_1 (2.74 and 2.39 eV) states lead to moderate ΔE_{ST} values of 0.50 and 0.55 eV, respectively, for BT3O3Cz (monomer) and BT2O6Cz (dimer).[47] These results rationalize the intense TADF for the shorter chain and intense RTP for the longer chain rotors. All the computational results are summarized in Table A5.5. DFT and TDDFT calculations were carried out to compute relaxed potential energy curves as a function of dihedral angle for the ground and a few singlet excited states (S_1, S_7, S_8 and S_{10}) of BT2O3Cz. For each constrained geometry optimization, the dihedral angle (DA) of the molecular rotor was held constant, while all other bond lengths and angles were allowed to fully relax. Thirty-six different geometries were generated for the BT2O3Cz where the rotor DA in between Cz and alkyl chains (inset: DA shown by red arrow in the SC-geometry of BT2O3Cz) was varied in 10° increments. The relaxed potential energy surface results are shown in Figure 5.11a. The energy difference between the emissive higher-lying excited states (S_7, S_8 and S_{10}) and the S_1 state was found to be approximately 7,300 cm^{-1} (Table A5.6). Thus, as per the energy gap law, this much difference is sufficient to help the retardation of internal conversion to dark S_1 state and exhibits high brightness emission from S_7. In contrast, states $>S_1$ possessing large oscillator strength relaxes radiatively with bright emission by violating Kasha's rule. By restricting access to the crossing of potential energy surfaces due to the high energy barrier in S_7, it allows the excited molecule on higher excited states ($>S_1$) to show bright emission, which justifies the experimentally obtained AIE in the aggregated state where the formation of the aggregates restricted the access to the crossing of potential energy surfaces and kept the excited molecule on higher excited states. Collectively, the present observations were demonstrated in the modified Jablonski diagram which illustrates that the multi-mode emission originated from high-lying triplet excited states by violating Kasha's rule.

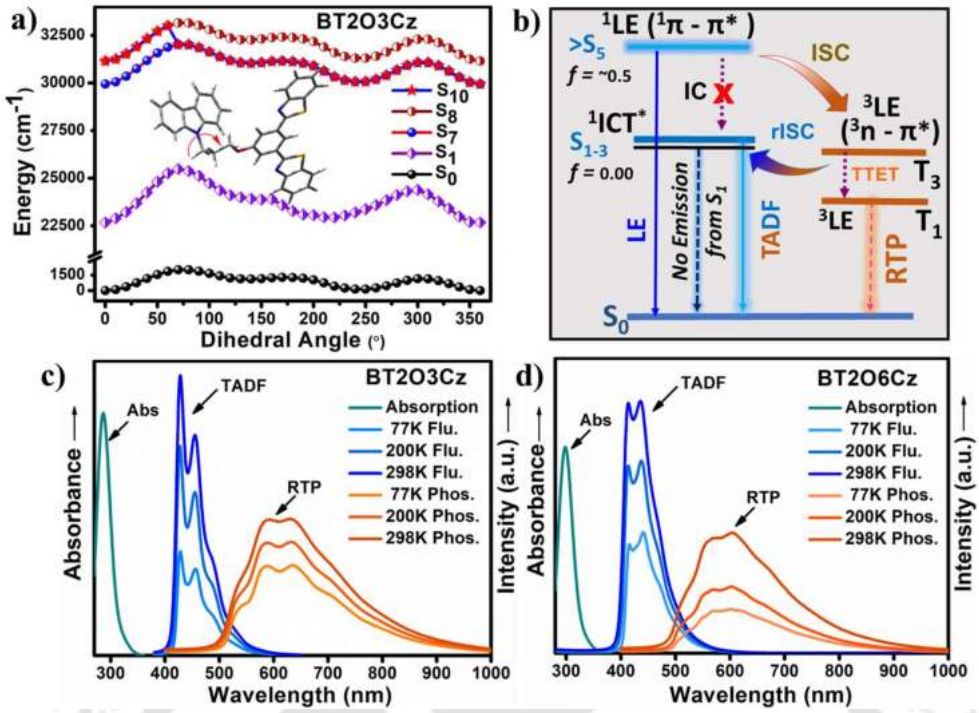

Figure 5.11. (a) Relaxed potential energy surfaces for BT2O3Cz rotor as a function of the dihedral angle at B3LYP/6-31G(d,p) from TDDFT studies (inset: DA shown by red arrow in the SC-geometry of BT2O3Cz). (b) A proposed modified Jablonski diagram illustrating the multi-mode emission originated from high-lying singlet-triplet excited states by violating the Kasha's rule. (c & d) Simulated absorption, dual fluorescence and dual phosphorescence spectra for BT2O3Cz and BT2O6Cz rotors from ORCA_ESD (Abs), ORCA_ESD (fluoro) and ORCA_ESD (phos) at B3LYP/DEF2-SVP/DEF2-SVP/C level of study including temperature-dependent fluorescence and phosphorescence spectra were computed using ESD at 77, 200 and 298 K.

In order to evaluate the origin of the delayed decay and precisely define the nature of excited states, natural transition orbitals (NTOs) for different singlet and triplet excited states in BT2O3Cz and BT2O6Cz were computed (Summarized in Table A5.7-A5.10).Further, to investigate emission spectra from the triplet states, the faster ISC processes from S_n to T_m manifold were also studied. The $S_1 \rightarrow T_1$ transition is of ^{1}ICT $\rightarrow$ ^{3}ICT type, whereas the $S_1 \rightarrow T_3$ and other higher transition $S_n \rightarrow T_m$ (n> 1, m > 3) are of ^{1}ICT $\rightarrow$ ^{3}LE types which influence the SOC *via* mixing of ISC transitions between higher possible excited states. To verify the robustness of the above-mentioned analysis from TDDFT, a recently developed excited state dynamics (ESD)[51] method was utilized using ORCA 4.2.0. Prior to ESD studies, static TDDFT calculations were also performed, and the obtained results were found to be consistent with the results calculated using the Gaussian16 software.

Table 5.2: SOC-matrix element (SOCME) calculated by SOC-TDDFT using ORCA 4.2.0 software with ORCA_ESD module.

SOC_TDDFT_BT2O3Cz					**SOC_TDDFT_BT2O6Cz**			
State	$\langle \mathbf{S_0}\|\mathbf{H_{SO}}\|\mathbf{T_m}\rangle^a$	$\langle \mathbf{S_1}\|\mathbf{H_{SO}}\|\mathbf{T_m}\rangle^a$	$\langle S_4\|\mathbf{H_{SO}}\|\mathbf{T_m}\rangle^a$	Configuration[b]	$\langle S_0\|\mathbf{H_{SO}}\|\mathbf{T_m}\rangle^a$	$\langle S_1\|\mathbf{H_{SO}}\|\mathbf{T_m}\rangle^a$	$\langle S_4\|\mathbf{H_{SO}}\|\mathbf{T_m}\rangle^a$	Configuration[b]
T1	0.052	0.087	0.095	H-6→ L+1(13)	0.193	0.024	0.043	H-6→ L(27)
T2	0.481	0.167	0.022	H-3→L(25)	0.364	0.052	0	H-6→L+1(25)
T3	0.112	0	0.405	H→ L (98)	0.042	0	0	H-5→ L+2 (20)
T4	0.036	0.100	0.014	H-1→ L+2(76)	0.215	0.1621	0.30	H→ L(99)
T5	0.428	0.462	0.024	H-7→ L(11)	0.022	0	0.110	H-4→ L+1(24)
T6	0.163	0.041	0.010	H→ L+2(91)	0.147	0	0.010	H-11→ L+2(12)

[a]$\sqrt{\Sigma\langle S_n|H_{SO}|T_m\ (MS=0,\pm1)\rangle^2}$; [b]Only transitions with contributions larger than 10% are shown.

Further, the SOC matrix elements (SOCME)[52] $\langle S_0|H_{SOC}|T_m\rangle$, $\langle S_1|H_{SOC}|T_m\rangle$ and $\langle S_4|H_{SOC}|T_4\rangle$ for BT2O3Cz and BT2O6Cz were calculated and the results are summarized in Table 5.2. It was observed that the SOCME values were large between S_1/S_4 and T_5/T_3 for BT2O3Cz. On the other hand, for BT2O6Cz, the values are large between S_1/S_4 and T_4 states due to the large excitons populations in these states, thereby contributing to the effective hot-exciton based emission. This observation supports the mixing of ISC transitions in which the triplet manifold has been harvested to attest the dual-state phosphorescence emission from T_1 and $T_3/T_4/T_5$ due to triplet-triplet energy transfer (TTET) process, which defines the exchange of both spin and energy between a pair of molecules or intramolecular fragments located at a short distance of <10 Å and releases free energy (exothermic) *via* Dexter-type channel.[53] Vibrationally resolved emission (both fluorescence and phosphorescence) calculations using ESD with ORCA were performed at B3LYP /DEF2-SVP/DEF2-SVP/C level within a reasonable TD-DFT error.[54] Notably, the emission spectra confirmed the involvement of higher-lying singlets contributing to TADF emission; at 430/455 nm arising from S_7/S_4, respectively, for BT2O3Cz and at 415/435 nm from S_8/S_5 for BT2O6Cz, respectively (Figure 5.11c and 5.11d). The two distinct longer wavelength phosphorescence emissions centered at 580 and 640 nm for BT2O3Cz, and 565 and 605 nm for BT2O6Cz originated from T_3/T_4 and T_1 (*via* TTET process) state, respectively.[45] Moreover, in BT2O6Cz, the longer distance between donor and acceptor is beneficial for charge separation and showed relatively blue-shifted (15 and 35 nm) fluorescence and phosphorescence decay. Further, splitting of the states and corresponding emission were verified by temperature-dependent vibrationally resolved

fluorescence and phosphorescence. ORCA simulated emission spectra of AIEgens showed the intensity increment of delayed fluorescence and phosphorescence with rising temperature from 100K to 300K providing concrete evidence to support the singlet and triplet excitons release process *via* TADF and RTP simultaneously. Based on the combined single-crystal analyses, TDDFT calculations and simulated emission spectra, a plausible mechanism with a modified Jablonski diagram is presented (Figure 5.11b). In particular, the distinct self-assembly behavior of the molecular rotors in their monomeric and dimeric forms through a variety of non-covalent interactions promoted the multi-mode emission that originated from the higher-lying singlet and triplet excited states violating the Kasha's rule. In contrast, H/J-aggregates in dimer accelerate the enhanced ISC and triplet exciton stabilization assisting to exhibit red RTP. Altogether, the experimental and computational results demonstrated that AIEgens possess unique fluorescence-phosphorescence emission covering the entire visible region by suppressing the non-radiative deactivation by higher lying excited state emission release. Interestingly, anomalous AIE emission involving higher-lying singlet states were realized by spacer-based structural modalities for the first time.

5.3.6. Mechanoresponsive Properties of AIEgens

AIEgenic molecular rotors with structural rigidity and flexibility correspond to the mechanical properties of intramolecular/intermolecular interaction and distinct molecular packing resulting in impressive emission switching behavior in solid state by applying various mechanical stimuli.[4,36,37]

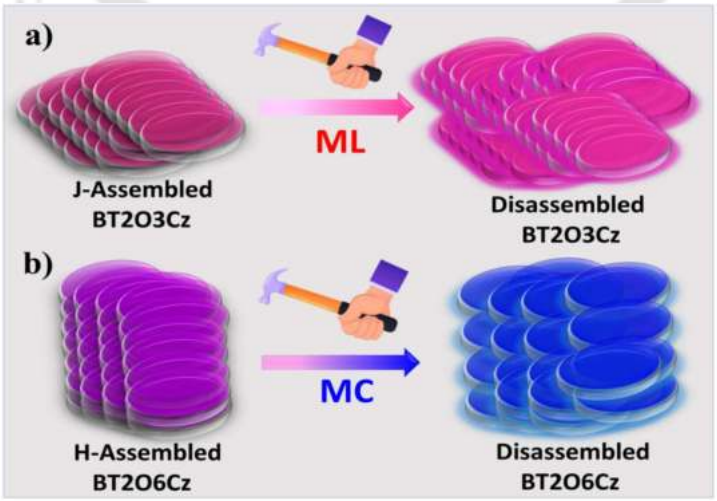

Figure 5.12. (a & b) Schematic illustration of distinct mechanoluminescence (ML) and mechanochromic (MC) behavior.

The short-chain BT2O3Cz exhibited reversible mechanoluminescence (ML) behavior with good mechanical, whereas longer chain BT2O6Cz exhibited reversible mechanochromism (MC) upon applying mechanical force (Figure 5.12a, b). A significant PL emission enhancement was observed for BT2O3Cz due to robust molecular rigidity, however, geometrically more relaxed BT2O6CZ showed intense blue-emission while the phosphorescence emission peak was found to be suppressed under mechanical stimuli (Figure 5.13a, b). This phenomenon was clarified by shifting of CIE co-ordinate after grinding with the value of (0.25, 0.25), (0.16, 0.10) BT2O3Cz and BT2O6Cz (Figure A5.7). Moreover, PXRD results for BT2O3Cz demonstrated intact, sharp and intense diffraction peaks after grinding in various states (pristine, grinding and solvent fuming), however, diffraction peaks for long-chain emitters nearly disappeared upon grinding (Figure 5.13c, d). Additionally, single molecular-based mechano-responsive behavior was further investigated *via* a stretchable and transparent elastomer film by embedding a minute fraction (0.05%) of AIEgens in Polydimethylsiloxane (PDMS) matrix,[55] (which is known to be one of the most deformable polymer) and the homogeneous mixture kept at 100 °C for 3h (Figure 5.14a, b).

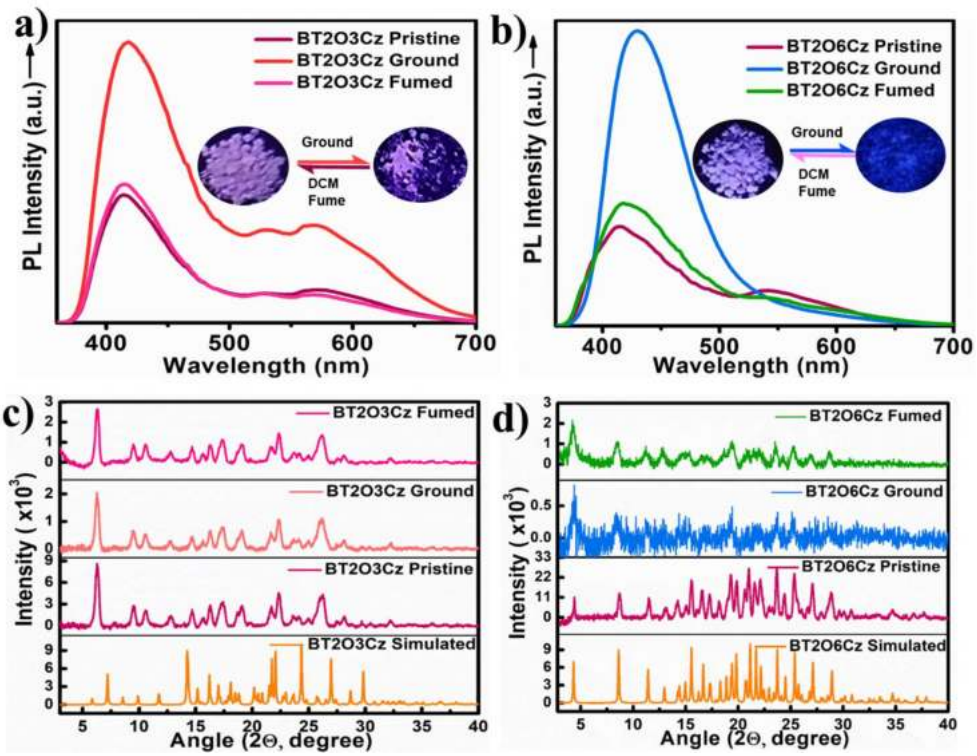

Figure 5.13. (a) PL spectra for Mechanoluminescence behavior of BT2O3Cz emitter. (b) PL spectra for Mechanochromism behavior of the BT2O6Cz emitter at pristine grounded and fumed state, respectively. (c, d) PXRD pattern for BT2O3Cz and BT2O6Cz emitter at pristine grounded and fumed state, respectively.

Noticebly, BT2O3Cz and BT2O6Cz elastomer displayed blue and white emission at 330 nm excitation. However, two simultaneous emission enhancements and switching phenomena for BT2O3Cz and BT2O6Cz were observed under horizontal mechanical stress to the film, akin to the bulk solid crystals mechano-responsive behavior (Figure 5.15a, b).[56, 57] Upon mechanical stretching both the emitters exhibited enhanced PL emission and their single molecular phosphorescence emission from amorphous polymer matrix was found to be at 585 and 650 nm respectively (Figure 5.15c, d). Notably, BT2O6Cz showed intense phosphorescence due to high order non-covalent interactions with long alkyl chains that rigidified the elastomer more effectively. Solid-state mechano-responsive phenomenon was supported by differential scanning calorimetry (DSC) results, which revealed dissimilar endothermic phase transition (melting) at 200 °C and 145 °C for BT2O3Cz and BT2O6Cz. However, an exothermic crystalline phase transition was observed at 107 °C for BT2O3Cz, and this was not found after grinding, depicting the transformation of amorphous material under mechanical stress (Figures A5.8 and A5.9). Regardless of their distinct mechanical stability, both the emitters were thermally stable up to ~400 °C, confirmed by thermogravimetric analysis (TGA) (Figure A5.10). These results indicate that intramolecular packing offers more rigid packing than intermolecular interactions, which could contribute to the emission in distinct ML and MC behavior by restricting the non-radiative transitions.

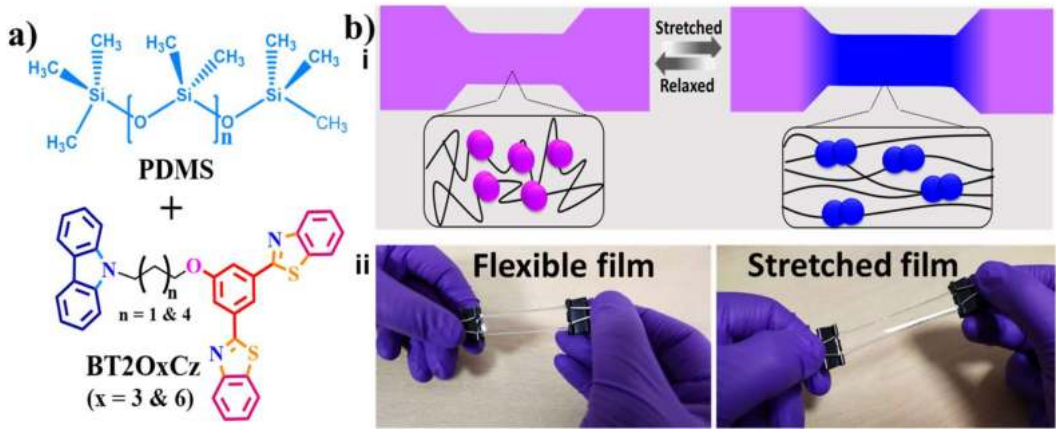

Figure 5.14. (a) Transparent and flexible elastomer were prepared by PDMS and BT2OxCz (0.05%). (b) The mixture was filled in a covered glass slide and kept at 100 ºC for 3h, after solidification, films become flexible elastomers and use for optical studies.

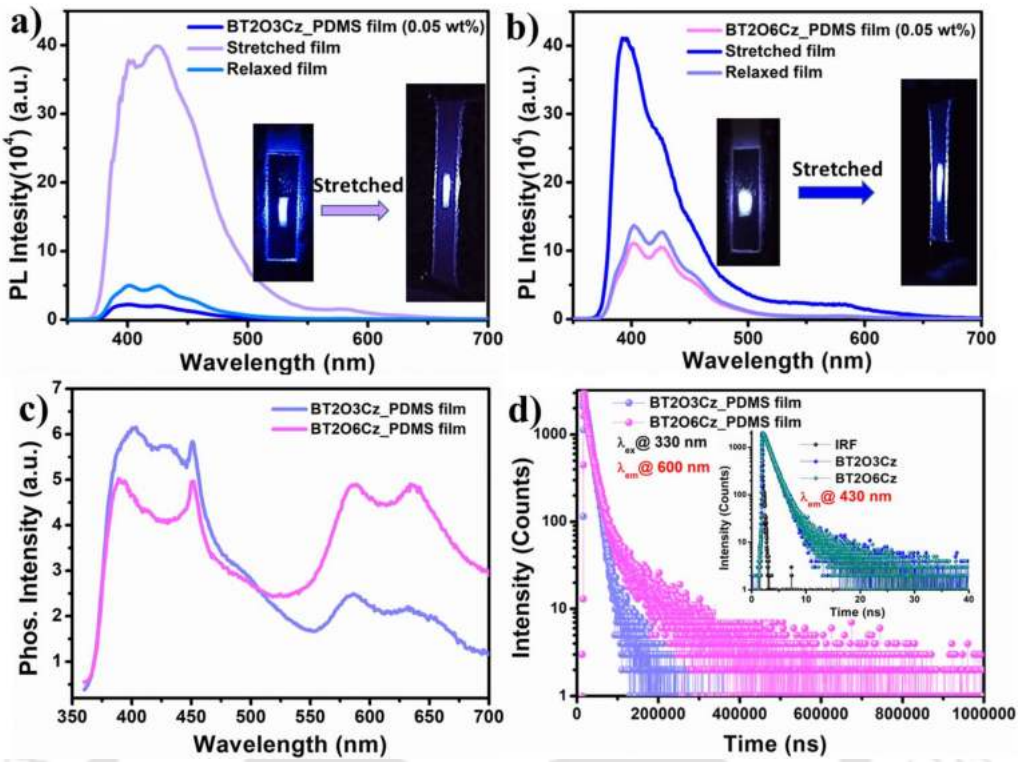

Figure 5.15. (a & b) Steady-state PL spectra of normal stretched and relax mode (inset: photographs of color changes observed in normal and stretch conditions). (c & d) Phosphorescence emission spectra, including prompt and delayed lifetime recorded for the respective band located at 430 and 600 nm respectively.

5.4. Conclusion

In summary, four through-space charge transfer (TSCT) molecular rotors, BT2OxCz (alkyl spacer x = 3, 4, 5 and 6) are reported that display multifunctional properties involving high lying S_n (singlet) and T_m (triplet) manifold charge-separated states and suppressing Kasha's rule. The bridging alkyl chain length between D-A plays a crucial role in controlling the excited-state relaxation process and fine-tuning the emission behavior in the solution and aggregated state, respectively. This work presents the first example of Anti-Kasha's based novel AIEgenic materials and displayed dual fluorescence and phosphorescence originating from extremely higher excited states (>S_5 and T_3) in a single component system. Precisely, deep quantum-mechanical computations (static and dynamic) by TD-DFT and ESD and numerous experimental studies were performed to justify the underlying mechanistic insights of the involvement of higher-lying excited states (>S_1/T_1) and revealed the origin of AIE emission in the condensed state as SOKR. In addition, ESD studies strongly supported the co-existence of thermally elevated fluorescence-phosphoresce emission (TADF and RTP), respectively. The integrated heavy atom-free and amorphous

AIEgens with shorter chain BT2O3CZ, BT2O4CZ and BT2O5CZ displayed TADF, while longer chain BT2O6Cz was more susceptible to exhibit RTP in water owing to their dissimilar H-/J-aggregation packing modes. Moreover, the important role of triplet emission for the enhanced and color switching behavior of all the opted rotors under mechanical stimuli and stretching of flexible ML-active elastomer have also been demonstrated. Through this work, a new concept revealing the unique emission mechanism of WLE in crystals and unusual AIE property in water *via* SOKR, including their intrinsic mechanoresponsive (ML and MC) behavior by varying the alkyl chain length, has been precisely demonstrated. Such an approach presents a new strategy to obtain efficient multifunctional materials by stressing the importance of modulating and optimizing the bridging groups for achieving anti-Kasha based new AIEgenic materials and advanced optoelectronic functions.

5.5. References

[1] H. Tsujimoto, D.-G. Ha, G. Markopoulos, H. S. Chae, M. A. Baldo, T. M. Swager, *J. Am. Chem. Soc.,* **2017,** *139*, 4894-4900.

[2] D. Liu, J. Y. Wei, W. W. Tian, W. Jiang, Y. M. Sun, Z. Zhao, B. Z. Tang, *Chem. Sci.,* **2020,** *11*, 7194-7203.

[3] D. Wang, B. Z. Tang, *Acc. Chem. Res.,* **2019,** *52*, 2559-2570.

[4] G. Huang, Q. Xia, W. Huang, J. Tian, Z. He, B. S. Li, B. Z. Tang, *Angew. Chem., Int. Ed.,* **2019,** *58*, 17814-17819.

[5] C. W. T. Leung, Y. Hong, S. Chen, E. Zhao, J. W. Y. Lam, B. Z. Tang, *J. Am. Chem. Soc.,* **2013,** *135*, 62-65.

[6] F. Hu, S. Xu, B. Liu, *Adv. Mater.,* **2018,** *30*, 1801350.

[7] Z. Liu, H. Zou, Z. Zhao, P. Zhang, G.-G. Shan, R. T. K. Kwok, J. W. Y. Lam, L. Zheng, B. Z. Tang, *ACS Nano,* **2019,** *13*, 11283-11293.

[8] J. F. Lovell, T. W. B. Liu, J. Chen, G. Zheng, *Chem. Rev.,* **2010,** *110*, 2839-2857.

[9] J. F. Lovell, C. S. Jin, E. Huynh, H. Jin, C. Kim, J. L. Rubinstein, W. C. W. Chan, W. Cao, L. V. Wang, G. Zheng, *Nat. Mater.,* **2011,** *10*, 324-332.

[10] J. Mei, N. L. C. Leung, R. T. K. Kwok, J. W. Y. Lam, B. Z. Tang, *Chem. Rev.,* **2015,** *115*, 11718-11940.

[11] Y. Hong, J. W. Y. Lam, B. Z. Tang, *Chem. Commun.,* **2009,** 29, 4332-4353.

[12] D. Ding, K. Li, B. Liu, B. Z. Tang, *Acc. Chem. Res.,* **2013,** *46*, 2441-2453.

[13] Y. Chen, J. W. Y. Lam, R. T. K. Kwok, B. Liu, B. Z. Tang, *Mater. Horiz.,* **2019,** *6*, 428-433.

[14] A. P. Demchenko, V. I. Tomin, P.-T. Chou, *Chem. Rev.,* **2017,** *117*, 13353-13381.

[15] M. Kasha, *Discuss. Faraday Soc.,* **1950,** *9*, 14-19.

[16] S. Scuppa, L. Orian, A. Donoli, S. Santi, M. Meneghetti, *J. Phys. Chem. A,* **2011,** *115*, 8344-8349.

[17] O. Yushchenko, G. Licari, S. Mosquera-Vazquez, N. Sakai, S. Matile, E. Vauthey, *J. Phys. Chem. Lett.,* **2015,** *6*, 2096-2100.

[18] D. Malpicci, E. Lucenti, C. Giannini, A. Forni, C. Botta, E. Cariati, *Molecules,* **2021,** *26*. 6999.

[19] H. Qian, M. E. Cousins, E. H. Horak, A. Wakefield, M. D. Liptak, I. Aprahamian, *Nat. Chem.,* **2017,** *9*, 83-87.

[20] Y.-H. Wu, H. Xiao, B. Chen, R. G. Weiss, Y.-Z. Chen, C.-H. Tung, L.-Z. Wu, *Angew. Chem., Int. Ed.* **2020,** *59*, 10173-10178.

[21] B. H. Jhun, D. Y. Jeong, S. Nah, S. Y. Park, Y. You, *J. Mater. Chem. C,* **2021,** *9*, 7083-7093.

[22] M. Murai, S.-Y. Ku, N. D. Treat, M. J. Robb, M. L. Chabinyc, C. J. Hawker, *Chem. Sci.,* **2014,** *5*, 3753-3760.

[23] P. A. M. Van Den Bogaardt, R. P. H. Rettschnick, J. D. W. Van Voorst, *Chem. Phys. Lett.,* **1976,** *41*, 270-273.

[24] J. E. Kwon, S. Y. Park, *Adv. Mater.,* **2011,** *23*, 3615-3642.

[25] S. I. Druzhinin, P. Mayer, D. Stalke, R. von Bülow, M. Noltemeyer, K. A. Zachariasse, *J. Am. Chem. Soc.,* **2010,** *132*, 7730-7744.

[26] Y. Gong, Y. Zhou, B. Yue, B. Wu, R. Sun, S. Qu, L. Zhu, *J. Phys. Chem. C,* **2019,** *123*, 22511-22518.

[27] P. P. Neelakandan, D. Ramaiah, *Angew. Chem., Int. Ed.,* **2008,** *47*, 8407-8411.

[28] X. Ji, B. Shi, H. Wang, D. Xia, K. Jie, Z. L. Wu, F. Huang, *Adv. Mater.,* **2015,** *27*, 8062-8066.

[29] J. Guo, J. Fan, L. Lin, J. Zeng, H. Liu, C.-K. Wang, Z. Zhao, B. Z. Tang, *Adv. Sci.,* **2019,** *6*, 1801629.

[30] C. A. Masmanidis, H. H. Jaffe, R. L. Ellis, *J. Phys. Chem.,* **1975,** *79*, 2052-2061.

[31] M. A. El-Sayed, *Acc. Chem. Res.,* **1971,** *4*, 23-31.

[32] D. Barman, M. Annadhasan, R. Chandrasekar, P. K. Iyer, *Chem. Sci.,* **2022***,13,* 9004-9015.

[33] Y. Tu, J. Liu, H. Zhang, Q. Peng, J. W. Y. Lam, B. Z. Tang, *Angew. Chem., Int. Ed.,* **2019,** *58*, 14911-14914.

[34] Y. Xu, P. Xu, D. Hu, Y. Ma, *Chem. Soc. Rev.,* **2021,** *50*, 1030-1069.

[35] Z. He, W. Zhao, J. W. Y. Lam, Q. Peng, H. Ma, G. Liang, Z. Shuai, B. Z. Tang, *Nat. Commun.,* **2017,** *8*, 416.

[36] B. Huang, W.-C. Chen, Z. Li, J. Zhang, W. Zhao, Y. Feng, B. Z. Tang, C.-S. Lee, *Angew. Chem., Int. Ed.,* **2018,** *57*, 12473-12477.

[37] J. Wang, Z. Chai, J. Wang, C. Wang, M. Han, Q. Liao, A. Huang, P. Lin, C. Li, Q. Li, Z. Li, *Angew. Chem., Int. Ed.,* **2019,** *58*, 17297-17302.

[38] T. Itoh, *Chem. Rev.,* **2012,** *112*, 4541-4568.

[39] S. M. A. Fateminia, Z. Mao, S. Xu, Z. Yang, Z. Chi, B. Liu, *Angew. Chem., Int. Ed.,* **2017,** *56*, 12160-12164.

[40] X.-F. Wang, W.-J. Guo, H. Xiao, Q.-Z. Yang, B. Chen, Y.-Z. Chen, C.-H. Tung, L.-Z. Wu, *Adv. Funct. Mater.,* **2020,** *30*, 1907282.

[41] F. Gao, R. Du, C. Han, J. Zhang, Y. Wei, G. Lu, H. Xu, *Chem. Sci.,* **2019,** *10*, 5556-5567.

[42] N. Mataga, Y. Kaifu, M. Koizumi, *B. Chem. Soc. Jpn.,* **1956,** *29*, 465-470.

[43] X.-F. Wang, H. Xiao, P.-Z. Chen, Q.-Z. Yang, B. Chen, C.-H. Tung, Y.-Z. Chen, L.-Z. Wu, *J. Am. Chem. Soc.,* **2019,** *141*, 5045-5050.

[44] C. Feng, S. Li, L. Fu, X. Xiao, Z. Xu, Q. Liao, Y. Wu, J. Yao, H. Fu, *J. Phys. Chem. Lett.,* **2020,** *11*, 8246-8251.

[45] R. W. Chambers, T. Kajiwara, D. R. Kearns, *J. Phys. Chem.,* **1974,** *78*, 380-387.

[46] X.-N. Li, M. Yang, X.-L. Chen, J.-H. Jia, W.-W. Zhao, X.-Y. Wu, S.-S. Wang, L. Meng, C.-Z. Lu, *Small,* **2019**, *15*, 1903270.

[47] Y. Wang, J. Yang, Y. Tian, M. Fang, Q. Liao, L. Wang, W. Hu, B. Z. Tang, Z. Li, *Chem. Sci.,* **2020,** *11*, 833-838.

[48] M. J. Frisch, *et. al*., Gaussian, Inc., Wallingford CT, 2016.

[49] F. Neese, F. Wennmohs, U. Becker, C. Riplinger, *J. Chem. Phys.,* **2020,** *152*, 224108.

[50] L. Shi, C. Yan, Z. Guo, W. Chi, J. Wei, W. Liu, X. Liu, H. Tian, W.-H. Zhu, *Nat. Commun.,* **2020**, *11*, 793.

[51] M. K. Etherington, J. Gibson, H. F. Higginbotham, T. J. Penfold, A. P. Monkman, *Nat. Commun.,* **2016,** *7*, 13680.

[52] C. A. M. Salla, G. Farias, M. Rouzières, P. Dechambenoit, F. Durola, H. Bock, B. de Souza, I. H. Bechtold, *Angew. Chem., Int. Ed.,* **2019,** *58*, 6982-6986.

[53] W. Zhao, T. S. Cheung, N. Jiang, W. Huang, J. W. Y. Lam, X. Zhang, Z. He, B. Z Tang, *Nat. Commun.,* **2019***, 10*, 1595.

[54] B. de Souza, G. Farias, F. Neese, R. Izsák, *J. Chem. Theory Comput.* **2019,** *15*, 1896-1904.

[55] R. Taniguchi, T. Yamada, K. Sada, K. Kokado, *Macromolecules* **2014**, *47*, 6382-6388.

[56] Y. Zhang, Q. Sun, L. Yue, Y. Wang, S. Cui, H. Zhang, S. Xue, W. Yang, *Adv. Sci.,* **2022**, *9*, 2103402.

[57] Y. Sagara, H. Traeger, J. Li, Y. Okado, S. Schrettl, N. Tamaoki, C. Weder, *J. Am. Chem. Soc.* **2021**, *143*, 5519–5525.

Appendix: Additional data for **Chapter 5**

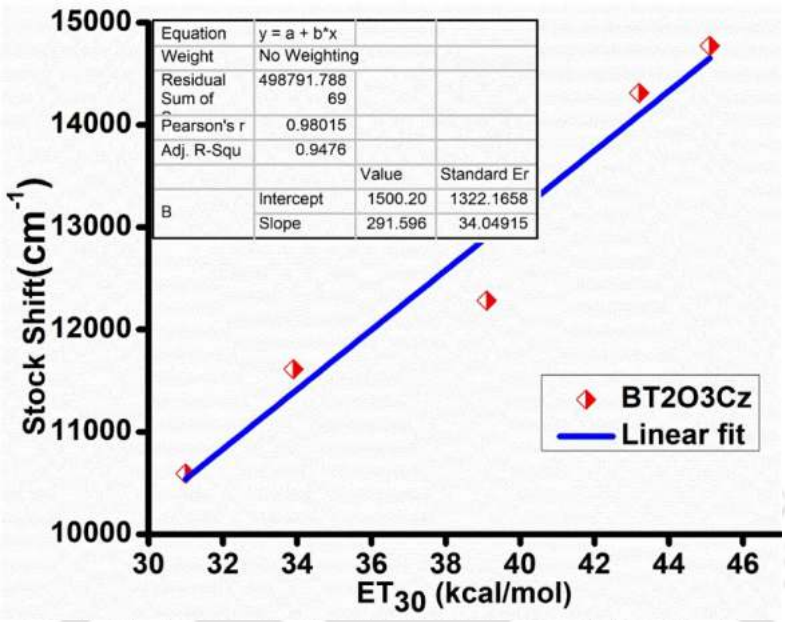

Figure A5.1. The extent of solvatochromism was tested by the Lippert-Mataga plot Stokes shift of BT2O3Cz in different solvents, plotted against their ET(30) values and fitted with straight line. Notably, the Stokes shift and emission maxima of BT2O3Cz show a regular increment and positive slope with the increase of solvent polarity.[2]

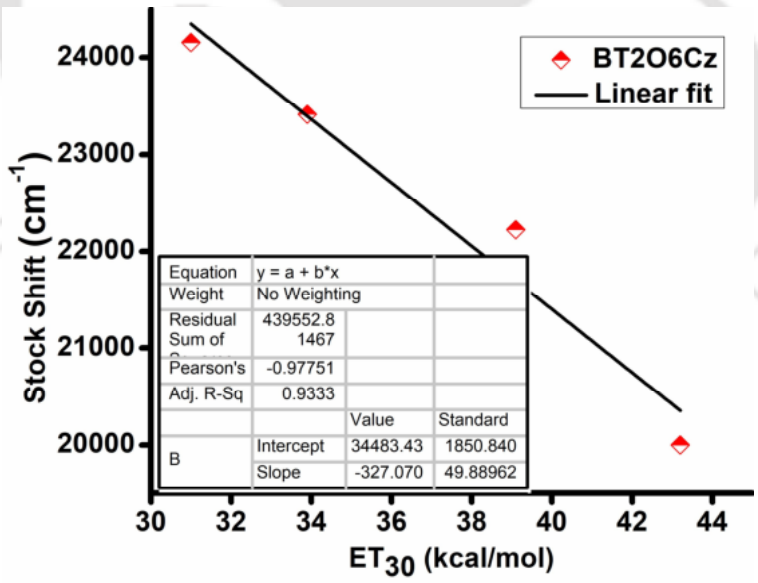

Figure A5.2. The extent of solvatochromism was tested by the Lippert-Mataga plot Stokes shift of BT2O5Cz in different solvents, plotted against their ET(30) values and fitted with straight line. Notably, the Stokes shift and emission maxima of BT2O6Cz show a negative slope with the increase of solvent polarity.[2]

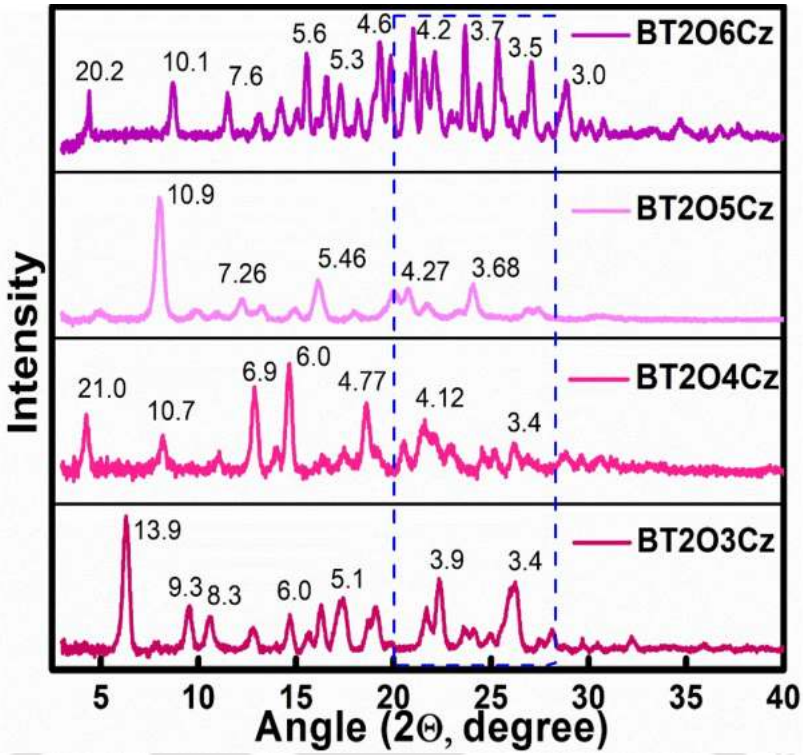

Figure A5.3. PXRD pattern for BT2OxCz, longer chain BT2O6Cz exhibiting high order packing and multiple peaks rather than shorter chain AIEgens.

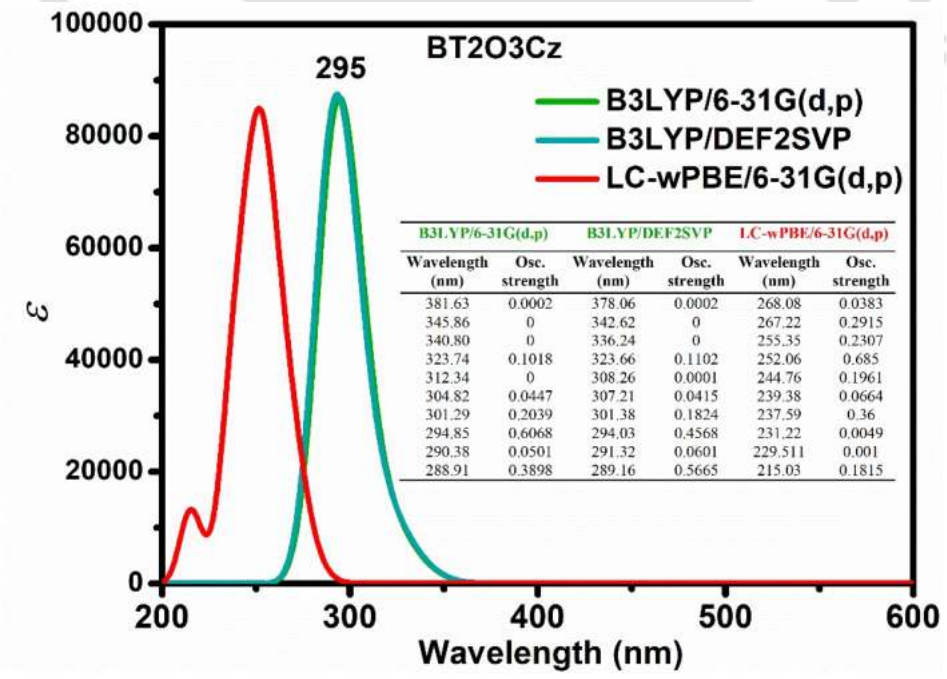

B3LYP/6-31G(d,p)		B3LYP/DEF2SVP		LC-wPBE/6-31G(d,p)	
Wavelength (nm)	Osc. strength	Wavelength (nm)	Osc. strength	Wavelength (nm)	Osc. strength
381.63	0.0002	378.06	0.0002	268.08	0.0383
345.86	0	342.62	0	267.22	0.2915
340.80	0	336.24	0	255.35	0.2307
323.74	0.1018	323.66	0.1102	252.06	0.685
312.34	0	308.26	0.0001	244.76	0.1961
304.82	0.0447	307.21	0.0415	239.38	0.0664
301.29	0.2039	301.38	0.1824	237.59	0.36
294.85	0.6068	294.03	0.4568	231.22	0.0049
290.38	0.0501	291.32	0.0601	229.511	0.001
288.91	0.3898	289.16	0.5665	215.03	0.1815

Figure A5.4. Theoretical UV-visible spectrum for BT2O6Cz calculated from three different function and basis sets and their comparasion table (inset). B3LYP/6-31G(d,p) and B3LYP/DEF2SVP exhibited well matched results with experimental results.

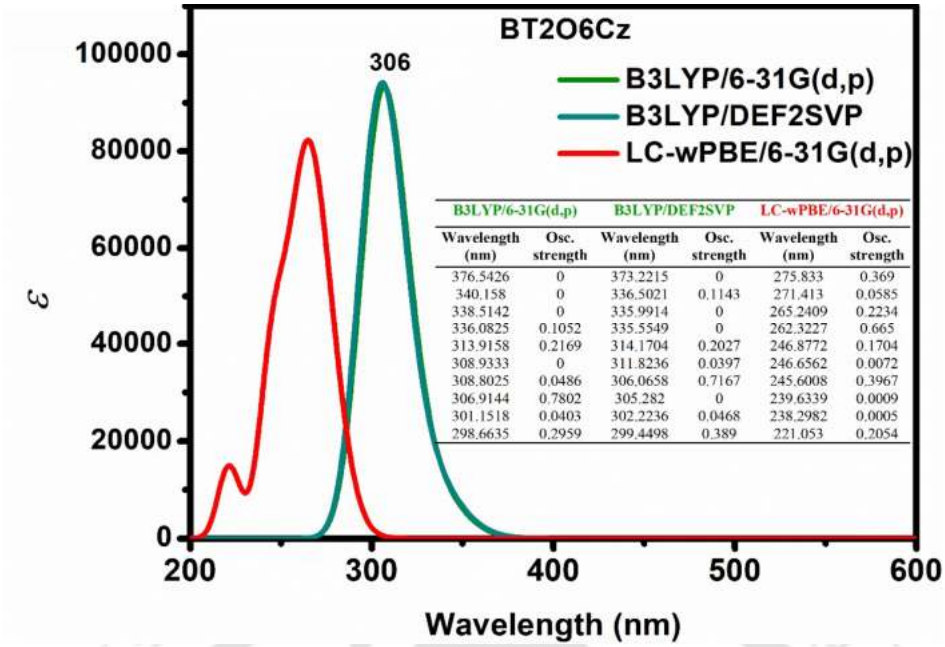

B3LYP/6-31G(d,p)		B3LYP/DEF2SVP		LC-wPBE/6-31G(d,p)	
Wavelength (nm)	Osc. strength	Wavelength (nm)	Osc. strength	Wavelength (nm)	Osc. strength
376.5426	0	373.2215	0	275.833	0.369
340.158	0	336.5021	0.1143	271.413	0.0585
338.5142	0	335.9914	0	265.2409	0.2234
336.0825	0.1052	335.5549	0	262.3227	0.665
313.9158	0.2169	314.1704	0.2027	246.8772	0.1704
308.9333	0	311.8236	0.0397	246.6562	0.0072
308.8025	0.0486	306.0658	0.7167	245.6008	0.3967
306.9144	0.7802	305.282	0	239.6339	0.0009
301.1518	0.0403	302.2236	0.0468	238.2982	0.0005
298.6635	0.2959	299.4498	0.389	221.053	0.2054

Figure A5.5. Theoretical UV-visible spectrum for BT2O6Cz calculated from three different function and basis sets and their comparasion table (inset). B3LYP/6-31G(d,p) and B3LYP/DEF2SVP exhibited well matched results with experimental results.

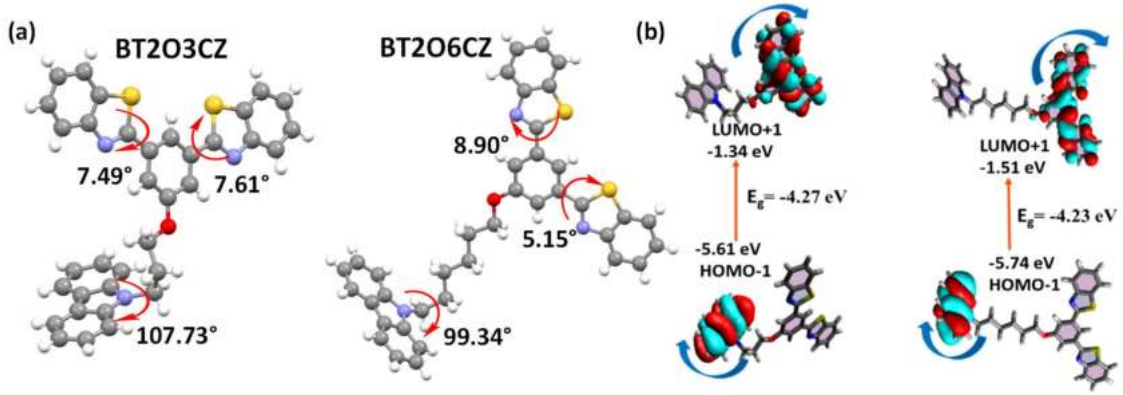

Figure A5.6. Dihedral angle of each rotor groups present in BT2O3Cz and BT2O6Cz SC-structure (a). Higher frontier molecular orbital (FMO) contribution of BT2O3Cz and BT2O6Cz respectively showed prominent localization of electron densities over their respective donor and acceptor units (b) at B3LYP/6-31G(d,p) level.

Table A5.1. Adiabatic energy transitions with major frontier orbital contribution for BT2O3CZ at B3LYP/6-31G (d,p) level for singlet states.

State	Energy (eV)	Energy (cm^{-1})	Wavelength (nm)	Osc. Strength	Symmetry	Major contributions
S_1	3.24	26203.34029	381.6307345	0.0002	HOMO→LUMO	100%
S_2	3.58	28913.36317	345.8608375	0	H-1→LUMO	100%
S_3	3.63	29342.45013	340.8031694	0	HOMO→L+1	100%
S_4	3.82	30888.61497	323.7438781	0.1019	H-3→LUMO	55%
S_5	3.96	32016.17806	312.342091	0	H-1→L+1	100%
S_6	4.06	32805.79485	304.8241948	0.0447	HOMO→L+2	88%
S_7	4.11	33190.52131	301.2908386	0.2039	H-3→LUMO	22%
S_8	4.20	33914.00063	294.8634727	0.6071	H-3→LUMO	17%
S_9	4.26	34436.6479	290.3883104	0.0501	H-5→LUMO	21%
S_{10}	4.29	34612.47677	288.9131589	0.3902	H-5→LUMO	53%

Table A5.2. Adiabatic energy transitions with major frontier orbital contribution for BT2O3CZ at B3LYP/6-31G (d,p) level for triplet states.

State	Energy (eV)	Energy (cm^{-1})	Wavelength (nm)	Osc. Strength	Symmetry	Major contributions
T_1	2.74	22172.18125	451.0156166	0	H-2→LUMO	66%
T_2	3.12	25170.95062	397.2833665	0	H-3→LUMO	33%
T_3	3.22	26011.38034	384.4471101	0	H-1→L+2	77%
T_4	3.24	26193.66164	381.7717484	0	HOMO→LUMO	98%
T_5	3.33	26935.69171	371.2546204	0	H-6→LUMO	14%
T_6	3.38	27288.96255	366.4485222	0	HOMO→L+2	90%
T_7	3.54	28587.51518	349.8030499	0	H-5→LUMO	21%
T_8	3.58	28914.16973	345.8511897	0	H-1→LUMO	100%
T_9	3.60	29057.73641	344.1424293	0	H-4→L+1	13%
T_{10}	3.64	29358.58122	340.6159149	0	HOMO→L+1	95%

Table A5.3. Adiabatic energy transitions with major frontier orbital contribution for BT2O6CZ at B3LYP/6-31G(d,p) level for singlet states.

State	Energy (eV)	Energy (cm^{-1})	Wavelength (nm)	Osc. Strength	Symmetry	Major contributions
S_1	3.29	26557.41768	376.5426337	0	HOMO→LUMO	100%
S_2	3.64	29398.10238	340.1580099	0	HOMO→L+1	100%
S_3	3.66	29540.86252	338.5141512	0	H-1→LUMO	100%
S_4	3.68	29754.59944	336.0824944	0.1053	H-3→LUMO	75%
S_5	3.94	31855.67373	313.9158219	0.2169	H-2→ LUMO	85%
S_6	4.01	32369.4489	308.9332794	0	H-1→L+1	100%
S_7	4.01	32383.16032	308.8024733	0.0486	HOMO→L+2	92%
S_8	4.03	32582.37927	306.9143575	0.7802	H-3→LUMO	14%
S_9	4.11	33205.84584	301.1517926	0.0402	H-5→LUMO	16%
S_{10}	4.15	33482.49401	298.6635343	0.296	H-5→LUMO	62%

Table A5.4. Adiabatic energy transitions with major frontier orbital contribution for BT2O6CZ at B3LYP/6-31G(d,p) level for triplet states.

State	**Energy (eV)**	**Energy (cm^{-1})**	**Wavelength (nm)**	**Osc. Strength**	**Symmetry**	**Major contributions**
T_1	2.58	20842.173	479.7964205	0	H-3→L+1	14%
T_2	2.93	23652.20863	422.7934971	0	H-3→LUMO	35%
T_3	3.17	25575.84094	390.9939862	0	H-1→L+2	74%
T_4	3.20	25870.23331	386.5446392	0	H-6→LUMO	18%
T_5	3.29	26557.41768	376.5426337	0	HOMO→LUMO	100%
T_6	3.32	26796.96435	373.1765983	0	HOMO→L+2	93%
T_7	3.41	27520.44367	363.3662349	0	H-5→LUMO	11%
T_8	3.45	27846.29166	359.1142448	0	H-5→LUMO	10%
T_9	3.61	29186.78512	342.6208114	0	H-6→LUMO	21%
T_{10}	3.64	29398.10238	340.1580099	0	HOMO→L+1	100%

Table A5.5: Summary table of the computational results obtained by Gaussian 16 package at B3LYP/6-31G(d,p) level for isolated BT2O3Cz and BT2O6Cz dimer.

Emitters	λ_{abs} (nm)	HOMO (H)(eV)	HOMO -1 (eV)	LUMO (L)eV)	LUMO+1 (eV)	Eg (eV)	ΔE_{ST} (eV)	Oscillator strength (*f*)	μ_d (Debye)
BT2O3Cz	295	-5.28	-5.60	-1.67	-1.32	3.61	0.50	0.204(S_7)	2.5713
BT2O4Cz	298	-5.38	-5.77	-1.85	-1.53	3.53	0.62	0.254(S_6)	1.9951
BT2O5Cz	312	-5.35	-5.75	-1.84	-1.53	3.51	0.63	0.303(S_6)	2.9153
BT2O6Cz	343	-5.30	-5.38	-1.84	-1.63	3.45	0.64	0.020 (S_5)	1.9857

Table A5.6. Ground and Excited State Electronic Energies for Compound BT2O3Cz.

Rotor Angle	Electronic Energy (cm^{-1})				
	S_0	S_1	S_7	S_8	S_{10}
0	0	22673.92403	29947.31326	31154.42373	31154.42373
10	100.9583298	22891.20391	30059.24532	31253.18731	31253.18731
20	373.106871	23227.00009	30353.34133	31525.33585	31525.33585
30	744.0189957	23690.09156	30750.59041	31905.02696	31905.02696
40	1158.826046	24251.94662	31180.76068	32322.02876	32322.02876
50	1551.685634	24815.99641	31580.20451	32714.88835	32714.88835
60	1854.560624	25265.91941	31878.69001	33008.98435	33008.98435
70	2010.387611	25478.8098	32023.54326	33156.03235	32023.54326
80	2003.803372	25377.85147	32012.56953	33149.44812	32012.56953
90	1865.534355	25127.65039	31865.52153	33013.37384	31865.52153
100	1652.643964	24732.59605	31641.65741	32800.48345	31641.65741
110	1413.416617	24361.68393	31384.87209	32554.67187	31384.87209
120	1218.084197	24107.09336	31178.56594	32361.53419	31178.56594
130	1125.904852	23992.96655	31066.63388	32269.35485	31066.63388
140	1112.736374	23920.53992	31038.10217	32264.96536	31038.10217

150	1152.241808	23883.22924	31071.02337	32313.24977	31071.02337
160	1231.252674	23896.39771	31130.28152	32383.48166	31130.28152
170	1277.342347	23582.54899	31152.22898	32414.2081	31152.22898
180	1255.394884	23279.674	31121.50253	32385.6764	31121.50253
190	1189.552495	23093.12057	31044.68641	32315.44452	31044.68641
200	1040.309746	23062.39412	30904.22265	32174.98076	30904.22265
210	746.213742	22948.26731	30627.68462	31891.85849	30627.68462
220	438.94926	22941.68307	30331.39387	31591.17824	30331.39387
230	243.6168393	23047.0309	30149.22992	31398.04057	30149.22992
240	151.4374947	23202.85788	30068.02431	31305.86122	30068.02431
250	149.2427484	23378.43759	30074.60855	31305.86122	30074.60855
260	261.1748097	23593.52273	30188.73536	31415.59854	30188.73536
270	471.8704545	23852.50279	30403.82049	31628.48893	30403.82049
280	739.6295031	24115.87234	30673.77429	31896.24798	30673.77429
290	989.8305813	24317.789	30923.97537	32146.44906	30923.97537
300	1141.268076	24385.82614	31077.60761	32300.0813	31077.60761
310	1134.683837	24153.18303	31075.41286	32293.49706	31075.41286
320	963.4936257	23782.27091	30908.61214	32122.30685	30908.61214
330	675.9818604	23413.55353	30623.29512	31834.79508	30623.29512
340	351.159408	22987.77275	30300.66742	31507.77788	30300.66742
350	94.3740909	22706.84522	30039.49261	31250.99257	30039.49261
360	0	22673.92403	29947.31326	31154.42373	29947.31336

Table A5.11. Natural transition orbitals (NTOs) for different singlet excited states in BT2O3Cz.

Geometry	Hole	Electron	λ	Character
S_1	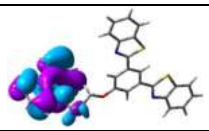	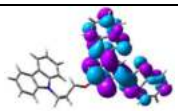	0.99	^{1}ICT
S_2	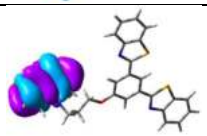	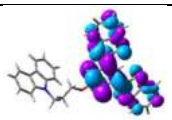	0.99	^{1}ICT
S_3		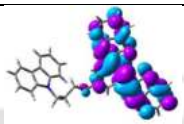	0.99	^{1}ICT
S_4	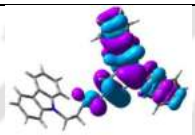	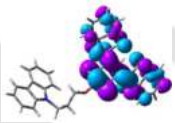	0.87	^{1}LE
S_6	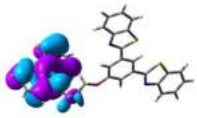		0.88	^{1}LE
S_7	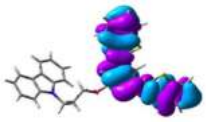	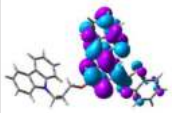	0.91	^{1}LE

Table A5.12. Natural transition orbitals (NTOs) for different singlet excited states in BT2O3Cz.

Geometry	Hole	Electron	λ	Character
T_1	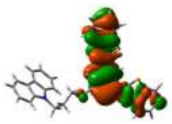	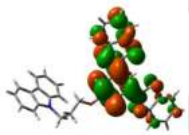	0.78	^{3}LE
T_2	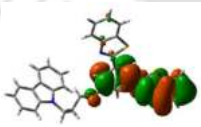		0.61	^{3}LE
T_3	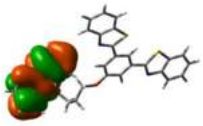	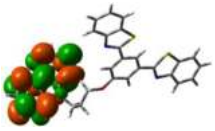	0.86	^{3}LE
T_4	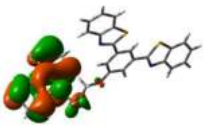	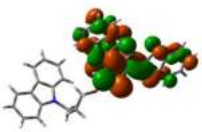	0.98	^{3}ICT

T_5	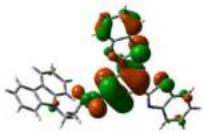	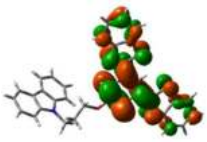	0.77	^{3}LE
T_6	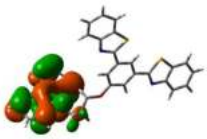		0.96	^{3}LE
T_7	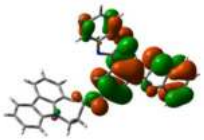		0.56	^{3}LE
T_8			0.99	^{3}ICT
T_9		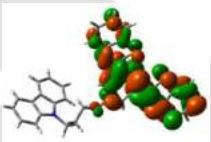	0.53	^{3}HLCT
T_{10}		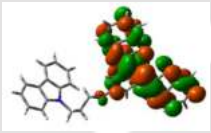	0.98	^{3}HLCT

Table A5.13. Natural transition orbitals (NTOs) for different singlet excited states in BT2O6Cz.

Geometry	Hole	Electron	λ	Character
S_1	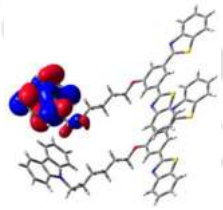	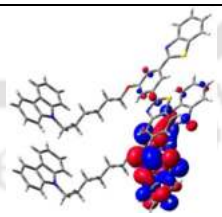	1.00	^{1}ICT
S_5	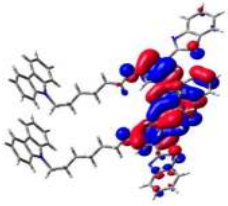	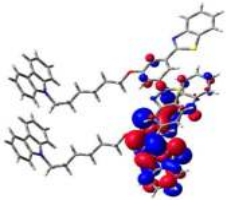	0.97	^{1}LE

Table A5.14. Natural transition orbitals (NTOs) for different triplet excited states in BT2O6Cz.

Geometry	Hole	Electron	λ	Character
T_1	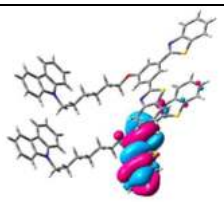	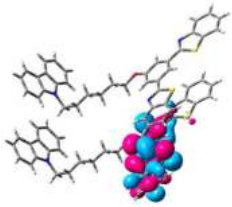	0.90	^{3}LE
T_3	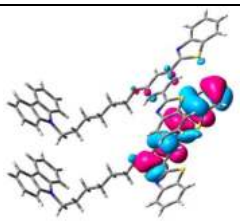	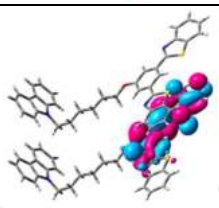	0.78	^{3}LE
T_4	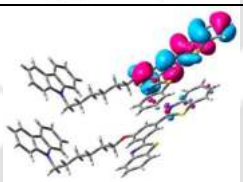	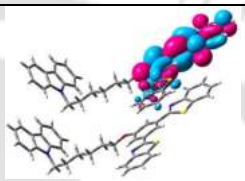	0.70	^{3}LE
T_5	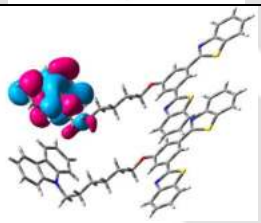	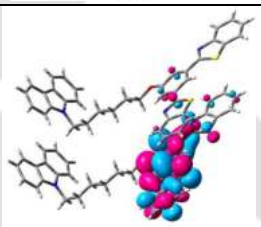	0.90	^{3}ICT

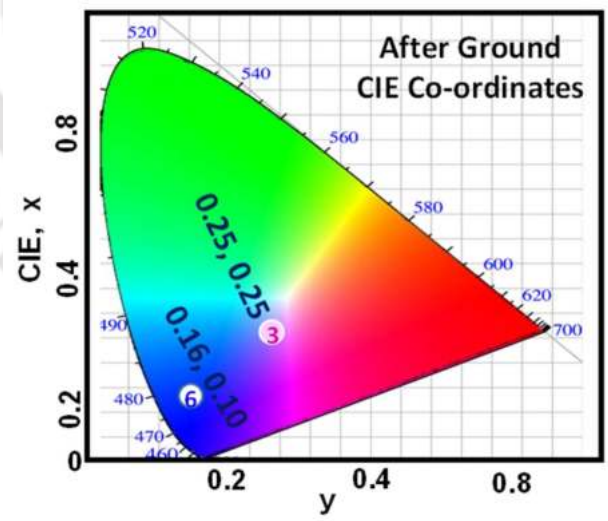

Figure A5.7. CIE coordinate diagram for Mechanoluminescence BT2O3Cz and Mechanochromism BT2O6Cz emitter at grounded state respectively.

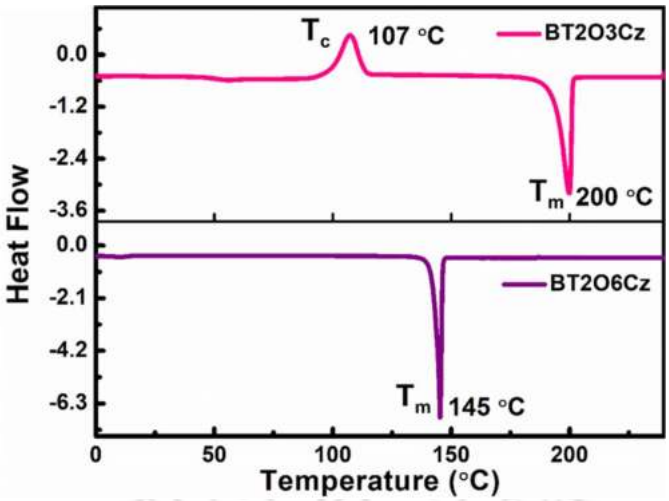

Figure A5.8. Differential scanning calorimetry (DSC) to investigate phase transition of the short and long chain BT2O3Cz and BT2O6Cz respectively (before grinding).

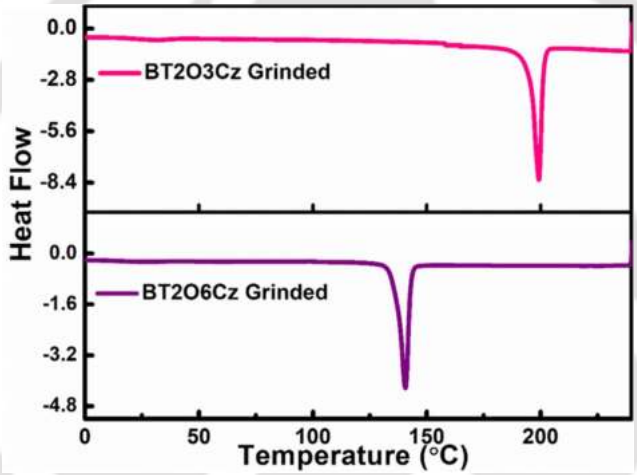

Figure A5.9. Differential scanning calorimetry (DSC) to investigate phase transition of the short and long chain BT2O3Cz and BT2O6Cz respectively (after grinding).

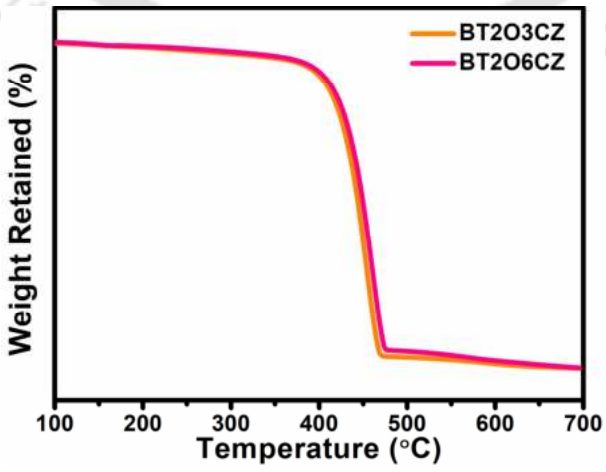

Figure A5.10. Thermogravimetric analysis (TGA) to investigate thermal stability of the short and long chain BT2O3Cz and BT2O6Cz respectively.[2]

CHAPTER 6

Modulation of Donor in Purely Organic Triplet Harvesting AIE-TADF Photosensitizer for Image-guided Photodynamic Therapy

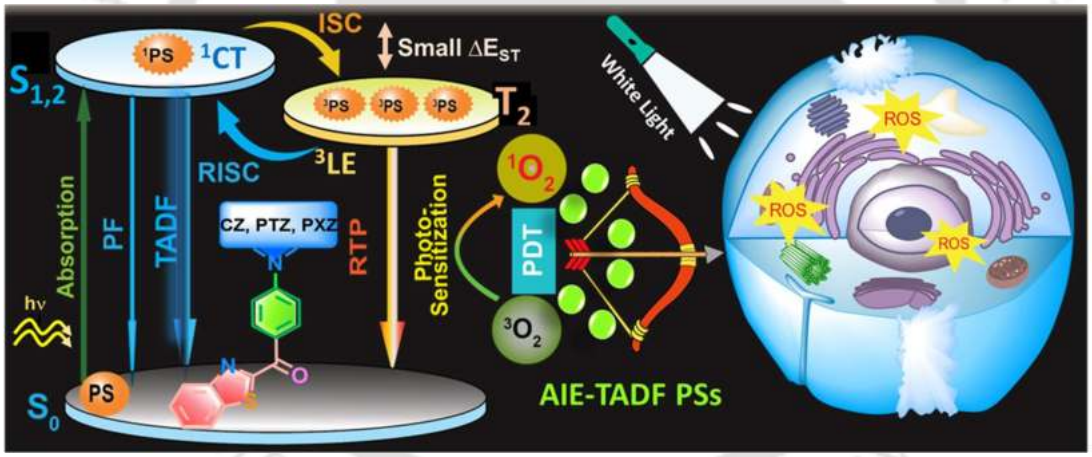

Barman, D., Rajamalli, P., Bidkar, A.P., Narang, K., Ghosh, S. S., Zysman-Colman, E., Iyer, P. K. (*Communicated*)

Abstract

Image-guided photodynamic therapy (PDT) has been acknowledged as one of the most demonstrative therapeutic modalities for cancer treatment, owing to its precision, non-invasiveness and improved imaging ability. Unlike, conventional photosensitizers (PSs) with low contrast imaging, weaker sensitivity and dark cytotoxicity, herein, we have designed and synthesized a series of purely organic PSs denoted as BTMCZ, BTMPTZ and BTMPXZ, exhibiting thermally activated delayed fluorescence (TADF) and aggregation induced emission (AIE) characteristics. Experimental and theoretical studies revealed that modulation of donor in the PSs enables to finely adjust energy gap (ΔE_{ST}) via second-order spin-orbit perturbation, involving lowest singlet (^{1}CT) and higher-lying triplet (^{3}LE) states along with rigid crystal packing of H-, X, and J-type aggregation greatly influencing Color-tunable up-converted luminescence. Further, confocal-microscopy-based cellular uptake study confirms the internalization of nano-probe PSs and BTMCZ enables to generate reactive oxygen species (ROS) under white-light irradiation, which efficiently kills the cancer cells.

6.1 Introduction

Image-guided photodynamic therapy (PDT) represents a well-consolidated and attractive approach to the treatment of cancer in recent years.[1,2] Regardless of few well-established advanced clinical cancer treatment methods such as chemotherapy and radiotherapy, these treatments inevitably cause toxic side effects, induce bodily damage and other serious problems that can even lead to the death of a patient.[3,4] In contrast, photo-regulated therapy has several advantages, including high spatiotemporal specificity, high repeatability, low drug resistance, negligible side effects and noninvasive in nature.[5,6,7] Typically, this therapy involves three simple components, such as a photon-harvesting chromophores called photosensitizer (PS), an excitation light source with a specific wavelength and molecular oxygen.[8,9] In principle, after external photo-excitation of PS, the excited PS, may directly decay by emitting light or followed by intersystem crossing (ISC) process between singlet and triplet excited state from its either lowest (S_1/T_1) or higher manifold (S_n/T_m) states, when their respective energy gap (ΔE_{ST}) and oscillator strength (*f*) is sufficiently small.[10] Subsequently, energy transfer occurs from the T_1/T_m of the PS to the surroundings molecular oxygen ($^3O_2$), generating the primary cytotoxic agent termed reactive oxygen species (ROS), which causes oxidative damage to the targets.[11] Primarily, the efficient generation of $^1O_2$ in this photodynamic process is immensely controlled by ISC efficiency of the sensitizer with minimized concentration quenching of the excited state. Substantially, photosensitization and generation of ROS is not only beneficial for PDT but also found great research interest in the fields of sensors,[12] synthetic organic chemistry (used as photocatalytic agent),[13] and wastewater treatment,[14,15] respectively. Therefore, in order to harvest triplets and construct an efficient PS, typically, assimilation of heavy atoms into organic molecular frameworks is one of the widely used approaches to enhance spin-orbit perturbations (SOP), thereby improving ISC efficiency and $^1O_2$ generation.[16,17] Conversely, the inclusion of heavy atoms such as bromine, iodine, selenium and certain lanthanides has often been found to show intrinsic effects of "dark cytotoxicity" and high synthetic cost thereby limiting their use in the clinical and other applications.[18] Besides, to reduce the excited-state concentration quenching effect, formulation of low diameter nanoparticles strategies was proposed, embedding with certain functionalized phospholipids-polymer embedded PSs and resulting biocompatible nano-assemblies.[19,21] However, polymer encapsulated nanoaggregates lead to significantly decreased fluorescence intensity and PDT efficiency using hydrophobic planar porphyrin-

based derivatives due to the notorious aggregation-caused quenching (ACQ) effect.[22] Therefore, exploration of encapsulation-free triplet-harvesting PSs design strategy for purely organic small molecules is relatively challenging task. It is thus important to search alternative strategies by avoiding heavy atoms and planar molecular structures of PS to minimize dark toxicity and severe ACQ effects. Recent advances demonstrated that aggregation-induced emission (AIE),[23] opposite to ACQ effect, displayed strong emission in aggregated/solid-state owing to its propeller-like π-conjugated structures[24] and/or in a twisted donor-acceptor (D-A) system.[25] AIEgens are easily prevent energy dissipation by circumventing non-radiative decays, beneficial for the real-time tracking with high-resolution imaging of cells and tissues in biomedical exploration.[26] Besides, D-A structures, in particular, have been demonstrated to harness long-lived triplets depicted as thermally activated delayed fluorescence (TADF) [27] with the aid of ambient state reverse ISC (RISC) at reduced ΔE_{ST}, resulting in long fluorescence lifetimes of microsecond (μs) to millisecond (ms) scale, enabling the probe more potential for eliminating tissue auto-fluorescence and offering an effective strategy to regulate $^1O_2$ generation for PDT.[28] ROS generation efficiency depends on the ISC and RISC rate, where rate constants could be estimated using the equation 1 and 2: [29,30]

$$k_{ISC} \propto \frac{\langle S_1|H_{SO}|T_1\rangle^2}{\Delta E_{ST}} \qquad \text{Equation 6.1}$$

$$k_{RISC} \propto \exp\left(-\frac{\Delta E_{ST}}{k_B T}\right) \qquad \text{Equation 6.2}$$

Where, H_{SO} is the Hamiltonian for the SOP and ΔE_{ST} is the energy gap between the lowest singlet (S_1) and lowest triplet excited state (T_1) or certain higher energy states (S_n/T_m). Notably, RISC can be accelerated by ISC mixing of T_1 with S_1 or S_n/T_m states via strong SOP. Hence, these equations build a good relationship among ISC/RISC rate, ΔE_{ST}, and $^1O_2$ generation.

Markedly, triplet-harvesting fluorogens, especially AIE-TADF emitters are well familiarized in the field of OLEDs,[31] however, recently, few of these classes of materials have attractive properties in particular importance for photocatalysis and biomedical applications owing to their photo-induced electron and/or energy transfer ability.[27,32] Therefore, taking advantage of the unique dynamic excited-state properties of AIEgens deliberately motivated us to design a new D-A-based efficient PS for image-guided PDT.[33] Therefore, modulation of the excited states and population of triplets at higher yields are found to be an effective strategy to develop efficient PDT active PS. Noticeably, nearly all

the reported triplet-harvesting PSs rely on conventional knowledge of spin flipping between S_1 and T_1 only at limited SOC and ISC efficiency. Thus far, a molecular probe having higher vibronic SOC ascribing an efficient ISC-RISC based TADF PS, has not been reported to the best of our knowledge. [34] In this work, a series of AIE active triplet harvesting PSs were rationally designed and synthesized, denoted as BTMCZ, BTMPTZ and BTMPXZ. Modulation of the donor into newly explored acceptor benzo [d] thiazol-2-yl) methanone core leads to desirable ΔE_{ST}, *f*, high photoluminescence quantum yield (PLQY) and perceiving H-, J-, and X-type supramolecular arrangements prompted color tunable and long-lived emission. Collectively by adjusting different electron donating strengths and structural rigidity/planarity/flexibility of the donor segments, we could control the singlet-triplet excitons release simultaneously.

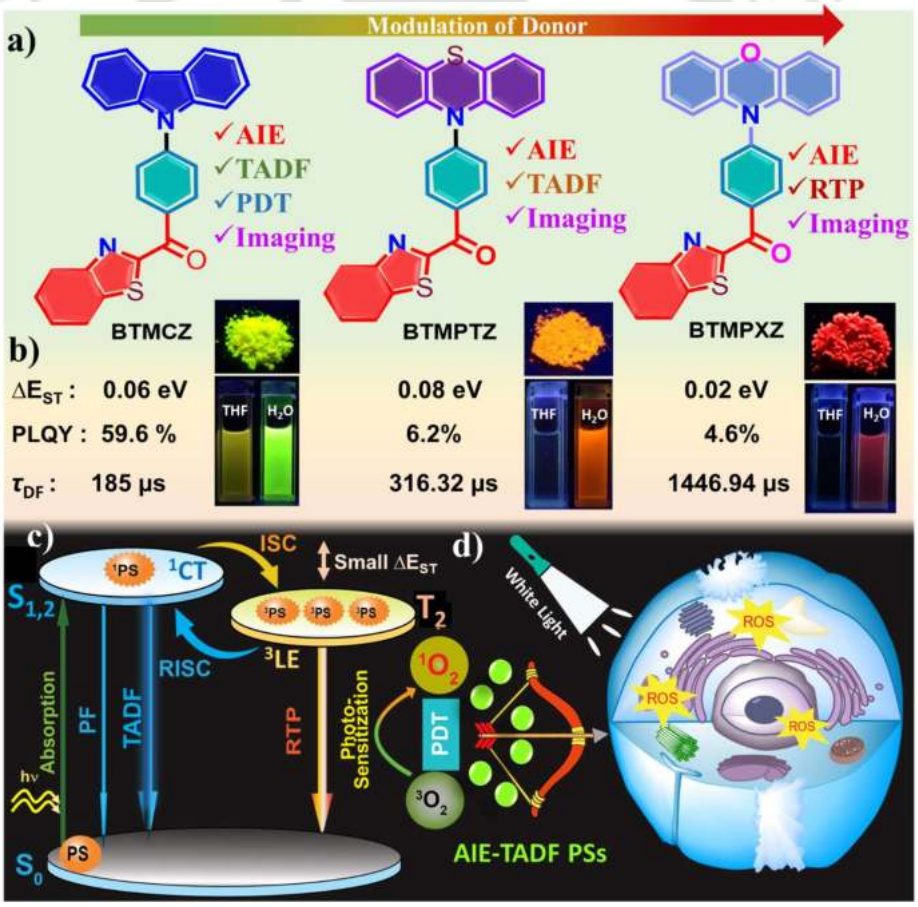

Figure 6.1. (a) Chemical structure of BTMCZ, BTMPTZ, BTMPXZ. (b) Color-tunable optical properties in aggregated and solid state (images were taken under 365 nm UV-lamp). (c) Illustration of Jablonski diagram for multi-emissions (PF, TADF and RTP) involving active singlet (1CT) and triplet (3LE) states. (d) Representation of ROS generation mechanism for PDT activity.

Of particular note, we have investigated a complex second-order spin-vibronic coupling mechanism which is induced by the involvement of charge-transfer singlet (^{1}CT) and charge-transfer triplet (^{3}CT) states via energetically closest local triplet (^{3}LE) state, resulting in efficient TADF and RTP emissions respectively. Remarkably, triplet-harvesting capabilities of the PSs further motivated us to utilize the PSs for the ROS generation and image-guided PDT study. Unlike many polymer-embedded PSs, we report encapsulation free AIE-TADF nanoparticles (NPs) for biological applications.[35] In addition all the PSs showed bright fluorescence imaging in cancer cells, confirming the successful internalization of PSs molecules inside cells. BTMCZ showed efficient 1O2 generation both in solution and in cells, including impressive PDT efficacy owing to its higher PLQY, narrow band TADF emission and improved RISC as compare to BTMPTZ and BTMPXZ. Therefore, we strongly believe that our synthesized photosensitizer BTMCZ could be a good candidate for cancer treatment.

6.2. Experimental section

6.2.1. Materials

Benzothiazole, 4-bromo-Acetophenone, carbazole, phenoxazine, and phenothiazine, potassium carbonate, palladium acetate, triphenylphsphine and toluene were purchased from Sigma-Aldrich and used as such without further purification**.** All the solvents used like toluene, chloroform and hexane were purified prior to use according to the standard protocol and stored in molecular sieves.

6.2.2. Synthesis and Characterizations

6.2.2.1. Synthesis and Characterization of benzo[d]thiazol-2-yl (4 bromophenyl) methanone (BTMBr)

Benzo[d]thiazol-2-yl(4-bromophenyl)methanone (BTMBr) is synthesized by in-situ cross-coupling reaction. 1-(4-bromophenyl)ethanone (1.38 g, 10 mmol), benzothiazole (2.03 g 15 mmol), iodine (3.80 g, 15 mmol) and potassium hydroxide (1.12 g, 20 mmol) were taken in DMSO : water (3:1) at room temperature. The mixture was heated up to 100 °C and the completion of the reaction was monitored using analytical TLC technique. After 24 h the reaction mixture was cooled to at room temperature after that dichloromethane (50 ml) was added to it. Then the crude mixture was extracted with dichloromethane and washed with aqueous sodium thiosulfate solution for several times.

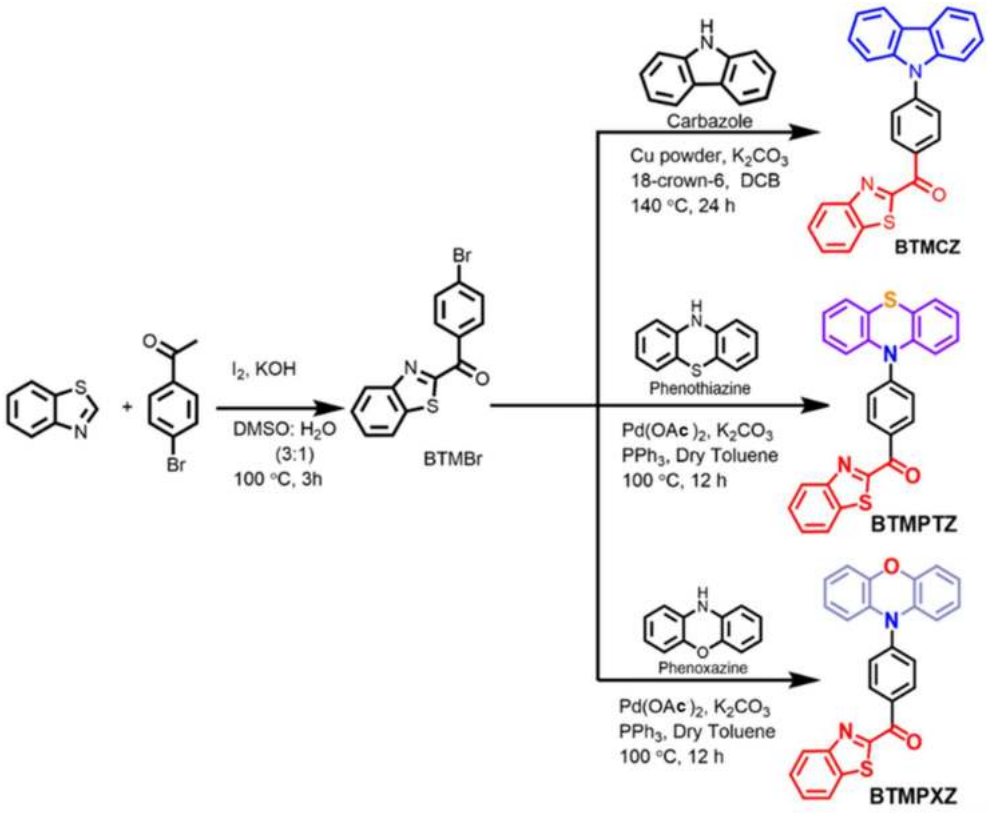

Scheme 6.1: Route of synthesis of BTMBr, BTMCZ, BTMPXZ and BTMPTZ.

Then it was dried over anhydrous Na_2SO_4 and concentrated under reduced pressure. Then the compound was finally purified by column chromatography using silica gel with 5% dichloromethane in hexane as eluent.

Yellow solid (1.722 g, 67% yield).

^{1}H NMR (600 MHz, $CDCl_3$,) δ (ppm): 8.48 (d, J = 8.1 Hz, 2H), 8.25 (d, J = 8.1 Hz, 1H), 8.03 (d, J = 8.0 Hz, 1H), 7.72 (d, J = 8.2 Hz, 2H), 7.61 (dt, J = 22.7, 7.4 Hz, 2H). ^{13}C NMR (151 MHz, $CDCl_3$, δ ppm) 185.01, 165.29, 151.13, 137.52, 133.69, 132.80, 131.90, 129.55, 127.85, 127.10, 125.80, 122.24. HRMS (ESI) peaks of m/z value was calculated for C14H8BrNOS, 317.9588 and 319.9568, observed 318.1823 and 320.1813.

6.2.2.2. Synthesis and Characterization of BTMCZ [4-(9H-carbazol-9-yl) phenyl) (benzo [d] thiazol-2-yl) methanone]

In this reaction all the reagents are taken at a time in an oven dried 100 ml round-bottom flask at inert condition (Ag-gas), taking 3.18 mmole (1g) of BTMBr, and 4.77 mmol (797 mg) of carbazole, 3.18 mmol (202 mg) of Cu powder and 16.25 mmole (2.2 g) of K_2CO_3 in the RB followed by the addition of about 30 ml of diclorobenzene. Then into the reaction mixture, a pinch amount of 18-crown-6 (3.25 mmol, 850 mg) was added. The reaction was

refluxed for 24 hours at 140 °C. After 24 hours a brown color solution was observed. TLC was checked and the reaction was stopped (TLC solvent was 1:3 v/v DCM: Hexane). The solvent was removed with the help of vacuum RV and the reaction mixture was worked up with DCM and distilled H_2O followed by Brine (NaCl) for several times until the base was removed from the organic portion and the organic layer was dried with anhydrous Na_2SO_4. The residue was purified by silica gel (100-200 mesh) with coulomb chromatography using solvent (Hexane/dichloromethane 9:1 v/v; 8:2 v/v; 7:3 v/v with the respect of polarity of the products) as the eluent to obtain a desired product (yellow color in pristine powder form).

^{1}H NMR (600 MHz, $CDCl_3$), δ (ppm): δ 8.88 (d, J = 8.4 Hz, 3H), 8.31 (d, J = 8.8 Hz, 1H), 8.17 (d, J = 7.8 Hz, 3H), 8.07 (d, J = 7.5 Hz, 2H), 7.84 (d, J = 8.5 Hz, 2H), 7.63 (d, J = 15.1 Hz, 3H), 7.62 – 7.58 (m, 3H), 7.47 – 7.45 (m, 3H), 7.36 – 7.33 (m, 3H). ^{13}C NMR (151 MHz, $CDCl_3$) δ 184.09 (s), 167.13 (s), 153.94 (s), 143.05 (s), 140.12 (s), 137.10 (s), 133.25 (s), 127.83 (s), 127.12 (s), 126.30 (s), 125.80 (s), 124.00 (s), 122.29 (s), 120.77 (s), 120.50 (s), 109.99 (s). HRMS (ESI) peaks of m/z value was calculated 405.1062 and observed 405.3795 at 298K in Acetonitrile solvent.

6.2.2.3. Synthesis and Characterization of BTMPTZ [4-(10H-phenothiazin-10 yl) phenyl) (benzo [d] thiazol-2-yl) methanone]

For this reaction the reagent K_2CO_3 was dried in an oven for overnight in about 200 °C to remove the trace of moistures. In an inert atmosphere (Ag-gas), taking 3.18 mmol (1g) of BTMBr, and 6.36 mmol (1.26 g) of phenothiazine, 1.59 mmol (357 mg) of $Pd(OAC)_2$, 4.77 mmol (1.25 g) of PPh_3, and 15.9 mmol (2.16 g) of K_2CO_3 powder in a 100 ml RB followed by the addition of about 20 ml of dry toluene. The reaction was refluxed for 12 hours at 100 °C. After 12 hours a gradual color change was observed from yellow to orange to black color solution was observed. TLC was checked and the reaction was stopped (TLC solvent was 1:3 v/v DCM: Hexane). The solvent was removed with the help of vacuum RV and the reaction mixture was worked up with DCM and distilled H_2O followed by Brine (NaCl) for several times until the base was removed from the organic portion and the organic layer was dried with anhydrous Na_2SO_4. The residue was purified by silica gel (100-200 mesh) with coulomb chromatography using solvent (Hexane/dichloromethane 9:1 v/v; 8:2 v/v 7:3 v/v with the respect of polarity of the products) as the eluent to obtain a desired product (red color in pristine powder form).

^{1}H NMR (600 MHz, $CDCl_3$), δ (ppm): δ 8.56 (d, J = 9.3 Hz, 5H), 8.20 (d, J = 8.5 Hz, 1H), 8.01 (d, J = 8.0 Hz, 2H), 7.58 – 7.51 (m, 14H), 7.44 (d, J = 9.1 Hz, 2H), 7.34 – 7.29 (m, 16H), 7.22 – 7.18 (m, 13H). ^{13}C NMR (151 MHz, $CDCl_3$) δ 183.09 (s), 168.06 (s), 153.92 (s), 149.93 (s), 141.24 (s), 136.90 (s), 133.52 (s), 132.52 (s), 128.71 (s), 128.29 (s), 127.30 (d, J = 9.0 Hz), 126.79 (s), 125.92 (s), 125.53 (d, J = 6.1 Hz), 122.13 (s), 116.62 (s).

HRMS (ESI) peaks of m/z value was calculated 437.0782 and observed 437.3701 at 298K in HPLC Acetonitrile solvent.

6.2.2.4. Synthesis and Characterization of BTMPXZ [4-(10H-phenoxazin-10 yl)phenyl)(benzo[d]thiazol-2-yl)methanone]

For this reaction the reagent K_2CO_3 was dried in an oven for overnight in about 200 °C to remove the trace of moistures. In an inert atmosphere (Ag-gas), taking 3.18 mmol (1g) of BTMBr, and 6.36 mmol (1.16 g) of phenoxazine, 1.59 mmol (350 mg) of $Pd(OAC)_2$, 4.77 mmole (1.25 g) of PPh_3 and 15.9 mmol (2.16 g) K_2CO_3 powder in a 100 ml RB followed by the addition of about 20 ml of dry toluene. The reaction was refluxed for 12 hours at 100 °C. After 12 hours a gradual color change was observed black color solution was observed. TLC was checked and the reaction was stopped (TLC solvent was 1:3 v/v DCM: Hexane). The solvent was removed with the help of vacuum RV and the reaction mixture was worked up with DCM and distilled H_2O followed by Brine (NaCl) for several times until the base was removed from the organic portion and the organic layer was dried with anhydrous Na_2SO_4. The residue was purified by silica gel (100-200 mesh) with coulomb chromatography using solvent (Hexane/dichloromethane 9:1 v/v; 8:2 v/v 7:3 v/v with the respect of polarity of the products) as the eluent to obtain a desired product (yellowish red color in pristine powder form).

^{1}H NMR (600 MHz, $CDCl_3$), δ (ppm): δ 8.83 (d, J = 8.7 Hz, 8H), 8.29 (d, J = 10.2 Hz, 1H), 8.06 (d, J = 7.2 Hz, 2H), 7.64 – 7.57 (m, 24H), 6.75 – 6.69 (m, 17H), 6.65 – 6.62 (m, 8H), 6.08 (d, J = 9.4 Hz, 9H). ^{13}C NMR (151 MHz, $CDCl_3$) δ 184.27 (s), 166.85 (s), 153.90 (s), 144.51 (s), 144.10 (s), 137.11 (s), 134.58 (s), 134.14 (s), 133.58 (s), 130.78 (s), 127.90 (s), 127.15 (s), 125.83 (s), 123.34 (s), 122.28 (s), 121.97 (s), 115.77 (s), 113.62 (s).

HRMS (ESI) peaks of m/z value was calculated 421.1011 and observed 421.3841 at 298K in HPLC Acetonitrile solvent.

6.2.3. Measurements and Methods

6.2.3.1. Structural Characterization

All the reactions were carried out in oven dried (~100 °C) round bottom flasks under argon atmosphere unless otherwise mentioned. The ^{1}H and ^{13}C NMR spectra were recorded by using deuterated solvents ($CDCl_3$) in Bruker 600 MHz NMR spectrometer. Chemical shifts (δ) are expressed relative to the resonances of the residual non-deuterated solvent for ^{1}H [$CDCl_3$: ^{1}H (δ) = 7.26 ppm], and ^{13}C [$CDCl_3$:^{13}C(δ) = 77.0 ppm]. Absolute values of the coupling constants are given in Hertz (Hz), regardless of their sign. Multiplicities are abbreviated as singlet (s), doublet (d), doublet of doublets (dd), triplet (t), multiplet (m), and broad (br).

6.2.3.2. Optical Characterization

The fluorescence and absorption spectra were measured with PerkinElmer, Model Lambda-25 spectrometer and Horiba-Fluoromax4 with Varian Cary Eclipse spectrometer respectively. The absolute quantum yields were measured by using the Horiba Fluoromax (Jobin Yvon equipped with Integrating sphere) absolute quantum yield spectrometer. The time-resolved fluorescence lifetimes were investigated with the time-resolved fluorescence studies were performed using an Edinburgh Life Spec II instrument. Temperature-dependent (77K-300K) PL and lifetime measurements were carried out using a liquid nitrogen-cooled optical cryostat (Optistat, Oxford Instruments) attached to an Edinburgh FLS-1000 instrument.

6.2.3.3. Morphology Visualization

The morphology and crystallinity of the synthesized BTMCZ, BTMPTZ and BTMPXZ were examined by scanning electron microscopy (FESEM) (Zeiss, Model: Sigma-300) in water drop casted samples, on which gold-sputtered under vacuum to achieve a thin layer of conductive gold coating on the micro/nano crystalline samples. Atomic force microscopy (AFM) analysis were performed drop-casted sample over silicon substrate, in AFM, Asylum Cypher, Oxford Instruments. Transmission electron microscopy (TEM, JEOL JEM-2100F). Dynamic light scattering (DLS) measurements were taken with a Zetasizer Nano ZS90 (model no ZEN3690)
instrument. All digital pictures were taken with a canon power shot SX420 IS digital camera.

6.2.3.4. Single Crystal X-ray Diffraction (XRD) data

Single-crystal structures of BTMCZ, BTMPTZ and BTMPXZ were obtained on X-ray diffractometer on Agilent. The single crystal x-ray diffractometer (SC-XRD) is equipped

with Mo X-ray source (Mova), CCD detector (Eos), Oxford cryo system (80-500K) and crystal AlisPRO software and Autochem softwares. SCXRD data were collected at 293 K. All the crystal structures were solved by SHELXT with direct methods. All of the non-hydrogen atoms were located by SHELXT directly and refined anisotropically by SHELXL2018 with least squares methods. The revised data have been deposited with the CCDC (accession codes CCDC **2122178, 2122179, 2122180,** and **2122181**). The stacking structure and intermolecular interactions of the BTMCZ, BTMPTZ and BTMPXZ were analyzed via Murcury and Materials Studio software. The powder X-ray diffraction measurements of the powder and thin films were performed using a Rigaku SmartLab X-ray diffractometer where copper Kα (λ = 1.54 Å) was used as the source with 9 kW power. The XRD patterns for the 2θ range of 5°−50° were measured at the scan rate 0.3°/s.

6.2.3.5. Computational Studies

Vertical and transitions energies with the highest occupied molecular orbital (HOMO), lowest unoccupied molecular orbital (LUMO), of single-component crystals were calculated by density functional theory (DFT). All DFT and TDDFT calculations in this study were performed by employing the combination of Becke3-Lee-Yang-Parr (B3LYP) hybrid functional and 6-31G(d,p) basis set using the Gaussian 16 package. The calculated structures, energy level very much close to experimental results.

6.2.3.6. Long-term Cellular Imaging

To evaluate the long-term imaging efficiency of BTMCZ, BTMPTZ and BTMPXZ inside the cellular environment, MCF-7 cells were seeded on 96 well plates at the density of 6000 cells per well cells/well. Following the attachment, cells were treated with 10 μm of BTMCZ, BTMPTZ and BTMPXZ at one time and incubated for 6 h. Cells were washed with PBS and nearly 30% of the cells were further subcultured in the growth medium, whereas the rest of the cells were employed for CLSM imaging. Accordingly, the process was repeated and the CLSM images were recorded. To compare the fluorescence intensity, imaging of the one-time treated cells was carried out at 6 h, 24 h, 48 h, and 72 h. Cells at these time points were washed with PBS, fixed with 4% formaldehyde and images were taken in a confocal microscope using 405 nm laser as an excitation source. The protocol to evaluate the long-term imaging potential of the probes has been schematically presented in Figure S6.

6.2.3.7. Cell Viability Assay

The effect of BTMCZ, BTMPTZ, and BTMPXZ on cell viability was studied on human embryonic kidney (HEK, non-cancerous) and MCF7 (breast cancer cells). For this, cells were seeded on 96 well plates at the density of 6000 cells per well. Plates were incubated in CO_2 incubator overnight for cell attachment. Following this, cells were treated with BTMCZ, BTMPTZ and BTMPXZ at various concentrations. In the case of light irradiated groups, white light (60 mW cm^{-2}) was focused to treated wells for 5 minutes. After 24 hours of treatment, MTT dye was added to individual wells (5µL, 5mg/mL in PBS), and plates were incubated for 2 h. In the end, to measure the absorbance from MTT dye, 150 µL DMSO solution was added to each well, and absorbance was recorded at 470 nm.

6.2.3.8. DCF-DA Assay for ROS Detection

MCF-7 cells in 96 well plates (10000 per well in BD Falcon black wall) were treated with BTMCZ, BTMPTZ, and BTMPXZ. Additional treatment groups were kept to confirm the ROS generated from light irradiation. Treated and light irradiated cells were stained with DCF-DA dye (20 µM in PBS, Sigma Aldrich), and the fluorescence was recorded in 96 well plate reader (TECAN 2.0). The fold change in ROS for treated groups was calculated by comparing the FL signal with untreated wells.

6.2.3.9. Apoptosis Assay

Annexin-V- FITC PI-based apoptosis detection kit (BD Pharmingen) was used to study the percent of cells undergoing apoptosis. MCF-7 cells in 6 well plates (1.2×10^5 cells per well) were treated with BTMCZ, BTMPTZ, and BTMPXZ along with light irradiation for 5 minutes. Treated cells were trypsinized and collected in a binding buffer provided in the kit. Cells were stained with Annexin-V- FITC, and PI, and analyzed on a flow cytometer (Cytoflex).

6.2.3.10. TUNEL Assay

To detect the TUNEL-positive cells with DNA damage were stained using a kit from BD Pharmingen (APO-DIRECT TUNEL detection). Cells treatment was done similarly to the apoptosis assay, and cells were stained with APO direct reagents to analyze on a Flow cytometer (Cytoflex).

6.3. Results and Discussion

6.3.1. Materials Design Strategy

By considering important aspects of light-harvesting materials, a series of donor-π-bridge-acceptor (D-π-A) based photo-functional organic materials viz. BTMCZ, BTMPTZ and BTMPXZ has been developed in the pursuit of an efficient PSs design for image-guided PDT study (Figure 6.1a). Unlike, traditional Tetraphenylethylene (TPE) and its derivatives-based AIEgens reported so far,[36] we report novel design for achieving simultaneous AIE and TADF/RTP properties. The AIE-TADF luminogens were conceived by modulating three different rigid, flexible and planar donors such as carbazole (CZ), phenothiazine (PTZ) and phenoxazine (PXZ) with an acceptor benzo [d] thiazol-2-yl) methanone core (BTM) connected via a central phenyl bridge creating a nonplanar geometry in D-π-A architecture thereby accomplishing delayed emission in aggregated/solid state successively. The integrated compounds; 4-(9H-carbazol-9-yl) phenyl) (benzo [d] thiazol-2-yl) methanone (BTMCZ), 4-(10H-phenothiazin-10-yl) phenyl) (benzo [d] thiazol-2-yl) methanone (BTMPTZ) and 4-(10H-phenoxazin-10-yl)phenyl)(benzo[d]thiazol-2-yl) methanone (BTMPXZ) was synthesized with a good yield via Cu(0) and Pd(0) catalyzed C-N coupling reactions using benzo[d]thiazol-2-yl(4-bromophenyl) methanone (BTMBr) with CZ, PTZ and PXZ, respectively. BTMBr was synthesized via in-situ cross-coupling reaction using 1-(4-bromophenyl) ethanone and benzothiazole (Scheme 6.1). Synthesized compounds were well characterized by NMR (^{1}H and ^{13}C), HRMS and SC-XRD, respectively (Figure A6.1-A6.12). By incorporating different strength of donor units into the BTM core, the resultant emitters showed color-tunable green to red emissions, including AIE-TADF and AIE-RTP in solid/aggregated state. From their experimental and computational studies, it was observed that the rigid donor CZ-containing molecules exhibited higher AIE-TADF and PDT efficiency rather than the structurally flexible PTZ and PXZ donor-containing congeners (Figure 6.1b).

Nonetheless, a wealth of knowledge and a sound understanding is highly important for the creation of and effective theranostic agent including chemical synthesis, diagnostic strategies, therapeutic efficiency, toxicity and side effects of materials. We proposed few photophysical and electronic requisites for achieving a new class of TADF PSs, which includes: 1) sterically hindered D-π-A architecture embedding electron-rich N-heteroaromatics (D) and electron-deficient benzo [d] thiazol-2-yl) methanone (A) connected through a free rotor phenyl unit. 2) Strategically manipulated HOMO and

LUMO in π-conjugated structure lead to narrow energy splitting (ΔE_{ST}) between favorable excited singlet and triplet states accelerating the RISC process, and harvesting long-lived TADF.[37] 3) Involvement of charge-transfer singlet (^{1}CT) and charge-transfer triplet (^{3}CT) states *via* energetically closest local triplet (^{3}LE) state lead to a complex second-order spin-vibronic coupling,[38] resulting in efficient TADF and RTP emission successively. 4) Utilization of high triplet energy-containing rigid donor e.g. carbazole, resulting in a high yield of triplets and narrow band TADF emission which could easily transform triplet oxygen to singlet oxygen (ROS) with photo-excitation.[39] 5) Presence of multiple heteroatoms in the chemical structure is favoring for generating rigid supramolecular framework via numerous non-covalent interactions (NCIs), thereby preventing excited state quenching[40]. These stringent requirements strongly promote to realize delayed luminescence in the solid state, thereby becoming a suitable candidate for ROS generation and photo-regulated therapeutic applications. The proposed Jablonski diagram illustrates the prominent photophysical processes and utilization of triplet for ROS generation and cancer cell killing mechanism using integrated AIE-TADF PSs (Figure 6.1c).

6.3.2. Photofunctional Properties

To investigate the ground and excited state optical properties of the afforded luminogens, firstly, solvatochromism studies were conducted to verify the charge-transfer (CT) characteristics using various polarity solvents. By recording absorption spectra in the different polarity solvents, multiple absorption peaks were observed at 280, 320 and 390 nm for BTMCZ, 310 and 395 nm for BTMPTZ, 318 and 465 nm for BTMPXZ, signifying the presence of π-π*/n-π* and ICT feature corresponding to each peaks (Figure A6.13a, b & c). However, no significant wavelength shift was noted by varying different polarity solvents confirming a stable ground state. The fluorescence spectra showed single and dual emission (DE) with an obvious color-tunable bathochromic shift was observed with increasing solvent polarity, 145 nm red-shift for BTMCZ, 100 nm for BTMPTZ and 70 nm for BTMPXZ, respectively (Figure A6.14a, b & c). These large red-shifted emissions are because of the twisted intramolecular charge-transfer (TICT) effect which is beneficial to ensued TADF behavior.[41] Notably, BTMCZ displayed strong CT emission with structureless broad spectra, while other two congeners exhibited structured DE spectra with an additional stable locally excited (LE) emission at 450 nm along with TICT emission.[38] Further, fluorescence spectra in the thin film of BTMCZ showed strong green emission near λ_{max} centered at 512 nm, BTMPTZ and BTMPXZ showed orange and red emission,

λ_{max} located at 620 and 640 nm respectively. The phosphorescence spectra at 77K displayed corresponding λ_{max} at 520, 580 and 630 nm respectively. Moreover, the PL spectra of the thin films showed higher intensity and sharper emission than those in solution which is presumably due to the structural rigidification that inhibits non-radiative decay loss.[40]

To precisely investigate triplet-harvesting luminescence properties of the PSs, ΔE_{ST} values were calculated from the onset of the fluorescence and phosphorescence spectra recorded using thin films for all the emitters (Figure 6.2a, b and c). The ΔE_{ST} values were found to be 0.06, 0.08 and 0.02 eV for BTMCZ, BTMPTZ and BTMPXZ, respectively. Further delayed emission characteristics were verified by recording transient PL spectra under air and vacuum in the dry toluene solution. The characteristic transient PL decay curve are composed of prompt and delayed components, while prompt fluorescence decays with the lifetime values of 4.62 ns (vacuum) and 4.60 ns (air) for BTMCZ, 8.21 ns (vacuum) and 7.55 ns (air) for BTMPTZ, 12.73 ns (vacuum) and 11.10 ns (air) for BTMPXZ respectively (Figure A6.15a, b & c).

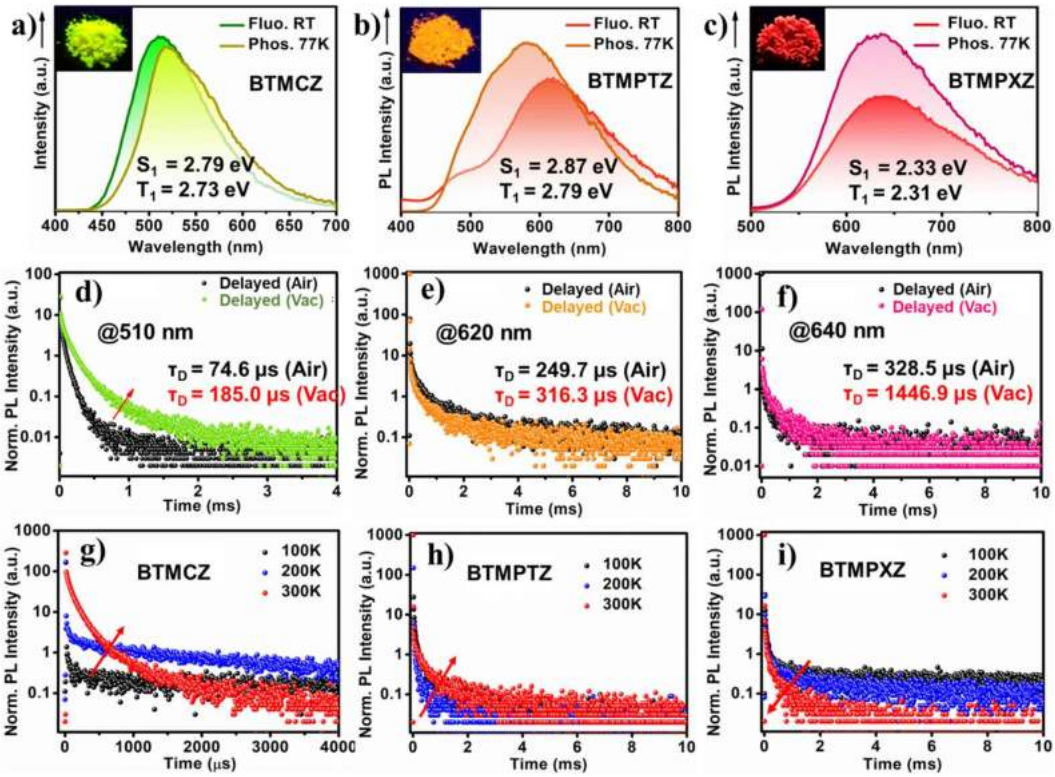

Figure 6.2. Evidence for TADF and RTP (a-i): Fluorescence and phosphorescence spectra in the thin films for BTMCZ (a), BTMPTZ (b) and BTMPXZ (c). Transient PL decay profile under Air and under Vacuum for BTMCZ, BTMPTZ and BTMPXZ (d, e and f). Transient PL decay curve under temperature gradient of 100 K, 200K and 300K for BTMCZ (g), BTMPTZ (h), BTMPXZ (i) respectively.

For delayed components, under vacuum, all the emitters exhibited significantly longer delayed decay lifetime with increased values of 185 μs (vacuum) to 74.6 μs (air) for BTMCZ, 316.3 μs (vacuum) to 249.7 μs (air) for BTMPTZ, 1446.9 μs (vacuum) to 328.5 μs (air) for BTMPXZ, respectively (Figure 6.2d, e & f). These, large enhancement of delayed lifetimes can be rationalized as thermally unconverted delayed emission resulted from T_1/T_m to S_1 with additional fluorescence. In the thin film under vacuum the PLQYs are 62.1%, 8.1% and 5.6%, respectively for BTMCZ, BTMPTZ and BTMPXZ, whereas in the presence of oxygen the values are decreased to 36.6%, 4.9% and 6.1%. Therefore, the decrease of PLQY of these PSs in the presence of molecular oxygen signifies, PSs possess delayed luminescence. Moreover, the high PLQY value of BTMCZ is due to the narrower ΔE_{ST}, rigid donor carbazole substituents lead tight molecular packing resulting substantial higher triplet population, thereby facilitating efficient RISC. The labile T_1 is very sensitive and readily quenched by the molecular oxygen that restricts RISC, leading to the decrease of the fluorescence intensity and lesser PLQY for other two congeners. In the case of BTMPXZ, due to the stronger donor strength of PXZ unit it showed longer lifetime and lesser PLQY. Since, BTMPXZ experienced higher triplet population by large density of NCIs, and therefore RTP emission is activated. Moreover, relatively short delayed emission lifetimes with high PLQY for BTMCZ are an important feature to realizing efficient triplet up-conversion process and efficient TADF. The radiative (k_r) and non-radiative (k_{nr}) decay constants were calculated from their respective delayed lifetime and PLQY values, using the formula $k_r = \phi/\tau$ and $k_{nr} = 1\text{-}\phi/\tau$ for all the PSs. Therefore, K_r are calculated to be 6.72 x 10^7 s^{-1}, 4.08 x 10^7 s^{-1} and 6.14 x 10^7 s^{-1} while K_{nr} values are 1.40 x10^4 s^{-1}, 0.87 x10^4 s^{-1} and 0.42 x10^4 s^{-1} for BTMCZ, BTMPTZ and BTMPXZ respectively. Further, to confirm the presence of TADF and RTP characteristics, temperature-dependent transient PL measurements were performed using a streak camera for the thin films of the emitters at different elevated temperatures of 100K, 200K and 300K, respectively (Figure 6.2g, h, & i). The intense emission and long tail was observed for prompt and delayed emission respectively, notably, the delayed component gradually increases with the increase of temperatures from 100K to 300K for BTMCZ and BTMPTZ. Surprisingly, BTMPXZ displayed exactly an opposite transient curve at elevated temperature (300K) where delayed decay decreases, and a direct phosphorescence emission predominantly appeared below 200K. However, the delayed component for BTMCZ showed high up-conversion at 200K and reduced at 300K, because of higher non-radiative decays at the higher temperature.[42]

6.3.3. Computational Calculations

To investigate the origin of intrinsic emission, quantum-mechanical calculations were performed for BTMCZ, BTMPTZ and BTMPXZ from their optimized single-crystal structure geometry using Gaussian 16 program.[43] Time-dependent density functional theory (TD-DFT) were employed at B3LYP/6-31G (d,p) level up to the 10th states at their different spin multiplicities. Consistent with previous results, well-separated electron-density distributions were observed in all three cases, whereas, the highest occupied molecular orbital (HOMO) were located at donors (CZ, PTZ, and PXZ) and lowest unoccupied molecular orbital (LUMO) centered at acceptor (BTM) cores, respectively.

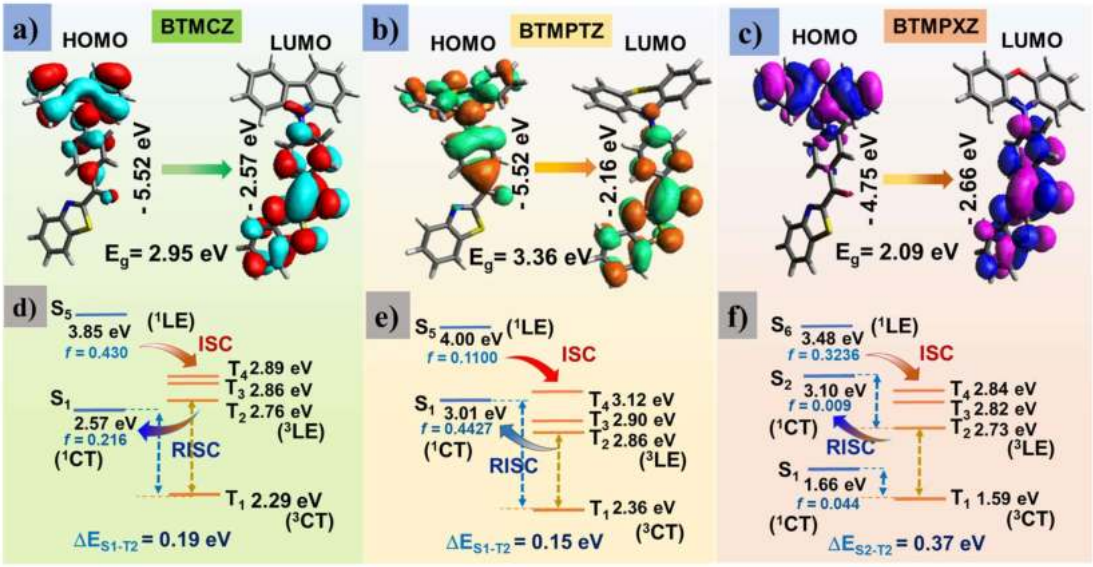

Figure 6.3. (a-c) Computational calculations: Electron density distributions and energies of HOMO and LUMO for BTMCZ (a), BTMPTZ (b) and BTMPXZ (c). (d-f) Emission energies and possible active manifold of ISC channels and the corresponding energy splitting are shown for BTMCZ (d), BTMPTZ (e) and BTMPXZ (f) respectively.

The HOMO/LUMO and band gaps values of BTMCZ, BTMPTZ, and BTMPXZ, depicting their corresponding variable band gaps and CT behavior, respectively (Figure 6.3a, b and c). Nonetheless, a small energy difference between lowest excited singlet and triplet was found to be 0.28, 0.65 and 0.07 eV for BTMCZ, BTMPTZ and BTMPXZ (Figure 6d, e and f). Moreover, by computing natural transition orbital (NTO) calculations for all three molecules, S_1 and >S1 found to have pure ^{1}ICT and ^{1}LE characters while T_1 and >T_1 have a ^{3}ICT and ^{3}LE characters (Figure A6.16). For an effective SOP, the active NTOs correspond to transitions that are allowed involving ^{1}ICT → ^{3}LE and ^{1}LE → ^{3}LE/^{3}ICT

within singlet and triplet (S_n and T_m) manifolds resulting in TADF and/or RTP property. In these cases, unlike the basic prerequisite for small ΔE_{ST} values between T_1 and S_1 the effective RISC is not favorable for efficient TADF due to the pure CT nature of S_1 (^{1}CT) and T_1 (^{3}CT) states.[37] In contrast, a second order spin-vibronic coupling is preferentially considered, evolving closely lying S_1(^{1}CT) and higher lying T_2(^{3}LE). A large energy difference between T_1 and T_2, lead to another level of small $\Delta E_{S1\text{-}T2}$ values such as 0.19, 0.15 and 0.37 eV for BTMCZ, BTMPTZ and BTMPXZ. These results strongly favored the enhanced RISC process for achieving second-order coupling. Especially smaller ΔE_{ST} playing major contribution for BTMCZ to become an efficient TADF emitter.[38] Remarkably, these ΔE_{ST} values are very much consistent with the experimental values. Besides, active ISC manifold channels were also investigated by sequential higher excited singlets and triplets related to the ground state with their corresponding major frontier orbital contributions summarized in Table A6.1-A6.6.

6.3.4. Supramolecular Structures and Luminescence

To decipher different supramolecular interactions and molecular packing arrangements induced TADF, RTP emission in solid state, the single-crystal X-ray structures were analyzed carefully. Crystal structures of BTMCZ (CCDC 2123178), BTMPTZ (CCDC 2123179) and BTMPXZ (CCDC 2123181) were obtained by very slow evaporation of chloroform/hexane (7:3) solvents. Three needle-shaped crystals of BTMCZ, BTMPTZ and BTMPXZ exhibited monoclinic, triclinic and monoclinic crystal systems with P 21/n, P-1 and C 2/c space group (crystal structure information summarized in Table A6.1). All the molecules exhibited multiple intra- and intermolecular interactions via hydrogen bonding due to the presence of N/O/S atoms and other NCIs such as weak CH-O, CH-N CH-π, π-π, and CT. All the crystal structures are self-assembled by their nearby set of molecules and form dimers, evolving the intra- and inter-NCIs through S and N atoms that are closely lying to the active hydrogen in their respective unit cells, while bulk crystal packing showed distinct H-type, J-type and X-type aggregation (as shown in Figure 6.4a, b for BTMCZ, Figure 6.4c, d for BTMPTZ, Figure 6.4e, f for BTMPXZ). Interestingly, we found a polymorphic crystal structure of BTMPTZ by varying the crystal growth condition denoted as BTMPTZ_P1. The polymorph showed slightly different packing, NCI distances, further confirming the structural flexibility in the BTMPTZ molecule (Figure A6.17). All the crystal structure-packing interaction are summarized in Table A6.2. Therefore, these high-order NCIs enable to form a rigid and dense supramolecular 3D network, benefiting to

restrict vibrational relaxation and preventing excitons quenching effect to a greater extent[44] Notably, their different and unique mode of crystal packing (H-, J- and X-aggregation) directly influenced their distinct color-tunable emission behavior of BTMCZ, BTMPTZ and BTMPXZ, respectively. Moreover, the torsion angle between donors and acceptors increases by varying donor units from CZ, PTZ to PXZ in BTMCZ, BTMPTZ, BTMPXZ, depicting higher hindered geometry and longer delayed lifetime. Subsequently, these key factors enabled considerably weak π-π stacking, therefore leading to bright solid-state emission and/or AIE effect.[44] Additionally, in the bulk crystal packing showed H-aggregated assembly for BTMCZ leads to overall denser herringbone like molecular packing rather than boat-like and chair interlocked J- and X-aggregated BTMPTZ and BTMPXZ in their crystalline state, which inhibited internal conversions and photochemical reactions which facilitated delayed fluorescence[45] (Figure. 6.4g, h & i). Furthermore, dissimilar NCI induced tunable emission colors were correlated with X-ray powder diffraction (XPRD) peaks. XPRD were recorded with the crystalline powder obtained from as-synthesized pristine compounds.

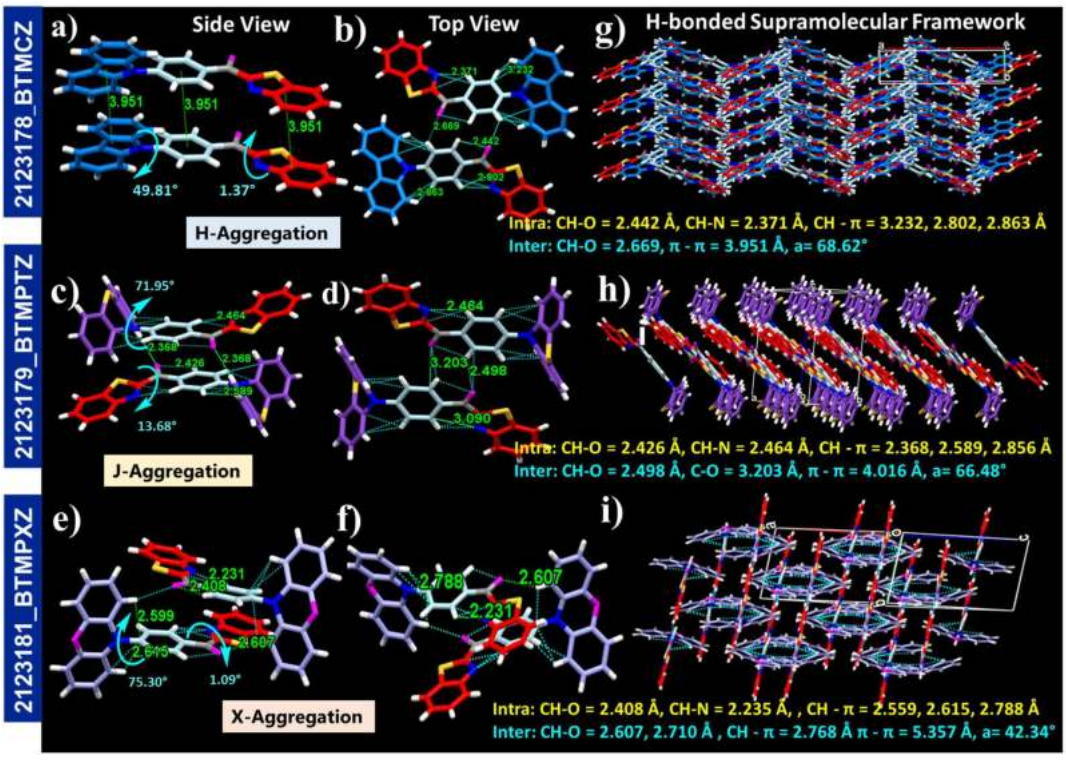

Figure 6.4. (a, b & c) Single-crystal X-ray structures of BTMCZ, BTMPTZ and BTMPXZ with their side (i) and top (ii) view of crystal structures and non-covalent interactions (NCI). (d, e and f) H-aggregation, X-aggregation and J-aggregation packing motif. (g, h and i) Variant supramolecular interaction induced crystal structure packing; wave-like, tubular and chair type bulk crystals structure packing along a, b, c-axis in BTMCZ, BTMPXZ and BTMPTZ respectively.

Notably, XPRD peaks pattern is exactly matched with the simulated patterns obtained from SC structures (Figure A6.18). The BTMCZ, BTMPTZ and BTMPXZ crystals grew preferentially along the [002], [011] and [110] phases, respectively.

Moreover, the gradual increment of multiple diffraction peaks was observed at low d-space region (2θ = 20-30°) (highlighted in red dotted line) from BTMCZ, BTMPTZ to BTMPXZ owing to their numerous intermolecular interactions and unique H/J/X aggregated packing motif. In addition, different intermolecular NCIs are simulated by functions of reduced density gradient (RDG) as a function of sign(λ_2)ρ. RDG plots were calculated for all the luminogens using TDDFT geometry with Multiwfn software[45] (Figure A6.19a, b & c). RDG plots revealed different twisted geometry, multiple π-planes and presence of many heteroatoms which confirmed the presence of obvious high density of weak interactions (green region) and larger steric hindrance (brown region) between D and A segments in BTMCZ BTMPTZ and BTMPXZ which could effectively restrict the molecular vibrations and prevent energy loss of the excited molecules and revealing TADF susceptibility.[46]

Table 6.1: Summary of photophysical studies for the integrated PSs in aggregated/solid state.

PSs	λ_{UV} (nm) CT		λ_{PL} (nm)		HOMO (eV)	LUMO (eV)	ΔE_{ST} (eV)	ΔE_{ST} (eV)	τ_{avP} (ns)	τ_{avD} (μs)		ϕ_{PL}	k_r ($x10^{77}$ s^{-1})[a]	k_{nr} ($x10^{47}$ s^{-1})[b]
	Soln	H_2O	Film	H_2O	Theo.		Theo.	Exp.		Air	Vac	Film/ H_2O	Film Air/ RT	Film Air/ RT
BTMCZ	390	410	512	525	-5.52	-2.57	0.19	0.06	4.60	74.6	185	62.1/ 59.6	6.72	1.40
BTMPTZ	395	420	620	615	-5.52	-2.16	0.15	0.08	8.21	249.7	316.3	8.1/6. 2	4.08	0. 87
BTMPXZ	465	490	640	650	-4.75	-2.66	0.37	0.12	12.7	328.5	1446. 9	5.6/4. 5	6.14	0. 42

Radiative and non-radiative decay rate [$^a k_r = \phi/\tau$, $^b k_{nr} = (1-\phi)/\tau$] calculated from QY and delayed lifetime of crystals at RT in air.

6.3.5. AIE, Nano Morphology and ROS Generation

Further, the condensed state absorption and emission studies for BTMCZ, BTMPTZ and BTMPXZ luminogens were performed by varying different water/THF fractions (f_w) at constant sample concentrations (~5 x 10^{-5} M). A broad CT-absorption band was observed at 99% f_w, centered at 410, 420 and 490 nm for BTMCZ, BTMPTZ and BTMPXZ

respectively (Figure A6.20a, b & c). All the AIEgens exhibited 25 nm red-shifted absorption with increasing f_w into the THF (80% - 99% f_w) confirming the formation of various molecular self-assembly with H-, J- and X-type aggregation for BTMCZ, BTMPXZ and BTMPTZ, confirmed by SC-XRD analysis. Likewise, the steady state emission spectra and their relative intensities were recorded at various f_w. In the emission spectra a sharp increment of emission intensity was observed at higher 99% f_w, fluorescence wavelength maximum located at 525, 615 and 650 nm for BTMCZ, BTMPTZ and BTMPXZ respectively (Figure 6.5a, b & c). Although, no noticeable change was observed for AIE emission maxima (~525 nm) with increasing f_{ws} for BTMCZ, however, a locally excited peak occurs at 480 nm along with a CT peak at 615 and 650 nm for BTMPTZ and BTMPXZ. Moreover, absolute PLQY in aggregated state and in solution was observed to be 59.64% and 30.85% for BTMCZ, 6.22% and ≤0% for BTMPTZ, 4.68% and ≤0% for BTMPXZ respectively.

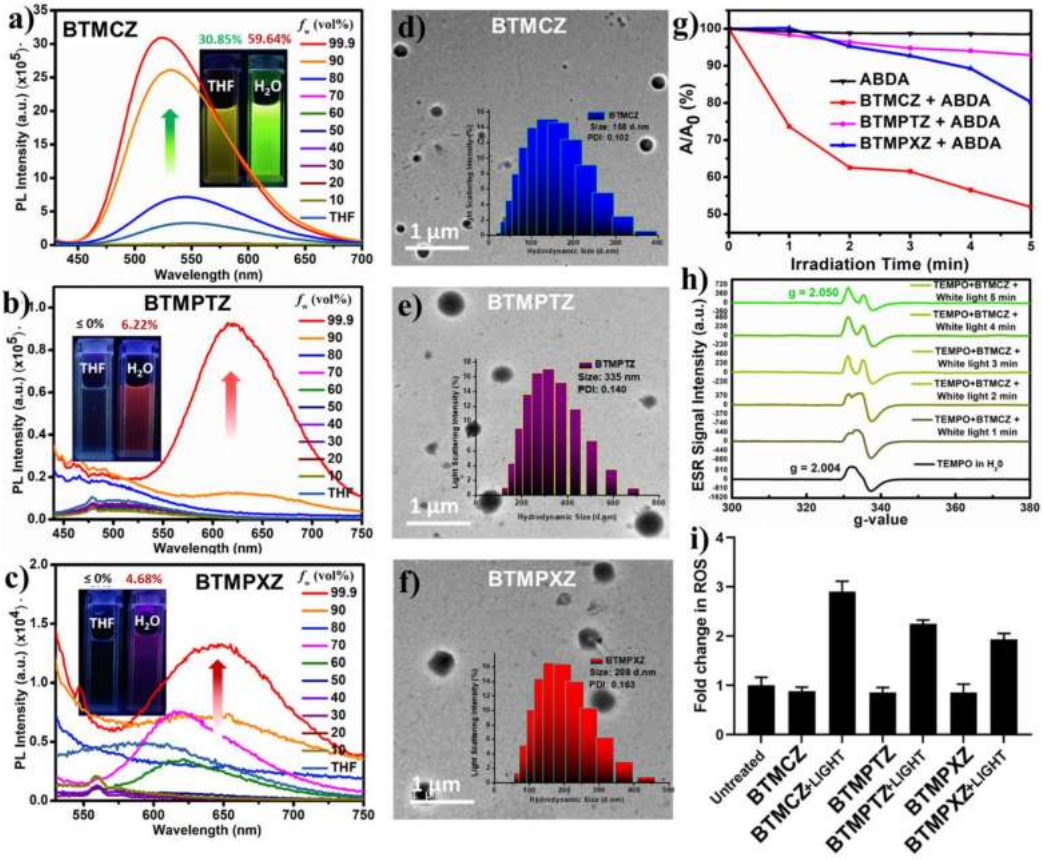

Figure 6.5. (a, b & c) Fluorescence spectra for BTMCZ, BTMPTZ and BTMPXZ at varying THF/H2O fractions. (d, e and f) Nano-aggregates visualization by FETEM (1 µm scale bar), inset: size distributions by DLS study for BTMCZ, BTMPTZ and BTMPXZ, respectively. (g) Identification of ROS generation by ABDA treatment, monitoring absorption of ABDA in the presence of PS and white light irradiation at different time span (0-5 min). (h) ROS detected by ESR spectra for BTMCZ in the presence of TEMPO and white light.(i) ROS detections inside the cancerous cells in the absence and presence of white light.

The enhanced emission in solution and aggregated state and accompanying results could be attributed to strong CT characteristics and restricted intramolecular free rotation due to the structural rigidity and flexibility of non-planar D-π-A architecture. The supramolecular nano-range self-assembly behavior in water for BTMCZ, BTMPTZ and BTMPXZ were studied by atomic force microscopy (AFM) and transmission electron microscopy (TEM) respectively. Extremely uniform spherical nanoparticles with slightly varying morphology and size of ~235, 380 and 425 nm for BTMCZ, BTMPTZ and BTMPXZ were observed in TEM (scale: 1 μm) (Figure 6.5d, e & f) Similar size values and surface morphologies were also seen in AFM (scale: 400 nm) (Figure A6.21a, b & c). Further, Zeta-potential recorded in H_2O for all the three PSs at 10^{-5} M concentration showed a desirable surface charge with the value of -31.6 ± 5.02, -28.7 ± 6.13 and -31.4 ± 7.61 meV for BTMCZ, BTMPTZ and BTMPXZ signifying potential stability of the NPs in colloidal system (Figure A6.22-A6.24). Furthermore, ROS generation ability of the AIEgens was determined quantitatively using 9,10-anthracenediyl-bis(methylene)dimalonic acid (ABDA).The intrinsic absorption of ABDA decreases under white light irradiation for all the AIEgens (Figure 6.5g). Interestingly, in the case of BTMCZ the absorbance of ABDA decreases significantly, depicting the generation of efficient $^1O_2$ in presence of light. The unique chemical structure of BTMCZ with its high PLQY, low ΔE_{ST} and effective TADF capabilities enables ROS generation and potential for PDT study.[47] Therefore, considering BTMCZ as the model PS, electron paramagnetic resonance (EPR) studies were conducted with radical sensitive agent (2,2,6,6-Tetramethylpiperidin-1-yl)oxyl (TEMPO) to verify the presence of $^1O_2$ under white-light irradiation time of 60s to 300s where a characteristic radical ($^1O_2$) peak was observed (g factor = 2.050) in addition to TEMPO peak (g factor = 2.004) at 77K (Figure 6.5h). In addition, ROS generation was performed in cell, and as expected BTMCZ showed the highest ROS generation capabilities rather other two congeners (Figure 6i).

6.3.6. Photodynamic Therapy and Bio-imaging

Prior to studying the PDT and biological effect of the PSs, microscopy-based uptake study was carried out to confirm the internalization of PSs molecules inside the cells. The MCF-7 cells incubated with PSs (at 10 μM) and counterstained with propidium iodide (for nucleus) were imaged using a confocal microscope. The compound panel shown in Figure 6.6a-d, corresponds to the fluorescence signal collected from PSs molecules. Interestingly, the presence of fluorescence in cytoplasm of the MCF-7 cells confirms the successful internalization of PSs molecules inside cells.

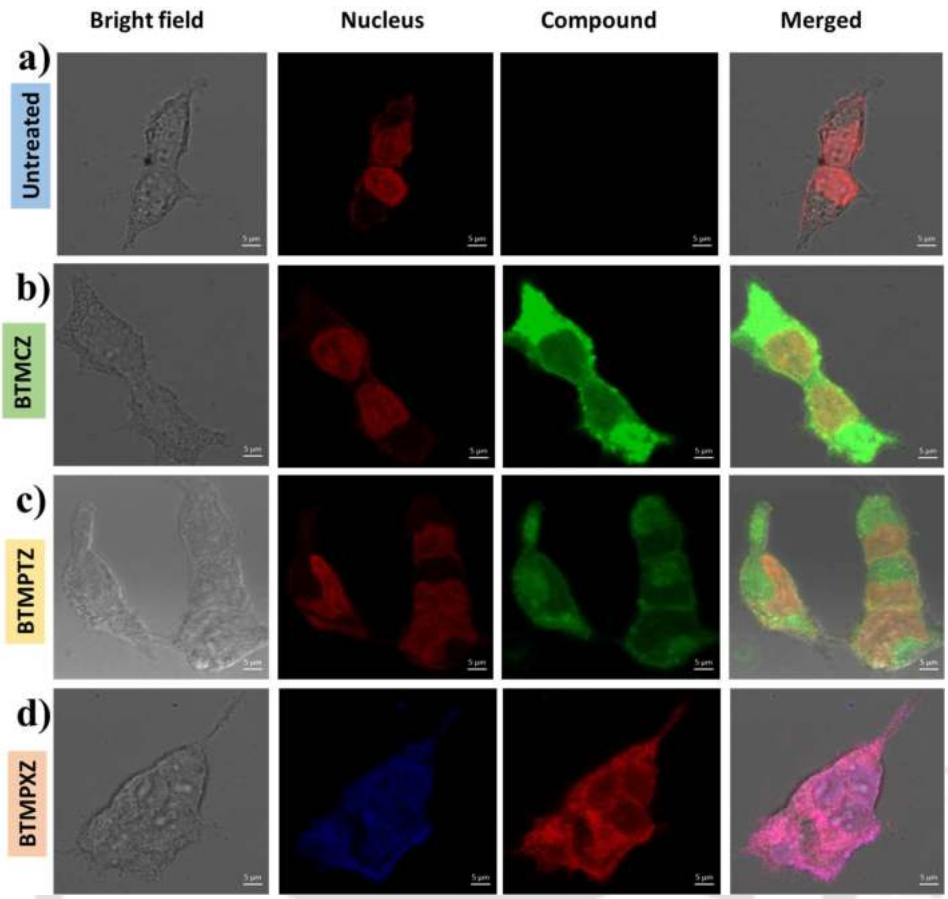

Figure 5.6. (a-d) Confocal images of MCF-7 cancer cells after incubation them with BTMCZ, BTMPTZ and BTMPXZ PSs (10 µg mL^{-1}) for 2 h; the fluorescence of the PSs was collected between 500 and 650 nm upon excitation at 405 nm; all the images share the same scale bar of 5 µm.

Additionally, nuclear staining with PI confirms that PSs molecules were localized in the cytoplasm of the cells. This ensures the possibility of imaging application of the PSs molecules (Figure A6.25). Furthermore, to gain insights into the working of PSs, it is essential to understand the distribution and interaction of externally added molecules inside the cells. Internalization or uptake of the molecules depends on their size, surface charge, and affinity to the cell surface proteins.[48]

Though the average size and structures of the BTMCZ, BTMPTZ, and BTMPXZ were different, we could confirm the internalization and localization of the PSs inside the cells. Following this, the dark cytotoxicity, as well as the light-induced cell death, was quantified using an MTT-based cell viability assay. For this, HEK293 (non-cancerous) and MCF-7 (breast cancer) cells were treated with increasing concentrations of the PSs. As shown in Figures 6.7a, b, & c, we did not observe significant dark toxicity of BTMCZ, BTMPTZ, and BTMPXZ in HEK293 cells, even up to 100 uM concentration.

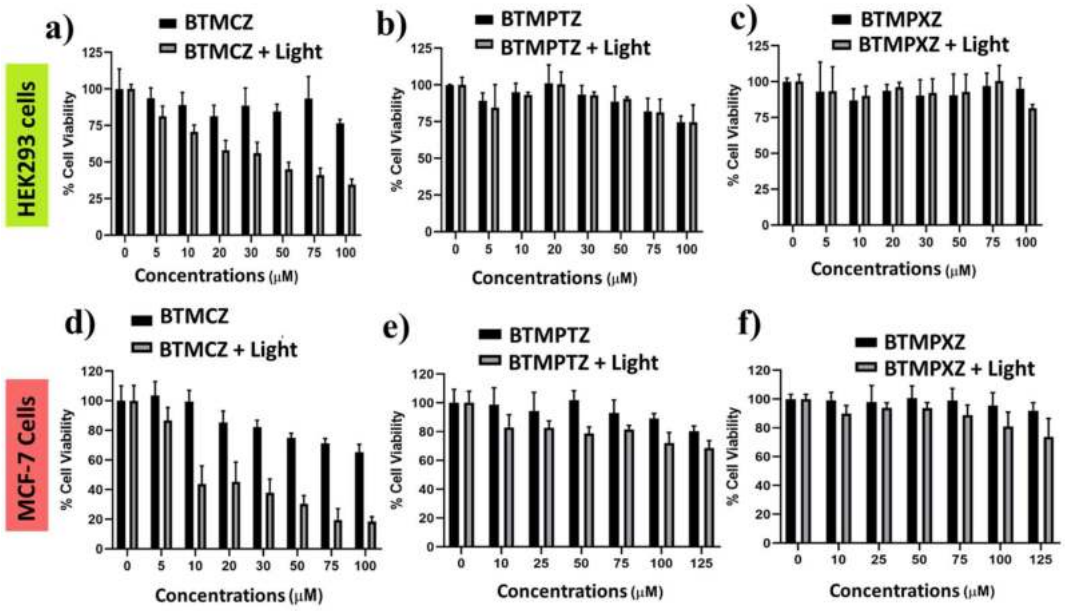

Figure 6.7. Cell viability of different PS-treated HEK293 cell (a, b & c) and MCF-7 cancer cells (d,e & f) under white light irradiation (60 mW cm^{-2}, 5 min) and under dark.

Surprisingly, BTMCZ caused significant cell death at the lowest concentration tested in the presence of light. Though cell death was not reached to IC_{50} without light, IC_{50} for the BTMCZ+ Light treatment group shown in Figure 6.7a for HEK293 cells was 19.6±12.1 μM. Similar to this, the BTMCZ+Light treatment (Figure 6.7d) showed a significant increase in dead cell population after light irradiation. The IC_{50} concentrations were found to be 11.8±4 μM in BTMCZ+Light group for MCF-7 cells. No significant dark toxicity or photodynamic effect was evident in HEK293 and MCF-7 cells in case of BTMPTZ and BTMPXZ (Figure 6.7e, f). This corroborates our experiments with ABDA (Figure 6.5i) and DCF-DA, where high levels of ROS were seen for BTMCZ compared to BTMPTZ, and BTMPXZ. A large number of therapeutic approaches are being developed which induce the generation of ROS inside the cells. Anticancer approaches work by either generating the ROS or by damaging the ROS scavenger machinery of the cells. The increased proliferation, and hyperactivated cell signaling processed inside the cancer cells generated ROS imbalance.[49] This results in the higher susceptibility of cancer cells to the ROS generated from PSs, compared to healthy cells. Our results also suggest similar observations, where an IC_{50} for healthy cells (HEK293) was much higher (19.6±12.1 μM) than the MCF-7 cells (11.8±2 μM). Additionally, a known PDT agent, methylene blue has a comparable range of IC_{50} amounts (10-25 μM) in different cancer cells.

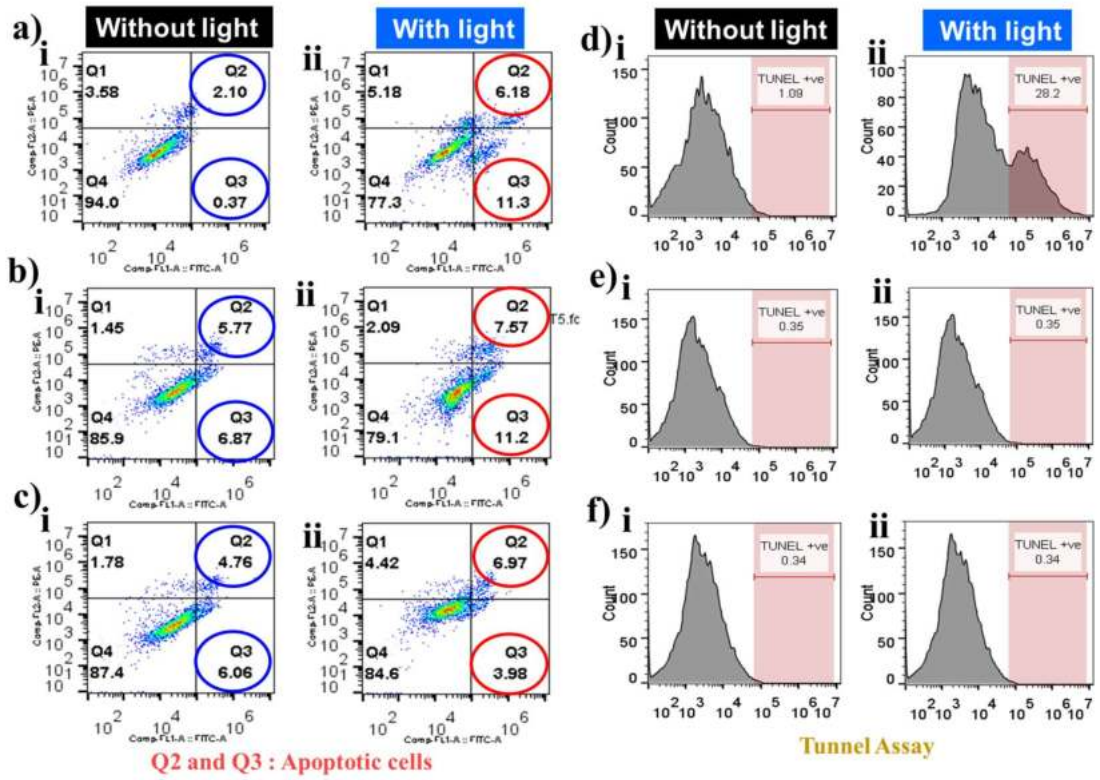

Figure 6.8. (a, b & c) Apoptosis study of MCF-7 cells without and with white-light irradiation (i &ii) for BTMCZ, BTMPTZ and BTMPXZ, IR-TPP treated MCF-7 cells without light irradiation (IR-TPP-L) and IR-TPP treated MCF-7 cells with 5 min white light irradiation (60 mW cm−2, 5 min) (IR-TPP+L) by flow cytometry. (d-f) Tunnel Assay for PSs without light and with light (i & ii).

6.3.7. Cell Death Study

The inhibition of cell growth could happen due to necrosis or apoptosis. The cell death process was studied using a cell signaling pathway directed by fluorescent dye-tagged antibodies. The dot plot shown in Figure 6.8a, b & c for MCF-7 cells shows the number of cells stained with FITC tagged antibody detecting apoptotic cells (x-axis), whereas y-axis shows PI-positive dead cells. The total number of dead or apoptotic cells in BTMCZ-treated wells without any light was 6.05%, which increased to 22.6 % in BTMCZ+light treatment (Figure 6.8aii). In the case of BTMPTZ and BTMPXZ treatment, total dead cells were found to be 14.09% and 12.6 5, which was slightly elevated to 22.7% and 15.37 after light irradiation (Figure 6.8b, c). Similar to this, to study the molecular mechanism of he cell death, antibody-based DNA damage (TUNEL) assay was carried out.[50] The TUNEL assay results shown in Figures 6.8d, e & f confirm the increase in the TUNEL positive cells(28.2%) in the BTMCZ+light treatment, whereas no TUNEL positive cells were recorded in the BTMPTZ and BTMPXZ therapy with light. The higher number of apoptotic

and TUNEL positive cells in BTMCZ+light treatment confirms the photodynamic events after light irradiation. These results are also consistent with the ABDA and ROS assay results shown in Figure 6.5h and 6.5i.

6.4. Conclusions

In summary, we have designed and synthesized a series of new triplet harvesting purely organic PSs using acceptor benzo [d] thiazol-2-yl) methanone (BTM) and different donor carbazole (CZ), phenothiazine (PTZ), and phenoxazine (PXZ) denoted as BTMCZ, BTMPTZ and BTMPXZ respectively. By incorporating structurally different donor units into the BTM core, the resultant emitters showed color-tunable green to red emissions, including up-converted luminescence such as TADF and RTP with AIE in solid/aggregated state. From their experimental and computational studies, it was observed that modulation of the donor in the PSs structure enables to finely adjust energy gap (ΔE_{ST}) *via* second-order spin-orbit perturbation involving higher-lying excited triplets (^{3}LE) and lowest singlet (^{1}CT) state, thereby harvesting excitons at a greater extent. Remarkably, integrated AIE-TADF PS could generate reactive oxygen species (ROS) under white-light irradiation and efficiently kill the cancer cells. Notably, the rigid donor CZ-containing molecules exhibited strong AIE-TADF property, narrower band emission and very high PLQY, hence, showing high PDT efficiency rather than the structurally flexible PTZ and PXZ donor-containing congeners. Moreover, unique crystal packing of H-, X, and J-type aggregation, resulting in supramolecular nano-range self-assemblies of AIE-nanoparticles and those are accumulated homogeneously in the cancer cells and therefore, a good cellular uptake and high-contrast imaging were also reported. Therefore, combined with the exceptional interest of TADF emitters into $^1O_2$, generation for improved PDT efficiency and bright imaging revealed promising approach to explore the triplet harvesting organic materials for biomedical exploration. We strongly believe that the concept of ROS generation using metal-free purely organic TADF/RTP materials pave the way for future PSs design for cancer treatment and other applications.

6.5. References

[1] a) X. Li, J. F. Lovell, J. Yoon, X. Chen, *Nat. Rev. Clin. Oncol*. **2020**, *17*, 657; b) F. Hu, S. Xu, B. Liu, *Adv. Mater.* **2018***, 30,* 1801350.

[2] a) Z. Zhou, J. Song, L. Nie, X. Chen, *Chem. Soc. Rev.* **2016**, *45*, 6597; b) X. Li, N. Kwon, T. Guo, Z. Liu, J. Yoon, *Angew. Chem., Int. Ed.* **2018**, *57*, 11522.

[3] a) J. Li, K. Pu, *Chem. Soc. Rev.* **2019**, *48*, 38–71; b) W. Fan, P. Huang, X. Chen, *Chem. Soc. Rev.* **2016**, *45*, 6488.

[4] a) E. Terreno, D. D. Castelli, A. Viale, S. Aime*, Chem. Rev.* **2010**, *110*, 3019– 3042; b) S. Hu, B. Huang, Y. Pu, C. Xia, Q. Zhang, S. Guo, Y. Wang, X. Huang, *J. Mater. Chem. B*, **2021**, *9*, 5645.

[5] Y. Jiang, K. Pu, *Acc. Chem. Res.* **2018**, *51*, 1840.

[6] D. Cui, J. Huang, X. Zhen, J. Li, Y. Jiang and K. Pu, *Angew. Chem., Int. Ed.* **2019**, *58*, 5920.

[7] J. Li, J. Huang, Y. Lyu, J. Huang, Y. Jiang, C. Xie and K. Pu, *J. Am. Chem. Soc*. **2019**, *141*, 4073.

[8] Kenry, B. Liu*, Acc. Mater. Res.* **2022***, 3,* 721.

[9] X. Cai, B. Liu, *Angew. Chem. Int. Ed.* **2020**, *59*, 9868.

[10] S. Xu, Y. Yuan, X. Cai, C.-J. Zhang, F. Hu, J. Liang, G. Zhang, D. Zhang, B. Liu. *Chem. Sci*. **2015**, *6*, *5824*.

[11] R. Bonnett, *Chem. Soc. Rev.* **1995**, *24*, 19.

[12] L. Wu, A. C. Sedgwick, X. Sun, S. D. Bull, X.-P. He, T. D. James, *Acc. Chem. Res.* **2019**, *52*, 2582.

[13] M. DeRosa, *Coord. Chem. Rev.* **2002**, *233,* 351.

[14] D. W. Felsher, *Nat. Rev. Cancer*, **2003**, *3,* 375.

[15] Y. Wu, Y. Zhen, Y. Ma, R. Zheng, Z. Wang and H. Fu, *J. Phys. Chem. Lett.* **2010**, *1*, 2499.

[16] J. Zhao, W. Wu, J. Sun and S. Guo, *Chem. Soc. Rev.* **2013**, *42*, 5323.

[17] C. Y. Yu, H. Xu, S. Ji, R. T. Kwok, J. W. Lam, X. Li, S. Krishnan, D. Ding, B. Z. Tang, *Adv. Mater.* **2017**, *29*, 1606167.

[18] S. H. Lim, C. Thivierge, P. Nowak-Sliwinska, J. Han, H. van den Bergh, G. Wagnieres, K. Burgess and H. B. Lee, *J. Med. Chem.,* **2010**, *53*, 2865.

[19] W. D. Jang, Y. Nakagishi, N. Nishiyama, S. Kawauchi, Y. Morimoto, M. Kikuchi, K. Kataoka, *J. Controlled Release* **2006**, *113*, 73.

[20] J. F. Lovell, T. W. B. Liu, J. Chen, G. Zheng, *Chem. Rev.* **2010**, *110*, 2839.

[21] J. F. Lovell, C. S. Jin, E. Huynh, H. Jin, C. Kim, J. L. Rubinstein, W. C. Chan, W. Cao, L. V. Wang, G. Zheng, *Nat. Mater.* **2011**, *10*, 324.

[22] D. Wang, M. M. S. Lee, G. Shan, R. T. K. Kwok, J. W. Y. Lam, H. Su, Y. Cai and B. Z. Tang, *Adv. Mater.* **2018**, *30*, 1802105.

[23] a) Y. Yuan, G. Feng, W. Qin, B. Z. Tang, B. Liu, *Chem. Commun.* **2014**, *50*, 8757; b) Y. Yuan, C.-J. Zhang, R. T. K. Kwok, S. Xu, R. Zhang, J. Wu, B. Z. Tang, B. Liu, *Adv. Funct. Mater.* **2015**, *25*, 6586; c) Y. Yuan, C.-J. Zhang, M. Gao, R. Zhang, B. Z. Tang, B. Liu, *Angew. Chem., Int. Ed.* **2015**, *54*, 1780.

[24] Y. Li, R. Tang, X. Liu, J. Gong, Z. Zhao, Z. Sheng, J. Zhang, X. Li, G. Niu, R. T. K. Kwok, W. Zheng, X. Jiang, B. Z. Tang, *ACS Nano* **2020**, *14*, 16840.

[25] a) Z. Zheng, T. Zhang, H. Liu, Y. Chen, R. T. K. Kwok, C. Ma, P. Zhang, H. H. Y. Sung, I. D. Williams, J. W. Y. Lam, K. S. Wong, B. Z. Tang, *ACS Nano* **2018**, *12*, 8145; b) Y. Liao, R. Wang, S. Wang, Y. Xie, H. Chen, R. Huang, L. Shao, Q. Zhu, Y. Liu, *ACS Appl. Mater. Interfaces* **2021**, *13*, 54783.

[26] a) B. Gu, W. Wu, G. Xu, G. Feng, F. Yin, P. Han J. Chong, J. Qu, K.-T. Yong, B. Liu, *Adv. Mater*. **2017**, *29*, 1701076; b) F. Hu, D. Mao, Kenry, X. Cai, W. Wu, D. Kong, B. Liu, *Angew. Chem. Int. Ed.* **2018**, *57*, 10182; c) V. –N. Nguyen, S. Qi, S. Kim, N. Kwon, G. Kim, Y. Yim, S. Park, J. Yoon, *J. Am. Chem. Soc.* **2019**, *141*, 16243.

[27] F. Fang, L. Zhu, M. Li, Y. Song, M. Sun, D. Zhao, J. Zhang, *Adv. Sci.* **2021**, 2102970.

[28] Y.-F. Xiao, J.-X. Chen, S. Li, W.-W. Tao, S. Tian, K. Wang, X. Cui, Z. Huang, X.-H. Zhang, C.-S. Lee, *Chem. Sci.* **2020**, *11*, 888.

[29] a) Y. L. Chen, S. W. Li, Y. Chi, Y. M. Cheng, S. C. Pu, Y. S. Yeh and P. T. Chou, *ChemPhysChem*, **2005**, *6*, 2012–2017; b) E. Bassan, A. Gualandi, P. G. Cozzi, P. Ceroni, *Chem. Sci.* **2021**,*12*, 6607-6628.

[30] Z. Zhu, D. Tian, P. Gao, K. Wang, Y. Li, X. Shu, J. Zhu, Q. Zhao, *J. Am. Chem. Soc.* **2018**, *140*, 17484.

[31] a) H. Uoyama, K. Goushi, K. Shizu, H. Nomura, C. Adachi, *Nature* **2012**, *492*, 234; b) Y. Liu, C. Li, Z, Ren, S. Yan M. R. Bryce, *Nat Rev Mater*. **2018**, *3,* 18020; c) M. Y. Wong, E. Zysman-Colman, *Adv. Mater.* **2017**, *29*, 1605444; d) P. Rajamalli, N. Senthilkumar, P. Y. Huang, C. C. Ren-Wu, H. W. Lin, C. H. Cheng, *J. Am. Chem. Soc.* **2017**, *139*, 10948.

[32] M. A. Brydena, E. Zysman-Colman, *Chem. Soc. Rev.* **2021**, *50*, 7587.

[33] a) J. Zhang, F. Fang, Bin Liu, J.-H Tan, W.-C. Chen, Z. Zhu, Y. Yuan, Y. Wan, X. Cui, S. Li, Q.-X. Tong, J. Zhao, X.-M. Meng, C.-S. Lee, *ACS Appl. Mater. Interfaces* **2019**, *11*, 41051; b) F. Ni, Z. Zhu, X. Tong, W. Zeng, K. An, D. Wei, S. Gong, Q. Zhao, X. Zhou, C. Yang, *Adv. Sci.* **2019**, *6*, 1801729.

[34] D. Barman, M. Annadhasan, R. Chandrasekar, P. K. Iyer, *Chem. Sci.* **2022**,*13*, 9004.

[35] F. Ni, N. Li, L. Zhan, C. Yang, *Adv. Opt. Mater.* **2020**, *8*, 1902187.

[36] a) G. Feng, B. Liu, *Acc. Chem. Res.* **2018**, *51*, 1404−1414; b) J. Dai, X. Wu, S. Ding, X. Lou, F. Xia, S. Wang, Y. Hong, *J. Med. Chem.* **2020**, *63*, 1996.

[37] a) Q. Zhang, B. Li, S. Huang, H. Nomura, H. Tanaka and C. Adachi, *Nat. Photonics*, **2014**, *8*, 326; b) S. Y. Lee, T. Yasuda, Y. S. Yang, Q. Zhang and C. Adachi, *Angew. Chem., Int. Ed.* **2014**, *53*, 6402.

[38] a) X.-K. Chen, S.-F. Zhang, J.-X. Fan, A.-M. Ren, *J. Phys. Chem. C* **2015**, *119*, 9728; b) M. K. Etherington, F. Franchello, J. Gibson, T. Northey, J. Santos, J. S. Ward, H. F. Higginbotham, P. Data, A. Kurowska, P. L. Dos Santos, D. R. Graves, A. S. Batsanov, F. B. Dias, M. R. Bryce, T. J. Penfold, A. P. Monkman, *Nat. Commun.* **2017**, *8*, 14987.

[39] Y. Im, M. Kim, Y. J. Cho, J.-A Seo, K. S. Yook, J. Y. Lee, *Chem. Mater.* **2017**, *29*, 1946.

[40] a) X.-N. Li, M. Yang, X.-L. Chen, J.-H. Jia, W.-W. Zhao, X.-Y. Wu, S.-S. Wang, L. Meng, C.-Z. Lu, *Small*, **2019**, *15*, 1903270; b) P. Rajamalli, F. Rizzi, W. Li, M. A. Jinks, A. K. Gupta, B. A. Laidlaw, I. D. W. Samuel, T. J. Penfold, S. M. Goldup, E. Zysman-Colman, *Angew. Chem. Int. Ed.* **2021**, *60*, 12066.

[41] a) H. Tanaka, K. Shizu, H. Nakanotani, C. Adachi, *Chem. Mater.* **2013**, *25*, 3766; b) H. Naito, K. Nishino, Y. Morisaki, K. Tanaka, Y. Chujo, *Angew. Chem., Int. Ed.* **2017**, *56*, 254 -259; c) N. A. Kukhta, M. R. Bryce, *Mater. Horiz.* **2021**, *8*, 33.

[42] a) J. Li, T. Nakagawa, J. MacDonald, Q. Zhang, H. Nomura, H. Miyazaki and C. Adachi, *Adv. Mater.* **2013**, *25*, 3319; b) T. Maldine , A. Bessière, J. Seguin, E. Teston, S. K. Sharma, B. Viana, A. J. J. Bos, P. Dorenbos, M. Bessodes, D. Gourier, D. Scherman, C. Richard, *Nat. Mater.* **2014**, *13*, 418.

[43] M. J.Frisch, et al., Gaussian 16 Revision C.01, Gaussian, Inc., Wallingford CT, USA, 2016.

[44] a) F. Ni, Z. Zhu, X. Tong, M. Xie, Q. Zhao, C. Zhong, Y. Zoub C. Yang, *Chem. Sci.* **2018**, *9*, 6150; b) T. Li, D. Yang, L. Zhai, S. Wang, B. Zhao, N. Fu, L. Wang, Y. Tao, W. Huang, *Adv. Sci.* **2017**, *4*, 1600166.

[45] a) T. Lu, F. W. Chen, *J. Comput. Chem.* **2012**, *33*, 580; b) Z. Yang, Z. Mao, C. Xu, X. Chen, J. Zhao, Z. Yang, Y. Zhang, W. Wu, S. Jiao, Y. Liu, M. P. Aldred, Z. Chi,*Chem. Sci*., **2019**, *10* , 8129.

[46] a) M. Luo, X. Li, L. Ding, G. Baryshnikov, S. Shen, M. Zhu, L. Zhou, M. Zhang, J. Lu, H. Ågren, X. –D. Wang, L. Zhu, *Angew. Chem. Int. Ed.* **2020**, *59*, 17018; b) D. Barman, K. Narang, R. Parui, N. Zehra, M. N. Khatun, L. R. Adil, P. K. Iyer, *Aggregate* **2022**, e172.

[47] a) S. Suzuki, S. Sasaki, A. S. Sairi, R. Iwai, B. Z. Tang, G.-i. Konishi, *Angew. Chem. Int. Ed.* **2020**, *59*, 9856; b) N. R. Paisley, S. V. Halldorson, M. V. Tran, R. Gupta, S. Kamal, W. R. Algar, Z. M. Hudson, *Angew. Chem. Int. Ed.* **2021**, *60*, 1863.

[48] J. Zhang, B. Xu, W. Tian, Z. Xie, *Chem. Sci.* **2018**, *9*, 2620.

[49] S. J. Kim, H. S. Kim, Y. R. Seo, *Oxidative Medicine and Cellular Longevity,* **2019**, *2019*, 1-12; https://doi.org/10.1155/2019/5381692.

[50] a) A. P. Bidkar, P. Sanpui, S. S. Ghosh, *ACS Appl. Nano Mater*. **2020**, *3*, 3807. b) N. Meher, A. P. Bidkar, D. Barman, S. S. Ghosh, P. K. Iyer, *Chem. Commun.* **2020**, *56*, 14861.

Appendix: Additional data for **Chapter 6**

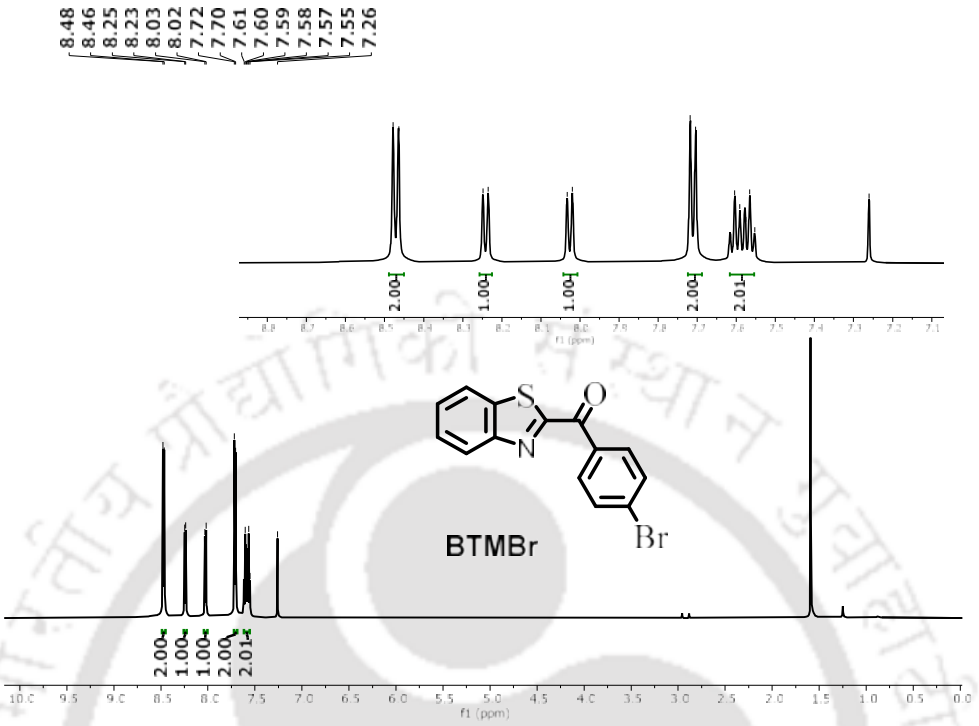

Figure A6.1. ^{1}H NMR spectra of BTMBr in $CDCl_3$ at 298K.

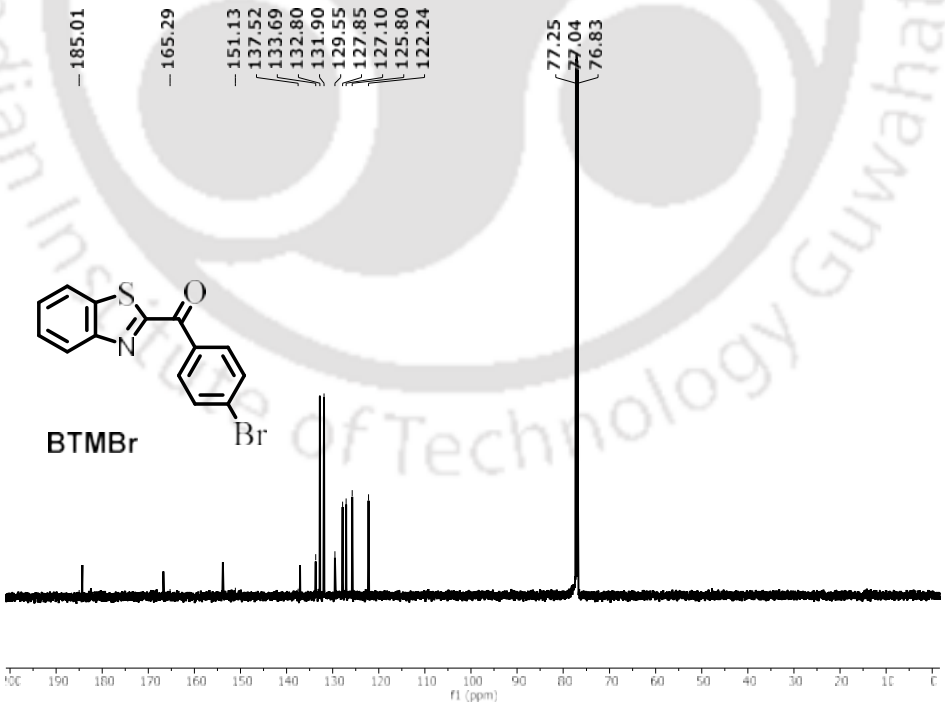

Figure A6.2. ^{13}C NMR spectra of BTMBr in $CDCl_3$ at 298K.

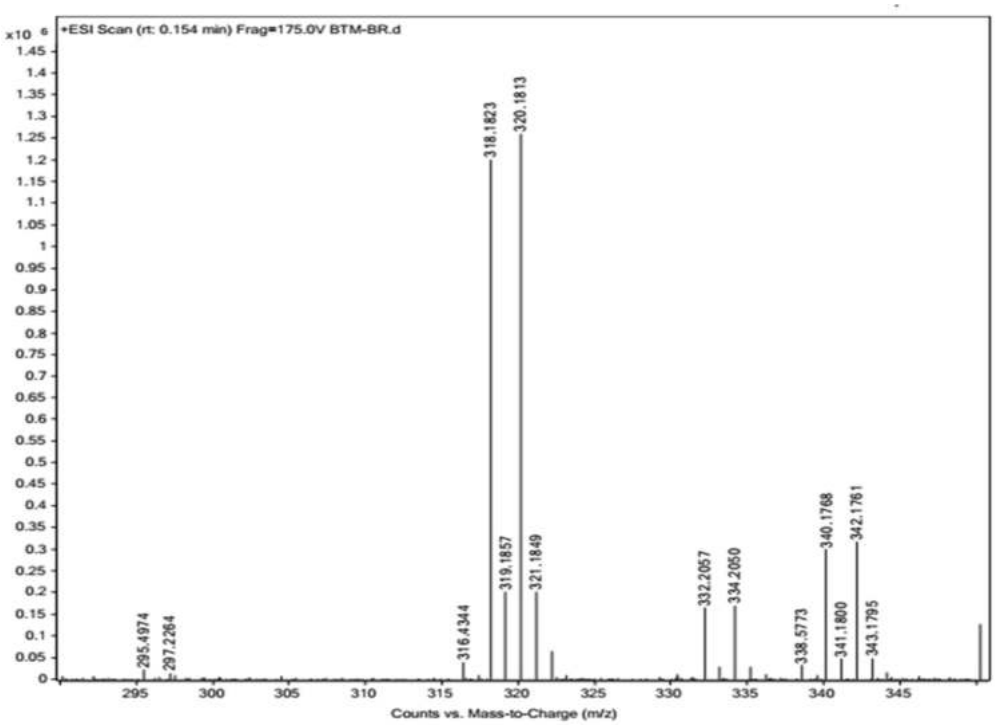

Figure A6.3. HRMS (ESI) peaks of m/z value for $[BTMBr + H]^+$ was calculated 317.9588 and 319.9568 while observed 318.1823 and 320.1813 at 298K in Acetonitrile solvent.

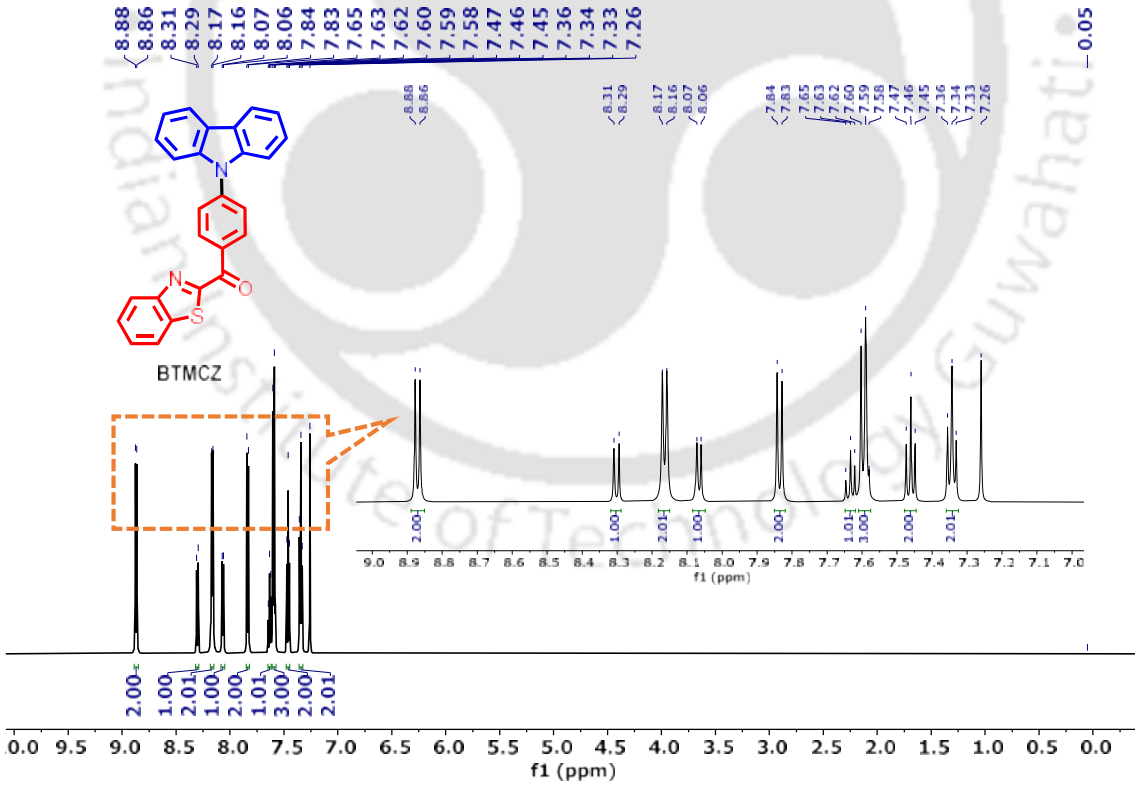

Figure A6.4. ^1H NMR spectra of BTMCZ in $CDCl_3$ at 298K.

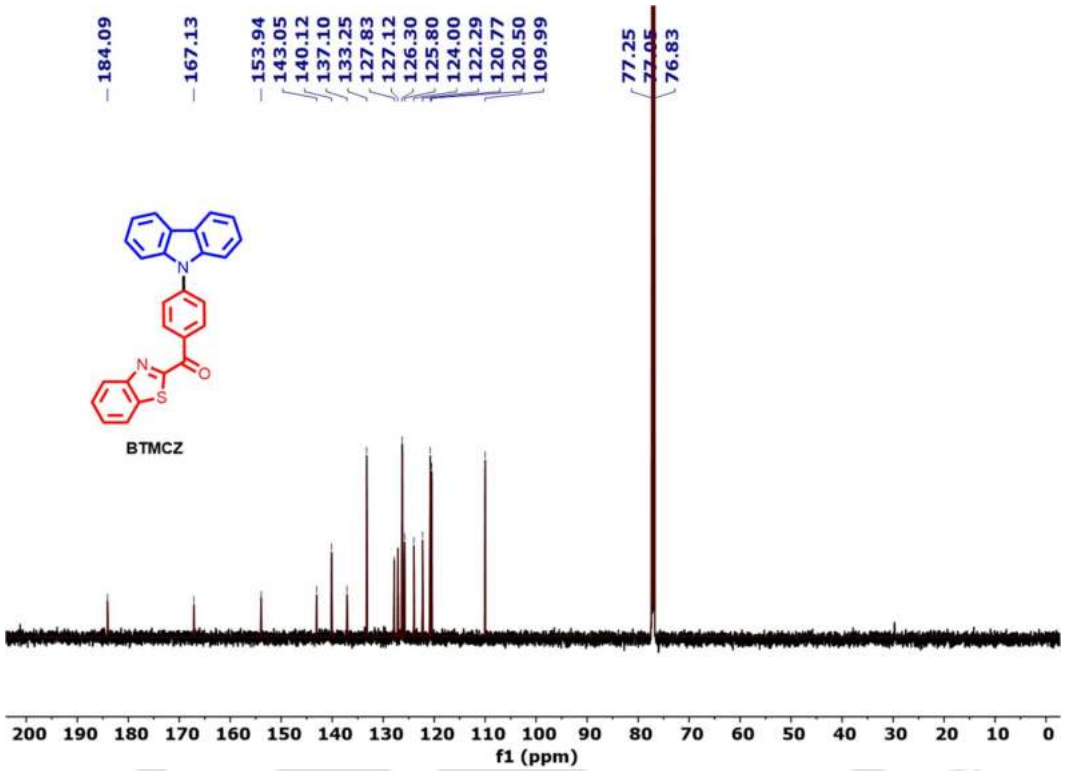

Figure A6.5. ^{13}C- NMR spectra of BTMCZ in $CDCl_3$ solvent at 298 K.

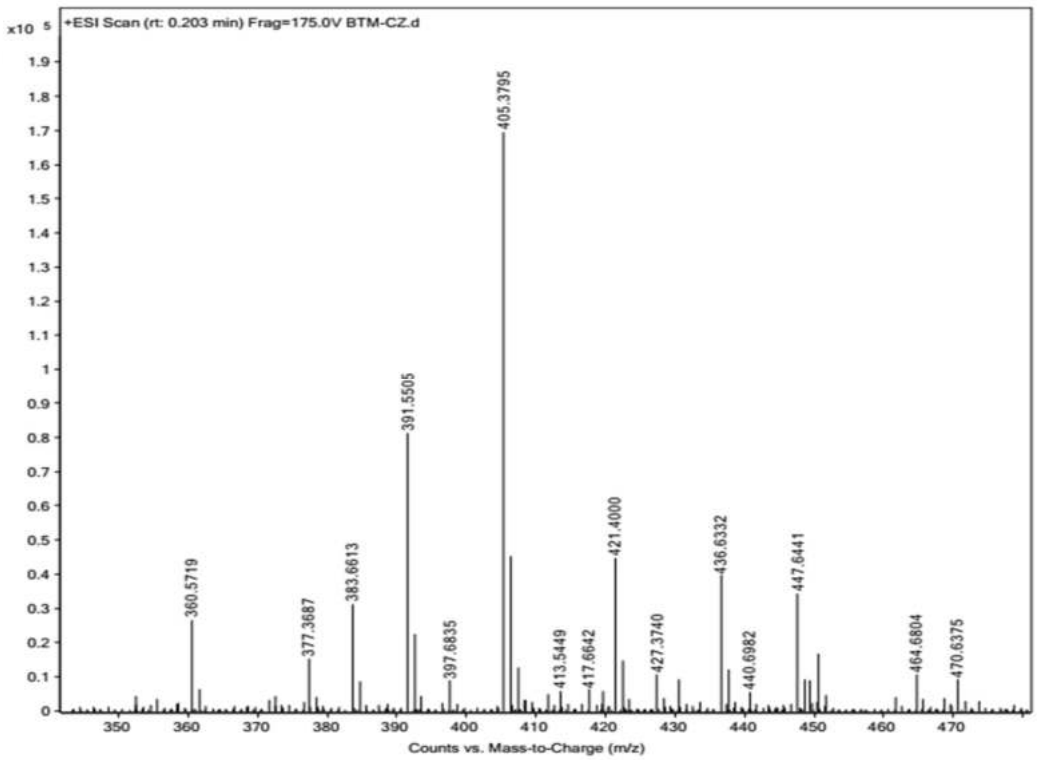

Figure A6.6. HRMS (ESI) peaks of m/z value for $[BTMCZ + H]^+$ was calculated 405.1062 and observed 405.3795 at 298K in Acetonitrile solvent.

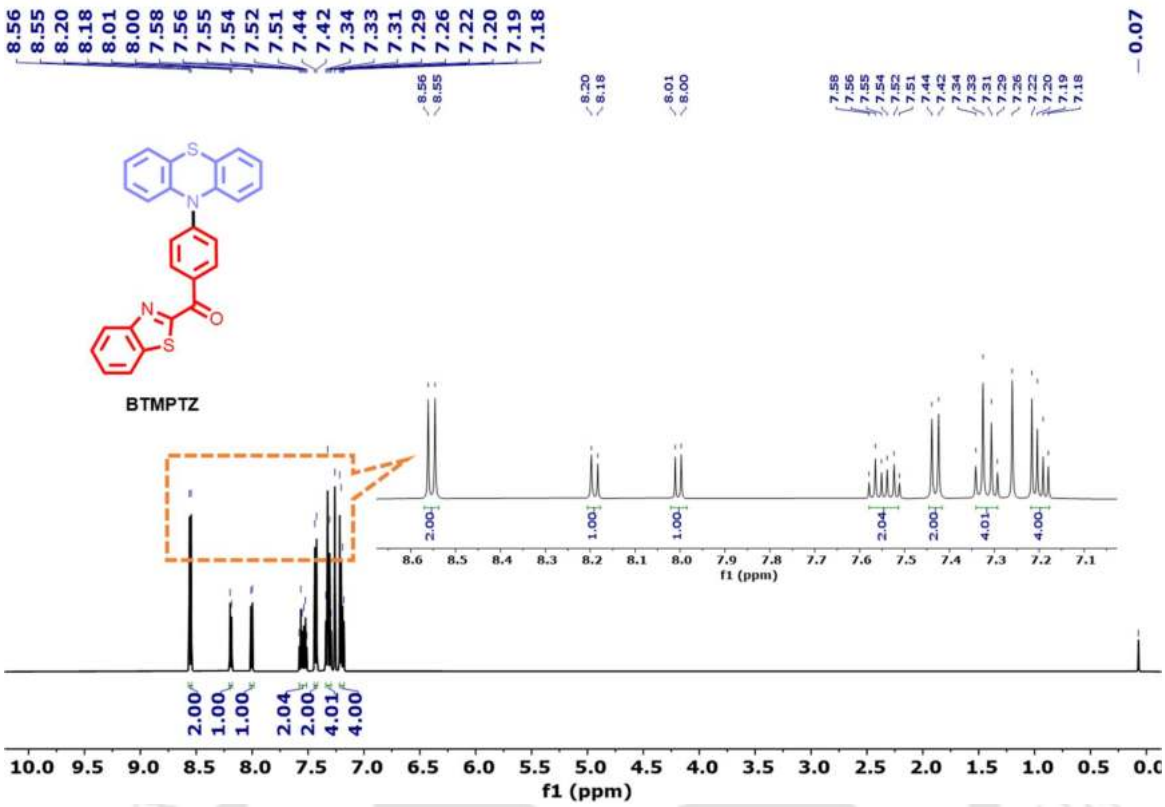

Figure A6.7. ^{1}H NMR spectra of BTMPTZ in $CDCl_3$ at 298K.

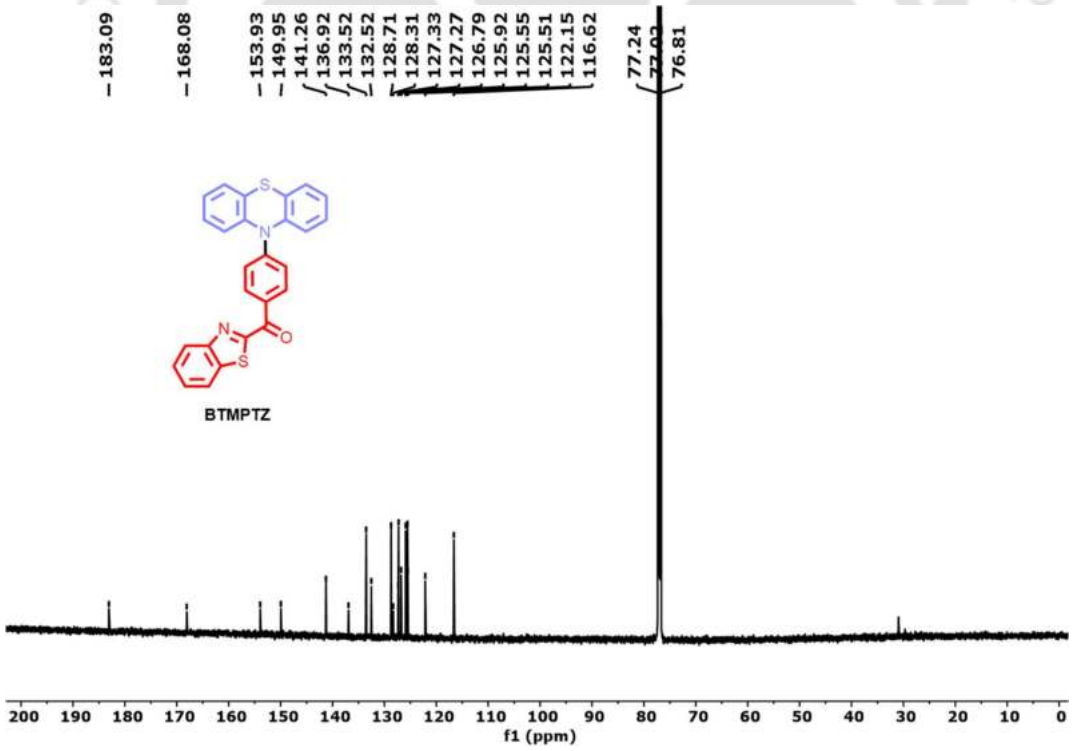

Figure A6.8. ^{13}C- NMR spectra of BTMPTZ in $CDCl_3$ solvent at 298 K.

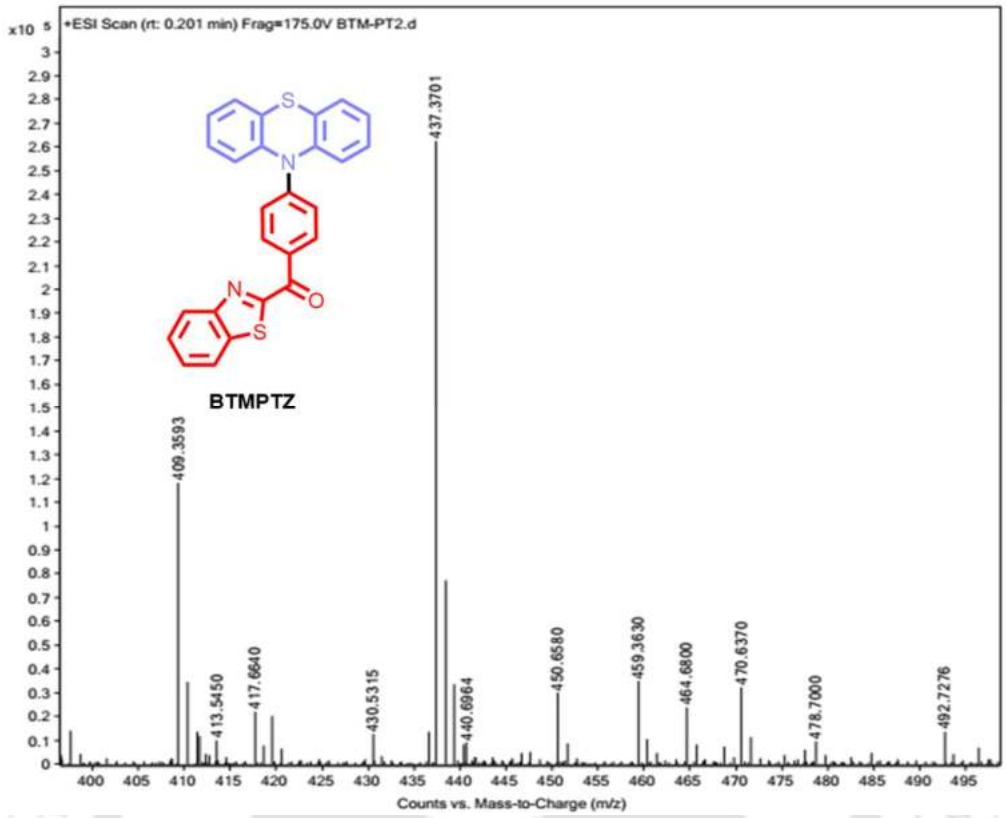

Figure A6.9. HRMS (ESI) peaks of m/z value for $[BTMPTZ + H]^+$ was calculated 437.0782 and observed 437.3701 at 298K in HPLC Acetonitrile solvent.

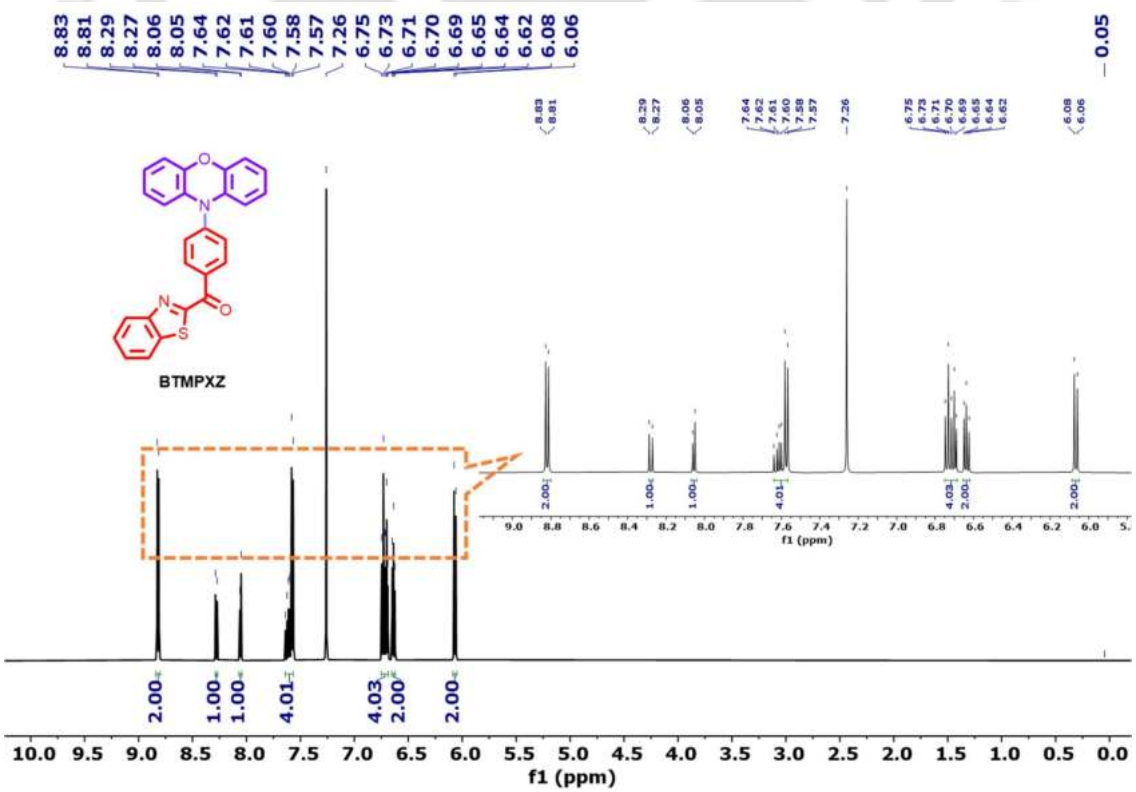

Figure A6.10. ^1H NMR spectra of BTMPXZ in $CDCl_3$ at 298K.

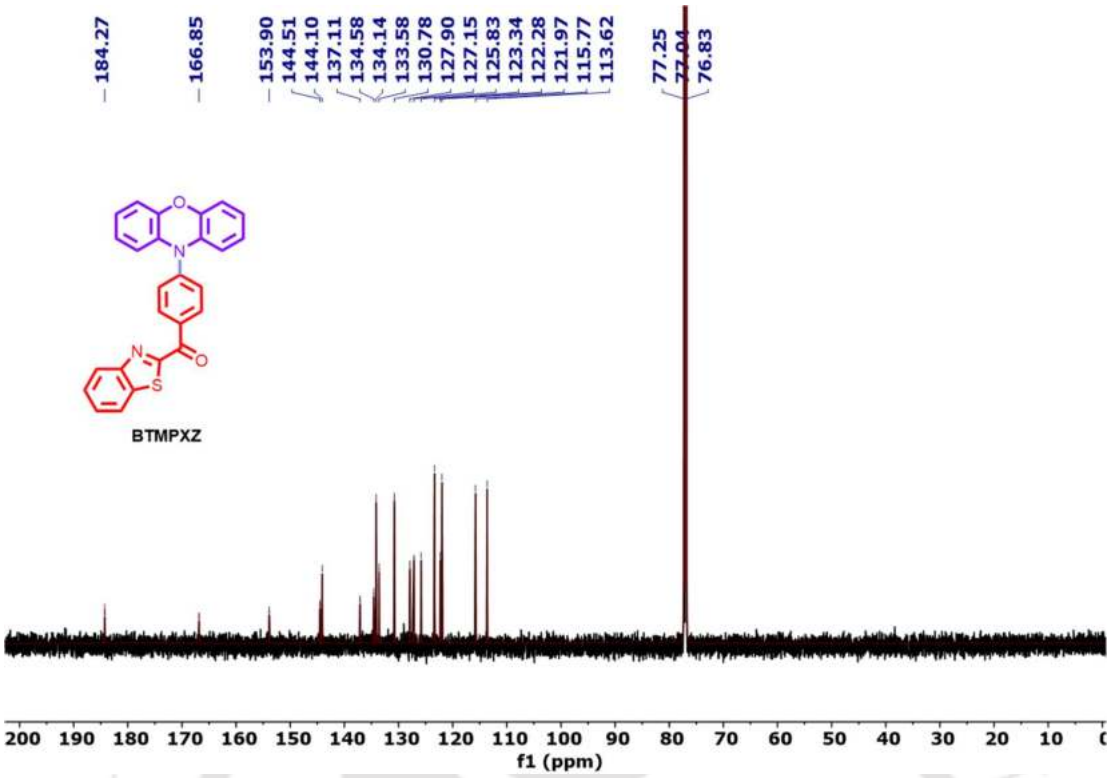

Figure A6.11. ^{13}C- NMR spectra of BTMPXZ in $CDCl_3$ solvent at 298 K.

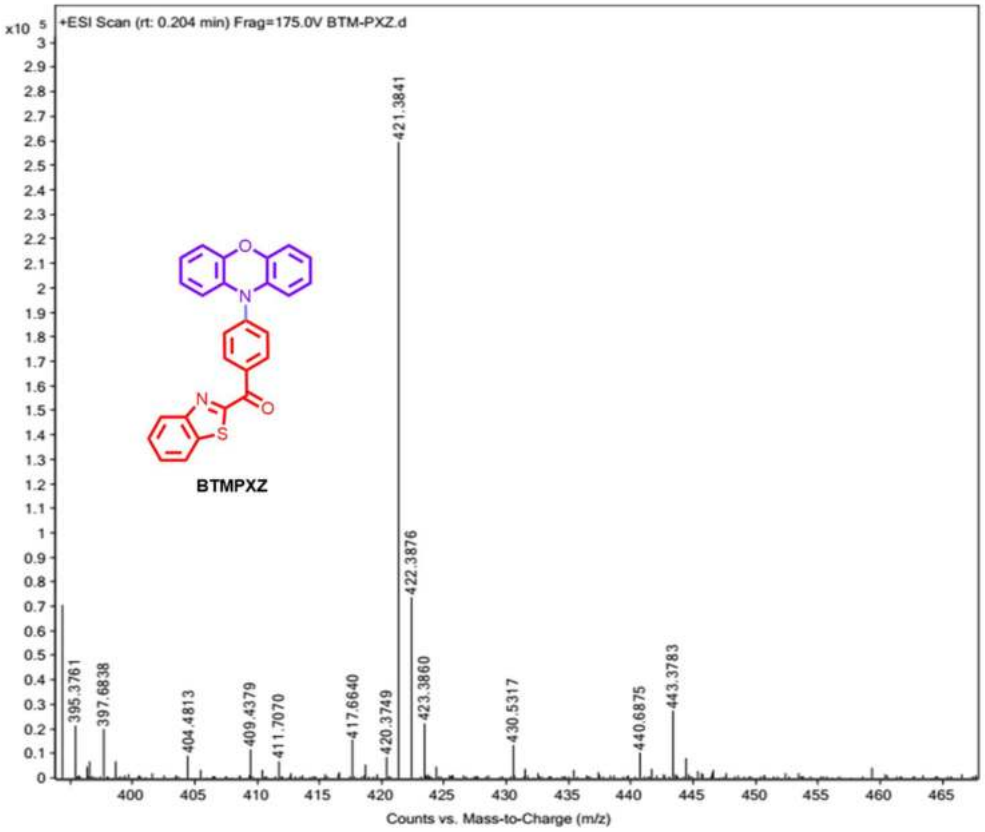

Figure A6.12. HRMS (ESI) peaks of m/z value for $[BTMPXZ + H]^+$ was calculated 421.1011 and observed 421.3841 at 298K in HPLC Acetonitrile solvent.

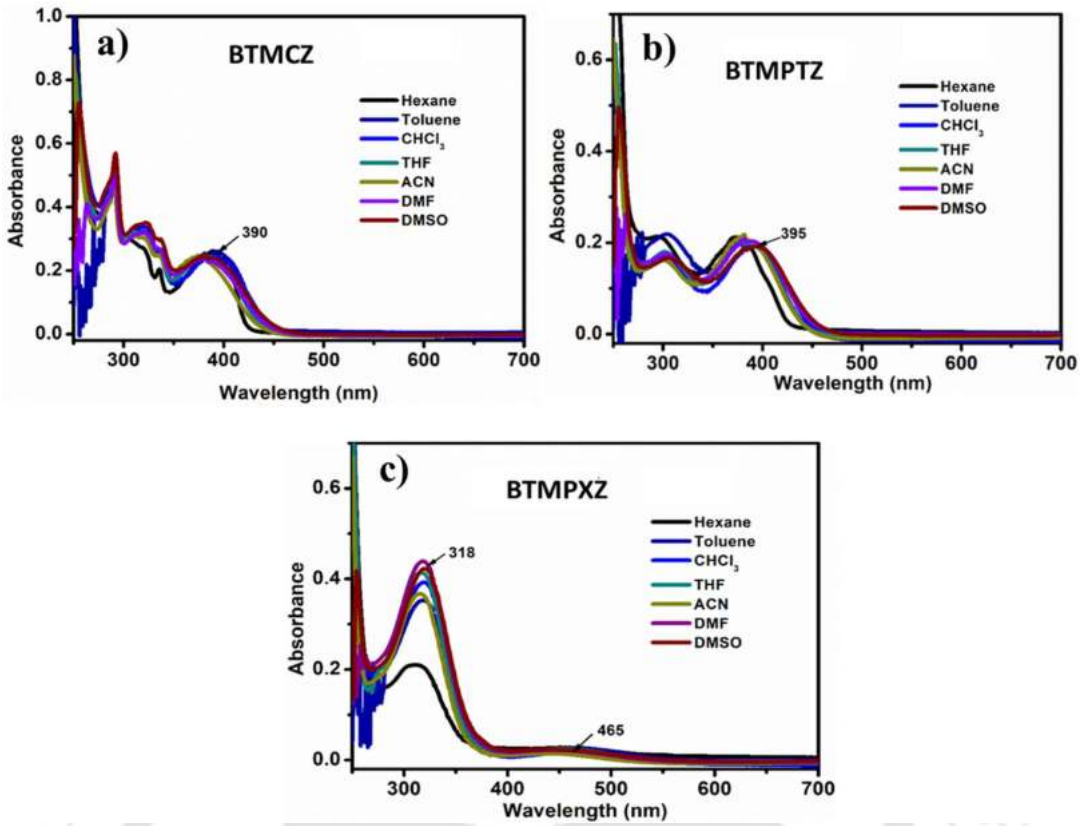

Figure A6.13. (a, b & c) UV-visible absorption spectra recorded by varying different solvent polarity for BTMCZ, BTMPTZ and BTMPXZ at 5 x 10^{-5}M concentration.

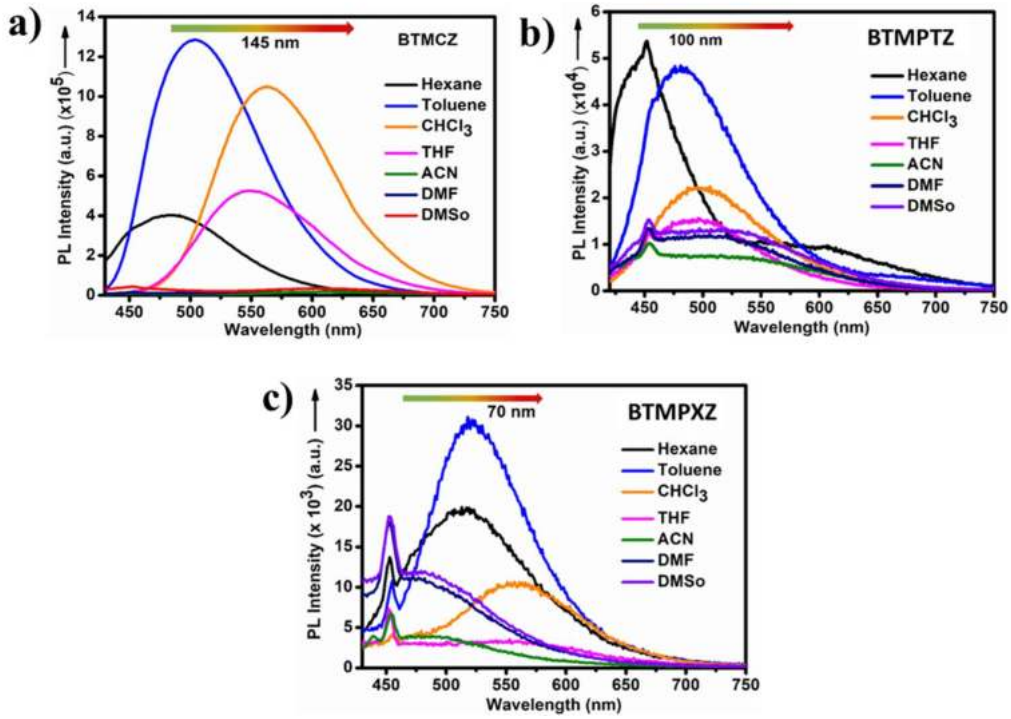

Figure A6.14. (a, b & c) Fluorescence spectra recorded by varying different solvent polarity for BTMCZ, BTMPTZ and BTMPXZ at 5 x 10^{-5}M concentration.

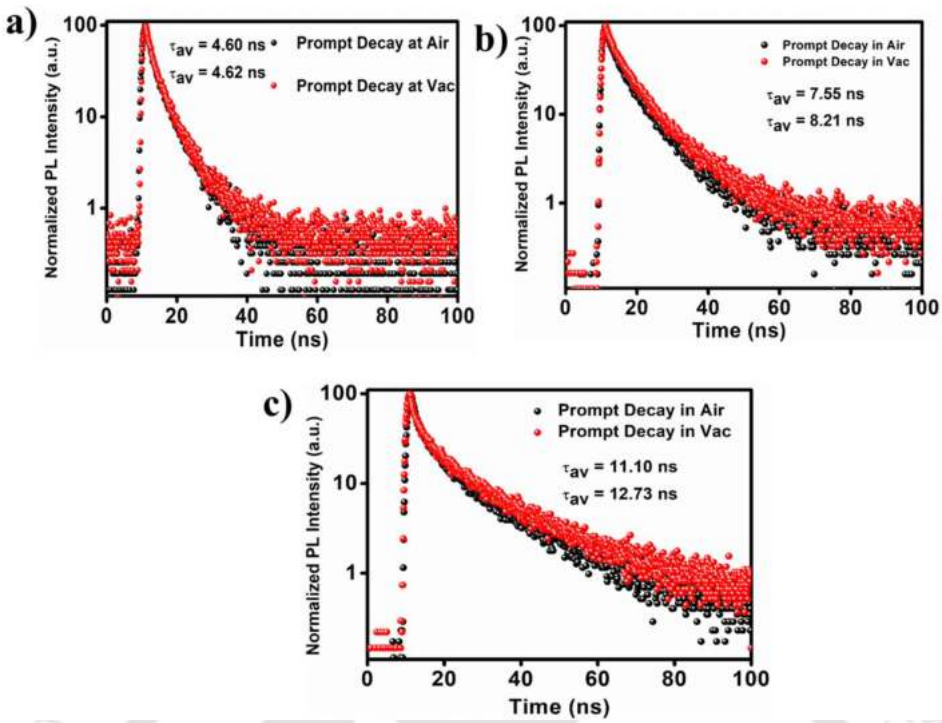

Figure A6.15. (a, b & c) Prompt fluorescence/LE state emission lifetime recorded under air and vacuum in the thin film of BTMCZ, BTMPTZ and BTMPXZ respectively.

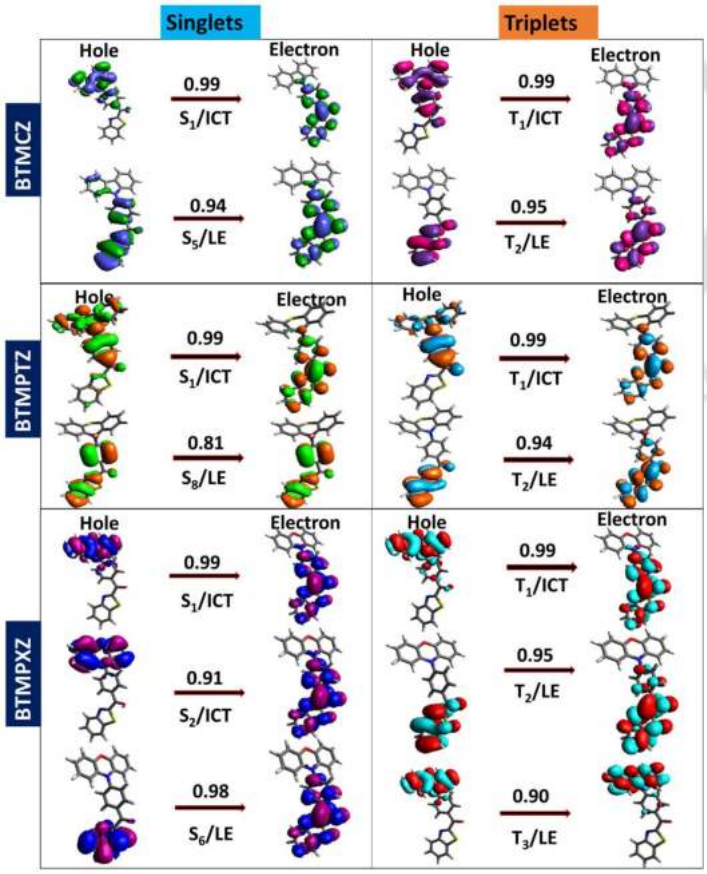

Figure A6.16. Natural transition orbitals (NTOs) for different singlet and triplet excited states in BTMCZ, PTMPTZ and BTMPXZ respectively.

Table A6.1. Crystallographic data and structure refinement parameters of BTMCZ, Polymorph of BTMPTZ and BTMPXZ.

Compound	BTMCZ	BTMPTZ	BTMPTZ-P1	BTMPXZ
Empirical formula	C26 H16 N2 O S	C26 H16 N2 O S2	C26 H16 N2 O S2	C25 H16 N4 O S
CCDC NO	2123178	2123179	2123180	2123181
Temperature/K	293	293	293	293
Crystal system	monoclinic	triclinic	triclinic	monoclinic
Space group	P 21/n	P -1	P -1	C 2/c
a/Å	17.2792(11)	7.7000(5)	7.6739(18)	25.075(6)
b/Å	3.9507(2)	11.1923(13)	11.1775(19)	10.236(2)
c/Å	31.1783(17)	13.1368(14)	13.088(3)	15.884(3)
α/°	90.00	73.553(10)	73.521(17)	90.00
β/°	102.318(6)	81.072(7)	81.035(19)	98.753(17)
γ/°	90.00	1046.47(18)	75.501(17)	90.00
Volume/Å^3	2079.4(2)	1046.47(19)	1037.9(4)	4029.4(15)
Z	4	2	2	8
ρ_{calc}mg/mm^3	1.292	1.385	1.397	1.386
m/mm^{-1}	0.176	0.276	0.278	0.188
F(000)	840	452.0	452	1744.0
Index ranges	-15≤ h ≤ 20, -4 ≤ k ≤ 2, -30 ≤ l ≤ 37	-9 ≤ h ≤ 9, -10 ≤ k ≤ 13, -14 ≤ l ≤ 15	-9 ≤ h ≤ 9, -13 ≤ k ≤ 13, -15 ≤ l ≤ 14	-21≤ h ≤ 29, -12 ≤ k ≤ 12, -18 ≤ l ≤ 16
Reflections collected	3665	3680	3648	3562
Independent reflections	2252	2498	3645	573
Data/restraints/ parameters	2252/0/271	2498/0/280	2404/0/280	573/0/280
Goodness-of-fit on F^2	1.157	1.031	0.978	0.0865
Final R indexes	R1 = 0.0940, wR2 = 0.3488	R1 = 0.0615, wR2 = 0.1866	R1 = 0.0504, wR2 = 0.1259	R1 = 0.0793, wR2 = 0.1911

Table A6.2. Crystal structural analysis with non-covalent interactions and dihedral angle information.

Single Crystals	Intra-molecular Interactions Close contact distance (Å)				Intermolecular Interactions Close contact distance (Å)			D-A Dihedral Angle (Degree)
	CH-O	CH-N	CH-π	π-CH	CH-O	CH- π	π -π	
BTMCZ	2.442	2.371	3.232	2.802	2.669	-	3.951	68.62
BTMPTZ	2.426	2.464	2.368	2.589	2.498	-	4.016	66.48
BTMPTZ_P1	2.429	2.463	2.520	2.595	2.341	-	3.994	66.90
BTMPXZ	2.408	2.235	2.559	2.615	2.607	2.768	5.357	42.34

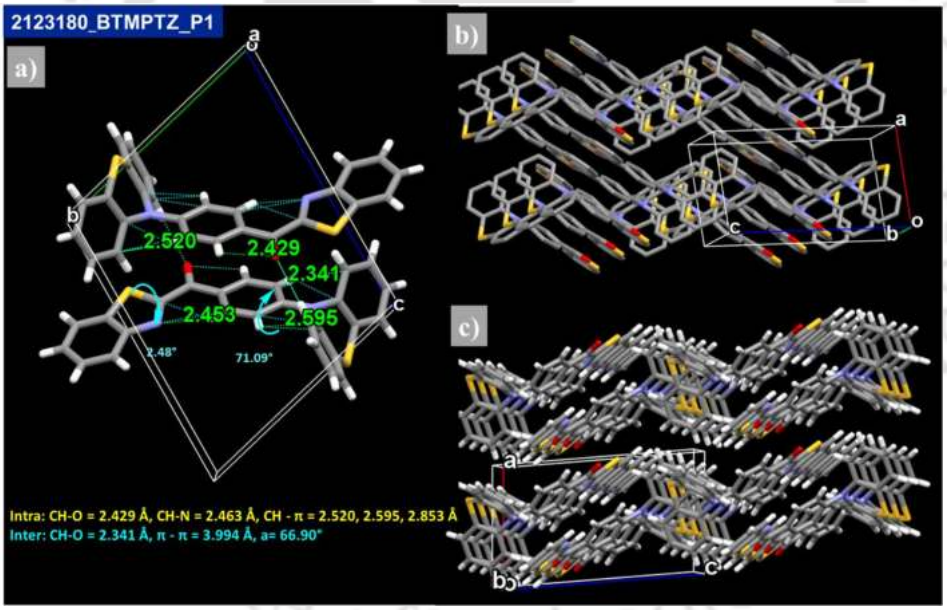

Figure A6.17. Polymorphism: (a) Unit cell crystal stucture for the polymorphic stucture of BTMPTZ denoted as BTMPTZ_P1. This polymorph was obtained by changing the solvent during crystal growth. As expected a significant variation in the crystal packing stucture, different distances in intermolecular/ intramolecular noncovalent interactions and dihedral angle was noted for this stucture than parent BTMPTZ, confirming polymorphism behavior due to the flexible nature of PTZ donor unit (b) J-aggregated self-assembly stucture for BTMPTZ_P1 (H-is omited for better clarity) (H-is omited for better clarity).(c) H-bonded supramolecular rigid 3D- crystal packing for BTMPTZ_P1 in bulk along axis c.

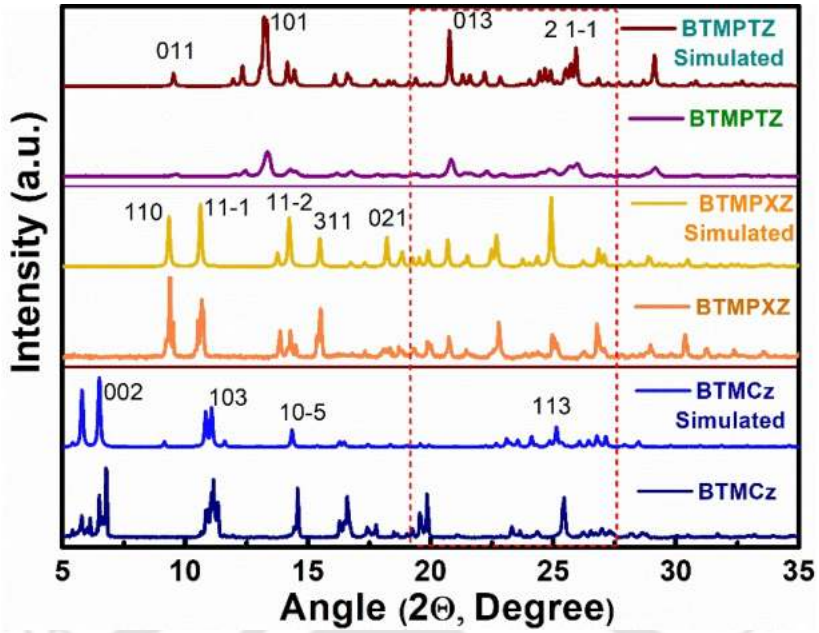

Figure A6.18: PXRD pattern for BTMCZ, BTMPTZ and BTMPXZ respectively.

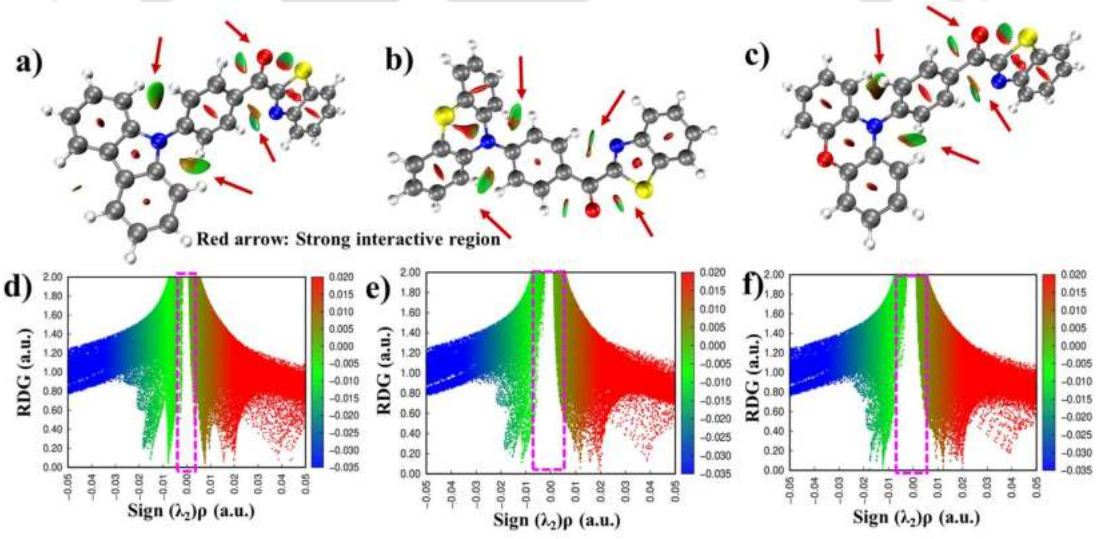

Figure A6.19: Reduced density gradient (RDG): distribution of RDG isosurfaces (a, b and c) with the scatter plot of RDG versus sign(λ_2)ρ isosurface map (d, e, and f) with an isovalue of 0.5 for BTMCZ, BTMPTZ and BTMPXZ respectively.

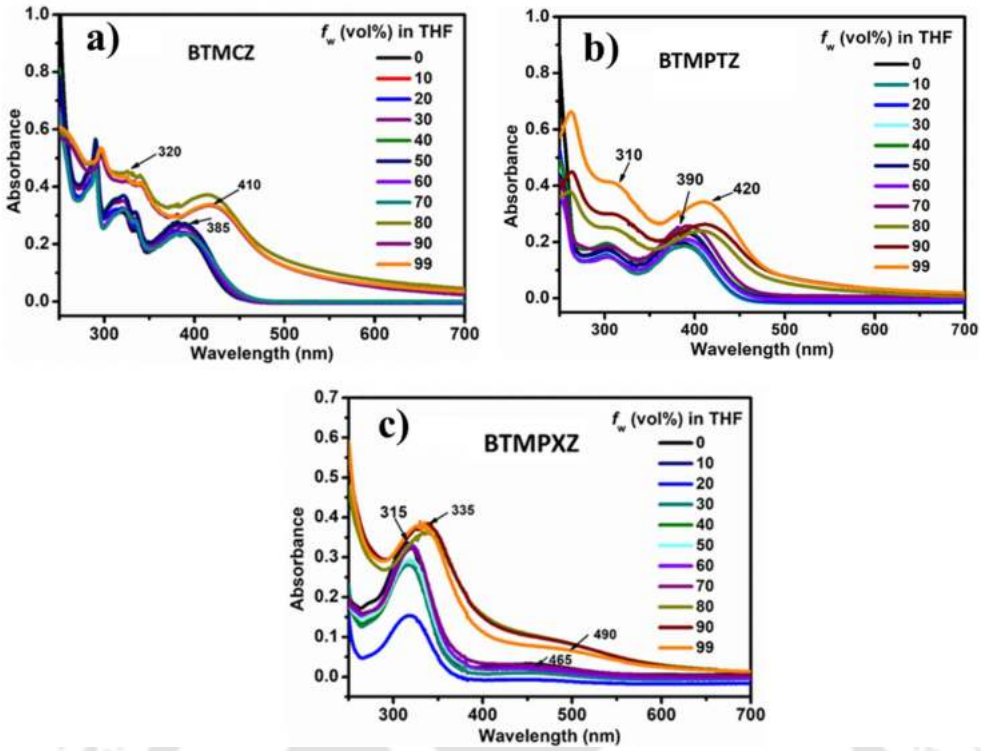

Figure A6.20: (a, b & c) UV-visible absorbance spectra recorded by varying various THF:H_2O mixtures for BTMCZ, BTMPTZ and BTMPXZ at 5 x 10^{-5}M concentration.

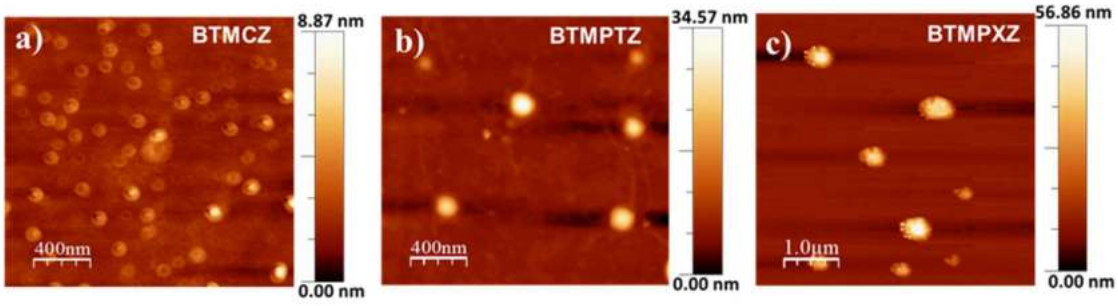

Figure A6.21: Atomic force microscopy (AFM) images recorded using aggregates from 99% w_f for BTMCZ, BTMPTZ and BTMPXZ.

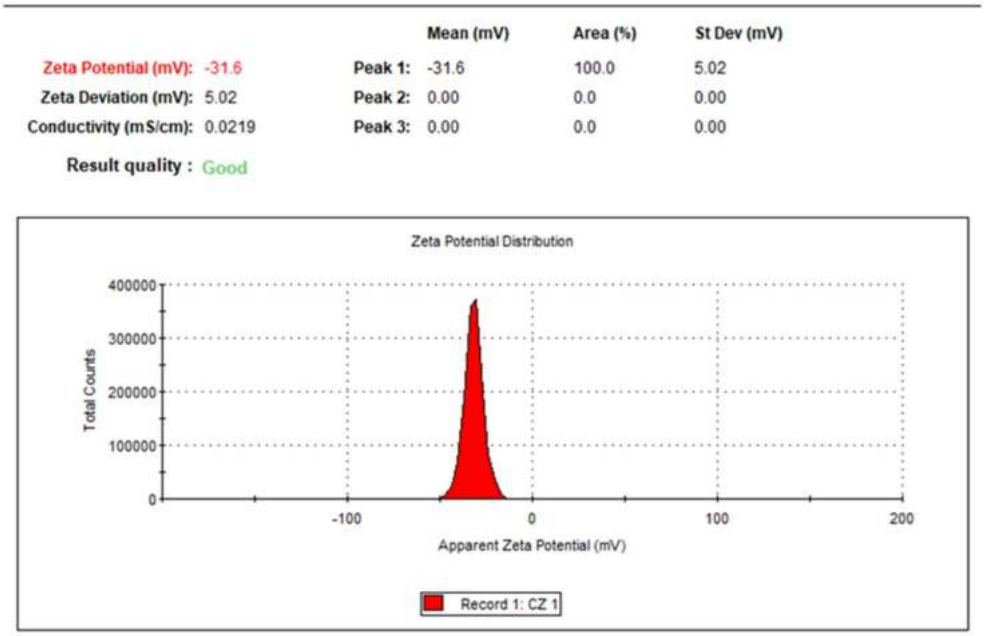

Figure A6.22: Zeta-potential recorded in H_2O for BTMCZ at 10^{-5} M concentration.

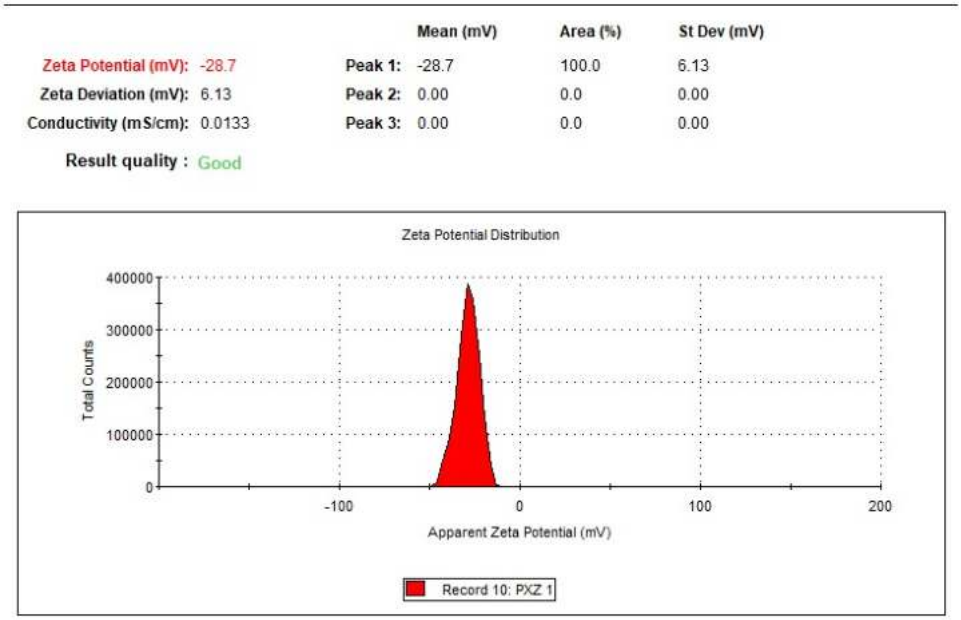

Figure A6.23: Zeta-potential recorded in H_2O for BTMPTZ at 10^{-5} M concentration.

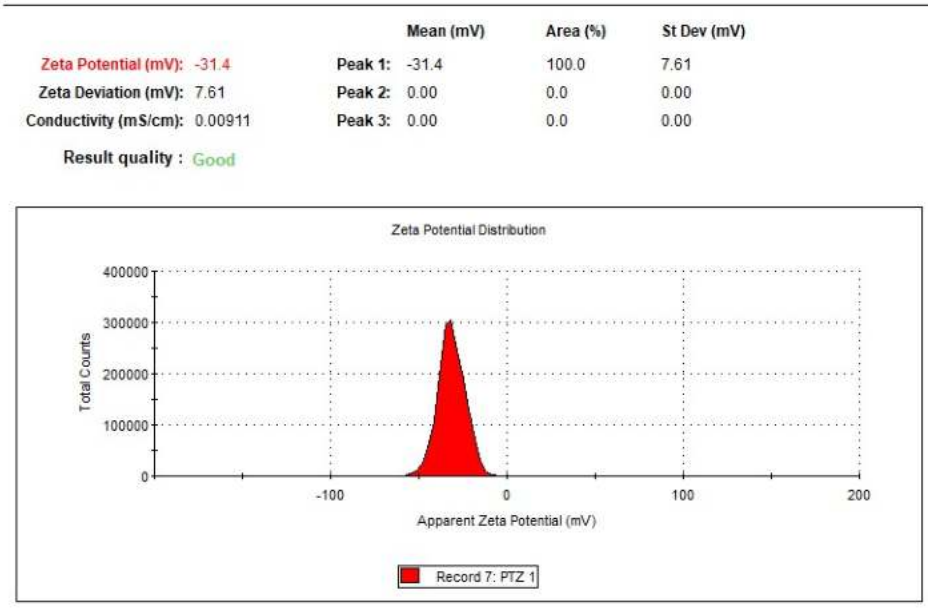

Figure A6.24: Zeta-potential recorded in H_2O for BTMPXZ at 10^{-5} M concentration.

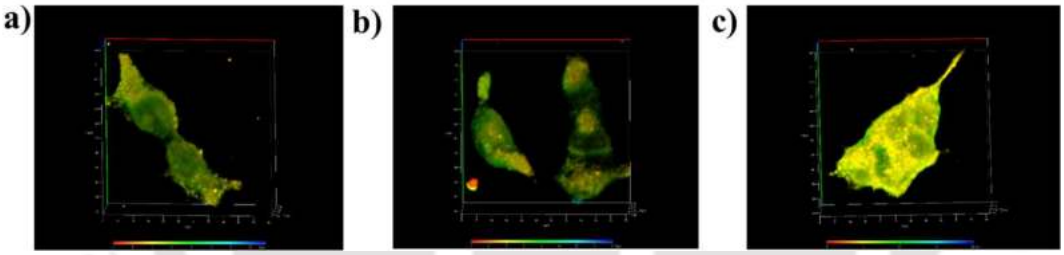

Figure A6.25. (a, b & c) Z-stacking analysis of the MCF-7, confirming the internalization and localization of the BTMCZ, BTMPTZ and BTMPXZ in the cytoplasm. (Scale bar: 5 µm)

CHAPTER 7

Manipulation of Triplet Excited-states Procuring Long-lived Delayed Fluorescence *via* Pull-push Electronic Effects in Structurally Tailored Novel AIEgens for Bio-imaging

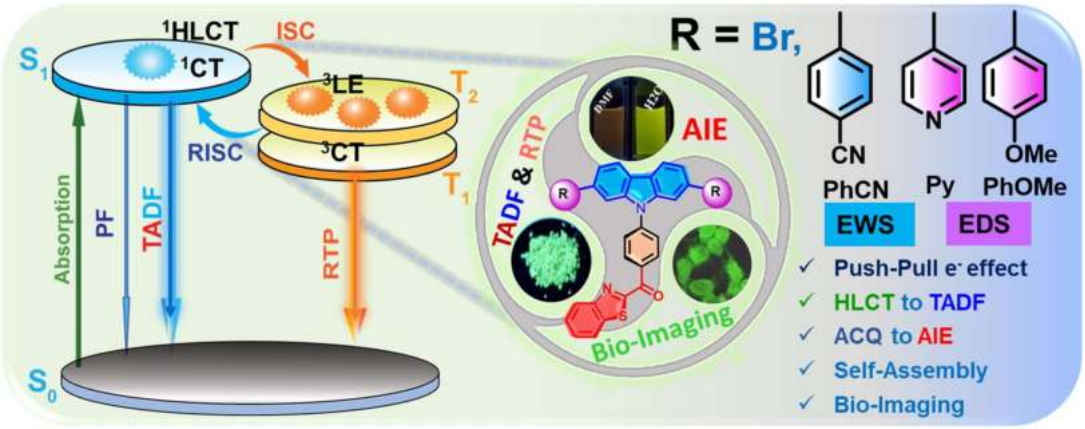

Barman, D., Rajamalli, P., Bidkar, A.P., Barman, D., Gogoi, R., Ghosh, S. S., Zysman-Colman, E., Iyer, P. K. (*Communicated)*

Abstract

Purely organic luminescent materials with aggregation induced emission (AIE) and thermally activated delayed fluorescence (TADF) have appeared as a new library of benign luminophores for versatile applications. Yet, the fundamental understanding of their exceptional 'structure-property relationship' is still in its infancy. Herein, four triplet harvestig luminogens namely BTMCZBr2, BTMCZCN2, BTMCZOMe2 and BTMCZPy2 were facilely synthesized to decipher their intrinsic structure-property functions and further used for cell imaging application. A novel benzothiazole-methanone acceptor core has been explored with common donor carbazole moiety. By introducing electron donating and withdrawing segments (EWS and EDS) in the carbazole donor, efficiently triggering the pull-push electronic effects *via* different locally excited (LE) and charge-transfer (CT) states, demonstrating a unique examples of long-lived luminescent organic materials. Interestingly, EWS substituted molecules BTMCzBr2 and BTMCzCN2 showed hybridized locally excited charge-transfer (HLCT) emission and long lifetime, while EDS contained molecules BTMCzOMe2 and BTMCzPy2 showed efficient TADF property and very high PLQY. Experimental studies and computational results revealed a clear understanding of the singlet-triplet excited state dynamics, appropriate structural modifications, controlled electronic effects, and supramolecular self-assembly which are important prerequisites to demonstarte the 'structure-property-functions correlations' at the electronic level. Single-crystal X-ray structures of EWS adopted organic solvents while EDG adopted water molecule in the crystal lattice and depicting different solvent polarity induced optical properties. Among four fluorophores, BTMCzPy2 was found to be an efficient AIE-TADF emitter and exhibited a good cellular uptake and bright cell-imaging efficacy.

7.1 Introduction

The discovery of metal-free organic luminescent materials and their associated fundamental mechanism is of great significance in building a unique "structure-property relationship" and is extremely expedited to newer applications. For instance, most organic chromophores and their emission solely depend on singlet excitons,[1,2] while their obscure mechanism of triplet emission limits their efficient utilization in many versatile fields.[3,4] Essentially, delicate tailoring in new molecular design and management of singlet and triplet energy states via favourable excited state dynamics for purely organic materials have emerged as a principle focus in the scientific community.[5,6] In particular, harnessing dark-emissive triplets endured a great challenge since the first discovery of triplet-harvesting thermally activated delayed fluorescence (TADF) in metal-free organic emitter by C. Adachi and co-workers in 2012.[7] Over the last few years, novel TADF materials have been performing theoretically 100% internal quantum efficiency (IQE) *via* reverse intersystem crossing (RISC) process with their extremely small singlet-triplet energy gap (ΔE_{ST}), have made enormous breakthroughs in organic light-emitting diodes (OLEDs).[8–10] Besides, TADF materials exhibit certain additional characteristics, *viz*. large structure diversity, long-lived emission, high photoluminescence quantum yield (PLQY), and reliable biosafety, which offer great promise for biomedical applications. Therefore, aside from OLEDs, by the merits of their unique photophysical properties, TADF emitters have attracted tremendous attention in conventional fluorescence imaging,[11] time-resolved fluorescence imaging (TRFI),[12] photo-catalysis,[13] sensing,[14] and photodynamic therapy (PDT).[15] Remarkably, fluorescence imaging has been demonstrated to be an indispensable tool owing to its ultra-high sensitivity and superior spatial-temporal resolution beneficial for visualizing the cellular structures and biochemical processes in complex biological environments.[16,17] However, the major issue for obtaining high-resolution images is the background auto-fluorescence while using fluorescent probes.[18]

In this prospect, TADF emitters featured large stock shifts *via* charge-transfer (CT) excited states which offer distinguishing excitation and emission signals and also help to mitigate self-absorption and background interferences, thereby improving the accuracy of bio-imaging.[19] Meanwhile, the rate of RISC and involvement of long-

lived triplets primarily control the delayed fluorescence (DF) in TADF emitters, as described in equation 1.[20]

$$k_{RISC} \propto \exp\left(-\frac{\Delta E_{ST}}{k_B T}\right) \qquad \text{Equation 7.1}$$

Unlike the well-explored mechanism of long-lived DF, typical TADF emitters originated from the straightforward RISC between the lowest excited singlet and triplet charge transfer (^{1}CT and ^{3}CT) states.[21] Few recent reports demonstrated that RISC might occur with the involvement of higher-lying locally excited triplet states (^{3}LE), which act as an intermediatory state between ^{1}CT, ^{3}CT *via* second-order spin vibronic coupling at a very low ΔE_{ST}.[22] This phenomenon could be attributed to a rapid triplet up-conversion and efficient long-lived emission.[23,24] However, due to the involvement of triplets, these emitters are highly sensitive to surrounding quenchers, e.g. oxygen and temperatures.[25] In addition, the hydrophobic nature of most organic dyes forms aggregates in a hydrophilic biological system, where highly planar π-conjugates cause strong π-π stacking and, therefore, display reduced emission behaviour.[26,27]

Hence, great care is required while using TADF emitters in the biological environment. Thus far, encapsulation of the TADF probe is a widely explored strategy to solve the triplet quenching issues, using additional assistance e.g. amphiphilic polymers either covalently or by co-precipitation (within water-soluble nanoparticle) is increasingly studied for the Labelling of cell membranes.[28] However, this strategy provides poor information about intracellular structures and biological processes.[29] Nevertheless, the construction of encapsulation-free pure TADF molecules for bio-imaging remains a real challenge. It is noted that the self-aggregation behaviour of highly twisted TADF emitter can prevent inside molecules from surface quenchers owing to the prohibition of energy dissipation through non-radiative channels.[30] In the aggregated state, chromophores possess a high density of supramolecular interactions and rigid molecular packing, which facilitates the overlapping of excitons from triplet to singlet excited state, enhancing delayed luminescence lifetime from microseconds to milliseconds.[31] In this sense, the concept of aggregation-induced delayed fluorescence (AIDF) is the potential to suppress the concentration quenching and TADF–oxygen interactions simultaneously.[32]

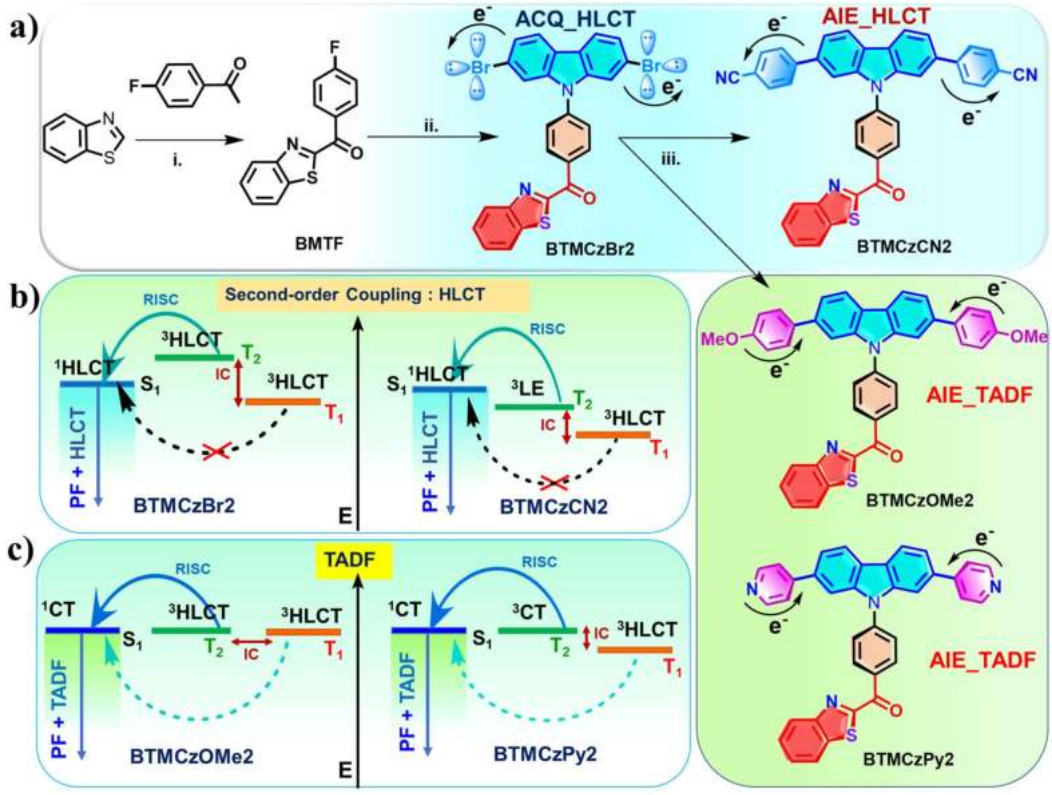

Figure 7.1. a) Schematic route of synthesis for target compounds BTMCzBr2, BTMCzCN2, BTMCZOMe2 and BTMCzPy2 respectively. b) Illustration of second-order coupling mechanism and HLCT emission pathways for BTMCzBr2 and BTMCzCN2. c) Representation of TADF mechanism via iso-energetic states for BTMCzOMe2 and BTMCzPy2.

Thus, aggregation is a key phenomenon that furnishes enhanced lifetimes and has shown promising appeal in biomedicine. However, lack of a systematic summary, ideal photophysical properties and reliable biosafety, the prospect of the current progress in TADF molecules is still in its infancy. Nonetheless, rational manipulation of the excited state and utilization of possible radiation energy from an engineered donor–acceptor (D-A) structure is relatively appealing. Herein, we present an effective strategy of pull-push electronic effects to tune the excitons dynamics for augmenting different delayed emission processes such as HLCT and TADF, respectively. As a proof of concept, four delayed fluorescence (DF) molecules are engineered viz. BTMCzBr2, BTMCzCN2, BTMCzOMe2 and BTMCzPy2, respectively. Remarkably, the former two compounds exhibited HLCT, and the latter two displayed TADF characteristics. By changing the electronically different substituents, the molecules followed different DF pathways and showed tunable optical properties, including AIE characteristics. Molecular simulation studies demonstrated that substitution of the

electronically different functional group could effectively regulate the ΔE_{ST} and LE/CT feature, which provided efficient long-lived emission and very high PLQY. Due to the presence of multiple rotor units in the DF cores, they exhibited a variety of color-tunable emission in the solution e.g. solvatochromism and AIE in the aggregated state. Moreover, by restricting the free rotation of the rotor groups in the aggregated state and the merits of pull-push electronic effect, non-radiative pathways are greatly controlled, resulting in poor AIE in BTMCzBr2 and BTMCzCN2 and intense AIE in BTMCzOMe2 and BTMczPy2. Single crystal X-ray analysis revealed that one of the HLCT molecule held a nonpolar solvent molecule (ethylacetate), while one of the TADF cores contained polar molecules (water), stabilizing their respective crystal structure and corroborating the different optical behaviour. Further, to investigate the biocompatibility of the compounds cell viability studies were tested. Unlike BTMCzBr2, all the emitters were found to be highly cell viable. Further, fluorescence imaging were performed in few sets of normal and cancer cells using all the emitters. Remarkably, the pyridine-substituted CZ-containing BTMCzPy2 molecule exhibited higher AIE-TADF and cellular uptake efficiency rather than the other congeners, due to its extreme CT emission, high TADF efficiency, and well defined nano-sphere like nanocrystalline morphology.

7.2. Experimental Section

7.2.1. Materials

Benzothiazole, 4-fluoro-Acetophenone, 2, 7-dibromo carbazole, 4-cyanophenyl) boronic acid, (4-methoxyphenyl)boronic acid, and pyridin-4-ylboronic acid, potassium carbonate, palladium acetate, triphenylphsphine, tetrakis-(triphenylphosphine)palladium(0) and toluene were purchased from Sigma-Aldrich and used as such without further purification**.** All the solvents used like toluene, chloroform and hexane were purified prior to use according to the standard protocol and stored in molecular sieves.

7.2.2. Synthesis and Characterizations

7.2.2.1. Synthesis of benzothiazol-2-yl(4-fluorophenyl)methanone [BTM-F]

1-(4-fluorophenyl)ethanone (1.38 g, 10 mmol), benzothiazole (2.03 g 15 mmol), iodine (3.80 g, 15 mmol) and potassium hydroxide (1.12 g, 20 mmol) were taken in DMSO : water (3:1) at room temperature. The mixture was heated up to 100 °C and the completion of the reaction was monitored using analytical TLC technique. After 24 h the reaction mixture was cooled to at room temperature after that dichloromethane (50 ml) was added to it.

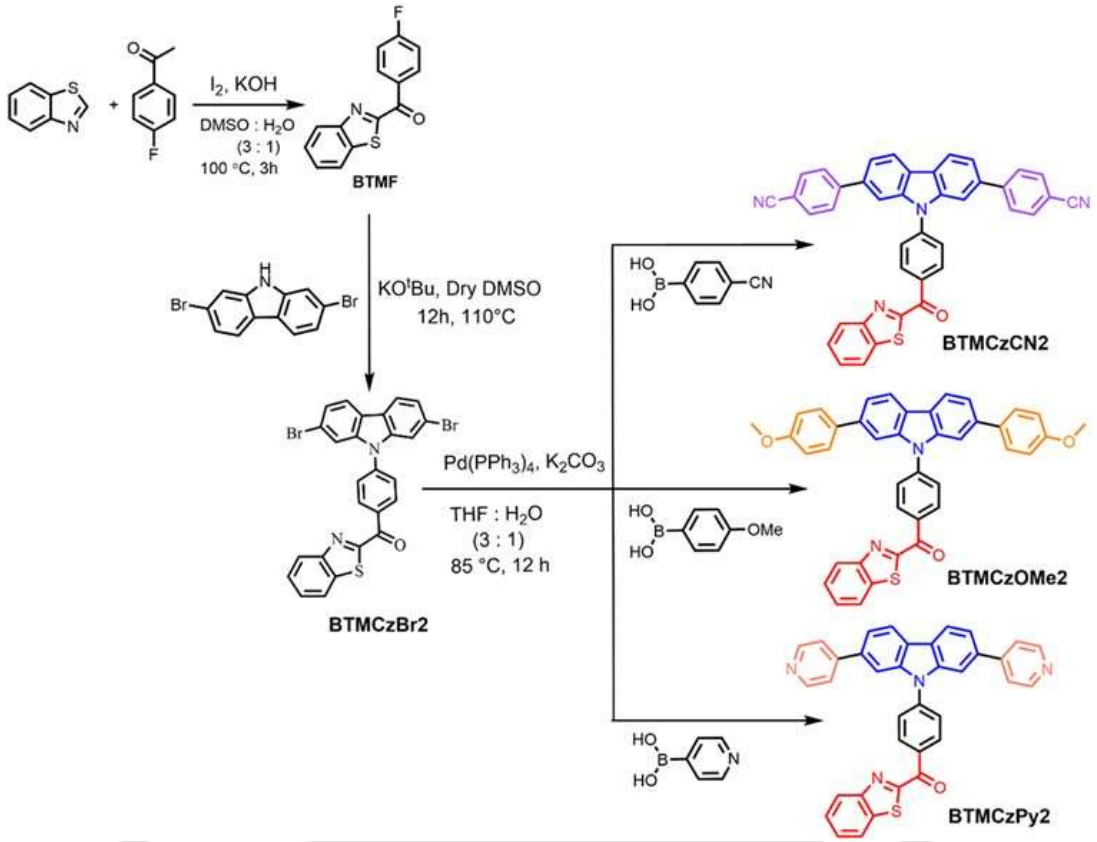

Scheme 7.1: Route of Synthesis for BTMCzBr2, BTMCzCN2, BTMCzOMe2 and BTMCzPy2.

Then the crude mixture was extracted with dichloromethane and washed with aqueous sodium thiosulfate solution for several times. Then it was dried over anhydrous Na2SO4 and concentrated under reduced pressure. Then the compound was finally purified by column chromatography using silica gel with 5% dichloromethane in hexane as eluent. Yellow solid (1.722 g, 67% yield).

Yellow solid (1.722 g, 67% yield). ^{1}H NMR (400 MHz, $CDCl_3$, δ ppm) 8.68 (dd, J = 8.8, 5.5 Hz, 2H), 8.25 (d, J = 7.4 Hz, 1H), 8.03 (d, J = 7.3 Hz, 1H), 7.63 – 7.54 (m, 2H), 7.23 (d, J = 8.7 Hz, 2H). ^{13}C NMR (101 MHz, $CDCl_3$, δ ppm) 183.62, 153.87, 137.02, 134.25, 127.74, 127.03, 125.73, 122.22, 115.88, 115.67.

HRMS (ESI) peaks of m/z value was calculated for $C_{14}H_7FNOS$ 257.0389, Found at 258.0340, $[M+1]^+$.

7.2.2.2. Synthesis and Characterization of benzothiazol-2-yl(4-(2,7-dibromo-9H-carbazol-9-yl) phenyl) methanone [BTMCzBr2]

2,7-Dibromo-9H-carbazol (2.07 g, 6.39 mmol) and potassium tert-butoxide (0.72 g, 6.4 mmol) were taken in a 100 mL round bottom flask. The mixture was degassed by multiple vacuum and argon purging cycle. Then dry DMSO (50mL) was added and heated at 80 °C with continuous stirring for 30 minutes. After that, BTM-F (1.50 g, 5.84 mmol) was added and refluxed for 12 hours under inert atmosphere. The reaction mixture was cooled down to room temperature and then poured into ice water. The crude product was extracted with ethyl acetate (50 mL×3), washed with brine solution and dried over anhydrous sodium sulfate. Ethyl acetate was evaporated under reduced pressure and the product was purified by column chromatography (silica gel-100 mesh) using 10% ethyl acetate in hexane.

Yellow green solid (1.77 g, 54% yield). ^{1}H NMR (400 MHz, $CDCl_3$, δ ppm) 8.90 (d, J = 8.6 Hz, 2H), 8.31 (d, J = 7.6 Hz, 1H), 8.07 (d, J = 8.6 Hz, 1H), 7.96 (d, J = 8.3 Hz, 2H), 7.76 (d, J = 8.6 Hz, 2H), 7.68 – 7.56 (m, 4H), 7.45 (d, J = 8.3 Hz, 2H). ^{13}C NMR (101 MHz, $CDCl_3$, δ ppm) 183.96, 166.84, 153.92, 141.53, 141.17, 137.14, 134.18, 133.51, 127.93, 127.18, 126.43, 125.86, 124.38, 122.29, 122.22, 121.64, 120.31, 113.22. HRMS (ESI) peaks of m/z value was calculated for $C_{26}H_{14}Br_2N_2OS$ is 561.9173, Found 562.9273, $[M+1]^+$.

7.2.2.3. Synthesis and Characterization of 4,4'-(9-(4-(benzo[d]thiazole-2-carbonyl)phenyl)-9H-carbazole-2,7-diyl)dibenzonitrile [BTMCzCN2]

The compound BTMCzBr2 (0.5 g, 0.88 mmol), (4-cyanophenyl) boronic acid (0.37 g, 2.2 mmol) and tetrakis-(triphenylphosphine)palladium(0) (0.3 mmol) were taken in a 50 mL round bottom flask and it was degassed for 30 minutes. Then the solid compounds were dissolved in 15 mL dry-THF and degassed for 10 min. 5 mL of 2.0 M potassium carbonate solution was added and then the mixture was stirred at 85 °C under argon atmosphere. Further, the progress of the reaction was monitored by analytical TLC. After 12 h, the reaction mixture was cooled down to room temperature and 50 mL water was added. The crude product was extracted with ethyl acetate and the organic layer was dried over anhydrous sodium sulfate. The solvent was evaporated under reduced pressure and the product was purified by column chromatography (neutral alumina) using 30% ethyl acetate in hexane.

Pale Yellow solid (0.26 g, 50% yield). ^{1}H NMR (600 MHz, $CDCl_3$, δ ppm) δ 8.91 (d, J = 8.5 Hz, 2H), 8.27 (d, J = 8.1 Hz, 3H), 8.08 (d, J = 8.8 Hz, 1H), 7.87 (d, J = 8.5 Hz, 2H), 7.78 – 7.73 (m, 10H), 7.66 – 7.60 (m, 4H). ^{13}C NMR (151 MHz, CDCl3) δ 184.14, 167.46, 153.85, 145.96, 142.65, 141.51, 138.12, 137.12, 134.10, 133.56, 132.68, 128.16, 128.05,

127.31, 126.70, 125.74, 123.62, 122.37, 121.42, 120.59, 118.99, 110.93, 108.33, 77.25, 77.04, 76.83.

HRMS (ESI) peaks of m/z value was calculated for $C_{40}H_{22}N_4OS$ is 607.1593 and observed 607.1681, $[M+1]^+$.

7.2.2.4. Synthesis and Characterization of benzo[d]thiazol-2-yl(4-(2,7-bis(4-methoxyphenyl)-9H-carbazol-9-yl)phenyl)methanone [BTMCzOMe2]

The compound BTMCzBr2 (0.50 g, 0.88 mmol), (4-methoxyphenyl)boronic acid (0.34 g, 2.2 mmol) and tetrakis-(triphenylphosphine)palladium(0) (0.3 mmol) were taken in a 50 mL round bottom flask and it was degassed for 30 minutes. Then the solid compounds were dissolved in 15 mL THF and degassed for 10 min. 5 mL of 2.0 M potassium carbonate solution was added and the mixture was stirred at 85 °C under argon atmosphere. The progress of the reaction was monitored by analytical TLC. After 12 h, the reaction mixture was cooled down to room temperature and 50 mL water was added. The crude product was extracted with ethyl acetate and the organic layer was dried over anhydrous sodium sulfate. The solvent was evaporated under reduced pressure and the product was purified by column chromatography (neutral alumina) using 30% ethyl acetate in hexane.

Yellow solid (0.26 g, 50% yield). ^{1}H NMR (600 MHz, $CDCl_3$, δ ppm) δ 8.88 (d, J = 8.6 Hz, 2H), 8.30 (d, J = 7.7 Hz, 1H), 8.17 (d, J = 8.0 Hz, 2H), 8.07 (d, J = 8.1 Hz, 1H), 7.89 (d, J = 8.6 Hz, 2H), 7.70 (d, J = 1.5 Hz, 2H), 7.61 (d, J = 8.7 Hz, 6H), 7.55 (d, J = 8.1 Hz, 2H), 7.00 (d, J = 8.7 Hz, 4H), 3.86 (s, 6H). ^{13}C NMR (151 MHz, $CDCl_3$) δ 184.14, 167.52, 159.78, 151.80, 143.50, 141.25, 139.38, 136.45, 134.24, 133.38, 128.57, 127.85, 127.14, 126.56, 125.80, 123.10, 122.29, 120.64, 120.25, 119.56, 114.27, 107.06, 77.25, 77.04, 76.83, 55.41.

HRMS (ESI) peaks of m/z value was calculated for C40H28N2O3S is 617.1899 and observed 617.1890, [M+1] +.

7.2.2.5. Synthesis of benzo[d]thiazol-2-yl(4-(2,7-di(pyridin-4-yl)-9H-carbazol-9-yl)phenyl)methanone [BTMCzPy2]

The compound BTM-DB-CZ (0.50 g, 0.88 mmol), pyridin-4-ylboronic acid (0.28 g, 2.2 mmol) and tetrakis-(triphenylphosphine)palladium(0) (0.3 mmol) were taken in a 50 mL round bottom flask and it was degassed for 30 minutes. Then the solid compounds were dissolved in 15 mL THF and degassed for 10 min. 5 mL of 2.0 M potassium carbonate solution was added and the mixture was stirred at 85 °C under argon atmosphere. The

progress of the reaction was monitored by analytical TLC. After 12 h, the reaction mixture was cooled down to room temperature and 50 mL water was added. The crude product was extracted with ethyl acetate and the organic layer was dried over anhydrous sodium sulfate. The solvent was evaporated under reduced pressure and the product was purified by column chromatography (neutral alumina) using 30% ethyl acetate in hexane.

Yellow solid (0.26 g, 50% yield). ^{1}H NMR (400 MHz, DMSO-d_6, δ ppm) δ 8.89 (d, J = 8.6 Hz, 2H), 8.68 (d, J = 4.8 Hz, 4H), 8.54 (d, J = 8.2 Hz, 2H), 8.38 (dt, J = 7.2, 3.7 Hz, 2H), 8.18 (d, J = 8.6 Hz, 2H), 7.94 (s, 2H), 7.85 (d, J = 6.3 Hz, 6H), 7.76 – 7.72 (m, 2H). ^{13}C NMR (151 MHz, DMSO-d_6)) δ 184.09, 166.85, 153.85, 150.16, 148.76, 142.13, 141.49, 137.09, 137.03, 134.08, 133.58, 132.75, 132.14, 132.07, 131.99, 131.98, 128.57, 128.49, 128.00, 127.26, 126.69, 125.76, 123.98, 122.34, 122.06, 121.48, 120.29, 108.55.

HRMS (ESI) peaks of m/z value was calculated for $C_{36}H_{22}N_4OS$ is 558.1514, Found 559.2857, $[M+1]^+$.

7.2.3. Measurements and Methods

7.2.3.1. Structural Characterization

All the reactions were carried out in oven dried (~100 °C) round bottom flasks under argon atmosphere unless otherwise mentioned. The ^{1}H and ^{13}C NMR spectra were recorded by using deuterated solvents (CDCl3) in Bruker 600 MHz NMR spectrometer. Chemical shifts (δ) are expressed relative to the resonances of the residual non-deuterated solvent for 1H [$CDCl_3$ & DMSO-d_6: ^{1}H (δ) = 7.26 ppm & 2.50 ppm], and ^{13}C [CDCl3 & DMSO-d6: ^{13}C(δ) = 77.0 ppm & 39.52 ppm]. Absolute values of the coupling constants are given in Hertz (Hz), regardless of their sign. Multiplicities are abbreviated as singlet (s), doublet (d), doublet of doublets (dd), triplet (t), multiplet (m), and broad (br).

7.2.3.2. Optical Characterization

The fluorescence and absorption spectra were measured with PerkinElmer, Model Lambda-25 spectrometer and Horiba-Fluoromax4 with Varian Cary Eclipse spectrometer respectively. The absolute quantum yields were measured by using the Horiba Fluoromax (Jobin Yvon equipped with Integrating sphere) absolute quantum yield spectrometer. The time-resolved fluorescence lifetimes were investigated with the time-resolved fluorescence studies were performed using an Edinburgh Life Spec II instrument. Temperature-dependent (77K-300K) PL and lifetime measurements were carried out using a liquid

nitrogen-cooled optical cryostat (Optistat, Oxford Instruments) attached to an Edinburgh FLS-1000 instrument.

7.2.3.3. Morphology Visualization

The morphology and crystallinity of the synthesized BTMCzBr2, BTMCzCN2, BTMCzOMe2 and BTMCzPy2 were examined by scanning electron microscopy (FESEM) (Zeiss, Model: Sigma-300) water drop casted samples, on which gold-sputtered under vacuum to achieve a thin layer of conductive gold coating on the micro/nano crystalline samples. Atomic force microscopy (AFM) analysis were performed drop-casted sample over silicon substrate, in AFM, Asylum Cypher, Oxford Instruments. Transmission electron microscopy (TEM, JEOL JEM-2100F). Dynamic light scattering (DLS) measurements were taken with a Zetasizer Nano ZS90 (model no ZEN3690)

7.2.3.4. Single-crystal X-ray Diffraction (XRD) data

Single-crystal structures of BTMCzCN2, BTMCzOMe2 and BTMCzPy2 were obtained on X-ray diffractometer on Agilent. The single crystal x-ray diffractometer (SC-XRD) is equipped with Mo X-ray source (Mova), CCD detector (Eos), Oxford cryo system (80-500K) and crystal AlisPRO software and Autochem softwares. SCXRD data were collected at 293 K. All the crystal structures were solved by SHELXT with direct methods. All of the non-hydrogen atoms were located by SHELXT directly and refined anisotropically by SHELXL2018 with least squares methods The revised data have been deposited with the CCDC (accession codes 2202461 for BTMCzCN2, 2202462 for BTMCzOMe2, and 1974995 for BTMCzPy2. The stacking structure and intermolecular interactions of the BTMCZ, BTMPTZ and BTMPXZ were analyzed via Murcury and Materials Studio software. The powder X-ray diffraction measurements of the powder and thin films were performed using a Rigaku SmartLab X-ray diffractometer where copper Kα (λ = 1.54 Å) was used as the source with 9 kW power. The XRD patterns for the 2θ range of 5°−50° were measured at the scan rate 0.3°/s.

7.2.3.5. Computational Studies

Vertical and transitions energies with the highest occupied molecular orbital (HOMO), lowest unoccupied molecular orbital (LUMO), of single-component crystals were calculated by density functional theory (DFT). All DFT and TDDFT calculations in this study were performed by employing the combination of Becke3-Lee-Yang-Parr (B3LYP) hybrid functional and 6-31G(d,p) basis set using the Gaussian 16 package.[2,3] The calculated structures, energy level very much close to experimental results.

7.2.3.6. Cell viability Assay

The effect of BTMCzBr2, BTMCzCN2**,** BTMCzOMe2 and BTMCzPy2 on cell viability was studied on human embryonic kidney (HEK, non-cancerous), human keratinocyte line (HACAT) and MDA-MB-231, MCF7 (breast cancer cells). For this, cells were seeded on 96 well plates at the density of 6000 cells per well. Plates were incubated in CO_2 incubator overnight for cell attachment. Following this, cells were treated with BTMCzBr2, BTMCzCN2**,** BTMCzOMe2 and BTMCzPy2 at various concentrations. After 24 hours of treatment, MTT dye was added to individual wells (5µL, 5mg/mL in PBS), and plates were incubated for 2 h. In the end, to measure the absorbance from MTT dye, 150 µL DMSO solution was added to each well, and absorbance was recorded at 470 nm.

7.2.3.7. Long-term Cellular Imaging

To evaluate the long-term imaging efficiency of BTMCzBr2, BTMCzCN2**,** BTMCzOMe2 and BTMCzPy2 inside the cellular environment, MCF-7 cells were seeded on 96 well plates at the density of 6000 cells per well cells/well. Following the attachment, cells were treated with 10 µm of of BTMCzBr2, BTMCzCN2**,** BTMCzOMe2 and BTMCzPy2at one time and incubated for 6 h. Cells were washed with PBS and nearly 30% of the cells were further subcultured in the growth medium, whereas the rest of the cells were employed for CLSM imaging. Accordingly, the process was repeated and the CLSM images were recorded. To compare the fluorescence intensity, imaging of the one-time treated cells was carried out at 6 h, 24 h, 48 h, and 72 h. Cells at these time points were washed with PBS, fixed with 4% formaldehyde and images were taken in a confocal microscope using 405 nm laser as an excitation source. The protocol to evaluate the long-term imaging potential of the probes has been schematically presented in Figure 7.12.

7.3. Results and Discussion

7.3.1. Materials Design Strategy

By considering important aspects of triplet-harvesting emitters, our design molecule possess a common carbazole (Cz) donor and new benzo [d] thiazol-2-yl) methanone (BTM) as an acceptor, while the carbazole donor is ornamented by a set of electron-withdrawing segments (EWS) e.g. bromine / p-benzonitrile moiety and electron-donating segments (EDS) e.g. 4-methoxy phenyl/4-pyridyl group respectively. Unlike, widely explored traditional Tetraphenylethylene (TPE) and its derivatives-based AIEgens have been reported so far,[33] we report a novel design for achieving simultaneous AIE and

HLCT/TADF, respectively. Moreover, a multi-step reactions were carried out to synthesize the target compounds viz. BTMCzBr2, BTmCzCN2, BTMCzOMe2 and BTMCzPy2 (Scheme 7.1). Firstly benzothiazol-2-yl (4-fluorophenyl) methanone [BTM-F] was synthesized via in-situ cross-coupling reaction using 1-(4-fluorophenyl) ethanone and benzothiazole (Figure 7.1ai).[34] Then, benzothiazol-2-yl (4-(2,7-dibromo-9H-carbazol-9yl) phenyl) methanone [BTMCzBr2] was synthesized *via* simple base substitution reaction using benzo[d]thiazol-2-yl (4-fluorophenyl) methanone and 2,7 dibromocarbazole (Figure 7.1aii). Whereas, the final compounds, 4,4'-(9-(4-(benzo[d]thiazole-2-carbonyl) phenyl)-9H-carbazole-2,7-diyl) dibenzonitrile [BTMCzCN2], benzo[d]thiazol-2-yl (4-(2,7-bis (4-methoxyphenyl)-9H-carbazol-9-yl) phenyl) methanone [BTMCzOMe2] and benzo[d]thiazol-2-yl (4-(2,7-di(pyridin-4-yl)-9H-carbazol-9-yl)phenyl) methanone [BTMCzPy2] were synthesized with a good yield (~70%) via Suzuki coupling reactions (Figure 7.aiii). Synthesized compounds were well characterized by NMR (^{1}H and ^{13}C), HRMS, and from SC-XRD structures, respectively (Figure A7.1-A7.15). By incorporating structurally different EWS and EDS into donor units, the resultant emitters showed color-tunable emissions and AIE-TADF in various state. From their experimental and computational studies, it was observed that the introduction of EWS in BTMCzBr2 and BTMMCzCN2, electrons density of central cores were extracted thereby weakening the CT feature and locally excited state is dominated with a new feature of HLCT characteristics via a second-order coupling process as shown in Figure 7.1b. Whereas, in BTMCZOMe2 and BTMCzPy2, the EDS pushed the electron densities towards the central core thereby, CT is highly intensified to exhibit efficient TADF (Figure 7.1c). With these, the development of triplet-harvesting purely organic molecules with AIE, HLCT and TADF features in the pursuit of a structural engineering and singlet-triplet custom control on exciton dynamics resulting improved photophysical properties, good biocompatibility and bright imaging.

7.3.2. Characterization of Triplet Harvesting Behavior of BTMCzR2

To decipher the intrinsic photophysical properties in the solid-state of the afforded chromophores, absorption, fluorescence and fluorescence lifetimes were recorded in the thin film. In the absorption spectra, a high and low-energy absorption band was observed centered at 305 and 360 nm for BTMCzBr2, 330 and 380 nm for BTMCzOMe2, 323 and 390 nm for BTMCzPy2 which is assigned as π-π* and intramolecular charge-transfer (ICT) peak. Whereas BTMCzCN2 exhibited one absorption band at 335 nm. In the fluorescence

spectra, a gradual bathochromic shift was observed from sky-blue to green emission by considering their respective excitation of CT absorption wavelength. BTMCzBr2, BTMCzCN2, BTMCzOMe2 and BTMCzPy2 showed emissions near λmax = 468, 480, 530 and 490 nm, respectively. Whereas, 77K phosphorescence spectra displayed the corresponding λ_{max} at 527, 555, 540, and 520 nm, respectively (Figure 7.2a-d). Moreover, the first two EWS-containing compounds showed a larger shift in their respective fluorescence and phosphorescence spectra than the latter two EDS-containing spectra, depicting different excited state dynamical properties in presence of EWS and EDS. Further, to investigate the up-converted luminescence properties energy gap between singlet and triplet (ΔE_{ST}) values was calculated from the onset of the room temperature fluorescence and low temperature (77K) phosphorescence spectra using thin films of all the emitters. The ΔE_{ST} values were found to be 0.14, 0.40, 0.09 and 0.04 eV for BTMCzBr2, BTMCzCN2, BTMCzOMe2 and BTMCzPy2, respectively. Further, transient PL spectra were recorded to verify delayed emission characteristics under air and vacuum in dry toluene solution.

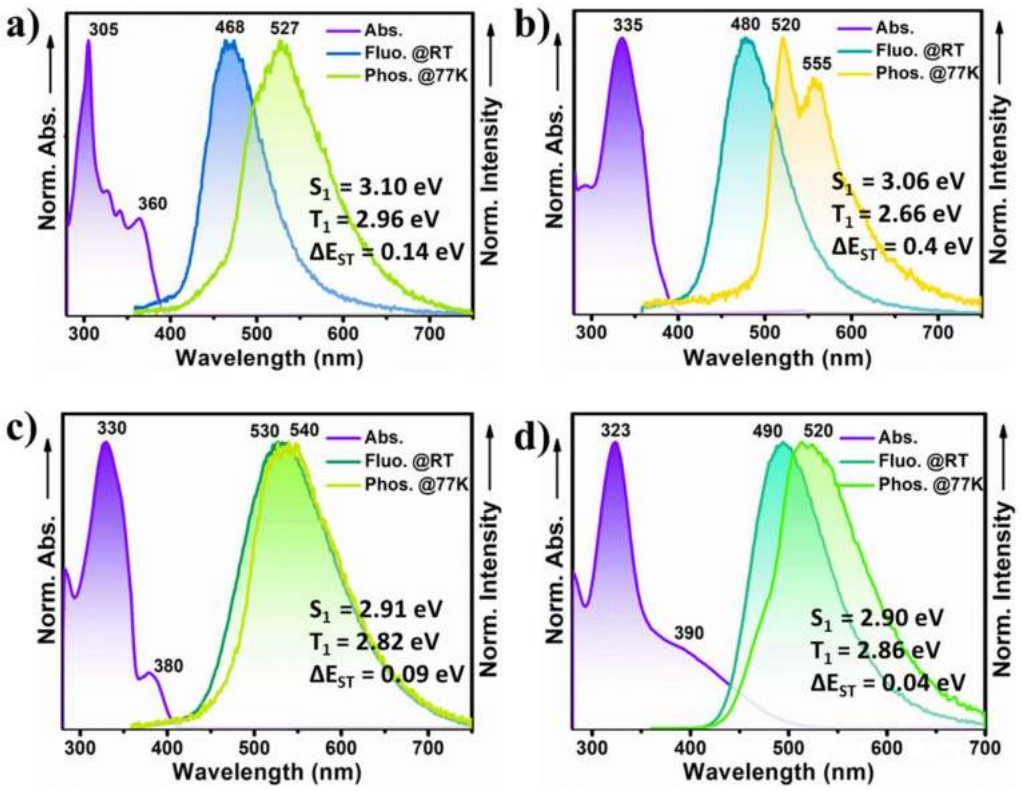

Figure 7.2. (a-d) Absorption, fluorescence (Fluo.) at room temperature (RT) and phosphorescence (Phos.) at 77K temperature; inset ΔE_{ST} calculated from the onset of fluorescence and phosphorescence spectra of BTMCzBr2, BTMCzCN2, BTMCzOMe2 and BTMCzPy2 respectively.

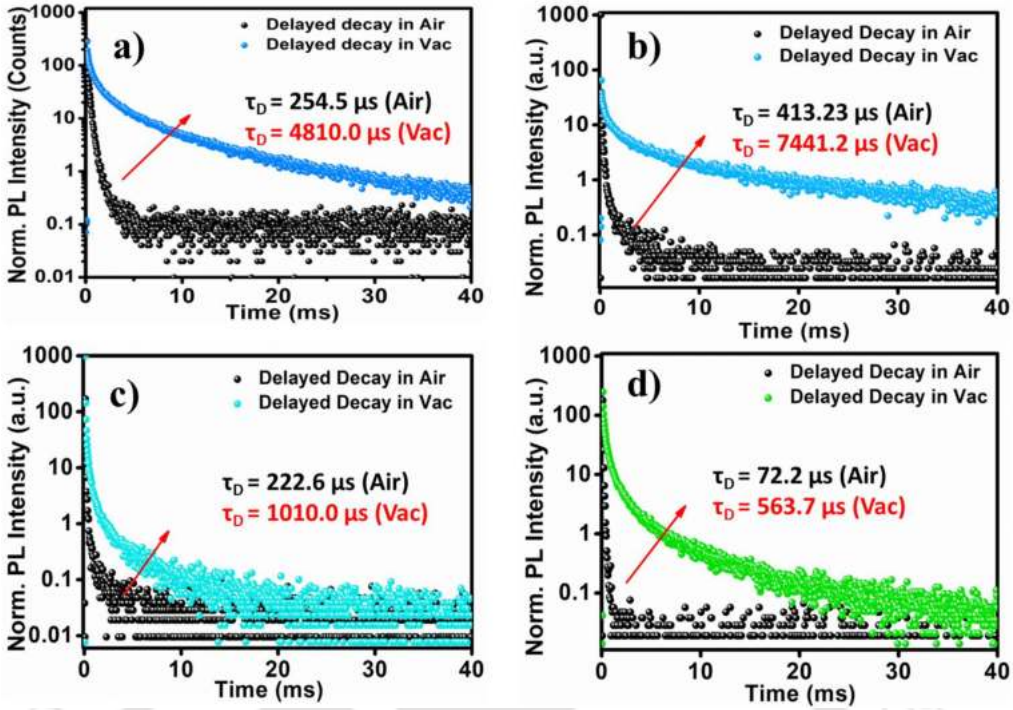

Figure 7.3. (a-d) TRPL delayed decay profile under air and vacuum for BTMCzBr2, BTMCzCN2, BTMCzOMe2 and BTMCzPy2 respectively.

TRPL curve showed a biexponetial decay curve and composed of prompt and delayed components while prompt fluorescence decay corresponds to S_1 to S_0 transition with the lifetime values of 4.02 ns (vacuum) and 2.00 ns (air) for BTMCzBr2, 3.80 ns (vacuum) and 2.41 ns (air) for BTMCzCN2, 11.37 ns (vacuum), 10.91 ns (air) for BTMCzOMe2 and 3.74 ns (vacuum), 3.31 ns (air) for BTMCzPy2 respectively (Figure A7.16). For delayed components, all the emitters exhibited significantly increased delayed lifetime in the vacuum than air, average lifetime values of 4810.0 µs (vacuum) to 254.5 µs (air) for BTMCzBr2, 7441.2 µs (vacuum) to 413.23 µs (air) for BTMCzCN2, 1010 µs (vacuum) to 222.6 µs (air) for BTMCzOMe2, 563.7 µs (vacuum) to 72.2 µs (air) for BTMCzPy2, respectively (Figure 7.3a-d).

These, large enhancements of delayed lifetime can be rationalized as thermally up-converted delayed emission of T_1/T_m to S_1 followed by an additional fluorescence. All the emitters exhibited improved PLQYs values of 7.3%, 22.3%, 25.0% and 24.6%, in oxygen-free atmosphere at room temperature for BTMCzBr2, BTMCzCN2, BTMCzOMe2 and BTMCzPy2, whereas in the presence of oxygen the values are decreased to 1.7%, 5.3%, 14% and 9.6% respectively. Therefore, in oxygenic condition, the decrease in PLQY and increase in lifetime signify the presence of a delayed component of the integrated emitters.

Moreover, the high PLQY value and relatively short delayed lifetime for BTMCzOMe2 and BTMCzPy2 are due to the smaller $\Delta E_{ST,}$ which substantially accelerates fast RISC. Moreover, the presence of EDS on carbazole donor leads to strong CT interactions and therefore promises to be an efficient TADF emitter. On the contrary, the lower PLQY and higher delayed lifetime of BTMCzBr2 and BTMCzCN2 is due to the larger $\Delta E_{ST,}$ further restricting RISC process. While the presence of EWS on donor Cz weakens CT interactions and another intermediary LE state, resulting in HLCT emission. The radiative (k_r) and non-radiative (k_{nr}) decays constants were calculated from their respective delayed lifetime and PLQY values, using the formula $k_r = \phi/\tau$ and $k_{nr} = 1\text{-}\phi/\tau$ for all the emitters. Therefore, K_r are calculated to be 1.746 x 10^{-4} μs^{-1}, 0.31 x 10^{-4} µs, 2.47 x 10^{-4} µs, and 4.36 x 10^{-4} µs while K_{nr} values are 0.646 x10^{-4} µs, 1.04 x10^{-4} µs, 7.42 x10^{-4} µs and and 13.37 x 10^{-4} µs for BTMCzBr2, BTMCzCN2, BTMCzOMe2 and BTMCZPy2, respectively. Further, to confirm the TADF and/or HLCT characteristics, temperature-dependent transient PL measurements were performed using a streak camera for the thin film at different elevated temperatures of 100K, 200K and 300K, respectively (Figure 7.4a-d). The gradual increment of intense prompt decay and long tail delayed decay was observed for all the emitters confirming that thermal energy accelerates the RISC process.

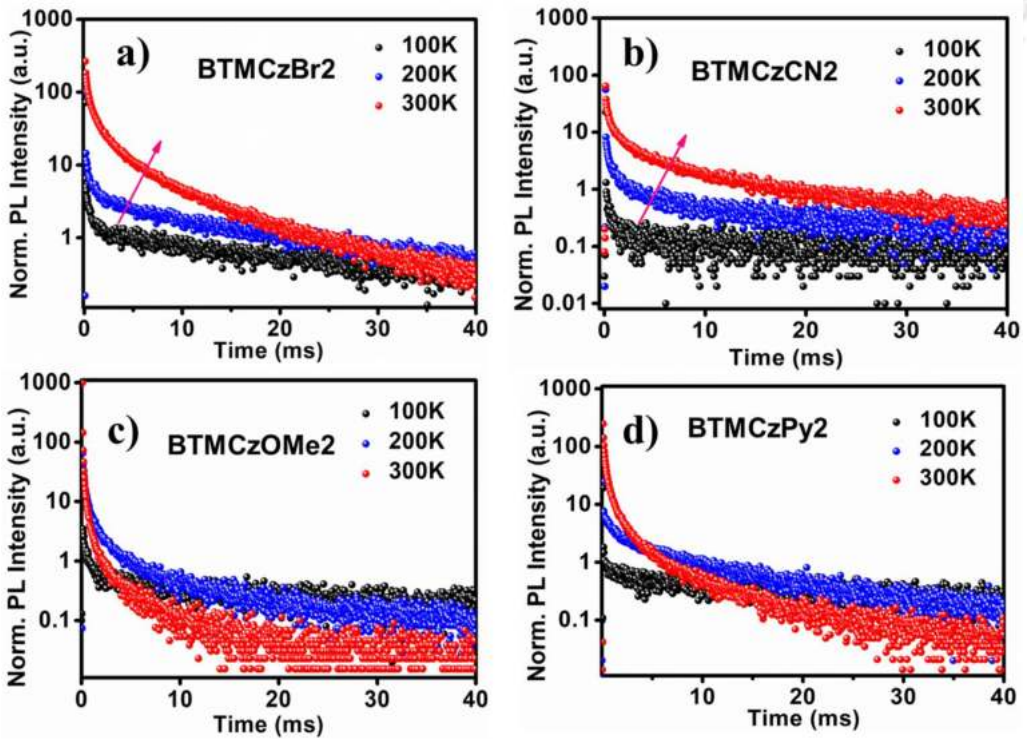

Figure 7.4. (a-d) Transient PL decay profile under temperature gradient of 100 K, 200K and 300K for For BTMCzBr2, BTMCzCN2, BTMCzOMe2 and BTMCzPy2 respectively.

Notably, the delayed component gradually increases with rising temperatures from 100K to 300K for BTMCzBr2 and BTMCzCN2. However, the delayed component for BTMCzOMe2 and BTMCzPy2 showed a higher up-conversion decay curve up to 200K and intensity reduced at 300K, due to the higher non-radiative decays at very high temperature.[35] Moreover, longer delayed emission in the solid state due the dense packing may restrained the triplet quenching from air which further implied that this long-lived emission could be beneficial to use even in oxygen containing biological environment.

7.3.3. Computational Calculations

Different types of Intrinsic DF emissions were computed using quantum-mechanical calculations for BTMCzBr2 BTMCzCN2, BTMCzOMe2 and BTMCzPy2 from their optimized single-crystal structure geometry using Gaussian 16 program.[36] Time-dependent density functional theory (TD-DFT) were employed at B3LYP/6-31G (d,p) level up to the 10th states at their different spin multiplicities. Vertical transition of TD-DFT results showed a similar well-separated electronic distribution for all the four cases, where, the highest occupied molecular orbital (HOMO) located at donors (CZ) and lowest unoccupied molecular orbital (LUMO) centred at acceptor (BTM) cores, respectively. The HOMO and LUMO values were found to be -5.85, -5.91, -5.15, -5.63 eV and -2.53, -2.67, -2.41, -2.50 eV for BTMCzBr2 BTMCzCN2, BTMCzOMe2 and BTMCzPy2 respectively depicting their adjustable band gaps and CT behaviour respectively (Figure 7.5a-d).

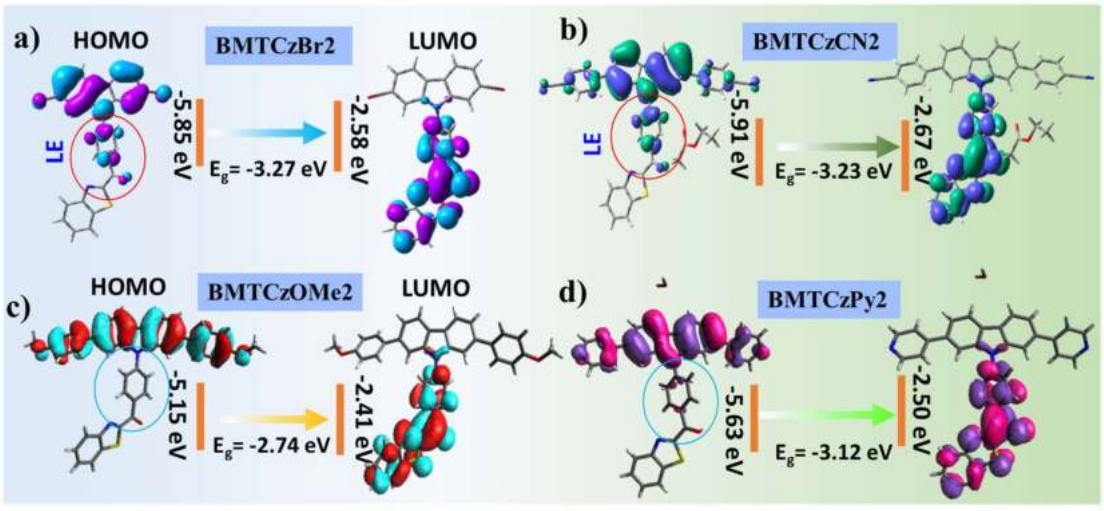

Figure 7.5. (a-d) Frontier molecular orbital (FMO) and electronic distribution in HOMO-LUMO and band gap profile for BTMCzBr2, BTMCzCN2, BTMCzOMe2, BTMCzPy2, respectively.

To further understand the dynamical mechanisms of TADF molecules, it is important to investigate the nature of each singlets/triplets energy state and favourable excited state dynamics. In particular some of the nearly orthogonal donor–acceptor (D–A) and donor-acceptor-donor (D–A–D) type structures exhibited strong coupling between singlet charge-transfer (^{1}CT) and triplet charge transfer state (^{3}CT) along with an intermediary nearest local triplet (^{3}LE) state, thus inducing the second-order SOC.[37] Nonetheless, a variable energy gap (ΔE_{ST}) between lowest excited singlet (S_1 = ^{1}HLCT, ^{1}CT) and triplet (T_1= ^{3}HLCT, ^{3}CT) was found to be 0.24, 0.27, 0.03 and 0.20 eV for BTMCzBr2 BTMCzCN2, BTMCzOMe2 and BTMCzPy2, respectively. Notably, for BTMCzBr2 and BTMCzCN2 the $\Delta E_{S1\text{-}T1}$ is relatively higher in value due to a larger overlap between HOMO and LUMO in the central phenyl ring; therefore, an intermediate ^{3}LE and/or ^{3}HLCT state closest to ^{1}CT/^{1}HLCT state ($\Delta E_{S1\text{-}T2}$= 0.01 and 0.1 eV) participating in the RISC process, leading to HLCT property of these emitters (Figure 7.6a-d). Whereas, in the case of BTMCzOMe2 and BTMCzPy2 the closest states (S_1, T_1, T_2) have pure CT character and contribute to efficient RISC and therefore exhibit TADF behaviour. Moreover, natural transition orbital (NTO) calculations for all four emitters confirmed the character of independent states (Figure A7.17-A7.20). Remarkably, these ΔE_{ST} values are very much consistent with the experimental values.

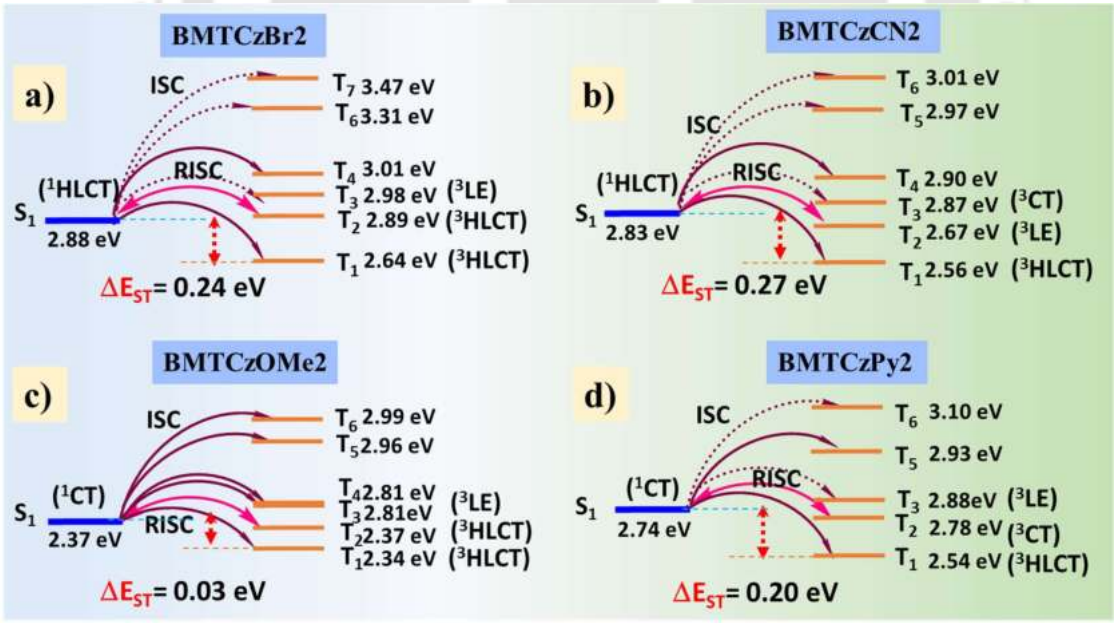

Figure 7.6. (a-d) Emission energy levels, ΔE_{ST} values and active ISC channels in the different spin-multiplicities for BTMCzBr2, BTMCzCN2, BTMCzOMe2, BTMCzPy2, respectively.

Besides, major possible ISC manifold channels were also investigated by sequential higher excited singlets and triplets related to the ground state. Thus, by changing the different substituents groups we could finely modulate their characteristics dynamic excited states. EWS contained emitters showed deeper HOMO and LUMO levels, including large spatial overlap and large energy gap, while EDS demonstrated to be shallower HOMO and LUMO with minimal overlap, corroborating a narrower energy gap respectively. These results reveal that different withdrawing and donating effect plays an important role in yielding high variable CT interaction and DF in the solid state.To reveal the impact of rigid packing and electronic environment induced optical properties of the emitters, a reduced density gradient (RDG) analysis was also performed.[38] As shown in Figure 7.7a-d, the surfaces are colored on a blue-green-red scale based on values of sign(λ_2)ρ, ranging the iso-surface value from 0.05 and 0.05. Figure 7.7e-h Blue and red color in the RDG scatter plots represented as strong attractive interaction and intense non-bonded overlaps between neighbouring heteroaromatic rings. All the emitters experienced strong interaction via multiple heteroatoms which could effectively restrict the intramolecular vibrations and prevent energy loss of the excited molecules, revealing DF susceptibility.[39]

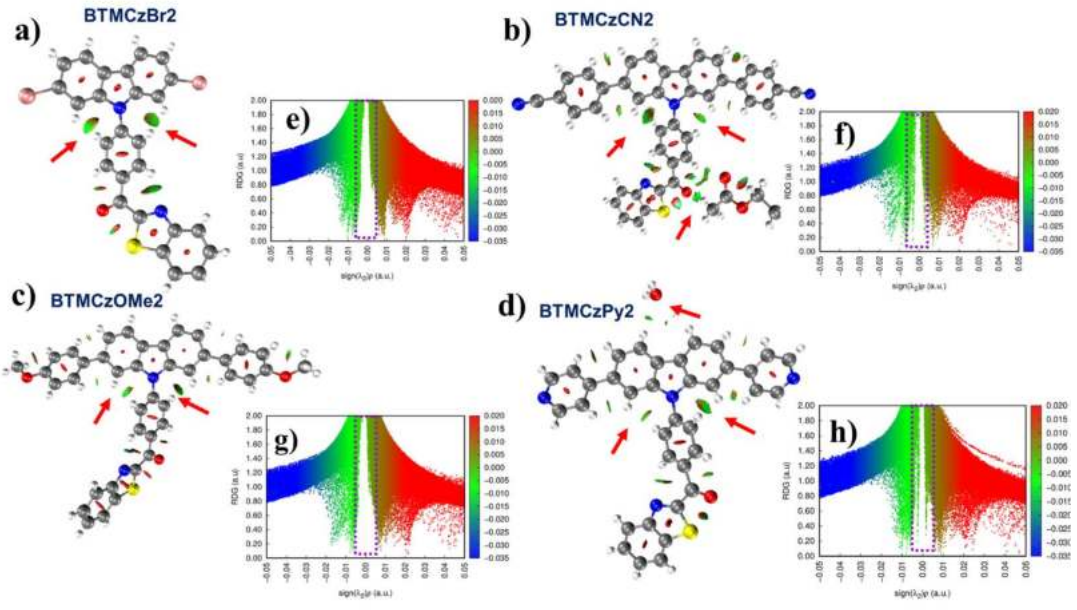

Figure 7.7: (a-d) The functions of the reduced density gradient (RDG) and sign (λ_2)ρ isosurface map with an isovalue of 0.5 and their corresponding RDG scatter plot (e-h) as a function of sign(λ_2)ρ for BTMCzBr2, BTMCzCN2, BTMCzOMe2, BTMCzPy2, respectively.

Table 7.1: Summary of photophysical and electronic properties for BTMCzBr2, BTMCzCN2, BTMCzOMe2 and BTMCzPy2, respectively.

Emitter	HOMO (eV)	LUMO (eV)	E_g /eV	Theo. ΔE_{ST} (eV)	Exp. ΔE_{ST} (eV)	λ_{max}, abs (nm)	λ_{max}, PL (nm)	λ_{max}, Phos (nm)	τ_P (ns) Air	τ_P (ns) Vac	τ_D (µs) Air	τ_D (µs) Vac	Φ_{Air} [%]	Φ_{N2} [%]	K_r ($x10^{-4}$, µs-1)	K_{nr} ($x10^{-4}$, µs-1)
BTMCzBr2	-5.85	-2.58	3.27	0.24	0.14	305, 360	468	527	2.00	4.02	254.50	4180.00	1.7	7.3	1.746	0.646
BTMCzCN2	-5.91	-2.67	3.24	0.27	0.40	335	480	520, 555	2.41	3.80	413.23	7441.2	5.3	22.3	0.31	1.04
BTMCzOMe2	-5.15	-2.50	2.74	0.03	0.09	330, 380	530	540	10.91	11.37	222.59	1010.00	14.0	25.0	2.47	7.42
BTMCzPy2	-5.63	-2.41	3.12	0.20	0.04	323, 390	490	520	3.31	3.74	72.19	563.70	9.6	24.6	4.36	13.37

Radiative and non-radiative decay rate [$^a k_r = \phi/\tau$, $^b k_{nr} = (1-\phi)/\tau$] calculated from fluorescence QY and delayed lifetime in water at RT.

7.3.4. Condensed State Optical Properties and Nano Morphology

The ground and excited state photophysical properties in solution and aggregated state were investigated using a constant sample concentration (5mM). Aggregation-induced emission behaviour was also analysed by UV-Vis absorption and fluorescence emission spectra using a good solvent (DMF) and a poor solvent (water) and different DMF/water fractions (0-99%) for BTMCzBR2, BTMCzCN2, BTMCzOMe2 and BTMCzPy2 respectively. All the compounds exhibited ~20 nm red-shifted absorption in aggregated state as compared to the solution state (in DMF). Unlike, BTMCzCN2, which exhibited lowest-energy CT absorption band at 360 nm, the other three compounds exhibited two absorption bands near 315 and 400 nm for BTMCzBr2, 345 and 420 nm for BTMCzOMe2, 333 and 420 for BTMCzPY2, was assigned to that of the π-π*and CT peak, the CT absorption mainly associated with intramolecular charge transfer (ICT) from the Cz moieties to the BTM core (Figure A7.21a-d). Correspondingly, in the fluorescence spectra, unlike BTMCzBr2 all other probes showed significant red-shift with enhanced emission intensity with increasing water fraction, deciphering prominent AIE-phenomenone[40] (Figure 7.8a-d). For BTMCzBr2 the LE state emission (410 nm) dominated over weak CT emission (580 nm), including a HLCT peak that appeared at 490 nm. In the case of BTMCzCN2 showed weak LE (410 nm) and CT (570 nm) while the highest intensity was found at 70% Wf which composed of HLCT character at 490 nm. The complete separation of LE (420 nm) and CT emission (540 nm) from solution to aggregated state was obtained for BTMCzOMe2. Notably, a prominent CT emission (530 nm) at 80% Wf was observed for BTMCzPy2 only.

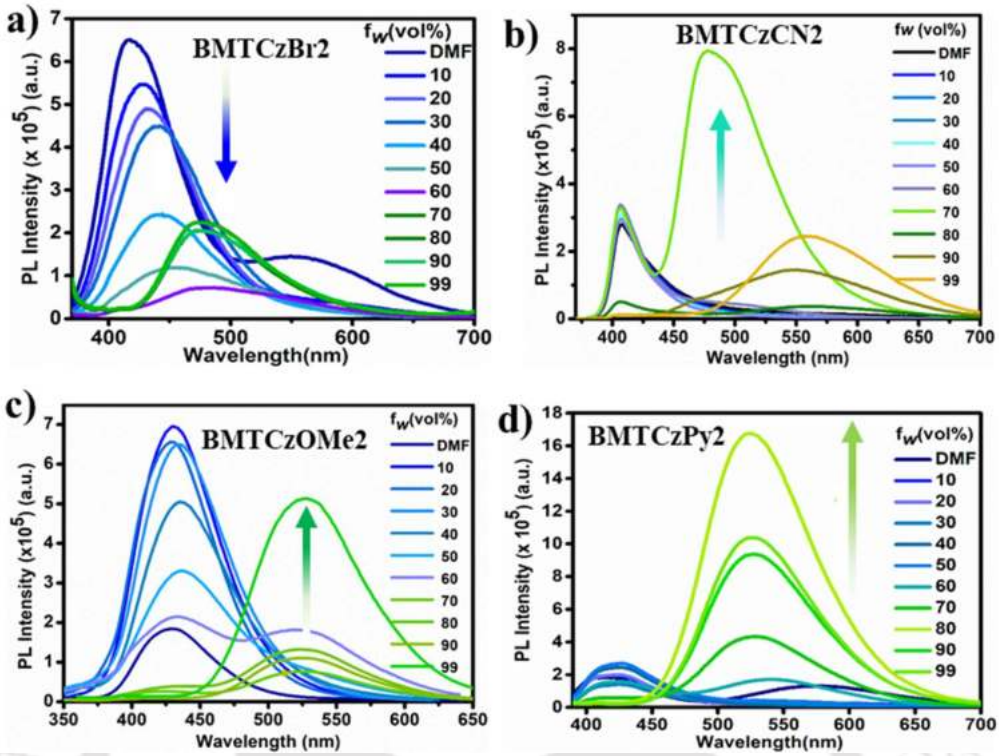

Figure 7.8. (a-d) AIE study: Fluorescence spectra at different DMF and water fractions (0-99%) at $5x10^{-5}$ M concentration. of BTMCzBr2, BTMCzCN2, BTMCzOMe2, BTMCzPy2, respectively.

The relative intensity plot demonstrated a clear understanding of the presence of both AIE, HLCT and TICT features in agreement with typical TADF compounds that have large Stokes shifts.These variable blue and red-shifted emissions are because of the dissimilar dipole-dipole interactions via the TICT effect between D-A probe and non-polar/polar solvents, depicting to ensued dynamical HLCT and TADF behaviour of the AIEgens.[41] Moreover, the directly attached bromine atom extensively extracts the electron density from the TADF core at the same time, it causes an excited state quenching effect; hence we could not see any emission in the aggregated state due to the heavy atom effect. Further, absorption studies were carried out using various polarity solvents such as hexane, toluene, chloroform, tetrahydrofuran, acetonitrile, dimethylformamide and dimethysulphoxide etc. The absorption spectra indicated the appearance of π-π* and CT absorption bands located at 300, and 380 nm for BTMCzBr2, only CT band at 340 nm for BTMCzCN2, 300 and 405 nm for BTMCzOMe2 whereas 325 and 385 nm for BTMCzPy2 respectively, (Figure A7.22a-d). However, no significant wavelength shift was noted by varying the different polarities of solvent, signifying a non-polarizable ground state.

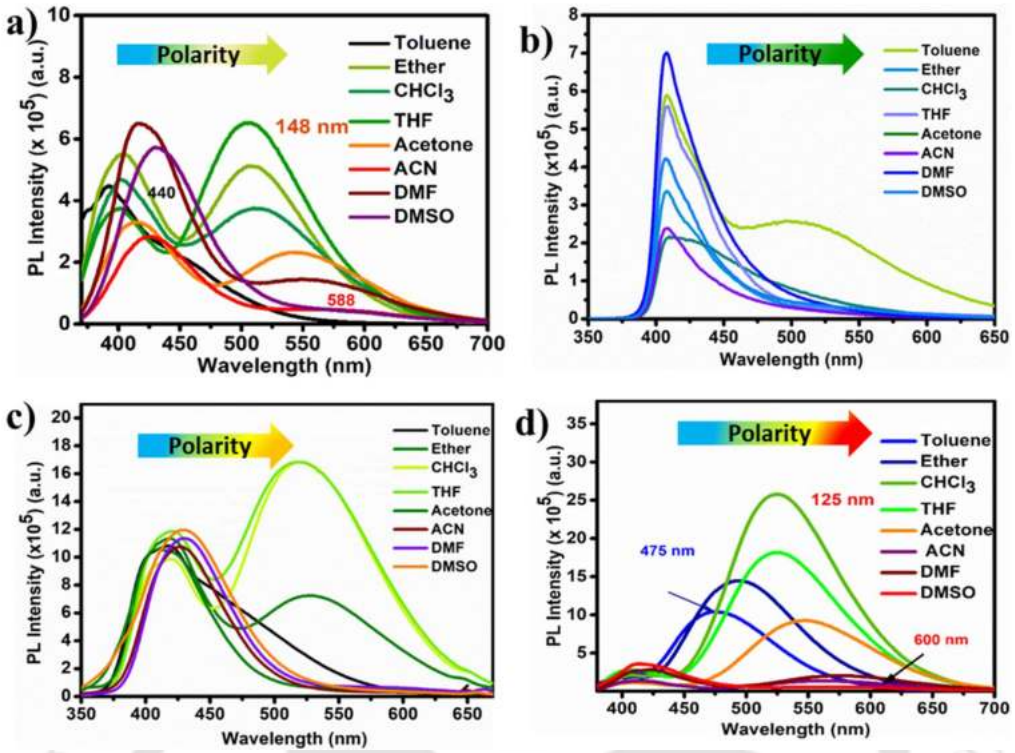

Figure 7.9. (a-d) Solvatochromism study: fluorescence spectra at different polarity solvents at constant sample comcentration of BTMCzBr2, BTMCzCN2, BTMCzOMe2, BTMCzPy2, respectively.

Whereas, fluorescence spectra displayed an obvious color-tunable bathochromic shift with increasing solvent polarity due to the strong CT effect, employing highly polar DMSO or ACN as the solvent led to emission quenching of the fluorophores (Figure 7.9a-d). Notably, variable locally excited (LE) and CT emission was observed by changing the EWS and EDS respectively. BTMCzCN2 and BTMCzPY2 exhibited prominent narrow LE and broad CT peak near 410 and 530 nm, while for BTMCzBr2 and BTMCzOMe2 a significant solvatochromism effect and a distinct LE to CT emission switching behaviour was noted with increasing solvent polarity. These results depicted the regulation of the LE and ICT characteristics could be a paradigm for the design of a turn-on type TADF probes.

Furthermore, morphological studies were performed to investigate nano aggregation properties of the AIE-TADF chromophores in the aggregated state. Low-magnification (scale bar: 200 nm) FESEM images (Figure 7.10a-d), low-magnification FETEM (scale bar: 500 nm and 1 μm) images (Figure 7.10e-h) and surface morphology by AFM images (Figure 7.10i-l) displayed nano-ribbon shaped nano aggregates for BTMCZBr2 and BTMCzCN2, whereas random and well-dispersed nano-range spherical morphology was observed for BTMCzOMe2 and BTMCzPy2 which confirms the aggregation in water

which could be a reason for AIE phenomenon. Notably, in the selected area (electron) diffraction (SEAD) images shown in the inset of FETEM images attributed to the amorphous nature of the former two AIEgens and nanocrystalline behaviour of the latter two AIEgens, respectively.

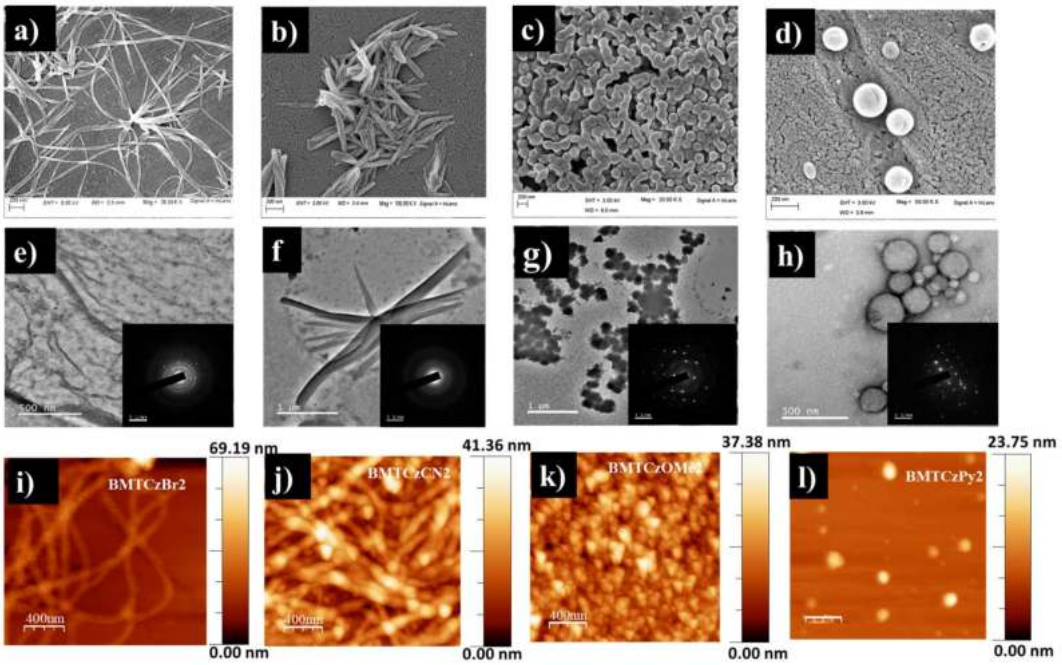

Figure 7.10. Microscopic images of self-assembly induced nano-aggregation: (a-d) FESEM images (Scale bar: 200 nm). (e-h) FETEM images (Scale bar: 500 nm and 1 µm; inset: SAED pattern). (i-l) AFM images (Scale bar: 400 nm) for BTMCzBr2, BTMCzCN2, BTMCzOMe2, BTMCzPy2, respectively.

7.3.5. Crystal Structure Analysis and Evolving Interactions

Single crystals of BTMCzCN2 (CCDC No: 2202461), BTMCzOMe2 (CCDC No: 2202462), and BTMCzPy2 (CCDC No: 1974995) were obtained *via* slow evaporation technique using ethylacetate/chloroform (2:8) solution respectively. The needle-shaped crystals of BTMCZCN2, BTMCzOMe2 and block-shaped crystal of BTMCzPy2 exhibited a similar monoclinic, crystal systems with P 21/c, P 21/n and C 2/c space group (crystal structure information summarized in Table A7.1). All the crystals structures are found to be highly non-planar due to their twisted dihedral angles for the pair of benzonitrile, anisole, and pyridine unit with respect to carbazole moiety are 33.42°/32.47°, 38.08°/39.81°, and 12.53°/35.37° respectively. A similar dihedral angle between the phenyl bridge and carbazole unit of 51.75°, 49.53° and 51.58° is observed for all three crystal structures, while a distinct dihedral angle of 11.10°, 0.36° and 155.09° between central phenyl ring and BTM unit is obtained for BTMCzCN2, BTMCzOMe2, and BTMCzPy2

respectively (Figure 7.11a, b, & c). Notably, in the crystal structures of BTMCzCN2, and BTMCzPy2 is stabilized by solvent molecules such as water and ethyl acetate, plays a vital role in molecular packing and optical properties. Ethylacetate stabilized the molecular packing in BTMCzCN2 crystal *via* multiple intermolecular hydrogen bonding interactions such as CH---O (2.417 Å, 2.502 Å, 2.614 Å) and CH---N (2.705 Å, 2.663 Å) with the BTMCzCN2. On the other hand, presence of water molecules in the BTMCzPy2 crystal hold a unique molecular assembly by hydrogen bonding (2.70 Å, 2.66 Å, and 1.87 Å) and forming a butterfly and penguin-like rigid structure. Conversely, no such solvent effect was observed in the case of BTMCZOMe2 crystal, moreover, several non-covalent intermolecular interactions like CH--π (2.807 Å, 2.735 Å), π - π (2.748 Å, 3.763 Å) and CH--CH (2.357 Å) assemble two adjacent molecules with head-to-head fashion to form ladder-like packing structure (Figure 7.11d, e, & f).

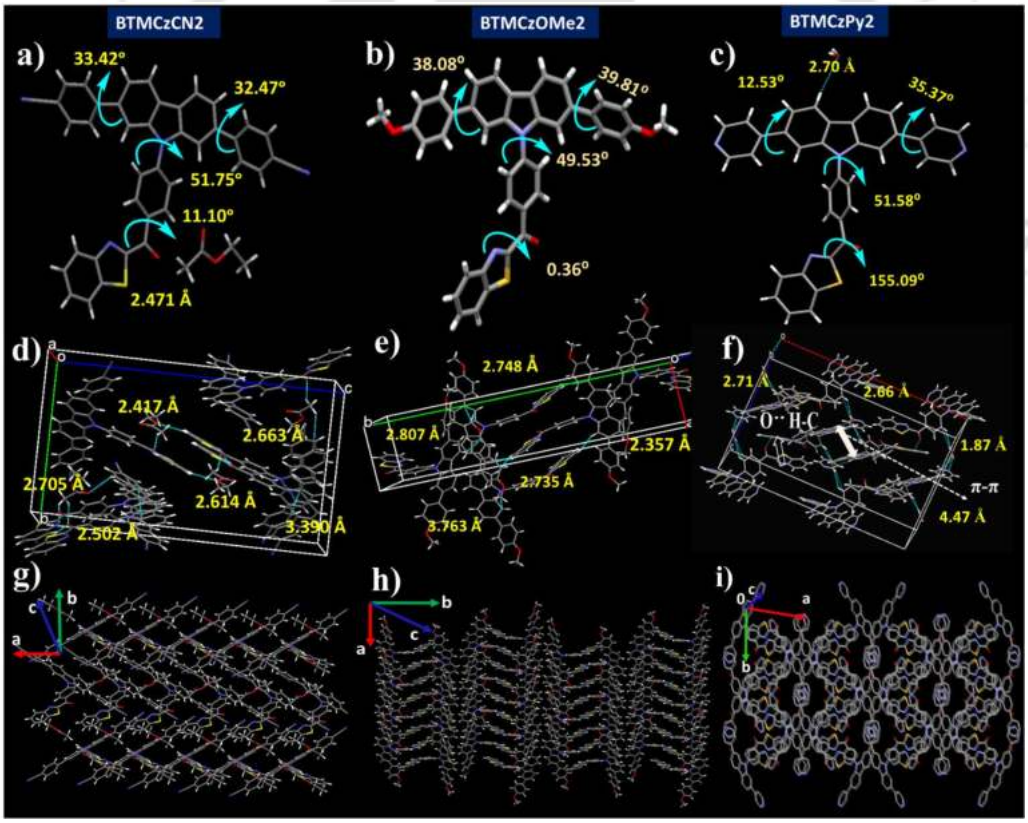

Figure 7.11. (a, b & c Single-crystal X-ray stuctures of BTMCzCN2, BTMCzOMe2 and BTMCzPy2 with their dihedral angles of each rotor units. (d, e & f) Unit cell packing structure and active non-covalent intermolecular interactions. (g, h & i) Varient supramolecular interaction induced crystal stucture packing; 3D-network, chair and butterfly like bulk crystals stucture packing along a axis in BTMCzCN2, BTMCzOMe2 and BTMCzPy2 respectively.

In the bulk crystals of BTMCzCN2 and BTMCzPy2 showed the head-to-head antiparallel and twisted packing wheareas BTMCzOme2 revealed the face-to-face parallel packing mode between the adjacent sets of molecules.Interestingly, all the crystals were found to be highly bright emissive due to the absence of obvious π-π stacking between the two stacking molecules and presence of weak hydrogen bonding in their respective multiple heteroatom containing crystals structures[42] (Figure 7.11g, h & i). Furthermore, non-covalent supramolecular intermolecular interactions induced tunable delayed emission were correlated with X-ray powder diffraction (XPRD) peaks. XPRD were recorded with the crystalline powder obtained from as-synthesized pristine compounds of BTMCzBr2, BTMCzCN2, BTMCzOMe2 and BTMCzPy2, respectively. Notably, XPRD peaks pattern is nearly matched with the simulated patterns obtained from SC- structures (Figure A7.23-A7.26). Moreover, appearance of multiple XRD peaks at low d-space region (2θ = 20-30°) depicted their numerous intermolecular interactions and unique aggregated packing motif. Therefore, intermolecular interaction as similar to other organic crystals can suppress the non-radiative decays and stabilize the triplet state for feasible RISC at room-temperature and thus DF lasting for tens of milliseconds.[43]

7.3.6. Cell Viability and Bio-imaging

By considering the excellent photophysical properties of all the four AIEgens with their large stock shift, long-lived emission, well-defined morphology, we further utilized the compounds for fluorescence imaging in living cells. The HACAT, MDAMB231, MCF-7 and HEK293 cells were treated with the BTMCZBr2, BTMCZPY2, BTMCZCN2, and BTMCZOMe2 at various concentrations (Figure 7.12a, b). The BTMCZBr2 and BTMCZPY2 show similar dose-response curve in all the four cell lines tested, without any significant dark toxicity (more than 90% cell viability). The BTMCZOMe2 showed slight decrease in cell viability at higher concentrations (30-75 μM). Additionally, the BTMCZCN2 cause reduction in viability in MDAMB231, MCF7, and HEK293 cells. All the four molecules shows no significant cell death in the range of 1 to 10 μM range, and thus were suitable candidate for for living cell imaging. For fluorescence microscopy imaging MCF-7 cells were incubated with BTMCZBr2, BTMCZPY2, BTMCZOMe2, and BTMCZCN2. As shown in Figure 7.12c, all the AIEgens show strong PL emission intensity from the MCF-7 cells, except BTMCZBr2 due to its low fluorescence quantum yield. However, the distribution of the AIEgens over the cell is completely distinct. In the case of BTMCZPY2, the molecule is homogeneously distributed all over the cell compared to the

other three molecules. The reason lies in the crystal structure as the water molecule plays a vital role in the crystal packing of BTMCZPY2, therefore due to its hydrophilic nature, it spread all over the cell uniformly.

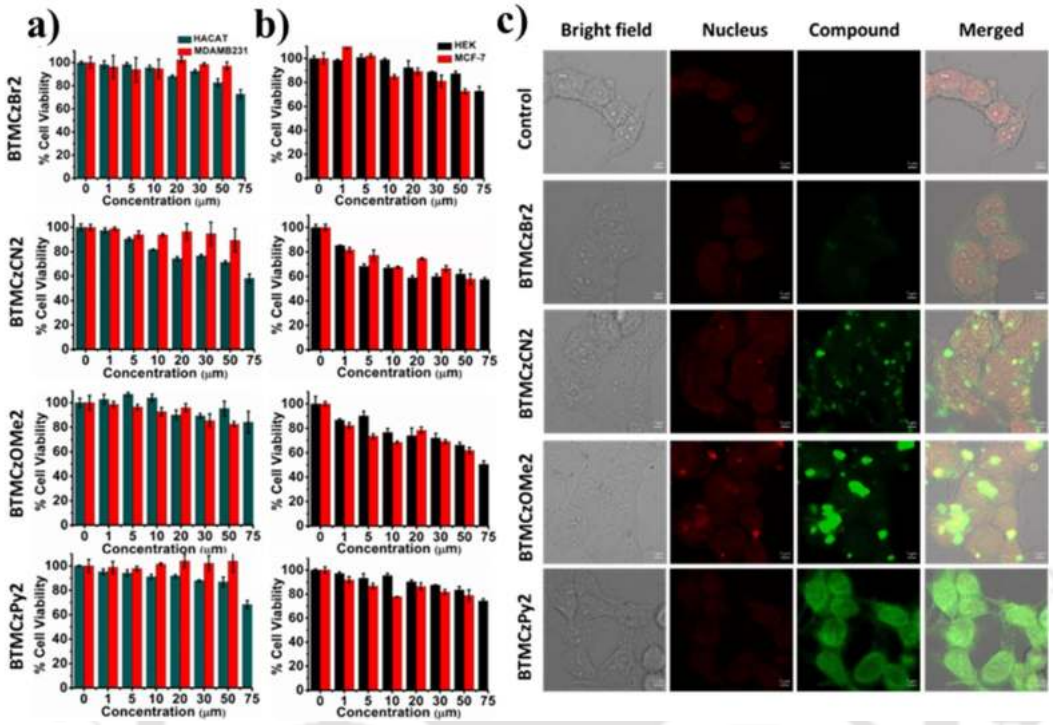

Figure 7.12. Cell viability of different AIEgens-treated with two sets of normal and cancer cells (a) HACAT and MDAMB231, (b) HEK cell and MCF-7 cells. (c) (a-d) Confocal images of MCF-7 cancer cells after incubation them with AIEgens (10 μg mL^{-1}) for 2 h; the fluorescence of the PSs was collected between 500 and 650 nm upon excitation at 405 nm; all the images share the same scale bar of 5 μm for BTMCzBr2, BTMCzCN2, BTMCzOMe2 and BTMCzPy2.

7.4. Conclusion

In summary, triplet-harvesting emitters possess a large structural diversity, emission adjustability, and low toxicity, therefore considered as potential for biological application. On this view, we have designed and synthesized four triplet harvestig luminogens namely BTMCZBr2, BTMCZCN2, BTMCZOMe2 and BTMCZPy2, deciphering their intrinsic structure-property functions and cell imaging application. The afforded molecules exhibited unique excited state charge transfer properties of HLCT and TADF respectively. Notably, unlike wellknown AIE- active tetraphenylene (TPE) core, a novel benzothiazole-methanone acceptor core has been explored with common donor carbazole moiety, displaying AIE behavior in condensed state. By introducing electron donating and withdrawing segments (EWS and EDS) in the carbazole donor, efficiently triggering the

pull-push electronic effects via LE and CT states, demonstrating a unique examples of long-lived luminescent organic materials. Interestingly, EWS substituted molecules BTMCzBr2 and BTMCzCN2 showed HLCT emission and long lifetime, while EDS contained molecules BTMCzOMe2 and BTMCzPy2 showed efficient TADF property and very high PLQY. Experimental studies and computational results revealed a clear understanding of the singlet-triplet excited state dynamics, appropriate structural modifications, controlled electronic effects, and supramolecular self-assembly which are important prerequisites to demonstarte the 'structure-property-functions correlations' at the electronic level. With the advantages of their different, PLQY, long-lived emission, dissimilar nano morphology, the molecules were employed in various normal and cancerious cell lines. Interstingly they showed a very good bio-compatibility, however, mong four fluorophores, BTMCzPy2 showed a good cellular uptake and bright cell-imaging efficacy.

7.5. References

[1] O. Ostroverkhova, *Chem. Rev.* **2016,** *116*, 13279–13412.

[2] J. Mei, N. L. C. Leung, R. T. K. Kwok, J. W. Y. Lam, B. Z. Tang, *Chem. Rev.* **2015**, *115*, 11718–11940.

[3] Z. Yang, Z. Mao, Z. Xie, Y. Zhang, S. Liu, J. Zhao, J. Xu, Z. Chi, M.P. Aldred, *Chem. Soc. Rev.* **2017,** *46*, 915–1016.

[4] Y. Tao, K. Yuan, T. Chen, P. Xu, H. Li, R. Chen, C. Zheng, L. Zhang, W. Huang, *Adv. Mater.* **2014**, *26*, 7931–7958.

[5] K.-H. Kim, J.-J. Kim, *Adv. Mater.* **2018**, *30*, 1705600.

[6] D. Barman, K. Narang, R. Gogoi, D. Barman, P.K. Iyer, *J. Mater. Chem. C* **2022**, *10*, 8536–8583.

[7] K. Goushi, K. Yoshida, K. Sato, C. Adachi, *Nat. Photonics*, **2012**, ***6***, 253–258.

[8] M.Y. Wong, E. Zysman-Colman, *Adv. Mater.* **2017**, *29*, 1605444.

[9] T. Hatakeyama, K. Shiren, K. Nakajima, S. Nomura, S. Nakatsuka, K. Kinoshita, J. Ni, Y. Ono, T. Ikuta, *Adv. Mater.* **2016**, *28*, 2777–2781.

[10] B. Xu, Y. Mu, Z. Mao, Z. Xie, H. Wu, Y. Zhang, C. Jin, Z. Chi, S. Liu, J. Xu, Y.-C. Wu, P.-Y. Lu, A. Lien, M. R. Bryce, *Chem. Sci.* **2016**, *7*, 2201–2206.

[11] J. Zhang, F. Fang, B. Liu, J.-H. Tan, W.-C. Chen, Z. Zhu, Y. Yuan, Y. Wan, X. Cui, S. Li, Q.-X. Tong, J. Zhao, X.-M. Meng, C.-S. Lee, *ACS Appl. Mater. Interfaces* **2019**, *11*, 41051–41061.

[12] X. Xiong, F. Song, J. Wang, Y. Zhang, Y. Xue, L. Sun, N. Jiang, P. Gao, L. Tian, X. Peng, *J. Am. Chem. Soc.* **2014**, *136*, 9590–9597.

[13] M. A. Bryden, E. Zysman-Colman, *Chem. Soc. Rev.* **2021**, *50*, 7587–7680.

[14] A. Steinegger, I. Klimant, S. M. Borisov, *Adv. Opt. Mater.* **2017**, *5*, 1700372.

[15] F. Fang, Y. Yuan, Y. Wan, J. Li, Y. Song, W.-C. Chen, D. Zhao, Y. Chi, M. Li, C.-S. Lee, J. Zhang, *Small* **2022**, *18*, e2106215.

[16] M. Luo, X. Li, L. Ding, G. Baryshnikov, S. Shen, M. Zhu, L. Zhou, M. Zhang, J. Lu, H. Ågren, X.-D. Wang, L. Zhu, *Angew. Chem. Int. Ed.* **2022,** *132*, 17166–17173.

[17] F. Ni, N. Li, L. Zhan, C. Yang, *Adv. Opt. Mater.* **2020**, *8*, 1902187.

[18] C. I. C. Crucho, J. Avó, A. M. Diniz, S. N. Pinto, J. Barbosa, P.O. Smith, M. N. Berberan-Santos, L.-O. Pålsson, F. B. Dias, *Front. Chem.* **2020**, *8*, 404.

[19] Q. Zhang, S. Xu, M. Li, Y. Wang, N. Zhang, Y. Guan, M. Chen, C.-F. Chen, H.-Y. Hu, *Chem. Commun.* **2019**, *55*, 5639–5642.

[20] X. -K. Chen, D. Kim, J. -L. Brédas, *Acc. Chem. Res.* **2018**, *51*, 2215–2224.

[21] H. Imahori, Y. Kobori, H. Kaji, *Acc. Mater. Res.* **2021** ***2***, 501–514.

[22] D. Barman, M. Annadhasan, R. Chandrasekar, P. K. Iyer, *Chem. Sci.* **2022**, *13*, 9004–9015.

[23] C. Lin, P. Han, S. Xiao, F. Qu, J. Yao, X. Qiao, D. Yang, Y. Dai, Q. Sun, D. Hu, A. Qin, Y. Ma, B. Z., Tang, D. Ma, *Adv. Funct. Mater.* **2021**, *31*, 2106912.

[24] S. H. Han, Y. H. Park, J. Y. Lee, *Adv. Opt. Mater.* **2018**, *6*, 1800997.

[25] G. Kreiza, D. Banevičius, J. Jovaišaitė, K. Maleckaitė, D. Gudeika, D. Volyniuk, J. V. Gražulevičius, S. Juršėnas, K. Kazlauskas, *J. Mater. Chem. C* **2019***, 7,* 11522–11531.

[26] X. CAI, B. Liu, *Angew. Chem. Int. Ed.* **2020**, *59*, 9868–9886.

[27] S. Guisán-Ceinos, A. R. Rivero, F. Romeo-Gella, S. Simón-Fuente, S. Gómez-Pastor, N. Calvo, A. H. Orrego, J. M. Guisán, I. Corral, F. Sanz-Rodriguez, M. Ribagorda, *J. Am. Chem. Soc.* ***2022****, 144*, *18*, 8185–8193.

[28] T. Li, D. Yang, L. Zhai, S. Wang, B. Zhao, N. Fu, L. Wang, Y. Tao, W. Huang, *Adv. Sci.* **2017**, *4*, 1600166.

[29] Q. Zhang, S. Xu, M. Li, Y. Wang, N. Zhang, Y. Guan, M. Chen, C. -F. Chen, H. -Y. Hu, *Chem. Commun.* **2019**, *55*, 5639–5642.

[30] M. Luo, X. Li, L. Ding, G. Baryshnikov, S. Shen, M. Zhu, L. Zhou, M. Zhang, J. Lu, H. Ågren, X. -D. Wang, L. Zhu, *Angew. Chem. Int. Ed.* **2020**, *59*, 17018–17025.

[31] F. Ni, Z. Zhu, X. Tong, M. Xie, Q. Zhao, C. Zhong, Y. Zou, C. Yang, *Chem. Sci.* **2018**, *9*, 6150–6155.

[32] F. Fang, L. Zhu, M. Li, Y. Song, M. Sun, D. Zhao, J. Zhang, *Adv. Sci.* **2021**, *8*, e2102970.

[33] Q. Gao, X. Wu, F. Jia, M. Liu, Y. Zhu, Q. Cai, A. Wu, *J. Org. Chem.* **2013**, *78*, 2792–2797.

[34] G. Feng, B. Liu, *Acc. Chem. Res.* **2018**, *51*, 1404−1414.

[35] P. Rajamalli, F. Rizzi, W. Li, M.A. Jinks, A. K. Gupta, B. A. Laidlaw, I. D. W. Samuel, T. J. Penfold, S. M. Goldup, E. Zysman-Colman, *Angew. Chem. Int. Ed.* **2021**, *133*, 12173–12180.

[36] S. Cekli, R. W. Winkel, E. Alarousu, O. F. Mohammed, K. S. Schanze, *Chem. Sci.* **2016**,*7*, 3621-3631.

[37] M. K. Etherington, J. Gibson, H. F. Higginbotham, T. J. Penfold, A. P. Monkman, *Nat. Commun.* **2016**, *7*, 13680.

[38] Q. Li, J. Hu, J. Lv, X. Wang, S. Shao, L. Wang, X. Jing, F. Wang, *Angew. Chem. Int. Ed.* **2020**, *59*, 20174–20182.

[39] J. Liu, T. Hu, Z. Li, X. Wei, X. Hu, H. Gao, G. Liu, Y. Yi, Y. Yamada-Takamura, C. -S. Lee, P. Wang, Y. Wang, *J. Phys. Chem. Lett.* **2019**, *10*, 1888–1893.

[40] B. Huang, W. –C. Chen, Z. Li, J. Zhang, W. Zhao, Y. Feng, B. Z. Tang, C. –S. Lee, *Angew. Chemie. Int. Ed.* **2018**, *57*, 12473-12477.

[41] S. Sasaki, G. P. C. Drummen, G. -I. Konishi, *J. Mater. Chem. C* **2016**, *4*, 2731–2743.

[42] Z. An , C. Zheng , Y. Tao , R. Chen , H. Shi , T. Chen , Z. Wang , H. Li , R. Deng , X. Liu and W. Huang , *Nat. Mater,* **2015**, *14* , 685-690.

[43] M. Okazaki, Y. Takeda, P. Data, P. Pander, H. Higginbotham, A. P. Monkman, S. Minakata, *Chem. Sci.* **2017**, *8*, 2677 – 2686.

Appendix: Additional data for **Chapter 7**

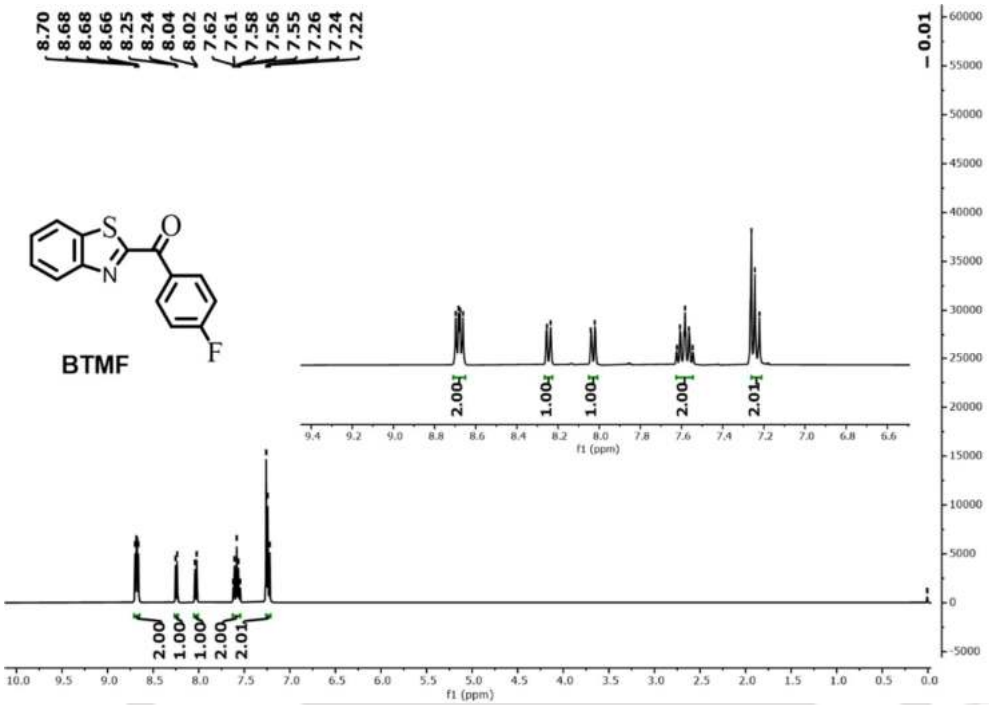

Figure A7.1. ^{1}H NMR spectra of BTMF in $CDCl_3$ at 298K.

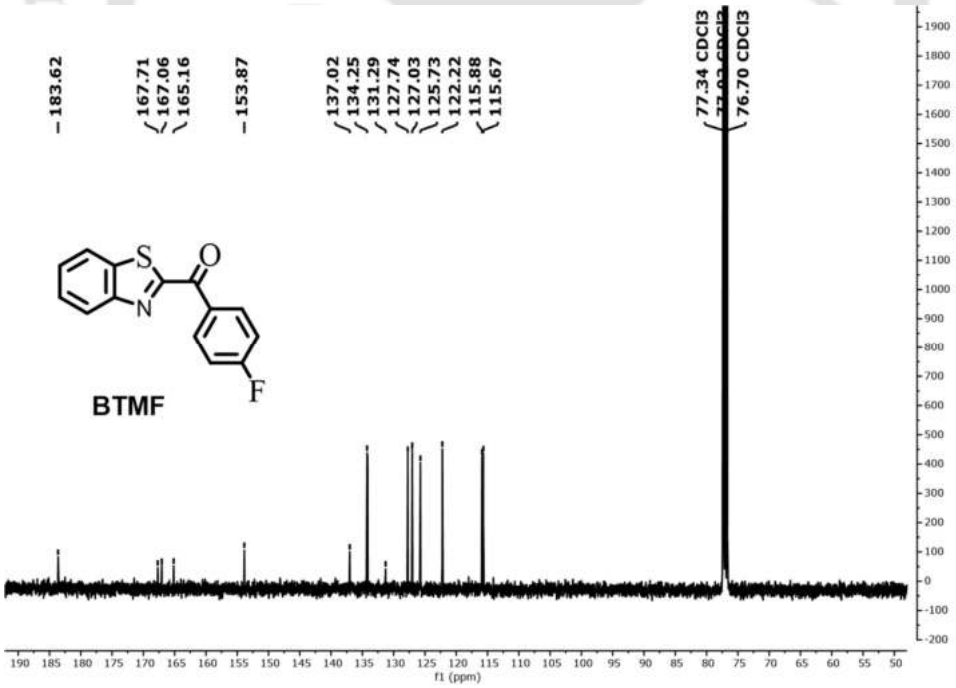

Figure A7.2: ^{13}C NMR spectra of BTMF in $CDCl_3$ at 298K.

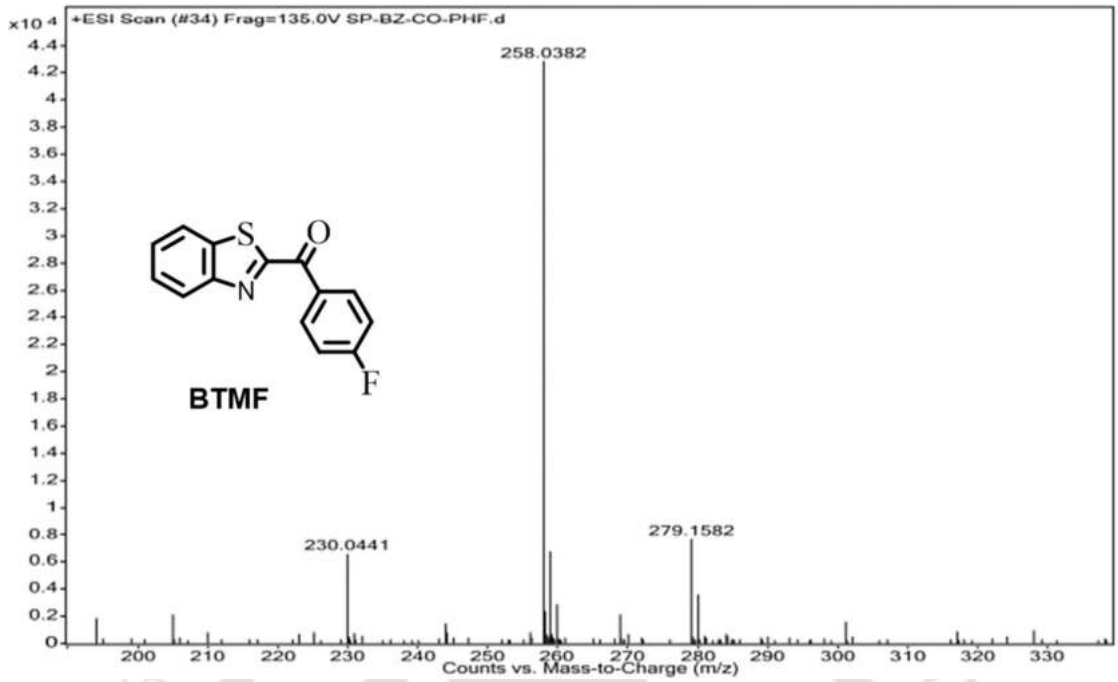

Figure A7.3. HRMS (ESI) peaks of m/z value for $[BTMF + H]^+$ was calculated 258.0389 and observed 258.0340 at 298K in Acetonitrile solvent.

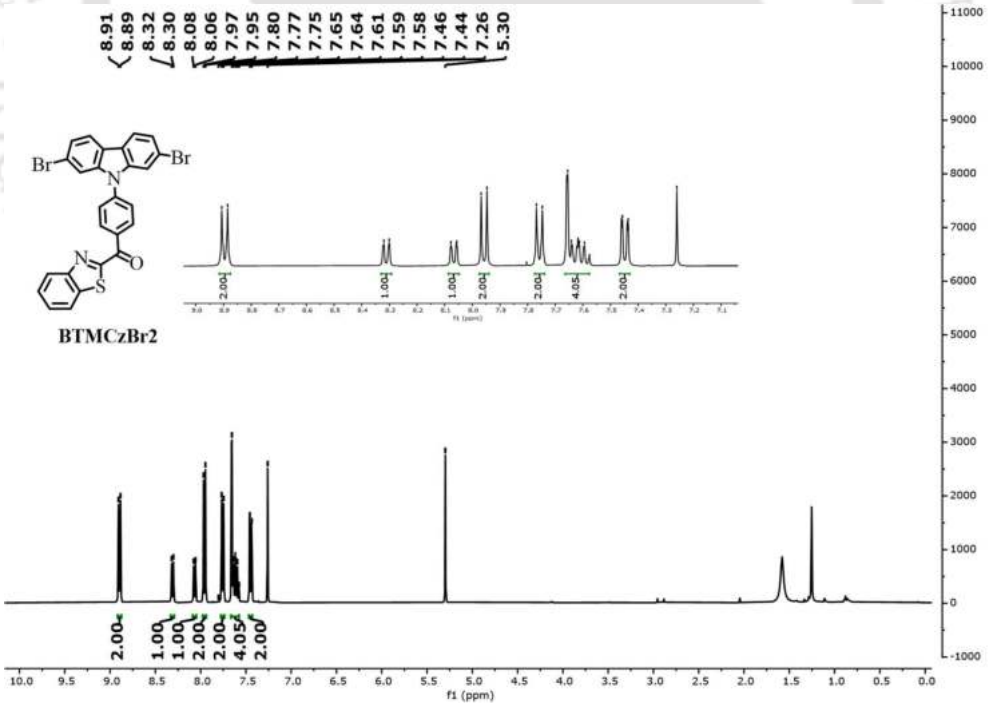

Figure A7.4. ^1H NMR spectra of BTMCzBr2 in $CDCl_3$ at 298K.

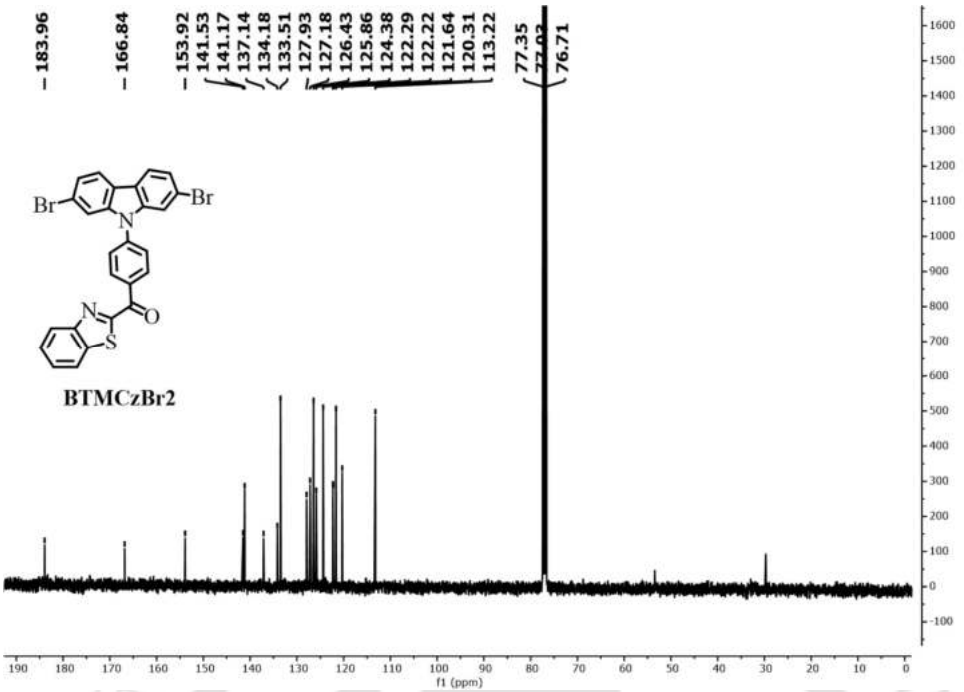

Figure A7.5. ^{13}C NMR spectra of BTMCzBr2 in $CDCl_3$ at 298K.

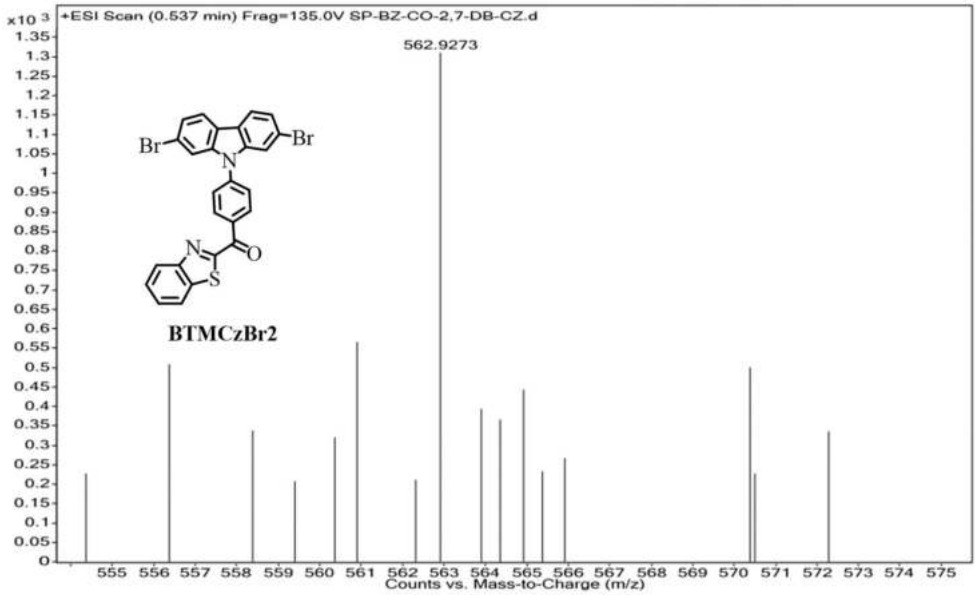

Figure A7.6. HRMS (ESI) peaks of m/z value for $[BTMCzBr2 + H]^+$ was calculated 562.9251 and observed 562.9273 at 298K in Acetonitrile solvent.

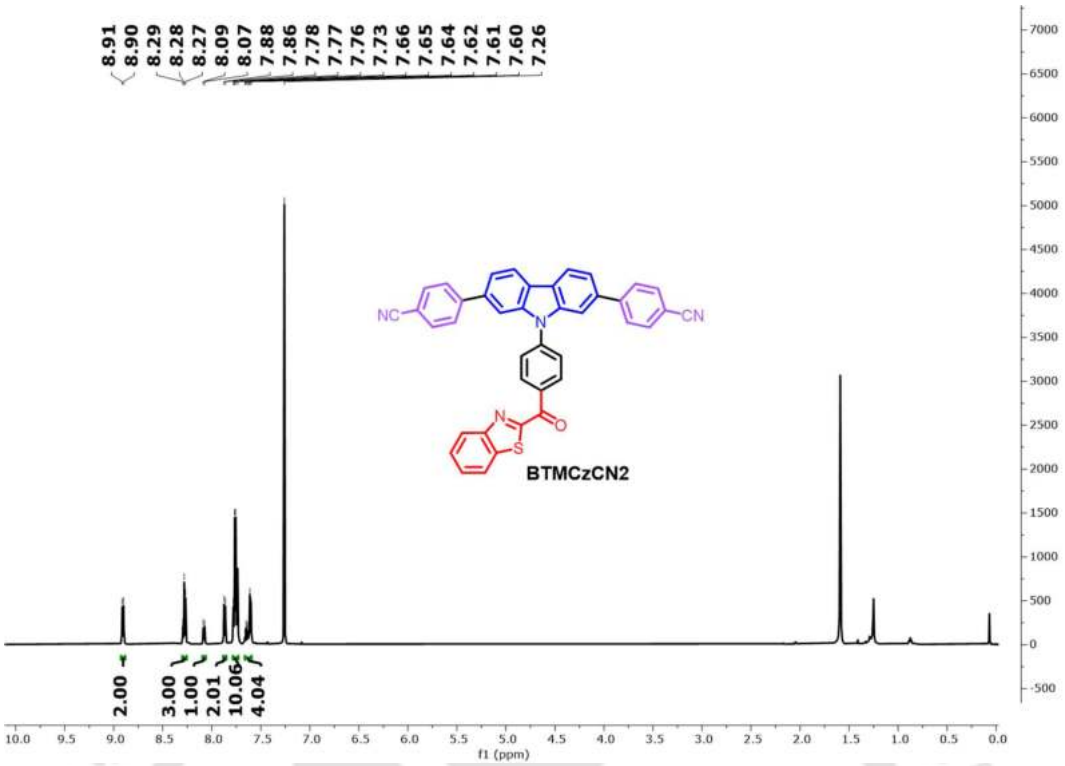

Figure A7.7. ^{1}H NMR spectra of BTMCzCN2 in $CDCl_3$ at 298K.

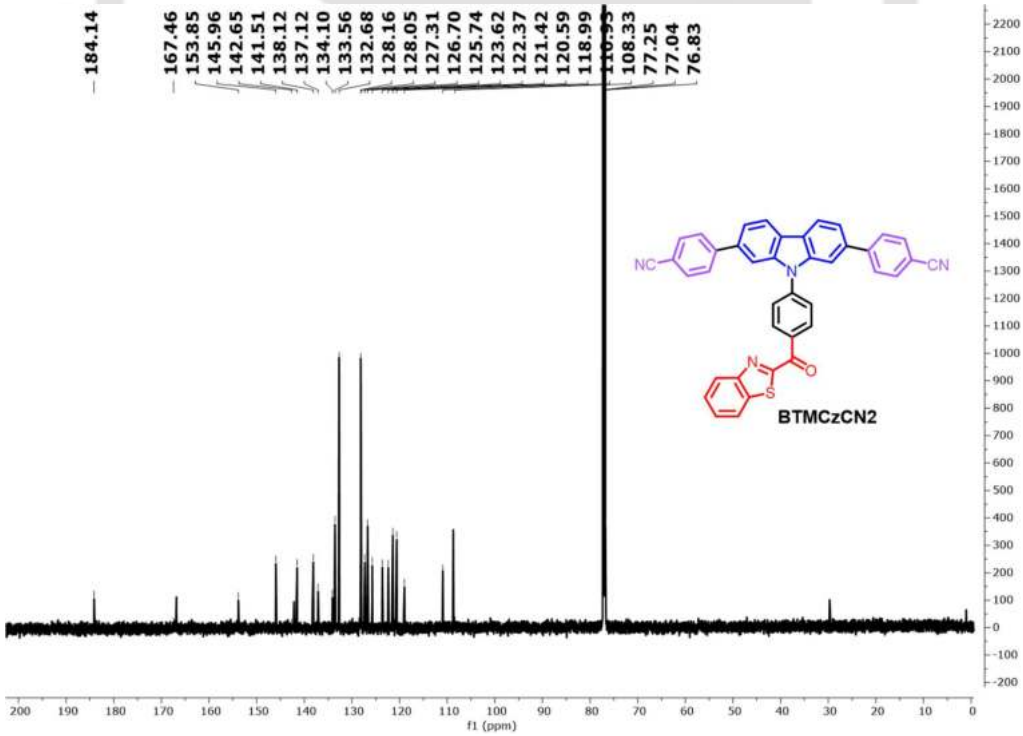

Figure A7.8. ^{13}C NMR spectra of BTMCzCN2 in $CDCl_3$ at 298K.

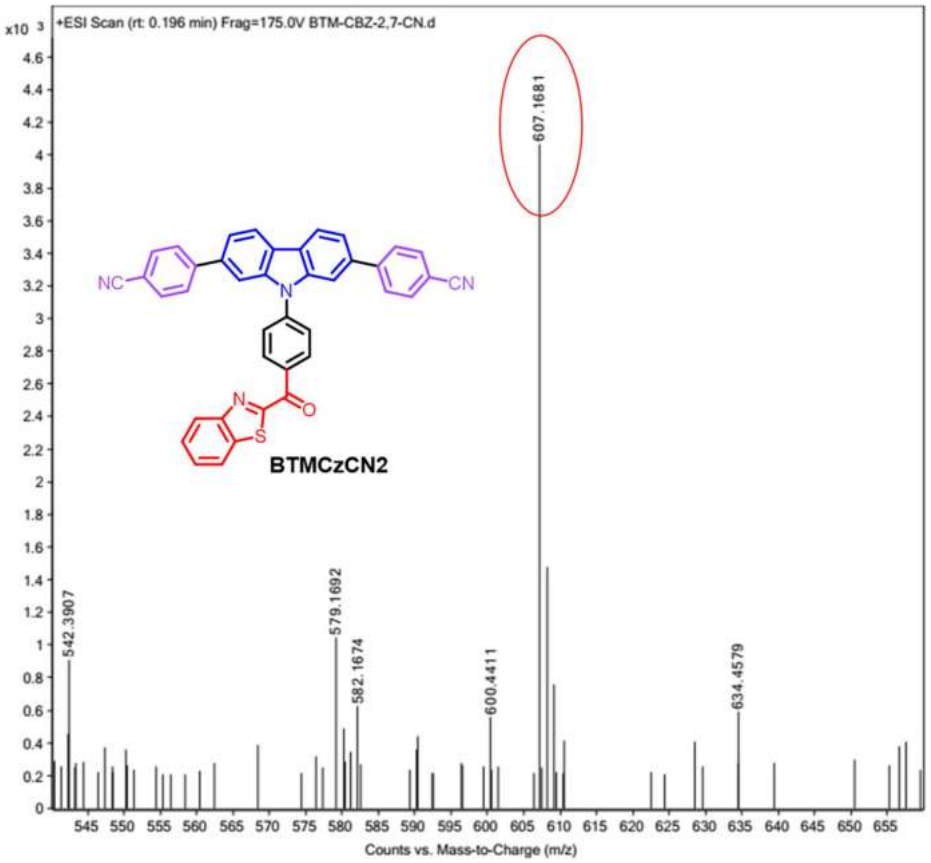

Figure A7.9. HRMS (ESI) peaks of m/z value for $[BTMCzCN2 + H]^+$ was calculated 607.1593 and observed 607.1681 at 298K in Acetonitrile solvent.

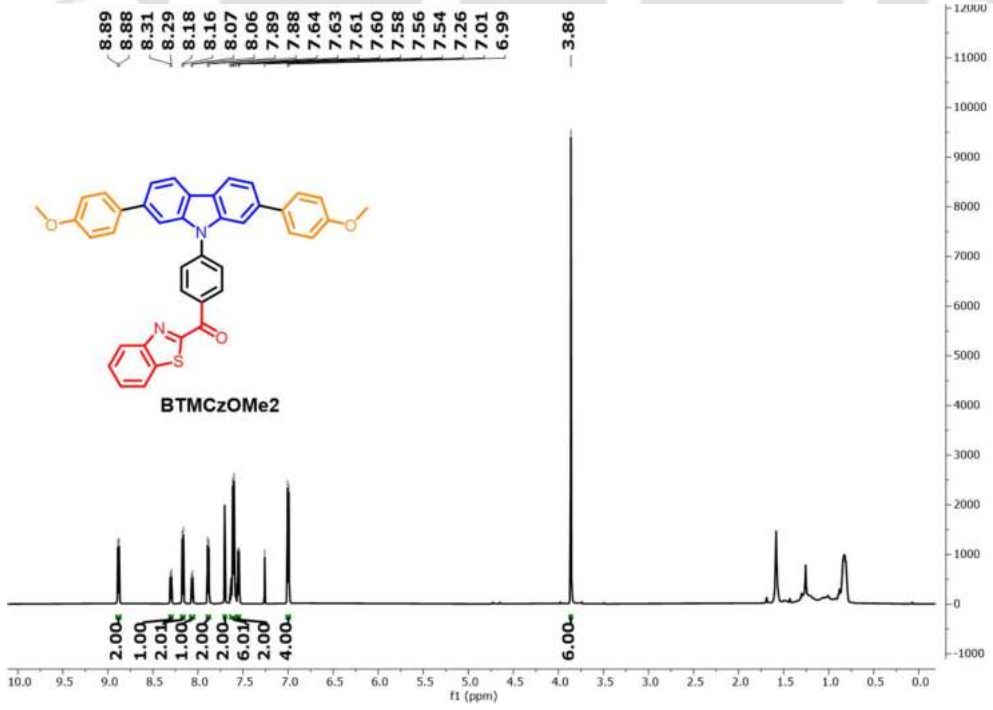

Figure A7.10. ^1H NMR spectra of BTMCzOMe2 in $CDCl_3$ at 298K.

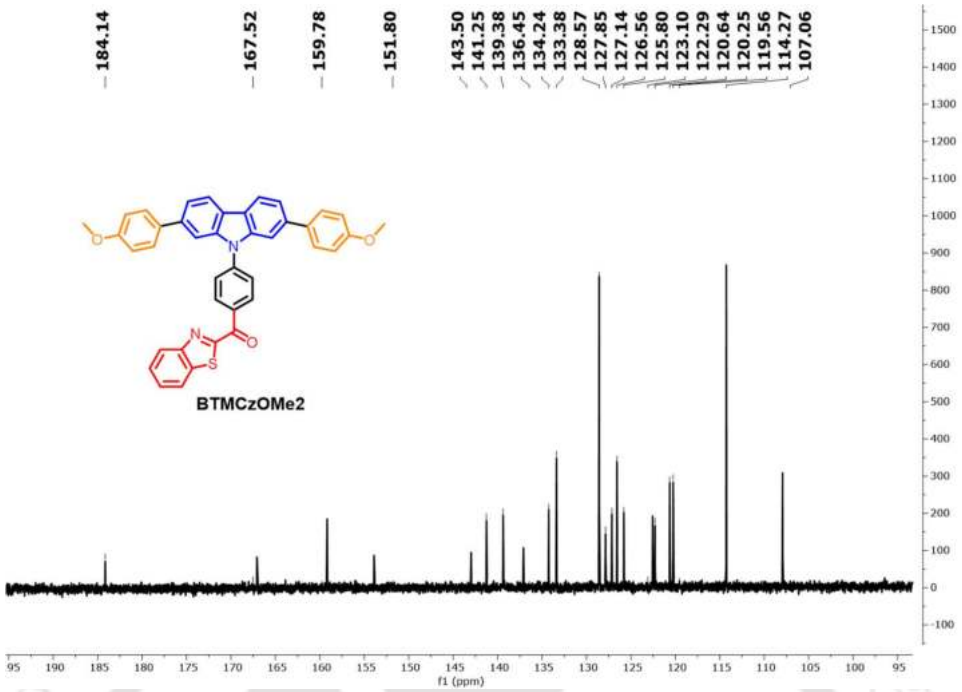

Figure A7.11. ^{13}C NMR spectra of BTMCzOMe2 in $CDCl_3$ at 298K.

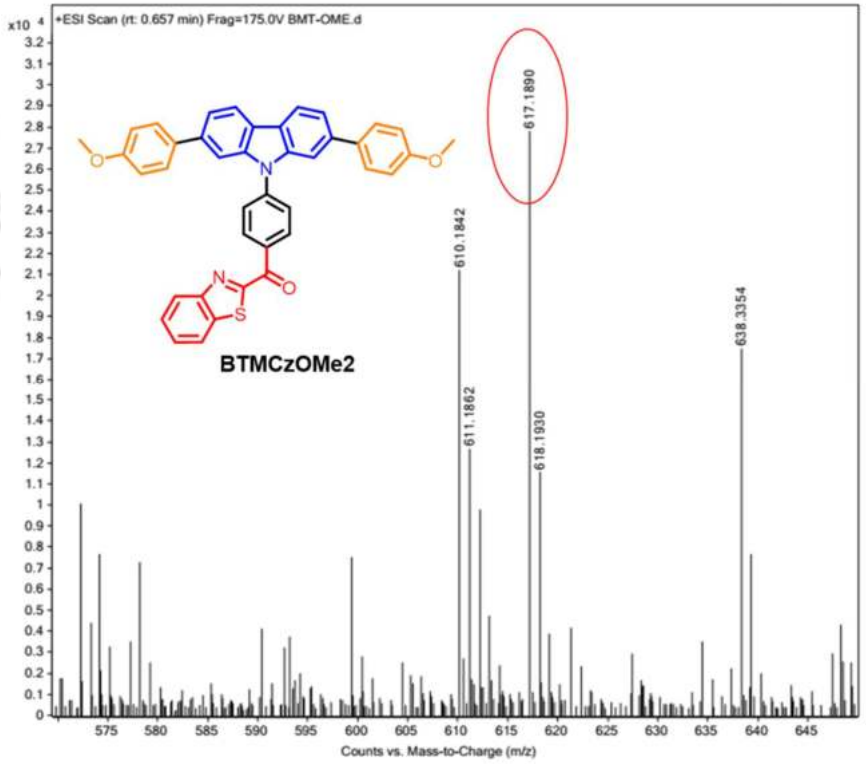

Figure A7.12. HRMS (ESI) peaks of m/z value for $[BTMCzOMe2 + H]^+$ was calculated 617.1899 and observed 617.1890 at 298K in Acetonitrile solvent.

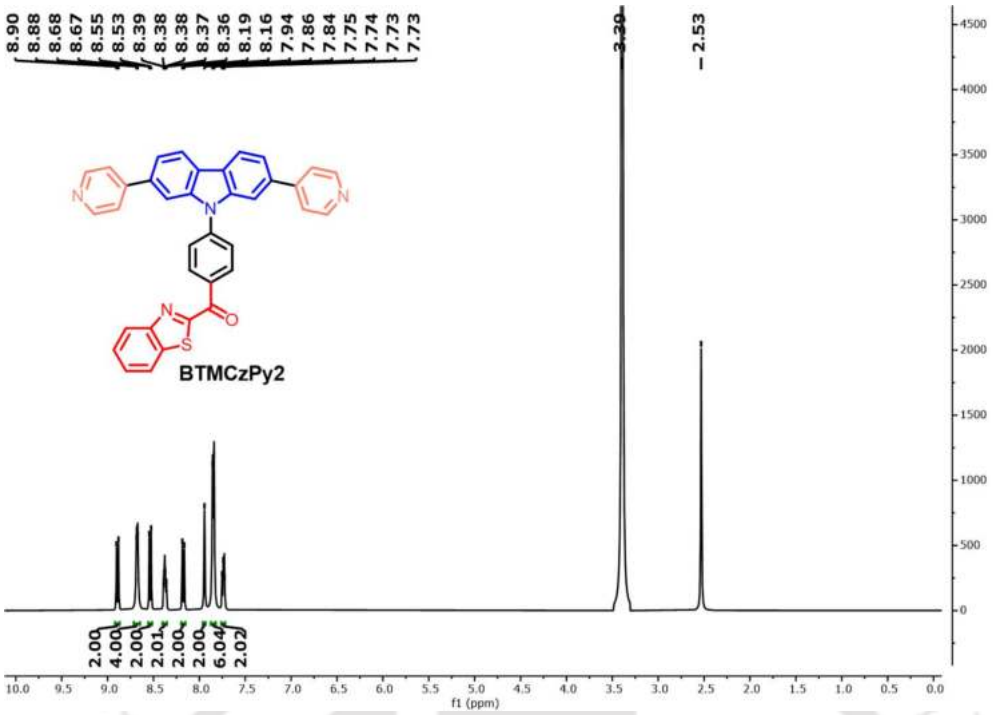

Figure A7.13. ^{1}H NMR spectra of BTMCzPy2 in $CDCl_3$ at 298K.

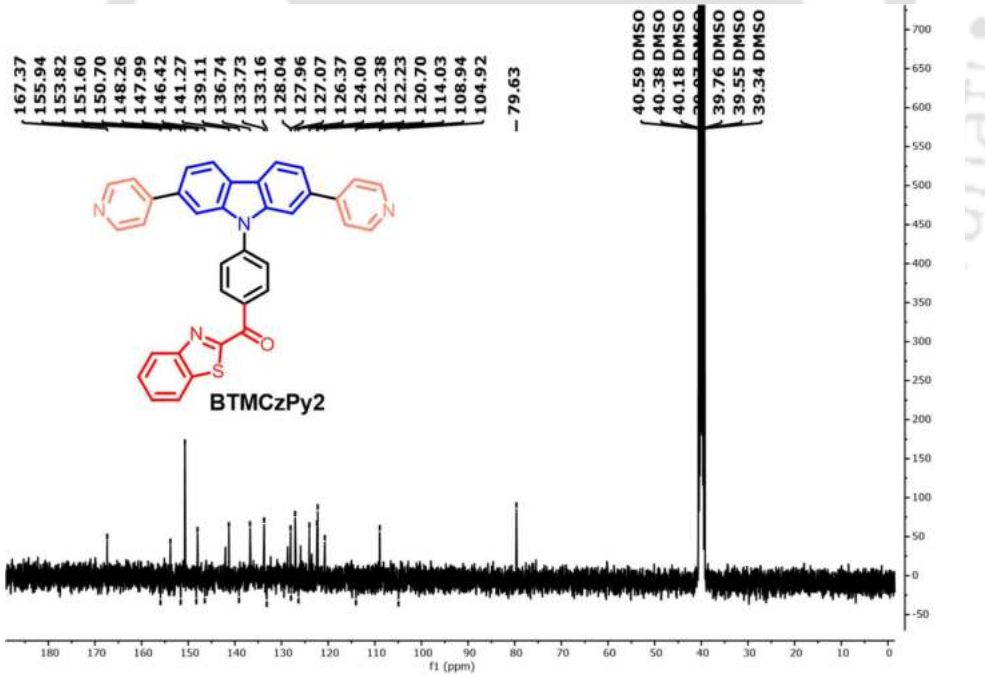

Figure A7.14. ^{13}C NMR spectra of BTMCzPy2 in $CDCl_3$ at 298K.

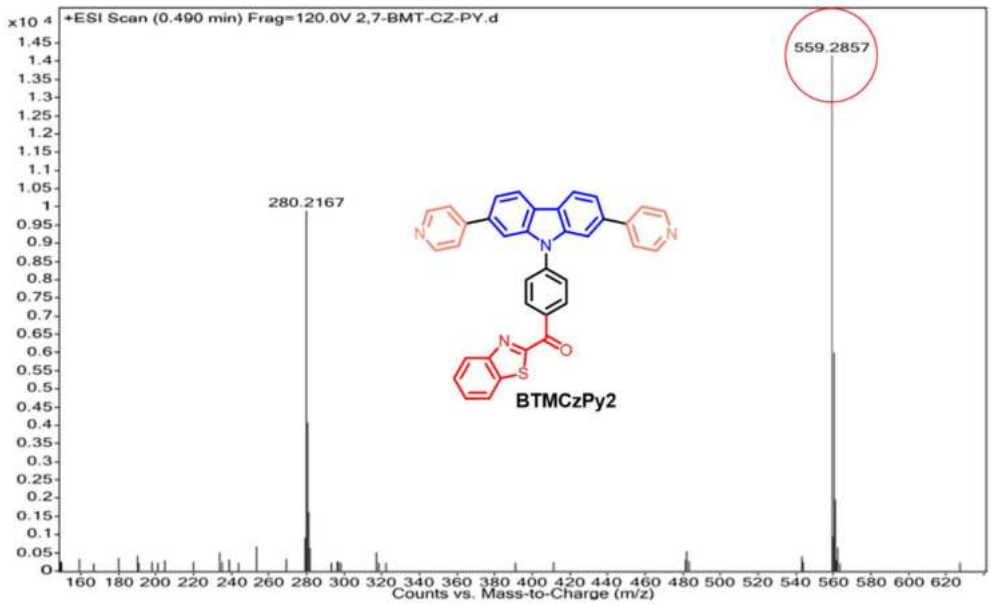

Figure A7.15. HRMS (ESI) peaks of m/z value for $[BTMCzPy2 + H]^+$ was calculated 559.1593 and observed 559.2857 at 298K in Acetonitrile solvent.

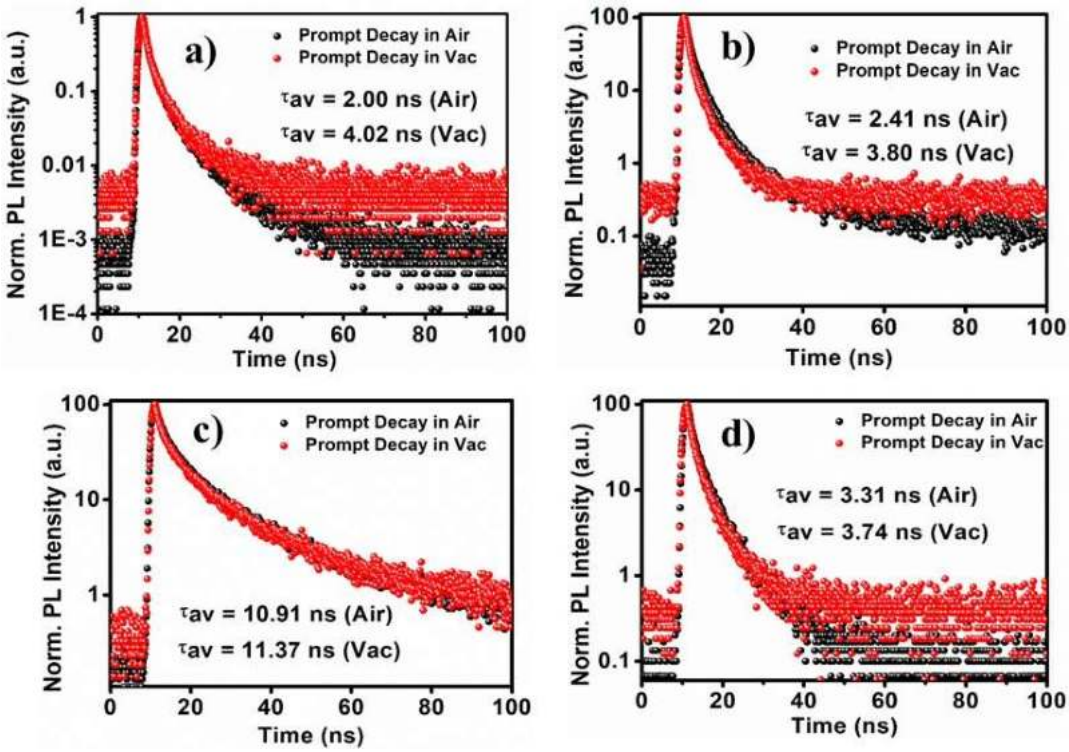

Figure A7.16: Prompt fluorescence/LE state emission lifetime recorded under air and vacuum in the thin film of BTMCzBr2, BTMCzCN2, BTMCzOMe2 and BTMCzPy2.

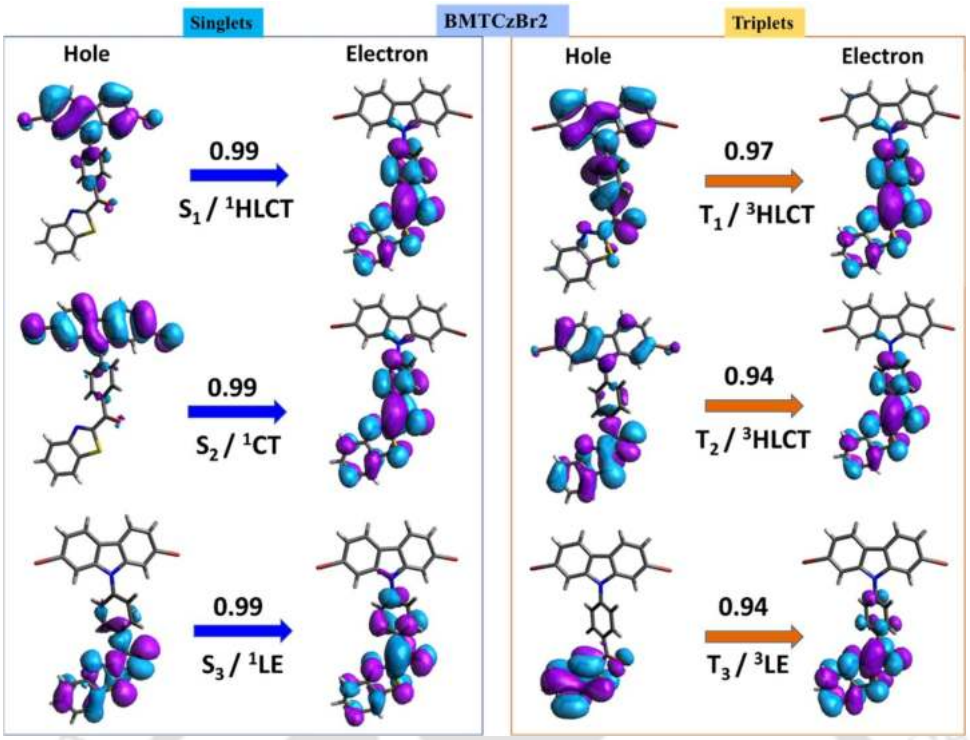

Figure A7.17. Natural transition orbitals (NTOs) for different singlet and triplet excited states in BTMCzBr2.

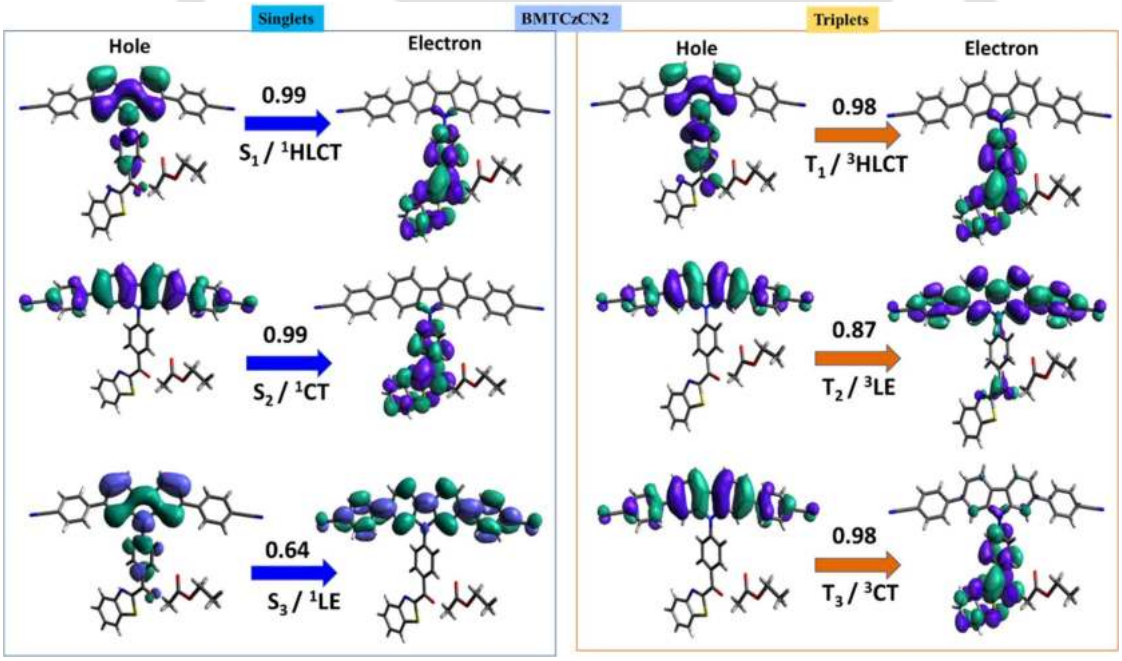

Figure A7.18 Natural transition orbitals (NTOs) for different singlet and triplet excited states in BTMCzCN2.

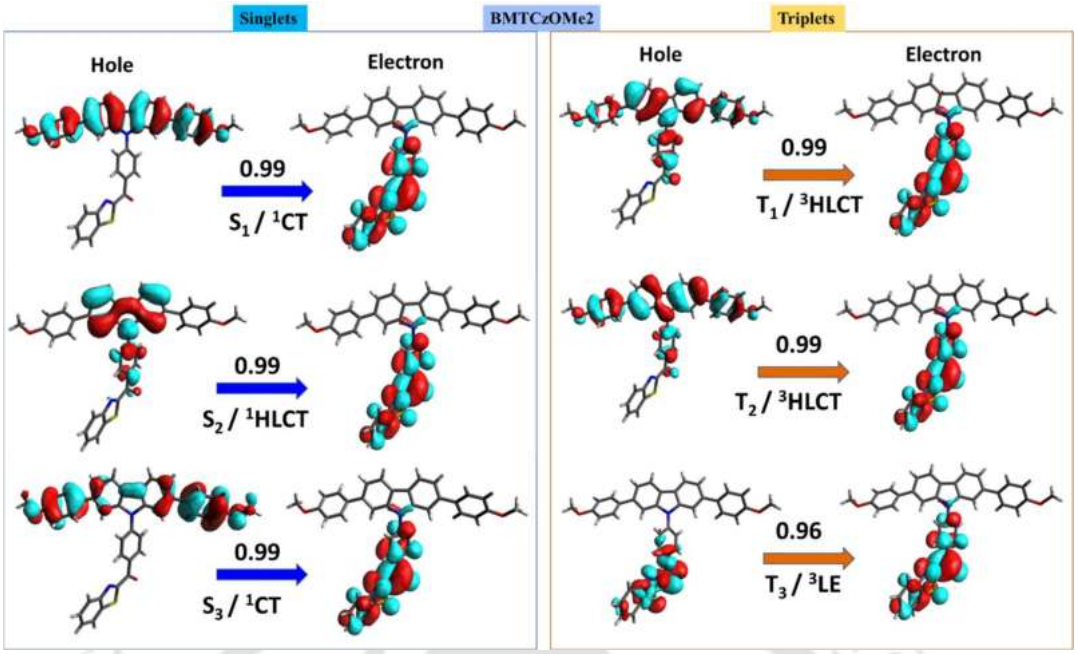

Figure A7.19. Natural transition orbitals (NTOs) for different singlet and triplet excited states in BTMCzOMe2.

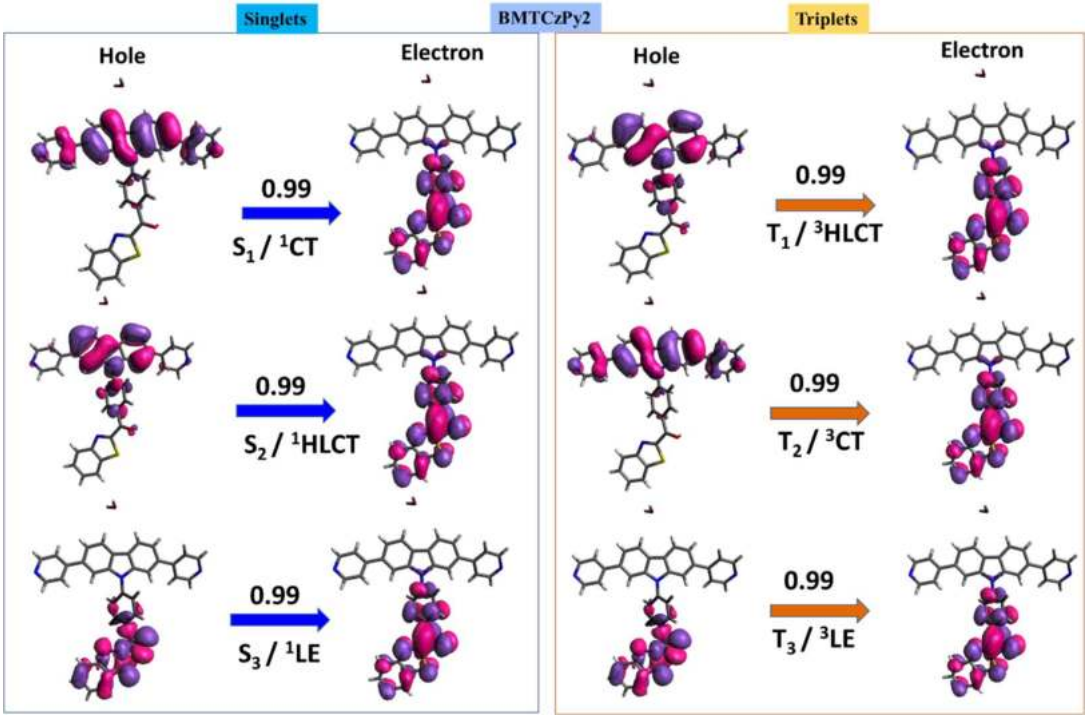

Figure A7.20. Natural transition orbitals (NTOs) for different singlet and triplet excited states in BTMCzPy2.

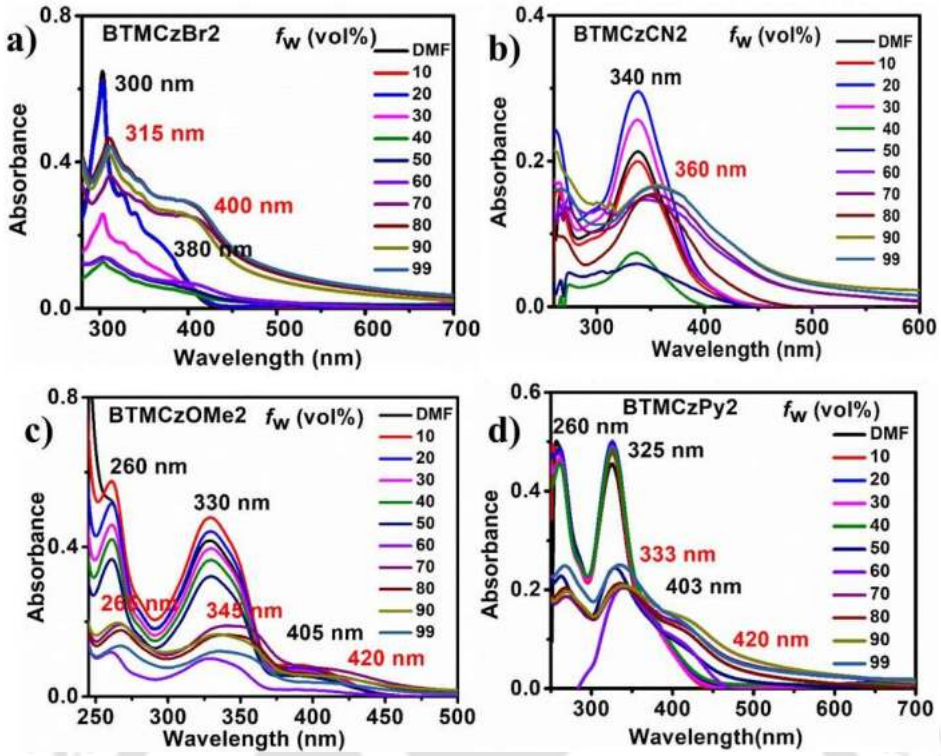

Figure A7.21. UV-visible absorbance spectra recorded by varying various THF:H_2O mixtures for BTMCZBr2, BTMCzCN2, BTMCzOMe2, and BTMCzPy2 at 5 x 10^{-5}M concentration.

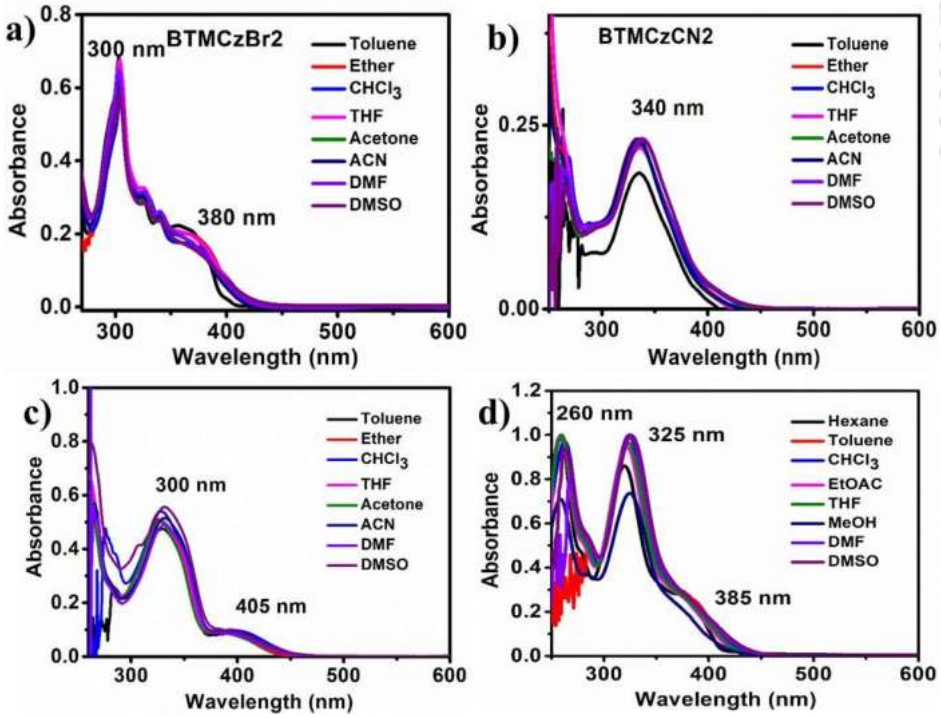

Figure A7.22. UV-visible absorption spectra recorded by varying different solvent polarity for BTMCzBr2, BTMCzCN2, BTMCzOMe2, and BTMCzPy2 at 5 x 10^{-5}M concentration.

Table A7.1. Crystallographic data and structure refinement parameters of BTMCzBr2, BTMCzCN2, BTMCzOMe2 and BTMCzPy2, respectively.

Compound	BTMCzCN2	BTMCzOMe2	BTMCzPy2
Empirical formula	C40 H22 N4 O S	C40 H28 N2 O3 S	C36 H22 N4 O S
CCDC NO	2202461	2202462	1974995
Temperature/K	293	293	293
Crystal system	monoclinic	monoclinic	monoclinic
Space group	P 21/c	P 21/n	C 2/c
a/Å	8.121(3)	8.1259(8)	30.111(12)
b/Å	15.889(5)	37.671(5)	11.9901(19)
c/Å	27.795(9)	10.2558(11)	15.791(8)
α/°	90.00	90.00	90.00
β/°	98.271(13)	91.372(9)	102.66(4)
γ/°	90.00	90.00	90.00
Volume/Å^3	2079.4(2)	3138.5(6)	5563(4)
Z	4	4	4
ρ_{calc}mg/mm^3	1.300	1.305	1.355
m/mm^{-1}	0.139	0.146	0.156
F(000)	1448.0	1288.0	2360.0
Index ranges	-9≤ h ≤ 9, -18 ≤ k ≤ 18, -33 ≤ l ≤ 33	-9≤ h ≤ 9, -23 ≤ k ≤ 44, -12 ≤ l ≤ 12	-26 ≤ h ≤35, -14 ≤ k ≤ 13, -16 ≤ l ≤ 18
Reflections collected	6287	5563	4946
Independent reflections	2542	1126	1745
Data/restraints/ parameters	2542/0/471	1126 /0/ 417	1745/0/388
Goodness-of-fit on F^2	1.223	0.870	1.121
Final R indexes	R1 = 0.0812 wR2 = 0.1730	R1 = 0.0806, wR2 = 0.1786	R1 = 0.1012, wR2 = 0.2326

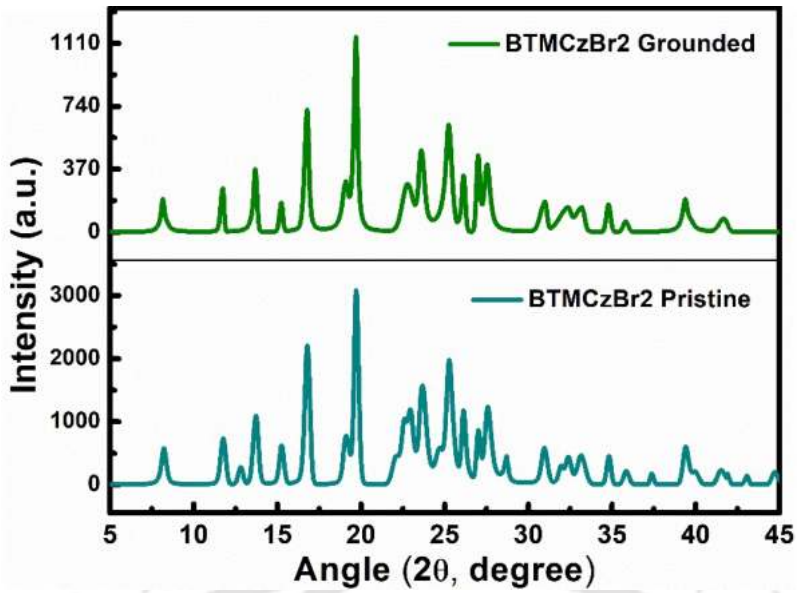

Figure A7.23. PXRD pattern for BTMCzBr2 sky-blue line as synthesized pristine compound where dark green line is the simulated pattern obtained from SC-XRD structure

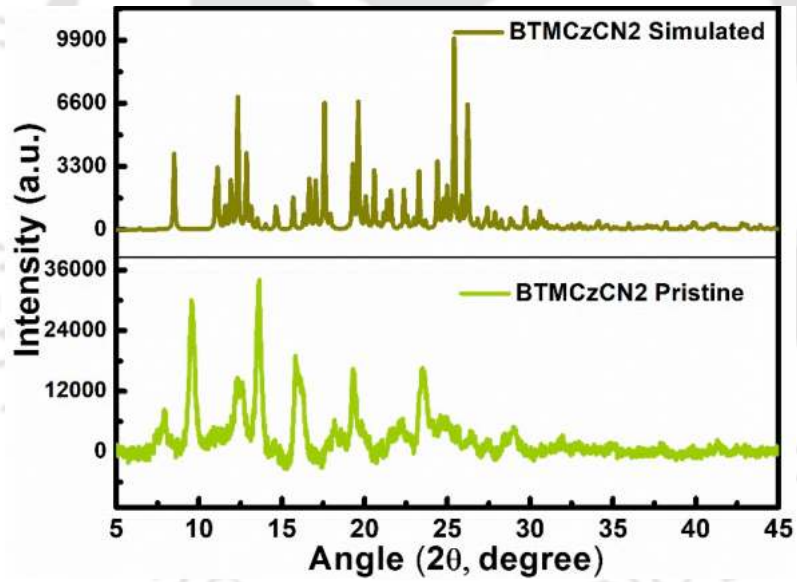

Figure A7.24. PXRD pattern for BTMCzCN2 yellow green line as synthesized pristine compound where dark yellow line is the simulated pattern obtained from SC-XRD structure.

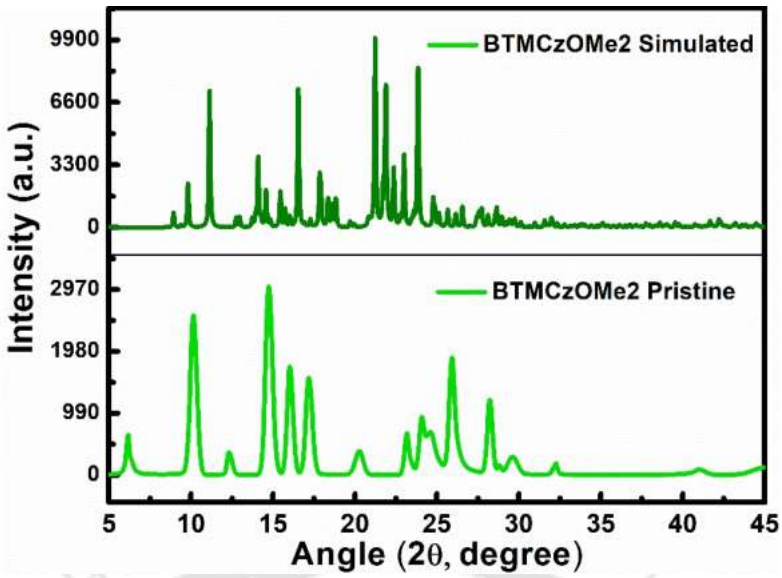

Figure A7.25. PXRD pattern for BTMCzOMe2 bright green line as synthesized pristine compound where dark green line is the simulated pattern obtained from SC-XRD structure.

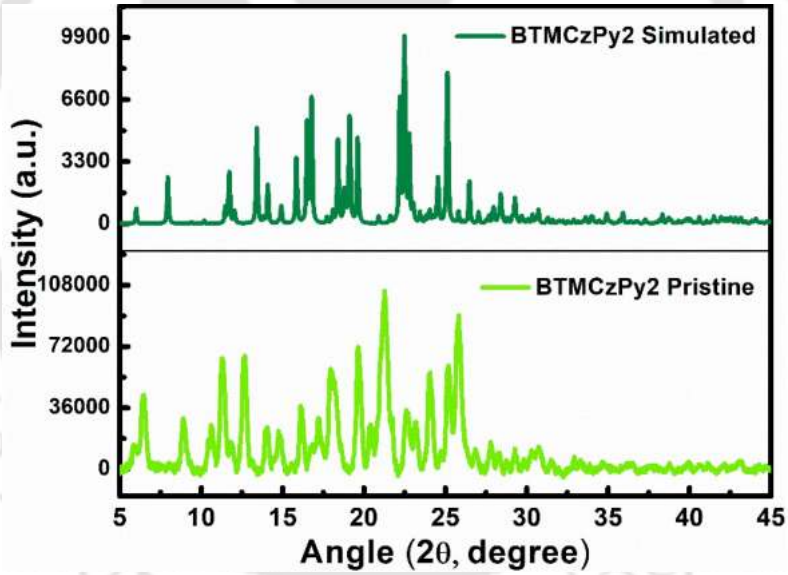

Figure A7.26. PXRD pattern for BTMCzPy2 bright green line as synthesized pristine compound where dark green line is the simulated pattern obtained from SC-XRD structure.

Thesis Overview

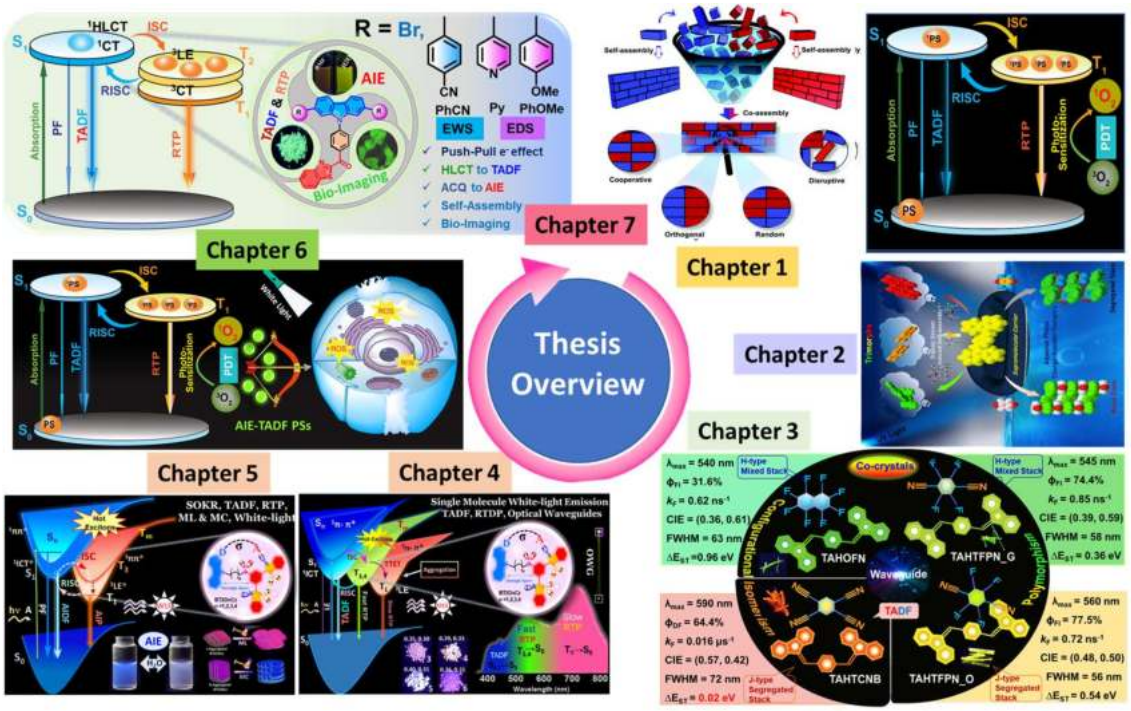

Curriculum vitae

Debasish Barman

debasish16@iitg.ac.in/debasish.chem16@gmail.com
CHEL304, Department of Chemistry
Indian Institute of Technology Guwahati
Guwahati-781039, Assam, India
+91 9734343773

EDUCATION

Indian Institute of Technology Guwahati — Guwahati, Assam
- PhD in Chemistry — Expected December, 2022

Indian Institute of Technology Guwahati — Guwahati, Assam
- M.Sc in Chemistry, CGPA **7.5**/10 — 2016

Vidyasagar University — Purba Medinipur, West Bengal
- B.Sc (Hons) in Chemistry, **64.25%** — 2014

RESEARCH EXPERIENCE

Indian Institute of Technology Guwahati — Guwahati, Assam
Graduate student (Doctoral) with Prof. Parameswar K Iyer — 2016- present

Pursuing my doctoral research on *"Modulation of Ground and Excited State Dynamics in Donor-Acceptor Organic Functional Small Molecules for Photonics and Biomedical Applications."*

Indian Institute of Technology Guwahati — Guwahati, Assam
Graduate student (Master's) with Dr. Kingsuk Mahata — 2015- 2016
Worked as summer project and M.Sc project entitled *"Towards Synthesis of a Novel Carbonyl Bridged N-doped Polycyclic Heterocarbons"* at IIT Guwahati, Guwahati, India.

TECHNICAL SKILLS/ TEACHING EXPERIENCE

1. **Materials Synthesis -** Organic multi-step reactions, various coupling reactions, column chromatography, inert-atmosphere reaction, low-temperature reactions, solvent drying, distillation.
2. **Characterization Techniques -** Nuclear magnetic resonance (**NMR**), high resolution mass spectrometry (**HRMS**), single crystal X-ray diffraction (**SC-XRD**), powder X-ray diffraction (**PXRD**), fourier-transform infrared spectroscopy (**FTIR**), dynamic light scattering (**DLS**), Field emission scanning electron microscopy (**FESEM**), field Emission transmission electron microscopy (**FETEM**), atomic force microscopy (**AFM**), UV-visible spectroscopy, fluorescence spectroscopy, time-resolved photoluminescence spectroscopy (**TRPL**), micro-Raman spectroscopy, thermal gravimetric analysis (**TGA**), differential scanning calorimetry (**DSC**), Cyclic Voltammetry (**CV**).
3. **Computational Calculations and Software's Proficiency –** Familiar with the density functional theory (**DFT**) and time-dependent density functional theory

(**TDDFT**) using Gaussiun, excited state dynamics study by **ORCA**, Crystal growth morphology by Material Studio, Multiwfn, Chemdraw, Origin, ImageJ, Vesta, Murcury, Avogadro, Adobe Illustrator, Windows-XP, 7, 8, 10, dos and MS Office.

4. **Organic Light-emitting Diode (OLED) Fabrication and Characterization -** Substrate patterning, sonication, cleaning, UV-ozone treatment, spin coating, thermal deposition, Keithley 2400 source meter, spectro-radiometer.
5. ***In vitro* Biological Techniques** – Basic learning on 2D cell culture techniques, cell viability/proliferation assays like fluorescence and colorimetric based; cell cytotoxicity assays like reactive oxygen species determination.

Indian Institute of Technology Guwahati Guwahati, Assam

Central Instrument Facility

- Authorized operator of Single Crystal X-ray Diffraction (SC-XRD) 2019- 2021

Department of Chemistry

- Guided five postgraduate projects 2018-2021 (Jan-May)
- Guided five graduate projects 2018-2021 (Jan-May)
- Guided two summer projects 2018, 2019 (Jun-August)
- Teaching Assistant, undergraduate Laboratory work 2017-2019 (July- November)

RESEARCH INTEREST

- Functional Organic Materials: Design and Synthesis
- Thermally Activated Delayed Fluorescence
- Room Temperature Phosphorescence
- Aggregation Induced Emission
- Organic Crystal and Co-crystal
- Optical Waveguide
- Cancer Therapy
- Bio-imaging
- OLED

PUBLICATIONS

1 **Barman, D**., Rajamalli, P., Bidkar, A. P., Gogoi, R., Barman, D., Ghosh, S. S., Zysman-Colman, E., Iyer, P. K. Manipulation of Triplet Excited States Procuring Long-lived Delayed Fluorescence *via* Pull-push Electronic Effects in Structurally Tailored Novel AIEgens for Bio-imaging. (*Under Communication*)

2 **Barman, D**., Rajamalli, P., Bidkar, A. P., Ghosh, S. S., Zysman-Colman, E., Iyer, P. K. Highly Efficient Purely Organic Triplet Harvesting AIE-TADF Photosensitizer for Image-guided Photodynamic Therapy. (*Under Communication)*

3 **Barman, D**., Iyer, P. K. Aggregation-Induced Hot-exciton Emission *via* Suppression of Kasha's Rule in Through-space Donor-alkyl Bridge-Acceptor Molecular Rotor. *J. Phys. Chem. C, 2023, XX, XXXX (Accepted).*

4 **Barman, D**., Annadhasan, M., Rajamalli, P., Chandrasekar, R., Iyer, P. K. Through-Space Charge-Transfer Induced Color-Tunable Luminescent Co-crystals: Polymorphism, Isomerism, Thermally Activated Delayed Fluorescence and Optical Waveguides (Chem. Sci. *Under Review*).

5 **Barman, D**., Annadhasan, M., Chandrasekar, R., Iyer, P. K. Hot-excitons Harvesting *via.* Through-Space Single-Molecule White-Light Emission and Optical-waveguides. *Chem. Sci.,* ***2022,*** 13, 9004-9015. https://doi.org/10.1039/D2SC02172B

6 Meher, N., **Barman, D.** Parui, R., Iyer, P. K. Recent Development on the Fluorescence Based Detection of Volatile Organic Compounds: A Review *J. Mater. Chem. C,* **2022**, *10*, 10224-10254. https://doi.org/10.1039/D2TC00265E

7 **Barman, D**., Narang, K., Gogoi, R., Barman, D., Iyer, P. K. Exceptional Class of Thermally Activated Delayed Fluorescent Emitters Comprising Pure Blue, Near-IR, Circularly Polarized Luminescence and Multifunctional Behaviour for Highly Efficient and Stable OLEDs. *J. Mater. Chem. C*, **2022**, *10*, 8536-8583. https://doi.org/10.1039/D1TC05906H

8 **Barman, D**., Narang, K., Parui, R., Zehra, N., Khatun, N., Adil, L. R., Iyer, P. K. Review on Recent Trends and Prospects in π-Conjugated Luminescent Aggregrates for Bio-medical Applications. *Aggregate.***2022**;e172. https://doi.org/10.1002/agt2.172

9 Das, D., Gopikrishna, P., Barman, D., Yathirajula, R. B., Iyer, P. K.; Substantial Efficiency Enhancement in Solution Processed Phosphorescent Light Emitting Diode with Polymer Host: Efficient Optimization of Charge Balance and Processing Conditions. *J. Phys. Chem. Solids,* **2022**, *163*, 110577. https://doi.org/10.1016/j.jpcs.2022.110577

10 **Barman, D**., Gopikrishna, P., Iyer, P. K. Stimuli-Responsive Trimorphs and Charge-Transfer Complexes of Twisted Molecular Donor. *Langmuir,* **2021**, *37*, 8024−8036. https://doi.org/10.1021/acs.langmuir.1c01172

11 Meher, N., Bidkar, A. P., **Barman, D.,** Ghosh, S. S., Iyer, P. K. A Conformational Tweak for Enhanced Cellular Internalization, Photobleaching Resistance and Prolonged Imaging Efficacy. *Chem. Commun.,* **2020**, *56*, 14861-14864. https://doi.org/10.1039/D0CC05557C

12 **Barman, D**., Gogoi, R., Narang, K., Iyer, P. K. Recent Developments on Multi-Functional Metal-Free Mechanochromic Luminescence and Thermally Activated Delayed Fluorescence Organic Materials. *Front. Chem.* **2020**, *8*, 483. https://doi.org/10.3389/fchem.2020.00483

13 Das, D., Gopikrishna, P., **Barman, D**., Yathirajula, R. B., Iyer, P. K. White light emitting diode based on purely organic fluorescent to modern thermally activated delayed fluorescence (TADF) and perovskite materials. *Nano Convergence*, **2019**, *6*, 31. https://doi.org/10.1186/s40580-019-0201-6

PATENT

1. **Barman, D.,** Iyer, P. K.; Highly Fluorescence 'J-shaped' Multifunctional Thermally Activated Delayed Fluorescence (TADF) and Stimuli Responsive Organic Luminogens (SROL) for Lighting Applications and a method for attaining said TADF from an Inaccessible Near-IR Room Temperature Phosphorescence (NIR-RTP). Ref. No. 201931020985, Appl. No. TEMP/E-1/22090/2019-KOL

2. **Barman, D.,** Iyer, P. K.; Singlet-triplet harvesting color-tunable bright luminescent organic cocrystals (*Applied*)

3. **Barman, D**., Iyer, P. K.; Rational Strategy for hot-exciton harvesting *via* through-space single-molecule white-light emission by Suppression of Kasha's Rule (*Applied*)

BOOK CHAPTER

1. **Barman, D.,** Parui, R., Narang, K., Gogoi, R., Iyer, P. K. Chapter Four: Aggregation Induced Emission materials with advanced photophysical properties for bio-medical applications, *Progress in Molecular Biology and Translational Science, Academic Press,* Elsevier, 2021, 185, 75-112. https://doi.org/10.1016/bs.pmbts.2021.07.001

FELLOWSHIPS AND AWARDS

- Received Merit-cum Means Fellowship (**MCM**) from Indian Institute of Technology Guwahati (IITG), from July 2014 to July 2016.
- Qualified national level Graduate Aptitude Test (**GATE**) 2016.
- Qualified national level Council of Scientific and Industrial Research Lectureship National Eligibility Test (**CSIR-LS-NET**) June 2018.
- Received Junior Research Fellowship (**JRF**) from Indian Institute of Technology Guwahati (IITG) through the Ministry of Human Resource Development (**MHRD**), Government of India (GOI), from July 2016 to July 2018.
- Received Best Poster Presentation Award on **Reflux a symposium**-2018.
- Received **Best Flash Talk** Presentation Award on 5th International Conference on Advanced Nanomaterials and Nanotechnology (**ICANN-2021**).
- Received **Best Poster** Presentation Award on 20th National Conference on Surfactants, Emulsions and Biocolloids **NATCOSEB-XX, 2021**.
- Received **Best Poster** Presentation Award on International Conference on Advanced Materials and Mechanical Characterization (**ICAMMC 2021**).
- Received **Best Oral** Presentation Award on Research & Industrial Conclave (**RIC-2022**)
- Received Best Poster Presentation Award on International Conference on Materials - Properties, Measurements and Applications (**ICMPMA 2022**)

CONFERENCES/SYMPOSIUMS/WORKSHOPS

1. **Presented Poster** International Conference on Materials - Properties, Measurements and Applications (ICMPMA 2022) held by Fatima Mata National College, Kerala, India on 9-13 May 2022.
2. **Presented Poster**: 28th CRSI National Symposium in Chemistry, held by Indian Institute of Technology Guwahati on March 25-27, 2022.
3. **Presented Oral Talk**: Research & Industrial Conclave (RIC-2022), an amalgamation of Academia, Industry & Startups held at IIT Guwahati, March 20th-23rd January, 2022.

4. **Presented Oral Talk**: 16th DAE-BRNS Biennial, Trombay Symposium on Radiation & Photochemistry (TSRP-2022), held on January 12-15, 2022, at Online Platform (DAE Convention Centre, Anushaktinagar, Mumbai).
5. **Presented Flash Talk**: 5th International Conference on Advanced Nanomaterials and Nanotechnology (ICANN-2021) held at IIT Guwahati, Guwahati, during Dec 15th -17st, 2021.
6. **Presented Poster**: 20th National Conference on Surfactants, Emulsions and Biocolloids NATCOSEB-XX. Organized by Indian Institute of Technology Guwahati in association with Indian Society for Surface Science and Technology, Kolkata on 9th – 11th December 2021**.**
7. **Presented Poster**: International Conference on Advanced Materials and Mechanical Characterization (ICAMMC 2021) organized by Department of Physics and Nanotechnology & Department of Mechanical Engineering, SRM Institute of Science and Technology, Kattankulathur on 2nd - 4th December 2021.
8. **Presented Oral Talk**: FCS2021 jointly organized by IISER Thiruvanthapuram and RGCB Thiruvanthapuram, held on Online November 29th – 4th December, 2021.
9. **Presented Poster**: 11th Asian Photochemistry Conference (APC 2021) held on Online during October 31 - November 4 2021, in Seoul South Korea.
10. **Presented Poster**: 5th International Conference on Advanced Nanomaterials and Nanotechnology (ICANN-2019) held at IIT Guwahati, Guwahati, during Dec 18th -21st, 2019.
11. **Presented Poster**: International Conference on Frontiers in Chemical Sciences (FICS - 2018) from 6-8 December, 2018.
12. **Attended Workshop:** National Centre for Flexible Electronics (NCFlexE) Samtel Centre for Display Technologies (SCDT) a Short Course on Flexible Electronics held at IIT Kanpur, on 2nd - 7th July, 2018.
13. **Presented Poster**: Reflux a symposium held at IIT Guwahati, 16th-18th March, 2018. **Presented Poster**: Research Conclave, an amalgamation of Academia, Industry & Startups held at IIT Guwahati, March 8th-11th, 2018.
14. **Presented Poster**: Chemconvene, Symposium, held at IIT Guwahati, on 26th July, 2017.
15. **Attended Workshop:** National Workshop on MEMS/NEMS and Theranostic Devices (NWNTD), from March 21st- 23rd, 2017, at IIT Guwahati, Assam, India.
16. **Attended Workshop:** "Day ACS ON CAMPUS" agenda held at IIT Guwahati, Guwahati, on Jan, 2017.

-----End-----